

The international journal of science / 19 August 2021

nature



OVARIAN AGEING

The genetics driving reproductive lifespan

Coronavirus
Has COVID helped us prepare for the next pandemic?

Negative effect
Ways to incentivize the removal of carbon dioxide

Social success
How hashtags helped bring Black researchers together

Nature.2021.08.21

[Sat, 21 Aug 2021]

- [This Week](#)
- [News in Focus](#)
- [Books & Arts](#)
- [Opinion](#)
- [Work](#)
- [Research](#)
- [Amendments & Corrections](#)

| [Next section](#) | [Main menu](#) |

Donation

| [Next section](#) | [Main menu](#) |

This Week

- **[The WHO is right to call a temporary halt to COVID vaccine boosters](#)** [17 August 2021]
Editorial • Richer countries should focus on ramping up vaccine supply to the billions who are still waiting for their first dose.
- **[Great Barrier Reef: accept ‘in danger’ status, there’s more to gain than lose](#)** [18 August 2021]
World View • The Australian government must embrace UNESCO’s assessment to marshal the resources needed to protect the unique coral ecosystem.
- **[An ink ‘writes’ tiny generators that are powered by heat](#)** [11 August 2021]
Research Highlight • Printing technique could help to produce minute power sources for use in lightweight sensors and wearable devices.
- **[Clouds plus trees equals cooler climes at mid-latitudes](#)** [12 August 2021]
Research Highlight • Planting forests outside the tropics can sequester carbon and counteract global warming.
- **[The giant centipede that devours fluffy baby seabirds](#)** [13 August 2021]
Research Highlight • The voracious Phillip Island centipede eats enough chicks and other large prey to play an important part in its home ecosystem.
- **[Found: the world’s oldest known mint and its jumbo product](#)** [09 August 2021]
Research Highlight • A mint discovered in China was churning out 14-centimetre-long ‘spade coins’ more than 2,500 years ago.
- **[How to weigh a black hole: monitor its fireworks](#)** [12 August 2021]
Research Highlight • The dusty disk around a black hole flashes on a characteristic schedule, offering a clue to its mass.
- **[Poo from young mice improves their elders’ memories](#)** [12 August 2021]
Research Highlight • Substances made by gut microbes could account for a cognitive boost from faecal transplants.

- **From drab to dazzling: seaweed yields sparkling coloured inks** [13 August 2021]

Research Highlight • Cheap, eco-friendly materials can be formed into vibrant 2D or 3D shapes.

| [Next section](#) | [Main menu](#) | [Previous section](#) |

- EDITORIAL
- 17 August 2021

The WHO is right to call a temporary halt to COVID vaccine boosters

Richer countries should focus on ramping up vaccine supply to the billions who are still waiting for their first dose.





•

[Download PDF](#)



Israel has begun rolling out a third dose of the Pfizer mRNA vaccine, even though the case for boosters has not yet been proved. Credit: Nir Alon/Alamy

The World Health Organization (WHO) has called for a moratorium on COVID-19 boosters until the end of next month, with the aim of ensuring that at least 10% of people in all countries are vaccinated before extra doses are handed out. It makes a compelling argument. As *Nature* went to press, 58% of people in high-income countries had received at least one vaccine dose; in low-income countries this number stood at just 1.3%.

Moreover, the case for boosters has not yet been proved. Most COVID-19 vaccines currently in use remain extremely effective months after administration, particularly against severe disease and death. In a period of vaccine scarcity, the choice to dole out boosters must be guided by evidence of benefit, and consideration given to the cost of delaying the delivery of vaccines to vulnerable people and health-care workers in other countries. So far, there is [little evidence that boosters are needed](#) to protect the fully vaccinated.

Sadly, [many countries are moving ahead with boosters regardless](#). Israel has begun giving third doses of Pfizer's mRNA vaccine to people over 50 and other vulnerable groups. France, Germany, the United Kingdom and the United States are all planning to provide boosters to certain groups. In the United States, more than one million people have managed to get an unauthorized third dose.



[COVID vaccine boosters: the most important questions](#)

In some cases, boosters might be warranted — if the evidence suggests that the usual doses aren't effective, for example. One study of people who have had an organ transplant, meaning they need to take drugs that suppress the immune system, found that almost half had no antibody response after two doses of mRNA vaccines ([B. J. Boyarsky *et al. JAMA* 325, 2204–2206; 2021](#)).

Boosters might also be needed if vaccines made from inactivated viral particles, namely those from the Chinese manufacturers Sinopharm and Sinovac, are found to provide inadequate protection against severe disease or death from variants such as Delta. A surge of COVID-19 in Indonesia that has affected many health-care workers fully vaccinated with Sinovac, and surges in other countries reliant on Sinovac's shot, have led officials to consider boosters using other vaccines — even though vaccines are far from the only factor implicated in rising disease rates.

All other vaccines currently in use seem to be more than 90% effective against hospitalization and death from COVID-19. Although some studies have found that vaccine-induced antibody levels wane after several months, this is typical for all vaccines and not necessarily indicative of waning protection against the coronavirus.



[COVID vaccines to reach poorest countries in 2023 — despite recent pledges](#)

Scientists don't yet know how much extra protection a booster shot might confer against disease, or for how long any boost will last. However, on average, an unvaccinated person exposed to the coronavirus is much more likely both to be infected and to spread that infection than is a vaccinated individual. Moreover, they are more than 90% more likely to be hospitalized or die from the disease. Choosing an unknown but potentially incremental benefit for a person in a wealthy country over a massive, life-saving one for a person elsewhere in the world is a losing strategy, because new variants will inevitably arise in places where the spread of COVID-19 continues unabated.

Instead of offering boosters to large swathes of people, wealthier nations need to be more active in getting the world vaccinated — and there are several ways to do this.

First, rich countries must come through on promises to support COVAX, the international alliance supplying vaccines to low-income countries. It remains

short on its modest goal to vaccinate the most vulnerable 20% of populations by the end of 2021.

However, global vaccine availability is limited — and will only become more so if boosters become commonplace — so vaccine donations alone won't suffice. Leaders of countries whose companies have benefited from public funds — such as BioNTech in Germany and Moderna in the United States — should use their clout to expand manufacturing. Many more wealthy nations need to support a proposal led by India and South Africa — that has the United States' backing — for a temporary waiver on vaccine patents.



[COVID boosters for wealthy nations spark outrage](#)

These deals must be matched by funds to get new manufacturers up and running quickly and safely, along with financing for countries to allow them to purchase vaccine doses and distribute them to their populations. Typically, this process occurs over years or even decades, but time is crucial in a pandemic — and needs are vast. Patent waivers won't solve the problem alone; neither will vaccine donations or a temporary moratorium on boosters. The world must push on all fronts simultaneously.

Allowing COVID-19 to spread in low and lower-middle-income countries — where, overall, fewer than 15% of people are vaccinated — could result

in millions of people dying or facing long-term complications from severe COVID-19. Economies will erode as businesses and schools remain closed. And surging COVID-19 levels will foster the evolution of new variants that could be yet more transmissible than Delta, deadlier than existing strains or able to evade the immune response. Last month, the International Monetary Fund warned that highly infectious variants could derail economic recovery around the world, and wipe US\$4.5 trillion from global gross domestic product by 2025.

If vaccines were not scarce, boosters would be less controversial. But to focus on boosters when more than half the world lacks vaccine doses is short-sighted and will only keep the pandemic burning longer. For wealthy countries, this strategy means they will be indefinitely chasing their tails in terms of new variants. And for the rest of the world, it means prolonging unnecessary suffering.

Nature **596**, 317 (2021)

doi: <https://doi.org/10.1038/d41586-021-02219-w>

Related Articles

-  [**COVID boosters for wealthy nations spark outrage**](#)
-  [**COVID vaccine boosters: the most important questions**](#)
-  [**COVID vaccines to reach poorest countries in 2023 — despite recent pledges**](#)



- [A patent waiver on COVID vaccines is right and fair](#)

Subjects

- [SARS-CoV-2](#)
- [Public health](#)
- [Vaccines](#)
- [Intellectual-property rights](#)
- [Policy](#)

nature careers

[Jobs](#) >

- [Group Leader \(f/m/d\) CRISPR/RNAi Technology for Target Identification \(Screening\) and Validation](#)

Evotec AG

Hamburg, Germany

- [Tier I Canada Research Chair in Infectious Disease & Immunity](#)

The University of British Columbia (UBC)

Vancouver, Canada

- [Clinical Research Nurse/Project Manager](#)

Oklahoma Medical Research Foundation (OMRF)

Oklahoma City, United States

- [Research Associate - Immunologist](#)

The University of British Columbia (UBC)
Vancouver, Canada

Nature Briefing

An essential round-up of science news, opinion and analysis, delivered to your inbox every weekday.

[Download PDF](#)

Related Articles



- [COVID boosters for wealthy nations spark outrage](#)



- [COVID vaccine boosters: the most important questions](#)



- [COVID vaccines to reach poorest countries in 2023 — despite recent pledges](#)



- [A patent waiver on COVID vaccines is right and fair](#)

Subjects

- [SARS-CoV-2](#)
 - [Public health](#)
 - [Vaccines](#)
 - [Intellectual-property rights](#)
 - [Policy](#)
-

This article was downloaded by **calibre** from <https://www.nature.com/articles/d41586-021-02219-w>

| [Section menu](#) | [Main menu](#) |

- WORLD VIEW
- 18 August 2021

Great Barrier Reef: accept ‘in danger’ status, there’s more to gain than lose



The Australian government must embrace UNESCO’s assessment to marshal the resources needed to protect the unique coral ecosystem.

- [Tiffany H. Morrison](#) 0

1. [Tiffany H. Morrison](#)

1. Tiffany H. Morrison is a political geographer specializing in marine interventions at James Cook University in Townsville, Australia.

[View author publications](#)

You can also search for this author in [PubMed](#) [Google Scholar](#)

-



•

[Download PDF](#)

No one denies the cascade of climate-induced coral bleaching that devastated huge portions of the Great Barrier Reef in 2016, nor the subsequent bleaching. No one questions the Queensland government's 2019 report (see go.nature.com/3ckg) that the reef's condition near the shore is poor.

Yet last month, the World Heritage Committee of the United Nations organization UNESCO caved to lobbying from the Australian government — pressured by fossil-fuel, agricultural and mining interests — and kept the

Great Barrier Reef off its list of ecosystems ‘in danger’. In my view, this decision is wrong, factually and strategically. It leaves both UNESCO and Australia weaker against the climate crisis.

I study the governance of approximately 250 ecosystems with World Heritage status because of their outstanding value to humanity — including attempts to curtail runaway industrial development of Vietnam’s Ha Long Bay and overzealous urbanization along Florida’s Everglades wetlands.

There are benefits to an in-danger listing: the Belize Barrier Reef Reserve System was placed on the list in 2009. The World Heritage Fund then provided technical and financial assistance for its restoration. By 2018, mangrove coverage was restored nearly to 1996 levels, with clearing in protected areas almost entirely curtailed. The whole maritime zone was under a moratorium on oil and gas production. Restoration work is ongoing, but the Belize reef is no longer on the list.



Save reefs to rescue all ecosystems

This July, UNESCO proposed to list the Great Barrier Reef as in danger owing to severe coral bleaching, poor water quality and inaction on climate change.

In arguing against the listing, the Australian government did not directly deny the reef's parlous state, but did play down its condition. The government also argued that the listing would decrease tourism revenues, that Australia had too little time to respond and should not be held responsible for global change, and that UNESCO should not supersede national sovereignty on climate-change policy.

Australian environment minister Sussan Ley lobbied committee members from more than a dozen countries to override UNESCO's recommendation. Australia avoided an in-danger listing in 2015 using similar tactics and by touting a sustainability plan. The following year saw the worst coral bleaching in the world's history.

But changes are in the wind. After back-to-back coral bleaching in 2016–17 and the tragic 2020 bush fires, more Australian voters, industries and even conservative politicians are calling for strong efforts against climate change.

Accepting an in-danger listing for the reef could tip the balance past gridlock. More than 70% of Australians think that formally acknowledging the reef's endangered state would spur action. In 1993, former US president Bill Clinton's administration requested that UNESCO certify Florida's Everglades as in danger. This helped to bring industry opponents on board to better manage coastal development. Had the Great Barrier Reef been listed as in danger in 2015, fossil-fuel developments in the catchment areas draining into the reef would have struggled to get approval.

Australia's most conservative politicians will argue that avoiding an in-danger listing in 2022 is necessary to boost economic development. But this will embarrass Australia later. As more marine heating occurs globally, Australia will struggle to defend its inaction on climate to the UN climate-change conference in November and to the World Heritage Committee next year. Even the Queensland Tourism Industry Council has said keeping the reef's status under the spotlight is a "call to the world to do more on climate change".



[Fevers are plaguing the oceans — and climate change is making them worse](#)

And undercutting the listing undermines the purpose of the World Heritage Committee. Since 1972, 41 ecosystems have been considered for the in-danger list — 27 of them more than once — but not officially inscribed, even though UNESCO and its advisory body had assessed these ecosystems as threatened, or more threatened than those already listed. The number of sites on the list has declined by almost one-third since 2001, although threats continue to grow and there are more ecosystems on the overall World Heritage List.

However, destabilizing strategies are mainly due to a small group of nations — including countries in the Organisation for Economic Co-operation and Development, such as Australia and Spain. World Heritage status and in-danger listings often work as intended: the managers of 73% of sites do comply with their responsibilities.

Concerned observers are helping the World Heritage Committee to protect itself from political manipulation. In February 2020, a consortium of 76 organizations and individuals petitioned UNESCO to consider climate change in its World Heritage decisions. A nascent international network known as World Heritage Watch hopes to provide more oversight and monitoring of self-interested states. Ecologists and non-profit organizations

are using remote sensing and citizen science to track and expose degradation of protected areas (see go.nature.com/2xn1) and hold governments accountable.

UNESCO and its World Heritage Committee grasp the stakes. A new draft policy clearly states that climate-related degradation of a World Heritage Area can be used as the basis for in-danger listing; it will probably be ratified later this year at the UNESCO General Assembly. This policy will shine a harsh light on the intensifying geopolitics of climate change. Advanced economies, such as Australia, with high per-capita emissions but limited climate action, will need to find alternative ways to protect resources and jobs.

Nature **596**, 319 (2021)

doi: <https://doi.org/10.1038/d41586-021-02220-3>

Related Articles



- [Fevers are plaguing the oceans — and climate change is making them worse](#)



- [Save reefs to rescue all ecosystems](#)

Subjects

- [Climate change](#)
- [Conservation biology](#)
- [Government](#)

Jobs >

- [**Group Leader \(f/m/d\) CRISPR/RNAi Technology for Target Identification \(Screening\) and Validation**](#)

Evotec AG

Hamburg, Germany

- [**Tier I Canada Research Chair in Infectious Disease & Immunity**](#)

The University of British Columbia (UBC)

Vancouver, Canada

- [**Clinical Research Nurse/Project Manager**](#)

Oklahoma Medical Research Foundation (OMRF)

Oklahoma City, United States

- [**Research Associate - Immunologist**](#)

The University of British Columbia (UBC)

Vancouver, Canada

Nature Briefing

An essential round-up of science news, opinion and analysis, delivered to your inbox every weekday.

[Download PDF](#)

Related Articles



- [Fevers are plaguing the oceans — and climate change is making them worse](#)

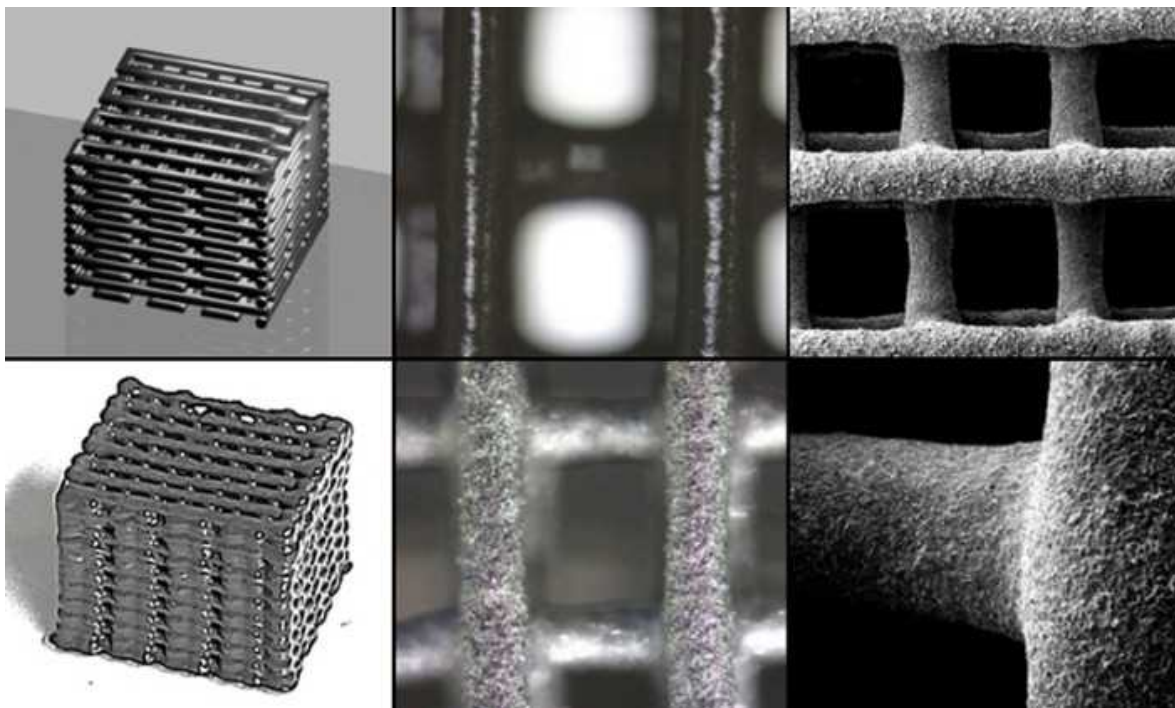


- [Save reefs to rescue all ecosystems](#)

Subjects

- [Climate change](#)
- [Conservation biology](#)
- [Government](#)

This article was downloaded by **calibre** from <https://www.nature.com/articles/d41586-021-02220-3>



A latticework box (model, top left; photograph, bottom left) built by layering 3D-printed ink filaments (middle and right columns). The ink's properties make it suitable for turning a heat flow into an electric current.
Credit: Fredrick Kim *et al./Nat. Electron.*

Energy

11 August 2021

An ink ‘writes’ tiny generators that are powered by heat

Printing technique could help to produce minute power sources for use in lightweight sensors and wearable devices.





•

With the help of a new 3D-printing ink, scientists have crafted a miniature generator that efficiently transforms the flow of heat into an electric current.

Thermoelectric materials generate electricity from the movement of a modest amount of heat from a warmer place to a cooler one. But scientists have struggled to make thermoelectric components small enough to be useful in items such as wireless sensors.

Han Gi Chae and Jae Sung Son at the Ulsan National Institute of Science and Technology in South Korea and their colleagues sought to make small, 3D-printed components by tinkering with the ink recipe. By optimizing the ink formula for microscale fabrication, the researchers were able to print

slender, sturdy columns 1.4 millimetres tall and less than 0.5 millimetres in diameter onto a silicon chip. When the team heated one side of these columns while cooling the other, the micro-generator produced enough electricity to run a wireless sensor network.

The authors hope that this technique will make it easier to incorporate thermoelectric generators into wearable electronics, perhaps allowing the generators to replace conventional batteries.

Nature Electron. (2021)

- [Energy](#)

This article was downloaded by **calibre** from <https://www.nature.com/articles/d41586-021-02182-6>

| [Section menu](#) | [Main menu](#) |



Clouds above temperate forests can help to reduce local temperatures.
Credit: Johner Images/Alamy

Climate sciences

12 August 2021

Clouds plus trees equals cooler climates at mid-latitudes

Planting forests outside the tropics can sequester carbon and counteract global warming.





•

Planting trees in the zone between the tropics and the poles creates more clouds, which help to cool the planet.

Forests pull heat-trapping carbon dioxide out of the atmosphere. In tropical regions, the trees are so dense that the resulting cooling outweighs warming from the heat absorbed by their dark foliage.

But forests at higher latitudes, such as those in parts of Europe and North America, are sparser than forests in the tropics. Scientists have debated whether mid-latitude forests' heat absorption outweighs the cooling from their CO₂ absorption.

Amilcare Porporato at Princeton University in New Jersey and his colleagues studied satellite data on global land cover and modelled cloud formation over various types of vegetation. They found that at latitudes between 30 and 45 degrees, clouds are more numerous, and form earlier in the day, above forests than above other types of vegetation. The extra clouds reflect additional light and mean that the forests have an overall cooling effect.

Efforts to plant new forests in these regions, or replant those that have been cut down, could be useful in battling climate change.

[Proc. Natl Acad. Sci. USA \(2021\)](#)

- [Climate sciences](#)

This article was downloaded by **calibre** from <https://www.nature.com/articles/d41586-021-02185-3>

| [Section menu](#) | [Main menu](#) |



Visual effects make the adult black-winged petrel look smaller than the Phillip Island centipede — but the latter is still a good size, at an average length of 19 centimetres. Credit: Luke Halpin ([CC BY 4.0](#))

Animal behaviour

13 August 2021

The giant centipede that devours fluffy baby seabirds

The voracious Phillip Island centipede eats enough chicks and other large prey to play an important part in its home ecosystem.





•

Phillip Island centipedes can reach nearly 25 centimetres long, and have an appetite to match their size: those living on their namesake island together kill and eat as many as 3,700 seabird chicks each year.

The centipedes (*Cormocephalus coynei*), which immobilize their prey with a potent venom, live only on Phillip and Nepean islands, some 1,400 kilometres east of Australia. Luke Halpin at Monash University in Clayton, Australia, and his colleagues studied the feeding habits of these centipedes on Phillip Island and monitored the chicks of the black-winged petrel (*Pterodroma nigripennis*), which nests there.

In typical island ecosystems, seabirds sit near the top of the food chain. But the researchers captured video of centipedes attacking and feeding on petrel chicks. The team calculated the number of chicks killed by centipedes in part by analysing tissue samples from centipedes and their prey.

By preying on animals such as seabirds and by scavenging fish, the centipedes trap marine nutrients and distribute them across the island, giving the creatures a crucial part in the ecosystem, the authors write.

[Am. Nat. \(2021\)](#)

- [Animal behaviour](#)

This article was downloaded by **calibre** from <https://www.nature.com/articles/d41586-021-02183-5>

| [Section menu](#) | [Main menu](#) |



Fragmented ‘spade coins’ found at an ancient mint are the earliest known metal currency in China and possibly the world. Credit: Hao Zhao

Archaeology

09 August 2021

Found: the world's oldest known mint and its jumbo product

A mint discovered in China was churning out 14-centimetre-long ‘spade coins’ more than 2,500 years ago.





•

The world's oldest known facility to mass-produce coins started operations some 2,600 years ago in what is now China's Henan province.

Hao Zhao at Zhengzhou University in China and his colleagues discovered the remains of the coin mint at a bronze foundry that was built around 780 bc. At first, it produced mainly weapons and objects used in rituals. But radiocarbon dating of charred millet seeds in one of the pits used for production waste shows that minting began between 640 and 550 bc — the earliest date that scientists have confirmed for an active mint.

The ruins yielded two fragments of finished spade coins — an early form of money, shaped like the agricultural tool, that circulated in China from the

seventh to the third century bc. One of the fragments was so well preserved that the researchers could reconstruct the shape of the intact coin, which probably measured about 14 centimetres in length.

The researchers also found an outer mould and several clay cores for casting spade coins. Some of the clay cores were unused, which suggests that the entire minting process, from making moulds to casting coins, took place on site.

[Antiquity \(2021\)](#)

- [Archaeology](#)

This article was downloaded by **calibre** from <https://www.nature.com/articles/d41586-021-02181-7>

| [Section menu](#) | [Main menu](#) |



The flickering light from matter spiralling into a supermassive black hole (artist's impression) is correlated with the black hole's mass. Credit: Mark A. Garlick/Simons Foundation

Astronomy and astrophysics

12 August 2021

How to weigh a black hole: monitor its fireworks

The dusty disk around a black hole flashes on a characteristic schedule, offering a clue to its mass.





•

Astrophysicists might have found a way to estimate the masses of supermassive black holes by observing their feeding frenzies.

The centres of most galaxies harbour supermassive black holes, which have masses up to several billion times that of the Sun. When actively feasting on matter, these black holes tend to have ‘an accretion disk’ that orbits them and gradually falls in, heating up and emitting light in the process. Each accretion disk’s brightness varies on a characteristic timescale, typically every several hundred days.

Yue Shen at the University of Illinois at Urbana–Champaign and his co-authors selected 67 active supermassive black holes for which masses have

been estimated by other means — and whose brightness varies on a well-measured timescale. They then found a correlation between those two variables: the more massive the black hole, the longer the timescale.

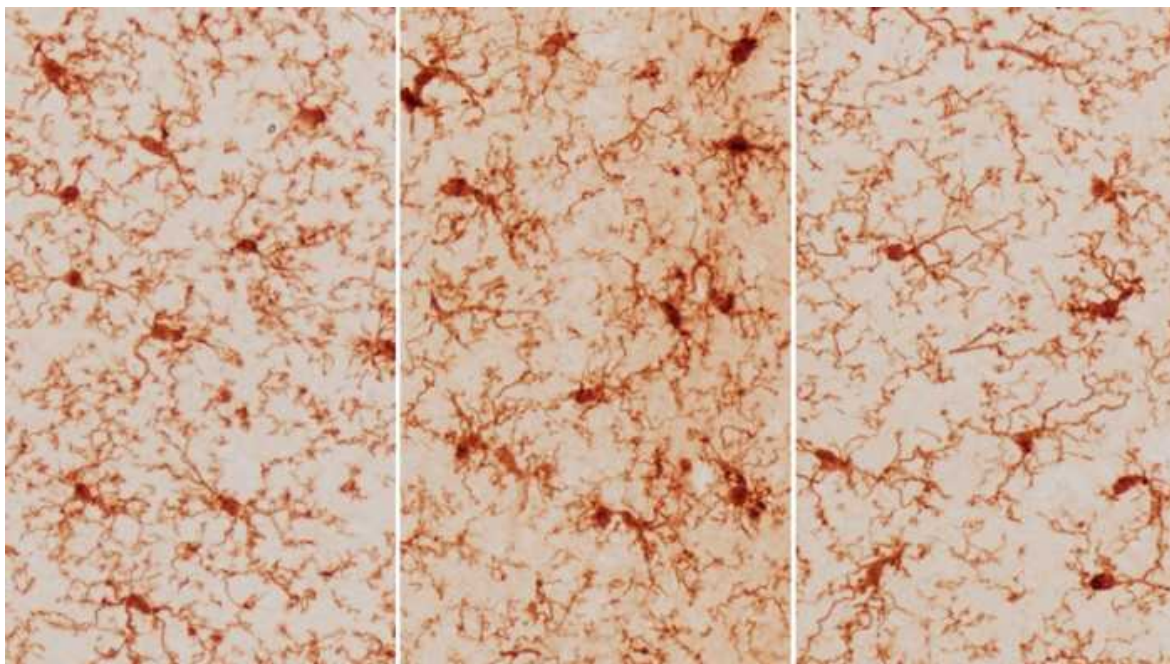
This correlation can be used to derive a black hole's mass from its characteristic flickering timescale. The authors say that a similar correlation exists in white-dwarf stars.

[Science \(2021\)](#)

- [Astronomy and astrophysics](#)

This article was downloaded by **calibre** from <https://www.nature.com/articles/d41586-021-02202-5>

| [Section menu](#) | [Main menu](#) |



Brain cells from a young mouse (left) look similar to those of an older mouse that received a faecal transplant from a younger one (right) — but not to cells of an older mouse that received faeces from an elderly one (middle).
Credit: M. Boehme *et al./Nature Aging*

Ageing

12 August 2021

Poo from young mice improves their elders' memories

Substances made by gut microbes could account for a cognitive boost from faecal transplants.





•

Poo transplants from young mice can enhance cognitive function in older animals.

John Cryan at University College Cork in Ireland and his colleagues collected faecal samples from young mice and transplanted them into the guts of elderly mice. They then put the old mice through a series of cognitive tests designed to measure memory, anxiety and learning capacity.

Old mice that received faecal transplants from youthful donors did better on these cognitive tests than did counterparts that got transplants from other old mice. When the researchers looked at the hippocampus — the brain region that regulates learning and memory — they found gene activity patterns and

metabolic changes that have been previously linked with improved cognitive function and immune function in the brain.

The researchers suspect that metabolic activity in the ‘young’ gut bacteria produces molecules that cross the blood–brain barrier and rejuvenate the ageing brain.

[Nature Aging \(2021\)](#)

- [Ageing](#)
-

This article was downloaded by **calibre** from <https://www.nature.com/articles/d41586-021-02184-4>

| [Section menu](#) | [Main menu](#) |



Seaweed-based inks coloured with mica, a glittery mineral that occurs in many shades. Credit: Andrea Starr/Pacific Northwest National Laboratory

Materials science

13 August 2021

From drab to dazzling: seaweed yields sparkling coloured inks

Cheap, eco-friendly materials can be formed into vibrant 2D or 3D shapes.





•

Shimmery, biodegradable inks in a rainbow of hues can be squeezed from a syringe to form multicoloured sculptures — without the heating usually required for 3D printing.

Three-dimensional printing techniques have opened a world of opportunities for artistic expression, but most such methods use plastic ‘inks’ that can soften when heated during printing. Anne Arnold and her colleagues at the Pacific Northwest National Laboratory in Richland, Washington, refined a heat-free alternative using low-cost polymers purified from brown seaweed.

The team dissolved the algal polymers in water to form viscous liquids, which are then combined with a solution of calcium chloride. The positively

charged calcium ions join together the negatively charged portions of various polymer strands, linking the polymers and turning the liquid inks into pliable gels that hold their shapes.

Pigments made of the mineral mica conferred lustrous colours to the colourless inks. Using a handheld syringe, the researchers ‘printed’ a 2D figure of a firefly and a 3D model of a brain.

A final application of calcium chloride solution maximized a printed piece’s longevity. But over time, the alga-based polymers will biodegrade, preventing discarded art from accumulating.

[ACS Omega \(2021\)](#)

- [Materials science](#)

This article was downloaded by **calibre** from <https://www.nature.com/articles/d41586-021-02186-2>

| [Section menu](#) | [Main menu](#) |

News in Focus

- **[Mars rover mishap, Beta variant's toll and UK open access](#)** [18 August 2021]
News Round-Up • The latest science news, in brief.
- **[Delta threatens rural regions that dodged earlier COVID waves](#)** [06 August 2021]
News • Data on the variant's spread in India make researchers fearful for areas in developing nations that lack health care and vaccines.
- **[How do vaccinated people spread Delta? What the science says](#)** [12 August 2021]
News • Emerging data suggest that Delta could spread more readily than other coronavirus variants among people vaccinated against COVID-19. But key questions remain.
- **[‘Tortured phrases’ give away fabricated research papers](#)** [05 August 2021]
News • Analysis reveals that strange turns of phrase may indicate foul play in science.
- **[Mammoth’s epic travels preserved in tusk](#)** [12 August 2021]
News • Chemical analysis of an ice age woolly mammoth’s tusk reveals the huge distances it travelled during its lifetime more than 17,000 years ago.
- **[Exotic four-quark particle spotted at Large Hadron Collider](#)** [10 August 2021]
News • Rare tetraquark is one of dozens of non-elementary particles discovered by the accelerator, and could help to test theories about strong nuclear force.
- **[Chelsea Clinton urges global sharing of COVID vaccine technology](#)** [09 August 2021]
News Q&A • The health-policy specialist who grew up in the White House is using her training and connections to convince world leaders to help make vaccines accessible to all nations.
- **[Has COVID taught us anything about pandemic preparedness?](#)** [13 August 2021]
News Feature • Researchers warn that plans to prevent the next global outbreak don’t consider the failures that have fuelled our current predicament.

- **Electric cars and batteries: how will the world produce enough?** [17 August 2021]

News Feature • Reducing the use of scarce metals — and recycling them — will be key to the world's transition to electric vehicles.

| [Next section](#) | [Main menu](#) | [Previous section](#) |

- NEWS ROUND-UP
- 18 August 2021

Mars rover mishap, Beta variant's toll and UK open access

The latest science news, in brief.





•

[Download PDF](#)



NASA's Perseverance rover drilled its first rock core on Mars on 6 August. The drill area appears as a small circular cone just to the right of the rover's shadow. Credit: NASA/JPL-Caltech

Why NASA's Mars Rover failed to collect its first rock core

After [drilling into its first rock](#) on Mars but failing to capture it in a storage tube on 6 August, NASA's Perseverance rover is rolling onwards. Rather than make a second attempt now at drilling in the same geologically interesting area in Mars's Jezero Crater, it will instead drill into different terrain next month, in the hope that those rocks will be more amenable to coring.

After a few days assessing what went wrong during the first attempt, NASA announced that the rover had [pulverized the sampled rock, turning it into](#)

powder and small fragments. They fell to the crater floor rather than sliding into the tube, as an intact core would have done.

Perseverance is attempting to become the first mission to drill and collect a suite of rock cores from the Martian surface. It is planned that other spacecraft will eventually bring the samples back to Earth, where scientists can study them. “This is just another reminder that there are still a lot of unknowns about Mars,” says Meenakshi Wadhwa, a planetary scientist at Arizona State University in Tempe who is NASA’s principal scientist for the sample-retrieval effort. “This planet still has the capacity to surprise us when we least expect it.”

Researchers were particularly excited about the rover’s first drilling attempt, which targeted one of the flat rocks that make up much of the floor of Jezero. Preliminary exploration of those rocks suggested that they might be volcanic in origin. Collecting a volcanic rock would allow geologists to eventually date its formation precisely, and thus pin down a chronology for much of Mars’s geological history.

But despite initial images suggesting that Perseverance had successfully drilled 7 centimetres into the surface (pictured) and extracted a slim cylinder of intact rock, NASA later discovered that the sampling tube was empty.

Rather than try again in this spot, Perseverance has already departed from the area and is heading towards a region named South Séítah, which probably contains layered sedimentary rocks that are more like the Earth rocks that engineers drilled during tests before the mission’s launch. The rover will try to drill a core there, perhaps in early September.



People in a temporary COVID-19 ward in Pretoria, South Africa, during the country's second wave. Credit: Phill Magakoe/AFP/Getty

Remember Beta? New data reveal variant's toll

People infected with the Beta coronavirus variant are more likely to die than are those infected with other variants. The Beta variant was first identified in late 2020 in South Africa.

Some evidence has suggested that severe cases of COVID-19 were more common during South Africa's Beta-driven second wave than during its first wave, caused by the ancestral version of SARS-CoV-2. To investigate this, Laith Jamal Abu-Raddad, an infectious-disease epidemiologist at Weill Cornell Medicine—Qatar in Doha, studied infected people in Qatar in early 2021 ([L. J. Abu-Raddad et al. Preprint at medRxiv https://doi.org/grcf, 2021](https://doi.org/grcf)).

During that period, two variants were circulating: Beta and Alpha, which originated in the United Kingdom in 2020. The team did not compare Beta with the Delta variant, which is now ripping across the globe.

People infected with Beta were 25% more likely than those infected with Alpha to develop severe disease, around 50% more likely to require critical care and 57% more likely to die. The findings have not yet been peer reviewed.

Abu-Raddad notes that Beta seems to be more resistant to immunity generated by vaccines and previous infection than are other variants, including Delta, and it could begin wreaking havoc again.

Major UK funder unveils strict open-access policy

From April 2022, scientists must make papers supported by Britain's national research-funding agency free to read immediately on publication, the funder UK Research and Innovation (UKRI) has announced in a keenly awaited [revision to its open-access \(OA\) policy](#).

As expected, the details closely match those laid out in Plan S, the bold pledge by many funders to publish all science outside paywalls. The new policy insists on immediate OA, where UKRI previously permitted a 6- or 12-month delay. Papers for which any author has UKRI funding must be published OA in a journal (sometimes called the gold OA route); if that is not possible, authors can post the accepted, peer-reviewed version of their manuscript online (sometimes called green OA). Articles must have liberal licences allowing anyone else to reuse and republish them. From 2024, long-form articles, such as books and monographs, must be made open within 12 months of publication.

UKRI says it will provide up to £46.7 million (US\$64 million) per year to support the implementation of the policy; some of this will go to universities, to help them to pay OA publication fees. However, it has not yet decided whether it will pay the per-paper fees charged by a particular category of 'hybrid' journal that includes *Nature* and other Nature-branded titles. This decision will be put out to consultation, the funder says.

UKRI has an annual budget of around £8 billion, and is one of the largest funders to take part in Plan S, along with the European Commission.

Nature **596**, 323 (2021)

doi: <https://doi.org/10.1038/d41586-021-02221-2>

Subjects

- [SARS-CoV-2](#)
- [Publishing](#)
- [Planetary science](#)

nature careers

[Jobs](#) >

- [Group Leader \(f/m/d\) CRISPR/RNAi Technology for Target Identification \(Screening\) and Validation](#)

Evotec AG

Hamburg, Germany

- [Tier I Canada Research Chair in Infectious Disease & Immunity](#)

The University of British Columbia (UBC)

Vancouver, Canada

- [Clinical Research Nurse/Project Manager](#)

Oklahoma Medical Research Foundation (OMRF)

Oklahoma City, United States

- [**Research Associate - Immunologist**](#)

The University of British Columbia (UBC)
Vancouver, Canada

Nature Briefing

An essential round-up of science news, opinion and analysis, delivered to your inbox every weekday.

[Download PDF](#)

Subjects

- [SARS-CoV-2](#)
- [Publishing](#)
- [Planetary science](#)

This article was downloaded by **calibre** from <https://www.nature.com/articles/d41586-021-02221-2>

| [Section menu](#) | [Main menu](#) |

- NEWS
- 06 August 2021
- Correction [13 August 2021](#)

Delta threatens rural regions that dodged earlier COVID waves

Data on the variant's spread in India make researchers fearful for areas in developing nations that lack health care and vaccines.

- [Smriti Mallapaty](#)
 1. Smriti Mallapaty
[View author publications](#)

You can also search for this author in [PubMed](#) [Google Scholar](#)





•

[Download PDF](#)



Government health workers carry a casket to a cemetery in Jakarta, Indonesia. Credit: Ed Wray/Getty

As the Delta variant of SARS-CoV-2 sweeps across Asia, researchers are increasingly concerned about COVID-19 spreading beyond urban centres to rural regions that were largely spared in earlier waves of the pandemic and have less access to testing, health care and vaccines.

“If the variants of concern, in particular Delta, reach far-flung areas, it will really challenge the health-care system,” says Cynthia Saloma, a molecular biologist at the University of the Philippines Diliman in Quezon City, who heads the Philippine Genome Center. Saloma says so far only a few cases of Delta have been sequenced in the Philippines, but the country is preparing for the worst. “The picture that is emerging in our neighbouring countries is really scary. We are all concerned.”

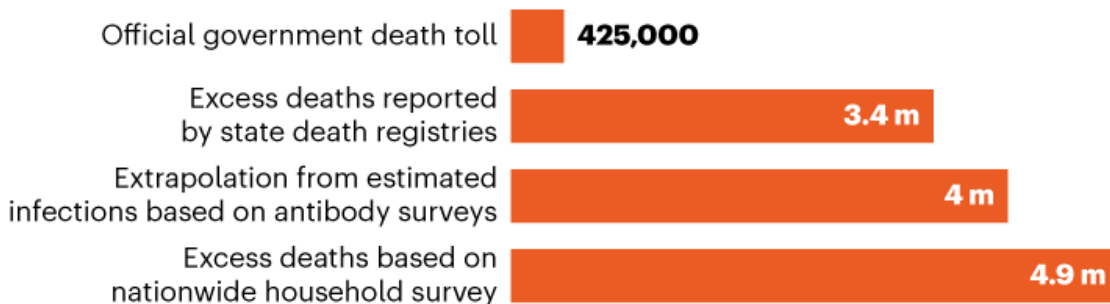
Research from India now suggests that during the nation’s brutal second wave earlier this year, the virus achieved much greater spread, beyond the urban sprawl, than during the first wave of 2020. This year’s surge was

largely driven by the Delta variant, which first came to [scientists' attention in India](#) in December.

“The variant is so much more transmissible, that health systems get overwhelmed with no time to prepare,” says Ramanan Laxminarayan, an epidemiologist at Princeton University, New Jersey, who is based in New Delhi. “The second wave has been absolutely devastating in rural India.”

COVID'S TRUE TOLL IN INDIA?

Estimates suggest that there were up to ten times more deaths in India due to COVID-19 than were officially recorded. One study, published by the Center for Global Development in Washington DC, uses three data sources to estimate a mortality figure of up to 4.9 million.



©nature

Source: Ref. 2

Rural impact in India

From Indonesia and Malaysia to Thailand and Bangladesh, countries across Asia have detected Delta in their communities, and many are experiencing their largest outbreaks yet. In Indonesia, where confirmed cases hit 50,000 per day in mid-July, daily deaths have now surpassed 1,700. But vaccination rates remain perilously low in many of these nations, leaving them highly vulnerable.

Researchers in India are only beginning to grasp the full scale of their second wave, which [hit a peak](#) of 391,000 recorded cases a day in early May

— but this data could be crucial for understanding the risk the variant poses to neighbouring nations.

In a [nationwide survey](#) of about 28,000 people (two-thirds of whom were unvaccinated and had therefore acquired immunity from infection) in June and July this year, researchers found that 68% had SARS-CoV-2 antibodies in their blood. This represented a huge increase from the 21% with antibodies, recorded in a similar survey in December 2020 to January 2021, prior to the second wave.

Although the previous survey found higher prevalence in urban areas, the latest estimates saw little difference between the numbers in urban and rural regions, which are home to 65% of India's population. This suggests that infections "have now penetrated very well in rural areas", says Manoj Murhekar, director of the country's National Institute of Epidemiology in Chennai, which co-led the June survey.

The death toll in India has been immense, and is probably much higher than official counts (see 'COVID's true toll in India?'). Studies of excess mortality suggest that up to 4.9 million people could have died in India since the pandemic began^{[1,2](#)} — much higher than 425,000, the official number of recorded deaths due to COVID-19. Half these deaths probably occurred in just three months over the second wave, say researchers.

"India has definitely had a significant problem with COVID-19 mortality reporting, which is now widely recognized, and a lot of those deaths are in rural India," says Laxminarayan.



Healthcare workers are racing to administer COVID vaccines across rural parts of India. Credit: Sumit Dayal/Bloomberg/Getty

Border regions

Researchers now fear that a similar scenario could engulf many low-income nations — in Asia and other regions, [such as Africa](#) — that also have large unvaccinated populations in rural regions with limited access to health care.

In Bangladesh, the first cases of Delta were identified in travellers from India in Dhaka and rural western districts in late April, and since then it has rapidly overtaken other variants. “It is like everything else has just disappeared,” says Senjuti Saha, a molecular geneticist at the Child Health Research Foundation in Dhaka.



India's massive COVID surge puzzles scientists

Daily case numbers in Bangladesh have now hit an average of around 14,000, with daily deaths at a high of more than 230. “The numbers are bonkers,” says Saha.

Most surprising to her has been the current outbreak’s persistence in rural regions. “This totally new population is getting affected, who have been protected for whatever reason all this time,” she says.

Previous outbreaks in Bangladesh were largely restricted to cities such as Dhaka and Chittagong, despite people frequently travelling from cities of work to their families in rural regions, says Saha. This could be due to the lower population density outside cities and the outdoor lifestyle in those places, she speculates. But in this latest surge, rural regions appear to be no barrier to Delta.

Lack of access to health care

The trend will make the pandemic much harder to control in Bangladesh, where health-care and testing facilities are concentrated in large cities, says Saha.

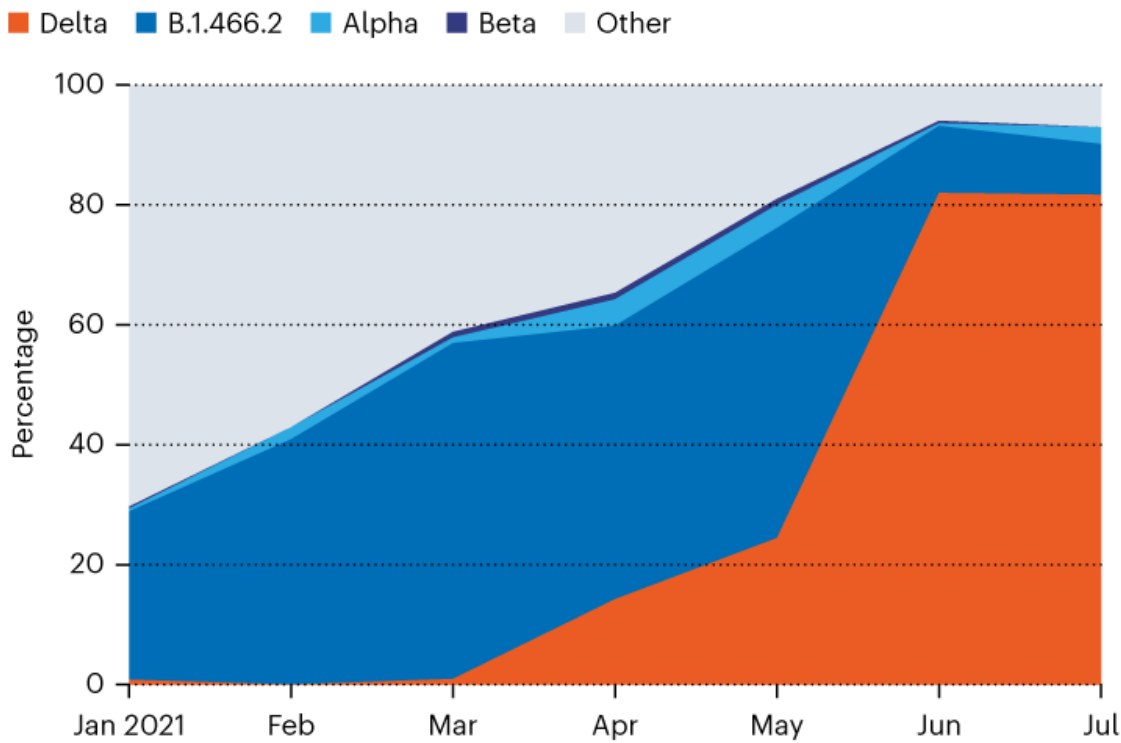
In Indonesia, which is experiencing a massive second wave, researchers are worried about the spread of COVID-19 to remote parts of the nation.

Bimandra Djaafara, an infectious-diseases epidemiologist at Imperial College London who has modelled the pandemic in Indonesia, worries about a “lack of access to healthcare facilities and oxygen, especially in rural areas and areas outside Java with poorer facilities”.

Henry Surendra, an epidemiologist at the Eijkman–Oxford Clinical Research Unit in Jakarta, is concerned about the risk of death in children in rural regions of Indonesia. In a study last year³, he found that about 10% of young children hospitalized for COVID-19 in Jakarta died of the disease. But even before the pandemic, child-mortality rates were higher in rural areas because of malnutrition and diseases such as malaria and tuberculosis. Children who already had other health problems could be at even higher risk of death from COVID-19, he says.

DELTA'S RISE IN INDONESIA

The highly transmissible Delta variant accounted for some 80% of the 1,225 samples sequenced in Indonesia since June. Alpha and Beta have also been detected, and so has B.1.466.2. That variant was first identified in Indonesia in November 2020.



©nature

Source: Safarina Malik/GISAID

Charting the spread

Delta has been detected in almost every province in Indonesia, and now makes up some 80% of all sequenced samples (see ‘Delta’s rise in Indonesia’). However, with [limited genomic sequencing](#) — especially in rural areas — tracking its spread has been challenging, says Safarina Malik, a molecular biologist at the Eijkman Institute for Molecular Biology in Jakarta.

The large majority of Indonesia’s 3,900 fully sequenced genomes — a tiny fraction of the confirmed cases — are from Jakarta and the surrounding island of Java, with only one sample each from the northeastern provinces of

Maluku Utara and Papua Barat. Sending samples to Java for sequencing can be tricky, says Malik, as airlines sometimes refuse to carry live virus.

Other nations have even more limited sequencing. In Bangladesh, for example, some 2,000 samples have been sequenced. Delta accounted for 89% of the 203 samples collected since June, says Marufur Rahman, a molecular biologist and physician at the Center for Medical Biotechnology in Dhaka. Delta has been isolated in 43 of 64 districts, but has likely extended beyond these regions as samples are not collected from all districts, says Rahman.

The Delta variant isn't the only reason for the pandemic's spread beyond urban centres, say researchers. Djaafara found that strict travel restrictions in Indonesia during Ramadan and Eid in 2020 helped to contain the spread of COVID-19 to rural parts of Java⁴. But cases were higher and movement was much less restricted during this year's Eid holidays in July, he says.

In Bangladesh, too, a huge number of people this year travelled for the Eid holidays despite restrictions, says Rahman.

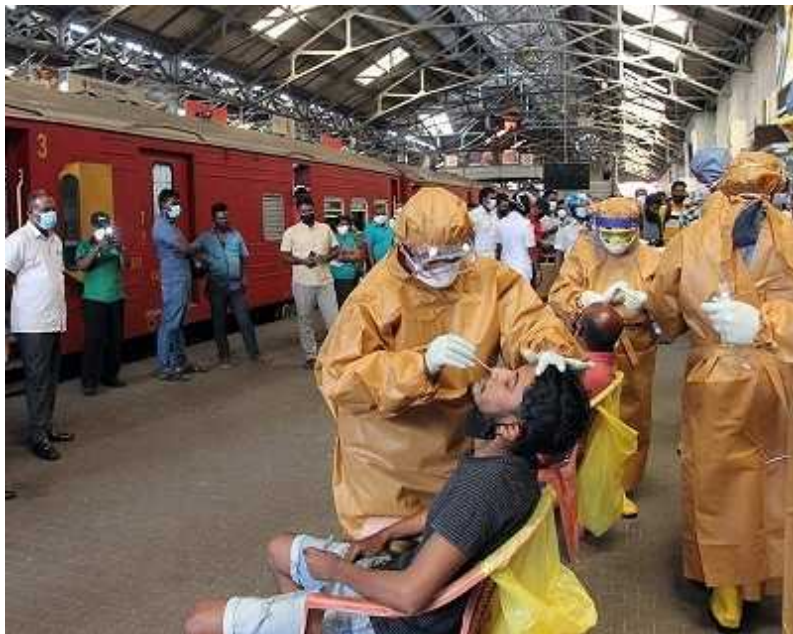


Oxygen tanks for hospitals treating COVID-19 patients are refilled at a factory in Dhaka, Bangladesh. Credit: Habibur Rahman/Eyepix/Barcroft Media/Getty

Vaccine gap

The rise of Delta in India and now nations across Asia highlights the crucial role of vaccination in stemming the pandemic, says Laxminarayan. “Delta just increases the vulnerability of countries that have poor vaccination coverage,” he says.

In Bangladesh, close to 6% of the population has received at least one dose of vaccine. In the Philippines, that figure is 11%. Indonesia has vaccinated some 17%, but most doses have gone to the more populated islands of Java and Bali, and getting doses to the nation’s thousands of smaller islands will be logistically difficult, say researchers.



[India's neighbours race to sequence genomes as COVID surges](#)

Malaysia, where there are more than 16,000 new cases of COVID-19 each day, is in a slightly better position. Yoke-Fun Chan, a virologist at the University of Malaya in Kuala Lumpur, says the country is “aggressively vaccinating”: so far, 45% of its population is partially or fully vaccinated.

“Rather than looking for the virus, now we are looking for solutions to stop the virus,” she says.

Although India serves as a warning to nations with large rural and remote populations, cities remain at risk across the developing world, too. In Indonesia, “the concern is not only that it could reach rural areas, but also what is happening in the big cities”, says Malik.

In May, Thailand detected its first cases of the Delta variant in Bangkok. Numbers have since surged to new heights, spilling to cities nationwide.

Part of the reason Thailand was able to maintain relatively low case numbers in previous waves of the pandemic is “because most of the outbreaks were not in Bangkok”, says Surakameth Mahasirimongkol, director of the genomic medicine and innovation support division at Thailand’s Ministry of Public Health. But Delta has now arrived in the heart of the capital and is proving very difficult to contain, he says.

Nature **596**, 325-326 (2021)

doi: <https://doi.org/10.1038/d41586-021-02146-w>

Updates & Corrections

- **Correction 13 August 2021:** A previous version of this story described Surakameth Mahasirimongkol as director of the departments of medical life sciences and genomic medicine at Thailand’s Ministry of Public Health. He is in fact the director of the genomic medicine and innovation support division. The story has been updated to reflect this.

References

1. 1.

Deshmukh, Y. et al. Preprint at medRxiv
<https://doi.org/10.1101/2021.07.20.21260872> (2021).

2. 2.

Anand, A., Sandefur, J. & Subramanian, A. Working Paper 589 (Center for Global Development, 2021).

3. 3.

Surendra, H. *et al. Lancet Reg. Health West Pac.* **9**, 100108 (2021).

[PubMed](#) [Article](#) [Google Scholar](#)

4. 4.

Djaafara, B. A. *et al. BMC Med.* **19**, 146 (2021).

[PubMed](#) [Article](#) [Google Scholar](#)

[Download references](#)

Related Articles



- [India's neighbours race to sequence genomes as COVID surges](#)



- [Coronavirus variants are spreading in India — what scientists know so far](#)



- [India's massive COVID surge puzzles scientists](#)

Subjects

- [Infection](#)
- [Epidemiology](#)
- [Developing world](#)
- [SARS-CoV-2](#)

nature careers

Jobs >

- [Group Leader \(f/m/d\) CRISPR/RNAi Technology for Target Identification \(Screening\) and Validation](#)

Evotec AG

Hamburg, Germany

- [Tier I Canada Research Chair in Infectious Disease & Immunity](#)

The University of British Columbia (UBC)

Vancouver, Canada

- [Clinical Research Nurse/Project Manager](#)

Oklahoma Medical Research Foundation (OMRF)

Oklahoma City, United States

- [Research Associate - Immunologist](#)

The University of British Columbia (UBC)

Vancouver, Canada

Nature Briefing

An essential round-up of science news, opinion and analysis, delivered to your inbox every weekday.

[Download PDF](#)

Related Articles



- [India's neighbours race to sequence genomes as COVID surges](#)



- [Coronavirus variants are spreading in India — what scientists know so far](#)



- [India's massive COVID surge puzzles scientists](#)

Subjects

- [Infection](#)
- [Epidemiology](#)
- [Developing world](#)
- [SARS-CoV-2](#)

This article was downloaded by **calibre** from <https://www.nature.com/articles/d41586-021-02146-w>

- NEWS
- 12 August 2021

How do vaccinated people spread Delta? What the science says

Emerging data suggest that Delta could spread more readily than other coronavirus variants among people vaccinated against COVID-19. But key questions remain.

- [Nidhi Subbaraman](#)
 1. Nidhi Subbaraman
[View author publications](#)

You can also search for this author in [PubMed](#) [Google Scholar](#)





•

[Download PDF](#)



COVID-19 vaccines are effective against serious illness. But researchers are increasingly concerned about ‘breakthrough’ infections driven by the Delta variant of SARS-CoV-2.Credit: Jeff J Mitchell/AFP/Getty

When early field data showed that [vaccinating people cuts transmission of the SARS-CoV-2 virus](#), researchers were cautiously optimistic. But they warned that many of those studies, although promising, took place before the fast-spreading Delta variant proliferated worldwide. Now, reports from various countries seem to confirm [what scientists feared](#) after the variant tore through India with alarming speed in April and May: Delta is more likely than other variants to spread through vaccinated people.

Data from COVID-19 tests in the United States, the United Kingdom and Singapore are showing that vaccinated people who become infected with Delta SARS-CoV-2 can carry as much virus in their nose as do unvaccinated people. This means that despite the protection offered by vaccines, a proportion of vaccinated people can pass on Delta, possibly aiding its rise.



Delta coronavirus variant: scientists brace for impact

“People who have a Delta virus and happen to have ‘breakthrough’ infections can carry these really high levels of virus, and can unwittingly spread the virus to others,” says David O’Connor, a virologist at the University of Wisconsin–Madison.

The findings underscore the importance of protective measures such as wearing masks indoors to reduce transmission. Researchers stress that COVID-19 vaccines are protective against serious illness and death, but the data on Delta transmission show that “people who are vaccinated still need to take precautions”, O’Connor says.

Testing transmissibility

O’Connor and colleagues at the Madison and Dane County health department looked at infections in Wisconsin in June and July.

The team used PCR tests, which are widely used to confirm COVID-19 infections, to estimate the concentration of virus in nasal-fluid samples. The tests detect the virus’s genetic material by amplifying DNA until it is detectable as a fluorescent signal. The number of amplification cycles needed to get a signal — a measure called the cycle threshold value or Ct —

serves as a proxy for viral concentration in the sample. The lower a sample's Ct, the more viral genetic material present.

In a preprint study published on medRxiv on 11 August¹, the researchers compared Ct values for 719 people between 29 June and 31 July, during which 90% of the 122 coronavirus samples they sequenced were the Delta variant. Of the 311 vaccinated people who tested positive for SAR-CoV-2 in that group, most had Ct values of less than 25, a level at which researchers expect the presence of infectious SARS-CoV-2. To confirm this, the team cultured 55 samples that had Ct values less than 25, from vaccinated and unvaccinated people, and detected infectious virus in nearly every one. Most unvaccinated people also had Ct values below this level.



COVID vaccines slash viral spread – but Delta is an unknown

“The bottom line is, this can happen — it can be true that vaccinated people can spread the virus. But we do not yet know what their relative role in overall community spread is,” says co-author Thomas Friedrich, a virologist at the University of Wisconsin–Madison.

Data from Provincetown, Massachusetts, suggest similar findings. An August report from the US Centers for Disease Control and Prevention (CDC) showed that following large gatherings in the beach town, nearly three-quarters of 469 new COVID-19 cases that occurred in the state were in vaccinated people². Both vaccinated and unvaccinated people had

comparably low Ct values, indicating high viral loads, and of the 133 samples sequenced, 90% were identified as Delta. The findings prompted the CDC to update its guidance on 27 July and once again recommend that people in areas of high transmission wear masks indoors.

The Provincetown results were linked to big gatherings, but Wisconsin didn't have similar activity, suggesting that small household gatherings could also help Delta to spread, Friedrich says.

Different biology

In Houston, Texas, where a Houston Methodist Hospital team has been sequencing and logging SARS-CoV-2 variants for almost every COVID-19 case in the hospital system, about 17% of Delta cases are in vaccinated people since March 2021, nearly three times the rate of breakthrough infections compared with all other variants combined. Patients with Delta SARS-CoV-2 also stayed in hospital slightly longer than did people infected with other variants. "There's potentially a slightly different biology to the infection," says James Musser, a molecular pathologist and director of the hospital's Center for Molecular and Translational Human Infectious Diseases Research. His team found that Ct levels were similar in vaccinated and unvaccinated people³.



How the Delta variant achieves its ultrafast spread

However, vaccinated people with Delta might remain infectious for a shorter period, according to researchers in Singapore who tracked viral loads for each day of COVID-19 infection among people who had and hadn't been vaccinated. Delta viral loads were similar for both groups for the first week of infection, but dropped quickly after day 7 in vaccinated people⁴. “Given the high virus levels seen in the first week of illness with Delta, measures such as masks and hand hygiene which can reduce transmission are important for everyone, regardless of vaccination status,” says co-author Barnaby Young, an infectious-disease clinician at the National Centre for Infectious Diseases in Singapore.

One massive analysis of Delta transmission comes from the UK REACT-1 programme, led by a team at Imperial College London, which tests more than 100,000 UK volunteers every few weeks. The team ran Ct analyses for samples received in May, June and July, when Delta was rapidly replacing other variants to become the dominant driver of COVID-19 in the country. The results suggested that among people testing positive, those who had been vaccinated had a lower viral load on average than did unvaccinated people. Paul Elliott, an epidemiologist at Imperial, says that these results differ from other Ct studies because this study sampled the population at random and included people who tested positive without showing symptoms.

These findings — along with an increase in cases in younger people who have not yet received both jabs — underscore the effectiveness of double vaccination against Delta, Elliott says. “We think it’s really, really important to get as many people double vaccinated, and particularly those younger groups, as soon as possible.”

Nature **596**, 327-328 (2021)

doi: <https://doi.org/10.1038/d41586-021-02187-1>

References

1. 1.

Riemersma, K. K. *et al.* Preprint at medRxiv
<https://doi.org/10.1101/2021.07.31.21261387> (2021).

2. 2.

Brown, C. M. *et al.* *MMWR Morb. Mortal. Wkly. Rep.* **70** 1059–1062 (2021).

[PubMed](#) [Article](#) [Google Scholar](#)

3. 3.

Musser, J. M. *et al.* Preprint at medRxiv
<https://doi.org/10.1101/2021.07.19.21260808> (2021).

4. 4.

Chia, P. Y. *et al.* Preprint at medRxiv
<https://doi.org/10.1101/2021.07.28.21261295> (2021).

[Download references](#)

Related Articles

-  [How the Delta variant achieves its ultrafast spread](#)
-  [Delta coronavirus variant: scientists brace for impact](#)



- [COVID vaccines slash viral spread – but Delta is an unknown](#)
- [How the coronavirus infects cells — and why Delta is so dangerous](#)

Subjects

- [Epidemiology](#)
- [SARS-CoV-2](#)
- [Vaccines](#)

nature careers

[Jobs >](#)

- [Group Leader \(f/m/d\) CRISPR/RNAi Technology for Target Identification \(Screening\) and Validation](#)

Evotec AG
Hamburg, Germany
- [Tier I Canada Research Chair in Infectious Disease & Immunity](#)

The University of British Columbia (UBC)
Vancouver, Canada
- [Clinical Research Nurse/Project Manager](#)

Oklahoma Medical Research Foundation (OMRF)
Oklahoma City, United States

- [Research Associate - Immunologist](#)

The University of British Columbia (UBC)

Vancouver, Canada

Nature Briefing

An essential round-up of science news, opinion and analysis, delivered to your inbox every weekday.

[Download PDF](#)

Related Articles



- [How the Delta variant achieves its ultrafast spread](#)



- [Delta coronavirus variant: scientists brace for impact](#)



- [COVID vaccines slash viral spread – but Delta is an unknown](#)

- [How the coronavirus infects cells — and why Delta is so dangerous](#)

Subjects

- [Epidemiology](#)
 - [SARS-CoV-2](#)
 - [Vaccines](#)
-

This article was downloaded by **calibre** from <https://www.nature.com/articles/d41586-021-02187-1>

| [Section menu](#) | [Main menu](#) |

- NEWS
- 05 August 2021
- Correction [10 August 2021](#)

‘Tortured phrases’ give away fabricated research papers

Analysis reveals that strange turns of phrase may indicate foul play in science.

- [Holly Else](#)
 1. Holly Else
[View author publications](#)

You can also search for this author in [PubMed](#) [Google Scholar](#)





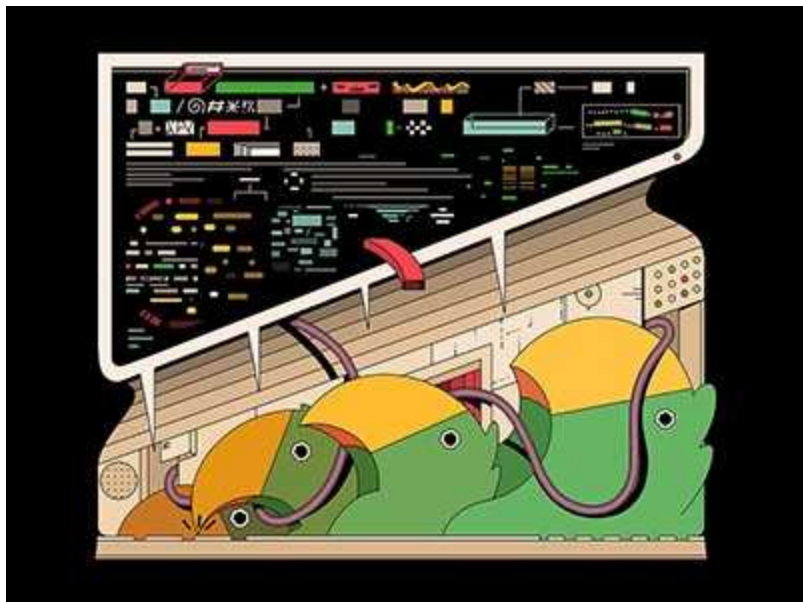
•

[Download PDF](#)

In April 2021, a series of strange phrases in journal articles piqued the interest of a group of computer scientists. The researchers could not understand why researchers would use the terms ‘counterfeit consciousness’, ‘profound neural organization’ and ‘colossal information’ in place of the more widely recognized terms ‘artificial intelligence’, ‘deep neural network’ and ‘big data’.

Further investigation revealed that these strange terms — which they dub “tortured phrases” — are probably the result of automated translation or

software that attempts to disguise plagiarism. And they seem to be rife in computer-science papers.



Robo-writers: the rise and risks of language-generating AI

Research-integrity sleuths say that Cabanac and his colleagues have uncovered a new type of fabricated research paper, and that their work, posted in a preprint on arXiv on 12 July¹, might expose only the tip of the iceberg when it comes to the literature affected.

To get a sense of how many papers are affected, the researchers ran a search for several tortured phrases in journal articles indexed in the citation database Dimensions. They found more than 860 publications that included at least one of the phrases, 31 of which were published in a single journal: *Microprocessors and Microsystems*.

“It harms science. You cannot trust these papers, so we need to find them and retract them,” says Guillaume Cabanac, a computer scientist at the University of Toulouse, France, who worked on the study.

Tortured phrases found in computer-science papers

Scientific term**Tortured phrase**

Big data Colossal information

Artificial intelligence Counterfeit consciousness

Deep neural network Profound neural organization

Remaining energy Leftover vitality

Cloud computing Haze figuring

Signal to noise Flag to commotion

Random value Irregular esteem

Suspecting that the tortured phrases are the result of automated translation or software that rewrites existing text, Cabanac and colleagues ran a selection of abstracts from *Microprocessors and Microsystems* and other journals through a tool that can identify whether texts have been generated by the [artificial-intelligence tool GPT](#). Of the *Microprocessors and Microsystems* papers flagged by the tool, manual checks revealed “critical flaws” in some of them, such as nonsensical text, as well as plagiarized text and images.

To dig deeper, the group downloaded all papers published in *Microprocessors and Microsystems* between 2018 and 2021, a time frame they chose because an upgraded version of GPT was released in 2019. They identified around 500 “questionable articles” based on various factors.

Their analysis revealed that papers published after February 2021 had an acceptance time that was five times shorter, on average, than those published before that date. A high proportion of these papers came from authors in China. And a subset of papers had identical submission, revision and acceptance dates, the majority of which appeared in special issues of the journal. This is suspicious, the authors say. Unlike standard issues, overseen by the editor-in-chief, special issues are usually proposed and overseen by a guest editor, and focus on a specific area of research.

Microprocessors and Microsystems was not the only affected title — the researchers also found evidence of tortured phrases in papers published in hundreds of other journals. “Preliminary probes show that several thousands of papers with tortured phrases are indexed in major databases,” they write, adding that “other tortured phrases related to the concepts of other scientific fields are yet to be exposed”.

Special-issue investigation

Around the time that Cabanac and his colleagues first noticed the tortured phrases, and unbeknown to them, the editor of *Microprocessors and Microsystems* began having concerns about the integrity and rigour of peer review for papers that had been published in some of the journal’s special issues.

The journal’s publisher, Elsevier, launched an investigation. This is still under way, but in mid-July the publisher added expressions of concern to more than 400 papers that appeared across six special issues of the journal.

The expressions of concern say that the papers in the affected special issues of *Microprocessors and Microsystems* are being “independently re-assessed” one by one, and the journal will give further updates on their status once the investigations have concluded.



The fight against fake-paper factories that churn out sham science

The publisher adds that a “configuration error in the editorial system” at the journal meant that neither the editor-in-chief nor the editor designated to handle the papers received them for approval as they should have. “This configuration error was a temporary issue due to system migration and was corrected as soon as it was discovered,” says the notice.

A spokesperson for Elsevier told *Nature* in a statement that the *Microprocessors and Microsystems* investigation has found that the authors probably used reverse-translation software to disguise plagiarism, and that this is the likely source of the tortured phrases.

The investigation has also revealed that 49 papers flagged as suspicious by Cabanac and his colleagues and published in standard issues of the journal were originally submitted to its special issues and were accepted by guest editors, “but were subsequently published in regular issues, at the authors’ request”, the statement says. These papers are already part of Elsevier’s investigation, it adds.

Elisabeth Bik, [a research-integrity analyst](#) in California known for her skill in spotting duplicated images in papers, says that the findings of Cabanac’s research are “shocking”. “This is a very new and disturbing type of fabricated paper,” she adds.

Jennifer Byrne, a molecular-oncology researcher at the University of Sydney, Australia, who also works on spotting fabricated papers, says that this is probably the tip of the iceberg because the researchers only looked in depth at one journal from one publisher. “These papers were also found because they were of very poor quality, but there could be more plausible AI-generated papers within the literature that are harder to detect,” she adds.

Nature **596**, 328-329 (2021)

doi: <https://doi.org/10.1038/d41586-021-02134-0>

Updates & Corrections

- **Correction 10 August 2021:** An earlier version of this article stated that more than 500 papers containing tortured phrases were identified in *Microprocessors and Microsystems*. The estimate of 500 questionable papers in this journal was in fact based on several factors.

References

1. 1.

Cabanac, G., Labb  , C. & Magazinov, A. Preprint at arXiv
<https://arxiv.org/abs/2107.06751> (2021).

[Download references](#)

Related Articles

-  [Robo-writers: the rise and risks of language-generating AI](#)



- [The fight against fake-paper factories that churn out sham science](#)
- [Publishers withdraw more than 120 gibberish papers](#)
- [Computer conference welcomes gobbledegook paper](#)

Subjects

- [Publishing](#)

nature careers

[Jobs](#) >

- [Group Leader \(f/m/d\) CRISPR/RNAi Technology for Target Identification \(Screening\) and Validation](#)

Evotec AG

Hamburg, Germany

- [Tier I Canada Research Chair in Infectious Disease & Immunity](#)

The University of British Columbia (UBC)

Vancouver, Canada

- [Clinical Research Nurse/Project Manager](#)

Oklahoma Medical Research Foundation (OMRF)

Oklahoma City, United States

- [Research Associate - Immunologist](#)

The University of British Columbia (UBC)
Vancouver, Canada

Nature Briefing

An essential round-up of science news, opinion and analysis, delivered to your inbox every weekday.

[Download PDF](#)

Related Articles



- [Robo-writers: the rise and risks of language-generating AI](#)



- [The fight against fake-paper factories that churn out sham science](#)
- [Publishers withdraw more than 120 gibberish papers](#)
- [Computer conference welcomes gobbledegook paper](#)

Subjects

- [Publishing](#)
-

This article was downloaded by **calibre** from <https://www.nature.com/articles/d41586-021-02134-0>

| [Section menu](#) | [Main menu](#) |

- NEWS
- 12 August 2021

Mammoth's epic travels preserved in tusk

Chemical analysis of an ice age woolly mammoth's tusk reveals the huge distances it travelled during its lifetime more than 17,000 years ago.

- [Ariana Remmel](#)
 1. Ariana Remmel
[View author publications](#)

You can also search for this author in [PubMed](#) [Google Scholar](#)





•

[Download PDF](#)



Woolly mammoths (illustration) roamed throughout the Arctic Circle during the last ice age.Credit: Orla/Getty

Researchers have reconstructed the geographical movements of a single woolly mammoth (*Mammuthus primigenius*) using chemical ‘GPS tags’ preserved in one of its tusks. The findings show that the animal travelled so widely across what is now Alaska that it could have circled Earth almost twice — a discovery that offers tantalizing clues about why the species went extinct.

Although researchers know a fair amount about the diet, genetics and ecology of woolly mammoths, insights into the life histories of individual animals are scarce.



Million-year-old mammoth genomes shatter record for oldest ancient DNA

“We can’t go back and watch these things like a modern ecologist might, but we can use chemistry to come up with good proxies,” says Chris Widga, a palaeontologist at East Tennessee State University in Johnson City. Every place on Earth has a distinct chemical signature based on differences in its geology. The ratios of various isotopes of elements such as strontium and oxygen in the bedrock and water create a unique profile specific to that location that remains consistent over millennia, and is incorporated into soil and plants. As mammoths grazed on the Arctic plains, these isotopic signatures were integrated into their ever-growing tusks, creating a permanent record of the animals’ whereabouts with almost daily resolution.

Until now, no one had analysed these chemical GPS tags across the full length of a tusk, which reflects the mammoth’s entire life. “This is by far the largest and most comprehensive study of its kind,” says Matthew Wooller, a palaeoecologist at the University of Alaska Fairbanks, who co-led the study with geoscientist Clement Bataille at the University of Ottawa in Canada and colleagues.

Their findings — published on 12 August in *Science*¹ — provide a glimpse of the life and death of a single woolly mammoth during the last ice age.

Mammoth soap opera

Previous analysis of the 1.7-metre-long tusk had showed that it belonged to a male mammoth that died around 17,100 years ago, when it was at least 28 years old. The researchers split the tusk down the middle to reveal the layers of growth, which look like a curving stack of ice cream cones. The base of this stack “is the day that it died and the tip is the day that it was born”, says Wooller. “Everything in between is the lifespan of the mammoth.”

The researchers used lasers to sample the tusk’s chemical composition at approximately 340,000 points along the full length of the cone tips. They then compared the isotopic profiles at each of these data points with a geological map of Alaska and northwest Canada, and used a computer algorithm to map out the most probable routes for the mammoth to have travelled, backtracking from where its remains were found.

“It’s a total soap opera, all the way up to the day it died,” Wooller says.



Cross section of a split mammoth tusk, stained blue to reveal growth lines. Researchers analysed the chemical compositions of the layers to track the mammoth's movements.Credit: J. R. Ancheta, University of Alaska Fairbanks

The bull spent much of its early life in the Yukon River basin and wider Alaskan interior, where it made repeated, long-distance journeys between smaller territories. The migratory behaviour is similar to those of modern elephant groups, which suggests that the young mammoth was moving with a herd.

At about 16 years old, the isotopic pattern in the tusk becomes more variable. The mammoth probably wandered longer distances in less regular patterns than during its juvenile years. This could indicate that it left its herd to roam freely, as has been observed in mature males from living elephant species. For around a decade, it travelled widely across its range, sometimes visiting areas in which other mammoth remains have been found.

In the last year and a half of the animal's life, its stamping grounds shrank to a single region near the northern coast of Alaska within the Arctic Circle. A distinctive isotope pattern recorded at the base of the tusk showed the "telltale hallmark of starvation in mammals", which was probably what caused its death, says Wooller.

"The fact that this study presents an 'iso-biography' for a single individual is part of what makes it so exciting," says Kate Britton, an archaeological scientist at the University of Aberdeen, UK. "We are gaining individual insight into the behaviour of an animal that roamed Alaska more than 17,000 years ago, and the strontium isotopes allow us to follow in its footsteps."

Splitting more tusks

Scientists still don't know exactly what caused woolly mammoths to go extinct, but many agree that the changing climate could have had a role.

Their extinction coincided with a period when the planet was warming and much of the mammoth's Arctic range was becoming hotter, wetter and more

forested. If mammoths regularly migrated as widely as this bull, that could explain why they were so negatively affected by habitat loss, Wooller says.



[Ancient stone tools hint at settlers' epic trek to North America](#)

Britton cautions against using one bull's movements to attribute behaviours to a whole species across time. But she's excited by how isotope profiles in tusks can offer insights across the full lifespan of extinct creatures, and hopes that the technique will be applied more widely.

Wooller and his colleagues want to analyse other mammoth tusks to compile a more robust collection of life histories. But that would mean splitting open — and thus partially destroying — precious museum specimens.

Christine Garcia, collections manager for geology at the California Academy of Sciences in San Francisco, is intrigued by the idea, but cautious. Although it's important to be mindful about the use of destructive sampling techniques, she says, this research "speaks to the potential value of a lot of these collections and how they can be useful". Now she wonders what other life stories are hidden among the isotopes of the mammoth tusks — and other specimens — in her own care.

Nature **596**, 329 (2021)

doi: <https://doi.org/10.1038/d41586-021-02206-1>

References

1. 1.

Wooller, M. J. *et al. Science* <https://doi.org/10.1126/science.abg1134> (2021).

[Article](#) [Google Scholar](#)

[Download references](#)

Related Articles



- [Million-year-old mammoth genomes shatter record for oldest ancient DNA](#)



- [Carbon dating, the archaeological workhorse, is getting a major reboot](#)



- [Ancient stone tools hint at settlers' epic trek to North America](#)



- [Ancient rock bears isotopic fingerprints of Earth's origins](#)

- [Monkey teeth tell tale of ancient migration](#)

Subjects

- [Zoology](#)
- [Evolution](#)
- [Palaeontology](#)

nature careers

[Jobs](#) >

- [Group Leader \(f/m/d\) CRISPR/RNAi Technology for Target Identification \(Screening\) and Validation](#)

Evotec AG

Hamburg, Germany

- [Tier I Canada Research Chair in Infectious Disease & Immunity](#)

The University of British Columbia (UBC)

Vancouver, Canada

- [Clinical Research Nurse/Project Manager](#)

Oklahoma Medical Research Foundation (OMRF)

Oklahoma City, United States

- [Research Associate - Immunologist](#)

The University of British Columbia (UBC)

Vancouver, Canada

Nature Briefing

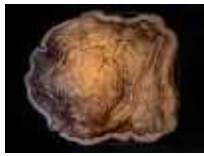
An essential round-up of science news, opinion and analysis, delivered to your inbox every weekday.

[Download PDF](#)

Related Articles



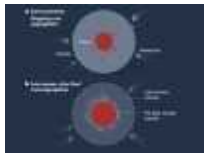
- [Million-year-old mammoth genomes shatter record for oldest ancient DNA](#)



- [Carbon dating, the archaeological workhorse, is getting a major reboot](#)



- [Ancient stone tools hint at settlers' epic trek to North America](#)



- [Ancient rock bears isotopic fingerprints of Earth's origins](#)

- [Monkey teeth tell tale of ancient migration](#)

Subjects

- [Zoology](#)
 - [Evolution](#)
 - [Palaeontology](#)
-

This article was downloaded by **calibre** from <https://www.nature.com/articles/d41586-021-02206-1>

| [Section menu](#) | [Main menu](#) |

- NEWS
- 10 August 2021
- Correction [17 August 2021](#)

Exotic four-quark particle spotted at Large Hadron Collider

Rare tetraquark is one of dozens of non-elementary particles discovered by the accelerator, and could help to test theories about strong nuclear force.

- [Davide Castelvecchi](#)
 1. Davide Castelvecchi
[View author publications](#)

You can also search for this author in [PubMed](#) [Google Scholar](#)





•

[Download PDF](#)



Installation of part of the LHCb detector — which has since spotted many of the LHC's new hadron types. Credit: Julien Marius Ordan/CERN

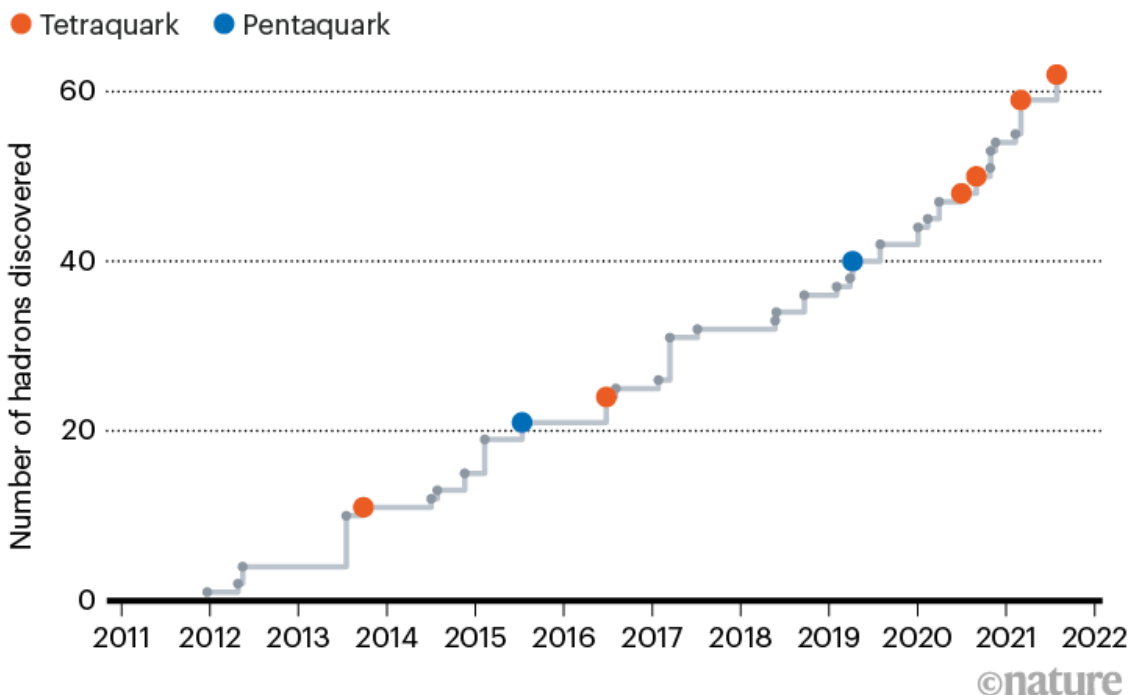
The Large Hadron Collider (LHC) is also a big hadron discoverer. The atom smasher near Geneva, Switzerland, is most famous for demonstrating the existence of the Higgs boson in 2012, a discovery that slotted into place the final keystone of the current classification of elementary particles. But the LHC has also netted dozens of the non-elementary particles called hadrons — those that, like protons and neutrons, are made of quarks.

The latest hadron made its debut at the virtual meeting of the European Physical Society on 29 July, when particle physicist Ivan Polyakov at Syracuse University in New York [unveiled a previously unknown exotic hadron](#) made of four quarks. This brought the LHC's hadron bounty up to 62 (see 'Particle discoveries') according to [a tally kept by Patrick Koppenburg](#), a particle physicist with Nikhef, the Dutch National Institute for Subatomic

Physics in Amsterdam. “These are all world firsts,” says Koppenburg, who is based at CERN, the European particle-physics laboratory that hosts the LHC.

PARTICLE DISCOVERIES

The Large Hadron Collider discovered an elementary particle, the Higgs boson, in 2012. But it has also discovered 62 non-elementary particles, called hadrons, so far. These include tetraquarks and pentaquarks — particles made of four and five quarks, respectively.



Source: [Patrick Koppenburg](#)

The established pantheon of particles, called the standard model, describes the basic building blocks of matter and the fundamental forces that act on them. It includes six flavours of quark, their six antimatter counterparts and several other elementary particles, including electrons and photons. The standard model also includes rules for how quarks form composite particles called hadrons. The quarks are held together by the strong nuclear force, one of the four fundamental forces. The two most common quarks in nature are called ‘up’ and ‘down’; their possible combinations include neutrons (one up and two downs) and protons (two ups and one down).

Protons are the only hadrons known to be stable in isolation — neutrons are stable only when they are incorporated into atomic nuclei. All other hadrons form only fleetingly, from the collision of other particles, and decay in a fraction of a second. So the LHC creates new kinds of hadron by causing high-energy, head-on collisions between protons.

Quark quartet

Most of the LHC's new hadron types have been spotted by LHCb, one of the four giant detectors in the 27-kilometre circular tunnel that holds the LHC, and the particle announced by Polyakov was no exception. Sifting through data on the debris from proton collisions, Polyakov and his collaborator Vanya Belyaev at the Institute for Theoretical and Experimental Physics in Moscow found the expected signature of a ‘tetraquark’ — a four-quark hadron — called T_{cc}^+ .

Tetraquarks are extremely unusual: most known hadrons are made of either two or three quarks. The first tetraquark was spotted at the High Energy Accelerator Research Organization (KEK) in Tsukuba, Japan, in 2003, and LHCb has seen several more. But the new one is an oddity. Previous tetraquarks were likely to be pairs of ordinary quark doublets attached to each other like atoms in a molecule, but theoretical physicist Marek Karliner thinks that the latest one could be a genuine, tightly bound quadruplet. “It is a big deal. It’s a new animal, not a hadronic molecule. It’s the first of its kind,” says Karliner, who is at Tel Aviv University in Israel and helped to predict the existence of a particle with the same properties as T_{cc}^+ in 2017¹.

In nature, tetraquarks probably existed only during the first instants of the Universe, when all matter was compressed in an extremely tight space, says Belyaev. But creating them anew helps physicists to test their theories about how particles interact through the strong nuclear force.

The data revealed the new particle’s properties so precisely that Belyaev was stunned. “My first reaction was: it’s my mistake,” he says. For example, the particle’s mass, which is around 4 times that of a proton, was nailed with a margin of error nearly 3,000 times better than in the discovery of the Higgs boson. Belyaev adds that T_{cc}^+ could have been discovered in data from the

early years of the LHC, but he and his LHCb colleagues didn't find it until now because they had a long list of other particles to look for.

Limitless possibilities

The search for new hadrons will go on. Dozens of combinations of quarks can give rise to hadrons. Karliner says that there are 50 possible 2-quark hadrons, all but one of which have been observed, and 75 possible quark triplets (and as many triplets of antiquarks), of which nearly 50 have been seen. "We are certain all the others exist, but they are difficult to make," Karliner says.

Moreover, for each combination of quarks, there is an almost limitless number of possible heavier 'excited states' — distinguished, for example, by how fast they spin — and each is classified as a separate particle. Many have been found experimentally, and in fact the majority of particles in Koppenburg's catalogue are excited states. "Who knows how many other states are there just hidden in plain sight, sitting in the data on a laptop," says Koppenburg, who, like Polyakov and Belyaev, is a member of the LHCb collaboration.

But he also wonders whether all these discoveries should be treated as discrete particles. "I tend to be increasingly convinced that we need a better definition of what a particle is," he says.

Nature **596**, 330 (2021)

doi: <https://doi.org/10.1038/d41586-021-02174-6>

Updates & Corrections

- **Correction 17 August 2021:** An earlier version of the 'Particle discoveries' graphic erroneously included '2021' twice on the *x* axis.

References

1. 1.

Karliner, M. & Rosner, J. L. *Phys. Rev. Lett.* **119**, 202001 (2017).

[PubMed](#) [Article](#) [Google Scholar](#)

[Download references](#)

Related Articles



- [Read the paper: Unveiling the strong interaction among hadrons at the LHC](#)
- [Muons: the little-known particles helping to probe the impenetrable](#)
- [Mysterious particles spotted in Saturn's atmosphere](#)
- [CERN's next director-general on the LHC and her hopes for international particle physics](#)
- [China, Japan, CERN: Who will host the next LHC?](#)

Subjects

- [Physics](#)
- [Particle physics](#)

nature careers

[Jobs](#) >

- [Group Leader \(f/m/d\) CRISPR/RNAi Technology for Target Identification \(Screening\) and Validation](#)

Evotec AG

Hamburg, Germany

- **Tier I Canada Research Chair in Infectious Disease & Immunity**

The University of British Columbia (UBC)

Vancouver, Canada

- **Clinical Research Nurse/Project Manager**

Oklahoma Medical Research Foundation (OMRF)

Oklahoma City, United States

- **Research Associate - Immunologist**

The University of British Columbia (UBC)

Vancouver, Canada

Nature Briefing

An essential round-up of science news, opinion and analysis, delivered to your inbox every weekday.

[Download PDF](#)

Related Articles



- **Read the paper: Unveiling the strong interaction among hadrons at the LHC**

- [Muons: the little-known particles helping to probe the impenetrable](#)
- [Mysterious particles spotted in Saturn's atmosphere](#)
- [CERN's next director-general on the LHC and her hopes for international particle physics](#)
- [China, Japan, CERN: Who will host the next LHC?](#)

Subjects

- [Physics](#)
- [Particle physics](#)

This article was downloaded by **calibre** from <https://www.nature.com/articles/d41586-021-02174-6>

| [Section menu](#) | [Main menu](#) |

- NEWS Q&A
- 09 August 2021

Chelsea Clinton urges global sharing of COVID vaccine technology

The health-policy specialist who grew up in the White House is using her training and connections to convince world leaders to help make vaccines accessible to all nations.

- [Amy Maxmen](#)
 1. Amy Maxmen
[View author publications](#)

You can also search for this author in [PubMed](#) [Google Scholar](#)





•

[Download PDF](#)



Once a White House resident, Chelsea Clinton is now a professor of health policy at Columbia University in New York. Credit: Jeenah Moon/Reuters/Alamy

Chelsea Clinton typically maintains a low public profile. But lately, she's using various platforms to decry the lack of COVID-19 vaccines in low- and middle-income countries while wealthy nations are stockpiling jabs and [considering third doses](#). She's leveraging her background in public health, as well as a lifetime of political connections, to implore world leaders to ramp up vaccine supplies so that everyone can get one.



[COVID boosters for wealthy nations spark outrage](#)

Before becoming a professor of health policy at the Columbia Mailman School of Public Health in New York City, Clinton had a ringside view of Washington DC politics growing up beside her parents, former US president Bill Clinton and Hillary Clinton, a former senator and secretary of state who was also the 2016 Democratic Party presidential nominee. Chelsea Clinton's graduate work in international relations and public health has also served her in her position as vice-chair of the Clinton Foundation, which aims to bolster public health and economic development in the United States and about three dozen other countries. At a time when politics and economics are swaying the direction of the pandemic as much as science is, Clinton feels prepared to speak about vaccines — the tools she thinks are central to ending the COVID-19 crisis.

Nature spoke to Clinton about her career path, vaccine hesitancy, and the need to make and distribute shots around the world.

After an upbringing in politics, what led you to public health?

My first real interest in public health began around three decades ago, when [basketball player] Magic Johnson gave his courageous speech about being

HIV-positive. And when my family moved to Washington DC, I was lucky to have a theatre teacher who did a lot of work with an HIV-positive theatre group. Through that group, I was introduced to the gross inequities around who had access to health care. I started to feel that my father, president at the time, wasn't doing enough around HIV and AIDS. I remember being at an Easter church service when [the AIDS activist group] ACT-UP barged in to shout at my father — and I thought it was appropriate, because I agreed with them.

When my father left the White House in 2001, I hoped he would devote energy to this. And he did, by helping to found the Clinton HIV/AIDS Initiative, which became the Clinton Health Access Initiative. I was in college then, and right after, I went to graduate school and wrote my master's thesis on the Global Fund [to Fight AIDS, Tuberculosis and Malaria], and why the world needed a new instrument to help finance prevention and treatment.

You have been advocating for COVID-19 vaccine equity. Are you relieved that the US government has donated shots to more than 60 countries?



[In shock move, US backs waiving patents on COVID vaccines](#)

I'm incredibly grateful that we've donated 110 million doses of a vaccine, yet it is deeply insufficient given the needs. I hope that we will accelerate the donations to the full 500 million doses that [US President Joe Biden's] administration committed to earlier. But even then, as many others have pointed out, we cannot donate our way out of this.

That's why I continue to advocate for the Biden administration to push pharmaceutical companies to license their technologies to the many facilities around the world that could begin to make the vaccines. I hope that the administration will see this not only as the morally right thing for the American government to do, but also as what's in our best interest to ensure that we're protecting American lives and livelihoods. We cannot move forward in a durable, sustainable way until we minimize the risk of future variants, which will happen only when we vaccinate the world.

In May, Biden backed proposals asking the World Trade Organization (WTO) to issue waivers on COVID-19 vaccine patents. What is the status of that?

Last I heard, the head of the WTO set an early-December deadline for an agreement on the TRIPS waiver [which would temporarily override the Trade-Related Intellectual Property Rights agreement protecting the organization's members]. That's four months away. I worry that our response doesn't match the urgency of the moment. We can't continue to dither. Donations are not a scalable strategy. And that is why I and many others are calling for not only broad-based IP [intellectual property] and the sharing of technical know-how, but also real investment to help ensure that people everywhere can be vaccinated. I think, at some point, we will wind up there. But it's very painful for me to think about how many lives will be lost between that point and where we are today.

I hope that, somehow, there will be another path out of this, but I don't see one outside of enabling significantly more vaccines to be produced in significantly more places, with continued funding to ensure that the vaccines

can be produced, that their quality can be assured and that they can be distributed to countries and get into arms.

Is there any alternative to a TRIPS waiver?



COVID vaccines have higher approval in less-affluent countries

Right now, [German chancellor] Angela Merkel seems to be strongly opposed to the TRIPS waiver, but if she still wanted Germany to help vaccinate the world she could compel [German biotech firm] BioNTech to license its patents and vaccine technology so that other manufacturers could step in. The German government gave meaningful research grants to BioNTech that helped them to develop the mRNA technology in their vaccine, which they immediately licensed to Pfizer [a pharmaceutical company based in New York City]. But BioNTech retains marketing and distribution rights for the vaccine in Germany and Turkey.

The United States could compel Moderna [a biotech firm in Cambridge, Massachusetts] to do much the same because the government funded much of their vaccine's development. The NIH [US National Institutes of Health] even owns some of those patents. Besides this being the moral and smart thing to do, it could restore our standing in the world. Multiple surveys indicated a steep decline in how the United States and Americans were

perceived during [former president] Donald Trump's administration. It would seem that there would be no better way to declare that the United States is a leader, and is committed to dignity, solidarity and to global health, than by facilitating access to vaccines around the world. As an American, this is very much what I would hope my country will do, and I also think that it would be good for the global economy and global security, and vital to public health.

Are you concerned about the lack of vaccine uptake within the United States?

Very much. At the Clinton Foundation, we've been working with schools, community organizations and faith leaders to help ensure that people have the information on vaccines that they need to be able to make the choice to get themselves vaccinated. I've actually been involved in the push-back against the anti-vaccine movement for many years. I'm ashamed to admit that I wasn't attuned to how potent it was until I was pregnant with my first child in 2014. I had a woman stop me as I was walking through my local park and say, 'Please tell me you're not going to vaccinate your child.' I told her that I certainly would because vaccines will protect my child, but I was taken aback by the vehemence of her responses and the depth of her belief that I was wrong. That prompted me to try to better understand the origins of the anti-vaccine movement in this country, and to support efforts that push back against it.

Do you think an anti-science movement in the United States has grown in the past few decades?

Although there were very intense political debates in the 1980s and early 1990s, we didn't have the broad-based politicization of science, and the kinds of attack against scientists and the scientific method, that we have today. I disagreed with [former president Ronald] Reagan and his administration on many things, but he led the effort against [ozone-depleting] chlorofluorocarbons, and led the effort to end the scourge of acid rain. In the early 1990s, the American public overwhelmingly listened when scientists warned that humans were contributing to global warming. But in

the mid-1990s, [conservative media outlet] Fox News started, as well as organized efforts to create think tanks to churn out papers that spurred doubt by questioning the science behind climate change. Today, we are in a radically different context than when I was a kid. A large portion of the public doubts the scientific method, and even demonizes scientists themselves.

How would you remedy the anti-science situation?



'It's a minefield': COVID vaccine safety poses unique communication challenge

I think we need to help scientists better articulate what they do, how they know what they do, and what they don't know and are still querying. For so long, I think many scientists have just felt like the data speak for themselves, but oftentimes people will pay a lot more attention to a personal testimony than to a chart — even if it's the coolest infographic ever.

I also think we need to lift up people that we sometimes disagree with. Right now, the governor of Arkansas is trying to overturn legislation — that he supported only a few weeks ago — that bans mask mandates. Arkansas public schools start up in a couple of weeks, and he wants school authorities to be able to mandate masks if they want to. I think we need to recognize

leaders when they reverse course to be more responsive to what public-health authorities say is necessary to protect people.

Nature **596**, 331 (2021)

doi: <https://doi.org/10.1038/d41586-021-02164-8>

This interview has been edited for length and clarity.

Related Articles



- [**This COVID-vaccine designer is tackling vaccine hesitancy — in churches and on Twitter**](#)



- [**In shock move, US backs waiving patents on COVID vaccines**](#)



- [**COVID boosters for wealthy nations spark outrage**](#)



- [**‘It’s a minefield’: COVID vaccine safety poses unique communication challenge**](#)



- [COVID vaccines have higher approval in less-affluent countries](#)



- [The epic battle against coronavirus misinformation and conspiracy theories](#)

Subjects

- [SARS-CoV-2](#)
- [Public health](#)
- [Vaccines](#)
- [Politics](#)
- [Policy](#)

nature careers

[Jobs](#) >

- [Group Leader \(f/m/d\) CRISPR/RNAi Technology for Target Identification \(Screening\) and Validation](#)

Evotec AG

Hamburg, Germany

- [Tier I Canada Research Chair in Infectious Disease & Immunity](#)

The University of British Columbia (UBC)

Vancouver, Canada

- [Clinical Research Nurse/Project Manager](#)

Oklahoma Medical Research Foundation (OMRF)

Oklahoma City, United States

- **Research Associate - Immunologist**

The University of British Columbia (UBC)

Vancouver, Canada

Nature Briefing

An essential round-up of science news, opinion and analysis, delivered to your inbox every weekday.

[Download PDF](#)

Related Articles



- **This COVID-vaccine designer is tackling vaccine hesitancy — in churches and on Twitter**



- **In shock move, US backs waiving patents on COVID vaccines**



- **COVID boosters for wealthy nations spark outrage**

-  **'It's a minefield': COVID vaccine safety poses unique communication challenge**
-  **COVID vaccines have higher approval in less-affluent countries**
-  **The epic battle against coronavirus misinformation and conspiracy theories**

Subjects

- [SARS-CoV-2](#)
- [Public health](#)
- [Vaccines](#)
- [Politics](#)
- [Policy](#)

This article was downloaded by **calibre** from <https://www.nature.com/articles/d41586-021-02164-8>

- NEWS FEATURE
- 13 August 2021

Has COVID taught us anything about pandemic preparedness?

Researchers warn that plans to prevent the next global outbreak don't consider the failures that have fuelled our current predicament.

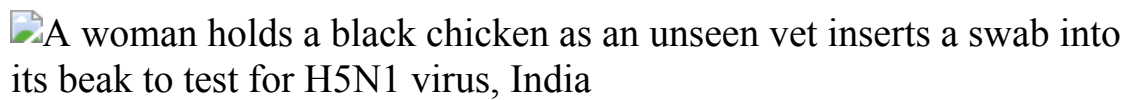
- [Amy Maxmen](#)
 1. Amy Maxmen
[View author publications](#)

You can also search for this author in [PubMed](#) [Google Scholar](#)





•



A veterinary doctor in Shahpur, India, tests a chicken for H5N1 influenza in January after migratory birds were reported dead in the area. Credit: Sanjay Baid/EPA-EFE/Shutterstock

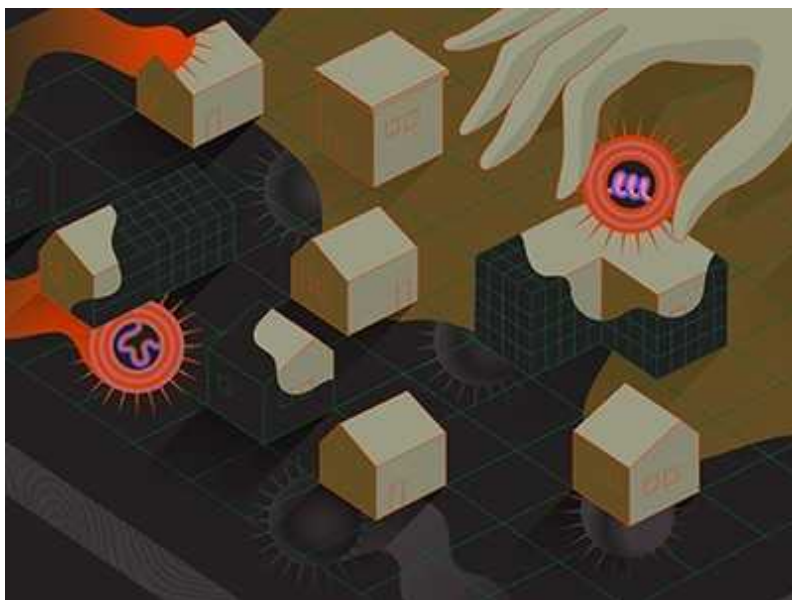
[Download PDF](#)

As nations struggle to control the COVID-19 pandemic, scientists warn that deadly outbreaks of other viruses are inevitable. History is clear on this: more than six distinct influenza pandemics and epidemics have struck in just

over a century. Ebola viruses have spilled over from animals about 25 times in the past five decades. And at least seven coronaviruses, including SARS-CoV-2, have brought illness and death.

Expecting to avoid another spillover is about as realistic as stopping lightning from sparking a forest fire. “Preventing a pandemic may not be possible, so being prepared is the key,” says Youngmee Jee, chief executive at the Pasteur Institute in South Korea.

Epidemiologists and researchers who specialize in biosecurity and public health have been outlining preparedness plans for at least 20 years. The core components consist broadly of surveillance to detect pathogens; data collection and modelling to see how they spread; improvements to public-health guidance and communication; and the development of therapies and vaccines.



[Two decades of pandemic war games failed to account for Donald Trump](#)

Governments and private funders have poured millions of dollars into building these capabilities. Researchers have painstakingly [tested and evaluated these plans](#) to identify and fill gaps. Still, COVID-19 has demonstrated that the world was even less prepared than most had imagined. And what makes some scientists nervous is that current discussions on how

to defend against the next pandemic are stuck on the same strategies as before.

“We can’t simply repeat the recipes that failed,” says David Fidler, a global-health policy researcher at the Council on Foreign Relations, a think tank in Washington DC. “People are still talking about doing the same things, and not asking, ‘Why did this all break down?’”

As new preparedness plans are shaping up around the world, *Nature* spoke to more than a dozen researchers to ask what stands in the way of a better system for identifying and controlling new outbreaks, and what must change.

Why aren’t warning systems better?

“Everything starts with smarter surveillance. If you don’t look, you don’t see. If you don’t see, you will always respond too late,” writes infectious-disease researcher Jeremy Farrar, director of the UK biomedical funder Wellcome, in his new book *Spike: The Virus vs the People — the Inside Story*. Unfortunately, too late is the norm. The world’s largest Ebola epidemics had been spreading for more than a month before anyone diagnosed the disease. Similarly, scientists agree that people in China had probably been infected by SARS-CoV-2 for several weeks before officials reported a mysterious pneumonia in Wuhan¹.



Scientists analyse coronavirus samples as part of wider pathogen surveillance in Ede, Nigeria. Credit: Pius Utomi Ekpei/AFP/Getty

Insufficient detection worries researchers because outbreaks get exponentially harder to contain once they've expanded beyond a limited area. The world recognized this danger for influenza viruses decades ago. In 1952, one of the first moves by the nascent World Health Organization (WHO) was to set up the Global Influenza Surveillance and Response System. It has since provided an early warning system for flu outbreaks, such as H5N1 avian influenza, and it has alerted researchers to the rise of resistance to certain antiviral drugs².

Unknown or unexpected pathogens are harder to monitor, but improvements in genome-sequencing techniques have made open-ended searches possible. For example, in Ede, Nigeria, scientists at the African Center of Excellence for Genomics of Infectious Diseases search for foreign DNA and RNA in blood samples from patients who have high fevers but test negative for the most common maladies in the region. Using this method, they discovered an unrecognized outbreak of yellow fever in 2017. “This is a very good method

for finding unknowns,” explains Judith Oguzie, an infectious-disease researcher at the centre.

Some researchers say this sort of surveillance should be extended to people who work in forests, on farms handling animals and in virology laboratories — anywhere people might come into close contact with pathogens. Oliver Pybus, a co-director of the pandemic genomics programme at the University of Oxford, UK, adds that new genomic technologies could allow researchers to detect viruses in waste water or air. And once an outbreak is ongoing, these same tools can help them to determine how far it has spread below the radar.



Researchers collect bats in Ratchaburi, Thailand.Credit: Adam Dean/Panos Pictures

High-tech tracking would provide lots of data, but Mosoka Fallah, the president of Refuge Place International in Monrovia, Liberia, says that basic surveillance needs to improve first. He says funders often support it as a finite project rather than a sustained process, and this defeats the purpose. A case in point: Liberia received more than US\$19 million from donors,

including the US government and the World Bank, to strengthen its health system and surveillance in the wake of the Ebola outbreak in 2014–16, but many of the funds have run dry. In 2019, the country was facing nationwide shortages in biomedical supplies, and many researchers and health workers weren't being paid.

At a large hospital in Bong County in Liberia, the district surveillance officer, J. Henry Capehart, explained that his team had been unable to monitor endemic infectious diseases, such as measles and Lassa fever, because there were no sample tubes to collect blood. Jefferson K. Sibley, the medical director at the hospital, said that a laboratory technician had recently died of Lassa fever because the hospital didn't have the antiviral drug to treat him. "It's terrible," said Sibley. Some people had stopped seeking care because the clinic had no way to help, meaning that their illnesses were also going undetected.

According to the [2019 Global Health Security Index](#), Liberia was among more than 70 countries sorely lacking in capacity to detect emerging epidemics, and among some 130 with health systems that would be inadequate in an outbreak. In these places, Fallah says, donors investing in surveillance must also strengthen the health system, or the efforts will continue to be in vain.

How can better data drive smarter decisions?

Epidemiologists learn about emerging diseases by crunching numbers, and the quality of their results depends on access to raw information. On the day after he took office, US President Joe Biden pledged to modernize the country's outdated system for public-health data and create a National Center for Epidemic Forecasting and Outbreak Analytics. The proposal, backed by \$500 million through the America Rescue Plan Act of 2021, aligns with earlier suggestions by epidemiologists such as Caitlin Rivers at the Johns Hopkins Center for Health Security in Baltimore, Maryland. She says that the world lost valuable time in January and February 2020, when she and her colleagues were struggling to make sense of scraps of data on COVID-19 from official reports, newspaper articles and social-media posts.



The US Centers for Disease Control and Prevention aims to guide local health partners. Credit: James Gathany/CDC/Smith Collection/Gado/Getty

Better data would have helped epidemiologists to determine more quickly and confidently, for example, that SARS-CoV-2 spreads through the air and that it can be transmitted by people without symptoms, says Rivers. That might have prompted scientists to advocate sooner for measures such as widespread testing and face masks. Predictions from mathematical models might have been more accurate, too, adds Jennifer Nuzzo, an epidemiologist at the Johns Hopkins Center for Health Security. “We were doing elegant math on crappy data,” she explains.

Biden’s forecasting centre will begin by focusing on the United States, where data collection was [patchy and sloppy throughout 2020](#). One problem has been that rules around patient privacy prevented hospitals and health departments from sharing data with researchers who wanted to analyse it. Rivers expects the centre to set standards on how to share data responsibly. Meanwhile, the UK government, in partnership with the WHO and Wellcome, launched the Global Pandemic Radar surveillance network in May to track disease outbreaks around the world, including the spread of

SARS-CoV-2 variants. The Rockefeller Foundation in New York City is developing a pandemic data platform, too. [Rick Bright](#), a former head of the US government's Biological Advanced Research and Development Authority, who is spearheading the Rockefeller project, says its position outside the government is a strength. "A non-governmental, non-political entity would have the ability to seal and protect those data, and to make sure that the world has access to all the same information at the same time," Bright argues.

Although these initiatives should improve the situation, they can't make data emerge from places where lab capacity for diagnostic testing is insufficient, and they could still fail to procure information from sources that don't want to share it. Countries with authoritarian leaders have a history of suppressing news of outbreaks ranging from H1N1 influenza to cholera.



Pandemic whistle-blower: we need a non-political way to track viruses

Many criticized China for being less than forthcoming at the beginning of the pandemic, but it hasn't been alone. For example, several counties in the United States refused to share details about outbreaks at companies and jails with the US Centers for Disease Control and Prevention. In India, local journalists exposed the fact that officials were not sharing the case numbers in a timely manner. "Technology is potentially very beneficial, but one has to be cautious about being misty-eyed and thinking it will solve problems if basic capacity and openness is not abundant," says Arvind Subramanian, an

economist at Brown University in Providence, Rhode Island. He [co-authored an investigation](#) estimating that India had under-reported deaths by 3 million or more from the start of the pandemic to June 2021 (ref. ³).

Nuzzo says that to get better raw data, researchers and policymakers need to think about incentives. For instance, most governments around the world report atmospheric conditions because agriculture markets and commerce rely on weather prediction. And community leaders in the United States push people to fill out a census because it can result in resources, she explains.

One incentive could be an agreement that groups sharing data will have access to the technologies that result, says Suerie Moon, a global-health researcher at the Graduate Institute of International and Development Studies in Geneva, Switzerland. She recalls how Indonesia withheld influenza samples in 2006, after it was denied access to flu vaccines that were developed using samples collected in the country. This issue culminated in a [2011 international framework for sharing influenza samples](#).

No such deal exists for SARS-CoV-2, and signs of discontent have surfaced. Several researchers in Africa and South America have [complained about requests to grant rich countries unrestricted access to their data on emerging variants](#) while they have little to no access to COVID-19 vaccines.

Moon says that sharing epidemiological and genomic data in an outbreak is a political issue that must be negotiated at a high level, similarly to the 2011 influenza framework and other multilateral treaties. Such discussions are ongoing, Moon says, but they have not formally begun to address key issues, including what the WHO is allowed to do if a country is suspected of withholding information.

Where does communication break down?

Public-health officials in Taiwan and South Korea were concerned about COVID-19 from the start. Recalling the epidemic of severe acute respiratory syndrome (SARS) in 2003, officials recommended face masks and ramped up mask manufacturing just as details on the first cases emerged, says

biomedical researcher Chien-Jen Chen, who was vice-president of Taiwan from 2016 to 2020. In both places, government agencies met almost daily to agree on cohesive updates for the public.



Wanted: rules for pandemic data access that everyone can trust

Chen tailored messages carefully, emphasizing that recommendations to curb the virus were intended to keep businesses and schools open. “We kept saying, we are doing this because we don’t want to lock down,” Chen explains. Time helped, too. “People began to feel more trusting as they saw how poorly other countries were doing.” As for misinformation, Chen says that a special team was appointed to scout out rumours and dispel them weekly on a dedicated website.

These experiences stand in stark contrast to countries where COVID-19 — and conflicting messages about it — spread out of control. In the United States, health officials didn’t recommend face masks until April 2020, but then-president Donald Trump undermined the recommendations by refusing to wear a mask himself. In Brazil, President Jair Bolsonaro contradicted scientists in the country by trivializing COVID-19, calling it “little flu”. He also fired two ministers of health who advocated control measures such as social distancing.

In May 2020, [the WHO passed a resolution](#) in which countries agreed to combat misinformation at home. [A committee of experts listed some key approaches to this in June last year](#), such as working with data scientists and social-media companies to amplify the reach of credible messages. Facebook had been removing some disinformation from its platform, and renewed attention to the subject prompted the company to go further, adding warnings and links to information from health organizations on posts about COVID-19.



Health workers in Mumbai use digital thermometers to screen people for COVID-19. Credit: Atul Locke/Panos Pictures

But presenting people with a link hardly helps when there are pre-existing biases against the scientific establishment, health authorities or the government, says Nahid Bhadelia, founding director of Boston University's Center for Emerging Infectious Diseases Policy and Research in Massachusetts, which launched in May. Researchers at this centre will develop evidence-based guidelines and communicate them in congressional briefings and through alliances they are building with grassroots organizations.

Bhadelia says the centre will fund research on how to help people debunk online misinformation, including articles and videos posing as science that contain false claims and glaring errors. “The pseudo-academization of conspiracy theories is at its nascent — and that is only going to get worse in the next pandemic,” she says.

But Peter Hotez, a vaccine advocate and scientist at Baylor College of Medicine in Houston, Texas, warns that scientists on their own aren’t equipped to counter the sentiments fuelled by far-right extremists, politicians and media organizations. “I’m on a zillion Zoom calls with scientists to fine-tune our messages, but these are messages in a bottle in the Atlantic Ocean,” he says. “Until there is an appetite among government agencies to take down an anti-science empire — to say it endangers the public — it won’t be heard.”

How can public-health measures be made stronger?

Throughout the pandemic, public-health and infectious-disease researchers have pleaded with leaders to enforce measures to curb COVID-19, often in vain. Bhadelia says a solution to this problem would be granting public-health departments more power during health crises, along with larger and more stable budgets. But, in many places, the opposite is happening.

According to a [May report from the US National Association of County & City Health Officials](#) in Washington DC, at least 15 states have passed or are considering laws to limit the legal authority of public-health agencies.



Will COVID force public health to confront America's epic inequality?

Another issue is that people cannot follow public-health recommendations that compromise their ability to provide food and shelter for themselves and their families. During the pandemic, vast inequality has led to disparities in disease among people who are paid low wages, work or live in crowded environments and don't have adequate labour protections. One study, for example, found an association between income inequality and COVID-19 cases and deaths in US counties⁴.

Addressing inequality — or at least incorporating strong measures to correct inequities during a health emergency — should be a crucial component of pandemic preparedness plans, but such solutions are rarely included, says Nuzzo. “People acknowledge this is important, but see it as too hard to fix,” she says. “We can’t come out of COVID-19 and not have equity be front and centre.”

How can vaccines and medicine reach the people who need them?

Drug companies developed vaccines in record time during COVID-19, and researchers say they could move even faster if early-stage work received more funding. Leading the charge is the Coalition for Epidemic

Preparedness Innovations (CEPI), which is raising money for a 5-year, \$3.5-billion strategy that includes developing vaccines for novel diseases within 100 days. In another proposal, Anthony Fauci, director of the US National Institute of Allergy and Infectious Diseases in Bethesda, Maryland, has suggested creating ‘prototype’ vaccines against about 20 families of viruses to speed up development in case of emergency.



A doctor in Wuhan, China, checks a patient's lung scans for damage in February 2020.Credit: AFP/Getty

However, governments have made little progress when it comes to ensuring that new drugs and vaccines are distributed rapidly around the world. This is evident today, where less than 2% of people in low-income countries have been vaccinated so far — more than seven months after regulators authorized the first vaccines.

Priti Krishtel, a health-justice lawyer and co-founder of the non-profit organization I-MAK, based in New York, says that mechanisms to improve the situation could provide models for future pandemics. Governments could agree to temporarily waive intellectual-property rights on vaccines during a

pandemic so that other manufacturers could help to increase the supply, for example, or policymakers could create rules ensuring that vaccines developed largely with public money are broadly licensed in an emergency.



The race for antiviral drugs to beat COVID — and the next pandemic

However, such agreements require buy-in from multiple countries. The same is true for surveillance, data sharing and other preparedness plans. That's an obstacle, says Stephen Morrison, a vice-president at the Center for Strategic and International Studies, a think tank in Washington DC. He says it's essential to pay attention to how nationalism, US–China tensions and an assault on the WHO paralysed attempts at a global response to COVID-19 in 2020. “We had the biggest global catastrophe since World War Two and yet there was no high-level diplomacy,” he says.

To move forwards, he argues that leaders must restore a degree of cooperation between the United States and China on pandemic preparedness, so that plans attract broad support. Fidler agrees, and adds that a stronger alliance between low- and lower-middle-income countries would lend them more bargaining power on the international stage. The political reality is dire, he says. “I think a lot of people in global health are stuck in the past, and they don't want to face the fact that we are in a very different, more difficult, and more dangerous international system now,” Fidler adds. “Global health has to operate in this, rather than pretend it doesn't exist.”

Despite the complexity, he and others maintain hope. Many world leaders now recognize the devastation that health crises create and are motivated to do something about it. For example, [a July report from a G20 panel](#) calls for \$75 billion in international financing for pandemic prevention and preparedness — twice as much as current spending levels. “There has been a change in consciousness,” Morrison says. “People are watching this horror show and realizing that something has to change.”

Nature **596**, 332-335 (2021)

doi: <https://doi.org/10.1038/d41586-021-02217-y>

References

1. 1.

The Independent Panel for Pandemic Preparedness & Response.
[COVID-19: Make it the Last Pandemic](#) (Independent Panel, 2021).

2. 2.

Hay, A. J. & McCauley, J. W. *Influenza Other Respir. Viruses* **12**, 551–557 (2018).

[PubMed](#) [Article](#) [Google Scholar](#)

3. 3.

Anand, A., Sandefur, J. & Subramanian, A. [Three New Estimates of India's All-Cause Excess Mortality during the COVID-19 Pandemic](#). CGD Working Paper 589 (Center for Global Development, 2021).

[Google Scholar](#)

4. 4.

Tan, A. X., Hinman, J. A., Magid, H. S. A., Nelson, L. M. & Odden, M. C. *JAMA Netw. Open* **4**, e218779 (2021).

[PubMed](#) [Article](#) [Google Scholar](#)

[Download references](#)

Related Articles



- [**Will COVID force public health to confront America's epic inequality?**](#)



- [**Two decades of pandemic war games failed to account for Donald Trump**](#)



- [**The race for antiviral drugs to beat COVID — and the next pandemic**](#)



- [**Pandemic whistle-blower: we need a non-political way to track viruses**](#)



- [**Wanted: rules for pandemic data access that everyone can trust**](#)

Subjects

- [**SARS-CoV-2**](#)

- [Epidemiology](#)
- [Policy](#)

nature careers

[Jobs](#) >

- [Group Leader \(f/m/d\) CRISPR/RNAi Technology for Target Identification \(Screening\) and Validation](#)

Evotec AG

Hamburg, Germany

- [Tier I Canada Research Chair in Infectious Disease & Immunity](#)

The University of British Columbia (UBC)

Vancouver, Canada

- [Clinical Research Nurse/Project Manager](#)

Oklahoma Medical Research Foundation (OMRF)

Oklahoma City, United States

- [Research Associate - Immunologist](#)

The University of British Columbia (UBC)

Vancouver, Canada

Nature Briefing

An essential round-up of science news, opinion and analysis, delivered to your inbox every weekday.

[Download PDF](#)

Related Articles

-  [**Will COVID force public health to confront America's epic inequality?**](#)
-  [**Two decades of pandemic war games failed to account for Donald Trump**](#)
-  [**The race for antiviral drugs to beat COVID — and the next pandemic**](#)
-  [**Pandemic whistle-blower: we need a non-political way to track viruses**](#)
-  [**Wanted: rules for pandemic data access that everyone can trust**](#)

Subjects

- [SARS-CoV-2](#)
- [Epidemiology](#)

- [Policy](#)
-

This article was downloaded by **calibre** from <https://www.nature.com/articles/d41586-021-02217-y>.

| [Section menu](#) | [Main menu](#) |

- NEWS FEATURE
- 17 August 2021

Electric cars and batteries: how will the world produce enough?

Reducing the use of scarce metals — and recycling them — will be key to the world's transition to electric vehicles.

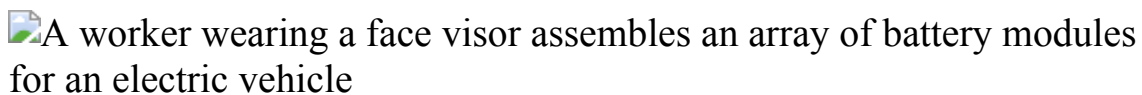
- [Davide Castelvecchi](#)
 1. Davide Castelvecchi
[View author publications](#)

You can also search for this author in [PubMed](#) [Google Scholar](#)





-



Batteries for an electric car are assembled at the Audi production plant in Brussels. Credit: Audi AG

[Download PDF](#)

The age of the electric car is upon us. Earlier this year, the US automobile giant General Motors announced that it aims to stop selling petrol-powered and diesel models by 2035. Audi, based in Germany, plans to stop producing such vehicles by 2033. Many other automotive multinationals have issued

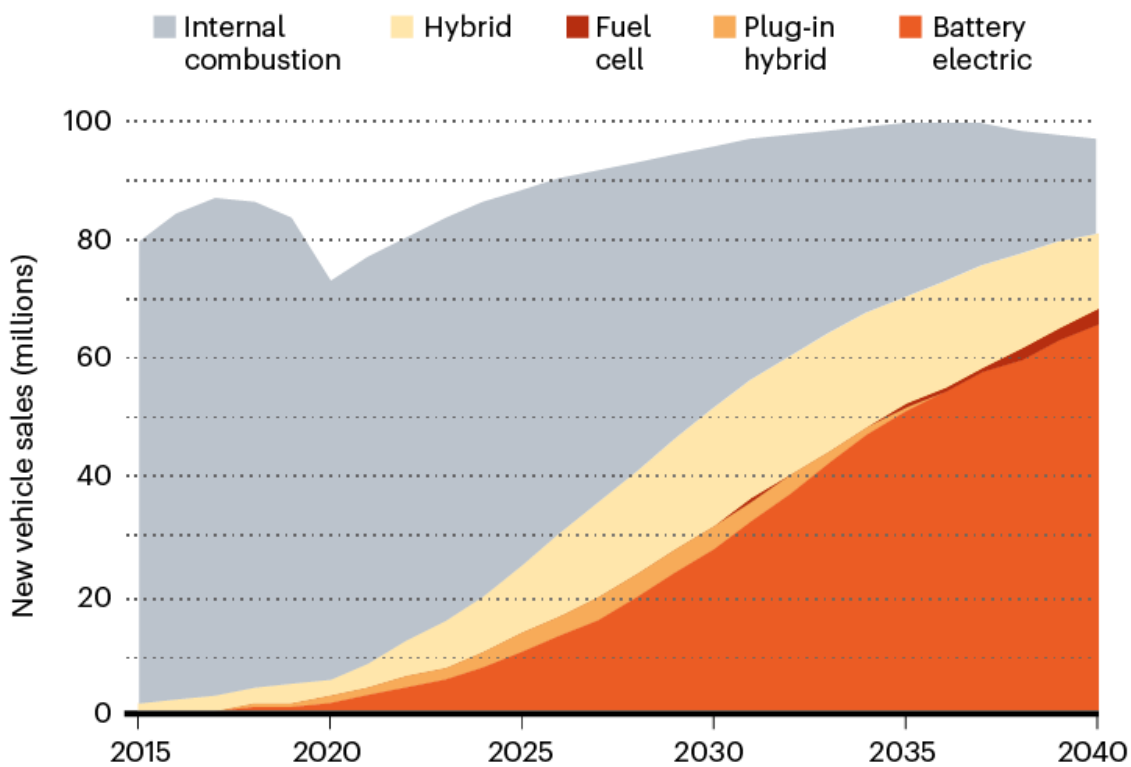
similar road maps. Suddenly, major carmakers' foot-dragging on electrifying their fleets is turning into a rush for the exit.

The electrification of personal mobility is picking up speed in a way that even its most ardent proponents might not have dreamt of just a few years ago. In many countries, government mandates will accelerate change. But even without new policies or regulations, half of global passenger-vehicle sales in 2035 will be electric, according to the BloombergNEF (BNEF) consultancy in London.

This massive industrial conversion marks a “shift from a fuel-intensive to a material-intensive energy system”, declared the International Energy Agency (IEA) in May¹. In the coming decades, hundreds of millions of vehicles will hit the roads, carrying massive batteries inside them (see ‘Going electric’). And each of those batteries will contain tens of kilograms of materials that have yet to be mined.

GOING ELECTRIC

A forecast suggests that by 2035, more than half of new passenger vehicles sold worldwide will be electric, even without further policies to promote switching.



©nature

Source: Ref. 2

Anticipating a world dominated by electric vehicles, materials scientists are working on two big challenges. One is how to cut down on the metals in batteries that are scarce, expensive, or problematic because their mining carries harsh environmental and social costs. Another is to improve battery recycling, so that the valuable metals in spent car batteries can be efficiently reused. “Recycling will play a key role in the mix,” says Kwasi Ampofo, a mining engineer who is the lead analyst on metals and mining at BNEF.

Battery- and carmakers are already spending billions of dollars on reducing the costs of manufacturing and recycling electric-vehicle (EV) batteries — spurred in part by government incentives and the expectation of forthcoming regulations. National research funders have also founded centres to study better ways to make and recycle batteries. Because it is still less expensive,

in most instances, to mine metals than to recycle them, a key goal is to develop processes to recover valuable metals cheaply enough to compete with freshly mined ones. “The biggest talker is money,” says Jeffrey Spangenberger, a chemical engineer at Argonne National Laboratory in Lemont, Illinois, who manages a US federally funded lithium-ion battery-recycling initiative, called ReCell.

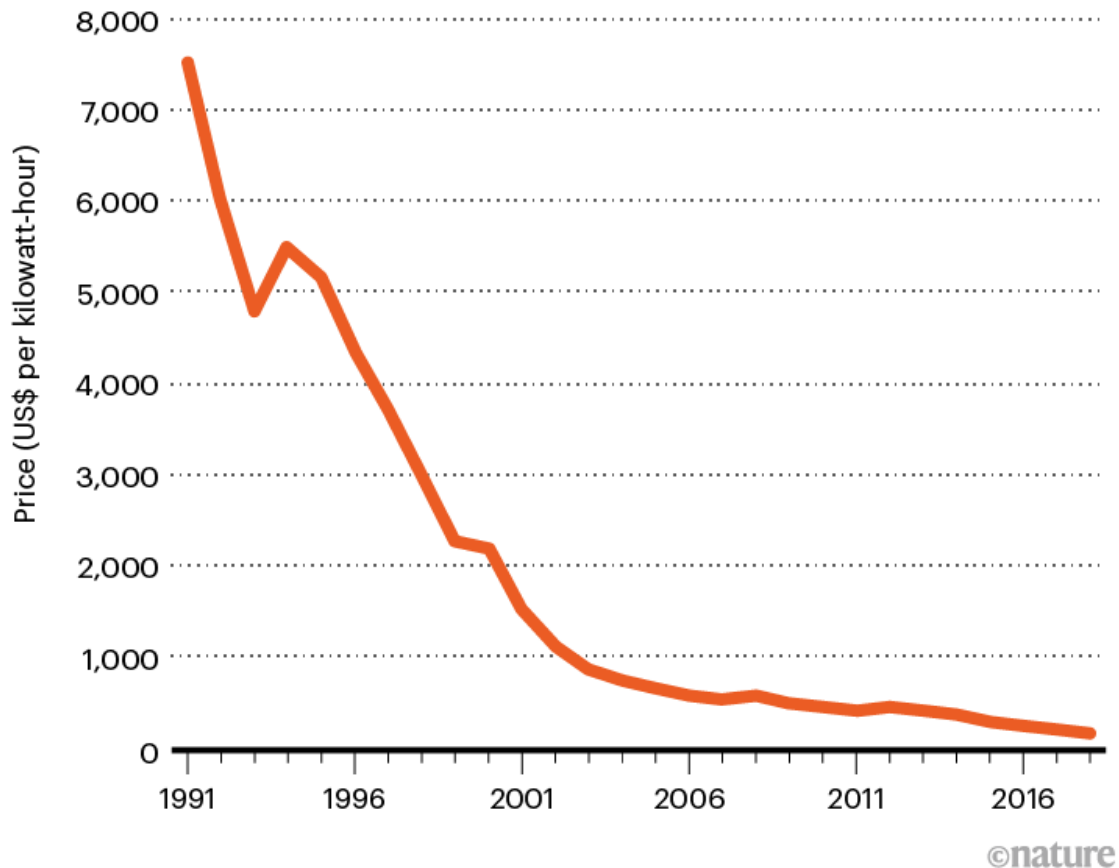
Lithium future

The first challenge for researchers is to reduce the amounts of metals that need to be mined for EV batteries. Amounts vary depending on the battery type and model of vehicle, but a single car lithium-ion battery pack (of a type known as NMC532) could contain around 8 kg of lithium, 35 kg of nickel, 20 kg of manganese and 14 kg of cobalt, according to figures from Argonne National Laboratory.

Analysts don’t anticipate a move away from lithium-ion batteries any time soon: their cost has plummeted so dramatically that they are likely to be the dominant technology for the foreseeable future. They are now 30 times cheaper than when they first entered the market as small, portable batteries in the early 1990s, even as their performance has improved. BNEF projects that the cost of a lithium-ion EV battery pack will fall below US\$100 per kilowatt-hour by 2023, or roughly 20% lower than today (see ‘Plummeting costs of batteries’). As a result, electric cars — which are still more expensive than conventional ones — should reach price parity by the mid-2020s. (By some estimates, electric cars are already cheaper than petrol vehicles over their lifetimes, thanks to being less expensive to power and maintain.)

PLUMMETING COSTS OF BATTERIES

The price of lithium-ion cells has fallen by more than 97% since 1991.



Source: M. S. Ziegler & J. E. Trancik *Energy Environ. Sci.*
<https://doi.org/gfx> (2021).

To produce electricity, lithium-ion batteries shuttle lithium ions internally from one layer, called the anode, to another, the cathode. The two are separated by yet another layer, the electrolyte. Cathodes are the main limiting factor in battery performance — and they are where the most valuable metals lie.

The cathode of a typical lithium-ion battery cell is a thin layer of goo containing micro-scale crystals, which are often similar in structure to minerals that occur naturally in Earth's crust or mantle, such as olivines or spinels. The crystals pair up negatively charged oxygen with positively charged lithium and various other metals — in most electric cars, a mix of

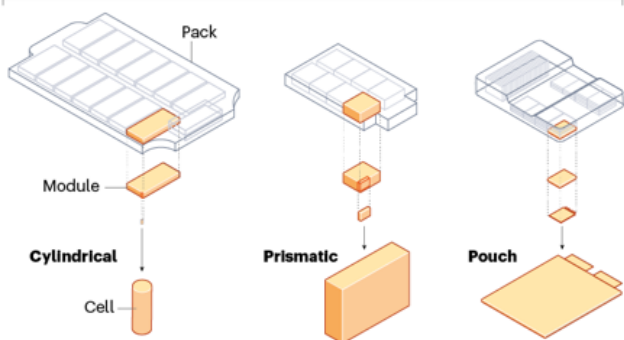
nickel, manganese and cobalt. Recharging a battery rips lithium ions out of these oxide crystals and pulls the ions to a graphite-based anode where they are stored, sandwiched between layers of carbon atoms (see ‘Electric heart’).

ELECTRIC HEART

The battery packs in electric vehicles are built from thousands of cells, with electronics to manage charging and discharging. To prevent overheating, some units include an active cooling system. A battery pack holds tens of kilograms of valuable metals; researchers hope to make recycling them easier and to reduce the amounts needed in future designs.

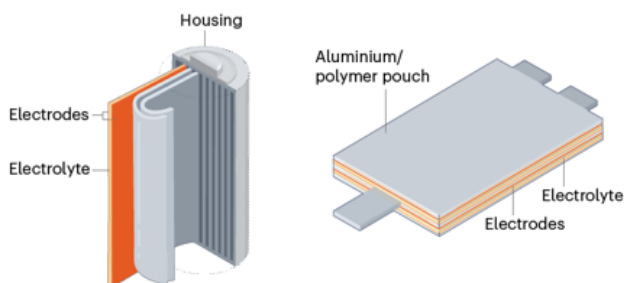
Battery packs

Battery cells come in cylindrical, prismatic and pouch varieties, and are arranged into modules that are assembled into packs. These packs are typically welded and glued together, which makes them hard to take apart at the end of their life cycle.



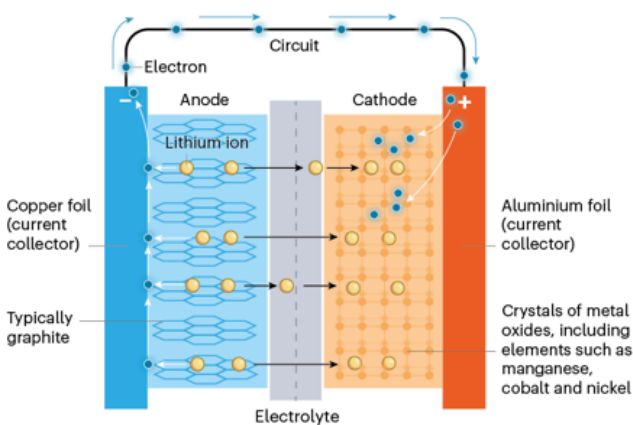
Cell structure

Inside cells, sheet-like electrodes (anodes and cathodes) are curled up or sandwiched together, with an electrolyte taking up the space in between.



Cell chemistry

Lithium-ion cells generate electricity when lithium ions flow from the anode through an electrolyte to the cathode, forcing electrons to flow around an outside circuit. Charging reverses that process.



©nature

Source: Adapted from G. Harper *et al.* *Nature* **575**, 75–86 (2019) and G. Offer *et al.* *Nature* **582**, 485–487 (2020).

Lithium itself is not scarce. A June report by BNEF² estimated that the current reserves of the metal — 21 million tonnes, according to the US Geological Survey — are enough to carry the conversion to EVs through to the mid-century. And reserves are a malleable concept, because they represent the amount of a resource that can be economically extracted at current prices and given current technology and regulatory requirements. For most materials, if demand goes up, reserves eventually do, too.

As cars electrify, the challenge lies in scaling up lithium production to meet demand, Ampofo says. “It’s going to grow by about seven times between 2020 and 2030.”

This could result in temporary shortages and dramatic price swings, he says. But market hiccups will not change the picture in the long term. “As more processing capacity is built, these shortages are likely to work themselves out,” says Haresh Kamath, a specialist in energy storage at the Electric Power Research Institute in Palo Alto, California.



Salt deposits in a lithium production facility at the Uyuni salt flats in Potosí, Bolivia. Credit: Carlos Becerra/Bloomberg/Getty

The increase in lithium mining carries its own environmental concerns: current forms of extraction require copious amounts of energy (for lithium extracted from rock) or water (for extraction from brines). But more-modern techniques that extract lithium from geothermal water, using geothermal energy to drive the process, are considered more benign. And despite this environmental toll, mining lithium will help to displace destructive fossil-fuel extraction.

Researchers are more worried about cobalt, which is the most valuable ingredient of current EV batteries. Two-thirds of global supply are mined in the Democratic Republic of the Congo. Human-rights activists have raised concerns over conditions there, in particular over child labour and harm to workers' health; like other heavy metals, cobalt is toxic if not handled properly. Alternative sources could be exploited, such as the metal-rich 'nODULES' found on the sea floor, but they present their own environmental hazards. And nickel, another major component of EV batteries, could also face shortages³.

Managing metals

To address the issues with raw materials, a number of laboratories have been experimenting with low-cobalt or cobalt-free cathodes. But cathode materials must be carefully designed so that their crystal structures don't break up, even if more than half the lithium ions are removed during charging. And abandoning cobalt altogether often lowers a battery's energy density, says materials scientist Arumugam Manthiram at the University of Texas in Austin, because it alters the cathode's crystal structure and how tightly it can bind lithium.

Manthiram is among the researchers who have solved that problem — at least in the lab — by showing that cobalt can be eliminated from cathodes without compromising performance⁴. "The cobalt-free material we reported has the same crystal structure as lithium cobalt oxide, and therefore the same energy density," or even better, says Manthiram. His team did this by fine-

tuning the way in which cathodes are produced and adding small quantities of other metals — while retaining the cathode's cobalt-oxide crystal structure. Manthiram says it should be straightforward to adopt this process in existing factories, and has founded a start-up firm called TexPower to try to bring it to market within the next two years. Other labs around the world are working on cobalt-free batteries: in particular, the pioneering EV maker Tesla, based in Palo Alto, California, has said it plans to eliminate the metal from its batteries in the next few years.

Sun Yang-Kook at Hanyang University in Seoul, South Korea, is another materials scientist who has achieved similar performance in cobalt-free cathodes. Sun says that some technical problems might remain in creating the new cathodes, because the process relies on refining nickel-rich ores, which can require expensive pure-oxygen atmospheres. But many researchers now consider the cobalt problem essentially solved. Manthiram and Sun "have shown that you can make really good materials without cobalt and [that] perform really well", says Jeff Dahn, a chemist at Dalhousie University in Halifax, Canada.



Workers extract cobalt near a mine between Lubumbashi and Kolwezi, in the Democratic Republic of the Congo. Credit: Federico Scoppa/AFP/Getty

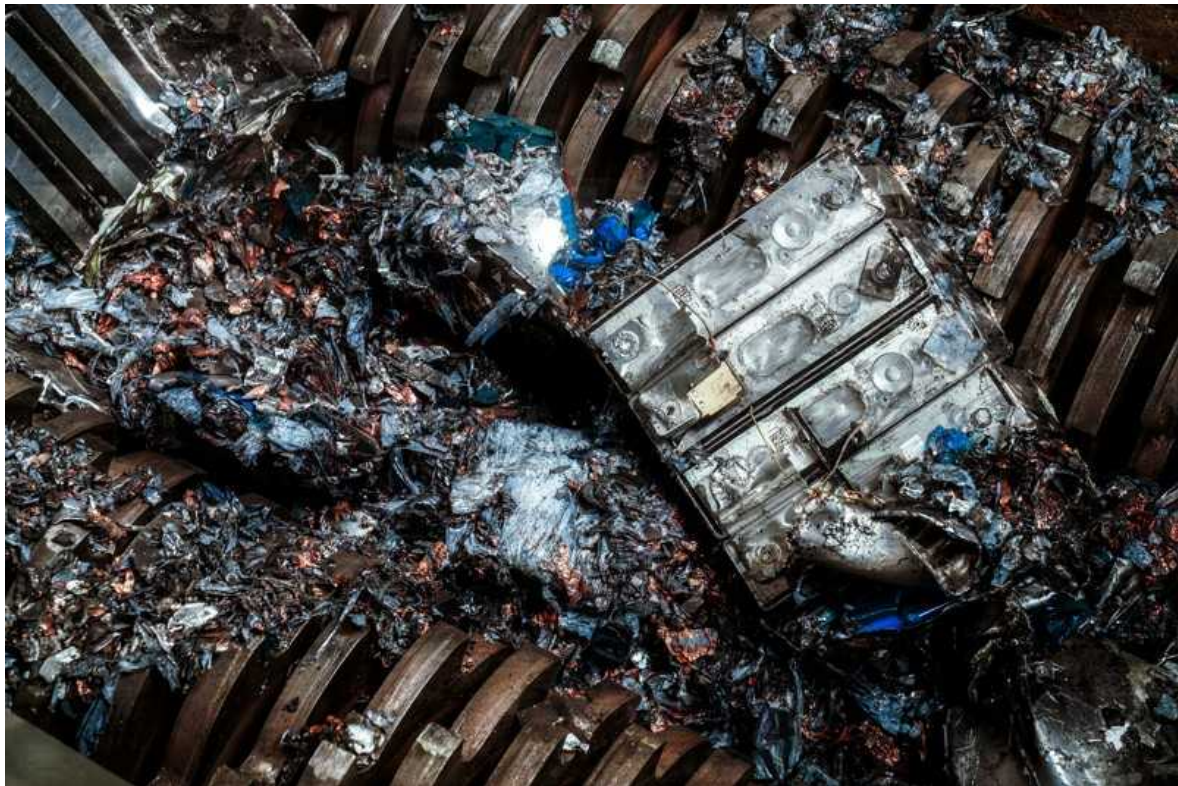
Nickel, although not as expensive as cobalt, isn't cheap, either. Researchers want to remove it as well. "We have addressed the cobalt scarcity, but because we're scaling so rapidly, we are heading straight for a nickel problem," says Gerbrand Ceder, a materials scientist at the Lawrence Berkeley National Laboratory in Berkeley, California. But removing both cobalt and nickel will require switching to radically different crystal structures for cathode materials.

One approach is to adopt materials called disordered rock salts. They get their name because of their cubic crystal structure, which is similar to that of sodium chloride, with oxygen playing the part of chlorine and a mix of heavy metals replacing the sodium. Over the past decade, Ceder's team and other groups have shown that certain lithium-rich rock salts allow the lithium to easily slip in and out — a crucial property to enable repeated charging⁵. But, unlike conventional cathode materials, disordered rock salts do not require cobalt or nickel to remain stable during that process. In particular, they can be made with manganese, which is cheap and plentiful, Ceder says.

Recycle better

If batteries are to be made without cobalt, researchers will face an unintended consequence. The metal is the main factor that makes recycling batteries economical, because other materials, especially lithium, are currently cheaper to mine than to recycle.

In a typical recycling plant, batteries are first shredded, which turns cells into a powdered mixture of all the materials used. That mix is then broken down into its elemental constituents, either by liquefying it in a smelter (pyrometallurgy) or by dissolving it in acid (hydrometallurgy). Finally, metals are precipitated out of solution as salts.



A mechanical shredder grinds up battery modules, here shown at the Duesenfeld recycling plant in Germany. Credit: Wolfram Schroll/Duesenfeld

Research efforts have focused on improving the process to make recycled lithium economically attractive. The vast majority of lithium-ion batteries are produced in China, Japan and South Korea; accordingly, recycling capabilities are growing fastest there. For example, Foshan-based Guangdong Brunn — a subsidiary of CATL, China's largest maker of lithium-ion cells — can recycle 120,000 tonnes of batteries per year, according to a spokesperson. That's the equivalent of what would be used in more than 200,000 cars, and the firm is able to recover most of the lithium, cobalt and nickel. Government policies are helping to encourage this: China already has financial and regulatory incentives for battery companies that source materials from recycling firms instead of importing freshly mined ones, says Hans Eric Melin, managing director of Circular Energy Storage, a consulting company in London.

The European Commission has proposed strict battery-recycling requirements which could be phased in from 2023 — although prospects for the bloc to develop a domestic recycling industry are uncertain⁶. The

administration of US President Joe Biden, meanwhile, wants to spend billions of dollars to foster a domestic EV battery-manufacturing industry and support recycling, but hasn't yet proposed regulations beyond existing legislation classing batteries as hazardous waste that must be safely disposed of. Some North American start-up firms say they can already recover the majority of a battery's metals, including lithium, at costs that are competitive with those of mining them, although analysts say that, at this stage, the overall economics are only advantageous because of the cobalt.



Ground-up battery powder, or 'black mass', gets cleaned from plates at Li-Cycle's battery recycling facility in Kingston, Ontario, Canada. Credit: Christinne Muschi/Bloomberg/Getty

A more radical approach is to reuse the cathode crystals, rather than break down their structure, as hydro- and pyrometallurgy do. ReCell, the US\$15-million collaboration managed by Spangenberger, includes three national labs, three universities and numerous industry players. It is developing techniques that will enable recyclers to extract the cathode crystals and resell them. One crucial step, after the batteries have been shredded, is to separate the cathode materials from the rest using heat, chemicals or other methods.

“The reason we’re so enthusiastic about retaining the crystal structure is that it took a lot of energy and know-how to put that together. That’s where a lot of the value is,” says Linda Gaines, a physical chemist at Argonne and the principal analyst for ReCell.

These reprocessing techniques work with a range of crystal structures and compositions, Gaines says. But if a recycling centre receives a waste stream that includes many types of battery, various types of cathode material will end up in the recycling cauldron. This could complicate efforts to separate out the different cathode-crystal types. Although processes developed by ReCell can easily separate nickel, manganese and cobalt from other kinds of cells, such as those that use lithium iron phosphate, for example, they will have a hard time separating two types that both contain cobalt and nickel, but in different proportions. For this and other reasons, it will be crucial for batteries to carry some kind of standardized barcode that tells recyclers what’s inside, Spangenberger says.



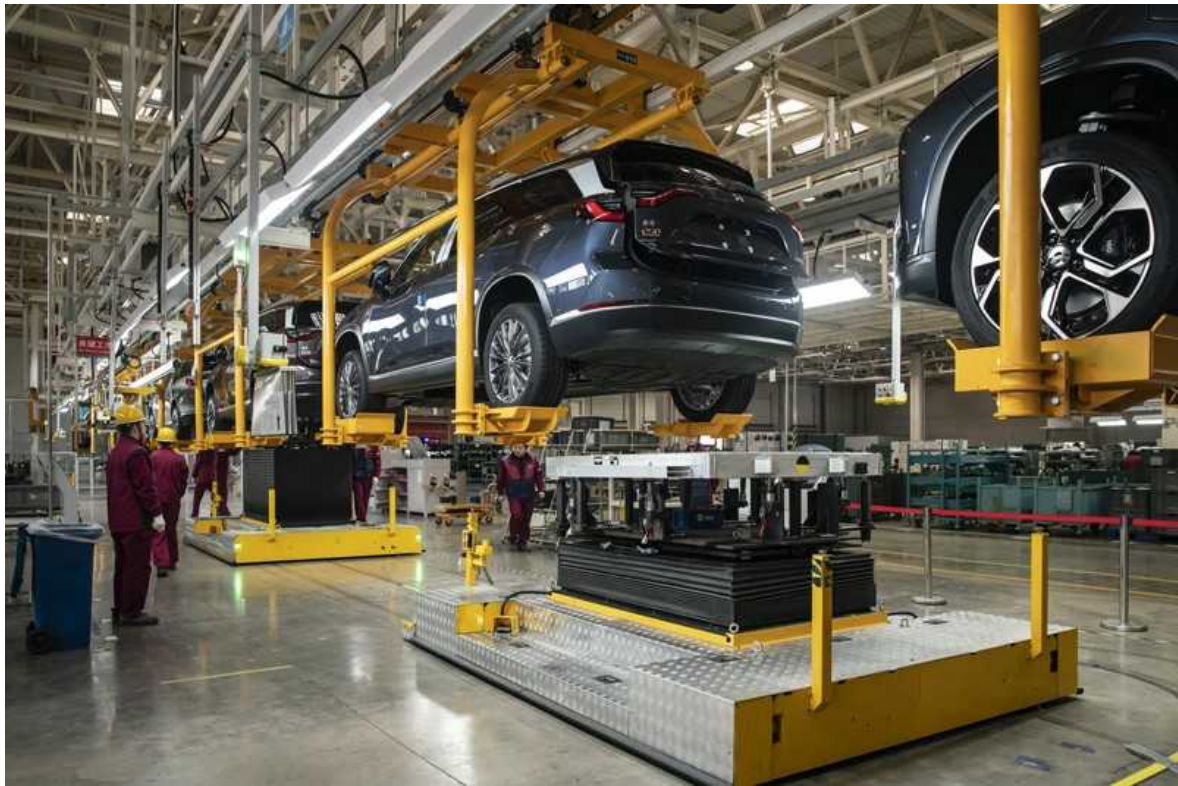
A worker at car firm Renault prepares to dismantle a battery. The firm says it is recycling all its electric vehicle batteries — for the moment, only a couple of hundred a year.Credit: Olivier Guerrin, Photothèque Veolia

Another potential hurdle is that the chemistry of cathodes is constantly evolving. The cathodes that manufacturers will use 10–15 years from now — at the end of the life cycle of present-day cars — could very well be different from today's. The most efficient way to get the materials out could be for the manufacturer to collect its own batteries at the end of the life cycle. And batteries should be designed from the ground up in a way that makes them easier to take apart, Gaines adds.

Materials scientist Andrew Abbott at the University of Leicester, UK, argues that recycling will be much more profitable if it skips the shredding stage and takes the cells apart directly. He and his collaborators have developed a technique for separating out cathode materials using ultrasound⁷. This works best in battery cells that are packed flat rather than rolled up (as common ‘cylindrical’ cells are), and, Abbott adds, can make recycled materials much cheaper than virgin mined metals. He is involved in a £14-million (US\$19-million) UK government research scheme on battery sustainability, called ReLiB.

Crank up the volume

Whichever recycling processes become standard, scale will help. Although media reports tend to describe the coming deluge of spent batteries as a looming crisis, analysts see it as a big opportunity, says Melin. Once millions of large batteries begin to reach the end of their lives, economies of scale will kick in and make recycling more efficient — and the business case for it more attractive.



An electric car production pipeline at Nio's factory in Hefei, China.Credit: Qilai Shen/Bloomberg/Getty

Analysts say the example of lead-acid batteries — the ones that start petrol-powered cars — gives reason for optimism. Because lead is toxic, those batteries are classified as hazardous waste and have to be disposed of safely. But an efficient industry has developed to recycle them instead, even though lead is cheap. “Over 98% of lead-acid batteries are recovered and recycled,” Kamath says. “The value of a lead-acid battery is even lower than a lithium-ion battery. But because of volume, it makes sense to recycle anyway,” Melin says.

It might take a while until the market for lithium-ion batteries reaches its full size, in part because these batteries have become exceptionally durable: present car batteries might last up to 20 years, Kamath says. In a typical electric car sold today, the battery pack will outlive the vehicle it was built into, says Melin.

That means that when old EVs are sent to scrap, the batteries are often neither thrown away nor recycled. Instead, they are taken out and reused for

less-demanding applications, such as stationary energy storage or powering boats. After ten years of use, a car battery such as the Nissan Leaf's, which originally held 50 kilowatt-hours, will have lost at most 20% of its capacity.

Another May report from the IEA, an organization noted for its historically cautious forecasts, included a road map⁸ to achieve global net-zero emissions by mid-century, which includes conversion to electric transport as a cornerstone. The confidence that this is achievable reflects a growing consensus among policymakers, researchers and manufacturers that challenges to electrifying cars are now entirely solvable — and that if we want to have any hope of keeping climate change to a manageable level, there is no time to lose.

But some researchers complain that electric vehicles seem to be held to an impossible standard in terms of the environmental impact of their batteries. “It would be unfortunate and counterproductive to discard a good solution by insisting on a perfect solution,” says Kamath. “That does not mean, of course, that we should not work aggressively on the battery disposal question.”

Nature **596**, 336-339 (2021)

doi: <https://doi.org/10.1038/d41586-021-02222-1>

References

1. 1.

International Energy Agency. *The Role of Critical Minerals in Clean Energy Transitions* (IEA, 2021); available at <https://www.iea.org/reports/the-role-of-critical-minerals-in-clean-energy-transitions>

[Google Scholar](#)

2. 2.

BloombergNEF. *Electric Vehicle Outlook 2021* (BNEF, 2021); available at <https://about.bnef.com/electric-vehicle-outlook>

[Article](#) [Google Scholar](#)

3. 3.

Baars, J., Domenech, T., Bleischwitz, R., Melin, H. E. & Heidrich, O. *Nature Sustain.* **4**, 71–79 (2021).

[Article](#) [Google Scholar](#)

4. 4.

Li, W., Lee, S. & Manthiram, A. *Adv. Mater.* **32**, 2002718 (2020).

[Article](#) [Google Scholar](#)

5. 5.

Yang, J. H., Kim, H. & Ceder, G. *Molecules* **26**, 3173 (2021).

[PubMed](#) [Article](#) [Google Scholar](#)

6. 6.

Melin, H. E. *et al.* *Science* **373**, 384–387 (2021).

[Article](#) [Google Scholar](#)

7. 7.

Lei, C. *et al.* *Green Chem.* **23**, 4710–4715 (2021).

[Article](#) [Google Scholar](#)

8. 8.

International Energy Agency. *Net Zero by 2050: A Roadmap for the Global Energy Sector* (IEA, 2021); available at

<https://www.iea.org/reports/net-zero-by-2050>

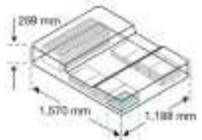
[Google Scholar](#)

[Download references](#)

Related Articles



- [Lithium-ion batteries need to be greener and more ethical](#)



- [Recycling lithium-ion batteries from electric vehicles](#)

Subjects

- [Chemistry](#)
- [Energy](#)
- [Technology](#)
- [Materials science](#)

nature careers

[Jobs](#) >

- [Group Leader \(f/m/d\) CRISPR/RNAi Technology for Target Identification \(Screening\) and Validation](#)

Evotec AG

Hamburg, Germany

- [**Tier I Canada Research Chair in Infectious Disease & Immunity**](#)

The University of British Columbia (UBC)

Vancouver, Canada

- [**Clinical Research Nurse/Project Manager**](#)

Oklahoma Medical Research Foundation (OMRF)

Oklahoma City, United States

- [**Research Associate - Immunologist**](#)

The University of British Columbia (UBC)

Vancouver, Canada

Nature Briefing

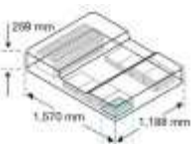
An essential round-up of science news, opinion and analysis, delivered to your inbox every weekday.

[Download PDF](#)

Related Articles



- [**Lithium-ion batteries need to be greener and more ethical**](#)



- [Recycling lithium-ion batteries from electric vehicles](#)

Subjects

- [Chemistry](#)
- [Energy](#)
- [Technology](#)
- [Materials science](#)

This article was downloaded by **calibre** from <https://www.nature.com/articles/d41586-021-02222-1>

| [Section menu](#) | [Main menu](#) |

Books & Arts

- **[Can start-ups fast-track fusion energy?](#)** [16 August 2021]
Book Review • The drive to net zero has changed the calculus of the Promethean dream.
 - **[Amazing ants, brain maps, and mammals before the dinosaurs: Books in brief](#)** [11 August 2021]
Book Review • Andrew Robinson reviews five of the week's best science picks.
-

- BOOK REVIEW
- 16 August 2021

Can start-ups fast-track fusion energy?

The drive to net zero has changed the calculus of the Promethean dream.

- [Melanie Windridge](#) ⁰
 1. [Melanie Windridge](#)

1. Melanie Windridge is UK director of the Fusion Industry Association and founder of Fusion Energy Insights, based in London.

[View author publications](#)

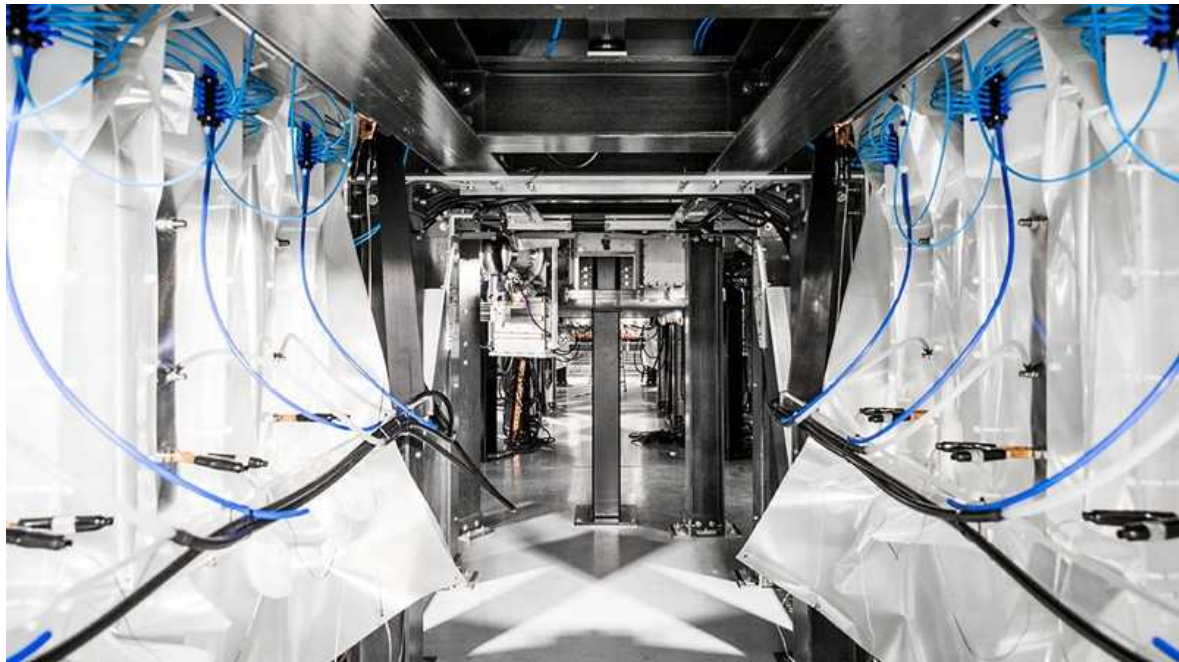
You can also search for this author in [PubMed](#) [Google Scholar](#)





•

[Download PDF](#)



First Light Fusion fires projectiles into a fusion target at around 15 kilometres per second.Credit: First Light Fusion

The Star Builders: Nuclear Fusion and the Race to Power the Planet

Arthur Turrell Scribner (2021)

To help the world reach net-zero emissions by 2050, Nick Hawker is betting on nuclear fusion. Co-founder of the start-up First Light Fusion, he says: “We need to be building plants, multiple, in the 2040s. And the first of a kind has to be built in the 2030s. Which means the physics problem has to be solved in the 2020s.” This pressure is the subject of *The Star Builders* — a book about those trying to harness the phenomenon that powers the Sun, as a source of almost limitless energy.

For decades, the quest for fusion power was a story of two government-funded pathways, culminating in mega projects: the US National Ignition Facility (NIF) and the international ITER collaboration, under construction in France. This history was detailed in Daniel Clery’s book *A Piece of the Sun* in 2013. Back then, some fusion start-up companies existed, but they weren’t taken seriously.



[After COVID-19, green investment must deliver jobs to get political traction](#)

Times have changed, technologies have changed and the stakes have changed. With global temperature rises now bringing floods and fires to every door, the need for emissions-free energy production has never been clearer. Arthur Turrell takes a good look at some of the 25 or so private fusion companies pushing towards commercialization, and appraises them alongside the public projects. Be it University of Oxford spin-off First Light Fusion in Yarnton, UK, smashing a projectile from a rail gun into a target, or Jeff Bezos-backed General Fusion in Burnaby, Canada, compressing magnetized plasma with pistons, he shows how private companies with different ideas, new kit and an eye on the bottom line are re-energizing the field.

Turrell's background is in plasma physics. (Full disclosure: we did our PhDs at Imperial College London around the same time, and I'm mentioned in the book's acknowledgements.) Now, he's a data scientist at the UK Office for National Statistics and the Bank of England. His is a clear and interesting introduction to the history, physics and economics of harnessing the energy produced by melding the nuclei of light atoms to make heavier ones. He argues that "investors are betting that private companies can succeed where governments have failed". I take slight issue with this framing, but more on that later.

Passion and expertise

So who are the people involved in the challenge — the star builders? We meet ex-astronaut Jeff Wisoff, who is now responsible for the safe operation of the NIF in Livermore, California. Jonathan Carling explains what drew him to become chief executive of Tokamak Energy in Milton Park, UK, after working in engineering at Rolls-Royce (he has since left Tokamak Energy). These characters' passion and expertise remind us that there are social and political factors affecting how fast this field can move, as well as technical and scientific ones.

Powerful statistics conjure the scale of the energy problem. Some 86% of the world's energy is still generated by fossil fuels. Air pollution is thought to contribute to the deaths of 8.8 million people worldwide each year, and Earth hasn't seen carbon dioxide levels this high for at least 800,000 years. Turrell quotes Ian Chapman, chief executive of the UK Atomic Energy Authority, as saying that in 2050, "We're going to need half as much energy again as we use now." Fusion could be a much-needed contributor. But no one has achieved the crucial milestone of break-even, the point at which the vast energy needed to create fusion reactions — which must run at temperatures of hundreds of millions of degrees — is recouped by the energy released.



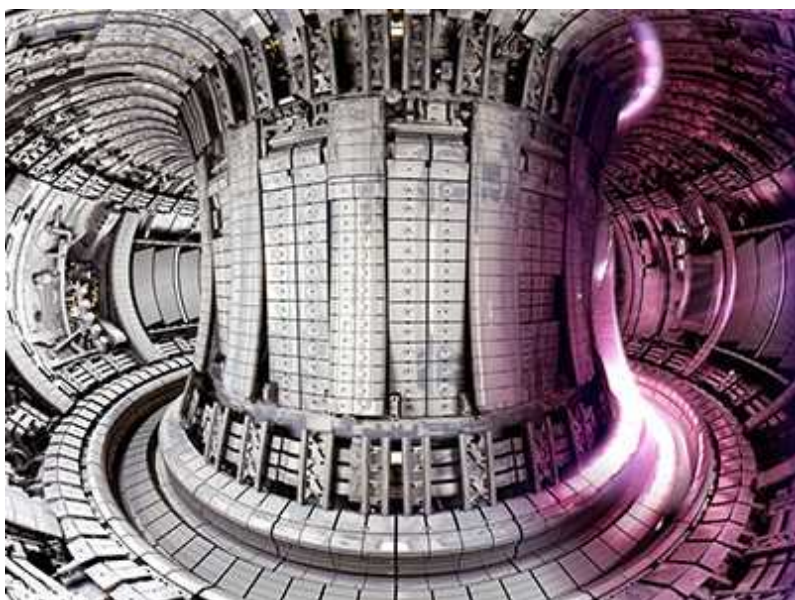
General Fusion in Canada uses steam-powered pistons to compress plasma to fusion conditions.Credit: General Fusion

Analogies also enliven the text. The hot plasma of deuterium and tritium in a tokamak — a multi-tonne magnetic toroid that is the most advanced method of containing controlled fusion reactions — has to be pure. So pure that vacuuming out all the other particles is like “removing all but a single star from the Milky Way”. Passengers cramming into a train carriage during rush hour (remember that?) come to represent increasing plasma density. Bremsstrahlung — radiation emitted by one charged particle as it is deflected by another — is like the wave when a speedboat turns.

But a ‘public versus private’ conceit is too simplistic. Start-ups, Turrell writes “are proposing to use millions of dollars, and some crazy ideas, to do what billions of dollars, and decades of scientific investigation, have been unable to”. In fact, the firms are building on foundations laid down by national laboratories and university research.

Audacious partnerships

Developing and integrating the technologies needed to form a working and economical fusion power plant is beyond the current scope of one company or public lab. The next phase could be like the public–private partnerships between NASA and companies SpaceX and Orbital Sciences to develop commercial transportation for the International Space Station, in which cost and risk were shared.



[Fuel for world’s largest fusion reactor ITER is set for test run](#)

Decades of investment in collaborative programmes such as ITER, the NIF and the Joint European Torus in Oxfordshire, UK, plus programmes in plasma physics and high-energy-density physics, have brought fusion science to a point at which start-ups are commercializing ideas and new technologies. Now, governments are introducing programmes to stimulate

the public and private sectors to work together. The key question is how best to make these partnerships flourish.

Star builders are optimistic by nature — you'd have to be, to tackle something so audacious. As a result, unrealistic timescales and over-promising have dogged fusion since the 1950s. More discussion on this would have been welcome. How much will fusion energy cost? And how long until it is powering our homes? The answers don't yet exist. But investors, governments, utility companies and the public can be forgiven for wanting answers — and the scientists for trying to provide them.

The discussion of the dangers of fusion is thoughtful and illuminating, from the low-to-zero possibilities of weapons proliferation or meltdown to the real risks from the radioactivity that high-energy neutrons create. Objectively, Turrell compares the numbers of deaths per exajoule of energy generated by current sources such as fossil fuels, renewables and nuclear fission. Fusion emerges as much safer than any of them.

In the end, *The Star Builders* is realistic and positive — an interesting snapshot of the current situation and key players. And, as if the challenge of clean energy weren't enough, Turrell has one last stretch for our imagination: to fusion propulsion for space travel. Humanity, he shows, is always reaching for the stars.

Nature **596**, 341-342 (2021)

doi: <https://doi.org/10.1038/d41586-021-02203-4>

Competing Interests

M.W. acts as a consultant for Tokamak Energy, one of the private companies featured in the book, and is UK director of the Fusion Industry Association (consultant rather than employee), which is the organization that represents private fusion companies.

Related Articles



- [After COVID-19, green investment must deliver jobs to get political traction](#)



- [Fuel for world's largest fusion reactor ITER is set for test run](#)



- [Lessons from cold fusion, 30 years on](#)



- [Pull together for fusion](#)

Subjects

- [Physics](#)
- [Energy](#)

nature careers

[Jobs](#) >

- [Group Leader \(f/m/d\) CRISPR/RNAi Technology for Target Identification \(Screening\) and Validation](#)

Evotec AG

Hamburg, Germany

- [**Tier I Canada Research Chair in Infectious Disease & Immunity**](#)

The University of British Columbia (UBC)

Vancouver, Canada

- [**Clinical Research Nurse/Project Manager**](#)

Oklahoma Medical Research Foundation (OMRF)

Oklahoma City, United States

- [**Research Associate - Immunologist**](#)

The University of British Columbia (UBC)

Vancouver, Canada

Nature Briefing

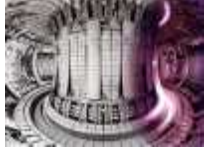
An essential round-up of science news, opinion and analysis, delivered to your inbox every weekday.

[Download PDF](#)

Related Articles



- [**After COVID-19, green investment must deliver jobs to get political traction**](#)

-  Fuel for world's largest fusion reactor ITER is set for test run
-  Lessons from cold fusion, 30 years on
-  Pull together for fusion

Subjects

- Physics
- Energy

This article was downloaded by **calibre** from <https://www.nature.com/articles/d41586-021-02203-4>

| [Section menu](#) | [Main menu](#) |

- BOOK REVIEW
- 11 August 2021

Amazing ants, brain maps, and mammals before the dinosaurs: Books in brief

Andrew Robinson reviews five of the week's best science picks.

- [Andrew Robinson](#) 0
 - 1. [Andrew Robinson](#)
 - 1. Andrew Robinson's many books include *Lost Languages: The Enigma of the World's Undeciphered Scripts* and *Einstein on the Run: How Britain Saved the World's Greatest Scientist*. He is based in London.

[View author publications](#)

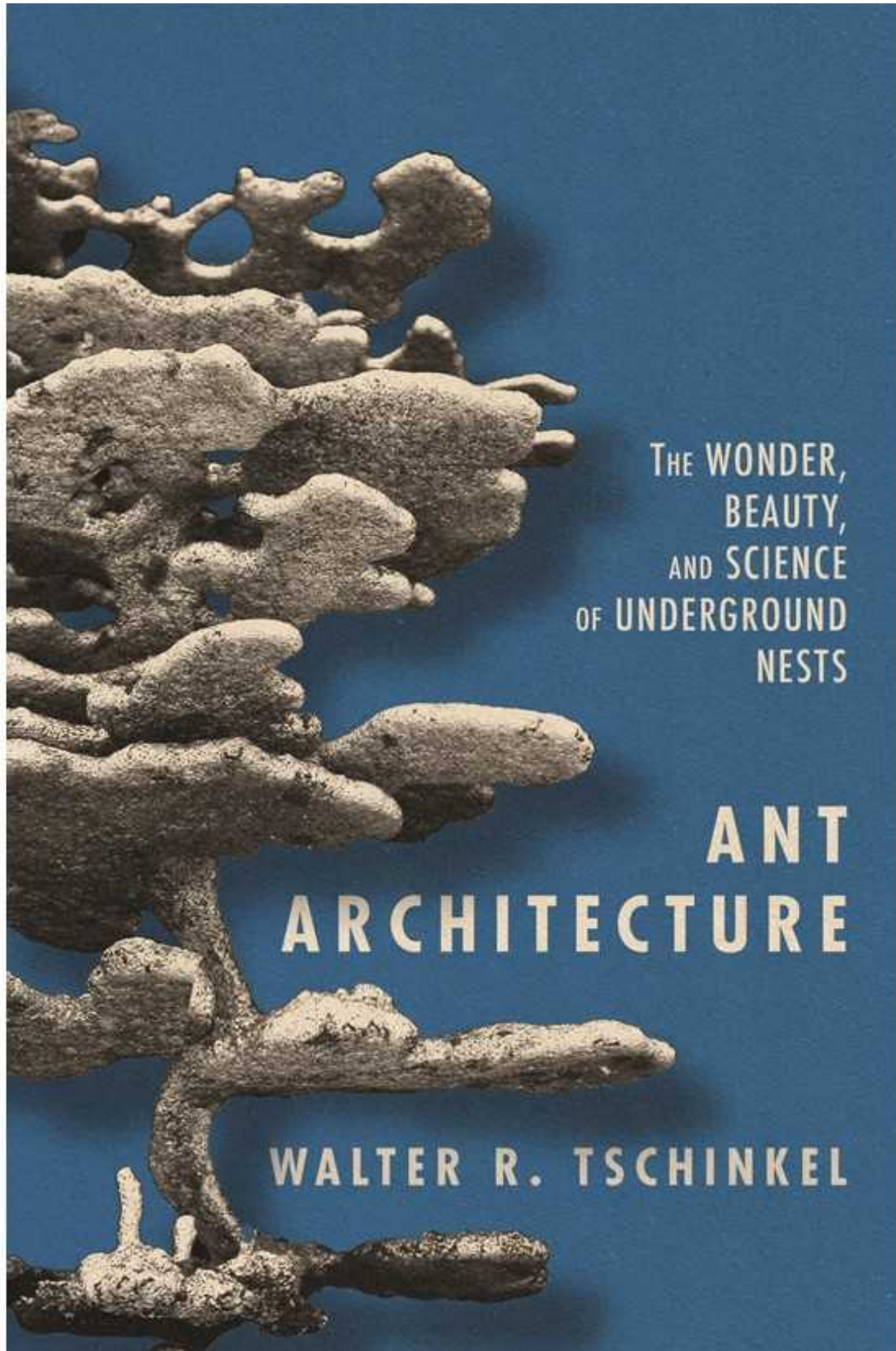
You can also search for this author in [PubMed](#) [Google Scholar](#)





•

[Download PDF](#)



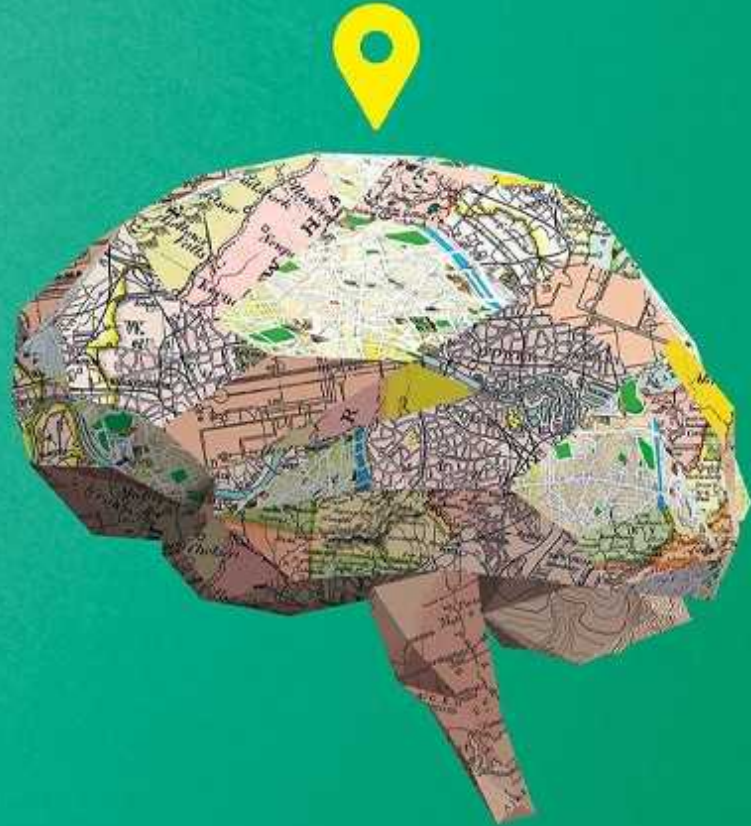
Ant Architecture

Walter R. Tschinkel *Princeton Univ. Press* (2021)

About 14,000 ant species are known, including 1,400 from Brazil. Their behaviour is intriguing. For example, to protect their nest at night, a few sterile *Forelius pusillus* workers conceal the entrance from outside with debris; they then march into the desert and die. Myrmecologist Walter Tschinkel focuses on his excavation of Florida nests in a highly personal, sometimes witty memoir flavoured with soil science, physics and chemistry. But, he admits, “most of the central mysteries of ant nests remain intact”, such as how the insects organize their digging.

'Profoundly illuminating ... a complete inspiration' Cass R. Sunstein

brainscapes



An Atlas of
Your Life on Earth

REBECCA SCHWARZLOSE

Brainscapes

Rebecca Schwarzlose *Profile* (2021)

If each human brain neuron were connected randomly to the other 86 billion, notes neuroscientist Rebecca Schwarzlose, the brain would be more than 20 kilometres wide. Instead, they link through maps of the “body, senses, movements, and crucial sources of information”. These “brainscapes” are the complex, partially understood subject of her clear, often vivid history. Much evidence derives from people with brain damage or other conditions, such as blind children who can remap their visual cortex for uses such as language processing.

—A HISTORY OF—
**WORLD
EGYPTOLOGY**

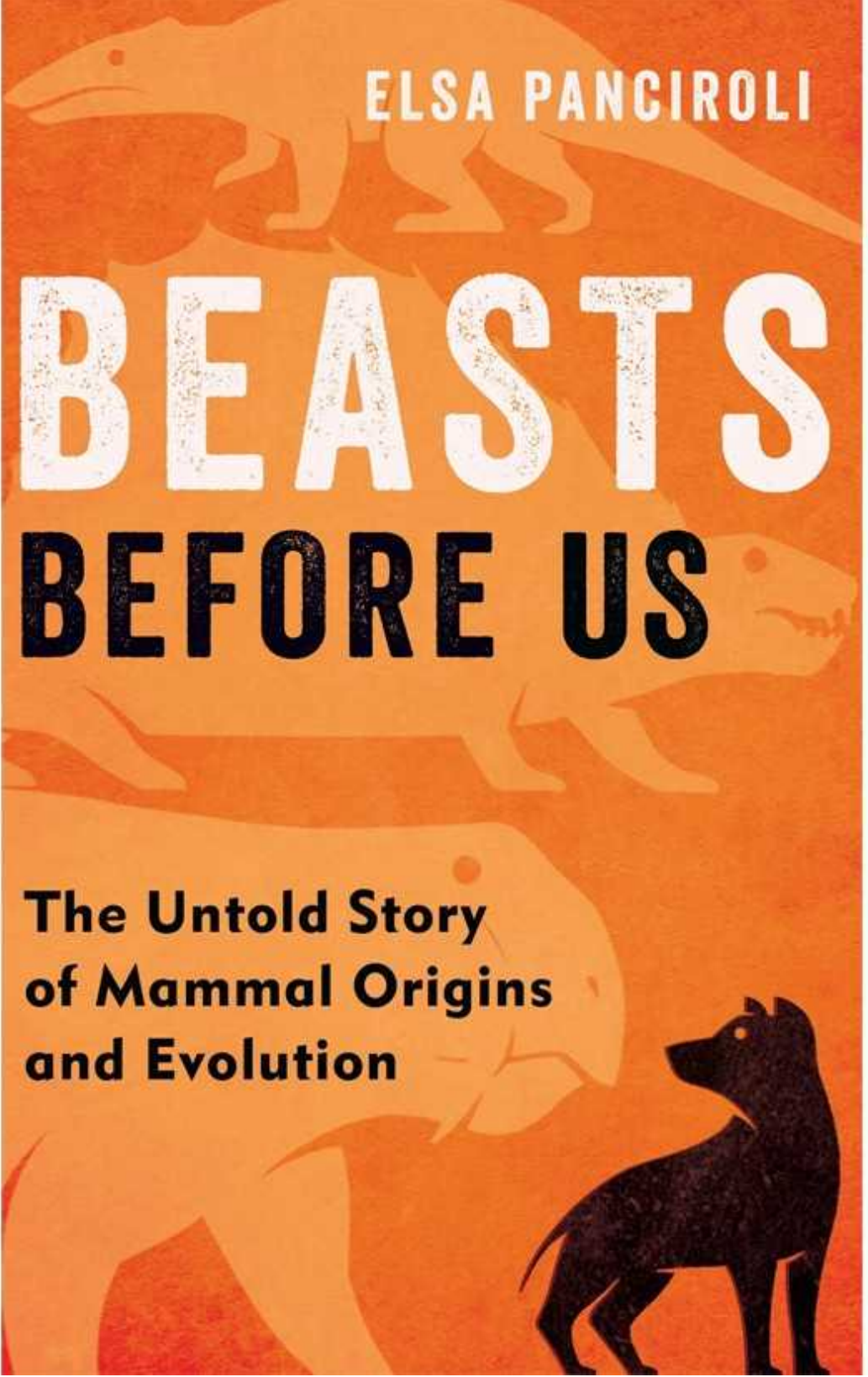
EDITED BY
ANDREW BEDNARSKI, AIDAN DODSON
AND SALIMA IKRAM



A History of World Egyptology

Edited by Andrew Bednarski, Aidan Dodson & Salima Ikram *Cambridge Univ. Press* (2021)

Egyptology began in an international atmosphere, with rival French and English researchers deciphering hieroglyphs in 1814–23, and a French–Italian expedition visiting Egypt in 1828–29. So it is appropriate that this encyclopedic history, with contributions from 19 nations, should analyse the subject's development globally, country by country. It is both immensely detailed and generally accessible, despite failing to include the Rosetta Stone in its copious index.



ELSA PANCIROLI

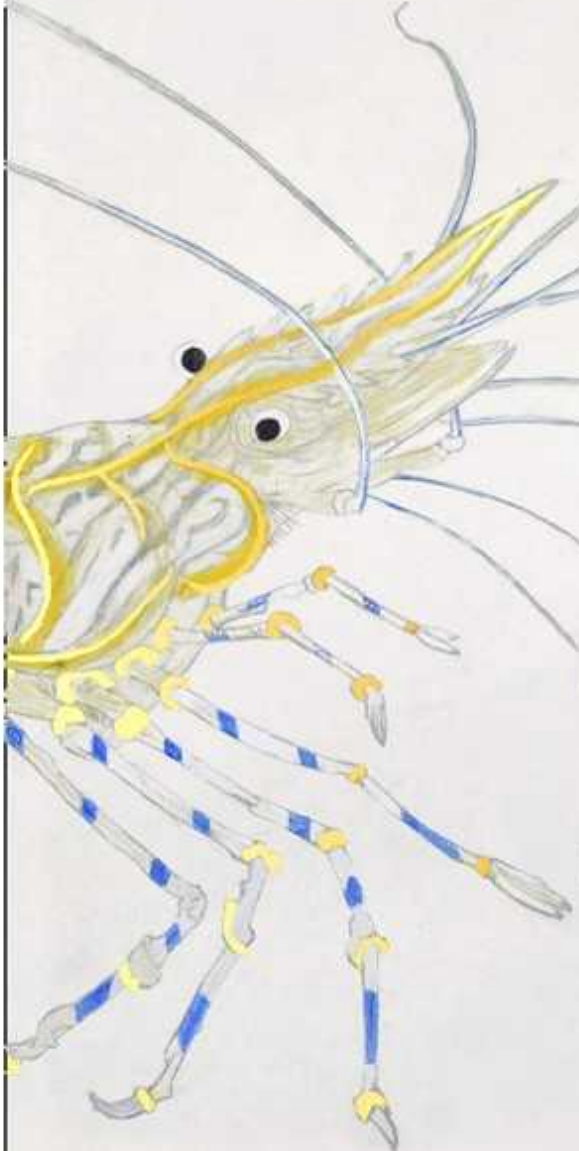
BEASTS BEFORE US

**The Untold Story
of Mammal Origins
and Evolution**

Beasts Before Us

Elsa Panciroli *Bloomsbury Sigma* (2021)

This pioneering study of the origin of mammals by palaeontologist Elsa Panciroli presents radical worldwide research from the past 20 years, based on new fossils and technologies. “If you thought it all began with the extinction of the non-bird dinosaurs” after a catastrophic asteroid impact 66 million years ago, says Panciroli, “think again.” Mammals go back much further. They first diverged from reptiles and birds in the Carboniferous period, more than 300 million years ago — long before the rise of the dinosaurs.



THE
SEA
IS
NOT
MADE
OF
WATER

Life Between
the Tides

ADAM
NICOLSON

The Sea is Not Made of Water

Adam Nicolson *William Collins* (2021)

Writer Adam Nicolson's latest nature book concerns the seashore. The intertidal zone, he reflects, is one of the most revelatory habitats on earth. Inspired by the Victorians, he uses poetry and science to engagingly chart his creation of new rock pools near his wife's family home in Scotland. They are, he writes, "governed by the movement of the planets; philosophical understandings can be applied to the ecology of invertebrates; the life of the crabs is attuned to the tides."

Nature **596**, 342 (2021)

doi: <https://doi.org/10.1038/d41586-021-02176-4>

Competing Interests

The author declares no competing interests.

Subjects

- [Arts](#)
- [Culture](#)

nature careers

[Jobs](#) >

- [Group Leader \(f/m/d\) CRISPR/RNAi Technology for Target Identification \(Screening\) and Validation](#)

Evotec AG

Hamburg, Germany

- [Tier I Canada Research Chair in Infectious Disease & Immunity](#)

The University of British Columbia (UBC)

Vancouver, Canada

- [**Clinical Research Nurse/Project Manager**](#)

Oklahoma Medical Research Foundation (OMRF)

Oklahoma City, United States

- [**Research Associate - Immunologist**](#)

The University of British Columbia (UBC)

Vancouver, Canada

Nature Briefing

An essential round-up of science news, opinion and analysis, delivered to your inbox every weekday.

[Download PDF](#)

Subjects

- [**Arts**](#)
- [**Culture**](#)

This article was downloaded by **calibre** from <https://www.nature.com/articles/d41586-021-02176-4>

Opinion

- **Track disability in COVID-19 statistics** [17 August 2021]
Correspondence •
- **Bespoke open databases would be cheaper and easier to analyse** [17 August 2021]
Correspondence •
- **Richly resourced researchers: work with developing-world scientists** [17 August 2021]
Correspondence •
- **Use photos of Black doctors and patients to heal not hurt**
[17 August 2021]
Correspondence •

- CORRESPONDENCE
- 17 August 2021

Track disability in COVID-19 statistics

- [Fei Qi](#) [ORCID: http://orcid.org/0000-0002-6893-2758](http://orcid.org/0000-0002-6893-2758) 

1. [Fei Qi](#)

1. Hainan University, Haikou, China.

[View author publications](#)

You can also search for this author in [PubMed](#) [Google Scholar](#)





•

[Download PDF](#)

The 2006 UN Convention on the Rights of Persons with Disabilities stipulates that parties to the convention should use statistical data to formulate and implement policies that “address the barriers faced by persons with disabilities in exercising their rights”. Yet, more than a year into the pandemic, very few public-health or medical institutions are recording the disability status of those who contract COVID-19.

Before the pandemic, an estimated 15% of the global population had a disability (see go.nature.com/3xbjqu3). COVID-19 is now adding to those

ranks apace. Even so, most institutions (including US public-health authorities) continue to rely on other statistical indicators — such as the age, sex and ethnicity of those who test positive — in formulating COVID-19 policy.

This dearth of data makes it harder to gauge the impact of COVID-19 on people with disabilities and to study the effects of legal and policy interventions. Australia, for example, does not mention disabled people in its COVID-19 emergency-response plan ([A. Kavanagh et al. *Disabil. Health J.* 14, 101050; 2021](#)).

When such data do exist, they indicate that disabled people are disproportionately affected. In the United Kingdom, for example, their risk of death from COVID-19 was around 2–3 times higher than that for non-disabled people. Even after normalizing for age, geography, co-morbidities, sex and residence type, a raised risk remained (see go.nature.com/3arf76s).

Nature **596**, 343 (2021)

doi: <https://doi.org/10.1038/d41586-021-02233-y>

Competing Interests

The author declares no competing interests.

Related Articles

- [See more letters to the editor](#)

Subjects

- [SARS-CoV-2](#)
- [Public health](#)
- [Research data](#)

Jobs >

- [**Group Leader \(f/m/d\) CRISPR/RNAi Technology for Target Identification \(Screening\) and Validation**](#)

Evotec AG

Hamburg, Germany

- [**Tier I Canada Research Chair in Infectious Disease & Immunity**](#)

The University of British Columbia (UBC)

Vancouver, Canada

- [**Clinical Research Nurse/Project Manager**](#)

Oklahoma Medical Research Foundation (OMRF)

Oklahoma City, United States

- [**Research Associate - Immunologist**](#)

The University of British Columbia (UBC)

Vancouver, Canada

Nature Briefing

An essential round-up of science news, opinion and analysis, delivered to your inbox every weekday.

[Download PDF](#)

Related Articles

- [See more letters to the editor](#)

Subjects

- [SARS-CoV-2](#)
- [Public health](#)
- [Research data](#)

This article was downloaded by **calibre** from <https://www.nature.com/articles/d41586-021-02233-y>.

| [Section menu](#) | [Main menu](#) |

- CORRESPONDENCE
- 17 August 2021

Bespoke open databases would be cheaper and easier to analyse

- [Nikolaus Obweger](#) ORCID: <http://orcid.org/0000-0003-3404-1989>⁰
- [Henrik M. Rønnow](#) ORCID: <http://orcid.org/0000-0002-8832-8865>¹
&
- [Tomoko Yokoi](#) ORCID: <http://orcid.org/0000-0002-6671-2946>²

1. Nikolaus Obweger

1. Bern University of Applied Sciences, Bern, Switzerland

[View author publications](#)

You can also search for this author in [PubMed](#) [Google Scholar](#)

2. Henrik M. Rønnow

1. Institute of Physics, École Polytechnique Fédérale de Lausanne,
Switzerland.

[View author publications](#)

You can also search for this author in [PubMed](#) [Google Scholar](#)

3. [Tomoko Yokoi](#)

1. IMD Business School, Lausanne, Switzerland.

[View author publications](#)

You can also search for this author in [PubMed](#) [Google Scholar](#)

-



•

[Download PDF](#)

The open-data movement encourages the sharing and interlinking of heterogeneous research data through large infrastructures. We argue that a greater number of smaller databases for similar or related research domains could cut the financial, environmental, social and governance costs involved.

All-inclusive data repositories need large up-front investments and continued funding (see go.nature.com/3xvk0yp). Their energy consumption is huge, and significant work is needed to reformat vast amounts of data for

easy sharing. The organization of deposited data can also vary and create confusion ([Y. Demchenko *et al. Int. Conf. Collab. Technol. Syst.* 48–55; IEEE, 2013](#)).

Streamlining data according to research domain and using a single format would simplify data processing and analysis, and be cheaper to run. These bespoke databases must not be balkanized: for example, different types of wildfire data — from the atmosphere, the ground or modelling, say — would need to be lodged in a single repository in one format. This approach can better tailor incentivizing mechanisms for data sharing. For instance, experiments at large facilities, such as synchrotrons, increasingly make their data available through citable DOIs.

Nature **596**, 343 (2021)

doi: <https://doi.org/10.1038/d41586-021-02234-x>

Competing Interests

The authors declare no competing interests.

Related Articles

- [See more letters to the editor](#)

Subjects

- [Research data](#)
- [Databases](#)

nature careers

[Jobs](#) >

- [Group Leader \(f/m/d\) CRISPR/RNAi Technology for Target Identification \(Screening\) and Validation](#)

Evotec AG

Hamburg, Germany

- **Tier I Canada Research Chair in Infectious Disease & Immunity**

The University of British Columbia (UBC)

Vancouver, Canada

- **Clinical Research Nurse/Project Manager**

Oklahoma Medical Research Foundation (OMRF)

Oklahoma City, United States

- **Research Associate - Immunologist**

The University of British Columbia (UBC)

Vancouver, Canada

Nature Briefing

An essential round-up of science news, opinion and analysis, delivered to your inbox every weekday.

[Download PDF](#)

Related Articles

- **See more letters to the editor**

Subjects

- [Research data](#)
 - [Databases](#)
-

This article was downloaded by **calibre** from <https://www.nature.com/articles/d41586-021-02234-x>

| [Section menu](#) | [Main menu](#) |

- CORRESPONDENCE
- 17 August 2021

Richly resourced researchers: work with developing-world scientists

- [Brady Lund](#) ORCID: <http://orcid.org/0000-0002-4819-8162>⁰ &
- [Amrollah Shamsi](#) ORCID: <http://orcid.org/0000-0001-6528-9341>¹

1. [Brady Lund](#)

1. Emporia State University, Emporia, Kansas, USA.

[View author publications](#)

You can also search for this author in [PubMed](#) [Google Scholar](#)

2. [Amrollah Shamsi](#)

1. Bushehr, Iran.

[View author publications](#)

You can also search for this author in [PubMed](#) [Google Scholar](#)





•

[Download PDF](#)

We contend that researchers in the global north — blessed as they are with infrastructure that most researchers in developing countries could only dream of — have a moral obligation to collaborate with and support those scientists. This will help to mitigate their own hegemony over the scholarly-research ecology.

Scientists from just a few wealthy nations have long dominated publication in the most highly cited research journals, determining the most appropriate

and compelling research topics and influencing how language is used to describe their fields.

For decades, international research collaborations were difficult because of language barriers and travelling requirements. The Internet has rendered these factors irrelevant. As the pace of COVID-19 research has shown, ideas and documents can be exchanged online almost instantly. Translation software enables comprehensive discussion between researchers who speak different languages.

Yet research collaborations between the global north and south remain all too rare in most disciplines. In our view, researchers from high-income countries should set aside their inherent self-interest and expand their spheres of collaboration to help forge genuine equity in scholarship.

Nature **596**, 343 (2021)

doi: <https://doi.org/10.1038/d41586-021-02235-w>

Competing Interests

The authors declare no competing interests.

Related Articles

- [See more letters to the editor](#)

Subjects

- [Research management](#)
- [Communication](#)

nature careers

[Jobs](#) >

- [Group Leader \(f/m/d\) CRISPR/RNAi Technology for Target Identification \(Screening\) and Validation](#)

Evotech AG

Hamburg, Germany

- [Tier I Canada Research Chair in Infectious Disease & Immunity](#)

The University of British Columbia (UBC)

Vancouver, Canada

- [Clinical Research Nurse/Project Manager](#)

Oklahoma Medical Research Foundation (OMRF)

Oklahoma City, United States

- [Research Associate - Immunologist](#)

The University of British Columbia (UBC)

Vancouver, Canada

Nature Briefing

An essential round-up of science news, opinion and analysis, delivered to your inbox every weekday.

[Download PDF](#)

Related Articles

- [See more letters to the editor](#)

Subjects

- [Research management](#)
- [Communication](#)

This article was downloaded by **calibre** from <https://www.nature.com/articles/d41586-021-02235-w>

| [Section menu](#) | [Main menu](#) |

- CORRESPONDENCE
- 17 August 2021

Use photos of Black doctors and patients to heal not hurt

- [Paula Littlejohn](#) 0

1. [Paula Littlejohn](#)

1. University of British Columbia, Vancouver, Canada.

[View author publications](#)

You can also search for this author in [PubMed](#) [Google Scholar](#)





•

[Download PDF](#)

You are right to draw attention to the problem of the under-representation of Black scientists in pictures (see [Nature 595, 626; 2021](#)). In the medical sphere, photos of people of colour are not deployed equitably.

For example, I'm struck by how health organizations' promotional websites in the United States and Canada frequently use photos of Black people to illustrate poor health, but pictures of white people to show vitality or to incite sympathy around a cause. Moreover, in such images, doctors are almost always white men. This repeated visual association of poor health

with Black bodies — often the patient, rarely the expert — perpetuates dangerous stereotypes, when the real health risk is structural racism (see [*Nature* 592, 674–680; 2021](#)).

At the same time, pictures of patients of colour can be missing where they are crucial. UK medical student Malone Mukwende was so dismayed at the lack of imagery on how to diagnose clinical symptoms on darker skin tones in his textbooks, that he wrote the 2020 handbook *Mind the Gap* and launched a website to share more diverse examples (go.nature.com/2wlx6g6).

What to do? Appreciate the damage caused by overuse and underuse of photos. Complain about both. And use images more intentionally: to educate, not to perpetuate inequality. They are powerful.

Nature 596, 343 (2021)

doi: <https://doi.org/10.1038/d41586-021-02236-9>

Competing Interests

The authors declare no competing interests.

Related Articles

- [See more letters to the editor](#)

Subjects

- [Medical research](#)
- [Publishing](#)

nature careers

[Jobs](#) >

- [Group Leader \(f/m/d\) CRISPR/RNAi Technology for Target Identification \(Screening\) and Validation](#)

Evotech AG

Hamburg, Germany

- [Tier I Canada Research Chair in Infectious Disease & Immunity](#)

The University of British Columbia (UBC)

Vancouver, Canada

- [Clinical Research Nurse/Project Manager](#)

Oklahoma Medical Research Foundation (OMRF)

Oklahoma City, United States

- [Research Associate - Immunologist](#)

The University of British Columbia (UBC)

Vancouver, Canada

Nature Briefing

An essential round-up of science news, opinion and analysis, delivered to your inbox every weekday.

[Download PDF](#)

Related Articles

- [See more letters to the editor](#)

Subjects

- [Medical research](#)
- [Publishing](#)

This article was downloaded by **calibre** from <https://www.nature.com/articles/d41586-021-02236-9>

| [Section menu](#) | [Main menu](#) |

Work

- **The hashtags that brought Black scientists together** [16

August 2021]

Career Feature • Online communities forged last year sparked collaborations and conversations about diversity and equity in academic research.

- **Exploring ‘the most spooky, weird kind of science’** [16

August 2021]

Where I Work • Alessandro Rossi applies quantum physics to the study of measurements in a ‘mind-boggling’ marriage of disciplines.

- CAREER FEATURE
- 16 August 2021

The hashtags that brought Black scientists together

Online communities forged last year sparked collaborations and conversations about diversity and equity in academic research.

- [Virginia Gewin](#) 0

1. Virginia Gewin

1. Virginia Gewin is a freelance writer in Portland, Oregon.

[View author publications](#)

You can also search for this author in [PubMed](#) [Google Scholar](#)





•

[Find a new job](#)

[Download PDF](#)



Plant biologist Nokwanda Makunga felt seen and validated during #BlackBotanists week in July 2020. Credit: Kaylan Reddy

Black researchers in dozens of scientific fields took to social media in 2020 to find, connect with and promote one another using hashtags such as #BlackinCancer, #BlackinPhysics, #BlackBotanists or #BlackinSTEM.

With each field of research taking centre stage for its own week of social-media events, the results challenged institutions to take meaningful steps to recruit more people of colour, and create a more welcoming academic environment to retain them.

These online initiatives were in response to racial unrest sparked by the murder of George Floyd, an unarmed Black man, by police officer Derek Chauvin in Minneapolis, Minnesota. On 25 May 2020, the day that Floyd was murdered, a white woman made a false accusation of assault against Christian Cooper, a Black birdwatcher in New York City's Central Park. What began with #BlackBirders week evolved into a succession of [20](#)

#BlackinSTEM weeks that [ran until December](#). They brought together global communities of Black scientists who plan to continue annual social-media events, and have even formed non-profit organizations dedicated to the task.

As the second year of such events gets under way, *Nature* interviewed five researchers who organized and took part in the #BlackinSTEM weeks. They discuss the impacts and rewards, including career opportunities, collaborations and meaningful institutional actions.

NOKWANDA MAKUNGA: Feeling more visible and valued

Plant biologist at Stellenbosch University, South Africa, and an organizer of #BlackBotanists.

#BlackBotanists was such a wonderful week of joy (6–11 July 2020). Participants shared why they love plants, their favourite plants and their research. Our lead organizer, Tanisha Williams, a postdoctoral botany researcher at Bucknell University in Lewisburg, Pennsylvania, sent out a tweet on the back of #BlackinNature and #BlackBirders weeks, asking who wanted to get involved. #BlackBotanists week was built organically from there, with each person putting their individual skills to use. I coordinated the media package; others facilitated social-media events such as Instagram Live broadcasts.

By the end of the first day, the #BlackBotanists hashtag had been used and/or liked by more than 40,000 people. By the end of the week, the top 50 tweeters had interacted with more than 223,000 people from around the world. To keep the hashtag relevant, all the organizers display it on our profiles and use it periodically, particularly during the monthly talks we have organized. As we warm up for this year's #BlackBotanists week, we are starting to engage with it again. We are striving for global interaction. One thing we are doing differently this year is making an effort to connect with people who aren't academic botanists.



What Black scientists want from colleagues and their institutions

From a personal perspective, I felt seen, validated and valued during that week last year. We were able to create a global community.

I don't see my role as a way of pushing my career. My role as a Black female scientist who works at a university with a long history of apartheid and continuing low diversity is to inspire others who are like me to pursue this career. That said, we did get loads of media attention, which is important to achieve the international standing that's necessary for me to get to the next level of my career.

In South Africa, we have an unusual researcher rating system. Every six years, our scientists get a rating of A, B or C, corresponding to being a leading international researcher, an internationally acclaimed researcher, or an established researcher, respectively. One's rating can affect promotions and grants. I am currently rated C, but I'm hopeful that my international activities since #BlackBotanists will bolster my rating. I was able to give virtual talks to groups at Cornell University in Ithaca, New York; the University of Minnesota in Minneapolis; and the University of Ohio in Athens. Furthermore, as a result of my higher visibility, I have also collaborated with researchers in Canada and elsewhere.

Some things are changing here. At the beginning of this year, the head of my department asked me to be involved with the social-impacts committee, which aims to connect the university to the greater community. That could mean developing a ‘science week’ so prospective students can visit, or raising money for lab coats at local schools that are in need.

She also encouraged me to continue to be a voice for Black botanists. I’ve always communicated about science, but that doesn’t necessarily help my career; some have questioned my seriousness about science itself, so there is a conflict. But that’s changing. Funders in South Africa are starting to recognize the importance of science communication and want to see evidence of such activities on grant applications.

TRAVIS HODGES: Being a role model and finding a community

Travis Hodges participated in #BlackinNeuro and is a neuroscience postdoctoral fellow at the University of British Columbia in Vancouver, Canada.



#BlackinNeuro week boosted networking for neuroscientist Travis Hodges (second from front). Credit: Paul Joseph

A lot of minorities in the sciences don't know others in STEM (science, technology, engineering and mathematics) who are like them. My gaining visibility from my role in the #BlackinSTEM weeks has helped new students to find me, and helped me to find other researchers in my own field whom I didn't know existed. Undergraduates and prospective graduate students now message me for advice about going to graduate school. I'm so glad they have someone to talk to and get advice from, which I didn't have. I was the only Black kid in my class besides my cousin, who did an undergraduate degree in psychology. I didn't see any role models out there.

In the University of British Columbia (UBC) psychology department, I'm the only postdoc who is Black. There are a couple of faculty members of colour in neuroscience broadly; one is Black. They are creating a diversity, equity and inclusivity (DEI) task force to hire more people of colour. I've been invited to join it, as well as UBC's diversity and inclusivity task force

for women's-health researchers, an international group that formed here. We are trying to create new ways to be more inclusive, primarily by raising funds to offer lab experience to students of colour. Without that, it's hard to advance in a science career. I've shared the obstacles I faced, including people telling me that I wouldn't be able to get a PhD, or discouraging me from finishing my degrees. It's also important to explain to white colleagues why these responsibilities can't always fall to one person.



The time tax put on scientists of colour

I point potential allies to the International Behavioral Neuroscience Society's website, [which has resources](#), including talks on YouTube, highlighting the experiences of people of colour and suggestions for making science more inclusive in future. That list of resources did not exist a year ago.

We are just now starting to ask why the UBC psychology department doesn't have anything about DEI on its website, and trying to implement some changes. I know the process is going to be tough. Faculty members who don't want to change have built walls around themselves. I do see a willingness to change among the higher administration officials; I'm thankful for that.

The #BlackinNeuro hashtag is enduring and is being integrated into neuroscience conferences. We are using it in outreach to pull in more students of colour. As the hashtag gets embedded into professional societies, it will continue to bring in people and sustain itself. I think it's here to stay.

On a personal level, more people are ready to collaborate with me, and finding each other is easier. I also get a lot more views on LinkedIn and ResearchGate. For me, networking is the biggest thing that came out of this; having this community during the pandemic had special meaning. My own research on the negative health impacts of stress in rats has shown me how important it is to have a good support system to defend against anxiety. Having that support rise up during the pandemic was amazing, and has helped me to get through.

NIKEA PITTMAN: Making connections, finding mentors

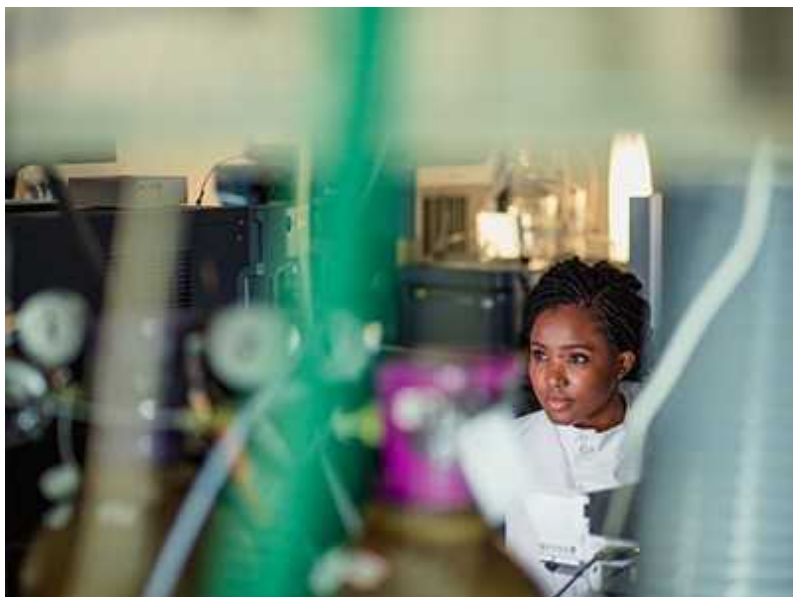
Nikea Pittman is an organizer of #BlackinMicro and a postdoc in biochemistry at the University of North Carolina at Chapel Hill.



Biochemist Nikea Pittman launched a course. Credit: Anna Wheless

The door is open for conversations about race now. Most people probably still aren't comfortable with the subject. The biggest change I've seen at institutions is a lot of committees and task forces rising up to address not only the recruitment but, just as importantly, the retention, of trainees of colour. There's been a rush for big institutions and professional societies to show that they care about recruitment and retention of Black academics in science, technology, engineering and mathematics (STEM), but a lot of that didn't feel genuine: if that message comes out only whenever a Black person is shot or an Asian person is assaulted, it's not genuine. It is nice to see that more people — although I wouldn't say it's a majority — are now aware that being an ally means investing the time and taking on the work, as opposed to [pushing labour back on to people of colour](#).

I noticed that the University of Washington in Seattle started an anti-racism summer reading programme for its incoming medical students, which included a mandatory assignment on race in academia. That inspired me to go to the head of my graduate programme and suggest we pitch a mini course for first-year PhD students on racial identity and its impact on their training. It started out as a small dream, but I recruited eight other postdocs to develop a curriculum and we ran a course for 120 incoming PhD students; we are expanding it next year.



'Blood, sweat and tears': Building a network for Black scientists

The biggest shock of the #BlackinMicro(biology) week (28 September to 4 October 2020) was suddenly realizing that my white-majority colleagues have had a certain level of support and networking all along — and I'd been missing out. It doesn't exist for a lot of underrepresented scientists; often, the feeling of 'otherness' can make it hard to network at conferences. By using the #BlackinSTEM hashtags when seeking help, I don't feel as if I have to first prove myself to be a good scientist despite my race. For example, using the #BlackinChem hashtag, I posted a question to structural biologists about metal-binding enzymes, and I got several responses within a day.

I made tons of connections with other Black postdocs and faculty members. I continue to meet people through the groups that have arisen since then; for

example, #BlackinMicro is now a non-profit organization. It's one of the first times I've felt I could have professional connections with Black female colleagues who experience the same challenges as I do. Surprisingly, almost all the connections I made were with Black women, not men.

The other surprise was the number of people who invited me to give research talks, although a lot of these invitations seemed off target, unrelated to the work I do. I also had two invitations to apply for tenure-track positions, even though I was just finishing the first year of a postdoc. Maybe their intentions were in the right place, but I felt as if people didn't always take the time to check my career stage. I replied to both, saying that I'm still working on my research plan and that I'd appreciate an opportunity next year. One invitation turned into a real conversation; the sender said they had looked at my qualifications and were trying to establish working relationships earlier than they had in the past.

It's been eye-opening to see how much each #BlackinSTEM group accomplished, often with a handful of organizers, all of whom treated it as a second or third 'job', and to compare that with progress at institutions. The contrast is stark. Each #BlackinSTEM group started with zero funding and no organization, and with people who didn't know each other and 'met' on a hashtag. But it's a challenge for institutions to show what they have achieved over the past year, and what they will do going forward.

SIGOURNEY BELL: Becoming founts of knowledge

Co-founder of #BlackinCancer and a PhD student studying paediatric cancer at Cancer Research UK's Cambridge Institute.



Sigourney Bell says it's been helpful to have a community to turn to for support. Credit: Sigourney Bell

I co-created #BlackinCancer week (11–17 October 2020) along with Henry Henderson, an oncology consultant at the biopharmaceutical company AbbVie, in Nashville, Tennessee. We met on Twitter (I'm based in Cambridge, UK) and had a conversation about bringing together a network of Black cancer researchers, which led to further conversations about the range of challenges Black biomedical scientists face — most notably, that we grapple with the Black community's [inherent distrust of the biomedical community](#). As Black cancer researchers, we become the fount of knowledge for our own communities.

While we started organizing, I had a Zoom call with Angeline Dukes, president of the #BlackinNeuro organization and a PhD student at University of California, Irvine. Since #BlackinNeuro was one of the first groups to have its week of events, the members were a go-to source of information for all the other weeks that were being organized, and they kept a calendar to

help avoid overlaps. She explained what had gone well and what hadn't. Following that call, we committed to making everything accessible to all communities; we added closed captioning to all the talks and image descriptions for blind users with screen readers, to make sure our adverts and posters were as accessible as possible.

We used Slack, the online collaboration platform, to assemble what ended up being a 16-person organizing committee. And we focused on a different theme each day — from cancer myths to the legacy of Black scientists of the past. [We created resources](#), from seminars on cancer basics to videos featuring Black survivors of cancer, to inform our family and friends so that they could be empowered around their own health care and help to bring more Black researchers into the pipeline. (In the United States, Black people have higher death rates than all other racial and ethnic groups for some types of cancer.)

The 7,270 #BlackinCancer tweets by 2,328 participants were seen 80.5 million times on Twitter. I personally gained around 500 or 600 Twitter followers, mostly fellow scientists, during our week. I now spend at least 4–5 hours a week in #BlackinCancer meetings or talks, including a biweekly board meeting for the foundation we are creating as a result of the initiative.



[Career resources for African scientists](#)

Even before #BlackinCancer week, we were reaching out to organizations. We have [our own channel](#) on the Nature Portfolio Communities website to promote scientists with publications. We also helped to put together a programme of events, including a public panel discussion and videos or slides to be shared using the #BlackFamCan hashtag, for the US Food and Drug Administration's National Black Family Cancer Awareness Week in June. Between last October and now, I've given probably 15–20 talks — largely on equity, diversity and inclusion for research organizations and pharmaceutical companies, or to inform students about what we do and how we can support them.

Following #BlackinCancer week, the Emerald Foundation, a private biomedical-research foundation based in New York City, contacted us and ended up funding a new US\$75,000, two-year postdoctoral fellowship award. The award can also be used to transition to a tenure-track position, in which case it will increase to \$100,000. It is a genuine step forward in boosting the number of Black researchers in science.

#BlackinCancer will be an annual thing for the foreseeable future. We don't want this year's week to be a replica of last year's, so we are aiming for more engagement rather than just pumping information out there. Cancer Research UK (CRUK) has been a big funder of #BlackinCancer week and has taken this very seriously; we are working with them on increasing diversity in clinical trials. We are also working to develop a mentorship programme for Black students in the United Kingdom and the United States. We will be able to offer undergraduates training in science communication, awards for presentation, and the opportunity to secure a paid eight-week laboratory placement.

During #BlackinCancer week, I felt hyper-visible, yet it's still really hard to find Black researchers in the United Kingdom, as I am. I have yet to meet anyone else who works on paediatric brain tumours as I do. Our organizing committee is made up of me and 15 Americans.

Cancer Research UK asked me for quotes about our work and put them on social media. Unfortunately, there were a handful of antagonistic responses — for example, asking why we don't have a white history month or

someone saying they would never donate to CRUK again. It was really hard for me to read these; I cried over the comments.

For the first few weeks after George Floyd's death, I didn't go a day without crying. It was a million times more real for me, because of my boyfriend, a tall Black man — as Floyd was — who lives in Houston, Texas, where Floyd grew up. As the only Black person in my research group now, and in my institute at the time, it's been helpful to have a community to turn to and say, 'I'm really struggling right now.'

LUKE DAVIS: Allies, be emboldened to take action

Luke Davis participated in #BlackinMath and #BlackPhysics, and is a postdoctoral researcher in theoretical physics at the University of Luxembourg.



Theoretical physicist Luke Davis hopes that #BlackinSTEM will challenge existing hierarchies.Credit: Tunrayo Adeleke-Larodo

I made the move from the United Kingdom to Luxembourg in October 2020 to accept a postdoctoral research position at the University of Luxembourg. The institution, inaugurated only in 2003, seems to have a focus on diversity, because it has pushed that from the get-go. However, as with all institutions in Europe, there is still a lot of work to be done to create an equitable academic environment for people of colour.

I know of two other Black theoretical physicists here, which is quite a lot because I knew only one other PhD physics student who identified as Black when I was at University College London.

Although the #BlackinPhysics and #BlackinMath weeks (26 October to 1 November and 9–15 November 2020, respectively) helped to alleviate the burden of lockdown, they also hit me on a deeper level. The transatlantic nature of the connections was able to bridge the gaps between Black American, Black UK and Black European scientists. I estimate that my Twitter followers increased by about 30% as a result.

I've always been honest on social media with my opinions about race; I'm blunt. One thing I tweet about is the power hierarchy at the top. If we can't get to the top, then nothing will happen.

My hope is that potential allies will be emboldened by the #BlackinSTEM movement to take specific steps to increase equity and inclusion in academia. If you are on a promotion committee, make sure the deliberations are transparent.

Challenge the system to enforce rational metrics for promotions or new faculty hires instead of allowing potentially prejudiced decisions. Take the energy from the #BlackinSTEM weeks, and use it day to day — that's true allyship.

Nature **596**, 449–452 (2021)

doi: <https://doi.org/10.1038/d41586-021-02223-0>

These interviews have been edited for clarity and length.

Related Articles



- [**‘Blood, sweat and tears’: Building a network for Black scientists**](#)



- [**What Black scientists want from colleagues and their institutions**](#)



- [**The time tax put on scientists of colour**](#)



- [**Career resources for African scientists**](#)

Subjects

- [Careers](#)
- [Scientific community](#)
- [Lab life](#)
- [Media](#)

nature careers

[**Jobs**](#) >

- [Group Leader \(f/m/d\) CRISPR/RNAi Technology for Target Identification \(Screening\) and Validation](#)

Evotec AG

Hamburg, Germany

- [Tier I Canada Research Chair in Infectious Disease & Immunity](#)

The University of British Columbia (UBC)

Vancouver, Canada

- [Clinical Research Nurse/Project Manager](#)

Oklahoma Medical Research Foundation (OMRF)

Oklahoma City, United States

- [Research Associate - Immunologist](#)

The University of British Columbia (UBC)

Vancouver, Canada

Nature Briefing

An essential round-up of science news, opinion and analysis, delivered to your inbox every weekday.

[Download PDF](#)

Related Articles



- [‘Blood, sweat and tears’: Building a network for Black scientists](#)



- [What Black scientists want from colleagues and their institutions](#)



- [The time tax put on scientists of colour](#)



- [Career resources for African scientists](#)

Subjects

- [Careers](#)
- [Scientific community](#)
- [Lab life](#)
- [Media](#)

This article was downloaded by **calibre** from <https://www.nature.com/articles/d41586-021-02223-0>

- WHERE I WORK
- 16 August 2021

Exploring ‘the most spooky, weird kind of science’

Alessandro Rossi applies quantum physics to the study of measurements in a ‘mind-boggling’ marriage of disciplines.

- [Josie Glausiusz](#) ⁰

1. Josie Glausiusz

1. Josie Glausiusz is a science journalist in Israel.

[View author publications](#)

You can also search for this author in [PubMed](#) [Google Scholar](#)





•



Alessandro Rossi, quantum scientist from the UK NPL and the University of Strathclyde working on a dilution refrigerator system.

Alessandro Rossi is a measurement fellow at the National Physical Laboratory in London and a senior lecturer and UKRI Future Leaders fellow at the University of Strathclyde in Glasgow, UK. Credit: Alecsandra Dragoi for *Nature*

[Download PDF](#)

In my work as a quantum engineer, I wear two hats. At the National Physical Laboratory (NPL) in London, where this photo was taken in April,

I research quantum metrology, the scientific study of measurements based on quantum-physics principles. The instrument in this image is a dilution refrigerator, which allows us to cool our semiconductor quantum devices to 0.007 kelvin: that's a fraction of a degree above absolute zero (-273.15°C), a temperature that, in nature, exists nowhere in the Universe.

In experiments at the NPL, we clock the transfer of single electrons so accurately that I know exactly how many of them move in a unit of time. By controlling electrons one at a time in this refrigerator system, I can generate an electric current very, very precisely. This level of control is useful for my research at the University of Strathclyde in Glasgow, UK, where my colleagues and I are developing quantum computers using semiconductor technology. By moving electrons one at a time, we can transfer information between various parts of a semiconductor-based quantum computer.

Quantum computing uses quantum bits, or qubits, that can exist in different states simultaneously. This means that quantum computers can perform certain calculations exponentially faster than classical computers. They can also simulate chemical reactions, because they work on the same quantum principles that govern interactions between individual atoms and molecules.

The idea that something can be in two states or two places at the same time is counter-intuitive. I feel that I myself live a contradiction. I study quantum physics — the most unreliable, spooky, weird type of science — and apply it to metrology, which is supposed to be among the most reliable, precise and repeatable of disciplines. To think how these two things come together successfully is mind-boggling.

Nature **596**, 454 (2021)

doi: <https://doi.org/10.1038/d41586-021-02224-z>

Related Articles

-  [Bridging the gap between biologists and physicists](#)
-  ['All my art is curiosity-driven': the garden studio where art and physics collide](#)
-  [Measuring curvatures in the ripples of space-time](#)

Subjects

- [Careers](#)
- [Quantum physics](#)

nature careers

[Jobs](#) >

- [Group Leader \(f/m/d\) CRISPR/RNAi Technology for Target Identification \(Screening\) and Validation](#)
Evotec AG
Hamburg, Germany
- [Tier I Canada Research Chair in Infectious Disease & Immunity](#)
The University of British Columbia (UBC)

Vancouver, Canada

- **Clinical Research Nurse/Project Manager**

Oklahoma Medical Research Foundation (OMRF)

Oklahoma City, United States

- **Research Associate - Immunologist**

The University of British Columbia (UBC)

Vancouver, Canada

Nature Briefing

An essential round-up of science news, opinion and analysis, delivered to your inbox every weekday.

[Download PDF](#)

Related Articles



- **Bridging the gap between biologists and physicists**



- **'All my art is curiosity-driven': the garden studio where art and physics collide**



- [Measuring curvatures in the ripples of space-time](#)

Subjects

- [Careers](#)
- [Quantum physics](#)

This article was downloaded by **calibre** from <https://www.nature.com/articles/d41586-021-02224-z>

| [Section menu](#) | [Main menu](#) |

Research

- **Genomic analysis identifies variants that can predict the timing of menopause** [04 August 2021]

News & Views • A broad analysis has identified genetic variants that influence age at natural menopause. The results implicate mechanisms such as DNA-damage repair and give insights into the potential for predicting and treating early menopause.

- **'Polluter pays' policy could speed up emission reductions and removal of atmospheric CO₂** [16 August 2021]

News & Views • To meet climate targets, technologies that remove atmospheric carbon dioxide will probably be needed. An analysis shows how their development and use could be accelerated if carbon emitters are obliged to remove their own CO₂.

- **Supersolids go two-dimensional** [18 August 2021]

News & Views • Supersolids are exotic materials whose constituent particles can simultaneously form a crystal and flow without friction. The first 2D supersolid has been produced using ultracold gases of highly magnetic atoms.

- **Deranged chromatin drives uterine fibroid tumours** [04 August 2021]

News & Views • A previously unknown subgroup of uterine fibroid tumours is driven by mutations that result in disruption of the DNA–protein complex chromatin. The findings could inform the management of this common condition.

- **A cocktail of pesticides, parasites and hunger leaves bees down and out** [04 August 2021]

News & Views • Pollinators are under threat. A meta-analysis reveals that the combination of agrochemicals, parasites and malnutrition has a cumulative negative effect on bees, and that pesticide–pesticide interactions increase bee mortality.

- **Lenghu on the Tibetan Plateau as an astronomical observing site** [18 August 2021]

Article • The results of site testing at a local summit near Lenghu Town in Qinghai Province on the Tibetan Plateau indicate that the site is suitable as an astronomical observing site.

- **Two-dimensional supersolidity in a dipolar quantum gas** [18 August 2021]

Article • Two-dimensional supersolidity is demonstrated using highly magnetic, ultracold dysprosium atoms.

- **Ghost hyperbolic surface polaritons in bulk anisotropic crystals** [18 August 2021]
Article • Hyperbolic phonon polaritons that exhibit long-distance, ray-like propagation and oblique wavefronts are described at the surface of an anisotropic bulk crystal.
- **How to design an icosahedral quasicrystal through directional bonding** [18 August 2021]
Article • Model patchy colloids with directional bonding are designed that assemble into icosahedral quasicrystals through the propagation of an icosahedral network of bonds and may be realized using DNA origami particles.
- **Mobility gradients yield rubbery surfaces on top of polymer glasses** [18 August 2021]
Article • Surface enhancements in glass mobility are complicated in polymers by the interplay of the surface mobile layer thickness with a second length scale (the size of the polymer chains), giving rise to a transient rubbery surface even in polymers with short chains.
- **Operationalizing the net-negative carbon economy** [08 July 2021]
Article • To enable net-negative CO₂ emissions, the repayment of previously accrued carbon debt by establishing the responsibility for the net removal of CO₂ by carbon-emitting parties through carbon removal obligations is necessary.
- **The Montreal Protocol protects the terrestrial carbon sink** [18 August 2021]
Article • Modelling suggests that the Montreal Protocol may be mitigating climate change by protecting the land carbon sink, as well as by protecting the ozone layer and reducing greenhouse gas emissions.
- **Agrochemicals interact synergistically to increase bee mortality** [04 August 2021]
Article • A meta-analysis of studies in which bees were exposed to combinations of agrochemicals, nutritional stressors and/or parasites revealed evidence for synergistic effects on mortality when bees were exposed to multiple agrochemicals at field-realistic levels.
- **Genetic insights into biological mechanisms governing human ovarian ageing** [04 August 2021]
Article • Hundreds of genetic loci associated with age at menopause, combined with experimental evidence in mice, highlight mechanisms of reproductive ageing across the lifespan.
- **Deficient H2A.Z deposition is associated with genesis of uterine leiomyoma** [04 August 2021]
Article • Analyses of samples from 728 women with uterine leiomyomas (uterine fibroids), and public data, show that somatic and germline mutations in the SRCAP histone-loading

complex genes are associated with the condition.

- **Locally ordered representation of 3D space in the entorhinal cortex** [11 August 2021]

Article • Recordings from the brains of freely flying bats show that grid cells that represent 3D space have multiple firing fields and are organized with local rather than global order.

- **Systems vaccinology of the BNT162b2 mRNA vaccine in humans** [12 July 2021]

Article • Profiling the immune responses of 56 volunteers vaccinated with BNT162b2 reveals how this mRNA vaccine primes the innate immune system to mount a potent response to SARS-CoV-2 after booster immunization.

- **Age-related immune response heterogeneity to SARS-CoV-2 vaccine BNT162b2** [30 June 2021]

Article • Individuals over eighty years of age are less likely to mount a good immune response against SARS-CoV-2 (measured by neutralization titres) after the first dose of the BNT162b2 mRNA vaccine, but achieve good neutralization after the second dose.

- **Protective efficacy of Ad26.COV2.S against SARS-CoV-2 B.1.351 in macaques** [23 June 2021]

Article • SARS-CoV-2 challenge of rhesus macaques demonstrates that the Ad26.COV2.S vaccine induces robust protection against both the WA1/2020 isolate and the B.1.351 variant of concern.

- **In silico saturation mutagenesis of cancer genes** [28 July 2021]

Article • A new computational approach to in silico mutagenesis screening allows comprehensive mapping of cancer driver mutations.

- **BARD1 reads H2A lysine 15 ubiquitination to direct homologous recombination** [28 July 2021]

Article • A tandem BRCT-domain-associated ubiquitin-dependent recruitment motif in BARD1 recruits BRCA1 to DNA double-strand breaks (DSBs) to promote homologous recombination and antagonize the 53BP1 DSB repair pathway that mediates non-homologous end joining.

- **Mechanisms of BRCA1–BARD1 nucleosome recognition and ubiquitylation** [28 July 2021]

Article • The authors elucidate the mechanisms for the ubiquitylation specificity and recruitment of the ubiquitin ligase complex BRCA1–BARD1 to damaged DNA within chromatin to facilitate homologous recombination.

- **Structure and mechanism of blood–brain-barrier lipid transporter MFSD2A** [04 August 2021]

Article • The cryo-electron microscopy structure of mouse MFSD2A sheds light on the mechanism that underlies its lipid transport functions, which have a pivotal role in regulating the blood–brain barrier.

| [Next section](#) | [Main menu](#) | [Previous section](#) |

- NEWS AND VIEWS
- 04 August 2021

Genomic analysis identifies variants that can predict the timing of menopause

A broad analysis has identified genetic variants that influence age at natural menopause. The results implicate mechanisms such as DNA-damage repair and give insights into the potential for predicting and treating early menopause.

- [Krina T. Zondervan](#) 

1. [Krina T. Zondervan](#)

1. Krina T. Zondervan is in the Nuffield Department of Women's and Reproductive Health, University of Oxford, Women's Centre, John Radcliffe Hospital, Oxford OX3 9DU, UK, and at the Wellcome Centre for Human Genetics, University of Oxford, UK.

[View author publications](#)

You can also search for this author in [PubMed](#) [Google Scholar](#)



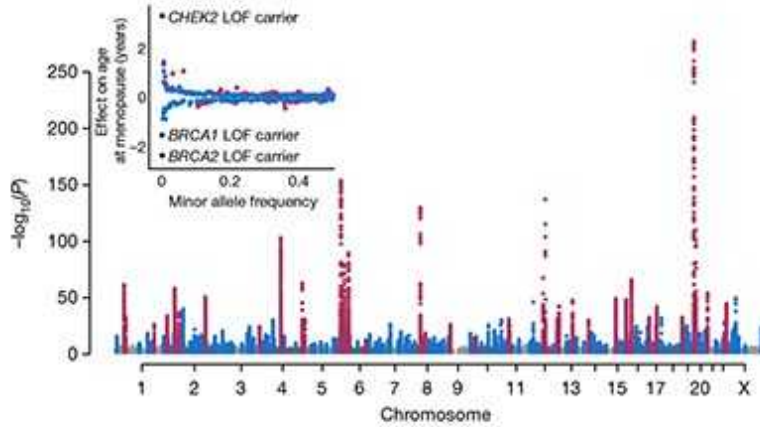


•

[Download PDF](#)

Menopause is the permanent cessation of menstrual cycles in women following the loss of ovarian function¹. It occurs, on average, between 47 and 52 years of age globally², but around 4% of women undergo it before the age of 45 (early menopause) or even 40 (primary ovarian insufficiency; POI)³. Being able to predict when menopause will occur would give women and their partners greater flexibility in choosing when to have a child. This knowledge, and treatments to delay menopause, might be particularly welcomed by women at high risk of early menopause or POI. Ruth *et al.*⁴

[now report genetic findings](#) that could bring us a step closer to predicting and treating early menopause.



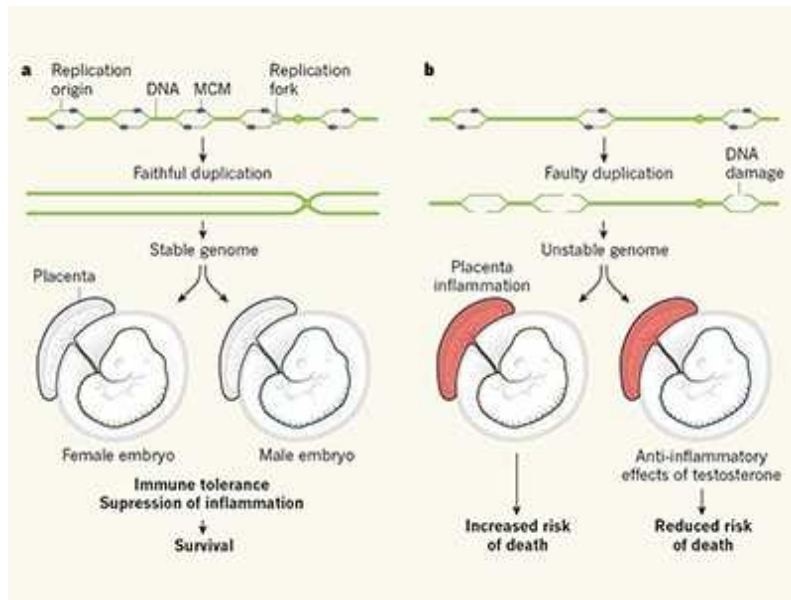
[Read the paper: Genetic insights into biological mechanisms governing human ovarian ageing](#)

Age at natural menopause (ANM) is determined by the complex interaction of both non-genetic and genetic factors. Non-genetic factors associated with earlier ANM include poor childhood nutrition and smoking, whereas being overweight is associated with later ANM^{1,2}. Genetic factors are thought to account for about 50% of the variation in menopausal timing⁵. Previous genetic studies^{6,7} have implicated a role for DNA-damage-response (DDR) mechanisms in the timing of menopause. DDR is a molecular process that is crucial for the error-free replication of cells, including the generation of egg cells in the ovary, and for the repair of DNA damage caused by environmental factors such as cigarette smoke⁸.

Ruth *et al.* conducted the largest genetic analysis so far in women whose ANM occurred between the ages of 40 and 60 years, testing millions of common genetic variants from across the genome for an association with ANM. Differences in genetic ancestry could distort results, and the analyses were therefore initially restricted to 200,000 women of European ancestry. Approximately half of this sample was derived from the UK Biobank, a large, population-based study containing extensive clinical, biological and

genomic data⁹. Ruth *et al.* found 290 independent areas of the genome that contained common genetic variants associated with ANM, a fivefold increase from previous results¹⁰. The impact of each variant on ANM varied from very small (3.5 weeks) to considerable (1.5 years).

The authors found that the results from this initial analysis were highly consistent with those from another (non-UK Biobank) data set that they analysed, containing data from about 300,000 women. Most of the implicated variants were also associated with ANM in a third data set that included 100,000 women of East Asian ancestry, although the magnitudes of the variants' effects varied from those seen in women of European descent. Thus, a genetic test that predicts ANM accurately in one ethnic group might not do so in another.



Unstable genomes promote inflammation

Altogether, the genetic variants explained around 10–12% of variation in ANM, a reasonable proportion for a trait with complex genetic underpinnings. Using the non-UK Biobank data sets, the authors built a polygenic score (PGS) to predict a woman's ANM on the basis of the cumulative effect of the common genetic variants that she carries. The authors showed that the PGS was a weak predictor of the ANM of women in the UK Biobank sample, providing slightly, yet significantly, more accurate predictions than did smoking status. Ruth and colleagues noted that women

in the top 1% of the PGS score distribution (that is, predicting a lower ANM) had an almost fivefold higher risk of POI than did women with average PGS scores — the same increase in risk as that associated with rare mutations in the *FMRI* gene, for which women can currently be tested. The utility and cost-to-benefit ratio of determining the PGS for women in the general population, and in those with a family history of early menopause or POI, remains to be assessed.

Ruth *et al.* found that many of the variants implicated in their analysis affected genes involved in DDR, including the genes *BRCA1* and *CHEK2*, which have been suggested previously to affect ANM¹. Using publicly available gene-expression data from 44 tissue types, the authors found that ANM-associated genes were preferentially expressed in blood-derived stem cells — cell types that have a high turnover and therefore depend heavily on DDR function. The expression of these genes in reproductive tissues such as the ovaries and fallopian tubes, and in human egg and fetal cells, was more variable and requires more-detailed investigation.

Collectively, the genetic data suggested a broader involvement of DDR processes in ANM than previously realized. Earlier research showed that feeding pregnant mice a high-fat, high-sugar diet results in their female offspring having a lowered reproductive potential (reduced ovarian reserve)¹¹. Ruth *et al.* observed changes in the expression of 2 of 35 assessed DDR-related genes (*Dmc1* and *Brskl*) in ovarian tissue from the female offspring of mice on this diet, suggesting that maternal diet can affect DNA repair in offspring. However, the impact of changes in expression of the two genes on ovarian ageing was not tested.

The authors then focused on two DDR genes: *CHEK2*, which was implicated in their genomic analysis, and *CHEK1*, which is involved in the same biological (checkpoint kinase) pathway. *CHEK1* helps DNA repair, whereas *CHEK2* plays a part in the destruction of eggs compromised by DNA damage¹² (Fig. 1a).

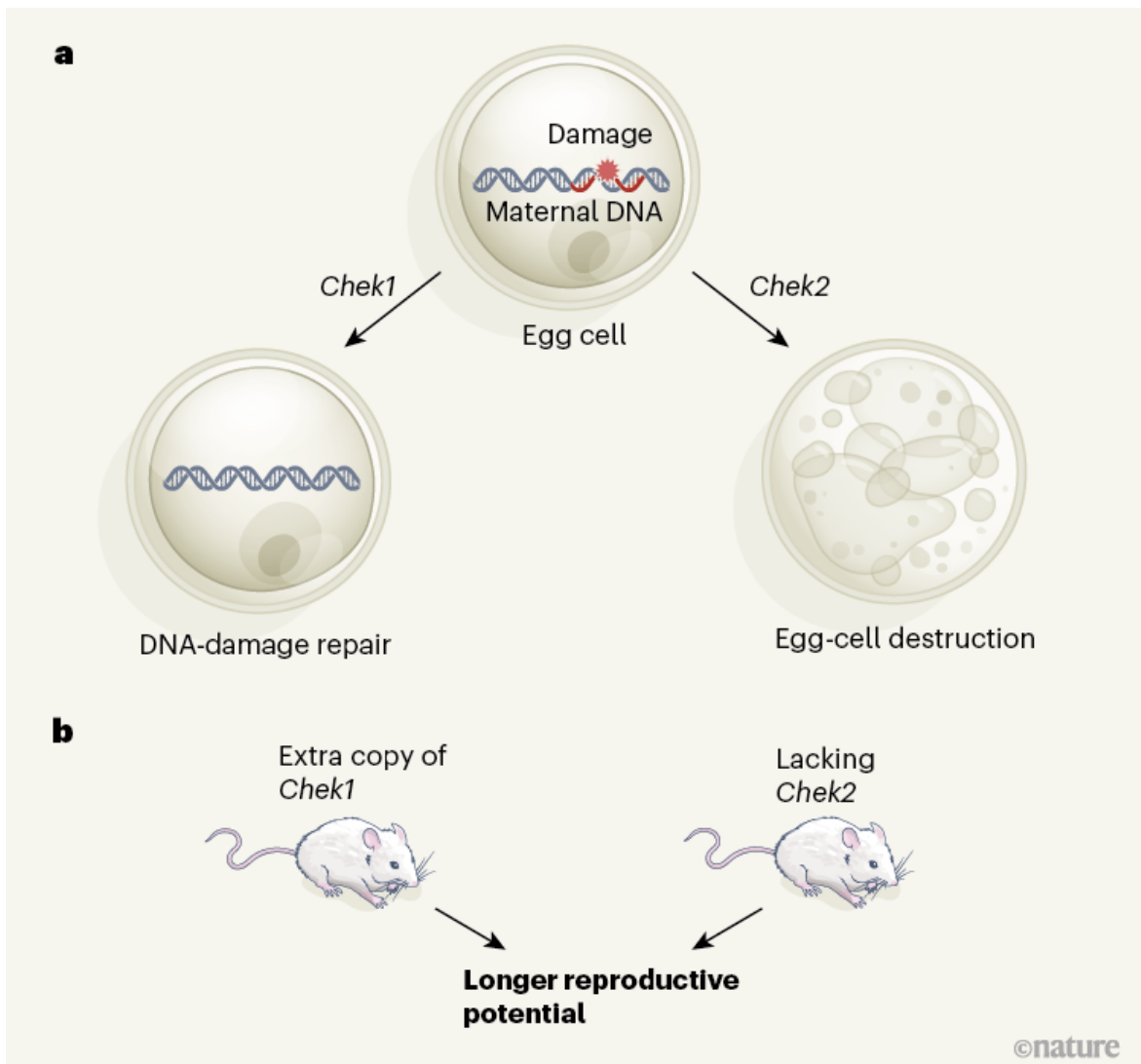
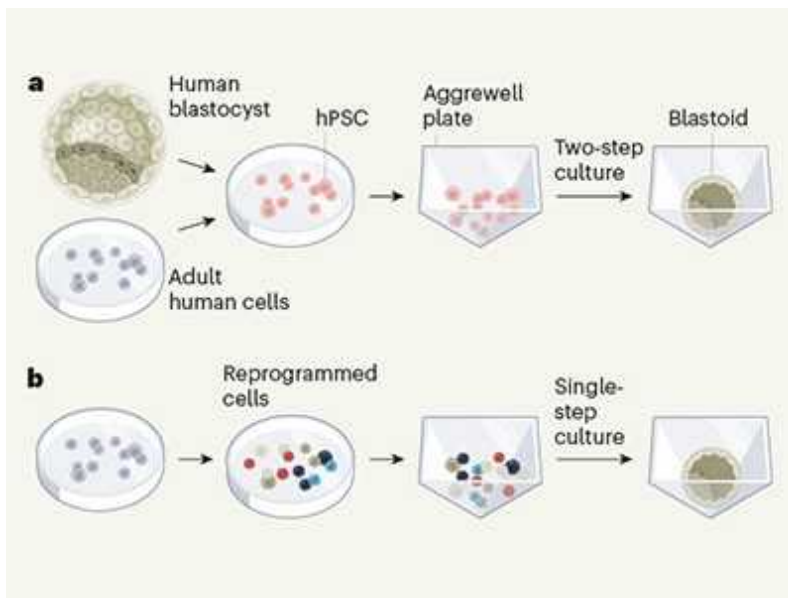


Figure 1 | Manipulating DNA-damage-response genes affects reproductive lifespan. **a**, *Chek1* and *Chek2* are genes involved in the complex response to DNA damage (simplified diagram shown here). When the DNA of egg cells in ovaries is damaged, *Chek1* expression promotes DNA repair, whereas *Chek2* expression promotes destruction of the affected cell. **b**, Through their large-scale genomic analysis, Ruth *et al.*⁴ found that variants of the human *CHEK2* gene and other genes involved in the response to DNA damage are associated with differences in age at natural menopause. In line with this, the authors showed that mice carrying an extra copy of the *Chek1* gene, or lacking expression of the *Chek2* gene altogether, had a longer reproductive age span than that of regular mice.

Inactivating *Chek2* in mice reduced ovarian degeneration and, in animals that were around the age of the mouse equivalent of menopause, increased the ovarian response to hormonal stimulation, consistent with these animals having a greater ovarian reserve than that of control mice (Fig. 1b). Fertilization rates in mice lacking *Chek2* were unaffected, as were embryonic development and litter size.

Chek1 is needed for embryo development, and its inactivation specifically in egg cells led to female infertility. By contrast, introducing an extra copy of *Chek1* resulted in increased ovarian reserve in older mice (Fig. 1b). Thus, limiting the destruction of egg cells or upregulating the DNA-repair process could extend reproductive lifespan in mice.



First complete model of the human embryo

The authors comment that the mice with an extra copy of *Chek1* gave rise to several generations of healthy, fertile offspring, although how the offspring's health was assessed was unclear. Multi-generational effects of reducing *Chek2* expression were not investigated. Any treatments that reduce *CHEK2* expression might have adverse effects, however, because *CHEK2* is a tumour-suppressor gene, and certain *CHEK2* mutations increase the risk of various cancers¹³. *CHEK2* inhibitors are under development for treating cancer, but are unlikely to be suitable for non-cancer-related disorders.

What are the potential health consequences of delaying ANM? Ruth *et al.* created a statistical instrument to infer how variation in the 290 ANM-associated genomic regions affected various health outcomes in publicly available genomic data sets. This approach revealed that each year of ‘genetically delayed’ ANM increases the risk of hormone-dependent cancers such as endometrial cancer (5%) and oestrogen-receptor-positive breast cancer (3.8%), consistent with epidemiological evidence¹⁴. By contrast, genetic variants that delayed ANM were inferred to increase bone density and reduce the risk of fractures, and not to affect the risk of cardiovascular disease or Alzheimer’s disease, lipid levels, body mass or longevity. Notably, the authors’ statistical instrument was based on all known variants influencing later ANM, not just those affecting DDR mechanisms. The effects of manipulations targeting only DDR mechanisms should be investigated.

Many factors determine the reproductive age span, and most — including specific nutritional influences — remain unknown. However, Ruth *et al.* deliver a considerable advance in our understanding of the genetic and molecular mechanisms that underpin ovarian ageing and ANM. The results will also incentivize further detailed studies into the role of DDR mechanisms in ANM.

The appeal of a future in which women can extend ANM will centre around balancing the risks and benefits, as is the case now for the use of hormone-replacement therapy. For women at risk of early menopause and POI, the benefits might be more likely to outweigh the risks. Although caution should be exercised in translating the findings into genetic tests for early menopause and POI, Ruth and colleagues’ findings pave the way for more-detailed studies that could lead to women being able to predict their menopausal age and to consider options to extend their reproductive age span.

Nature **596**, 345-346 (2021)

doi: <https://doi.org/10.1038/d41586-021-01710-8>

References

1. 1.

Davis, S. R. *et al.* *Nature Rev. Dis. Primers* **1**, 15004 (2015).

[PubMed](#) [Article](#) [Google Scholar](#)

2. 2.

Schoenaker, D. A. M., Jackson, C. A., Rowlands, J. V. & Mishra, G. D. *Int. J. Epidemiol.* **43**, 1542–1562 (2014).

[PubMed](#) [Article](#) [Google Scholar](#)

3. 3.

Golezar, S., Ramezani Tehrani, F., Khazaei, S., Ebadi, A. & Keshavarz, Z. *Climacteric* **22**, 403–411 (2019).

[PubMed](#) [Article](#) [Google Scholar](#)

4. 4.

Ruth, K. S. *et al.* *Nature* **596**, 393–397 (2021).

[Article](#) [Google Scholar](#)

5. 5.

Murabito, J. M., Yang, Q., Fox, C., Wilson, P. W. F. & Cupples, L. A. *J. Clin. Endocrinol. Metab.* **90**, 3427–3430 (2005).

[PubMed](#) [Article](#) [Google Scholar](#)

6. 6.

Stolk, L. *et al.* *Nature Genet.* **44**, 260–268 (2012).

[PubMed](#) [Article](#) [Google Scholar](#)

7. 7.

Titus, S. *et al.* *Sci. Transl. Med.* **5**, 172ra21 (2013).

[PubMed](#) [Article](#) [Google Scholar](#)

8. 8.

Chatterjee, N. & Walker, G. C. *Environ. Mol. Mutagen.* **58**, 235–263 (2017).

[PubMed](#) [Article](#) [Google Scholar](#)

9. 9.

Bycroft, C. *et al.* *Nature* **562**, 203–209 (2018).

[PubMed](#) [Article](#) [Google Scholar](#)

10. 10.

Day, F. R. *et al.* *Nature Genet.* **47**, 1294–1303 (2015).

[PubMed](#) [Article](#) [Google Scholar](#)

11. 11.

Aiken, C. E. *et al.* *FASEB J.* **30**, 1548–1556 (2016).

[PubMed](#) [Article](#) [Google Scholar](#)

12. 12.

Bolcun-Filas, E., Rinaldi, V. D., White, M. E. & Schimenti, J. C. *Science* **343**, 533–536 (2014).

[PubMed](#) [Article](#) [Google Scholar](#)

13. 13.

Cybulski, C. *et al.* *Am. J. Hum. Genet.* **75**, 1131–1135 (2004).

[PubMed](#) [Article](#) [Google Scholar](#)

14. 14.

Collaborative Group on Hormonal Factors in Breast Cancer. *Lancet Oncol.* **13**, 1141–1151 (2012).

[PubMed](#) [Article](#) [Google Scholar](#)

[Download references](#)

Competing Interests

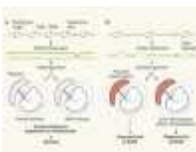
Financial competing interests: Scientific collaborations in translational research with Bayer AG and Roche Diagnostics, Inc. through the University of Oxford.

Non-financial competing interests: Board member of the World Endometriosis Society and the World Endometriosis Research Foundation. Research Advisory Committee member of Wellbeing of Women UK.

Related Articles



- [Read the paper: Genetic insights into biological mechanisms governing human ovarian ageing](#)



- [Unstable genomes promote inflammation](#)



- [First complete model of the human embryo](#)

- [See all News & Views](#)

Subjects

- [Genetics](#)
- [Ageing](#)

nature careers

Jobs >

- [Group Leader \(f/m/d\) CRISPR/RNAi Technology for Target Identification \(Screening\) and Validation](#)

Evotech AG

Hamburg, Germany

- [Tier I Canada Research Chair in Infectious Disease & Immunity](#)

The University of British Columbia (UBC)

Vancouver, Canada

- [Clinical Research Nurse/Project Manager](#)

Oklahoma Medical Research Foundation (OMRF)

Oklahoma City, United States

- [Research Associate - Immunologist](#)

The University of British Columbia (UBC)

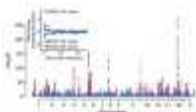
Vancouver, Canada

Nature Briefing

An essential round-up of science news, opinion and analysis, delivered to your inbox every weekday.

[Download PDF](#)

Related Articles



- [Read the paper: Genetic insights into biological mechanisms governing human ovarian ageing](#)



- [Unstable genomes promote inflammation](#)



- [First complete model of the human embryo](#)
- [See all News & Views](#)

Subjects

- [Genetics](#)
- [Ageing](#)

This article was downloaded by **calibre** from <https://www.nature.com/articles/d41586-021-01710-8>

- NEWS AND VIEWS
- 16 August 2021

‘Polluter pays’ policy could speed up emission reductions and removal of atmospheric CO₂

To meet climate targets, technologies that remove atmospheric carbon dioxide will probably be needed. An analysis shows how their development and use could be accelerated if carbon emitters are obliged to remove their own CO₂.

- [David A. Stainforth](#) ✉

1. [David A. Stainforth](#)

1. David A. Stainforth is at the Grantham Research Institute on Climate Change and the Environment, London School of Economics and Political Science, London WC2A 2AE, UK, and in the Department of Physics, University of Warwick, Warwick, UK.

[View author publications](#)

You can also search for this author in [PubMed](#) [Google Scholar](#)



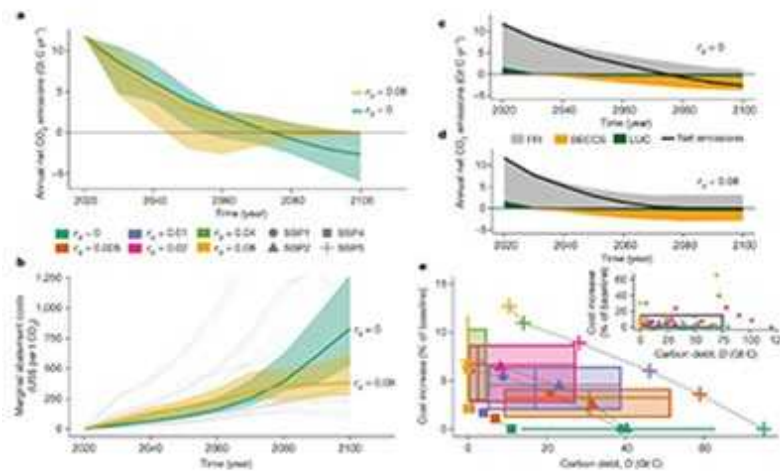


•

[Download PDF](#)

The 2015 Paris agreement on climate change set a goal of limiting global warming to 2 °C, or preferably 1.5 °C, above pre-industrial levels. Achieving either of these targets is expected to require not just reductions in carbon emissions, but also technologies that remove carbon dioxide from the atmosphere. [Writing in Nature](#), Bednar *et al.*¹ explore policy mechanisms that support the development and implementation of such technologies. They propose an emissions-trading scheme that provides permits for emissions consistent with a specific global-warming goal, but that allows further emissions as long as the emitter commits to removing the extra

carbon later on. The authors argue that emitters should be charged for the temporary ‘storage’ of this carbon in the atmosphere. They show that this would lead both to earlier reductions in carbon emissions (decarbonization) and to earlier application of CO₂-removal technologies than would otherwise occur.



[Read the paper: Operationalizing the net-negative carbon economy.](#)

Any agreed limit to future global warming can be associated, albeit with some uncertainty, with a carbon budget: a maximum value for the total cumulative emissions of CO₂ since pre-industrial times². If the budget is exceeded, as is expected to be the case for the Paris-agreement targets, CO₂-removal technologies will be required to extract the excess emissions. If the extraction is delayed too long, the target will be missed, but there is some flexibility with regard to timing. This raises several questions: who is responsible for implementing the technology, who pays, and what is the best timing?

Technologies to remove CO₂ are currently emerging or are expected to be developed in the future. If successful, the costs of such technologies will probably decline over time as a result of continuing research and large-scale application. Moreover, temporal discounting — the different value placed on goods or expenditure at different points in time — makes future expenditure

cheaper in terms of today's money than the same expenditure today. These factors lead to the expectation that CO₂-removal technologies will mostly be adopted late in this century. But this delay implies that the responsibility for mitigating climate change will be transferred to future generations. Bednar *et al.* study the consequences of applying a ‘polluter pays’ principle in which those responsible for excess emissions (that is, emissions greater than a carbon budget) are obliged to later implement the CO₂-removal technologies: they take on carbon debt³.

There are, of course, risks in relying on today's emitters to support future CO₂ removal. They might default or lobby governments to cancel the debt, or perhaps more CO₂ removal will be required than is currently expected. Bednar *et al.* propose that these risks can be addressed by applying interest on carbon debt — not only committing emitters to remove carbon, but also charging them for storing it in the atmosphere until it is removed. This interest counteracts the benefits of delay arising from temporal discounting and leads to more-rapid decarbonization, as well as earlier implementation of CO₂ removal (Fig. 1).

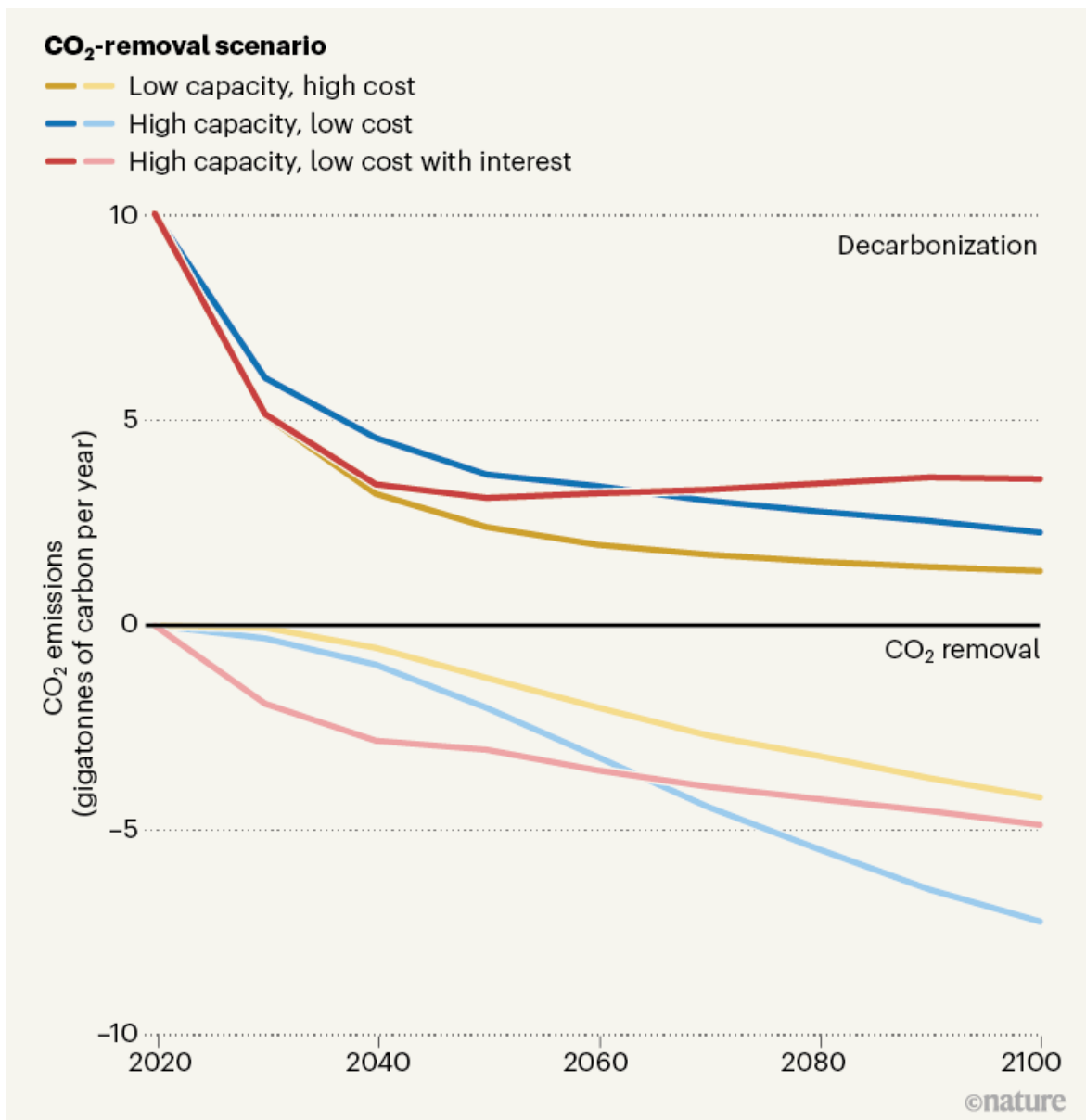


Figure 1 | The effects of charging interest on carbon debt. Bednar *et al.*¹ studied how various scenarios affect the time course of decarbonization (the reduction of carbon emissions) and the amount of CO₂ removed from the atmosphere by future technologies (plotted as negative emissions), assuming a goal of restricting global warming to 1.5 °C above pre-industrial levels. If CO₂-removal technologies have low capacity and high costs (yellow lines), rapid, short-term decarbonization combined with gradual uptake of these technologies is expected. With higher capacity and lower costs of CO₂ removal (blue lines), less-rapid decarbonization is expected with more CO₂

removal, particularly towards the end of this century. If carbon emitters are required to pay interest on any emissions above an agreed limit, decarbonization and CO₂ removal are both expected to occur earlier than in the previous scenario (red lines). (Data are for three scenarios in the supplementary information of ref. 2, and are shown only as an example of the effects of varying assumptions. Data on predicted effects of land-use change are not presented.)

The authors propose that current emissions-trading schemes (ETSs) could be adapted to include carbon-removal obligations (CROs), interest on CROs and limits on emissions permits that are consistent with a carbon budget. These changes increase the flexibility of such schemes to, for instance, avoid ‘stranded assets’ — situations in which valuable emissions-producing facilities have to be shut down earlier than would otherwise be necessary. They would, however, require complicated management and regulatory systems involving commercial and central banks to oversee the risks and ensure that commitments are met.

Further work is needed to address how an ETS with CROs (ETS-CRO) could be operated and managed in practice. The broader message from Bednar and colleagues’ study, however, is that an intergenerationally equitable approach to the implementation of CO₂-removal technologies would lead to them being used sooner than would otherwise be the case, along with more-rapid decarbonization. This conclusion does not depend on the implementation of the proposed ETS-CRO.



Trade-offs for equitable climate policy assessed

For example, an alternative way to apply the ‘polluter pays’ principle could be through a state-owned carbon-removal fund supported by carbon taxes. This would also face risks associated with uncertain carbon budgets or funds being diverted for short-term political expediencies. The justification for applying interest on future carbon-removal commitments would therefore still apply, along with the conclusion that CO₂-removal technologies would be implemented sooner.

The widespread and early adoption of such technologies requires confidence that a large-scale market for them will exist in the next few decades. Even if technical and practical barriers to their implementation can be overcome, this confidence will also be necessary to generate investment for large-scale commercial development and deployment — which is itself required to bring down costs and stimulate wider uptake.

There are lessons here from the renewable-energy industries: the price of solar panels, for instance, has fallen by more than 80% in the past decade, driven largely by the scaling-up of manufacturing facilities⁴. This scaling-up and price reduction, and the associated massive expansion of solar-energy generation capacity, could arguably have been achieved a decade or more earlier had there been sufficient confidence in the scale of the market. In the

same way, a risk for CO₂-removal technologies is that policies that would secure a market for their use lag behind their technological development, holding back investment.

The ETS-CRO proposed by Bednar *et al.* creates a market for CO₂-removal technologies because organizations with CROs will want to invest in those technologies. Yet its complexity represents a barrier. Researchers, policymakers and the finance industry need to work together to explore this proposal, alongside other options for building a reliable expectation that there will be a market for these technologies in the relatively near term, and to implement a policy in which the polluter pays for exceeding carbon budgets. But perhaps the most important policy message of Bednar and colleagues' work is that the possibility of future CO₂-removal technologies does not justify limiting the pace of decarbonization today.

Nature **596**, 346–347 (2021)

doi: <https://doi.org/10.1038/d41586-021-02192-4>

References

1. 1.

Bednar, J. *et al.* *Nature* **596**, 377–383 (2021).

[Article](#) [Google Scholar](#)

2. 2.

Masson-Delmotte, V. *et al.* (eds) *Global Warming of 1.5°C* (IPCC, 2018).

[Google Scholar](#)

3. 3.

Geden, O. *WIREs Clim. Change* **7**, 790–797 (2016).

[Article](#) [Google Scholar](#)

4. 4.

IRENA. *Renewable Power Generation Costs in 2019* (IRENA, 2020).

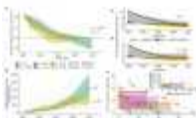
[Google Scholar](#)

[Download references](#)

Competing Interests

The author declares no competing interests.

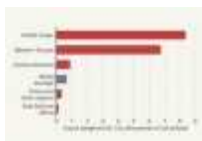
Related Articles



- [Read the paper: Operationalizing the net-negative carbon economy](#)



- [Trade-offs for equitable climate policy assessed](#)



- [The future costs of methane emissions](#)
- [See all News & Views](#)

Subjects

- [Climate change](#)

- [Climate sciences](#)
- [Environmental sciences](#)

nature careers

[Jobs](#) >

- [Group Leader \(f/m/d\) CRISPR/RNAi Technology for Target Identification \(Screening\) and Validation](#)

Evotech AG

Hamburg, Germany

- [Tier I Canada Research Chair in Infectious Disease & Immunity](#)

The University of British Columbia (UBC)

Vancouver, Canada

- [Clinical Research Nurse/Project Manager](#)

Oklahoma Medical Research Foundation (OMRF)

Oklahoma City, United States

- [Research Associate - Immunologist](#)

The University of British Columbia (UBC)

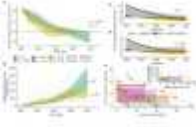
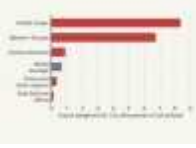
Vancouver, Canada

Nature Briefing

An essential round-up of science news, opinion and analysis, delivered to your inbox every weekday.

[Download PDF](#)

Related Articles

-  [**Read the paper: Operationalizing the net-negative carbon economy**](#)
-  [**Trade-offs for equitable climate policy assessed**](#)
-  [**The future costs of methane emissions**](#)
- [**See all News & Views**](#)

Subjects

- [Climate change](#)
- [Climate sciences](#)
- [Environmental sciences](#)

This article was downloaded by **calibre** from <https://www.nature.com/articles/d41586-021-02192-4>

- NEWS AND VIEWS
- 18 August 2021

Supersolids go two-dimensional

Supersolids are exotic materials whose constituent particles can simultaneously form a crystal and flow without friction. The first 2D supersolid has been produced using ultracold gases of highly magnetic atoms.

- [Bruno Laburthe-Tolra](#) ⁰
 1. [Bruno Laburthe-Tolra](#)

1. Bruno Laburthe-Tolra is at the Laser Physics Laboratory, Paris North University, 93430 Villetteuse, France.

[View author publications](#)

You can also search for this author in [PubMed](#) [Google Scholar](#)

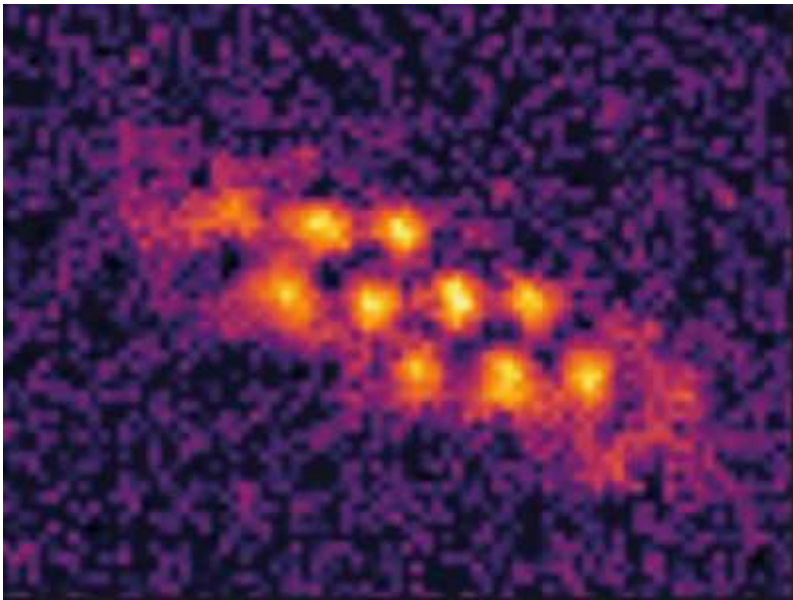




•

[Download PDF](#)

Despite their name, materials known as supersolids¹ are not super rigid. Instead, they combine the ordered structure of a solid with the properties of a superfluid — a substance that flows without friction. To picture a supersolid, consider an ice cube immersed in liquid water, with frictionless flow of the water through the cube. In 2019, supersolids were made using ultracold magnetic atoms^{2–4}, but the ordered structure existed in only one dimension. Now, in [a paper in *Nature*](#), Norcia *et al.*⁵ report the observation of a 2D supersolid formed by ultracold dysprosium atoms.



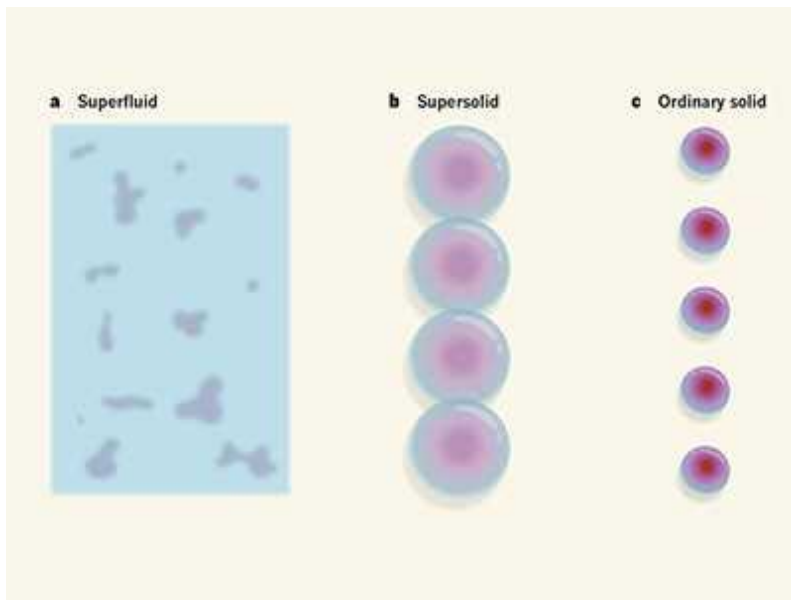
[Read the paper: Two-dimensional supersolidity in a dipolar quantum gas](#)

When a liquid becomes a solid, its density becomes strongly modulated as the ordered array of particles that constitutes a crystal emerges. This regular order, which characterizes solids ranging from ice to metals, is invisible to the naked eye and breaks a type of symmetry known as translational symmetry. For a material to become a supersolid, it must similarly break translational symmetry. Moreover, it needs to exhibit superfluidity, which requires it to behave like a wave that has a well-defined oscillation throughout the material.

Scientists first searched for supersolidity using helium atoms at cryogenic temperatures⁶. When the pressure is varied, such atoms can transition between a solid phase and a superfluid phase, suggesting the possible coexistence of solid and superfluid behaviours. Helium atoms are great candidates for observing supersolidity because, according to quantum mechanics, such ultralight atoms can easily behave like waves. Unfortunately, supersolid helium has remained elusive⁶.

Ultracold atomic gases, produced at temperatures of only about 100 nanokelvin, are other promising candidates for supersolidity because they can become a superfluid through Bose–Einstein condensation — a quantum-mechanical phenomenon in which all the atoms spontaneously organize into a collective macroscopic wave. By placing Bose–Einstein condensates into

patterns of laser light, researchers have observed self-arranged arrays of atoms that exhibit superfluidity^{7,8}. However, the periodicity of these crystals is determined by the laser's wavelength, which means that the material's lattice structure cannot vibrate like that of a conventional solid. Such systems therefore lack some of the degrees of freedom of supersolids.



Quantum gases show flashes of a supersolid

For these reasons, scientists were excited in 2019 when three groups announced the production of supersolids based on magnetic Bose–Einstein condensates^{2–4}. These condensates, made using strongly magnetic dysprosium or erbium atoms, are driven by the competition between two types of attractive and repulsive interaction. The experiments operate close to the limit at which the attraction between atoms is strong enough to make the system collapse. Under these conditions, the atoms form an array of droplets. The shape of each droplet is controlled by the competition between the atomic interactions and by an effective pressure resulting from quantum fluctuations. Furthermore, the spatial arrangement of the droplets is governed by the long-range magnetic repulsion between them.

In addition to this self-arranged array of droplets, there is a relatively large background gas of roughly uniform density that helps to provide the atomic wave with the well-defined oscillation that is needed for superfluidity. To picture this system, think of a lattice of droplets (corresponding to the solid

nature of the supersolid) coexisting with a uniform background gas (corresponding to the superfluid nature of the supersolid) — similar to the image mentioned above of an ice cube immersed in water, with the water flowing through the cube. But bear in mind that the crystal and background gas consist of the same atoms and form a single phase of matter: the supersolid.

Whereas these seminal studies made 1D droplet arrays and supersolids, Norcia and colleagues modified the optical trap that confines the atoms to produce a 2D droplet array and supersolid (Fig. 1). This demonstration is a key advance because one direct way to prove that a system exhibits superfluidity is to study its properties under rotation, and this analysis cannot be achieved if the system has only one dimension.

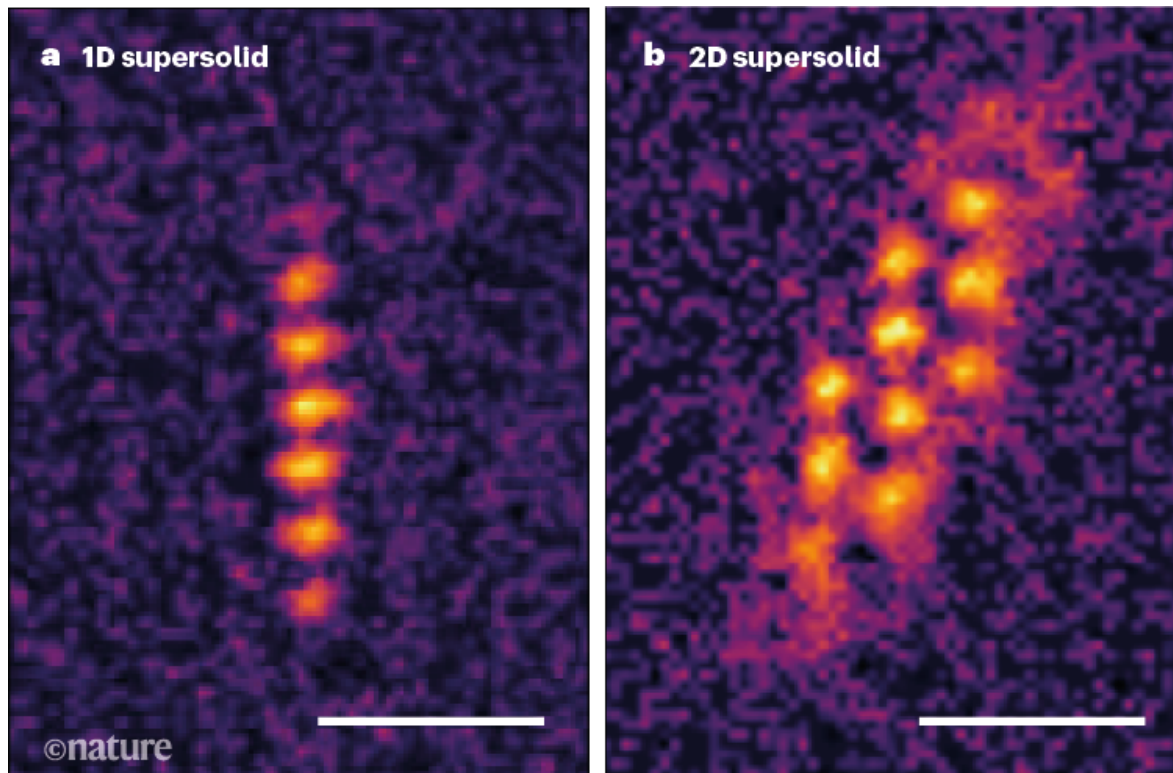


Figure 1 | Supersolids formed by an ultracold atomic gas. Supersolids are materials that combine the ordered structure of a solid with the frictionless flow of a substance called a superfluid. Norcia *et al.*⁵ made one- and two-dimensional supersolids using an ultracold gas of dysprosium atoms. The colours represent the density of the systems from low (black) to high (yellow). Scale bars, 10 micrometres. (Adapted from Fig. 2b,d of ref. 5.)

A superfluid can be rotated only by twisting its corresponding wave in such a way that the superfluid hosts a vortex, similar to a whirlpool in water. The formation of this vortex requires a certain amount of energy, so that, in practice, the superfluid does not rotate until a sufficiently large rotational force is applied to the system. This peculiar behaviour causes the superfluid to have an unconventional moment of inertia — a quantity that measures the extent to which an object resists rotational acceleration. For a supersolid, it is qualitatively expected that the crystal component will rotate like a rigid body, whereas the background gas will not¹. Comparing the moment of inertia of the authors' supersolid with that of an ordinary solid would be one way to determine the fraction of the supersolid that exhibits superfluidity.

Another question still to be addressed is to what extent the properties of the supersolid are driven by its limited size. The properties of systems that have long-range interactions, such as the magnetic interactions in the present case, are often driven by the structure of the system's outer edges. In Norcia and colleagues' experiment, the droplet array has a structure that is extremely sensitive to the trap, indicating a high sensitivity to such boundary effects⁹. It remains to be seen whether systems larger than the authors' supersolid can be made.

In the present experiment, the background gas of the supersolid has a healing length (a quantity that, for example, determines the size of a vortex core) that is probably much smaller than the material. This observation indicates that the system is already large enough to host vortex arrays¹⁰ and other excitations associated with the symmetries and structure of a supersolid. The full study of the dynamical properties of this phase of matter will be an exciting research topic in the next few years.

Nature **596**, 348-349 (2021)

doi: <https://doi.org/10.1038/d41586-021-02191-5>

References

1. 1.

Leggett, A. J. *Phys. Rev. Lett.* **25**, 1543–1546 (1970).

[Article](#) [Google Scholar](#)

2. 2.

Tanzi, L. *et al.* *Phys. Rev. Lett.* **122**, 130405 (2019).

[PubMed](#) [Article](#) [Google Scholar](#)

3. 3.

Böttcher, F. *et al.* *Phys. Rev. X* **9**, 011051 (2019).

[Article](#) [Google Scholar](#)

4. 4.

Chomaz, L. *et al.* *Phys. Rev. X* **9**, 021012 (2019).

[Article](#) [Google Scholar](#)

5. 5.

Norcia, M. A. *et al.* *Nature* **596**, 357–361 (2021).

[Article](#) [Google Scholar](#)

6. 6.

Chan, M. H. W., Hallock, R. B. & Reatto, L. *J. Low Temp. Phys.* **172**, 317–363 (2013).

[Article](#) [Google Scholar](#)

7. 7.

Li, J.-R. *et al.* *Nature* **543**, 91–94 (2017).

[PubMed](#) [Article](#) [Google Scholar](#)

8. 8.

Léonard, J., Morales, A., Zupancic, P., Esslinger, T. & Donner, T. *Nature* **543**, 87–90 (2017).

[PubMed](#) [Article](#) [Google Scholar](#)

9. 9.

Roccuzzo, S. M., Stringari, S. & Recati, A. Preprint at <https://arxiv.org/abs/2104.01068> (2021).

10. 10.

Gallemí, A., Roccuzzo, S. M., Stringari, S. & Recati, A. *Phys. Rev. A* **102**, 023322 (2020).

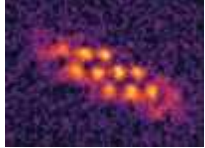
[Article](#) [Google Scholar](#)

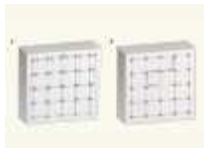
[Download references](#)

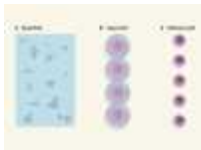
Competing Interests

The author declares no conflicts of interest.

Related Articles

-  [Read the paper: Two-dimensional supersolidity in a dipolar quantum gas](#)

-  [A solid more fluid than a fluid](#)



- [Quantum gases show flashes of a supersolid](#)
- [See all News & Views](#)

Subjects

- [Atomic and molecular physics](#)
- [Quantum physics](#)
- [Condensed-matter physics](#)

nature careers

[Jobs](#) >

- [Group Leader \(f/m/d\) CRISPR/RNAi Technology for Target Identification \(Screening\) and Validation](#)

Evotec AG
Hamburg, Germany
- [Tier I Canada Research Chair in Infectious Disease & Immunity](#)

The University of British Columbia (UBC)
Vancouver, Canada
- [Clinical Research Nurse/Project Manager](#)

Oklahoma Medical Research Foundation (OMRF)
Oklahoma City, United States

- [Research Associate - Immunologist](#)

The University of British Columbia (UBC)

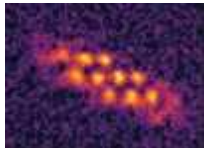
Vancouver, Canada

Nature Briefing

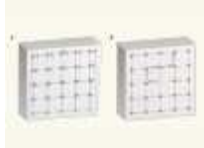
An essential round-up of science news, opinion and analysis, delivered to your inbox every weekday.

[Download PDF](#)

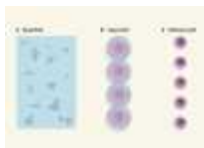
Related Articles



- [Read the paper: Two-dimensional supersolidity in a dipolar quantum gas](#)



- [A solid more fluid than a fluid](#)



- [Quantum gases show flashes of a supersolid](#)
- [See all News & Views](#)

Subjects

- [Atomic and molecular physics](#)
- [Quantum physics](#)

- [Condensed-matter physics](#)
-

This article was downloaded by **calibre** from <https://www.nature.com/articles/d41586-021-02191-5>

| [Section menu](#) | [Main menu](#) |

- NEWS AND VIEWS
- 04 August 2021

Deranged chromatin drives uterine fibroid tumours

A previously unknown subgroup of uterine fibroid tumours is driven by mutations that result in disruption of the DNA–protein complex chromatin. The findings could inform the management of this common condition.

- [Zehra Ordulu](#) ✉

1. [Zehra Ordulu](#)

1. Zehra Ordulu is in the Department of Pathology, Massachusetts General Hospital, Harvard Medical School, Boston, Massachusetts 02114, USA, and the Department of Pathology, University of Florida, Gainesville.

[View author publications](#)

You can also search for this author in [PubMed](#) [Google Scholar](#)



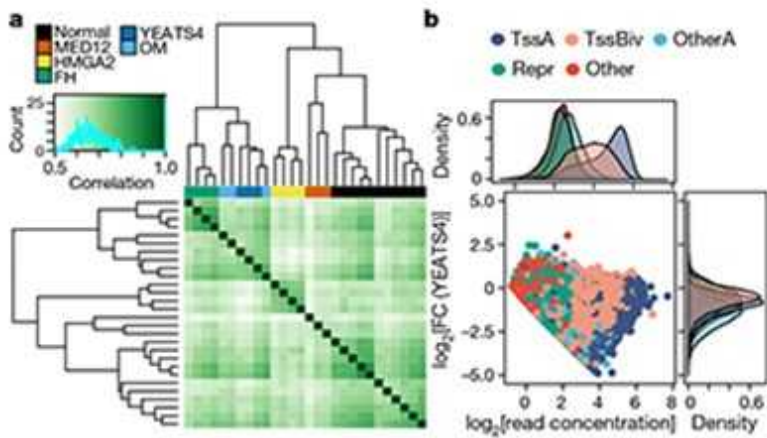


•

[Download PDF](#)

More than 70% of women are at risk of developing benign tumours of the uterus wall called uterine leiomyomas (ULs) by the age of 50¹. These tumours, which are also known as fibroids or myomas, can cause debilitating symptoms in women such as excessive bleeding, and even infertility, with surgery being the only curative treatment. ULs therefore remain the leading cause of hysterectomies in the United States². Understanding the molecular mechanisms that result in UL development could assist in the discovery of new approaches to clinical care. [Writing in](#)

[Nature](#), Berta *et al.*³ provide insights into the molecular basis of UL formation.



[Read the paper: Deficient H2A.Z deposition is associated with genesis of uterine leiomyoma](#)

Previous work has identified at least three mutually exclusive categories of UL, defined according to the genetic alterations they show: those with mutations in the gene *MED12* (70%); those in which *HMGAI* is activated (15%); and tumours in which *FH* is mutated (1%)⁴. However, a subset of ULs do not harbour any of these alterations. To characterize the molecular subgroups of ULs more comprehensively, Berta *et al.* used various molecular techniques to study the genomes of 2,263 tumours from 728 women.

The authors identified the previously known molecular subgroups in the sampled tumours, and used RNA sequencing to assess gene expression in subgroup-representative tumours and in all available tumours with unknown drivers. Nearly 40% of the tumours from the latter group showed high expression of *HMGAI* — perhaps not surprisingly, given earlier work⁵ implicating *HMGAI* alterations in UL. More interestingly, the authors also identified a previously uncharacterized subclass of UL in this ‘unknown driver’ category. Tumours in this subclass carried alterations in the genes

encoding proteins that make up the SRCAP complex, which is involved in remodelling of the genetic material in the nucleus.

DNA is packaged up in the nucleus in the form of chromatin. The DNA strand is wrapped around protein cores, each consisting of eight histone subunits, to form structural units of chromatin called nucleosomes. The SRCAP complex is an epigenetic remodeler: it regulates the structure of chromatin without altering the sequence of DNA bases. Specifically, it catalyses the incorporation of the histone variant H2A.Z into chromatin⁶. H2A.Z is involved in the regulation of gene transcription, the maintenance of genome integrity and DNA repair. Overexpression of H2A.Z is implicated in several types of cancer⁶.

Berta *et al.* found alterations in six of the nine genes that encode proteins in the SRCAP complex, with *YEATS4* being the most commonly altered gene. Inactivation of both copies of SRCAP-complex genes was a common finding (Fig. 1). This inactivation was caused either by loss of the non-mutated copy of the gene or, in the case of *YEATS4* alterations, by epigenetic silencing of the remaining copy of the gene. Moreover, the authors identified six individuals who had at least two tumours with mutations in SRCAP-complex genes, suggesting that certain individuals might be particularly predisposed to such alterations, perhaps because of environmental factors or because of inherited genetic variants, known as germline alterations.

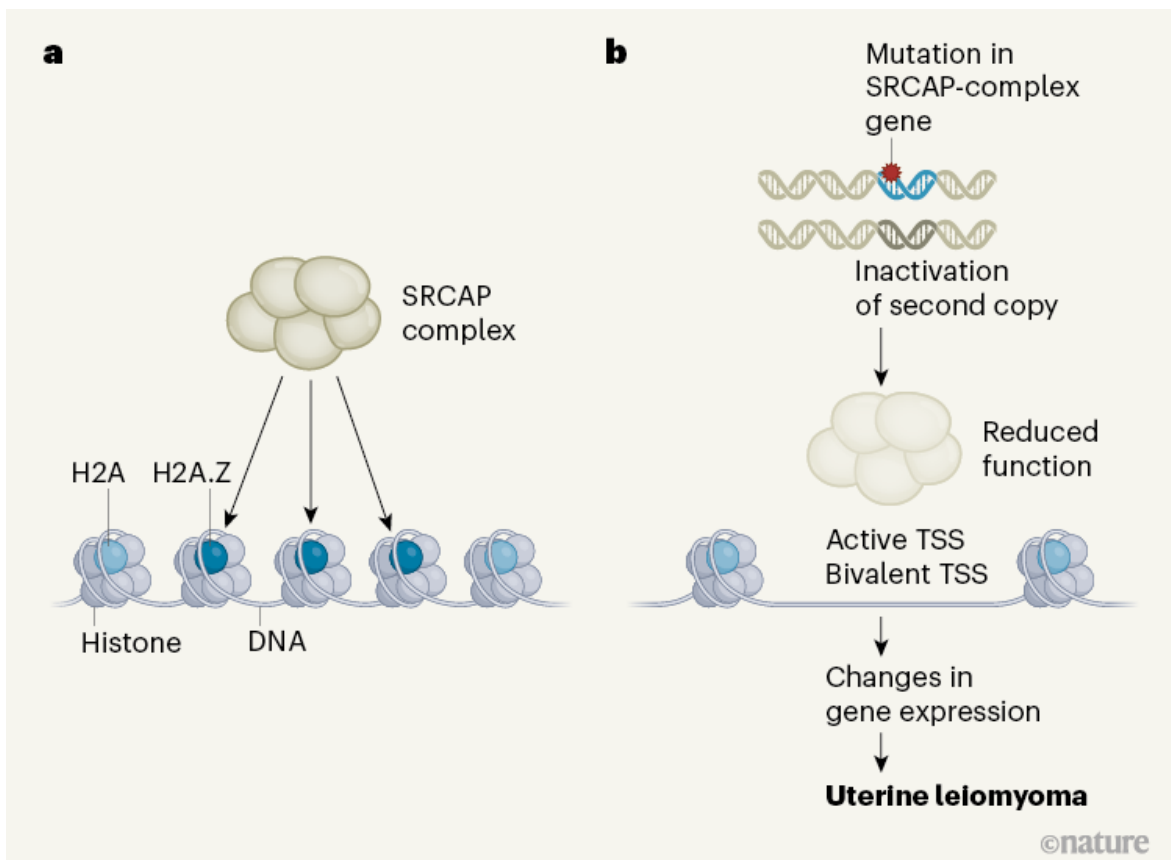
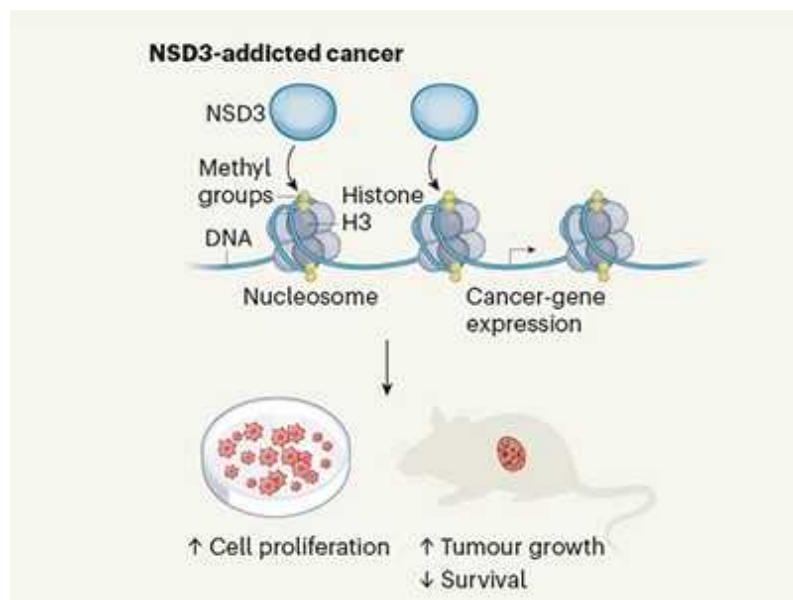


Figure 1 | A molecular mechanism underlying formation of uterine leiomyoma tumours. **a**, The SRCAP complex of proteins remodels chromatin (DNA wrapped around complexes of histone proteins) by loading it with the histone H2A variant H2A.Z, which regulates gene expression. **b**, Berta *et al.*³ examined genomic alterations in 2,263 uterine leiomyoma tumours from 728 women. Some tumours were driven by mutations in genes encoding protein components of the SRCAP complex, combined with another ‘second-hit’ genetic alteration (such as a deletion). The resulting inactivation of both copies of a SRCAP-complex gene can reduce SRCAP-complex function. This leads to deficient loading of H2A.Z at exposed regions of chromatin that contain transcription start sites (TSSs) that are active and bivalent (that is, bearing repressive and activating regulators). Overall, this results in underexpression of some genes and overexpression of others — including certain genes involved in the spatial organization of growing tissue.

The authors therefore studied germline alterations in the protein-coding portion of the genomes of 25,506 women, stored in the UK Biobank. They

found that mutations predicted to reduce the function of the proteins encoded by *YEATS4* and another SRCAP-complex gene, *ZNHIT1*, were strong candidates for an increased risk of UL. The authors validated the UL risk associated with such mutations in a replication group of 78,905 women, obtained from the UK Biobank. Remarkably, in both groups overall, the number of these germline alterations in SRCAP genes was greater than the number of *FH* mutations, which are well known to predispose women to UL⁷.

Given the role of the SRCAP complex in loading H2A.Z into chromatin, the authors examined H2A.Z status in samples of myometrium (normal uterine wall) and ULs. SRCAP-altered tumours showed a striking loss of H2A.Z, whereas myometrium, *MED12*-mutated tumours and *FH*-mutated tumours showed strong expression, and *HMGAI*- or *HMGAA2*-altered tumours had moderate expression.



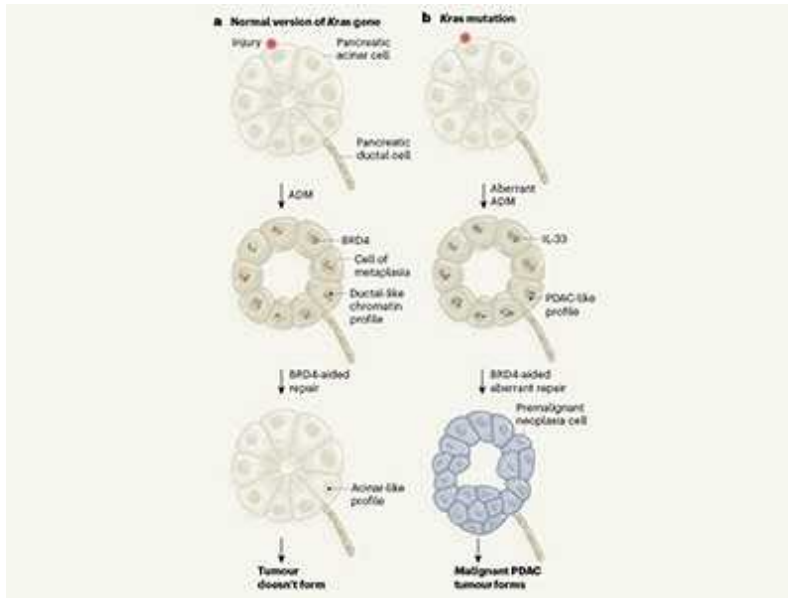
An epigenetic tipping point in cancer comes under the microscope

The authors then analysed H2A.Z binding to chromatin, making use of chromatin immunoprecipitation (ChIP) sequencing, a method that analyses protein–DNA interactions. Compared with myometrium, SRCAP-altered tumours showed reduced H2A.Z–chromatin binding, compatible with the loss of H2A.Z protein expression in this subgroup. Intriguingly, *MED12*-mutated tumours also had a global decrease in H2A.Z–chromatin binding,

despite having strong H2A.Z expression. *HMGA2*-altered tumours that had lower H2A.Z protein expression than normal also showed decreased binding of H2A.Z.

Findings of a different assay evaluating chromatin organization were complementary to the ChIP-sequencing results. Overall, Berta *et al.* observed that chromatin activation (whereby the DNA is exposed) in *YEATS4*-mutated tumours preferentially occurred at transcription start sites (TSSs) that were active or bivalent (that is, bearing both repressive and activating epigenetic regulators). These activated chromatin regions showed reduced H2A.Z binding compared with that in myometrium. These findings are in line with previous animal studies reporting that the loss of SRCAP-complex function results in reduced H2A.Z–chromatin binding⁶. In association with this epigenetic modification at these TSSs, *YEATS4*-mutated tumours had changes in the expression of various genes (Fig. 1). Many of the genes showing increased expression were associated with the spatial organization of cells in growing tissues.

All UL subgroups exhibited increases in the expression of three sets of genes: those encoding the CBX2, CBX4 and CBX8 protein components of the canonical polycomb repressor complex 1 (cPRC1) that epigenetically silences genes to regulate development; genes encoding the developmental transcription factors SATB2 and HOXA13; and genes encoding the enzymes SRD5A2 and HSD17B6, which synthesize the sex hormone dihydrotestosterone. By contrast, expression of the gene encoding CBX7, also a component of cPRC1, was reduced. Given that mutations in *MED12* are the most common genomic alterations in UL, it is interesting that MED12 protein was previously shown to act with CBX7-containing PRC1 to repress the expression of genes involved in mouse cell differentiation⁸. Berta and colleagues' findings suggest that, regardless of the mutation status of the tumours, altered PRC1 function might lead to abnormal differentiation of cells that are encouraged to divide by overexpressed developmental transcription factors, potentially leading to UL formation. In addition, inhibiting the enzymes SRD5A2 and HSD17B6 might be a potential therapeutic strategy for treating some ULs.



Mutation alters chromatin changes during injury response to drive cancer

Berta and colleagues' study is a tour de force in the molecular subclassification of UL. Some questions remain, however. Although there are some hints of the presence of H2A.Z alterations in UL subgroups without SRCAP-complex mutations, the underlying mechanisms are still unknown. Even in SRCAP-altered tumours, a detailed understanding of how ULs might result from diminished H2A.Z–chromatin binding requires further study. The reasons why some individuals accumulate SRCAP-complex-deficient ULs are also not obvious, although the germline-alteration findings suggest a hereditary component. However, environmental factors, such as changes in an individual's hormonal milieu, might also affect the abnormal differentiation of the bivalent regions of the myometrium genome, and warrant further study. Moreover, SRCAP-complex genes are not currently targeted by clinical sequencing assays, so it might be challenging to translate these findings into routine clinical practice.

Uterine leiomyomas affect millions of women and cost more than US\$1 billion in health care annually in the United States². A comprehensive understanding of the genomic underpinnings of the distinct molecular subgroups of ULs might eventually inform clinical decision-making, from diagnosis to therapy. Berta and co-workers' study describes how SRCAP-complex alterations lead to decreased loading of H2A.Z into chromatin in UL, recapitulating observations in previous model systems⁶. The association

of germline SRCAP-complex gene mutations with predisposition of women to develop ULs not only further supports the authors' genomic findings in the tumours, but also can have immediate clinical implications for the genetic counselling of affected women and their family members. Through multiple layers of '-omics' data, the authors suggest an epigenetic mechanism for UL development whereby deranged chromatin leads to the expression of genes involved in tumour formation.

Nature **596**, 349–351 (2021)

doi: <https://doi.org/10.1038/d41586-021-02005-8>

References

1. 1.

Baird, D. D., Dunson, D. B., Hill, M. C., Cousins, D. & Schectman, J. M. *Am. J. Obstet. Gynecol.* **188**, 100–107 (2003).

[PubMed](#) [Article](#) [Google Scholar](#)

2. 2.

Morgan, D. M. *et al.* *Am. J. Obstet. Gynecol.* **218**, 425–425 (2018).

[PubMed](#) [Google Scholar](#)

3. 3.

Berta, D. G. *et al.* *Nature* **596**, 398–403 (2021).

[Article](#) [Google Scholar](#)

4. 4.

Mehine, M., Mäkinen, N., Heinonen, H.-R., Aaltonen, L. A. & Vahteristo, P. *Fertil. Steril.* **102**, 621–629 (2014).

[PubMed](#) [Article](#) [Google Scholar](#)

5. 5.

Williams, A. J., Powell, W. L., Collins, T. & Morton, C. C. *Am. J. Pathol.* **150**, 911–918 (1997).

[PubMed](#) [Google Scholar](#)

6. 6.

Giaimo, B. D., Ferrante, F., Herchenröther, A., Hake, S. B. & Borggrefe, T. *Epigenet. Chromatin* **12**, 37 (2019).

[PubMed](#) [Article](#) [Google Scholar](#)

7. 7.

Tomlinson, I. P. M. *et al.* *Nature Genet.* **30**, 406–410 (2002).

[PubMed](#) [Article](#) [Google Scholar](#)

8. 8.

Papadopoulou, T., Kaymak, A., Sayols, S. & Richly, H. *Cell Cycle* **15**, 1479–1493 (2016).

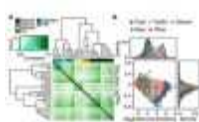
[PubMed](#) [Article](#) [Google Scholar](#)

[Download references](#)

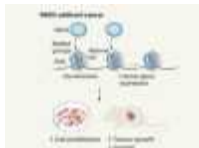
Competing Interests

The author declares no competing interests.

Related Articles



- [Read the paper: Deficient H2A.Z deposition is associated with genesis of uterine leiomyoma](#)



- [An epigenetic tipping point in cancer comes under the microscope](#)



- [Mutation alters chromatin changes during injury response to drive cancer](#)
- [See all News & Views](#)

Subjects

- [Genomics](#)
- [Genetics](#)
- [Epigenetics](#)
- [Medical research](#)

nature careers

[Jobs](#) >

- [Group Leader \(f/m/d\) CRISPR/RNAi Technology for Target Identification \(Screening\) and Validation](#)

Evotec AG

Hamburg, Germany

- [**Tier I Canada Research Chair in Infectious Disease & Immunity**](#)

The University of British Columbia (UBC)

Vancouver, Canada

- [**Clinical Research Nurse/Project Manager**](#)

Oklahoma Medical Research Foundation (OMRF)

Oklahoma City, United States

- [**Research Associate - Immunologist**](#)

The University of British Columbia (UBC)

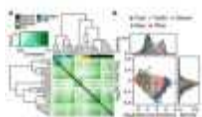
Vancouver, Canada

Nature Briefing

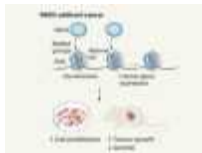
An essential round-up of science news, opinion and analysis, delivered to your inbox every weekday.

[Download PDF](#)

Related Articles



- [**Read the paper: Deficient H2A.Z deposition is associated with genesis of uterine leiomyoma**](#)



- [An epigenetic tipping point in cancer comes under the microscope](#)



- [Mutation alters chromatin changes during injury response to drive cancer](#)
- [See all News & Views](#)

Subjects

- [Genomics](#)
- [Genetics](#)
- [Epigenetics](#)
- [Medical research](#)

This article was downloaded by **calibre** from <https://www.nature.com/articles/d41586-021-02005-8>

- NEWS AND VIEWS
- 04 August 2021
- Correction [20 August 2021](#)

A cocktail of pesticides, parasites and hunger leaves bees down and out

Pollinators are under threat. A meta-analysis reveals that the combination of agrochemicals, parasites and malnutrition has a cumulative negative effect on bees, and that pesticide–pesticide interactions increase bee mortality.

- [Adam J. Vanbergen](#) ORCID: <http://orcid.org/0000-0001-8320-5535> 0
 1. [Adam J. Vanbergen](#)

1. Adam J. Vanbergen is in the Department of Plant Health and Environment, INRAE (the National Research Institute for Agriculture, Food and Environment), Dijon 21000, France.

[View author publications](#)

You can also search for this author in [PubMed](#) [Google Scholar](#)





•

[Download PDF](#)

Worldwide, an estimated 20,000 species of wild and managed bees pollinate flowers, aiding plant reproduction¹. In doing so, they form a key link in the tangled web of species interactions that support biodiverse and healthy ecosystems^{1,2}. Moreover, humans enjoy a variety of sociocultural and economic benefits from pollinator biodiversity^{2,3}, and pollination secures crop yields that supply essential nutrients and healthy, diverse diets^{1,4}.

[Writing in Nature](#), Siviter *et al.*⁵ report a pollinator threat that jeopardizes these benefits.

Pollinators and pollination are threatened by environmental pressures, including many that are a consequence of human activity (Fig. 1). These pressures include land-use and climate change^{2,6}, intensive agriculture⁷, the spread of invasive alien species and problems with pests and disease-causing agents (pathogens)^{2,8}. The individual effects of these pressures on pollinators are well established^{1,2}, raising the question of whether an interplay between these various pressures exacerbates the overall risk that they pose to pollinators and pollination^{9–11}. This issue has been recognized by the Intergovernmental Science-Policy Platform on Biodiversity and Ecosystem Services, which stated² in 2016 that “many drivers that directly impact the health, diversity and abundance of pollinators … can combine in their effects and thereby increase the overall pressure on pollinators”.

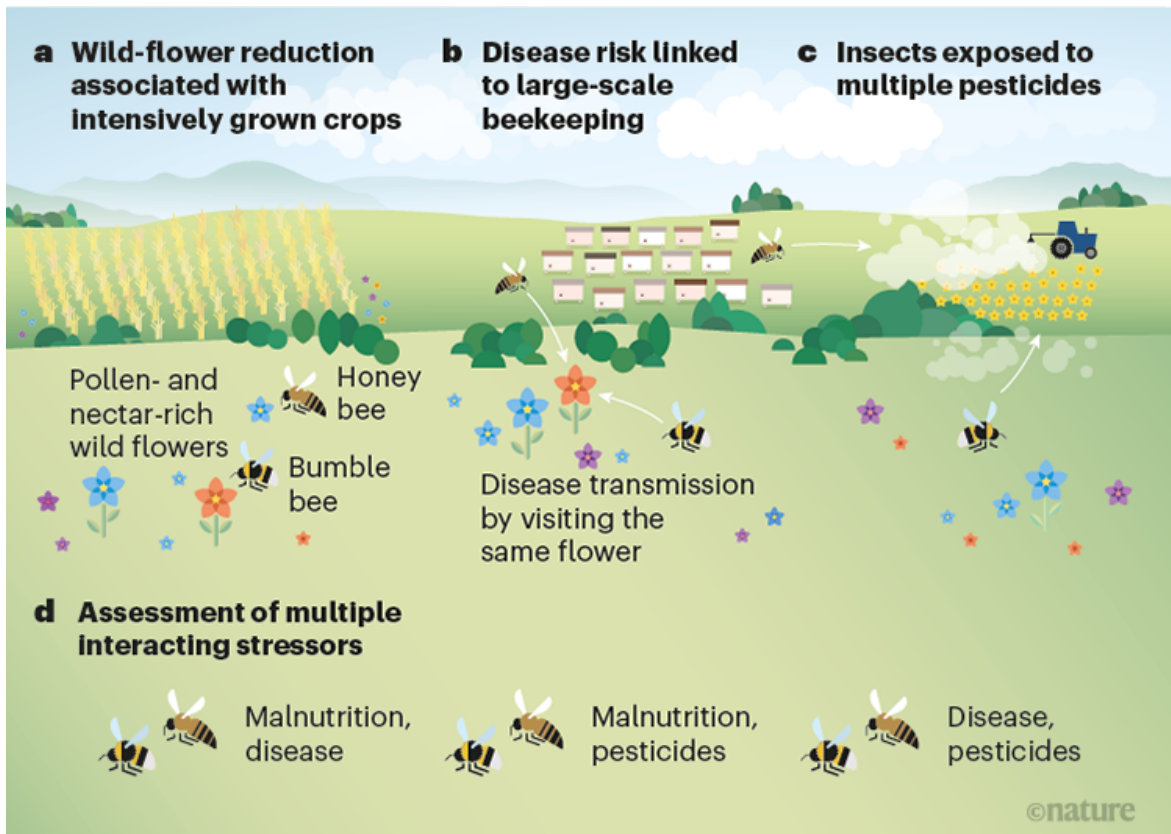
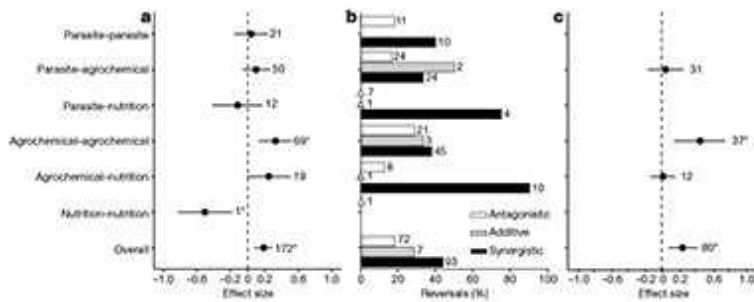


Figure 1 | The effect of multiple stressors on bees. Agricultural intensification has put pollinators under pressure. **a**, Practices associated with intensive farming reduce food availability for pollinators^{1,2,7,12}. **b**, Managed high-density bee colonies for crop pollination are associated with these pollinators being at risk of disease and parasite infection². This poses a

risk of illness spreading to wild bees. **c**, Exposure to a variety of pesticides poses another risk to pollinators. **d**, Siviter *et al.*⁵ present a meta-analysis that indicates the consequences for bees of combinations (some examples shown) of these challenges.

Intensive agriculture is a multifactorial source of stress on pollinator populations^{1,7,10,11}. Pollinating insects, such as bees, face the physiological challenge of acute or chronic harm from exposure to various agrochemicals, including fungicides and pesticides, that are used to protect crop plants. They also face nutritional stress arising from the lack of pollen- and nectar-providing wild flowers in large-scale, intensive crop monocultures^{1,2,7,12}. Moreover, the industrial transport and use of managed high-density colonies of honey bees (*Apis mellifera*) for crop pollination can increase pollinator exposure to parasites or pathogens², and might result in disease spillover to wild pollinators¹³. Over the past decade, the lethal or sublethal effect of combinations of agrochemical, pathogenic or nutritional stressors on bees has been tested in many individual experiments^{2,9,10}.



[Read the paper: Agrochemicals interact synergistically to increase bee mortality](#)

Siviter *et al.* advance this knowledge through a quantitative meta-analysis of the effect of interactions between agrochemical, pathogenic and nutritional

stressors on multiple aspects of bee health and fitness. Their analysis is notable because of the breadth of bee responses considered (for example, foraging behaviour, memory, mortality and colony reproduction), and for comparisons of the interactions of multiple classes of stressor (for example, agrochemical–parasite, parasite–nutrition, agrochemical–agrochemical and parasite–parasite interactions).

The authors conducted a monumental literature search that yielded almost 15,000 relevant individual studies. Siviter and colleagues combed through these publications to focus on the experiments that investigated the combined effect of parasites (microorganisms and invertebrates), agrochemicals and nutritional stressors on bee health. The authors selected studies that used a balanced and replicated experimental design, and that provided accessible data (means, standard deviations and sample sizes) for each treatment. This rigorous focus and quality control resulted in a final set of 90 studies being selected for further analysis.

These studies provide a total of 356 effect sizes (measurements indicating the magnitude of a relationship between factors of interest and a particular outcome) for different stressor and bee-response combinations. The authors accounted for data issues that might have confounded their accurate detection of bee responses. Such challenges included those arising from statistical non-independence of multiple effects reported from a single study, publication biases (for example, the lack of negative results), species skews (honey bee data sets predominated), and how experimental treatments such as pesticide dose compare with what might be realistically encountered in the field (termed field realism).



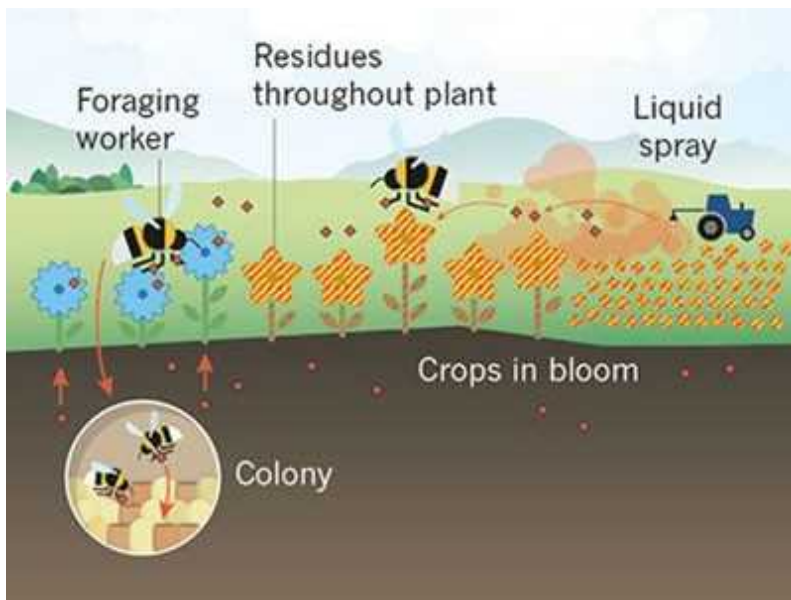
Robust evidence of declines in insect abundance and biodiversity

Siviter and colleagues tested whether the stressor interactions were synergistic, meaning that their combined effect was greater than the sum of their individual effects, as would be the case if the effect of one stressor on a bee elevates the effect of another stressor. The authors also examined alternative scenarios in which the effects of multiple stressors were antagonistic (the effect of one stressor lessens the effect of another) or additive (the combined effect is equivalent to the sum of the individual effects).

A consistent message from their analysis is that bee mortality is increased by a synergistic interaction between multiple stressors — the worst-case scenario, indicating a disproportionate effect of multiple stressors on bee survival. Interactions between different agrochemicals, rather than other stressors, drove this overall effect, and this finding held true when accounting for the field realism of the agrochemical doses. This result confirms that the cocktail of agrochemicals that bees encounter in an intensively farmed environment can create a risk to bee populations^{1,2,9,14}. Multi-stressor interactions involving parasites and nutritional stress (including in combination with agrochemicals) produced additive effects on bee mortality overall.

The authors' deeper analysis of the biological complexity, however, revealed large differences between particular parasite groups in terms of the full range of additive, antagonistic and synergistic effects on bee mortality, when considering interactions between different parasites or between different parasites and nutritional stress. This variability in response, together with the lower sample sizes for the interactions involving stressors other than agrochemicals, indicate a caveat to consider and also suggest a need for more research on the combined effects of biological sources of stress.

It is intriguing that Siviter and colleagues found that additive, not synergistic, effects predominated for the non-lethal effects of stressors on fitness proxies (such as modifications of bee behaviour or reproduction, changes in parasite load or immune function). Such non-lethal changes could ultimately affect bee mortality rates. Consequently, how the observed synergistic effects of agrochemicals on bee mortality arise remains to be established. More work is therefore needed to identify the mechanism that links exposure to behavioural or physiological changes and mortality.



An alternative to controversial pesticides still harms bumblebees

The majority of the studies in the data set were of managed populations of *A. mellifera*, so the authors also separately analysed responses at the level of bee genus (*Apis*, *Bombus*, *Megachile* and *Osmia*). *Apis* mortality was affected by a synergistic multi-stressor interaction qualitatively similar to the

full analysis of all bee genera. Other bee genera exhibited additive or antagonistic mortality responses from many fewer studies. This raises an important point. There is a need for research efforts and regulators to widen their focus from *A. mellifera* — a single, mostly managed bee species — to other pollinator model organisms, whose different ecology and evolutionary history might result in different responses to stressors¹⁰.

Siviter and colleagues' findings of the cumulative negative effect of multi-stressor interactions on bees reinforces the call to evaluate such interactions to avoid unforeseen risks to biodiversity and healthy ecosystems^{1,9,10}. In some regions of the world, regulatory risk-assessment frameworks for plant-protection products are being developed to deal with sublethal, long-term and potentially synergistic effects among stressors¹⁵ (see go.nature.com/3f4ax5r), but their biological and geographical scope must be extended. The authors acknowledge that the high levels of variability between the studies and parameters investigated demand an appropriately cautious interpretation. However, this highlights the need for worldwide reconsideration of risk-assessment approaches for pesticide regulation.

Given the widespread loss of habitat resources — such as pollen and nectar sources — from intensively managed agricultural landscapes^{7,12}, nutritional deficits occurred surprisingly infrequently as a mechanism underlying bees' physiological stress (they accounted for only 58 out of the 365 measurements of effect sizes). A greater consideration of how nutritional stress interacts with exposure to pathogens and agrochemicals is therefore an obvious research gap to fill. Moreover, ensuring that experimental treatments are calibrated to simulate realistic environmental conditions would greatly aid risk assessments. This might include three-way combinations of field-realistic chemical doses and parasite levels, and a spatio-temporal dietary diversity similar to that found in semi-natural or highly human-modified landscapes.

The next challenge is to look beyond these parasite–nutrition–agrochemical interactions to consider other risks to pollination. Future studies must ultimately consider, through a combination of correlative and experimental approaches, the interplay of nutrition–pathogen–agrochemical interactions alongside the effects of other human-driven changes (such as climate

change, pollution, land-use changes and the spread of invasive species)^{1,2,11}. Although such assessments would be non-trivial to carry out, they will be vital for understanding and ranking the relative risks to pollinators and pollination that are coming from multiple combinations of pressures resulting from global changes.

Nature **596**, 351–352 (2021)

doi: <https://doi.org/10.1038/d41586-021-02079-4>

Updates & Corrections

- **Correction 20 August 2021:** This article incorrectly stated that an estimated 20,000 species of wild and managed insects pollinate flowers. It should have said that an estimated 20,000 species of wild and managed bees pollinate flowers.

References

1. 1.

Potts, S. G. *et al.* *Nature* **540**, 220–229 (2016).

[PubMed](#) [Article](#) [Google Scholar](#)

2. 2.

IPBES. *The Assessment Report of the Intergovernmental Science-Policy Platform on Biodiversity and Ecosystem Services on Pollinators, Pollination and Food Production* (IPBES Secretariat, 2016).

[Google Scholar](#)

3. 3.

Hill, R. *et al.* *Nature Sustain.* **2**, 214–222 (2019).

[Article](#) [Google Scholar](#)

4. 4.

Chaplin-Kramer, R. *et al.* *Science* **366**, 255–258 (2019).

[PubMed](#) [Article](#) [Google Scholar](#)

5. 5.

Siviter, H. *et al.* *Nature* **596**, 389–392 (2021).

[Article](#) [Google Scholar](#)

6. 6.

Soroye, P., Newbold, T. & Kerr, J. *Science* **367**, 685–688 (2020).

[PubMed](#) [Article](#) [Google Scholar](#)

7. 7.

Kovács-Hostyánszki, A. *et al.* *Ecol. Lett.* **20**, 673–689 (2017).

[PubMed](#) [Article](#) [Google Scholar](#)

8. 8.

Vanbergen, A. J., Espíndola, A. & Aizen, M. A. *Nature Ecol. Evol.* **2**, 16–25 (2018).

[PubMed](#) [Article](#) [Google Scholar](#)

9. 9.

Goulson, D., Nicholls, E., Botías, C. & Rotheray, E. L. *Science* **347**, 1255957 (2015).

[PubMed](#) [Article](#) [Google Scholar](#)

10. 10.

Vanbergen, A. J. & the Insect Pollinators Initiative. *Front. Ecol. Environ.* **11**, 251–259 (2013).

[Article](#) [Google Scholar](#)

11. 11.

González-Varo, J. P. *et al.* *Trends Ecol. Evol.* **28**, 524–530 (2013).

[PubMed](#) [Article](#) [Google Scholar](#)

12. 12.

Baude, M. *et al.* *Nature* **530**, 85–88 (2016).

[PubMed](#) [Article](#) [Google Scholar](#)

13. 13.

Manley, R. *et al.* *Ecol. Lett.* **22**, 1306–1315 (2019).

[PubMed](#) [Article](#) [Google Scholar](#)

14. 14.

Woodcock, B. A. *et al.* *Nature Commun.* **7**, 12459 (2016).

[PubMed](#) [Article](#) [Google Scholar](#)

15. 15.

European Food Safety Authority. *EFSA J.* **11**, 3295 (2013).

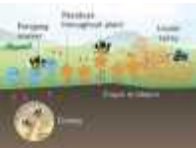
[Article](#) [Google Scholar](#)

[Download references](#)

Competing Interests

The author declares no competing interests.

Related Articles

- 
[Read the paper: Agrochemicals interact synergistically to increase bee mortality](#)
- 
[An alternative to controversial pesticides still harms bumblebees](#)
- 
[Robust evidence of declines in insect abundance and biodiversity](#)
- [See all News & Views](#)

Subjects

- [Ecology](#)
- [Agriculture](#)

nature careers

Jobs >

- [Group Leader \(f/m/d\) CRISPR/RNAi Technology for Target Identification \(Screening\) and Validation](#)

Evotec AG

Hamburg, Germany

- [**Tier I Canada Research Chair in Infectious Disease & Immunity**](#)

The University of British Columbia (UBC)

Vancouver, Canada

- [**Clinical Research Nurse/Project Manager**](#)

Oklahoma Medical Research Foundation (OMRF)

Oklahoma City, United States

- [**Research Associate - Immunologist**](#)

The University of British Columbia (UBC)

Vancouver, Canada

Nature Briefing

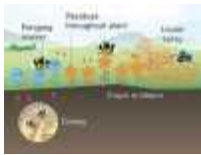
An essential round-up of science news, opinion and analysis, delivered to your inbox every weekday.

[Download PDF](#)

Related Articles



- [**Read the paper: Agrochemicals interact synergistically to increase bee mortality**](#)



- An alternative to controversial pesticides still harms bumblebees



- Robust evidence of declines in insect abundance and biodiversity
- See all News & Views

Subjects

- Ecology
- Agriculture

This article was downloaded by **calibre** from <https://www.nature.com/articles/d41586-021-02079-4>

| [Section menu](#) | [Main menu](#) |

Lenghu on the Tibetan Plateau as an astronomical observing site

[Download PDF](#)

- Article
- Open Access
- [Published: 18 August 2021](#)

Lenghu on the Tibetan Plateau as an astronomical observing site

- [Licai Deng](#) [ORCID: orcid.org/0000-0001-9073-9914](#)^{1,2,3},
- [Fan Yang](#) ^{1,2},
- [Xiaodian Chen](#) [ORCID: orcid.org/0000-0001-7084-0484](#)^{1,2,3},
- [Fei He](#) [ORCID: orcid.org/0000-0003-0542-2686](#)^{4,5},
- [Qili Liu](#) [ORCID: orcid.org/0000-0001-6590-1676](#)⁶,
- [Bo Zhang](#) [ORCID: orcid.org/0000-0002-6434-7201](#)¹,
- [Chunguang Zhang](#) [ORCID: orcid.org/0000-0001-6774-8038](#)^{1,2,3},
- [Kun Wang](#) [ORCID: orcid.org/0000-0002-5745-827X](#)²,
- [Nian Liu](#) [ORCID: orcid.org/0000-0003-0778-0663](#)²,
- [Anbing Ren](#) [ORCID: orcid.org/0000-0002-2037-2480](#)²,
- [Zhiqian Luo](#) [ORCID: orcid.org/0000-0002-5717-1340](#)²,
- [Zhengzhou Yan](#)²,
- [Jianfeng Tian](#) [ORCID: orcid.org/0000-0003-0672-3579](#)¹ &
- [Jun Pan](#)¹

[Nature](#) volume 596, pages 353–356 (2021) [Cite this article](#)

- 4379 Accesses
- 137 Altmetric
- [Metrics details](#)

Subjects

- [Astronomical instrumentation](#)
- [Astronomy and astrophysics](#)

Abstract

On Earth's surface, there are only a handful of high-quality astronomical sites that meet the requirements for very large next-generation facilities. In the context of scientific opportunities in time-domain astronomy, a good site on the Tibetan Plateau will bridge the longitudinal gap between the known best sites^{1,2} (all in the Western Hemisphere). The Tibetan Plateau is the highest plateau on Earth, with an average elevation of over 4,000 metres, and thus potentially provides very good opportunities for astronomy and particle astrophysics^{3,4,5}. Here we report the results of three years of monitoring of testing an area at a local summit on Saishiteng Mountain near Lenghu Town in Qinghai Province. The altitudes of the potential locations are between 4,200 and 4,500 metres. An area of over 100,000 square kilometres surrounding Lenghu Town has a lower altitude of below 3,000 metres, with an extremely arid climate and unusually clear local sky (day and night)⁶. Of the nights at the site, 70 per cent have clear, photometric conditions, with a median seeing of 0.75 arcseconds. The median night temperature variation is only 2.4 degrees Celsius, indicating very stable local surface air. The precipitable water vapour is lower than 2 millimetres for 55 per cent of the night.

[Download PDF](#)

Main

The geographic information of the site, Lenghu in Qinghai Province, is summarized in Methods and Extended Data Fig. 1. The main site parameters—including cloudiness and night-sky background brightness, air temperature, pressure, humidity, wind speed and direction, dust, precipitable water vapour (PWV), and, most importantly, seeing (using a differential image motion monitor (DIMM)^{7,8})—have been monitored starting at different times from March 2018 onwards (summarized in Extended Data Table 1). As DIMM seeing must be measured in the vicinity of a telescope project and at a similar height from the ground as the telescope, a 10-m tower was built to mount the DIMM. Shortly after the initial site reconnaissance, to start the site monitoring as soon as possible, the building materials and tools were carried to the site by a helicopter and the scientific devices were manually carried up to the mountain in September 2018, before the road reached the site. This could not have been accomplished without the great assistance from the local government of Lenghu Town. All the measurements and preliminary statistics of the raw data are updated daily and are available at <http://lenghu.china-vo.org/index.html>. Comprehensive comparisons of the key site characteristics of Lenghu with those of the other known best astronomical sites in the world are summarized in Table 1. A detailed analysis is given in the following.

Table 1 Comparison of key site characteristics with other known best sites in the world

[Full size table](#)

Available observing time

For any modern observatories for night optical/infrared astronomy and planetary sciences⁹, the first factor to consider is undoubtedly the clarity of nights, followed by the darkness of the night sky (that is, avoiding light pollution), among other parameters important for advanced modes of observations. Light pollution is mainly the result of human activities. Qinghai Province on the Tibetan Plateau has a very low population; therefore, problematic artificial light sources are at present non-existent. However, this does not mean that industrial development will not occur in the future. If the local population were to grow with economic development, then control of light pollution could be lost. This potential conflict between scientific research and industry needs a resolution¹⁰. Owing to the enforceable and long-term night-sky protection policy issued by the local municipal government in 2017, *a priori*, such a potential threat to astronomical observations has been lifted. Night-sky protection in the whole area of Lenghu will be guaranteed by law.

First, we determined how dark the local night sky is. We monitored the night-sky brightness using a widely used commercial sky quality meter (SQM)¹¹, which has a wide passband from 400 nm to 600 nm centred at the Johnson V-band and accurately measures the integrated light of the entire visible sky, with the sensitivity optimized towards the zenith and a quick drop-off to less than 20% once the zenith angle is greater than 60°. The integrated full visible sky brightness is converted into zenith brightness in mag arcsec⁻² (ref. ¹²). The night-sky brightness reaches 22.3 mag arcsec⁻² during a fully clear new moon time, in the extreme case when the bright part of the Galactic Disk is far away from the local zenith. The average night-sky brightness is around 22.0 mag arcsec⁻² when the Moon is below the horizon, comparable to the other three sites in Table 1. Artificial light contributions are completely negligible.

To evaluate the observable time at Lenghu, we used a homemade all-sky camera (LH-Cam) with a 12-mm fish-eye lens customized for this site¹³. All-sky images have been captured every 20 min during the day and every 5 min between dusk and dawn without interruption since March 2018, regardless of the weather conditions. Another measure to evaluate the observable time makes use of the same SQM¹⁴. The SQM reading changes smoothly with the rotation of the starry sky during a clear night, and any cloud passage through the visible sky modifies the sequence of SQM magnitudes, resulting in a chaotic light curve (Methods, Extended Data Fig. 2). Our SQM

photometer thereby enables us to study the overall cloudiness with a 1-min cadence. Combining LH-Cam and SQM data, we were able to reliably measure the clear time at the site. Observational data from 2018 to 2020 show that the site can provide, on average, over 90 fully clear photometric nights per year, 240 nights per year with more than 4 h of contiguous fully clear time and more than 280 nights with at least 2 h of contiguous clear time of photometric conditions. The fractional photometric time at the Lenghu site is 70%, which is slightly lower than the other three sites in Table 1.

DIMM seeing statistics

Seeing, the blurring of stars due to atmospheric turbulence along the light path, is one of the key parameters to assess the quality of observations at a site for seeing-limited scientific goals, and a good integrated seeing measurement using a DIMM is the starting point for advance observational modes applying adaptive optics¹⁵.

Measurements by DIMM are widely used and have become a standard assessment for integrated atmospheric optical turbulence^{7,8,16}. A multi-aperture scintillation sensor can provide further information on how the total seeing is composed of different layers in the atmosphere above the site¹⁷. The same make of DIMM (the one provided by Alcor-System) applied in this study has also been used for many different site-selection campaigns^{18,19}. Measurements are calculated for an average wavelength of 550 nm and corrected to the zenith (airmass unity).

Figure 1 shows the histogram of seeing taken from October 2018 until the end of 2020. We collected nearly a half a million data points in total. After removing the data not taken at clear time (mostly with cirrus passage over the local sky), or with spurs due to hot spots on the detector (Methods), we have 383,825 valid measurements. The seeing measurements follow a log-normal distribution. The median seeing is 0.75 arcseconds, and about 75% of the data are below 1 arcsecond. The DIMM dome is operated remotely and is only allowed to open when the wind speed is 10 m s^{-1} or lower, and the seeing measurement stops immediately when the wind speed exceeds 12 m s^{-1} for 3 min or 15 m s^{-1} for 1 min during observations. When the power or Internet connection was poor, and, of course, when weather turned bad, no DIMM data were taken. Seeing data were collected for 457 nights, evenly distributed during the whole period until 31 December 2020. We tested the temporal variation²⁰ and the wind dependence of seeing and found that the seeing is stable for most of the observable time. The prevailing wind direction at the site is around 280° throughout the year, which is also the wind direction for the best median seeing. The median seeing is below 0.7 arcseconds between wind directions of 255° and 324° (Extended Data Fig. 3).

Fig. 1: The night seeing at the Lenghu site.



The DIMM seeing data are collected from October 2018 to December 2020. The histogram is in red and the cumulative probability is in blue. The black solid line fits the histogram with a log-normal distribution.

[Full size image](#)

For the extreme observational requirements of very faint and/or high-redshifted targets in cutting-edge astrophysical problems, both high spatial resolution and long-time exposure are needed. Good natural seeing is a critical requirement for adaptive optics to work, especially for large-aperture telescopes¹⁵. A comparison of the total seeing at Lenghu with other known best sites in the world is shown in Table 1. The median value at Lenghu is the same as that at Mauna Kea (0.75 arcseconds) and is better than those at Cerro Paranal and La Palma.

In terms of total seeing, Lenghu is comparable to the best-established sites (in Chile, Hawaii and the Canary Islands), and is clearly the best one on the Tibetan Plateau (Methods, Extended Data Table 2, Extended Data Fig. 4). The best sites, with the

addition of Lenghu, form a network of the best-possible conditions in both seeing and observing duty cycle of the time domain, second only to conditions in Antarctica^{16,17}.

The length of the observable time that is good in terms of both seeing and clear time is a key parameter to determine when considering a potential future observing site. To quantitatively evaluate the quality of the Lenghu site, a site quality matrix is defined based on the length of contiguous available observing time (cAOT) and the median value of DIMM seeing (DMn) on each night (Methods, Extended Data Table 3). For Lenghu, this score is 65%, which is comparable to 66% for both Cerro Paranal (1999–2012) and La Silla (2000–2008).

Air stability

Local air stability analysis based on our weather data has been carried out. The intranight temperature variation is one of the essential elements that make up the total seeing. As of the end of December 2020, we have collected weather data for 756 days at a temporal resolution of 1 min. Wind and temperature, and the spatial/temporal variabilities of both, affect local air stability dynamically and thermodynamically. The median wind speed at the site during the period is 4.5 m s^{-1} , indicating that the dynamic activity of the air at the site is rather low. The amplitudes of the temperature variation on an observing night directly reflect the air stability at the surface level of the site. For an amplitude of 10° or higher, the seeing is typically above 1.5 arcseconds, as we learnt from experience at a different site also on the Tibetan Plateau¹³. Figure 2 shows the annual temperature variation pattern with the intranight variation amplitude (peak to valley) indicated by vertical bars. In two full years, the average amplitude of the intraday temperature variation is only 5.6 K, and the average amplitude is only 2.4 K for the observing time between dusk and dawn. This is an advantage over all the sites surveyed for the Thirty Meter Telescope¹ and shown in Table 1. The median night temperature during winter (December, January and February) is -14.5°C , which is comparable to the Ngari and Muztagh Ata test sites and much lower than the Daocheng test site¹⁸. Considering the mean warming trend of about 0.3°C per decade at Lenghu²¹, the median night temperature in winter will remain below -10°C towards the end of this century.

Fig. 2: Annual temperature variation pattern in 2019–2020.



The upper tip, upper top of the box, mid-bar in the box, bottom of the box and lower tip represent the standard deviation of the maximum temperature, the mean maximum temperature, the mean temperature, the mean minimum temperature and the standard deviation of the minimum temperature, respectively, on night for each month with blue for 2019 and red for 2020. The inset shows the histogram of the amplitude of the night temperature variations.

[Full size image](#)

Turbulence profile

Optical turbulence along the light path from the top of the atmosphere to the site surface can be measured by several methods²². Limited by the power supply currently available at the site, direct measurements are yet to be routinely done. Traditional meteorological balloon experiments were carried out three times during the current stage of site selection. These missions measured atmospheric parameters that can be used to infer the turbulence strength along the path with acceptable accuracy. Balloon

flights were performed in August and November 2020, representing typical conditions during summer and winter, which found that the height of the tropopause is around 11 km. Above 11 km, the refractive index structure constant $\langle C_N^2 \rangle$, where N is the refractive index, decreases monotonically, meaning that the turbulence strength decreases accordingly. The large fluctuations of the curves are due to the accuracy of the detectors. The $\langle C_N^2 \rangle$ is around $10^{-17.5} - 10^{-17} \text{ m}^{-2/3}$ between 4 km and 11 km (Methods, Extended Data Fig. 5). On 16 November, the two turbulence profiles show a similar trend, but the turbulence strength at night (red profile) is lower than that during the dawn (grey profile). Between 6 km and 9 km altitude, the turbulence profile shows a clear difference in August and November, which suggests a possible seasonal pattern.

Precipitable water vapour

All mega astronomical observing facilities designed now are aimed at cutting-edge scientific goals, such as the physics of the extremely early Universe and searching for signs of life on exoplanets. To realize such goals, ground-based observations are normally conducted through adaptive-optics-fed instruments working at infrared wavelengths. The PWV, the total amount of water vapour within the column between the telescope and the top of Earth's atmosphere, is a determining factor for such scientific goals.

At the Lenghu site, the infrastructure is still under construction; therefore, devices such as the scheduled infrared/submillimetre instruments cannot be supported on site yet. However, in both atmospheric studies and astronomical site qualifications^{23,24}, the PWV can be reliably modelled with an accuracy of better than 25% based on environmental quantities, including geographic and weather information (Methods). This method has been shown to be applicable for other sites on the Tibetan Plateau^{4,25,26}. To anchor the modelled PWV to actual measurements, we applied Global Navigation Satellite Systems (GNSS) data²⁷ from a week in January 2021. This cross-check shows that our modelling of PWV using onsite weather station data is consistent with the GNSS method. Figure 3 shows the monthly mean PWV distribution modelled for the Lenghu site (Methods). The PWV is lower than 2 mm for 55% of the night. Compared with the PWV of the Mauna Kea and La Palma sites²⁸, Lenghu has a different pattern, possibly due to different climate patterns. During 2019–2020, the Lenghu PWV was high in summer and very low in winter. At night, PWV at the Lenghu site is better than that at Mauna Kea, meaning that Lenghu has a much higher potential than other known sites for infrared wavelengths (Table 1, Fig. 3).

Fig. 3: Monthly averaged PWV at the Lenghu site in 2019–2020.



The reference curves of Mauna Kea (dotted) and La Palma (dashed) are taken from García-Lorenzo & Eff-Darwich²⁸. The PWV of Cerro Paranal is taken from the ESO website. Dots are all monthly averaged values.

[Full size image](#)

Methods

Geographic information

The Lenghu site is at a local summit on Saishiteng Mountain, which is located to the east of the Altyn Mountains and on the northern edge of the Qaidam Basin. Its geographical coordinates are 38.6068° N, 93.8961° E, and it has an elevation of 4,200 m. The Lenghu site occupies a unique geographic position in the Eastern Hemisphere and bridges the huge gap between Mauna Kea (155.8246° W), Atacama (70.4042° W) and the Canary Islands (17.8577° W). This will form a perfect network of ground-based, high-quality observatories ready for great scientific discoveries, including

searching signs of life on exoplanets, electromagnetic counterparts of gravitational wave outbursts, high-value transient events alerted by space-borne triggers that need to be done in very narrow time window^{[32,33](#)} and much more.

According to the climate record collected at three local weather stations for past 30 years, the average annual precipitation is around 18 mm, with over 3,500 h of annual sunshine^{[34,35](#)}. Land transport from the site to the local supporting base, Lenghu Town, and then to the developed areas of China by road and railway networks is convenient. The nearest international airport, highway access and the cargo railway stations of Dunhuang are all within only 250 km of the town. The altitude of Lenghu Town is only 2,700 m and is 80 km away from the site, which provides comfortable conditions for a supporting base for the site. This infrastructure enables good logistics for future activity at the site (Extended Data Fig. [1](#)).

AOT statistics

The clear night is derived by using both LH-Cam images analysis and the smoothness of integrated sky brightness records of the SQM. Lenghu has almost no artificial light pollution. Therefore, on LH-Cam images, any cloud will block the star background on a new moon night or when the moon is 18° or more under the horizon, leaving a dark patch on the image. When the moon is in the view of the camera, clouds will be directly visible. On sky brightness curves of the SQM, clouds make darkening or brightening fluctuations patterns depending on the moon age, and the amplitudes of such variations are correlated well with cloud coverage/thickness on the images^{[14](#)}, as demonstrated in Extended Data Fig. [2](#). In the left panel, three LH-cam images show a typical clear time (right), small clumpy cloud passage between clear time (left) and overcast (middle) cases, on the night of 6 October 2019, together with the SQM light curve. The right panel shows the distribution of clear time (cyan) in 2019 as an example of annual observing time statistics, based on the method described above.

A comparison of Tibetan sites

In addition to Lenghu, other sites, namely Ngari, Muztagh Ata and Daocheng, on the Tibetan Plateau were also tested during an earlier general site survey by the Large Optical/infrared Telescope team. An intensive site testing programme was carried out for the Chinese 12-m telescope from 2016 to 2018 at the three sites. The testing results are concluded in an overview paper^{[18](#)}. The Ngari site was later found to be good for the primordial gravitational wave project^{[4](#)}. The concerns regarding strong wind, cloud cover in summer and light pollution from the nearby Shiquanhe Town^{[36](#)} are potential challenges to further development of optical/infrared astronomy at the Ngari site. The other two sites are now being developed for different purposes. It turns out that Lenghu has the best observing conditions of all the sites tested on the plateau. A direct

comparison of the key parameters of AOT and seeing are shown in Extended Data Table 2 and Extended Data Fig. 4, respectively. As the seeing data offered by the Large Optical/infrared Telescope team for Ngari, Muztagh Ata and Daocheng were all truncated at 3.0 arcseconds, the seeing data of Lenghu are processed accordingly, as presented in Extended Data Fig. 4.

In Extended Data Table 2, we adopted the method of the Large Optical/infrared Telescope team for AOT calculation, based on all-sky camera images. They divide the total visible sky by two circles with zenith angles of 44.7° and 65° , namely the inner and the outer circles. When there is no cloud in the inner and the outer circles, it is defined as ‘clear’ (or photometric in ref. 18); when only the inner circle is clear, it is defined as ‘outer’ (spectroscopic).

Site quality matrix scores

Extended Data Table 3 shows the site quality matrix for the Lenghu site based on all the nights that have both DMn and cAOT statistics. The DMn and cAOT are divided into five levels and four levels, respectively. Each element is assigned a weight according to the values of the DMn and cAOT (in parenthesis). The total score of the site is denoted by the ratio between the weighted summation of the number of nights and the total number of nights (457 in our case). For Lenghu, this score is 65%. An ideal site with all nights in yellow would score 100%. For the Delingha site, the median of all seeing measurements is 1.58 arcseconds¹³. Half of the AOT for Delingha (about 250 in total¹³) would be in blue (score 0.5) with the other half in brown (score 0.3), and the total score would be approximately 40%, which is typical for current existing classical observatories in China. For the Xinglong site (150 km from Beijing), where the Large Sky Area Multi-Object Fibre Spectroscopic Telescope (LAMOST) is hosted, the expected score would be even lower than the Delingha site for the same level of seeing, but with less observable time.

Using the publicly available seeing and AOT data from the European Southern Observatory (ESO) website, the sites at Cerro Paranal and La Silla are evaluated on the site quality matrix scale. Both the seeing and AOT data released on the ESO website are monthly average values. For the AOT of the ESO sites, a photometric night calls for six or more hours of consecutive photometric night. Therefore, only the third column of Table 1 ($cAOT > 6$ h) is used for the site quality estimations for the Cerro Paranal and La Silla sites. The monthly fractions of photometric nights are transferred to cAOT nights, and then the nights are divided into five levels according to the seeing divisions in Table 1. Finally, the total scores for Cerro Paranal (1999–2012) and La Silla (2000–2008) are both 66%. It is noted that these scores are upper limits for the sites as the nights with $cAOT < 6$ h (therefore, lower scores) cannot be assessed owing to the lack of daily weather data.

Turbulence profiles

To understand the local meteorological pattern at the mountain region where our site is located, three balloon experiments were conducted at the Lenghu weather station. Once at 23:15 UT on 12 August 2020, and twice on 16 November 2020, at 11:18 UT and 23:44 UT. These balloon missions provided a vertical spatial resolution of 6.4 m. The mean potential temperature profile $\theta(h)$ is calculated by

$$\text{Equation 1: } \theta(h) = T(h) \left(\frac{P(h)}{\text{mathrm}{1,000}} \right)^{-0.286}$$

where h is the altitude, $T(h)$ is the temperature profile in K and $P(h)$ is the pressure profile in hPa. The structure function of the temperature fluctuation $\langle (C_T)^2 \rangle$ is evaluated by the AXP model³⁷. The refractive index structure constant $\langle (C_N)^2 \rangle$ is then estimated by the Gladstone formula

$$\text{Equation 2: } \langle (C_N)^2 \rangle(h) = \langle C_T^2 \rangle(h) \left(\frac{79 \times 10^{-6} P(h)}{T(h)^2} \right)^2$$

The turbulence profiles calculated using the parameters obtained during the balloon flights are shown in Extended Data Fig. 5. Above 11 km, $\langle (C_N)^2 \rangle$ decreases monotonously with no seasonal pattern. $\langle (C_N)^2 \rangle$ is around $10^{-17.5}$ and 10^{-17} between 4 km and 11 km. On 16 November, the two turbulence profiles show a similar trend, but the turbulence strength at night (red profile) is lower than that in the morning (grey profile). At an altitude of 6–9 km, the turbulence profile shows a clear difference in August and November, which suggests possible seasonal changes.

PWV

The PWV can be calculated by the equation

$$\text{Equation 3: } \text{PWV} = \frac{1}{\rho g} \int_0^z p q dz$$

where ρ is the density of liquid water, g is the acceleration of gravity, p_z is the pressure of the ground and q is the specific humidity. The value of q is calculated by the water vapour pressure e by the equation

$$\text{Equation 4: } q = \frac{0.622e}{p - 0.378e}$$

The saturation water vapour pressure is usually converted from temperature by the Goff–Gratch formula³⁸. We used the temperature, pressure and humidity of the ground weather station to estimate the amount of PWV. Here we adopted a temperature drop rate of 6.5 K km^{-1} , an exponential decay of air pressure with temperature, and the height of the tropopause is 11 km as measured by the balloon experiments (Extended data Fig. 5). The mean and median values of PWV modelled for the whole testing period are 3.13 mm and 2.01 mm, respectively (Extended Data Fig. 6).

By checking the data, we found that PWV changes substantially with season. We calculated the mean PWV by month and compared it with the PWV of La Palma and Mauna Kea (Fig. 3). Our two-year PWV values show a similar trend, that is, PWV values in winter are much lower than those in summer. The standard deviation in each month is about half of the average monthly PWV. From October to March, the mean PWV value is 1.55, which is 27% and 73% of the PWV values in La Palma and Mauna Kea, respectively²⁸.

To explore the possible deviations of our PWV, we also adopted the empirical equation between PWV and specific pressure of water vapour, $\text{PWV} = a_0 e + a_1$. The coefficients a_0 and a_1 change with elevation and latitude. Here we adopted the coefficients of Tibetan Plateau²⁵ (assuming an elevation of 4,200 m) and Ngari (also called Ali) site²⁶ (southwest part of the Tibetan Plateau) to re-estimate the PWV. Comparing the PWV estimates using the two sets of coefficients, our modelling of the PWV of the Lenghu site is consistent, but slightly overestimated by 0.15 mm and 0.01 mm, respectively.

Dust grains

Dust and aerosol above an observing site can create problematic extinction for astronomical observations, and their presence in the ground layer can be troublesome for both optical surfaces and mechanical bearings. To measure local dust and aerosol, we implemented a dust meter (GRIMM EM180) in December 2019. We have so far collected a full year of uninterrupted data regarding the dust grains and aerosols of the site, with a temporal resolution of 5 min. The mean and median values of particulate matter with a diameter smaller than $10 \mu\text{m}$ (PM_{10}) density are $20.7 \mu\text{g m}^{-3}$ and $11.7 \mu\text{g m}^{-3}$, respectively. The ambient dust level of the Lenghu site is comparable to the sites in Atacama³⁹. Twice in 2020, a high value of PM_{10} was recorded, of around $100 \mu\text{g m}^{-3}$, during sandstorms that originated from the Taklimakan and local Gobi deserts. Dust grain densities higher than $50 \mu\text{g m}^{-3}$ occurred 31 times in 2020, with a typical duration of several hours. Owing to the high altitude of the site, dust is less serious than at the La Palma site⁴⁰, which suffers from proximity to the Sahara Desert,

and precautions can be implemented at the Lenghu site to protect the equipment for the few days per year affected by dust.

Data availability

The seeing and weather data for the Lenghu site in 2018–2020 are available on a public website at <http://lenghu.china-vo.org/index.html>. The LH-Cam data are available from the corresponding authors on request. The monthly environmental parameters (seeing, cloudiness and PWV) for the Cerro Paranal and La Silla sites are publicly available from the ESO website at <https://www.eso.org/gen-fac/pubs/astclim/paranal/>. The tomographic data used in Extended Data Fig. 1 are provided by AW3D of the Japan Aerospace Exploration Agency (JAXA) available from <https://www.eorc.jaxa.jp/ALOS/en/aw3d30/data/index.htm>. (According to the data policy of JAXA, one can register a username and password to freely access the data.)

References

1. 1.

Schöck, M. et al. Thirty Meter Telescope site testing I: overview. *Publ. Astron. Soc. Pacif.* **121**, 384–395 (2009).

[ADS](#) [Article](#) [Google Scholar](#)

2. 2.

Vernin, J., Muñoz-Tuñón, C. & Sarazin, M. E-ELT site characterization status. *Proc. SPIE* **7012**, 70121T (2008).

[ADS](#) [Article](#) [Google Scholar](#)

3. 3.

Yao, Y. The astronomical site survey in west China. *J. Korean Astron. Soc.* **38**, 113–116 (2005).

[ADS](#) [Article](#) [Google Scholar](#)

4. 4.

Li, H., Li, S.-Y., Liu, Y., Li, Y.-P. & Zhang, X. Tibet’s window on primordial gravitational waves. *Nat. Astron.* **2**, 104–106 (2018).

[ADS](#) [Article](#) [Google Scholar](#)

5. 5.

Normile, D. China builds world-class observatories in Tibet. *Science* **364**, 316–317 (2019).

[ADS](#) [CAS](#) [Article](#) [Google Scholar](#)

6. 6.

Zhang, D. L. et al. Analysis on temporal and spatial variations for cloud radiation forcing over Qinghai-Xizang Plateau using CERES(SYN) data. *Plateau Meteorol.* **31**, 1192–1202 (2012).

[Google Scholar](#)

7. 7.

Sarazin, M. & Roddier, F. The ESO differential image motion monitor. *Astron. Astrophys.* **227**, 294–300 (1990).

[ADS](#) [Google Scholar](#)

8. 8.

Vernin, J. & Muñoz-Tuñón, C. Measuring astronomical seeing: the DA/IAC DIMM. *Publ. Astron. Soc. Pacif.* **107**, 265–272 (1995).

[ADS](#) [Article](#) [Google Scholar](#)

9. 9.

Wei, Y., Yao, Z. & Wan, W. China’s roadmap for planetary exploration. *Nat. Astron.* **2**, 346–348 (2018); correction **4**, 204 (2020).

[ADS](#) [Article](#) [Google Scholar](#)

10. 10.

Stone, R. Astronomers hope their prize telescope isn’t blinded by the light. *Science* **329**, 1002 (2010).

[ADS](#) [CAS](#) [Article](#) [Google Scholar](#)

11. 11.

Sky quality meter – LE *Unihedron* <http://unihedron.com/projects/sqm-le/> (2016).

12. 12.

Cinzano, P. *Night Sky Photometry with Sky Quality Meter* ISTIL Internal Report 9 (ISTIL, 2005).

13. 13.

Tian, J. F. et al. Optical observing conditions at Delingha station. *Publ. Astron. Soc. Pacif.* **128**, 105003 (2016).

[ADS](#) [Article](#) [Google Scholar](#)

14. 14.

Cavazzani, S. et al. Sky quality meter and satellite correlation for the night cloud-cover analysis at astronomical sites. *Mon. Not. R. Astron. Soc.* **493**, 2463–2471 (2020).

[ADS](#) [Article](#) [Google Scholar](#)

15. 15.

Tokovinin, A. Seeing improvement with ground-layer adaptive optics. *Publ. Astron. Soc. Pacif.* **116**, 941–951 (2004).

[ADS](#) [Article](#) [Google Scholar](#)

16. 16.

Ma, B. et al. Night-time measurements of astronomical seeing at Dome A in Antarctica. *Nature* **583**, 771–774 (2020).

[ADS](#) [CAS](#) [Article](#) [Google Scholar](#)

17. 17.

Lawrence, J. S., Ashley, M. C. B., Tokovinin, A. & Travouillon, T. Exceptional astronomical seeing conditions above Dome C in Antarctica. *Nature* **431**, 278–281 (2004).

[ADS](#) [CAS](#) [Article](#) [Google Scholar](#)

18. 18.

Feng, L. et al. Site testing campaign for the Large Optical/infrared Telescope of China: overview. *Res. Astron. Astrophys.* **20**, 080 (2020).

[ADS](#) [Article](#) [Google Scholar](#)

19. 19.

DIMM seeing monitor *Alcor-System* http://www.alcor-system.com/new/SeeingMon/DIMM_Complete.html (2016).

20. 20.

Racine, R. Temporal fluctuations of atmospheric seeing. *Publ. Astron. Soc. Pacif.* **108**, 372–374 (1996).

[ADS](#) [Article](#) [Google Scholar](#)

21. 21.

Liu, Z., Yang, M., Wan, G. & Wang, X. The spatial and temporal variation of temperature in the Qinghai-Xizang (Tibetan) Plateau during 1971–2015. *Atmosphere* **8**, 214 (2017).

[ADS](#) [Article](#) [Google Scholar](#)

22. 22.

Skidmore, W. et al. Thirty Meter Telescope site testing V: seeing and isoplanatic angle. *Publ. Astron. Soc. Pacif.* **121**, 1151–1166 (2009).

[ADS](#) [Article](#) [Google Scholar](#)

23. 23.

García-Lorenzo, B. et al. Infrared astronomical characteristics of the Roque de los Muchachos Observatory: precipitable water vapour statistics. *Mon. Not. R. Astron. Soc.* **405**, 2683–2696 (2010).

[ADS](#) [Google Scholar](#)

24. 24.

Giordano, C. et al. Atmospheric and seeing forecast: WRF model validation with in situ measurements at ORM. *Mon. Not. R. Astron. Soc.* **430**, 3102–3111 (2013).

[ADS](#) [Article](#) [Google Scholar](#)

25. 25.

Yang, J. & Qiu, J. A method for estimating precipitable water and effective water vapor content from ground humidity parameters. *Chin. J. Atmos. Sci.* **26**, 9–22 (2002).

[Google Scholar](#)

26. 26.

Qian, X., Yao, Y., Zou, L., Wang, H. & Yin, J. An empirical model for estimating precipitable water vapor on the Tibetan Plateau. *Publ. Astron. Soc. Pac.* **131**, 125001 (2019); corrigendum **132**, 099201 (2020).

[ADS](#) [Article](#) [Google Scholar](#)

27. 27.

Wang, X. et al. The correlation between GNSS-derived precipitable water vapor and sea surface temperature and its responses to El Niño–Southern Oscillation. *Remote Sens. Environ.* **216**, 1–12 (2018).

[ADS](#) [Article](#) [Google Scholar](#)

28. 28.

García-Lorenzo, B. & Eff-Darwich, A. Water vapour at La Palma and Mauna Kea. IAC <https://www.iac.es/en/documents/water-vapour-la-palma-and-mauna-kea> (2005).

29. 29.

General observing conditions and data for Paranal. ESO <http://www.eso.org/gen-fac/pubs/astclim/paranal/index.html> (1999).

30. 30.

Vernin, J. et al. European Extremely Large Telescope site characterization I: overview. *Publ. Astron. Soc. Pacif.* **123**, 1334–1346 (2011).

[ADS](#) [Article](#) [Google Scholar](#)

31. 31.

Patat, F. Night sky brightness during sunspot maximum at paranal. *Messenger* **115**, 18–21 (2004).

[ADS](#) [Google Scholar](#)

32. 32.

Bernardini, E. Astronomy in the time domain. *Science* **331**, 686–687 (2011).

[ADS](#) [CAS](#) [Article](#) [Google Scholar](#)

33. 33.

Clery, D. Big telescopes join the hunt for flashes in the sky. *Science* **367**, 724–725 (2020).

[ADS](#) [MathSciNet](#) [CAS](#) [Article](#) [Google Scholar](#)

34. 34.

Qi, D. L. et al. Variation characteristic analysis of solar radiation from 1980 to 2010 over Qaidam Basin of Tibet Plateau. *Anhui Nongye Kexue* **41**, 4484–4488, 4492 (2013).

[Google Scholar](#)

35. 35.

Xiao, L. G. et al. Sunshine hours variation characteristics and influencing factors in Qaidam Basin during 1961–2013. *Zhongguo Nongxue Tongbao* **33**, 106–114 (2017).

[Google Scholar](#)

36. 36.

Stone, R. World-class observatory rising on ‘roof of the world’. *Science* **337**, 1156–1157 (2012).

[ADS](#) [CAS](#) [Article](#) [Google Scholar](#)

37. 37.

Trinquet, H. & Vernin, J. A model to forecast seeing and estimate C^2_N profiles from meteorological data. *Publ. Astron. Soc. Pacif.* **118**, 756–764 (2006).

[ADS](#) [Article](#) [Google Scholar](#)

38. 38.

Goff, J. A. & Gratch, S. Low-pressure properties of water from –160 to 212 °F. *Trans. Am. Soc. Heat. Ventilat. Eng.* **52**, 95–122 (1946).

[Google Scholar](#)

39. 39.

Lombardi, G. et al. New dust measurements at ORM, and comparison with Paranal Observatory. *Proc. SPIE* **7733**, 77334G (2010).

[Article](#) [Google Scholar](#)

40. 40.

von Suchodoletz, H. et al. The influence of Saharan dust deposits on La Palma soil properties. *Catena* **103**, 44–52 (2013).

[Article](#) [Google Scholar](#)

[Download references](#)

Acknowledgements

This work is supported by the Lenghu municipal government. We acknowledge grants supporting this work from the Major Science and Technology Project of Qinghai Province 2019-ZJ-A10 and the National Natural Science Foundation of China (NSFC) 11633005. We thank the meteorological bureau of the local government for making balloon and historic weather data available. We are grateful to colleagues from the Purple Mountain Observatory of CAS for general discussions. Special gratitude is due to the organization committee of the Lenghu Industrial Park for constant support. We thank S. Justham for proofreading and suggestions.

Author information

Affiliations

1. CAS Key Laboratory of Optical Astronomy, National Astronomical Observatories, Chinese Academy of Sciences, Beijing, China

Licai Deng, Fan Yang, Xiaodian Chen, Bo Zhang, Chunguang Zhang, Jianfeng Tian & Jun Pan

2. Department of Astronomy, China West Normal University, Nanchong, China

Licai Deng, Fan Yang, Xiaodian Chen, Chunguang Zhang, Kun Wang, Nian Liu, Anbing Ren, Zhiqian Luo & Zhengzhou Yan

3. School of Astronomy and Space Science, University of Chinese Academy of Sciences, Beijing, China

Licai Deng, Xiaodian Chen & Chunguang Zhang

4. Key Laboratory of Earth and Planetary Physics, Institute of Geology and Geophysics, Chinese Academy of Sciences, Beijing, China

Fei He

5. College of Earth and Planetary Sciences, University of Chinese Academy of Sciences, Beijing, China

Fei He

6. Qinghai Observing Station, Purple Mountain Observatory, Chinese Academy of Sciences, Delingha, China

Qili Liu

Authors

1. Licai Deng

[View author publications](#)

You can also search for this author in [PubMed](#) [Google Scholar](#)

2. Fan Yang

[View author publications](#)

You can also search for this author in [PubMed](#) [Google Scholar](#)

3. Xiaodian Chen

[View author publications](#)

You can also search for this author in [PubMed](#) [Google Scholar](#)

4. Fei He

[View author publications](#)

You can also search for this author in [PubMed](#) [Google Scholar](#)

5. Qili Liu

[View author publications](#)

You can also search for this author in [PubMed](#) [Google Scholar](#)

6. Bo Zhang

[View author publications](#)

You can also search for this author in [PubMed](#) [Google Scholar](#)

7. Chunguang Zhang

[View author publications](#)

You can also search for this author in [PubMed](#) [Google Scholar](#)

8. Kun Wang

[View author publications](#)

You can also search for this author in [PubMed](#) [Google Scholar](#)

9. Nian Liu

[View author publications](#)

You can also search for this author in [PubMed](#) [Google Scholar](#)

10. Anbing Ren

[View author publications](#)

You can also search for this author in [PubMed](#) [Google Scholar](#)

11. Zhiqian Luo

[View author publications](#)

You can also search for this author in [PubMed](#) [Google Scholar](#)

12. Zhengzhou Yan
[View author publications](#)

You can also search for this author in [PubMed](#) [Google Scholar](#)

13. Jianfeng Tian
[View author publications](#)

You can also search for this author in [PubMed](#) [Google Scholar](#)

14. Jun Pan
[View author publications](#)

You can also search for this author in [PubMed](#) [Google Scholar](#)

Contributions

L.D. is the principal investigator of the project, who made the grand plan and participated in all instrumentation and data handling processes. F.Y. is the main person running the site monitoring system, and did most of the work on installation and maintenance, data taking and processing. X.C. did most of the modelling of PWV and the turbulence profile. F.H. did the GNSS data remote sensing of PWV and comparison. Q.L. performed on-site routine technical work. B.Z. did data archiving for this work. C.Z., K.W., N.L., A.R., Z.L. and J.P. took part in taking and reducing data. Z.Y. and J.T. worked on the initial hardware setup. J.P. also helped with the establishment of the site protection laws. All authors reviewed and commented on the manuscript.

Corresponding authors

Correspondence to [Licai Deng](#) or [Fan Yang](#) or [Xiaodian Chen](#) or [Fei He](#).

Ethics declarations

Competing interests

The authors declare no competing interests.

Additional information

Peer review information *Nature* thanks Michael Ashley and Marc Sarazin for their contribution to the peer review of this work. Peer reviewer reports are available.

Publisher's note Springer Nature remains neutral with regard to jurisdictional claims in published maps and institutional affiliations.

Extended data figures and tables

Extended Data Fig. 1 Geographic information for the Lenghu site.

The site is marked by the star. The national highways to Lenghu are shown by the black lines. The railway that connects Lenghu to the national railway network is shown by the dashed line. The nearest international airport in Dunhuang is 250 km away from Lenghu Town. The airport in Mangya is domestic.

Extended Data Fig. 2 Sky background light curve and observable time statistics.

a, Definition of clear time. Three representative images of LH-Cam for ‘clear’, ‘passage of cirrus’ and ‘cloudy’ conditions are shown along with the light curve on the night on 6 October 2019. DIMM seeing data are also shown as red dots. **b**, Nightly distribution of clear (cyan), unclear (grey, cloudy and cirrus) and instrument down time (red) in 2019. Each vertical line represents the night between dusk and dawn in UT hours of one night.

Extended Data Fig. 3 Temporal variation and the wind dependence of seeing.

a, Log-normal distribution of seeing. The maximum number (N) is normalized to 1. **b**, The fractional seeing variation between 1 min and 300 min according to the method of Racine²⁰. **c**, Seeing versus 2-min wind speed. **d**, Seeing versus wind direction. In **c**, **d**, the solid blue lines are the median and the two blue dotted lines are the 10% and 90% percentiles. The red dashed lines are the number distributions of wind speed and direction when we obtained the seeing measurements. The maximum number is also normalized to 1.

Extended Data Fig. 4 Comparison of the cumulative probability of seeing.

The red, grey, purple and blue curves represent the distributions at Lenghu (LH), Muztagh Ata (MA), Daocheng (DC) and Ngari (NG), respectively. As the seeing data at MA, DC and NG are truncated at 3.0 arcseconds, the seeing data at Lenghu are also truncated at 3.0 arcseconds for uniformity of comparison.

Extended Data Fig. 5 Turbulence profiles derived from balloon missions.

The blue, red and grey profiles denote vertical distributions of the refractive index structure constant ($\langle C_N^2 \rangle$) at 23:15 UT on 12 August 2020 and 11:18 UT and 23:44 UT on 16 November 2020, respectively. The dashed line shows the height of the tropopause at 11 km. The dotted lines denote heights of 6 km and 9 km.

Extended Data Fig. 6 Histograms of PWV of the site.

Quantiles of the distribution are indicated.

Extended Data Table 1 List of start times of the site parameter measurements

[Full size table](#)

Extended Data Table 2 Comparison of key parameters between Tibetan sites

[Full size table](#)

Extended Data Table 3 Site quality matrix for Lenghu

[Full size table](#)

Supplementary information

[Peer Review File](#)

Rights and permissions

Open Access This article is licensed under a Creative Commons Attribution 4.0 International License, which permits use, sharing, adaptation, distribution and reproduction in any medium or format, as long as you give appropriate credit to the original author(s) and the source, provide a link to the Creative Commons license, and indicate if changes were made. The images or other third party material in this article are included in the article's Creative Commons license, unless indicated otherwise in a credit line to the material. If material is not included in the article's Creative Commons license and your intended use is not permitted by statutory regulation or exceeds the permitted use, you will need to obtain permission directly from the copyright holder. To view a copy of this license, visit <http://creativecommons.org/licenses/by/4.0/>.

[Reprints and Permissions](#)

About this article



Cite this article

Deng, L., Yang, F., Chen, X. *et al.* Lenghu on the Tibetan Plateau as an astronomical observing site. *Nature* **596**, 353–356 (2021). <https://doi.org/10.1038/s41586-021-03711-z>

[Download citation](#)

- Received: 15 February 2021
- Accepted: 09 June 2021
- Published: 18 August 2021
- Issue Date: 19 August 2021
- DOI: <https://doi.org/10.1038/s41586-021-03711-z>

Comments

By submitting a comment you agree to abide by our [Terms](#) and [Community Guidelines](#). If you find something abusive or that does not comply with our terms or guidelines please flag it as inappropriate.

[Download PDF](#)

Advertisement

This article was downloaded by **calibre** from <https://www.nature.com/articles/s41586-021-03711-z>

- Article
- [Published: 18 August 2021](#)

Two-dimensional supersolidity in a dipolar quantum gas

- [Matthew A. Norcia](#)¹ na1,
- [Claudia Politi](#)^{1,2} na1,
- [Lauritz Klaus](#)^{1,2},
- [Elena Poli](#)²,
- [Maximilian Sohmen](#) [ORCID: orcid.org/0000-0002-5043-2413](#)^{1,2},
- [Manfred J. Mark](#) [ORCID: orcid.org/0000-0001-8157-4716](#)^{1,2},
- [Russell N. Bisset](#)²,
- [Luis Santos](#)³ &
- [Francesca Ferlaino](#) [ORCID: orcid.org/0000-0002-3020-6291](#)^{1,2}

[Nature](#) volume **596**, pages 357–361 (2021) [Cite this article](#)

- 1319 Accesses
- 389 Altmetric
- [Metrics details](#)

Subjects

- [Bose–Einstein condensates](#)
- [Matter waves and particle beams](#)
- [Phase transitions and critical phenomena](#)
- [Ultracold gases](#)

Abstract

Supersolid states simultaneously feature properties typically associated with a solid and with a superfluid. Like a solid, they possess crystalline order, manifesting as a periodic modulation of the particle density; but unlike a typical solid, they also have superfluid properties, resulting from coherent particle delocalization across the system. Such states were initially envisioned in the context of bulk solid helium, as a possible answer to the question of whether a solid could have superfluid properties^{1,2,3,4,5}.

Although supersolidity has not been observed in solid helium (despite much effort)⁶, ultracold atomic gases provide an alternative approach, recently enabling the observation and study of supersolids with dipolar atoms^{7,8,9,10,11,12,13,14,15,16}. However, unlike the proposed phenomena in helium, these gaseous systems have so far only shown supersolidity along a single direction. Here we demonstrate the extension of supersolid properties into two dimensions by preparing a supersolid quantum gas of dysprosium atoms on both sides of a structural phase transition similar to those occurring in ionic chains^{17,18,19,20}, quantum wires^{21,22} and theoretically in chains of individual dipolar particles^{23,24}. This opens the possibility of studying rich excitation properties^{25,26,27,28}, including vortex formation^{29,30,31}, and ground-state phases with varied geometrical structure^{7,32} in a highly flexible and controllable system.

Access options

Subscribe to Journal

Get full journal access for 1 year

\$199.00

only \$3.90 per issue

[Subscribe](#)

All prices are NET prices.

VAT will be added later in the checkout.

Tax calculation will be finalised during checkout.

Rent or Buy article

Get time limited or full article access on ReadCube.

from \$8.99

[Rent or Buy](#)

All prices are NET prices.

Additional access options:

- [Log in](#)
- [Access through your institution](#)
- [Learn about institutional subscriptions](#)

Fig. 1: Calculated phases of dipolar droplet array.

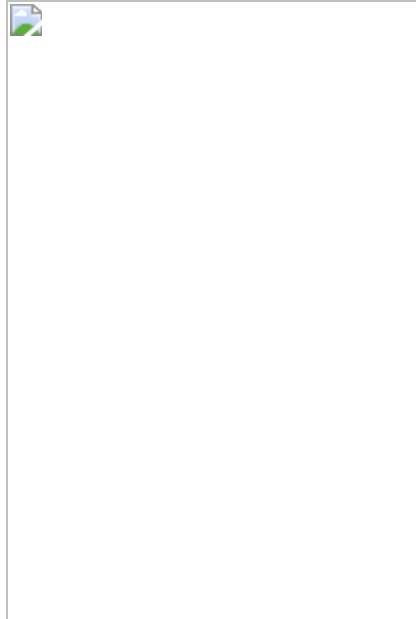


Fig. 2: Linear to zigzag transition in an anisotropic trap.

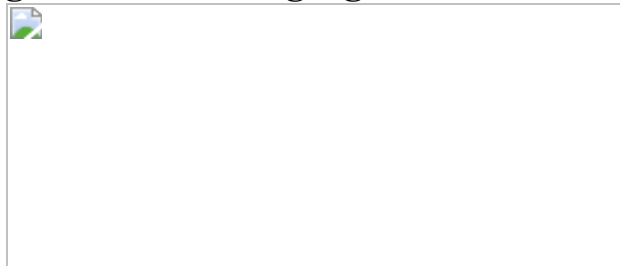
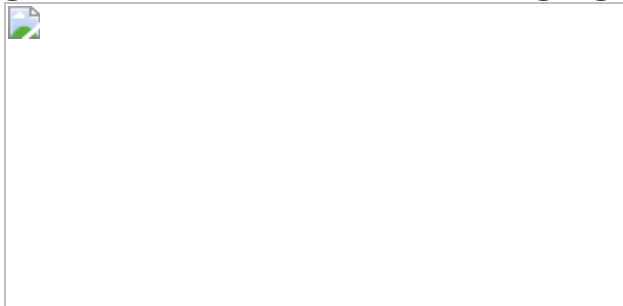


Fig. 3: Coherence in linear and zigzag states.



Data availability

Data pertaining to this work can be found at
<https://doi.org/10.5281/zenodo.4729519>.

Code availability

Code used for this work is available from the corresponding author upon reasonable request.

References

1. 1.

Gross, E. P. Unified theory of interacting bosons. *Phys. Rev.* **106**, 161–162 (1957).

[ADS](#) [CAS](#) [MATH](#) [Article](#) [Google Scholar](#)

2. 2.

Gross, E. P. Classical theory of boson wave fields. *Ann. Phys.* **4**, 57–74 (1958).

[ADS](#) [MathSciNet](#) [MATH](#) [Article](#) [Google Scholar](#)

3. 3.

Andreev, A. F. & Lifshitz, I. M. Quantum theory of defects in crystals. *Sov. Phys. JETP* **29**, 1107–1114 (1969).

[ADS](#) [Google Scholar](#)

4. 4.

Chester, G. V. Speculations on Bose–Einstein condensation and quantum crystals. *Phys. Rev. A* **2**, 256–258 (1970).

[ADS](#) [Article](#) [Google Scholar](#)

5. 5.

Leggett, A. J. Can a solid be “superfluid”? *Phys. Rev. Lett.* **25**, 1543–1546 (1970).

[ADS](#) [CAS](#) [Article](#) [Google Scholar](#)

6. 6.

Chan, M. H.-W., Hallock, R. & Reatto, L. Overview on solid ^4He and the issue of supersolidity. *J. Low Temp. Phys.* **172**, 317–363 (2013).

[ADS](#) [CAS](#) [Article](#) [Google Scholar](#)

7. 7.

Lu, Z.-K., Li, Y., Petrov, D. S. & Shlyapnikov, G. V. Stable dilute supersolid of two-dimensional dipolar bosons. *Phys. Rev. Lett.* **115**, 075303 (2015).

[ADS](#) [PubMed](#) [Article](#) [CAS](#) [PubMed Central](#) [Google Scholar](#)

8. 8.

Baillie, D. & Blakie, P. B. Droplet crystal ground states of a dipolar Bose gas. *Phys. Rev. Lett.* **121**, 195301 (2018).

[ADS](#) [CAS](#) [PubMed](#) [Article](#) [PubMed Central](#) [Google Scholar](#)

9. 9.

Roccuzzo, S. M. & Ancilotto, F. Supersolid behavior of a dipolar Bose–Einstein condensate confined in a tube. *Phys. Rev. A* **99**, 041601 (2019).

[ADS](#) [CAS](#) [Article](#) [Google Scholar](#)

10. 10.

Boninsegni, M. & Prokof'ev, N. V. Colloquium: Super-solids: what and where are they? *Rev. Mod. Phys.* **84**, 759–776 (2012).

[ADS](#) [CAS](#) [Article](#) [Google Scholar](#)

11. 11.

Tanzi, L. et al. Observation of a dipolar quantum gas with metastable supersolid properties. *Phys. Rev. Lett.* **122**, 130405 (2019).

[ADS](#) [CAS](#) [PubMed](#) [PubMed Central](#) [Article](#) [Google Scholar](#)

12. 12.

Böttcher, F. et al. Transient supersolid properties in an array of dipolar quantum droplets. *Phys. Rev. X* **9**, 011051 (2019).

[Google Scholar](#)

13. 13.

Chomaz, L. et al. Long-lived and transient supersolid behaviors in dipolar quantum gases. *Phys. Rev. X* **9**, 021012 (2019).

[CAS](#) [Google Scholar](#)

14. 14.

Guo, M. et al. The low-energy Goldstone mode in a trapped dipolar super-solid. *Nature* **574**, 386–389 (2019).

[ADS](#) [CAS](#) [PubMed](#) [Article](#) [PubMed Central](#) [Google Scholar](#)

15. 15.

Natale, G. et al. Excitation spectrum of a trapped dipolar supersolid and its experimental evidence. *Phys. Rev. Lett.* **123**, 050402 (2019).

[ADS](#) [CAS](#) [PubMed](#) [Article](#) [PubMed Central](#) [Google Scholar](#)

16. 16.

Tanzi, L. et al. Supersolid symmetry breaking from compressional oscillations in a dipolar quantum gas. *Nature* **574**, 382–385 (2019).

[ADS](#) [CAS](#) [PubMed](#) [Article](#) [PubMed Central](#) [Google Scholar](#)

17. 17.

Birkl, G., Kassner, S. & Walther, H. Multiple-shell structures of laser-cooled $^{24}\text{Mg}^+$ ions in a quadrupole storage ring. *Nature* **357**, 310–313 (1992).

[ADS](#) [CAS](#) [Article](#) [Google Scholar](#)

18. 18.

Raizen, M. G., Gilligan, J. M., Bergquist, J. C., Itano, W. M. & Wineland, D. J. Ionic crystals in a linear Paul trap. *Phys. Rev. A* **45**, 6493–6501 (1992).

[ADS](#) [CAS](#) [PubMed](#) [Article](#) [PubMed Central](#) [Google Scholar](#)

19. 19.

Fishman, S., De Chiara, G., Calarco, T. & Morigi, G. Structural phase transitions in low-dimensional ion crystals. *Phys. Rev. B* **77**, 064111

(2008).

[ADS](#) [Article](#) [CAS](#) [Google Scholar](#)

20. 20.

Shimshoni, E., Morigi, G. & Fishman, S. Quantum zigzag transition in ion chains. *Phys. Rev. Lett.* **106**, 010401 (2011).

[ADS](#) [PubMed](#) [Article](#) [CAS](#) [PubMed Central](#) [Google Scholar](#)

21. 21.

Hew, W. K. et al. Incipient formation of an electron lattice in a weakly confined quantum wire. *Phys. Rev. Lett.* **102**, 056804 (2009).

[ADS](#) [CAS](#) [PubMed](#) [Article](#) [PubMed Central](#) [Google Scholar](#)

22. 22.

Mehta, A. C., Umrigar, C. J., Meyer, J. S. & Baranger, H. U. Zigzag phase transition in quantum wires. *Phys. Rev. Lett.* **110**, 246802 (2013).

[ADS](#) [PubMed](#) [Article](#) [CAS](#) [PubMed Central](#) [Google Scholar](#)

23. 23.

Astrakharchik, G. E., Morigi, G., De Chiara, G. & Boronat, J. Ground state of low-dimensional dipolar gases: linear and zigzag chains. *Phys. Rev. A* **78**, 063622 (2008).

[ADS](#) [Article](#) [CAS](#) [Google Scholar](#)

24. 24.

Ruhman, J., Dalla Torre, E. G., Huber, S. D. & Altman, E. Nonlocal order in elongated dipolar gases. *Phys. Rev. B* **85**, 125121 (2012).

[ADS](#) [Article](#) [CAS](#) [Google Scholar](#)

25. 25.

Santos, L., Shlyapnikov, G. V. & Lewenstein, M. Roton-maxon spectrum and stability of trapped dipolar Bose–Einstein condensates. *Phys. Rev. Lett.* **90**, 250403 (2003).

[ADS](#) [CAS](#) [PubMed](#) [Article](#) [PubMed Central](#) [Google Scholar](#)

26. 26.

Ronen, S., Bortolotti, D. C. E. & Bohn, J. L. Radial and angular rotons in trapped dipolar gases. *Phys. Rev. Lett.* **98**, 030406 (2007).

[ADS](#) [PubMed](#) [Article](#) [CAS](#) [PubMed Central](#) [Google Scholar](#)

27. 27.

Wilson, R. M., Ronen, S., Bohn, J. L. & Pu, H. Manifestations of the roton mode in dipolar Bose–Einstein condensates. *Phys. Rev. Lett.* **100**, 245302 (2008).

[ADS](#) [PubMed](#) [Article](#) [CAS](#) [PubMed Central](#) [Google Scholar](#)

28. 28.

Bisset, R. N., Baillie, D. & Blakie, P. B. Roton excitations in a trapped dipolar Bose–Einstein condensate. *Phys. Rev. A* **88**, 043606 (2013).

[ADS](#) [Article](#) [CAS](#) [Google Scholar](#)

29. 29.

Gallemí, A., Rocuzzo, S. M., Stringari, S. & Recati, A. Quantized vortices in dipolar supersolid Bose–Einstein-condensed gases. *Phys. Rev. A* **102**, 023322 (2020).

[ADS](#) [Article](#) [Google Scholar](#)

30. 30.

Roccuzzo, S. M., Gallemí, A., Recati, A. & Stringari, S. Rotating a supersolid dipolar gas. *Phys. Rev. Lett.* **124**, 045702 (2020).

[ADS](#) [CAS](#) [PubMed](#) [Article](#) [PubMed Central](#) [Google Scholar](#)

31. 31.

Ancilotto, F., Barranco, M., Pi, M. & Reatto, L. Vortex properties in the extended supersolid phase of dipolar Bose–Einstein condensates. *Phys. Rev. A* **103**, 033314 (2021).

[ADS](#) [CAS](#) [Article](#) [Google Scholar](#)

32. 32.

Zhang, Y.-C., Maucher, F. & Pohl, T. Supersolidity around a critical point in dipolar Bose–Einstein condensates. *Phys. Rev. Lett.* **123**, 015301 (2019).

[ADS](#) [CAS](#) [PubMed](#) [Article](#) [PubMed Central](#) [Google Scholar](#)

33. 33.

Li, J.-R. et al. A stripe phase with supersolid properties in spin–orbit-coupled Bose–Einstein condensates. *Nature* **543**, 91–94 (2017).

[ADS](#) [CAS](#) [PubMed](#) [PubMed Central](#) [Article](#) [Google Scholar](#)

34. 34.

Léonard, J., Morales, A., Zupancic, P., Esslinger, T. & Donner, T. Supersolid formation in a quantum gas breaking a continuous translational symmetry. *Nature* **543**, 87–90 (2017).

[ADS](#) [PubMed](#) [PubMed Central](#) [Article](#) [CAS](#) [Google Scholar](#)

35. 35.

Kadau, H. et al. Observing the Rosensweig instability of a quantum ferrofluid. *Nature* **530**, 194–197 (2016).

[ADS](#) [CAS](#) [PubMed](#) [Article](#) [PubMed Central](#) [Google Scholar](#)

36. 36.

Ferrier-Barbut, I., Kadau, H., Schmitt, M., Wenzel, M. & Pfau, T. Observation of quantum droplets in a strongly dipolar Bose gas. *Phys. Rev. Lett.* **116**, 215301 (2016).

[ADS](#) [PubMed](#) [Article](#) [CAS](#) [PubMed Central](#) [Google Scholar](#)

37. 37.

Chomaz, L. et al. Quantum-fluctuation-driven crossover from a dilute Bose–Einstein condensate to a macrodroplet in a dipolar quantum fluid. *Phys. Rev. X* **6**, 041039 (2016).

[Google Scholar](#)

38. 38.

Wächtler, F. & Santos, L. Quantum filaments in dipolar Bose–Einstein condensates. *Phys. Rev. A* **93**, 061603 (2016).

[ADS](#) [Article](#) [CAS](#) [Google Scholar](#)

39. 39.

Bisset, R. N., Wilson, R. M., Baillie, D. & Blakie, P. B. Ground-state phase diagram of a dipolar condensate with quantum fluctuations. *Phys. Rev. A* **94**, 033619 (2016).

[ADS](#) [Article](#) [CAS](#) [Google Scholar](#)

40. 40.

Lavoine, L. & Bourdel, T. Beyond-mean-field crossover from one dimension to three dimensions in quantum droplets of binary mixtures. *Phys. Rev. A* **103**, 033312 (2021).

[ADS](#) [CAS](#) [Article](#) [Google Scholar](#)

41. 41.

Sohmen, M. et al. Birth, life, and death of a dipolar supersolid. *Phys. Rev. Lett.* **126**, 233401 (2021).

[ADS](#) [CAS](#) [PubMed](#) [Article](#) [PubMed Central](#) [Google Scholar](#)

42. 42.

Hadzibabic, Z., Stock, S., Battelier, B., Bretin, V. & Dalibard, J. Interference of an array of independent Bose–Einstein condensates. *Phys. Rev. Lett.* **93**, 180403 (2004).

[ADS](#) [PubMed](#) [Article](#) [CAS](#) [PubMed Central](#) [Google Scholar](#)

43. 43.

Schmidt, J.-N. et al. Roton excitations in an oblate dipolar quantum gas. *Phys. Rev. Lett.* **126**, 193002 (2021).

[ADS](#) [CAS](#) [PubMed](#) [Article](#) [PubMed Central](#) [Google Scholar](#)

44. 44.

Pyka, K. et al. Topological defect formation and spontaneous symmetry breaking in ion Coulomb crystals. *Nat. Commun.* **4**, 2291 (2013).

[ADS](#) [CAS](#) [PubMed](#) [Article](#) [PubMed Central](#) [Google Scholar](#)

45. 45.

Ulm, S. et al. Observation of the Kibble–Zurek scaling law for defect formation in ion crystals. *Nat. Commun.* **4**, 2290 (2013).

[ADS](#) [CAS](#) [PubMed](#) [Article](#) [PubMed Central](#) [Google Scholar](#)

46. 46.

Trautmann, A. et al. Dipolar quantum mixtures of erbium and dysprosium atoms. *Phys. Rev. Lett.* **121**, 213601 (2018).

[ADS](#) [CAS](#) [PubMed](#) [Article](#) [PubMed Central](#) [Google Scholar](#)

47. 47.

Chomaz, L. et al. Observation of roton mode population in a dipolar quantum gas. *Nat. Phys.* **14**, 442–446 (2018).

[PubMed](#) [PubMed Central](#) [Article](#) [CAS](#) [Google Scholar](#)

48. 48.

Lima, A. R. P. & Pelster, A. Quantum fluctuations in dipolar Bose gases. *Phys. Rev. A* **84**, 041604 (2011).

[ADS](#) [Article](#) [CAS](#) [Google Scholar](#)

[Download references](#)

Acknowledgements

We thank the Innsbruck Erbium team, T. Bland, G. Morigi and B. Blakie for discussions. We acknowledge R. M. W. van Bijnen for developing the code for our eGPE ground-state simulations. The experimental team is financially supported through an ERC Consolidator Grant (RARE, number 681432), an NFRI grant (MIRARE, number ÖAW0600) of the Austrian Academy of Science, the QuantERA grant MAQS by the Austrian Science Fund FWF number I4391-N. L.S. and F.F. acknowledge the DFG/FWF via FOR 2247/PI2790. M.S. acknowledges support by the Austrian Science

Fund FWF within the DK-ALM (number W1259-N27). L.S. thanks the funding by the Deutsche Forschungsgemeinschaft (DFG, German Research Foundation) under Germany's Excellence Strategy - EXC-2123 QuantumFrontiers - 390837967. M.A.N. has received funding as an ESQ Postdoctoral Fellow from the European Union's Horizon 2020 research and innovation programme under the Marie Skłodowska-Curie grant agreement number 801110 and the Austrian Federal Ministry of Education, Science and Research (BMBWF). M.J.M. acknowledges support through an ESQ Discovery Grant by the Austrian Academy of Sciences. We also acknowledge the Innsbruck Laser Core Facility, financed by the Austrian Federal Ministry of Science, Research and Economy. Part of the computational results presented have been achieved using the HPC infrastructure LEO of the University of Innsbruck.

Author information

Author notes

1. These authors contributed equally: Matthew A. Norcia, Claudia Politi

Affiliations

1. Institut für Quantenoptik und Quanteninformation, Österreichische Akademie der Wissenschaften, Innsbruck, Austria

Matthew A. Norcia, Claudia Politi, Lauritz Klaus, Maximilian Sohmen, Manfred J. Mark & Francesca Ferlaino

2. Institut für Experimentalphysik, Universität Innsbruck, Innsbruck, Austria

Claudia Politi, Lauritz Klaus, Elena Poli, Maximilian Sohmen, Manfred J. Mark, Russell N. Bisset & Francesca Ferlaino

3. Institut für Theoretische Physik, Leibniz, Universität Hannover, Hanover, Germany

Luis Santos

Authors

1. Matthew A. Norcia

[View author publications](#)

You can also search for this author in [PubMed](#) [Google Scholar](#)

2. Claudia Politi

[View author publications](#)

You can also search for this author in [PubMed](#) [Google Scholar](#)

3. Lauritz Klaus

[View author publications](#)

You can also search for this author in [PubMed](#) [Google Scholar](#)

4. Elena Poli

[View author publications](#)

You can also search for this author in [PubMed](#) [Google Scholar](#)

5. Maximilian Sohmen

[View author publications](#)

You can also search for this author in [PubMed](#) [Google Scholar](#)

6. Manfred J. Mark

[View author publications](#)

You can also search for this author in [PubMed](#) [Google Scholar](#)

7. Russell N. Bisset

[View author publications](#)

You can also search for this author in [PubMed](#) [Google Scholar](#)

8. Luis Santos

[View author publications](#)

You can also search for this author in [PubMed](#) [Google Scholar](#)

9. Francesca Ferlaino

[View author publications](#)

You can also search for this author in [PubMed](#) [Google Scholar](#)

Contributions

M.A.N., C.P., L.K., M.S., M.J.M. and F.F. contributed experimental work. E.P. and R.N.B. performed eGPE calculations. L.S. contributed variational model. All authors contributed to interpretation of results and preparation of manuscript.

Corresponding author

Correspondence to [Francesca Ferlaino](#).

Ethics declarations

Competing interests

The authors declare no competing interests.

Additional information

Peer review information *Nature* thanks the anonymous reviewers for their contribution to the peer review of this work.

Publisher's note Springer Nature remains neutral with regard to jurisdictional claims in published maps and institutional affiliations.

Extended data figures and tables

Extended Data Fig. 1 Fourier transforms of in-trap images.

The upper row shows individual in-trap images for different trap aspect ratios, as shown in Fig. 2b. The lower row shows the data for the same parameters in the Fourier domain, with k the associated wavenumber. As the trap aspect ratio is increased, the modulation goes from being present along a single direction to two, and a clear hexagonal pattern is visible.

Extended Data Fig. 2 Supersolid droplet array with more than two rows.

a, In-trap image of a droplet array with more than two rows. **b**, Averaged Fourier transform of 309 images in conditions of **a**, showing that a regular modulated structure persists in the more extended system. **c**, Calculated ground state from the eGPE for trap parameters $(f_x, f_y, f_z) = (22, 55, 140)$ Hz, and $N = 60,000$ atoms in the droplets, representative of the experimental conditions in **a**, **b**. **d**, Averaged TOF interference pattern for the conditions of **a**, **b**. The inset shows the measured 2D density profile and the main panel shows a radially averaged density, normalized to the peak density of the averaged image. The grey lines represent individual trials and the red line is the average. The repeatability of the modulation indicates the presence of phase coherence between droplets.

Extended Data Fig. 3 Prospects for larger and isotropic droplet arrays.

The panels show eGPE-calculated ground-state density profiles with fixed average atomic density (see text) and either fixed atom number and trap volume (upper row) or fixed f_x (lower row). Here N refers to the total number of atoms in the simulation (droplets plus halo), in contrast to the definition used elsewhere to compare with experimental conditions (droplets only).

Rights and permissions

[Reprints and Permissions](#)

About this article



Check for
updates

Cite this article

Norcia, M.A., Politi, C., Klaus, L. *et al.* Two-dimensional supersolidity in a dipolar quantum gas. *Nature* **596**, 357–361 (2021).
<https://doi.org/10.1038/s41586-021-03725-7>

[Download citation](#)

- Received: 10 February 2021
- Accepted: 14 June 2021
- Published: 18 August 2021
- Issue Date: 19 August 2021
- DOI: <https://doi.org/10.1038/s41586-021-03725-7>

Comments

By submitting a comment you agree to abide by our [Terms](#) and [Community Guidelines](#). If you find something abusive or that does not comply with our terms or guidelines please flag it as inappropriate.

[Access through your institution](#)

[Change institution](#)

[Buy or subscribe](#)

Associated Content

[Supersolids go two-dimensional](#)

- Bruno Laburthe-Tolra

News & Views 18 Aug 2021

Advertisement

This article was downloaded by **calibre** from <https://www.nature.com/articles/s41586-021-03725-7>

| [Section menu](#) | [Main menu](#) |

- Article
- [Published: 18 August 2021](#)

Ghost hyperbolic surface polaritons in bulk anisotropic crystals

- [Weiliang Ma^{1 na1}](#),
- [Guangwei Hu ORCID: orcid.org/0000-0002-3023-9632^{2,3 na1}](#),
- [Debo Hu ORCID: orcid.org/0000-0001-9432-1670^{4 na1}](#),
- [Runkun Chen^{1 na1}](#),
- [Tian Sun¹](#),
- [Xinliang Zhang ORCID: orcid.org/0000-0001-8513-3328¹](#),
- [Qing Dai ORCID: orcid.org/0000-0002-1750-0867⁴](#),
- [Ying Zeng¹](#),
- [Andrea Alù ORCID: orcid.org/0000-0002-4297-5274^{3,5}](#),
- [Cheng-Wei Qiu ORCID: orcid.org/0000-0002-6605-500X²](#) &
- [Peining Li ORCID: orcid.org/0000-0003-3836-3803¹](#)

[Nature](#) volume **596**, pages 362–366 (2021) [Cite this article](#)

- 2552 Accesses
- 22 Altmetric
- [Metrics details](#)

Subjects

- [Nanophotonics and plasmonics](#)
- [Polaritons](#)

- [Sub-wavelength optics](#)

Abstract

Polaritons in anisotropic materials result in exotic optical features, which can provide opportunities to control light at the nanoscale^{1,2,3,4,5,6,7,8,9,10}. So far these polaritons have been limited to two classes: bulk polaritons, which propagate inside a material, and surface polaritons, which decay exponentially away from an interface. Here we report a near-field observation of ghost phonon polaritons, which propagate with in-plane hyperbolic dispersion on the surface of a polar uniaxial crystal and, at the same time, exhibit oblique wavefronts in the bulk. Ghost polaritons are an atypical non-uniform surface wave solution of Maxwell's equations, arising at the surface of uniaxial materials in which the optic axis is slanted with respect to the interface. They exhibit an unusual bi-state nature, being both propagating (phase-progressing) and evanescent (decaying) within the crystal bulk, in contrast to conventional surface waves that are purely evanescent away from the interface. Our real-space near-field imaging experiments reveal long-distance (over 20 micrometres), ray-like propagation of deeply subwavelength ghost polaritons across the surface, verifying long-range, directional and diffraction-less polariton propagation. At the same time, we show that control of the out-of-plane angle of the optic axis enables hyperbolic-to-elliptic topological transitions at fixed frequency, providing a route to tailor the band diagram topology of surface polariton waves. Our results demonstrate a polaritonic wave phenomenon with unique opportunities to tailor nanoscale light in natural anisotropic crystals.

Access options

Subscribe to Journal

Get full journal access for 1 year

\$199.00

only \$3.90 per issue

[Subscribe](#)

All prices are NET prices.

VAT will be added later in the checkout.

Tax calculation will be finalised during checkout.

Rent or Buy article

Get time limited or full article access on ReadCube.

from \$8.99

[Rent or Buy](#)

All prices are NET prices.

Additional access options:

- [Log in](#)
- [Access through your institution](#)
- [Learn about institutional subscriptions](#)

Fig. 1: Ghost hyperbolic surface phonon polaritons at the interface of a bulk calcite crystal.

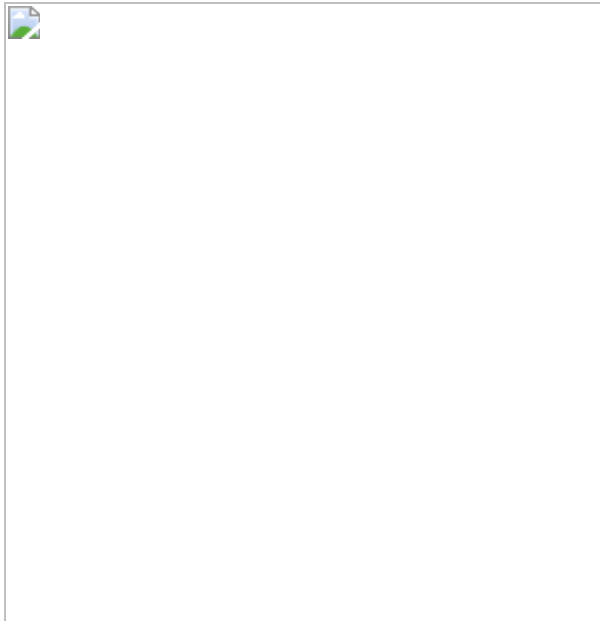


Fig. 2: Real-space imaging of g-HPs excited by an infrared antenna under oblique plane-wave illumination at the surface of bulk calcite.

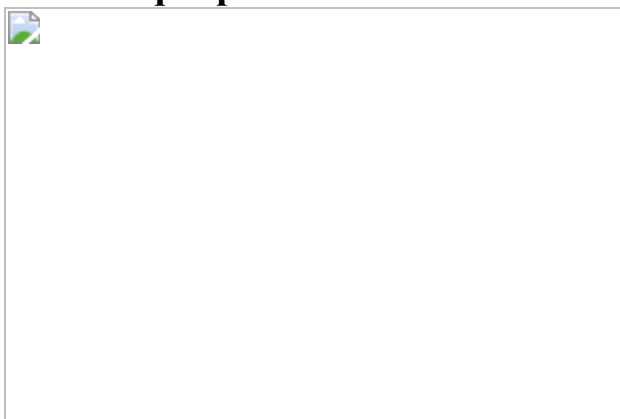
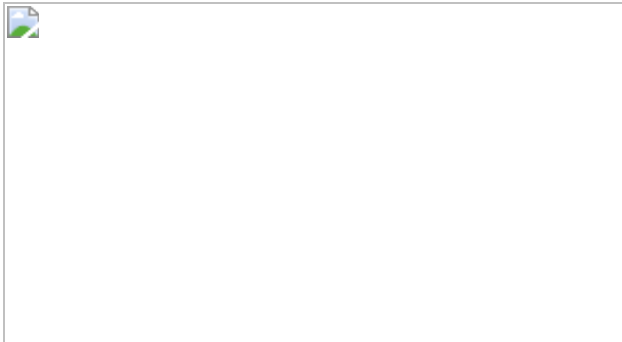


Fig. 3: Launching highly confined g-HPs for in-plane directional and diffraction-less polariton propagation.



Fig. 4: Tunable hyperbolicity and topological transition of polaritons in calcite.



Data availability

The data that support the findings of this study are available from the corresponding authors upon reasonable request.

Code availability

The code that support the findings of this study are available from the corresponding authors upon reasonable request.

References

1. 1.

Basov, D. N., Fogler, M. M. & García de Abajo, F. J. Polaritons in van der Waals materials. *Science* **354**, aag1992 (2016).

[Article](#) [Google Scholar](#)

2. 2.

Low, T. et al. Polaritons in layered two-dimensional materials. *Nat. Mater.* **16**, 182–194 (2017).

[ADS](#) [CAS](#) [Article](#) [Google Scholar](#)

3. 3.

Hu, G., Shen, J., Qiu, C.-W., Alù, A. & Dai, S. Phonon polaritons and hyperbolic response in van der Waals materials. *Adv. Opt. Mater.* **8**, 1901393 (2020).

[CAS](#) [Article](#) [Google Scholar](#)

4. 4.

Dai, S. et al. Tunable phonon polaritons in atomically thin van der Waals crystals of boron nitride. *Science* **343**, 1125–1129 (2014).

[ADS](#) [CAS](#) [Article](#) [Google Scholar](#)

5. 5.

Caldwell, J. D. et al. Sub-diffractive volume-confined polaritons in the natural hyperbolic material hexagonal boron nitride. *Nat. Commun.* **5**, 5221 (2014).

[ADS](#) [CAS](#) [Article](#) [Google Scholar](#)

6. 6.

Li, P. et al. Infrared hyperbolic metasurface based on nanostructured van der Waals materials. *Science* **359**, 892–896 (2018).

[ADS](#) [CAS](#) [Article](#) [Google Scholar](#)

7. 7.

Ma, W. et al. In-plane anisotropic and ultra-low-loss polaritons in a natural van der Waals crystal. *Nature* **562**, 557–562 (2018).

[ADS](#) [CAS](#) [Article](#) [Google Scholar](#)

8. 8.

Zheng, Z. et al. A mid-infrared biaxial hyperbolic van der Waals crystal. *Sci. Adv.* **5**, eaav8690 (2019).

[ADS](#) [CAS](#) [Article](#) [Google Scholar](#)

9. 9.

Taboada-Gutiérrez, J. et al. Broad spectral tuning of ultra-low-loss polaritons in a van der Waals crystal by intercalation. *Nat. Mater.* **19**, 964–968 (2020).

[ADS](#) [Article](#) [Google Scholar](#)

10. 10.

Sternbach, A. J. et al. Programmable hyperbolic polaritons in van der Waals semiconductors. *Science* **371**, 617–620 (2021).

[ADS](#) [CAS](#) [Article](#) [Google Scholar](#)

11. 11.

Alfaro-Mozaz, F. J. et al. Nanoimaging of resonating hyperbolic polaritons in linear boron nitride antennas. *Nat. Commun.* **8**, 15624 (2017).

[ADS](#) [CAS](#) [Article](#) [Google Scholar](#)

12. 12.

Giles, A. J. et al. Ultralow-loss polaritons in isotopically pure boron nitride. *Nat. Mater.* **17**, 134–139 (2018).

[ADS](#) [CAS](#) [Article](#) [Google Scholar](#)

13. 13.

Li, P. et al. Collective near-field coupling and nonlocal phenomena in infrared-phononic metasurfaces for nano-light canalization. *Nat. Commun.* **11**, 3663 (2020).

[ADS](#) [CAS](#) [Article](#) [Google Scholar](#)

14. 14.

Li, P. et al. Hyperbolic phonon-polaritons in boron nitride for near-field optical imaging and focusing. *Nat. Commun.* **6**, 7507 (2015).

[ADS](#) [CAS](#) [Article](#) [Google Scholar](#)

15. 15.

Dai, S. et al. Subdiffractive focusing and guiding of polaritonic rays in a natural hyperbolic material. *Nat. Commun.* **6**, 6963 (2015).

[ADS](#) [CAS](#) [Article](#) [Google Scholar](#)

16. 16.

Tielrooij, K.-J. et al. Out-of-plane heat transfer in van der Waals stacks through electron-hyperbolic phonon coupling. *Nat. Nanotechnol.* **13**, 41–46 (2018).

[ADS](#) [CAS](#) [Article](#) [Google Scholar](#)

17. 17.

Autore, M. et al. Boron nitride nanoresonators for phonon-enhanced molecular vibrational spectroscopy at the strong coupling limit. *Light Sci. Appl.* **7**, 17172 (2018).

[CAS](#) [Article](#) [Google Scholar](#)

18. 18.

Bylinkin, A. et al. Real-space observation of vibrational strong coupling between propagating phonon polaritons and organic molecules. *Nat. Photon.* **15**, 197–202 (2021).

[ADS](#) [CAS](#) [Article](#) [Google Scholar](#)

19. 19.

Castilla, S. et al. Plasmonic antenna coupling to hyperbolic phonon-polaritons for sensitive and fast mid-infrared photodetection with graphene. *Nat. Commun.* **11**, 4872 (2020).

[ADS](#) [CAS](#) [Article](#) [Google Scholar](#)

20. 20.

Hu, G. et al. Topological polaritons and photonic magic angles in twisted α -MoO₃ bilayers. *Nature* **582**, 209–213 (2020).

[ADS](#) [CAS](#) [Article](#) [Google Scholar](#)

21. 21.

Li, P. et al. Optical nanoimaging of hyperbolic surface polaritons at the edges of van der Waals materials. *Nano Lett.* **17**, 228–235 (2017).

[ADS](#) [CAS](#) [Article](#) [Google Scholar](#)

22. 22.

Dai, S. et al. Manipulation and steering of hyperbolic surface polaritons in hexagonal boron nitride. *Adv. Mater.* **30**, 1706358 (2018).

[Article](#) [Google Scholar](#)

23. 23.

D'yakonov, M. New type of electromagnetic wave propagating at an interface. *Sov. Phys. JETP* **67**, 714–716 (1988).

[Google Scholar](#)

24. 24.

Narimanov, E. Ghost resonance in anisotropic materials: negative refractive index and evanescent field enhancement in lossless media. *Adv. Photonics* **1**, 056003 (2019).

[Google Scholar](#)

25. 25.

Waseer, W. I., Naqvi, Q. A. & Mughal, M. J. Non-uniform plane waves (ghost waves) in general anisotropic medium. *Opt. Commun.* **453**, 124334 (2019).

[CAS](#) [Article](#) [Google Scholar](#)

26. 26.

Narimanov, E. Dyakonov waves in biaxial anisotropic crystals. *Phys. Rev. A (Coll. Park)* **98**, 013818 (2018).

[ADS](#) [CAS](#) [Article](#) [Google Scholar](#)

27. 27.

Narimanov, E. Electromagnenic Ghost Waves. in *Conference on Lasers and Electro-Optics* JTU2A.144 (Optical Society of America, 2018).

28. 28.

Walker, D., Glytsis, E. & Gaylord, T. Surface mode at isotropic–uniaxial and isotropic–biaxial interfaces. *J. Opt. Soc. Am. A* **15**, 248–260 (1998).

[ADS](#) [Article](#) [Google Scholar](#)

29. 29.

Kuś, M., Haake, F. & Delande, D. Prebifurcation periodic ghost orbits in semiclassical quantization. *Phys. Rev. Lett.* **71**, 2167–2171 (1993).

[ADS](#) [Article](#) [Google Scholar](#)

30. 30.

Zhou, S., Zhang, Q., Fu, S. F. & Wang, X. Z. Ghost surface phononic polaritons in ionic-crystal metamaterial. *J. Opt. Soc. Am. B* **35**, 2764–2769 (2018).

[ADS](#) [CAS](#) [Article](#) [Google Scholar](#)

31. 31.

Frech, R. & Nichols, H. Infrared reflectivity of calcite: Oblique phonons. *Phys. Rev. B* **17**, 2775–2779 (1978).

[ADS](#) [CAS](#) [Article](#) [Google Scholar](#)

32. 32.

Hellwege, K. H., Lesch, W., Plihal, M. & Schaack, G. Zwei-phononenabsorptionsspektren und dispersion der schwingungszweige in kristallen der kalkspatstruktur. *Z. Physik* **232**, 61–86 (1970).

[ADS](#) [CAS](#) [Article](#) [Google Scholar](#)

33. 33.

Breslin, V. M., Ratchford, D. C., Giles, A. J., Dunkelberger, A. D. & Owrutsky, J. C. Hyperbolic phonon polariton resonances in calcite nanopillars. *Opt. Express* **29**, 11760–11772 (2021).

[ADS](#) [CAS](#) [Article](#) [Google Scholar](#)

34. 34.

Huber, A., Ocelic, N., Kazantsev, D. & Hillenbrand, R. Near-field imaging of mid-infrared surface phonon polariton propagation. *Appl. Phys. Lett.* **87**, 081103 (2005).

[ADS](#) [Article](#) [Google Scholar](#)

35. 35.

Huber, A. J., Ocelic, N. & Hillenbrand, R. Local excitation and interference of surface phonon polaritons studied by near-field infrared microscopy. *J. Microsc.* **229**, 389–395 (2008).

[MathSciNet](#) [CAS](#) [Article](#) [Google Scholar](#)

36. 36.

Zhang, Q. et al. Interface nano-optics with van der Waals polaritons. *Nature* (in the press).

37. 37.

Hu, G., Krasnok, A., Mazor, Y., Qiu, C.-W. & Alù, A. Moiré hyperbolic metasurfaces. *Nano Lett.* **20**, 3217–3224 (2020).

[ADS](#) [CAS](#) [Article](#) [Google Scholar](#)

38. 38.

Schuller, E., Borstel, G. & Falge, H. J. Surface phonon-polaritons on general crystal cuts of α -quartz observed by attenuated total reflection. *Phys. Status Solidi B* **69**, 467–476 (1975).

[ADS](#) [CAS](#) [Article](#) [Google Scholar](#)

39. 39.

Lee, S. C., Ng, S. S., Hassan, H. A., Hassan, Z. & Dumelow, T. Surface phonon polariton responses of hexagonal sapphire crystals with non-polar and semi-polar crystallographic planes. *Opt. Lett.* **39**, 5467–5470 (2014).

[ADS](#) [Article](#) [Google Scholar](#)

40. 40.

Lane, M. D. Midinfrared optical constants of calcite and their relationship to particle size effects in thermal emission spectra of

granular calcite. *J. Geophys. Res. Planets* **104**, 14099–14108 (1999).

[ADS](#) [CAS](#) [Article](#) [Google Scholar](#)

41. 41.

Ocelic, N., Huber, A. & Hillenbrand, R. Pseudoheterodyne detection for background-free near-field spectroscopy. *Appl. Phys. Lett.* **89**, 101124 (2006).

[ADS](#) [Article](#) [Google Scholar](#)

[Download references](#)

Acknowledgements

We acknowledge support from T. Wang for micro-FTIR measurements, and Y. F. Hao and Y. S. Wang for antenna fabrication. P.L. acknowledges the support from the National Natural Science Foundation of China (grant no. 62075070). C.-W.Q. acknowledges support from the National Research Foundation, Prime Minister's Office, Singapore, under its Competitive Research Programme (CRP award NRF CRP22-2019-0006) and from grant R-261-518-004-720 from the Advanced Research and Technology Innovation Centre (ARTIC). G.H. acknowledges support from A*STAR under its AME Young Individual Research Grants (YIRG, no. A2084c0172). A.A. acknowledges support from the Office of Naval Research (grant no. N00014-19-1-2011), the Simons Foundation, the Air Force Office of Scientific Research MURI program, and the Department of Defense Vannevar Bush Faculty Fellowship. Q.D. acknowledges support from the National Natural Science Foundation of China (grant no. 51925203). D.H. acknowledges support from the National Natural Science Foundation of China (grant no. 11704085). X.Z. acknowledges support from the National Key Research and Development Program of China (grant no. 2018YFA0704403).

Author information

Author notes

1. These authors contributed equally: Weiliang Ma, Guangwei Hu, Debo Hu, Runkun Chen

Affiliations

1. Wuhan National Laboratory for Optoelectronics and School of Optical and Electronic Information, Huazhong University of Science and Technology, Wuhan, China

Weiliang Ma, Runkun Chen, Tian Sun, Xinliang Zhang, Ying Zeng & Peining Li

2. Department of Electrical and Computer Engineering, National University of Singapore, Singapore, Singapore

Guangwei Hu & Cheng-Wei Qiu

3. Photonics Initiative, Advanced Science Research Center, City University of New York, New York, NY, USA

Guangwei Hu & Andrea Alù

4. CAS Key Laboratory of Nanophotonic Materials and Devices, CAS Key Laboratory of Standardization and Measurement for Nanotechnology, CAS Center for Excellence in Nanoscience, National Center for Nanoscience and Technology, Beijing, China

Debo Hu & Qing Dai

5. Physics Program, Graduate Center, City University of New York, New York, NY, USA

Andrea Alù

Authors

1. Weiliang Ma

[View author publications](#)

You can also search for this author in [PubMed](#) [Google Scholar](#)

2. Guangwei Hu

[View author publications](#)

You can also search for this author in [PubMed](#) [Google Scholar](#)

3. Debo Hu

[View author publications](#)

You can also search for this author in [PubMed](#) [Google Scholar](#)

4. Runkun Chen

[View author publications](#)

You can also search for this author in [PubMed](#) [Google Scholar](#)

5. Tian Sun

[View author publications](#)

You can also search for this author in [PubMed](#) [Google Scholar](#)

6. Xinliang Zhang

[View author publications](#)

You can also search for this author in [PubMed](#) [Google Scholar](#)

7. Qing Dai

[View author publications](#)

You can also search for this author in [PubMed](#) [Google Scholar](#)

8. Ying Zeng

[View author publications](#)

You can also search for this author in [PubMed](#) [Google Scholar](#)

9. Andrea Alù

[View author publications](#)

You can also search for this author in [PubMed](#) [Google Scholar](#)

10. Cheng-Wei Qiu

[View author publications](#)

You can also search for this author in [PubMed](#) [Google Scholar](#)

11. Peining Li

[View author publications](#)

You can also search for this author in [PubMed](#) [Google Scholar](#)

Contributions

C.-W.Q. and P.L. conceived the study. W.M. fabricated the samples. G.H. performed the theory analysis coordinated by C.-W.Q. and A.A. D.H. and W.M. performed the s-SNOM measurements with the help of T.S. and Y.Z. G.H., R.C. and W.M. performed the simulations. P.L., C.-W.Q., A.A., Q.D. and X.Z. coordinated and supervised the work. W.M., G.H., A.A., C.-W.Q. and P.L. wrote the manuscript with input from all co-authors.

Corresponding authors

Correspondence to [Xinliang Zhang](#) or [Qing Dai](#) or [Andrea Alù](#) or [Cheng-Wei Qiu](#) or [Peining Li](#).

Ethics declarations

Competing interests

The authors declare no competing interests.

Additional information

Peer review information *Nature* thanks Thomas Folland and the other, anonymous, reviewer(s) for their contribution to the peer review of this work.

Publisher's note Springer Nature remains neutral with regard to jurisdictional claims in published maps and institutional affiliations.

Extended data figures and tables

Extended Data Fig. 1 Centimetre-sized calcite substrates with different optic axis-orientations and corresponding XRD patterns, angle-resolved far-field reflectance.

a–c, Optical microscope images of calcite substrates for $\theta = 90^\circ$, 23.3° , 48.5° (the crystal surface is along plane (001), (100), (104), respectively). **d**, Schematics of the characteristic planes and the corresponding angle θ with respect to optic axis. Black dashed arrow represents optic axis. Green, red and blue lines indicate the characteristic plane (100), (001), (104), respectively. **e**, X-ray diffraction (XRD) data of calcite substrates with different angles with respect to optic axis. XRD patterns of three calcite substrates with different θ exhibited strong diffraction peaks at 31.4° , 64.7° , 29.4° indicating the characteristic plane (001), (100) and (104) of calcite, respectively. **f**, Fourier-transform infrared reflection spectra of calcite substrates shown in **a–c** for different polarization angles of the incident light. The 0° polarization defined here is parallel with direction of red arrow in x - y plane. **g**, Theoretically fitted spectra using the dielectric permittivities according to Methods. The results for the calcite substrates for $\theta = 90^\circ$ (the surface is along plane (001)), $\theta = 23.3^\circ$ (the surface is along plane (100)) and $\theta = 48.5^\circ$ (the surface is along plane (104)), respectively.

Extended Data Fig. 2 Comparison of the modal patterns of the g-HPs, s-HPs and v-HPs.

a–c, Transverse cross-section of the simulated near-field distributions of a g-HPs mode (**a**), s-HPs mode (**b**) and the fundamental v-HPs waveguide mode M0 (**c**). These results are shown in Fig. 1. **d, e**, Near-field

distributions of the higher order v-HPs waveguide modes, M1 (**d**) and M2 (**e**). The s-HPs possess pure imaginary-valued k_z and thus exponentially decay inside the crystal. The v-HPs exhibiting real-valued wave vector k_z in the material. They thus can accumulate the phase variations in the vertical direction to form Fabry–Pérot interferences between the two interfaces, resulting in the different order waveguide modes. By contrast, as a consequence of the oblique wavefronts, the g-HPs exhibit an unusual propagation feature: their electric fields exponentially attenuate with sinusoidal phase oscillations inside calcite.

Extended Data Fig. 3 Comparison of in-plane polariton dispersion for s-HPs, g-HPs and v-HPs.

a–c, Schematic illustration of bulk calcite crystal with $\theta = 0^\circ, 23.3^\circ, 90^\circ$. **d–f**, Natural crystals can exhibit extreme dielectric anisotropy, arising when the permittivity tensor elements along orthogonal principal axes have opposite signs (for example, either type I: $\text{Re}(\varepsilon_{\perp}) > 0, \text{Re}(\varepsilon_{\parallel}) < 0$, or type II: $\text{Re}(\varepsilon_{\perp}) < 0, \text{Re}(\varepsilon_{\parallel}) > 0$, for uniaxial materials^{4,5}). These features result in polaritons—light–matter hybrid electromagnetic excitations—with a hyperbolic dispersion, that is, the polariton wavevector \mathbf{k} can support the hyperbolic isofrequency contours. Because of the two types of anisotropic dielectric permittivity, the hyperbolic dispersions are accordingly in the form of two types of open hyperboloids, which are the solutions of the equation of the wavevector \mathbf{k} given by $(\text{k}_z^2/\varepsilon_{\parallel}) + (\text{k}_x^2 + \text{k}_y^2/\varepsilon_{\parallel}) = k_0^2$, in which k_0 is the free-space wavevector. As a result, the polaritons in strongly anisotropic materials are called hyperbolic polaritons^{1,2,3}. The figure shows schematic illustrations of three-dimensional isofrequency and projected in-plane isofrequency contours (represented by the blue dashed line) at the k_x – k_y plane for s-HPs (**d**), g-HPs (**e**) and v-HPs (**f**) at the corresponding angle $\theta = 0^\circ, 23.3^\circ, 90^\circ$. The black dashed arrow represents the optic axis. **g**, A false-colour map showing the Fourier transform results of dipole-launched g-HPs. Dashed red, green

and white lines correspond to the theoretical IFCs of in-plane wave vectors for s-HPs, g-HPs and v-HPs respectively.

Extended Data Fig. 4 Numerical simulations of g-HPs considering the material loss.

a–c, Transverse cross-section of the simulated near-field distribution of a g-HP mode for different losses. It is clear that the g-HPs still exist in the presence of the loss. However, the propagation length is reduced when adding the loss. For all cases we use $(\{\varepsilon\}_{\parallel}) = 2.34$.

Extended Data Fig. 5 Evaluation of the effective wavevectors of g-HP rays.

a, Near-field image of antenna-launched g-HPs, shown in Fig. 2b. **b**, Magnified image of the g-HP ray, taken from the area marked in a. **c**, Fourier transform of b, indicating the composite of the super-composed mode.

Extended Data Fig. 6 Comparison of experimental and simulated near-field images of disk-launched g-HPs.

a–c, Disk-launched g-HPs at three different frequencies: $\omega = 1,450 \text{ cm}^{-1}$ (a), $\omega = 1,460 \text{ cm}^{-1}$ (b) and $\omega = 1,470 \text{ cm}^{-1}$ (c). Left, experimental near-field images of g-HPs. Middle, simulated near-field images of disk-launched g-HPs. Right, Fourier transform of the experimental near-field images shown in the left panels. Green and white lines are theoretical IFCs of in-plane wave vectors by considering the interference factors ($\pm k_0 \cos\varphi$) according to Supplementary Fig. 3. Considering that the metallic s-SNOM tip is not included in the calculations, we thus assign the experimental near-field distribution to disk-launched polaritons.

Supplementary information

Supplementary Information

This file contains Supplementary Information Sections 1-4 as follows: the theory to determine the g-HP propagation features; details of numerical simulations; Supplementary Figs 1-9 and Supplementary References.

Rights and permissions

[Reprints and Permissions](#)

About this article



Check for
updates

Cite this article

Ma, W., Hu, G., Hu, D. *et al.* Ghost hyperbolic surface polaritons in bulk anisotropic crystals. *Nature* **596**, 362–366 (2021).
<https://doi.org/10.1038/s41586-021-03755-1>

[Download citation](#)

- Received: 16 February 2021
- Accepted: 22 June 2021
- Published: 18 August 2021
- Issue Date: 19 August 2021
- DOI: <https://doi.org/10.1038/s41586-021-03755-1>

Comments

By submitting a comment you agree to abide by our [Terms](#) and [Community Guidelines](#). If you find something abusive or that does not comply with our

terms or guidelines please flag it as inappropriate.

[Access through your institution](#)

[Change institution](#)

[Buy or subscribe](#)

Advertisement

This article was downloaded by **calibre** from <https://www.nature.com/articles/s41586-021-03755-1>

| [Section menu](#) | [Main menu](#) |

- Article
- [Published: 18 August 2021](#)

How to design an icosahedral quasicrystal through directional bonding

- [Eva G. Noya](#) [ORCID: orcid.org/0000-0002-6359-1026](#)¹,
- [Chak Kui Wong](#) [ORCID: orcid.org/0000-0001-8930-5449](#)²,
- [Pablo Llombart](#)¹ &
- [Jonathan P. K. Doye](#) [ORCID: orcid.org/0000-0002-2226-9524](#)²

Nature volume **596**, pages 367–371 (2021) [Cite this article](#)

- 1525 Accesses
- 45 Altmetric
- [Metrics details](#)

Subjects

- [Coarse-grained models](#)
- [Self-assembly](#)
- [Structure of solids and liquids](#)

Abstract

Icosahedral quasicrystals (IQC)s are materials that exhibit long-range order but lack periodicity in any direction. Although IQCs were the first reported quasicrystals¹, they have been experimentally observed only in metallic

alloys², not in other materials. By contrast, quasicrystals with other symmetries (particularly dodecagonal) have now been found in several soft-matter systems^{3,4,5}. Here we introduce a class of IQCs built from model patchy colloids that could be realized experimentally using DNA origami particles. Our rational design strategy leads to systems that robustly assemble in simulations into a target IQC through directional bonding. This is illustrated for both body-centred and primitive IQCs, with the simplest systems involving just two particle types. The key design feature is the geometry of the interparticle interactions favouring the propagation of an icosahedral network of bonds, despite this leading to many particles not being fully bonded. As well as furnishing model systems in which to explore the fundamental physics of IQCs, our approach provides a potential route towards functional quasicrystalline materials.

Access options

Subscribe to Journal

Get full journal access for 1 year

\$199.00

only \$3.90 per issue

[Subscribe](#)

All prices are NET prices.

VAT will be added later in the checkout.

Tax calculation will be finalised during checkout.

Rent or Buy article

Get time limited or full article access on ReadCube.

from \$8.99

[Rent or Buy](#)

All prices are NET prices.

Additional access options:

- [Log in](#)
- [Access through your institution](#)
- [Learn about institutional subscriptions](#)

Fig. 1: From ideal quasicrystal to patchy-particle design.

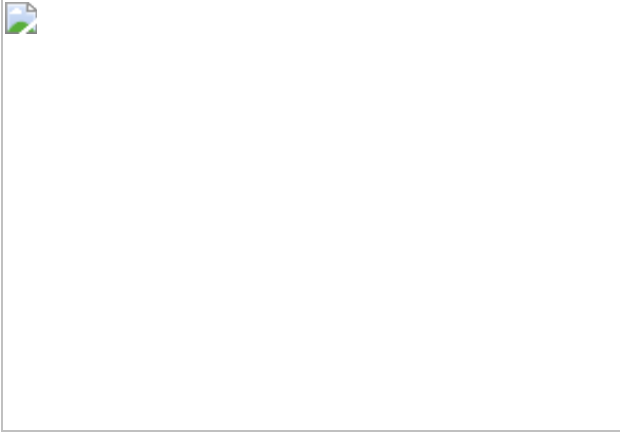


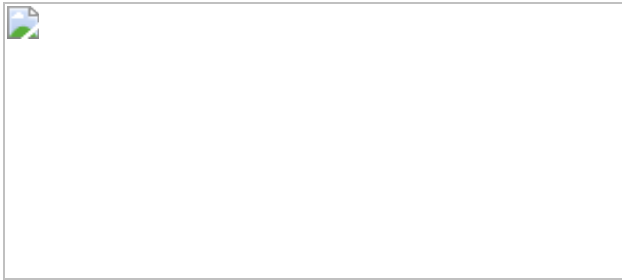
Fig. 2: Assembly of a body-centred IQC.



Fig. 3: A patchy-particle primitive IQC.



Fig. 4: Minimal quasicrystal-forming systems.



Data availability

Final configurations of all systems are available from the Oxford University Research Archive (<https://doi.org/10.5287/bodleian:R8eMnrapg>). [Source data](#) are provided with this paper.

Code availability

The patchy-particle Monte Carlo simulation code is available from https://github.com/evanova/MC_GPU. The simulation code incorporating the oxDNA model is available from <https://sourceforge.net/projects/oxdna/>.

References

1. 1.

Shechtman, D., Blech, I., Gratias, D. & Cahn, J. W. Metallic phase with long-range orientational order and no translational symmetry. *Phys. Rev. Lett.* **53**, 1951–1953 (1984).

[ADS](#) [CAS](#) [Article](#) [Google Scholar](#)

2. 2.

Takakura, H., Gómez, C. P., Yamamoto, A., Boissieu, M. D. & Tsai, A. P. Atomic structure of the binary icosahedral Yb–Cd quasicrystal. *Nat. Mater.* **6**, 58–63 (2007).

[ADS](#) [CAS](#) [Article](#) [Google Scholar](#)

3. 3.

Zeng, X. et al. Supramolecular dendritic quasicrystals. *Nature* **428**, 157–160 (2004).

[ADS](#) [CAS](#) [Article](#) [Google Scholar](#)

4. 4.

Haji-Akbari, A. et al. Disordered, quasicrystalline and crystalline phases of densely packed tetrahedra. *Nature* **462**, 773–777 (2009).

[ADS](#) [CAS](#) [Article](#) [Google Scholar](#)

5. 5.

Dotera, T. Quasicrystals in soft matter. *Isr. J. Chem.* **51**, 1197–1205 (2011).

[CAS](#) [Article](#) [Google Scholar](#)

6. 6.

Dotera, T., Oshiro, T. & Ziherl, P. Mosaic two-length scale quasicrystals. *Nature* **506**, 208–211 (2014).

[ADS](#) [CAS](#) [Article](#) [Google Scholar](#)

7. 7.

Savitz, S., Babadi, M. & Lifshitz, R. Multiple-scale structures: from Faraday waves to soft-matter quasicrystals. *IUCrJ* **5**, 247–268 (2018).

[CAS](#) [Article](#) [Google Scholar](#)

8. 8.

Subramanian, P., Archer, A. J., Knobloch, E. & Ruckridge, A. M. Three-dimensional icosahedral phase field quasicrystal. *Phys. Rev.*

Lett. **117**, 075501 (2016).

[ADS](#) [CAS](#) [Article](#) [Google Scholar](#)

9. 9.

Engel, M., Damasceno, P. F., Phillips, C. L. & Glotzer, S. C. Computational self-assembly of a one-component icosahedral quasicrystal. *Nat. Mater.* **14**, 109–116 (2015).

[ADS](#) [CAS](#) [Article](#) [Google Scholar](#)

10. 10.

Damasceno, P. F., Glotzer, S. C. & Engel, M. Non-close-packed three-dimensional quasicrystals. *J. Phys. Condens. Matter* **29**, 234005 (2017).

[ADS](#) [Article](#) [Google Scholar](#)

11. 11.

Reinhardt, A., Schreck, J. S., Romano, F. & Doye, J. P. K. Self-assembly of two-dimensional binary quasicrystals: a possible route to a DNA quasicrystal. *J. Phys. Condens. Matter* **29**, 014006 (2017).

[ADS](#) [Article](#) [Google Scholar](#)

12. 12.

Sadoc, J.-F. & Mosseri, R. *Geometric Frustration* (Cambridge Univ. Press, 1999).

13. 13.

Doye, J. P. K. & Wales, D. J. Structural consequences of the range of the interatomic potential: a menagerie of clusters. *J. Chem. Soc. Faraday Trans.* **93**, 4233–4243 (1997).

[CAS](#) [Article](#) [Google Scholar](#)

14. 14.

Dmitrienko, V. & Kléman, M. Tetrahedral structures with icosahedral order and their relation to quasi-crystals. *Crystallogr. Rep.* **46**, 527–533 (2001).

[ADS](#) [Article](#) [Google Scholar](#)

15. 15.

Liu, L., Li, Z., Li, Y. & Mao, C. Rational design and self-assembly of two-dimensional dodecagonal quasicrystals. *J. Am. Chem. Soc.* **141**, 4248–4251 (2019).

[CAS](#) [Article](#) [Google Scholar](#)

16. 16.

Tracey, D. F., Noya, E. G. & Doye, J. P. K. Programming patchy particles to form complex ordered structures. *J. Chem. Phys.* **151**, 224506 (2019).

[ADS](#) [Article](#) [Google Scholar](#)

17. 17.

Janot, C. *Quasicrystals: A Primer* (Oxford Univ. Press, 2002).

18. 18.

Cademartiri, L. & Bishop, K. J. M. Programmable self-assembly. *Nat. Mater.* **14**, 2–9 (2015).

[ADS](#) [CAS](#) [Article](#) [Google Scholar](#)

19. 19.

Liu, W., Halverson, J., Tian, Y., Tkachenko, A. V. & Gang, O. Self-organized architectures from assorted DNA-framed nanoparticles. *Nat. Chem.* **8**, 867–873 (2016).

[CAS Article](#) [Google Scholar](#)

20. 20.

Zhang, Z., Keys, A. S., Chen, T. & Glotzer, S. C. Self-assembly of patchy particles into diamond structures through molecular mimicry. *Langmuir* **21**, 11547–11551 (2005).

[CAS Article](#) [Google Scholar](#)

21. 21.

Vega, C., Sanz, E., Abascal, J. L. F. & Noya, E. G. Determination of phase diagrams via computer simulation: methodology and applications to water, electrolytes and proteins. *J. Phys. Condens. Matter* **20**, 153101 (2008).

[ADS Article](#) [Google Scholar](#)

22. 22.

Glotzer, S. C. & Solomon, M. J. Anisotropy of building blocks and their assembly into complex structures. *Nat. Mater.* **6**, 557–562 (2007).

[Article](#) [Google Scholar](#)

23. 23.

Li, W. et al. Colloidal molecules and patchy particles: complementary concepts, synthesis and self-assembly. *Chem. Soc. Rev.* **49**, 1955–1976 (2020).

[CAS Article](#) [Google Scholar](#)

24. 24.

Xiong, Y. et al. Three-dimensional patterning of nanoparticles by molecular stamping. *ACS Nano* **14**, 6823–6833 (2020).

[CAS](#) [Article](#) [Google Scholar](#)

25. 25.

Veneziano, R. et al. Designer nanoscale DNA assemblies programmed from the top down. *Science* **352**, 1534 (2016).

[ADS](#) [CAS](#) [Article](#) [Google Scholar](#)

26. 26.

Tian, Y. et al. Ordered three-dimensional nanomaterials using DNA-prescribed and valence-controlled material voxels. *Nat. Mater.* **19**, 789–796 (2020).

[ADS](#) [CAS](#) [Article](#) [Google Scholar](#)

27. 27.

Ma, N. et al. Directional assembly of nanoparticles by DNA shapes: towards designed architectures and functionality. *Top. Curr. Chem.* **378**, 36 (2020).

[CAS](#) [Article](#) [Google Scholar](#)

28. 28.

Man, W., Megens, M., Steinhardt, P. J. & Chaikin, P. M. Experimental measurement of the photonic properties of icosahedral quasicrystals. *Nature* **436**, 993–996 (2005).

[ADS](#) [CAS](#) [Article](#) [Google Scholar](#)

29. 29.

Steurer, W. Boron-based quasicrystals with sevenfold symmetry. *Phil. Mag.* **87**, 2707–2712 (2007).

[ADS](#) [CAS](#) [Article](#) [Google Scholar](#)

30. 30.

Snodin, B. E. K. et al. Introducing improved structural properties and salt dependence into a coarse-grained model of DNA. *J. Chem. Phys.* **142**, 234901 (2015).

[ADS](#) [Article](#) [Google Scholar](#)

31. 31.

Wilber, A. W., Doye, J. P. K., Louis, A. A. & Lewis, A. C. F. Monodisperse self-assembly in a model with protein-like interactions. *J. Chem. Phys.* **131**, 175102 (2009).

[ADS](#) [Article](#) [Google Scholar](#)

32. 32.

Ben Zion, M. Y. et al. Self-assembled three-dimensional chiral colloidal architecture. *Science* **358**, 633–636 (2017).

[ADS](#) [Article](#) [Google Scholar](#)

33. 33.

Anderson, J. A., Jankowski, E., Grubb, T. L., Engel, M. & Glotzer, S. C. Massively parallel Monte Carlo for many-particle simulations on GPUs. *J. Comput. Phys.* **254**, 27–38 (2013).

[ADS](#) [MathSciNet](#) [Article](#) [Google Scholar](#)

34. 34.

Rapaport, D. C. *The Art of Molecular Dynamics Simulation* (Cambridge Univ. Press, 2004).

35. 35.

Engel, M., Umezaki, M., Trebin, H.-R. & Odagaki, T. Dynamics of particle flips in two-dimensional quasicrystals. *Phys. Rev. B* **82**, 134206 (2010).

[ADS](#) [Article](#) [Google Scholar](#)

36. 36.

Rovigatti, L., Šulc, P., Reguly, I. Z. & Romano, F. A comparison between parallelization approaches in molecular dynamics simulations on GPUs. *J. Comput. Chem.* **36**, 1–8 (2015).

[CAS](#) [Article](#) [Google Scholar](#)

37. 37.

Bai, X.-C., Martin, T. G., Scheres, S. H. W. & Dietz, H. Cryo-EM structure of a 3D DNA-origami object. *Proc. Natl Acad. Sci. USA* **109**, 20012–20017 (2012).

[ADS](#) [CAS](#) [Article](#) [Google Scholar](#)

38. 38.

Snodin, B. E. K., Schreck, J. S., Romano, F., Louis, A. A. & Doye, J. P. K. Coarse-grained modelling of the structural properties of DNA origami. *Nucleic Acids Res.* **47**, 1585–1597 (2019).

[CAS](#) [Article](#) [Google Scholar](#)

39. 39.

Jun, H. et al. Automated sequence design of 3D polyhedral wireframe DNA origami with honeycomb edges. *ACS Nano* **13**, 2083–2093

(2019).

[CAS](#) [PubMed](#) [PubMed Central](#) [Google Scholar](#)

40. 40.

Douglas, S. M. et al. Rapid prototyping of 3D DNA-origami shapes with caDNAno. *Nucleic Acids Res.* **37**, 5001–5006 (2009).

[CAS](#) [Article](#) [Google Scholar](#)

41. 41.

Suma, A. et al. TacoxDNA: a user-friendly web server for simulations of complex DNA structures, from single strands to origami. *J. Comput. Chem.* **40**, 2586–2595 (2019).

[CAS](#) [Article](#) [Google Scholar](#)

42. 42.

Dietz, H., Douglas, S. M. & Shih, W. M. Folding DNA into twisted and curved nanoscale shapes. *Science* **325**, 725–730 (2009).

[ADS](#) [CAS](#) [Article](#) [Google Scholar](#)

[Download references](#)

Acknowledgements

We are grateful for financial support from the Agencia Estatal de Investigación and the Fondo Europeo de Desarrollo Regional (FEDER) under grant numbers FIS2015-72946-EXP(AEI) and FIS2017-89361-C3-2-P(AEI/FEDER,UE) (to E.G.N.) and the Croucher Foundation (to C.K.W.). We acknowledge the use of the University of Oxford Advanced Research Computing (ARC) facility and the Cambridge Service for Data Driven Discovery (CSD3).

Author information

Affiliations

1. Instituto de Química Física Rocasolano, Consejo Superior de Investigaciones Científicas, CSIC, Madrid, Spain
Eva G. Noya & Pablo Llombart
2. Physical and Theoretical Chemistry Laboratory, Department of Chemistry, University of Oxford, Oxford, UK
Chak Kui Wong & Jonathan P. K. Doye

Authors

1. Eva G. Noya
[View author publications](#)
You can also search for this author in [PubMed](#) [Google Scholar](#)
2. Chak Kui Wong
[View author publications](#)
You can also search for this author in [PubMed](#) [Google Scholar](#)
3. Pablo Llombart
[View author publications](#)
You can also search for this author in [PubMed](#) [Google Scholar](#)
4. Jonathan P. K. Doye
[View author publications](#)
You can also search for this author in [PubMed](#) [Google Scholar](#)

Contributions

E.G.N. and J.P.K.D. designed the research. E.G.N. wrote the Monte Carlo code used for the simulations of systems of patchy particles and built the ideal IQC and approximants used as target structures. E.G.N., C.K.W. and P.L. performed the patchy-particle simulations and analysed the data. C.K.W. designed the DNA origami particles and performed the simulations on these systems. All the authors discussed the results. J.P.K.D., E.G.N. and C.K.W. wrote the article.

Corresponding authors

Correspondence to [Eva G. Noya](#) or [Jonathan P. K. Doye](#).

Ethics declarations

Competing interests

The authors declare no competing interests.

Additional information

Peer review information *Nature* thanks Oleg Gang, Ron Lifshitz and the other, anonymous, reviewer(s) for their contribution to the peer review of this work.

Publisher's note Springer Nature remains neutral with regard to jurisdictional claims in published maps and institutional affiliations.

Extended data figures and tables

[Extended Data Fig. 1 Structure of the body-centred IQC.](#)

Projections of the BCI 5P (left) and 2P (right) IQCs along the five-fold axis, three-fold axis and two-fold axis (top to bottom). On the three-fold axis, self-similar triangular motifs follow a $1:\tau:\tau^2:\tau^3$ scaling that is a characteristic of IQCs.

Extended Data Fig. 2 Body-centred IQC diffraction patterns.

Comparison of the diffraction patterns of the ideal body-centred IQC and its $3/2$ approximant, with those of the assembled IQCs using the BCI $5P$, $3P$, $2P$ and $2P$ -mod models. All four assembled systems have diffraction patterns with clear five-fold symmetry confirming their IQC character. By contrast, the diffraction pattern of the approximant when viewed along the pseudo-five-fold axis shows clear deviations from fivefold symmetry. The diffraction patterns of the BCI $5P$ and $3P$ models most closely resemble those of the ideal IQC; the indexing of all peaks with a BCI indexing scheme is detailed in [Supplementary Information section 4E](#). The diffraction patterns for the BCI $2P$ and $2P$ -mod models exhibit additional features, particularly along the two-fold and five-fold axes; these include both diffuse scattering and extra weak peaks that cannot be indexed in a BCI indexing scheme (see [Supplementary Information](#)).

Extended Data Fig. 3 An ideal primitive IQC.

a, Primitive IQC model with a dodecahedral occupation domain viewed along the five-, three- and two-fold rotational axes (left to right). In the top row, only red and those blue particles that are bonded to red particles are shown; these views clearly show that not all the clusters are perfect. In the bottom row, all particles are shown. The yellow particles form an additional shell around the icosahedral cluster depicted in Fig. [3a](#) and all other matrix particles are coloured pink. **b**, Views of the $8/5$ rational approximant along the psuedo-five-, three- and two-fold rotational axes (left to right).

Extended Data Fig. 4 Structure of the primitive IQC.

Projections of the primitive icosahedral $3P$ WT (left) and $2P$ WT (right) models along the five-fold axis, three-fold axis and two-fold axis (top to bottom). On the three-fold axis, self-similar triangular motifs follow a $1:\tau:\tau^2:\tau^3$ scaling that is a characteristic of IQCs.

Extended Data Fig. 5 Primitve IQC diffraction patterns.

Comparison of the diffraction patterns of the ideal primitive IQC and its 8/5 approximant with those of the IQCs obtained from simulations. All four assembled systems have diffraction patterns with clear five-fold symmetry confirming their IQC character. By contrast, the diffraction pattern of the approximant when viewed along the pseudo-five-fold axis shows clear deviations from five-fold symmetry. Despite the assembled systems being simpler than the ideal IQC in terms of the number of environments, the diffraction patterns are very similar to that for the ideal IQC with the patterns along the two-fold axis showing the most differences. The primitive icosahedral $2P$ diffraction patterns could be satisfactorily indexed with a primitive icosahedral indexing scheme, but the better-resolved primitive icosahedral $3P$ patterns have additional weak peaks that require a face-centred icosahedral indexing scheme with a hypercubic lattice parameter that is double that of the primitive icosahedral indexing scheme, indicating some superstructural ordering (see [Supplementary Information section 4E](#)). The diffraction patterns for the systems with and without torsions show no clear differences, confirming their structural similarity.

Extended Data Fig. 6 Structural analysis of the body-centred IQCs.

The properties of the body-centred IQCs obtained with the $5P$, $3P$ and $2P$ models are compared with those of the ideal body-centred IQC and its $3/2$ rational approximant. **a**, PDFs considering only those particles within a sphere of radius $15\sigma_{LJ}$ centred at the centre of mass of the solid cluster. There is good coincidence between the broadened (due to thermal motion) peaks for the assembled IQCs and the distances present in the ideal IQC consistent with their similar structure. The PDFs for the BCI $5P$ and $3P$ systems are essentially the same, with the differences from the BCI $2P$ system still being relatively small. **b**, Radial density. The bulk densities of the ideal IQC, the BCI $5P$ and $3P$ systems and the $3/2$ approximant are very similar, but the bulk density for the BCI $2P$ system is lower, as expected, due to the absence of the red particles. The radial density of the assembled systems decreases from its bulk value to zero over $10\sigma_{LJ}$ – $15\sigma_{LJ}$, reflecting the irregular nature of the surface of the assemblies. **c**, Mole fraction of each particle type in the different structures. The incorporation of the

yellow and purple particles into the BCI 5P assembly is much lower than for the ideal IQC. The fraction of red and blue particles in the BCI 5P and 3P assemblies is also closer to that for the approximant than the ideal IQC. The BCI 2P assemblies have a substantially increased fraction of green particles. **d–i**, Probability of the number of dangling bonds for each particle type (**d–h**) and for all particle types (**i**). The assembled IQCs show a greater number of dangling bonds for the blue matrix particles than the ideal IQC, whereas the ideal IQC has a greater number of dangling bonds for the red and green particles that form the triacontahedral clusters.

Extended Data Fig. 7 Structural analysis of the primitive IQCs.

The properties of the primitive IQCs obtained with the 3P and 2P models with and without torsions are compared with those of the ideal primitive IQC. **a**, PDF considering only those particles within a sphere of radius $15\sigma_{\text{LJ}}$ centred at the centre of mass of the solid cluster. The peaks in the PDFs are consistent with the distances in the ideal IQC, even though the assembled systems do not have particles corresponding to many of the environments in the ideal IQC. The 2P system does not have the peak at $\sim 0.8\sigma_{\text{LJ}}$ that is due to the red–red bonds. **b**, Radial density. The bulk densities of the 3P systems are a bit lower than the ideal IQC with the 2P systems having even lower densities due to the absence of red particles. **c**, Mole fraction of each particle type in the different structures. Note that in the ideal structure the mole fractions do not add to 1, as there are additional local environments that are not included in this plot. Particularly noticeable is the much smaller number of red particles in the ideal IQC. **d–g**, Probability of the number of dangling bonds for each particle type (**d–f**) and for all particle types (**g**). The blue particles in the 3P systems have a particularly low probability of having no missing bonds, because when forming part of the inter-cluster matrix, they do not use their two patches that can only bond to the red particles that form the dodecahedral clusters; such particles contribute to the relatively large number of blue particles with two dangling bonds.

Extended Data Fig. 8 Bond orientational order.

a–d, Contributions to the BOOD for the BCI 5P (**a**), BCI 2P (**b**), primitive icosahedral 3P WT (**c**) and primitive icosahedral 2P WT (**d**) quasicrystals from the different patch–patch bonds types in these systems. For the BCI systems, the green–green and purple–purple bonds are directed along the two-fold axes, the blue–green and blue–purple along the three-fold axes, the blue–red, red–green, blue–yellow and yellow–purple along the five-fold axes and the blue–blue can be directed along five-fold (bonds formed through patches 1 to 3) and three-fold (bonds formed by patch 4) axes. For the primitive icosahedral systems, the red–red bonds are directed along the two-fold axes, and the green–blue and red–blue along the three-fold axes. Thus, for the primitive icosahedral 2P WT system the total BOOD only exhibits spots directed along the three-fold axes, whereas for the primitive icosahedral 3P WT system there are also spots along the two-fold axes. Contributions to the BOODs calculated using a distance cutoff exhibit additional spots but always directed along the rotational axes of the I_h point group ([Supplementary Fig. 7](#)). **e, f**, The relationship between the symmetry of the patchy particles and the I_h point group. All particles can be oriented so that their patch vectors point exclusively along the rotational axes of I_h . This is illustrated for the patchy particles in the BCI 5P (**e**) and primitive icosahedral 3P (**f**) models by depicting the direction of the patch vectors \mathbf{P}_i by circles (with the colours representing (one of) the particles with which they interact) on the surface of an icosahedron. The projections chosen are along the highest rotational axis of the particles. Edges on the back faces of the icosahedra are dashed and cyan. Similarly, for patch vectors on the back faces, the colour shade is lighter and ringed in cyan rather than black. The BOODs in **a–d** are fully consistent with the particles being oriented in this way with respect to the global icosahedral order of the IQCs. We also note that the preferred torsional angles of each patch–patch interaction are those that ensure the propagation of this global orientational order.

[Extended Data Fig. 9 Dynamics of the body-centred IQCs.](#)

Van Hove autocorrelation functions for the simulated body-centred IQCs, evaluated after one million Monte Carlo cycles and considering only those particles within a radius of $20\sigma_{LJ}$, which corresponds to the interior of the cluster where the radial density is constant ([Extended Data Fig. 6b](#)). The

majority of the particle mobility is associated with the blue matrix particles, whereas the red and green particles that form the inner shell of the icosahedral clusters have very limited mobility. The yellow particles in the $5P$ system are the most mobile but are only present at very low mole fraction.

Extended Data Fig. 10 Dynamics of the primitive IQCs.

Van Hove autocorrelation function for the simulated primitive IQCs, evaluated after one million Monte Carlo cycles and considering only those particles within a radius of $20\sigma_{\text{LJ}}$, which corresponds to the interior of the cluster where the radial density is constant (Extended Data Fig. [7b](#)). Although the overall pattern shows clear five-fold symmetry, the peaks merge into each other more than for the BCI systems. This is partly because the size of the allowed hops is shorter. The green particles are the most mobile, and the red particles, which form the inner shell of the icosahedral clusters, are least mobile. It is also noticeable that without torsions, the $3P$ system has greater mobility, and that the $2P$ patterns are less well defined, with the motion of the blue particles close to isotropic.

Supplementary information

Supplementary Information

This file contains supplementary text, supplementary equations s1 – s17, supplementary figures s1 – s15 and supplementary references.

Source data

Source Data Fig. 2

Source Data Fig. 3

Rights and permissions

[Reprints and Permissions](#)

About this article



Check for
updates

Cite this article

Noya, E.G., Wong, C.K., Llombart, P. *et al.* How to design an icosahedral quasicrystal through directional bonding. *Nature* **596**, 367–371 (2021).
<https://doi.org/10.1038/s41586-021-03700-2>

[Download citation](#)

- Received: 13 August 2020
- Accepted: 07 June 2021
- Published: 18 August 2021
- Issue Date: 19 August 2021
- DOI: <https://doi.org/10.1038/s41586-021-03700-2>

Comments

By submitting a comment you agree to abide by our [Terms](#) and [Community Guidelines](#). If you find something abusive or that does not comply with our terms or guidelines please flag it as inappropriate.

[Access through your institution](#)

[Change institution](#)

[Buy or subscribe](#)

Advertisement

This article was downloaded by **calibre** from <https://www.nature.com/articles/s41586-021-03700-2>

| [Section menu](#) | [Main menu](#) |

- Article
- [Published: 18 August 2021](#)

Mobility gradients yield rubbery surfaces on top of polymer glasses

- [Zhiwei Hao¹](#) na1,
- [Asieh Ghanekarade²](#) na1,
- [Ningtao Zhu¹](#),
- [Katelyn Randazzo³](#),
- [Daisuke Kawaguchi](#) [ORCID: orcid.org/0000-0001-8930-039X⁵](#),
- [Keiji Tanaka](#) [ORCID: orcid.org/0000-0003-0314-3843⁵](#),
- [Xinping Wang¹](#),
- [David S. Simmons](#) [ORCID: orcid.org/0000-0002-1436-9269²](#),
- [Rodney D. Priestley](#) [ORCID: orcid.org/0000-0001-6765-2933^{3,4}](#) &
- [Biao Zuo](#) [ORCID: orcid.org/0000-0002-4921-8823¹](#)

[Nature](#) volume 596, pages 372–376 (2021) [Cite this article](#)

- 2373 Accesses
- 105 Altmetric
- [Metrics details](#)

Subjects

- [Glasses](#)
- [Polymers](#)

Abstract

Many emerging materials, such as ultrastable glasses^{1,2} of interest for phone displays and OLED television screens, owe their properties to a gradient of enhanced mobility at the surface of glass-forming liquids. The discovery of this surface mobility enhancement^{3,4,5} has reshaped our understanding of the behaviour of glass formers and of how to fashion them into improved materials. In polymeric glasses, these interfacial modifications are complicated by the existence of a second length scale—the size of the polymer chain—as well as the length scale of the interfacial mobility gradient^{6,7,8,9}. Here we present simulations, theory and time-resolved surface nano-creep experiments to reveal that this two-scale nature of glassy polymer surfaces drives the emergence of a transient rubbery, entangled-like surface behaviour even in polymers comprised of short, subentangled chains. We find that this effect emerges from superposed gradients in segmental dynamics and chain conformational statistics. The lifetime of this rubbery behaviour, which will have broad implications in constraining surface relaxations central to applications including tribology, adhesion, and surface healing of polymeric glasses, extends as the material is cooled. The surface layers suffer a general breakdown in time–temperature superposition (TTS), a fundamental tenet of polymer physics and rheology. This finding may require a reevaluation of strategies for the prediction of long-time properties in polymeric glasses with high interfacial areas. We expect that this interfacial transient elastomer effect and TTS breakdown should normally occur in macromolecular systems ranging from nanocomposites to thin films, where interfaces dominate material properties^{5,10}.

Access options

Subscribe to Journal

Get full journal access for 1 year

\$199.00

only \$3.90 per issue

[Subscribe](#)

All prices are NET prices.
VAT will be added later in the checkout.
Tax calculation will be finalised during checkout.

Rent or Buy article

Get time limited or full article access on ReadCube.

from \$8.99

[Rent or Buy](#)

All prices are NET prices.

Additional access options:

- [Log in](#)
- [Access through your institution](#)
- [Learn about institutional subscriptions](#)

Fig. 1: Formation of wetting ridge and its topological profile.



Fig. 2: Polymer nano-rheology and surface chain dynamics.

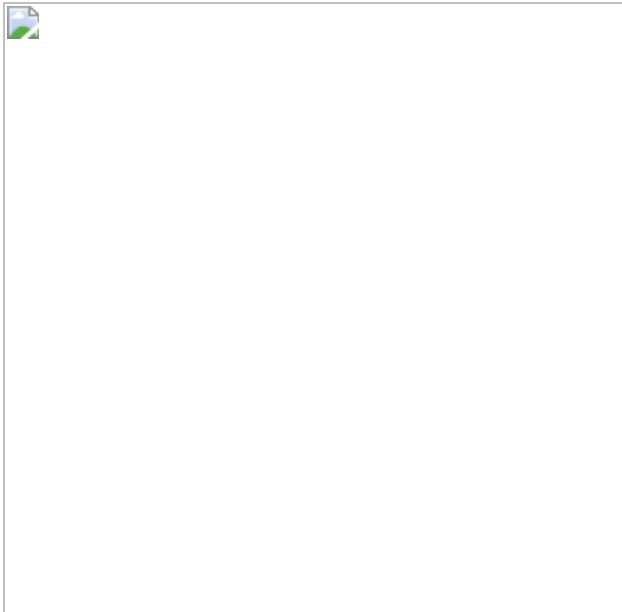
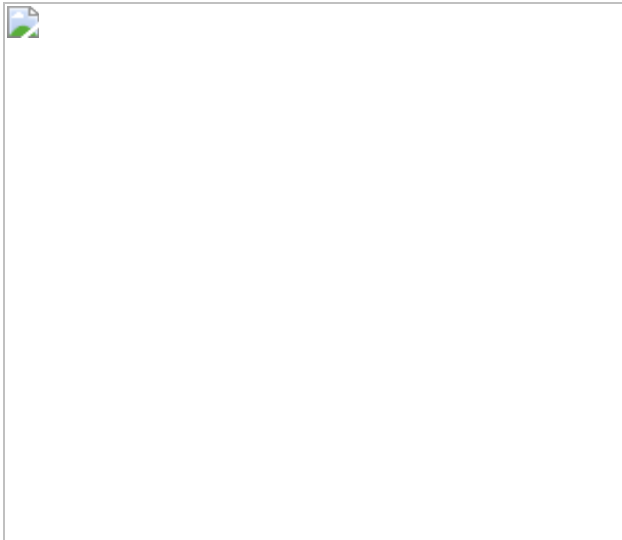


Fig. 3: Failure of TTS at the glassy polymer surface.



Fig. 4: Emergence of rubbery dynamics at the surface of the unentangled polymer.



Data availability

The data that support the findings of this study are available within the article and its [Supplementary Information](#). Raw simulation trajectories are available upon request from D.S.S.

Code availability

Simulations employ standard codes (LAMMPS) and methods that are freely available or documented in the literature.

References

1. 1.

Swallen, S. F. et al. Organic glasses with exceptional thermodynamic and kinetic stability. *Science* **315**, 353–356 (2007).

[ADS](#) [CAS](#) [Article](#) [Google Scholar](#)

2. 2.

Ediger, M. D. Perspective: highly stable vapor-deposited glasses. *J. Chem. Phys.* **147**, 210901 (2017).

[ADS](#) [CAS](#) [Article](#) [Google Scholar](#)

3. 3.

Dutcher, J. R. & Ediger, M. D. Glass surfaces not so glassy. *Science* **319**, 577–578 (2008).

[Article](#) [Google Scholar](#)

4. 4.

Jones, R. A. L. Glasses with liquid-like surfaces. *Nat. Mater.* **2**, 645–646 (2003).

[ADS](#) [CAS](#) [Article](#) [Google Scholar](#)

5. 5.

Napolitano, S., Glynos, E. & Tito, N. B. Glass transition of polymers in bulk, confined geometries, and near interfaces. *Rep. Prog. Phys.* **80**, 036602 (2017).

[ADS](#) [Article](#) [Google Scholar](#)

6. 6.

Schweizer, K. S. & Simmons, D. S. Progress towards a phenomenological picture and theoretical understanding of glassy dynamics and vitrification near interfaces and under nanoconfinement. *J. Chem. Phys.* **151**, 240901 (2019).

[ADS](#) [Article](#) [Google Scholar](#)

7. 7.

Ellison, C. J. & Torkelson, J. M. The distribution of glass-transition temperatures in nanoscopically confined glass formers. *Nat. Mater.* **2**, 695–700 (2003).

[ADS](#) [CAS](#) [Article](#) [Google Scholar](#)

8. 8.

Priestley, R. D., Ellison, C. J., Broadbelt, L. J. & Torkelson, J. M. Structural relaxation of polymer glasses at surfaces, interfaces, and in between. *Science* **309**, 456–459 (2005).

[ADS](#) [CAS](#) [Article](#) [Google Scholar](#)

9. 9.

Pye, J. E., Rohald, K. A., Baker, E. A. & Roth, C. B. Physical aging in ultrathin polystyrene films: evidence of a gradient in dynamics at the free surface and its connection to the glass transition temperature reductions. *Macromolecules* **43**, 8296–8303 (2010).

[ADS](#) [CAS](#) [Article](#) [Google Scholar](#)

10. 10.

Yu, L. Surface mobility of molecular glasses and its importance in physical stability. *Adv. Drug Deliv. Rev.* **100**, 3–9 (2016).

[CAS](#) [Article](#) [Google Scholar](#)

11. 11.

Jackson, C. L. & McKenna, G. B. The glass transition of organic liquids confined to small pores. *J. Non-Cryst. Solids* **131–133**, 221–224 (1991).

[ADS](#) [Article](#) [Google Scholar](#)

12. 12.

Keddie, J. L., Jones, R. A. L. & Cory, R. A. Size-dependent depression of the glass transition temperature in polymer films. *Europhys. Lett.* **27**, 59–64 (1994).

[ADS](#) [CAS](#) [Article](#) [Google Scholar](#)

13. 13.

Fakhraai, Z. & Forrest, J. A. Measuring the surface dynamics of glassy polymers. *Science* **319**, 600–604 (2008).

[CAS](#) [Article](#) [Google Scholar](#)

14. 14.

Paeng, K., Swallen, S. F. & Ediger, M. D. Direct measurement of molecular motion in freestanding polystyrene thin films. *J. Am. Chem. Soc.* **133**, 8444–8447 (2011).

[CAS](#) [Article](#) [Google Scholar](#)

15. 15.

Ediger, M. D. & Forrest, J. A. Dynamics near free surfaces and the glass transition in thin polymer films: a view to the future. *Macromolecules* **47**, 471–478 (2014).

[ADS](#) [CAS](#) [Article](#) [Google Scholar](#)

16. 16.

Yang, Z., Fujii, Y., Lee, F. K., Lam, C-H. & Tsui, O. K. C. Glass transition dynamics and surface layer mobility in unentangled polystyrene films. *Science* **328**, 1676–1679 (2010).

[ADS](#) [CAS](#) [Article](#) [Google Scholar](#)

17. 17.

Chai, Y. et al. A direct quantitative measure of surface mobility in a glassy polymer. *Science* **343**, 994–999 (2014).

[ADS](#) [CAS](#) [Article](#) [Google Scholar](#)

18. 18.

Li, Y. et al. Surface diffusion in glasses of rod-like molecules posaconazole and itraconazole: effect of interfacial molecular alignment and bulk penetration. *Soft Matter* **16**, 5062–5070 (2020).

[ADS](#) [CAS](#) [Article](#) [Google Scholar](#)

19. 19.

Flier, B. M. I. et al. Heterogeneous diffusion in thin polymer films as observed by high-temperature single-molecule fluorescence microscopy. *J. Am. Chem. Soc.* **134**, 480–488 (2012).

[CAS](#) [Article](#) [Google Scholar](#)

20. 20.

Xu, Q. et al. Decoupling role of film thickness and interfacial effect on polymer thin film dynamics. *ACS Macro Lett.* **10**, 1–8 (2021).

[ADS](#) [Article](#) [Google Scholar](#)

21. 21.

Toney, M. F. et al. Near-surface alignment of polymers in rubbed films. *Nature* **374**, 709–711 (1995).

[ADS](#) [CAS](#) [Article](#) [Google Scholar](#)

22. 22.

Maeda, N., Chen, N., Tirrell, M. & Israelachvili, J. N. Adhesion and friction mechanisms of polymer-on-polymer surfaces. *Science* **297**,

379–382 (2002).

[ADS](#) [CAS](#) [Article](#) [Google Scholar](#)

23. 23.

Tanaka, K., Takahara, A. & Kajiyama, T. Rheological analysis of surface relaxation process of monodisperse polystyrene films. *Macromolecules* **33**, 7588–7593 (2000).

[ADS](#) [CAS](#) [Article](#) [Google Scholar](#)

24. 24.

Ma, J. et al. Fast surface dynamics enabled cold joining of metallic glasses. *Sci. Adv.* **5**, eaax7256 (2019).

[ADS](#) [CAS](#) [Article](#) [Google Scholar](#)

25. 25.

Li, X. et al. Low-temperature processing of polymer nanoparticles for bioactive composites. *J. Polym. Sci. B* **54**, 2514–2520 (2016).

[CAS](#) [Article](#) [Google Scholar](#)

26. 26.

Chen, F., Lam, C.-H. & Tsui, O. K. C. The surface mobility of glasses. *Science* **343**, 975–976 (2014).

[ADS](#) [CAS](#) [Article](#) [Google Scholar](#)

27. 27.

Sokolov, A. P. & Schweizer, K. S. Resolving the mystery of the chain friction mechanism in polymer liquids. *Phys. Rev. Lett.* **102**, 248301 (2009).

[ADS](#) [Article](#) [Google Scholar](#)

28. 28.

Hung, J.-H., Mangalara, J. H. & Simmons, D. S. Heterogeneous rouse model predicts polymer chain translational normal mode decoupling. *Macromolecules* **51**, 2887–2898 (2018).

[ADS](#) [CAS](#) [Article](#) [Google Scholar](#)

29. 29.

Rubinstein, M. & Colby, R. H. *Polymer Physics* (Oxford Univ. Press, 2003).

30. 30.

Carré, A., Gastel, J.-C. & Shanahan, M. E. R. Viscoelastic effects in the spreading of liquids. *Nature* **379**, 432–434 (1996).

[ADS](#) [Article](#) [Google Scholar](#)

31. 31.

Shanahan, M. E. R. & Carré, A. Spreading and dynamics of liquid drops involving nanometric deformations on soft substrates. *Colloids Surf. A* **206**, 115–123 (2002).

[CAS](#) [Article](#) [Google Scholar](#)

32. 32.

Jerison, E. R., Xu, Y., Wilen, L. A. & Dufresne, E. R. Deformation of an elastic substrate by a three-phase contact line. *Phys. Rev. Lett.* **106**, 186103 (2011).

[ADS](#) [Article](#) [Google Scholar](#)

33. 33.

Lu, H., Chen, W. & Russell, T. P. Relaxation of thin films of polystyrene floating on ionic liquid surface. *Macromolecules* **42**, 9111–9117 (2009).

[ADS](#) [CAS](#) [Article](#) [Google Scholar](#)

34. 34.

Fetters, L. J., Lohse, D. J., Richter, D., Witten, T. A. & Zirkel, A. Connection between polymer molecular weight, density, chain dimensions, and melt viscoelastic properties. *Macromolecules* **27**, 4639–4647 (1994).

[ADS](#) [CAS](#) [Article](#) [Google Scholar](#)

35. 35.

Plazek, D. J. & O'Rourke, V. M. Viscoelastic behavior of low molecular weight polystyrene. *J. Polym. Sci. A-2* **9**, 209–243 (1971).

[CAS](#) [Article](#) [Google Scholar](#)

36. 36.

Yang, J. & Schweizer, K. S. Glassy dynamics and mechanical response in dense fluids of soft repulsive spheres. II. Shear modulus, relaxation-elasticity connections, and rheology. *J. Chem. Phys.* **134**, 204909 (2011).

[ADS](#) [Article](#) [Google Scholar](#)

37. 37.

Humphrey, W., Dalke, A. & Schulten, K. VMD — visual molecular dynamics. *J. Mol. Graph.* **14**, 33–38 (1996).

[CAS](#) [Article](#) [Google Scholar](#)

38. 38.

Lang, R. J. & Simmons, D. S. Interfacial dynamic length scales in the glass transition of a model freestanding polymer film and their connection to cooperative motion. *Macromolecules* **46**, 9818–9825 (2013).

[ADS](#) [CAS](#) [Article](#) [Google Scholar](#)

39. 39.

Khantha, M. & Balakrishnan, V. First passage time distributions for finite one-dimensional random walks. *Pramana* **21**, 111–122 (1983).

[ADS](#) [Article](#) [Google Scholar](#)

40. 40.

Kröger, M. Shortest multiple disconnected path for the analysis of entanglements in two- and three-dimensional polymeric systems. *Comput. Phys. Commun.* **168**, 209–232 (2005).

41. 41.

Si, L., Massa, M. V., Dalnoki-Veress, K., Brown, H. R. & Jones, R. A. L. Chain entanglement in thin freestanding polymer films. *Phys. Rev. Lett.* **94**, 127801 (2005).

[ADS](#) [Article](#) [Google Scholar](#)

42. 42.

Brown, H. R. & Russell, T. P. Entanglements at polymer surfaces and interfaces. *Macromolecules* **29**, 798–800 (1996).

[ADS](#) [CAS](#) [Article](#) [Google Scholar](#)

[Download references](#)

Acknowledgements

We thank N. L. Yamada for assisting with the neutron reflectivity measurements and O. K. C. Tsui and J. J. Zhou for discussions. B.Z. acknowledges financial support from the Natural Science Foundation of China (grant numbers 21973083 and 21504081), and R.D.P. and K.R. acknowledge support from the National Science Foundation (NSF) Materials Research Science and Engineering Center Program through the Princeton Center for Complex Materials (grant numbers DMR-1420541 and DMR-2011750) and the NSF through grant number CBET-1706012. D.S.S. and A.G. acknowledge support from the National Science Foundation through grant number CBET-1854308. X.W. thanks the Natural Science Foundation of China (grant numbers 21674100 and 21873085), and K.T. acknowledges the JST-Mirai Program (JPMJMI18A2). We also acknowledge the BL-16 line at J-PARC (programme no.2017L2501) for providing beam time.

Author information

Author notes

1. These authors contributed equally: Zhiwei Hao, Asieh Ghanekarade

Affiliations

1. Department of Chemistry, Key Laboratory of Surface & Interface Science of Polymer Materials of Zhejiang Province, National Engineering Lab for Textile Fiber Materials and Processing Technology (Zhejiang), Zhejiang Sci-Tech University, Hangzhou, China

Zhiwei Hao, Ningtao Zhu, Xinping Wang & Biao Zuo

2. Department of Chemical, Biological, and Materials Engineering, University of South Florida, Tampa, FL, USA

Asieh Ghanekarade & David S. Simmons

3. Department of Chemical and Biological Engineering, Princeton University, Princeton, NJ, USA

Katelyn Randazzo & Rodney D. Priestley

4. Princeton Institute for the Science and Technology of Materials, Princeton University, Princeton, NJ, USA

Rodney D. Priestley

5. Department of Applied Chemistry, Center for Polymer Interface and Molecular Adhesion Science, Kyushu University, Fukuoka, Japan

Daisuke Kawaguchi & Keiji Tanaka

Authors

1. Zhiwei Hao

[View author publications](#)

You can also search for this author in [PubMed](#) [Google Scholar](#)

2. Asieh Ghanekarade

[View author publications](#)

You can also search for this author in [PubMed](#) [Google Scholar](#)

3. Ningtao Zhu

[View author publications](#)

You can also search for this author in [PubMed](#) [Google Scholar](#)

4. Katelyn Randazzo

[View author publications](#)

You can also search for this author in [PubMed](#) [Google Scholar](#)

5. Daisuke Kawaguchi

[View author publications](#)

You can also search for this author in [PubMed](#) [Google Scholar](#)

6. Keiji Tanaka

[View author publications](#)

You can also search for this author in [PubMed](#) [Google Scholar](#)

7. Xinpeng Wang

[View author publications](#)

You can also search for this author in [PubMed](#) [Google Scholar](#)

8. David S. Simmons

[View author publications](#)

You can also search for this author in [PubMed](#) [Google Scholar](#)

9. Rodney D. Priestley

[View author publications](#)

You can also search for this author in [PubMed](#) [Google Scholar](#)

10. Biao Zuo

[View author publications](#)

You can also search for this author in [PubMed](#) [Google Scholar](#)

Contributions

B.Z. and R.D.P. conceived and supervised the experiments. Z.H., N.Z. and K.R. performed experiments. D.S.S. and A.G. conceived and analysed all simulations and theories. A.G. performed all simulations under the supervision of D.S.S. D.K. and K.T. provided neutron reflectivity data. All authors discussed the results and wrote the manuscript.

Corresponding authors

Correspondence to [David S. Simmons](#) or [Rodney D. Priestley](#) or [Biao Zuo](#).

Ethics declarations

Competing interests

The authors declare no competing interests.

Additional information

Peer review information *Nature* thanks the anonymous reviewer(s) for their contribution to the peer review of this work.

Publisher's note Springer Nature remains neutral with regard to jurisdictional claims in published maps and institutional affiliations.

Supplementary information

[Supplementary Information](#)

This file contains notes on the theoretical development, Supplementary Simulation Methods, Supplementary Data, Supplementary Table 1, Supplementary Figs 1-16 and Supplementary References.

Rights and permissions

[Reprints and Permissions](#)

About this article



Check for
updates

Cite this article

Hao, Z., Ghanekarade, A., Zhu, N. *et al.* Mobility gradients yield rubbery surfaces on top of polymer glasses. *Nature* **596**, 372–376 (2021).
<https://doi.org/10.1038/s41586-021-03733-7>

[Download citation](#)

- Received: 30 November 2020
- Accepted: 15 June 2021
- Published: 18 August 2021
- Issue Date: 19 August 2021
- DOI: <https://doi.org/10.1038/s41586-021-03733-7>

Comments

By submitting a comment you agree to abide by our [Terms](#) and [Community Guidelines](#). If you find something abusive or that does not comply with our terms or guidelines please flag it as inappropriate.

[Access through your institution](#)

[Change institution](#)

[Buy or subscribe](#)

Advertisement

This article was downloaded by **calibre** from <https://www.nature.com/articles/s41586-021-03733-7>

Operationalizing the net-negative carbon economy

[Download PDF](#)

- Article
- [Published: 08 July 2021](#)

Operationalizing the net-negative carbon economy

- [Johannes Bednar](#) [ORCID: orcid.org/0000-0002-8968-2591^{1,2}](#),
- [Michael Obersteiner](#) [ORCID: orcid.org/0000-0001-6981-2769^{1,2}](#),
- [Artem Baklanov](#) [ORCID: orcid.org/0000-0003-1599-3618^{1,3}](#),
- [Marcus Thomson⁴](#),
- [Fabian Wagner¹](#),
- [Oliver Geden](#) [ORCID: orcid.org/0000-0001-9456-4218^{1,5}](#),
- [Myles Allen](#) [ORCID: orcid.org/0000-0002-1721-7172²](#) &
- [Jim W. Hall²](#)

Nature volume **596**, pages 377–383 (2021) [Cite this article](#)

- 4891 Accesses
- 223 Altmetric
- [Metrics details](#)

Subjects

- [Climate-change mitigation](#)

Abstract

The remaining carbon budget for limiting global warming to 1.5 degrees Celsius will probably be exhausted within this decade^{1,2}. Carbon debt³ generated thereafter will need to be compensated by net-negative emissions⁴. However, economic policy instruments to guarantee potentially very costly net carbon dioxide removal (CDR) have not yet been devised. Here we propose intertemporal instruments to provide the basis for widely applied carbon taxes and emission trading systems to finance a net-

negative carbon economy⁵. We investigate an idealized market approach to incentivize the repayment of previously accrued carbon debt by establishing the responsibility of emitters for the net removal of carbon dioxide through ‘carbon removal obligations’ (CROs). Inherent risks, such as the risk of default by carbon debtors, are addressed by pricing atmospheric CO₂ storage through interest on carbon debt. In contrast to the prevailing literature on emission pathways, we find that interest payments for CROs induce substantially more-ambitious near-term decarbonization that is complemented by earlier and less-aggressive deployment of CDR. We conclude that CROs will need to become an integral part of the global climate policy mix if we are to ensure the viability of ambitious climate targets and an equitable distribution of mitigation efforts across generations.

[Download PDF](#)

Main

Delivering on the many national and corporate net-zero emission pledges will probably require the gross removal of atmospheric carbon dioxide (CO₂) on top of conventional emission reductions^{6,7}. To achieve the Paris Agreement, global gross CO₂ removals will need to exceed gross residual emissions^{4,8} after the middle of the century^{1,9}. The resultant net-negative emissions compensate for the carbon debt³ accrued by CO₂ emissions that overshoot the remaining carbon budget^{10,11}. Carbon debt is projected to amount to roughly the equivalent of 9 years of global emissions before the COVID-19 pandemic according to the 1.5 °C ‘middle of the road’ scenario P3/S2 of the Intergovernmental Panel on Climate Change (IPCC)¹ (Extended Data Table 1). Such large-scale deployment of CDR is controversial mainly for the implied economic and technological risks^{12,13,14,15,16} and environmental effects^{17,18}; and because reliance on CDR in mitigation scenarios often goes hand-in-hand with a substantial shift of the mitigation burden to future generations¹⁹.

Here we would like to highlight a fundamental economic problem associated with the existing assessments of climate mitigation scenarios, aiming to inform international climate negotiations. Existing economic policy instruments for emission control are inadequate to incentivize a global transformation towards a net-negative carbon economy without imposing excessive fiscal burden from 2050 onwards. Currently envisaged carbon tax schemes would turn into public subsidies under net-negative emissions with potentially prohibitive fiscal implications⁵. Emission trading schemes (ETS), on the other hand, are presently designed to handle only positive emission caps. Negative emissions are merely treated as offsets, suggesting that CO₂ emissions from one point in time cannot be compensated by an equivalent quantity of negative

emissions at another point in time, as required by most mitigation scenarios. Notably, we observe that pricing the depletion of the remaining carbon budget is fundamentally different to pricing overshoot emissions after the depletion of the budget, which has profound implications for the consistent earmarking of accrued revenues from a price on CO₂.

We argue that establishing the responsibility of emitters for carbon debt is a prerequisite to ensuring viable net-negative carbon futures. Carbon debt could therefore be treated similar to financial debt, including interest payments on physical liabilities (that is, as a CRO) to internalize the inherent risks. On the basis of this idealized global carbon policy proposal motivated by the IPCC's mitigation scenarios, our numerical results address the shortcomings of the existing climate mitigation literature²⁰. Despite the conceptual character of this study, we establish profound implications for national carbon policies, which are strongly influenced by the IPCC's global mitigation pathways in many high-emission countries²¹.

Carbon pricing for net-negative emissions

Integrated assessment models (IAMs) provide global carbon price paths that serve as a proxy for a wider range of cost-effective climate policy options to achieve specified greenhouse gas mitigation goals⁹. Such carbon prices typically increase exponentially with the interest rate as a consequence of the Hotelling rule, which defines the intertemporally optimal extraction schedule and price of a non-renewable resource^{22,23}, such as the carbon budget. If understood as a global common, revenues generated from pricing its depletion should consistently add to public budgets, for instance to compensate for the associated welfare effects, which may be unfairly distributed across society. However, in scenarios in which the carbon budget is overshot and subsequently replenished, the budget can no longer be regarded as a non-renewable resource. In this case, the Hotelling rule lends itself to an 'intertemporal interpretation' for carbon policy: revenues from carbon pricing after the depletion of the budget can be invested at the market interest rate to finance net carbon removal later in the century. Because marginal abatement costs increase at the market interest rate, this calculation is exact under perfect foresight conditions—as assumed in most IAMs—if the retained funds purchase net-negative emissions at marginal costs later on. Because emitters pay for future net CDR through the carbon price, this intertemporal interpretation is compatible with the 'polluter pays principle'. The resultant intertemporal financial transfer thereby addresses concerns of intergenerational equity because public budgets in the near-term no longer spuriously benefit from pricing an already depleted resource, while future generations thereafter are forced to replenish the carbon budget through other sources, such as income, sales or payroll taxes. According to the 'conventional interpretation' of the Hotelling rule,

revenues from carbon pricing are merely treated as contemporaneous additions to public budgets, with no clear earmarking of accrued funds. Notably, as both approaches are simply interpretations of the same underlying carbon price paths, emitters also pay the discounted future costs of net emission removal in case of the conventional interpretation. However, in the absence of consistent earmarking, the financial viability of net CDR in the second half of the twenty-first century is highly doubtful⁵, and intergenerational equity remains unaccounted for.

To operationalize a future net-negative carbon economy, carbon tax revenues could be partially retained and transferred over generations to finance net CDR in the style of a nuclear decommissioning trust fund or a sovereign wealth fund. The value of such a global net carbon removal fund is potentially enormous, yet in the range of comparable funds, peaking at roughly 100% of global gross domestic product (GDP) in the median of the Shared Socioeconomic Pathway (SSP) scenarios that are compatible with Representative Concentration Pathway 1.9 (RCP 1.9)²⁴ (Fig. 1). For comparison, Norway's large sovereign wealth fund has passed 250% of national GDP²⁵. Given this order of magnitude, intermediate investment portfolios could be a game changer to lift CDR out of the pilot phase even before pay-out of the fund. However, protecting financial resources from diversion for other purposes as political environments change, or as public finances become stressed, will surely be extremely challenging. For instance, sovereign borrowing to cushion the effects of the COVID-19 pandemic meant that by the end of 2020 the debt-to-GDP ratio of governments according to the Organisation for Economic Co-operation and Development had increased by about 13.4 percentage points²⁶. Severe crises in the future could induce considerable pressure for governments to appropriate savings originally reserved for net CDR.

Fig. 1: Idealized global tax scheme with net carbon removal fund.

 **figure1**

a, Bottom, public income and expenditure from a tax on net emissions expressed as a percentage of GDP. Hotelling-compatible (exponential) carbon prices from SSP–RCP 1.9 scenarios are multiplied by net emissions and divided by GDP (grey dashed lines). An idealized income/expenditure curve (black solid line) was derived from these scenarios using a strictly exponential median carbon price, median net emissions and GDP. Instead of reserving 100% of tax revenues after depletion of the carbon budget, we assert that a fraction $\phi = 0.76$ of revenues is earmarked for net carbon removal, from 2020 onwards. This share of income (green area) would need to be accrued into a net carbon removal fund invested at the market rate of interest to account for later expenditure when net emissions turn negative. See [Methods](#) for a definition of ϕ . **b**, Top, cumulative payments into the net carbon removal fund (green) and interest (orange) in theory pay exactly for cumulative tax expenditure (blue), such that the net value of the fund (brown solid line) gets exhausted as the warming target is achieved in 2100.

[Full size image](#)

The success of a net CDR fund also depends on the appropriate choice of several inherently uncertain parameters, including future abatement costs. If costs and other socioeconomic parameters are not estimated in line with the precautionary principle, or if regulators are reluctant to adequately reflect future carbon removal in near-term price instruments, insufficient financial resources would be collected as observed for nuclear decommissioning²⁷. Because the carbon debt and associated risks would be mutualized by a net CDR fund, missing financial resources would need to be replenished by public budgets.

Dynamic emission trading

Emission trading with fully liberalized banking and borrowing of allowances can be regarded as a response to these concerns. Decentralized decision-making and price determination in a competitive market is believed to improve efficiency by leveraging the ability of carbon markets to determine cost-effective time paths of mitigation²⁸. In an idealized global scheme, the remaining carbon budget would be distributed over time resulting in positive emission caps for consecutive auctioning periods. Emitters would decide in each period what fraction of their CO₂ emissions to compensate for by allowances and how much carbon debt to generate for compensation by future allowances—or future CDR in the absence of a positive emission cap. Effectively, emitters generating carbon debt would remain liable for the timing and delivery of net-negative emissions (Fig. 2) and can therefore balance present against future abatement based on individual expectations, such as those concerning technological breakthroughs. Stranded assets can be avoided by harmonizing abatement investments with natural renewal cycles of capital; and fluctuations in the business cycle can be addressed. Fixed price schedules under a carbon tax suggest lower costs for hedging risks related to the long-run costs of negative emissions and low-carbon investments. However, increased intertemporal flexibility in emission trading stabilizes the price—which reflects discounted future marginal abatement costs—compared with currently implemented ETS with no intertemporal trade of allowances^{29,30}. At least in principle, this ETS arrangement enables emitters to develop optimal investments over longer time horizons, increasing the dynamic efficiency of emission trading. Although emission caps can be overshot, the quantity of cumulative emissions remains exactly controlled under an ETS with intertemporal trade of carbon debt, which is, more generally, the main advantage of cap-and-trade schemes compared with carbon taxes. If caps no longer directly control emission reductions, they can be set to equitably distribute ETS revenues over time. However, as the carbon budget diminishes rapidly—the 1.5 °C compatible budget is projected to become depleted roughly within the

next 10 years¹—the importance of carbon debt management increasingly outweighs the requirement of an adequate temporal distribution of the remaining carbon budget.

Fig. 2: Idealized ETS with intertemporal trade of carbon debt.

 figure2



Illustrative 2 °C pathway with gross carbon emissions from FFI, LUC and non-specified sources of CDR including the schematic architecture of idealized global intertemporal emission trading. ETS emission caps b_t are obtained by distributing the carbon budget in tranches over consecutive periods. The amount by which emission caps b_t are exceeded by net emissions is conceptualized as ‘carbon debt’ (d_t). In this idealized illustration, d_t is compensated later by corresponding net-negative emissions ($e_{NN,t}$) such that $d_t = -e_{NN,t}$. In a conventional ETS, emission caps would be set to $b_t + d_t$, and $e_{NN,t}$ would have to be incentivized by public subsidies. d_t , b_t and $e_{NN,t}$ (in which t indicates 1, 2 and so on) are simplified discrete analogues of the continuous variables $d(t)$, $b(t)$ and $e_{NN}(t)$, respectively, which are described in the Methods.

Historical emissions are from a previously published study³⁹.

[Full size image](#)

Privately managed carbon debt within an ETS also has considerable drawbacks: the enforcement of carbon debt, assessment of creditworthiness of emitters, the potential for speculation on future softening of emission targets and subsequent deferral of mitigation (time inconsistency)—which is stronger the lower the solvency of emitters (adverse selection)—and the resultant incentive to lobby for cancellation of carbon debt (moral hazard) are crucial obstacles that explain why such intertemporal mechanisms are severely restricted in currently implemented ETS²⁸. Moreover, intertemporal trade of carbon debt by means of forward and future markets trading negative emissions over potentially long periods at a fixed price is perceived as infeasible, given the deep uncertainty in the parameters guiding a large-scale CDR rollout³¹.

Carbon removal obligations

Intertemporal emission trading would necessarily come at the cost of considerable regulation to address these drawbacks. We argue, however, that practices from the financial industry and monetary policy could be leveraged to reduce risks and adaptively balance potentially competing interests of economic development and climate mitigation by treating carbon debt in a similar manner to a financial debt obligation, and thereby invoking an interest on carbon debt. Economic growth, aggregate demand for carbon debt and individual financial ratings of debtors would define a general base rate, individual mark-ups, term structures and debt maturities. To assure its physical conservation and exert control over its aggregate level, carbon debt would initially be issued at the base rate by managing authorities—for example, Central Banks—to which commercial banks would be held liable in case of insolvent debtors. Commercial banks, or their equivalents, would issue debt to emitters and, assisted by rating agencies, assess and hedge their insolvency risk by determining individual mark-ups on the base rate. Carbon debt would enter the balance sheets of firms as a physical liability in tonnes (t) CO₂—a carbon removal obligation, for which interest payments would be due (Extended Data Fig. 7a). This chain of legal liabilities across layers of public and private actors reduces the moral hazard that governments would ultimately pick up the bill for net emission removal, and limit the issuance of CROs to debtors who are reluctant to fulfil their (interest) obligations. Individual interest mark-ups would also balance the push of the market for adverse selection and incentivize a debt transfer from agents losing ground under stringent climate policy to low-risk agents; or lead to more near-term abatement (see below) if risks are deemed non-insurable. The rate controls the volatility of the carbon price (Extended Data Fig. 1) and therefore directly affects the price–risk costs of scheduled abatement investments. More generally, interest and debt maturities would need to reflect the speculative nature of CDR, leading to short—but potentially renewable—repayment

terms and elevated rates in the near-term. A concrete phase-in scenario of CROs in the ETS of the European Union and beyond is described in Box 1.

For intertemporal emission trading to work efficiently—for instance to reduce issues of time inconsistency and price volatility—emission caps would need to be credibly announced as early as possible. As a consequence, regulators would lose the flexibility of adapting caps as new knowledge concerning the Earth system becomes available. In an idealized global scheme, emission caps need to exactly reflect the remaining carbon budget. Budget uncertainties related to the issuing of carbon debt, similar to those of permafrost thaw after a temperature overshoot², could be hedged by collecting risk funds through base rate payments and by incentivizing more-ambitious emission reductions to minimize the risk of climate feedback effects (see below). Such uncertainties should remain manageable by risk reserves, allowing for the budget to be replenished by drawing on risk funds rather than requiring a downwards correction of scheduled emissions caps. In the best case, uncertainties and base rates would decrease over time as updated estimates of the carbon budget converge to a value within the expected range of the previously announced budget. However, new findings might realistically also lead to exceeding of the abilities of risk management, requiring a combined effort of future generations to counter potentially abrupt climate change. Management of physical risks therefore remains limited to what is presently perceivable and realistically quantifiable.

Box 1 Hypothetical implementation of a CRO-ETS in the European Union and elsewhere

The total carbon debt of the European Union (EU) amounts to 22.5 Gt CO₂ already by 2050, or roughly 7 years⁴⁰ of present CO₂ emissions, according to the 1.5 °C-compatible mitigation scenarios LIFE and TECH from the European Commission⁴¹. (All numbers provided here include the UK and emissions from land use, land-use change and forestry (LULUCF). Carbon debt for compensation in the 2050–2100 period is determined by subtracting the 2018–2100 budget from the higher 2018–2050 budget. Budgets are average values from the 1.5 °C TECH and LIFE scenarios. Annual emissions in 2018 amount to 3.14 Gt CO₂ (ref. ⁴²).) In line with the EU's net-zero greenhouse gas target for 2050, CO₂ emissions must turn net-negative already by 2043⁴³. Despite the lack of any adequate mechanism to do so, sectors currently covered by the EU ETS will therefore need to deliver 50 Mt CO₂-equivalent net greenhouse gas removal by 2050 in the more-ambitious 1.5 °C TECH scenario. CDR volumes are expected to increase after 2050 in line with the economy-wide net-negative greenhouse gas emissions objective already enshrined in the EU Climate Law. Beyond 2050, negative caps in the EU ETS⁴⁴ will require considerable public

funding, which is likely to obstruct the implementation of ambitious net-CO₂ removal targets. With CROs in place, overburdening of public budgets can be avoided.

We envision the following scenario. With the revision for phase IV of the EU ETS initiated in 2021, the linear reduction factor of emission caps is brought in line with the European Commission's long-term cumulative net-CO₂ target of 26 Gt CO₂ (for the 2018–2100 period; 1.5 °C TECH and LIFE scenarios combined, including net removals), while the scheme is gradually extended to full sectoral coverage. The implied increase of the reduction factor is balanced by a simultaneous phase-in of CROs, and carbon debt management is added to the portfolio of the European Central Bank. The European Central Bank issues debt to commercial banks at a base rate, which in turn issue debt to firms that participate in the EU ETS, charging individual mark-ups depending on the financial ratings of those firms. To be able to repay the European Central Bank despite defaulting debtors, banks would have to develop their own CDR portfolios. The resultant increase in CDR supply and expertise in assessing carbon debt risks induces the development of a wider variety of CRO products, with different maturities. For securing the long-term supply with fossil fuels in hard-to-transition sectors, such as long-haul aviation and shipping^{45,46}, large energy firms would be incentivized to develop CDR for counterbalancing residual emissions⁴⁷. Alternatively, accrued carbon debt would be transferred to other agents, such as wealthy—potentially non-EU—tech firms, with presumably low credit risk and a proclivity for mitigation technology⁴⁸. For CDR suppliers^{49,50}, CROs are the basis of a business case and, because negative emissions do not have to be delivered immediately, CROs simultaneously act as loans to finance development.

It may be that the global implementation of a CRO-ETS under the United Nations Framework Convention on Climate Change, as conceptualized in this Article, is not realistic for the time being. However, given the potential opportunities for the financial sector and CDR investors, as well as the implications for public finance, non-EU countries or regions with ambitious climate targets and (pilot) ETS schemes, such as China, Japan, South Korea, Quebec or California⁵¹, would probably be under pressure to liberalize intertemporal trade of carbon debt and thereby establish responsibility for overshoot emissions. The EU-wide rollout would therefore be followed by attempts to actively influence regulation globally (for example, through ‘regulatory export’⁵²) and subsequent linkage with other national and regional schemes⁵³.

Climate mitigation under carbon debt

In IAMs, abatement costs are discounted at the market interest rate, implying a cost advantage for abatement in the distant future compared with near-term decarbonization in terms of net present value. The interest rate is therefore a key driver

of carbon debt accrual in IAMs^{32,33}. This ‘discounting effect’ is balanced by imposing interest on carbon debt. Longer CRO maturities indicate lower net present costs for CDR. Simultaneously, carbon debt interest is paid over a longer period, compensating for these gains. When the market rate of interest and the carbon debt interest rate (r_d) coincide, the gains from discounting are balanced exactly, as we analytically show in the Methods. In Fig. 3, we illustrate the sensitivity of 2 °C-compatible global mitigation pathways to interest on carbon debt, with rates constant over the 2020–2100 period ranging from $r_d = 0$ to $r_d = 0.08$. For each rate, 13 scenarios are computed based on different SSPs and IAMs that are used to calibrate the marginal abatement cost curves of our model (Extended Data Table 2).

Fig. 3: The 2 °C (RCP 2.6) mitigation scenarios for a range of interest rates on carbon debt.

 figure3

a, Net CO₂ emissions of all scenarios with $r_d = 0$ (turquoise) and $r_d = 0.08$ (yellow), including geometric median paths (bold solid lines) and minimum to maximum ranges (shaded areas). **b**, Marginal abatement costs of scenarios with $r_d = 0$ (turquoise) and $r_d = 0.08$ (yellow). Bold solid lines indicate geometric medians, shaded areas indicate 25–75% interquartile ranges. **c, d**, Geometric median net emissions as in **a**, including gross emissions from FFI, BECCS and LUC. **c**, $r_d = 0$. **d**, $r_d = 0.08$. **e**, Total discounted abatement costs (net present value, including interest costs) expressed as a percentage cost increase compared with the baseline ($r_d = 0$) are shown as function of total carbon debt D . The boxes indicate the 25–75% interquartile ranges around the median values of the costs and D . Symbols linked by grey solid lines indicate the medians grouped by

SSP. The entire dataset is shown in the top right corner, in which each scenario is reflected by a symbol, grouped by SSP (symbol type) and r_d (colour).

[Full size image](#)

For comparison, only the two extreme cases— $r_d = 0$ and $r_d = 0.08$ —are illustrated in Fig. 3a–d. Notably, when $r_d = 0.08$, the cumulative emission target is achieved without the accrual of carbon debt in the median path (Fig. 3d), suggesting that emissions remain at the net-zero level once achieved. This is accomplished by the contemporaneous compensation of residual CO₂ from fossil fuels and industry (FFI) with negative emissions from bioenergy with carbon capture and storage (BECCS) and land-use change (LUC). Complete decarbonization of FFI emissions is, however, not cost-effective owing to the high marginal costs of emission reductions from hard-to-abate sectors. Notably, net-negative emissions of individual scenarios in Fig. 3a turn back to zero before 2100, thereby minimizing the ‘problem of phasedown’³⁴. With reduced reliance on net-negative emissions, marginal costs are higher in the near-term due to the more-rapid reduction in FFI emissions and increase in BECCS, but considerably lower in 2100 (Fig. 3b). Figure 3e shows a reduction in the total carbon debt D as r_d is gradually increased. Carbon debt risks are therefore greatly reduced at a moderate cost increase of below 12.5% in more than 75% of scenarios in which $r_d > 0.02$.

A similar analysis was performed for the 1.5 °C global warming target; however, direct air capture and storage (DACS) is added to the mitigation technology mix, represented by six different DACS-specific marginal abatement cost curves with low, medium and high costs as well as low- and high-capacity limits. This results in a set of 78 scenarios for each rate r_d . Not surprisingly, the higher the potential for DACS to be deployed, the larger the level of D when $r_d = 0$. By contrast, when interest is invoked, this discounting effect is reversed and scenarios with large-capacity low-cost DACS simultaneously exhibit the lowest levels of D (Extended Data Fig. 2). The pathways in Fig. 4 show baseline (Fig. 4a, b) and reduced D (Fig. 4c, d) scenarios for those scenarios that achieve a reduction in D of at least 30% compared with their associated baselines (see Extended Data Figs. 3–5 for reductions of 5%, 15% and 45%, respectively). For illustration, we interpret the CRO-ETS baseline scenarios, in which $r_d = 0$, as conventional ETS scenarios because both schemes are theoretically equivalent in terms of the resultant emission profiles while they imply a qualitatively different timing of financial flows.

Fig. 4: The 1.5 °C (RCP 1.9) pathways under a conventional ETS or a CRO-ETS.

 **figure4**

a, b, A conventional ETS is used. **c, d**, A CRO-ETS is used. **a, c**, Geometric median net emissions (solid line) and gross emissions from FFI, BECCS, LUC and DACS. Net emissions from **a** are also displayed in **c** (dashed line) and vice versa. The total carbon debt D is shown as a box-and-whiskers plot. Boxes indicate the 25–75% interquartile range around the median values (bold line), whiskers indicate minimum to maximum ranges, points mark the outliers. **b, d**, Annual mitigation costs as a percentage of GDP, including the share of average abatement costs attributed to emission reductions (ABM), to the compensation of residual emissions by CDR (RES) and to net-negative emissions (NNE), as well as expenditures for allowances (ETS) and interest costs (INT). Total mitigation costs (that is, $ABM + RES + NNE + ETS + INT$) from **d** are also displayed in **b** (dashed line) and vice versa. Box-and-whiskers plots show the total discounted abatement costs (that is, $ABM + RES + NNE$) as a percentage of GDP, the number above the chart indicates out-of-range outliers. Pie charts in **d** summarize the properties of the underlying set of scenarios (see [Methods](#)). The distribution of r_d in CRO-ETS scenarios is depicted in **c**.

[Full size image](#)

Despite the earlier increase in DACS in Fig. [4c](#), causing emissions to turn net zero around 2050, an emission overshoot appears to be inevitable if warming is to be limited to 1.5 °C. Remaining net-negative emissions might cause problems of

phasedown in 2100, unless CRO maturities are further extended to enable a smooth transition to net-zero emissions; or more net-negative emissions are needed to stabilize the climate in the twenty-second century³⁵. Therefore, the median D is equal to roughly 7 years of global net emissions in 2019 in Fig. 4c. Yet, the role of CDR changes considerably: without considering risks, CDR seems to justify late-century compensation of carbon debt. In this case, the median D is equivalent to about 11 years of 2019 global net emissions, with compensation starting roughly 10 years later in Fig. 4a. However, when risks are accounted for by imposing interest, CDR supports a rapid decrease in net emissions by balancing the residual emissions. Controversially, the availability of cheap and large-scale CDR options, such as DACS, is key in 1.5 °C scenarios with reduced reliance on the accrual of carbon debt. As illustrated by the pie charts in Fig. 4d, the share of high-capacity DACS scenarios among feasible scenarios with respect to the 30% reduction requirement grows to 81% (50% in the underlying set) and the share of low-cost DACS scenarios to 54% (33% in the underlying set). Should CDR not become readily available as asserted in IAMs^{36,37,38}, this would be reflected in an elevated carbon debt interest rate, incentivizing emission reductions provided by other sources, such as the replacement of fossil fuel with renewable energy sources in hard-to-abate sectors—even if this leads to much higher costs.

Effect on financial flows over time

Figure 4, moreover, illustrates the distribution of annual mitigation cost shares, including investments in emission reductions and negative emissions and the financial flows associated with ETS allowances and interest for CROs. The share of abatement costs for emission reductions (ABM), negative emissions compensating for residual emissions (RES) and net-negative emissions (NNE) incurred in the near- versus the long-term increases with larger levels of r_d (compare Fig. 4d to Extended Data Figs. 3d–5d). Here, CROs with interest induce a more equitable temporal distribution of these cost items, in sum peaking at 2.4% in Fig. 4d compared to 4.5% of GDP in Fig. 4b. This is partly because the CRO-ETS requires carbon debtors to reserve financial resources early in the century, and such funds earn interest until they are spent for net-negative emissions. By contrast, net-negative emissions expenditures in Fig. 4b are incurred at the time of net carbon removal and would need to be funded by public sources in the absence of intertemporal financial transfers. Note that here we show average abatement costs. If marginal costs are paid by incentivizing net CDR on a market, public expenditures are much higher (for comparison, see Fig. 1). Pricing overshoot emissions under a conventional ETS, moreover, implies much larger revenues ('ETS') than under the CRO-ETS, where emission caps reflect exactly the remaining carbon budget. Median total discounted abatement costs, excluding ETS costs and interest costs ('INT'), increase from 1.6% to 2.0% of GDP when interest is

invoked within the CRO-ETS. Median interest costs in these scenarios are substantial, peaking at above 1.3% of GDP, and 0.4% to 1.5% in Extended Data Figs. 3–5. These numbers are, however, highly uncertain and will need to be determined considering the viability and scalability of near-term CDR options and other emission reduction technologies.

Enlarging IAM CDR portfolios to reduce technological risks and environmental effects would probably lead to further burdening of future generations in scenarios if CDR remains primarily a motivation for reducing net present costs by accrual of carbon debt. This is especially problematic if such results trickle down through the IPCC and international climate negotiations into national target setting because no viable mechanisms for the repayment of carbon debt have entered the policy debate at the moment. Simultaneously, mitigation pathways with reduced carbon debt heavily rely on CDR, requiring that risks be appropriately managed. Similar pathways result from lowering the market interest rate in IAMs³² or from adequately setting intermediate climate targets or constraints on net emissions²⁰. However, such measures would individually not resolve the more profound issue of finance of net-negative emissions discussed here.

Conclusion

In view of the rapid depletion of the global carbon budget, CROs seem to be indispensable for any robust climate mitigation framework. CROs imply a paradigm shift from pricing the permanent to pricing the temporary storage of CO₂ in the atmosphere, with carbon debtors being responsible for delivering net CDR. The implied flexibility for emitters also bears the largest drawback of intertemporal emission trading, if public bailout of carbon debtors becomes necessary. To minimize such risks, the ‘conservation of carbon debt’ needs to take top priority by controlling the total amount of carbon debt and by establishing liability across several layers of actors. Risk management under a CRO-ETS relies on imposing interest on carbon debt. For higher and risk-adjusted carbon debt interest rates, net-negative emission investments no longer benefit from net present cost gains when mitigation is deferred to the distant future. By implication, CDR under a CRO-ETS will need to prove its viability compared with conventional options for the reduction of emissions already in the near-term. This will promote bottom-up CDR market development with the accompanying benefits of price discovery, earlier technological learning, testing of scalability and identification of socio-environmental co-benefits and hazards, and ultimately, eliminating the uncertainties surrounding CDR.

Methods

Basic analytical setup

Emission reductions induced by a CRO-ETS are quantified using a Hotelling-type optimization problem (see ref. [32](#) for an analytical solution of the model). A global social planner is tasked to implement emission reductions at minimum costs to meet a cumulative emission target—that is, the remaining carbon budget B —by $T = 2100$ ($t_0 = 2020$). Exogenously given baseline emissions E_{base} —that is, future emission paths based on ‘business-as-usual’ climate policy assumptions, are reduced by a fraction a to obtain net emissions e :

$$\text{(1)} \quad \$\$ e(t) = \{E\}_{\{\{\text{rm}\{\text{base}\}\}\}}(t)(1-a(t)).\$$$

Total abatement costs c_{tot} are discounted at the market interest rate r to obtain the net present value of total abatement costs, which is minimized:

$$\text{(2)} \quad \$\$ \mathop{\min} \limits_{\{a(t), c\}} \int_{t_0}^T c(t, a(t)) e(t) e^{-rt} dt$$

subject to:

$$\text{(3)} \quad \$\$ \int_{t_0}^T e(t) dt = B.$$

Integrating over marginal abatement costs $\text{MAC}(a)$ gives the cost per tonne CO_2 for an instantaneous emission reduction of a compared to the baseline. Consequently, total abatement costs c_{tot} are defined as:

$$\text{(4)} \quad \$\$ c = \int_{t_0}^T a(t) \text{MAC}(a) dt$$

Assume that under an idealized CRO-ETS, a constant fraction $1 - \phi$ of net-positive emissions e_{NP} is equivalent to a (continuous) emission cap b (that is, the amount of conventional emission allowances issued over time) and $\phi < 1$ of e_{NP} equals carbon debt d (that is, the quantity of CROs issued). Then ϕ is defined as the ratio of cumulative net-negative emissions e_{NN} to cumulative net-positive emissions e_{NP} :

$$\text{(5)} \quad \$\$ \varphi = \frac{\int_{t_0}^T e_{\text{NN}}(t) dt}{\int_{t_0}^T e_{\text{NP}}(t) dt}$$

and net-negative emissions and net-positive emissions equal the negative and positive parts of net emissions ($e_{NP}, e_{NN} > 0$)

$$\$ \$ \{e\}_{\{\rm NN\}}(t) = \begin{array}{cc} e(t) & \text{if } e(t) < 0 \\ 0 & \text{if } e(t) \geq 0 \end{array} \$ \$$$

(6)

$$\$ \$ \{e\}_{\{\rm NP\}}(t) = \begin{array}{cc} 0 & \text{if } e(t) > 0 \\ e(t) & \text{if } e(t) \leq 0 \end{array} \$ \$$$

(7)

Carbon debt d and the continuous emission cap b are defined as:

$$\$ \$ d(t) = \varphi \{e\}_{\{\rm NP\}}(t), b(t) = (1 - \varphi) \{e\}_{\{\rm NN\}}(t), \$ \$$$

and total carbon debt D is obtained by integration over the planning horizon T (combining equations (5) and (8)):

$$\$ \$ D = \int_{t=0}^T d(t) dt = \int_{t=0}^T (1 - \varphi) \{e\}_{\{\rm NN\}}(t) dt. \$ \$$$

Consequently, we can write ϕ as:

$$\$ \$ \varphi = \frac{D}{B+D}. \$ \$$$

By implication, a fraction ϕ of cumulative net-positive emissions overshoots B and thereby generates D , and a fraction $1 - \phi$ depletes the budget B .

Instead of exogenously imposing ETS emission caps, ϕ allows us to endogenously compute caps b and carbon debt d to conceptualize the intertemporal allocation of carbon debt such that debt is solely compensated by net-negative emissions e_{NN} . On this basis, we can compute a ‘physical repayment term’ T_R linking the timing of net-positive to net-negative emissions (equation (12)). CROs in this idealized ETS therefore represent a long-term intertemporal net transaction for financing net-negative emissions. This aggregate can be regarded as a proxy for a multitude of smaller carbon debt transfers over shorter timeframes that are possible in real ETS implementations in which CROs can be compensated by (gross) carbon removal, issuance of new CROs or allowances at a later point in time.

Average abatement costs are obtained from total abatement costs by dividing by the abated quantity of CO₂:

$$\text{\$}\{c\}_{\text{\rm avg}}(t, a(t)) = \frac{c_{\text{tot}}(t, a(t))}{a(t) E_{\text{base}}}, \quad (11)$$

Next, we introduce interest payments that are due for carbon debt d over the repayment term $t \rightarrow t + T_R(t)$, that is, from issuance of the CRO until its retirement (Extended Data Fig. 7b–e). T_R is implicitly defined as:

$$\text{\int } \{t\}_{0}^t d(\tau) \text{d}\tau = \text{\int } \{t\}_{0}^{T_R} d(\tau) \text{d}\tau, \quad (12)$$

and instantaneous interest payments are obtained by multiplication of the quantity of CO₂ for which CROs have been issued ($d = \phi e_{NP}$) and the average abatement costs, c_{avg} , the moment of retirement of the CRO, $t + T_R(t)$, with the interest rate on carbon debt r_d :

$$i(t) = d(t) c_{\text{avg}}(t + T_R(t), a(t + T_R(t))) r_d. \quad (13)$$

Integrating and discounting instantaneous interest payments over the repayment term T_R gives the total net present interest costs at t for carbon debt $d(t)$:

$$\text{\int } i(t) \text{d}t = \int_0^{T_R} d(t) c_{\text{avg}}(t + T_R(t), a(t + T_R(t))) r_d \exp(-r_d \tau) \text{d}\tau. \quad (14)$$

Now we add interest costs to the standard objective function (equation (2)) to obtain the optimization problem for a CRO-ETS:

$$\text{\min } \{a(t), c_{\text{tot}}(t, a(t)), i(t)\} + \int_0^{T_R} d(t) c_{\text{avg}}(t + T_R(t), a(t + T_R(t))) r_d \exp(-r_d \tau) \text{d}\tau. \quad (15)$$

Mitigation cost discounting

If we set $r = r_d$, the objective function can be written as (Supplementary Information section 3):

$$\begin{aligned}
& \text{\$\$} \begin{array}{c} \mathop{\min} \limits_{a(t), e_NP(t)} (d(t) - \\
\{c\}_{\rm avg}(t, a(t)) \int_{t_0}^T (d(t) - \{c\}_{\rm avg}(t + T, a(t + T)))^{(t)} d(t) \\
+ (E_{\rm base}(t) - e_NP(t)) c_{\rm avg}(t, a(t)) \exp(-r(t - t_0))) \\
\end{array} \text{\$\$} \\
(16)
\end{aligned}$$

Notably, instead of pricing e_{NP} , carbon debt d in this new formulation is paid for the moment it is created; however, it is paid for at the average (undiscounted) future costs during removal at $t + T_R$, which is due to our definition of interest costs in equation (13). This is because when we set $r = r_d$, interest payments exactly compensate for the cost reduction in the net present value terms from discounting. The second term, $E_{\rm base}(t) - e_{NP}(t)$ equals emission reductions in the net-positive/net-zero domain. These reductions can be achieved by a mix of CDR, low-carbon and zero-carbon technologies; however, CDR is deployed only to offset contemporaneous emissions and not to recapture previously released CO₂.

Intuitively, r_d therefore controls to what extent cost discounting becomes a driver for accruing carbon debt. If r_d equals the market interest rate, future costs $c_{\rm avg}$ at $t + T_R$ —which depend on technological learning and the aggregate demand for abatement a in $t + T_R$ —determine whether the carbon debt route (d) proves competitive compared to instantaneous emission reductions ($E_{\rm base} - e_{NP}$). However, if d is reduced, e_{NP} needs to be reduced simultaneously to meet the emission target (less carbon debt leads to higher demand for near-term emission reductions and, therefore, an increase in near-term marginal costs). Because near-term emission reductions potentially include CDR, technological and socio-environmental learning associated with CDR is induced earlier, leading to a reduction in the uncertainty, which is key for operating in the net-negative domain later in the century. In this Article, we provide some intuition about the dynamic effects of invoking an interest on carbon debt, but do not determine optimal risk-reducing rates, which could—but do not necessarily need to—coincide with market interest rates. However, we expect, under circumstances in which physical and financial risks associated with carbon debt are managed by appropriately setting an interest rate on carbon debt, that r_d is driven by the market interest rate. In our model, an increase in the market interest rate induces deferral of mitigation due to discounting, leading to higher quantities of D , thereby also to an increase in risks and, finally, the necessity to correct r_d upwards to account for the increased risks.

Assessing the value of carbon debt

Net present cost gains from discounting are only cancelled exactly if the market interest rate is invoked on abatement costs at $t + T_R$. Costs are known in our model, but are potentially impossible to determine in the context of real emission control policy. Therefore, given their liability for issued debt, managing authorities and financial institutions need to estimate the financial value of carbon debt as a basis for interest payments and CRO maturities. The incentive to correctly value debt has a societal benefit of gradually reducing uncertainty with respect to CDR and other technologies relied on at large scales in mitigation scenarios. Notably, by prudently valuing debt, issuing bodies assure the quality of price signals on carbon markets, instead of relying on the carbon price to value debt. In fact, carbon prices on their own are insufficient benchmarks for valuing debt. For instance, a large demand for carbon debt would lead to a lower near-term carbon price if this is not balanced by an increase in r_d , which in turn would lead to an undervaluation of risks.

Supply and demand of CROs

The supply of allowances under a pure ETS is completely inelastic, whereas the supply in a tax system is infinitely elastic. By contrast, the supply of CROs (adding to the supply of allowances) is finitely elastic. Generally, the supply curve is increasing because the larger the demand for CROs, the more abatement is required in the future, making future abatement and thus CROs more expensive. Because the total discounted interest costs (i_{tot}) are reflected in the supply curve, by valuing carbon debt and setting the rate r_d accordingly, debt-issuing bodies can partly control its slope. The slope, however, determines the level of price volatility, for example, resulting from a demand shock, as depicted in Extended Data Fig. 1. By implication, price volatility is the largest in a pure ETS, and zero in a tax system. By increasing the interest costs in a CRO-ETS, the potential for volatile prices increases, and vice versa. On the other hand, net emissions are fixed in an idealized ETS and subject to demand fluctuations in a tax system. In a CRO-ETS, the cumulative quantity of net emissions is fixed, however, only if default risks are adequately managed.

Numerical solution of the model

The model used to solve the CRO optimization problem (equation (15)) is based on marginal abatement cost curves (MACCs; equation (4)) that are derived from scenarios reported in the SSP scenario database^{24,54}. MACCs are derived for each IAM and SSP by combining and fitting a curve to carbon prices from different RCPs in each time step. For instance, a MACC in 2040 for a specific IAM–SSP configuration is composed of the carbon prices reported for RCP 1.9–RCP 6.0. The set of parameters of each IAM–SSP configuration of our model is therefore composed of net emissions from the baseline scenario (E_{base}), the interest rate r (derived from the

slope of log-transformed carbon prices), the carbon budget B derived from the sum of net emissions compatible with specific climate targets and eight MACCs for the period from 2030 to 2100, that is, one per decade. We fix abatement rates a during optimization in which no MACCs could be derived because the reported prices p_i are (close to) zero over the whole range of a_i —that is, in 2020 for all configurations; for IMAGE–SSP 2 in 2030; for IMAGE–SSP 3 in 2030 and 2040; for IMAGE–SSP 5 in 2030. In decades in which abatement is fixed, costs are set to zero. Moreover, for the 1.5 °C and 2 °C case studies, carbon budgets were corrected using historical emission data³⁹ (scenarios reported in the SSP database start in 2005 or 2010 and were exceeded by estimated net emissions in the past decades). Baseline emissions in 2020 were replaced by the projection for 2019 in ref. ³⁹.

We fit the inverse of the generalized logistic function⁵⁵ to log-transformed prices p_i as reported in the SSP database. Abatement rates a_i are computed by subtracting net emissions in a scenario with a climate target from the net emissions in the baseline scenario and dividing by the baseline. The index i denotes the different RCPs within the same IAM–SSP configuration and the same year (see Supplementary Information section [2.1](#) for the cost curves of all IAM–SSP configurations):

$$\$ \$ \ln(p_i) = P + \frac{1}{k} \ln \left(\frac{1}{\nu} \left(\left(\frac{L-A}{a_i - A} \right)^{\nu} - 1 \right) \right) \quad (17)$$

MACs are therefore a power law defined for the interval (a, ∞) where $L < a < A$:

$$\$ \$ \text{rm{MAC}}(a_i) = b \left(\frac{1}{\nu} \left(\left(\frac{L-A}{a_i - A} \right)^{\nu} - 1 \right) \right)^c \quad (18)$$

where $b = \exp(P)$ and $c = \frac{1}{k}$. An interpretation of the parameters is provided in Extended Data Fig. [8a](#). $L \approx 0$ (subject to model fitting) and $A = \max(a_i) + \varepsilon$ (such that a can become $\max(a_i)$ without $\text{MAC}(a)$ becoming ∞)—that is, A is set to the maximum abatement (plus $\varepsilon = 0.01$) observed in each decade for each IAM–SSP configuration because this level cannot be exceeded. For numerical reasons, however, a is also constrained by A during optimization such that $a < A$.

In most IAMs, the carbon prices are either imposed exogenously as driver of mitigation (for example, in the recursive dynamic models AIM–CGE or GCAM4) or prices are derived after optimization from Lagrange multipliers of emission caps (for example, in the intertemporal optimization models MESSAGE–GLOBIOM, WITCH–GLOBIOM or REMIND–MAgPIE). In these cases, the carbon prices typically

increase exponentially with the interest rate, as explained by the Hotelling rule^{[22,23](#)}. In heavily constrained, detailed process-based IAMs, intertemporally optimal carbon prices are a good proxy of marginal costs; however, they do not necessarily reflect MACs exactly in each point of time, as a consequence of growth constraints or caps on total deployment levels of specific mitigation technologies. This is also the case here because we limit $a < A$ with an additional constraint and we fix a in cases in which no MACCs could be derived, suggesting that MAC and carbon prices (derived from the Lagrange multiplier of the budget constraint (equation (3))) do not necessarily coincide.

We compare MAC and carbon prices from our model with carbon prices as reported for the individual scenarios in the SSP database for all models, SSPs and RCPs (Supplementary Information section [2.2](#)). Reported carbon prices in the database for AIM–CGE do not follow an exact exponential curve because these prices reflect marginal costs from the SSP 1 scenario, which was initially constrained by emission caps to obtain the climate target. Then, prices were manually scaled and imposed on other SSP scenarios to achieve the respective climate targets^{[56](#)}. Therefore, AIM–CGE prices are better replicated by the MAC of our model than by carbon prices. The same is true for the IMAGE framework, which contains simulation as well as optimization components and does not report Hotelling-type carbon prices.

Furthermore, we show abatement costs for all SSPs, IAMs and RCPs computed with our model (Supplementary Information section [2.3](#)). Because abatement costs are not explicitly reported in the database, we compare costs from our model with close proxies—that is, GDP loss and consumption loss in SSP scenarios. For GCAM4 and IMAGE, GDP loss and consumption loss are either not reported or losses are close to zero. For GCAM4, we therefore added abatement costs for some scenarios as reported in the [supplementary information](#) of ref. ^{[57](#)}, which are well replicated by our model. No comparable data could be retrieved for the IMAGE model. For the other IAMs, abatement costs of our model mainly coincide with consumption loss. Net CO₂ emissions are also compared for all SSPs, IAMs and RCPs (Supplementary Information section [2.4](#)).

Abatement rates a cannot exceed A , hence only IAM–SSP configurations with RCP 1.9 data are used for our 2 °C case studies, because more-ambitious mitigation under a CRO-ETS requires our model to partly operate in the 1.5 °C abatement domain to achieve 2 °C. Therefore, thirteen IAM–SSP parameter sets of our model are used for the case studies: AIM–CGE (SSP 1 and SSP 2), GCAM4 (SSP 1, SSP 2 and SSP 5), IMAGE (SSP 1), MESSAGE–GLOBIOM (SSP 1 and SSP 2), REMIND–MAgPIE (SSP 1, SSP 2 and SSP 5), WITCH–GLOBIOM (SSP 1 and SSP 4); that is, six parameter sets for SSP 1, four for SSP 2, one for SSP 4 and two for SSP 5

(Extended Data Table 2). All 2 °C scenarios are shown graphically in Supplementary Information section 1.1 and numerically in Supplementary Information section 1.2.

Scenarios for DACS

For our 1.5 °C (RCP 1.9) case study, additional sources of abatement are required to assess compatible pathways of more-ambitious mitigation than suggested by RCP 1.9 scenarios. We therefore add DACS to the mitigation portfolio; however, we treat this technology in a stylized manner as completely stand-alone and independent of other abatement technologies (for example, the energy needs for DACS are assumed to be met by additional local renewable sources that do not interfere with the ramp-up of renewable energy as part of conventional abatement). DACS is less controversial than BECCS with respect to land use and has potentially limited environmental effects compared to other large-scale CDR options¹⁶, making it more independently scalable. However, capital and energy requirements are uncertain and potentially enormous. Costs range between US\$20 and US\$1,000 per t CO₂ (refs. [16,18,58,59,60](#)) and potentials for CDR range from 0.5–5 Gt CO₂ yr⁻¹ in 2050 to 15–40 Gt CO₂ yr⁻¹ in 2100¹⁸; however, these potentials are mainly constrained by cost considerations rather than biophysical limits⁶¹. Here we derive six idealized MACCs for DACS covering three cost ranges and two maximum abatement rates (Extended Data Fig. 8b). Instead of modifying the MACCs derived from SSP scenarios to account for DACS, we add a_{DACS} to equation (1):

$$\text{e}(t) = \{E\}_{\{\text{base}\}}(t)(1-a(t)-\{a\}_{\{\text{DACS}\}}(t)). \quad (19)$$

and change the total costs in equation (4) to:

$$\text{c}_{\{\text{tot}\}}(t,a(t)) = \{E\}_{\{\text{base}\}}(t)(\{\int_0^t a(\tau) \text{MAC}(\tau) d\tau\} + \{a\}_{\{\text{DACS}\}}(t)) \quad (20)$$

Moreover, MACs are always required to be equal:

$$\text{MAC}(t,a(t)) = \{\text{MAC}\}_{\{\text{DACS}\}}(a_{\{\text{DACS}\}}(t)) \quad (21)$$

To obtain a detailed technology downscaling of sources and sinks of CO₂ (fossil fuels and industry, including residual emissions from carbon capture and storage; BECCS and land-use emissions) we interpolate linearly between the closest abatement levels

reported in the SSP database—that is, $a_i < a < a_{i+1}$ (again, i denotes different RCPs within the same IAM–SSP configuration and the same year)—and add DACS after the interpolation.

The 1.5 °C scenarios used

For Fig. 4, the set of all 468 scenarios (13 IAM–SSP parameter sets, 6 rates r_d and 6 DACS parameters sets) is filtered for scenarios that achieved at least a 30% reduction in D compared with their baselines (that is, where $r_d = 0$). For scenarios depicted in Extended Data Figs. 3–5 this reduction in D needs to be at least 5%, 15% and 45%, respectively. From scenarios with different rates r_d but otherwise identical parameters, only the lowest rate is kept, resulting in a potential set of 78 scenarios, of which 26 are feasible regarding the 30% carbon debt reduction requirement in Fig. 4. Hence, in Fig. 4c,d the 26 scenarios for which $r_d > 0$ are compared to the associated 26 baselines in Fig. 4a,b in which $r_d = 0$. Baselines are interpreted as ‘conventional ETS’ scenarios, which are—in terms of emission paths—equivalent to CRO-ETS scenarios with $r_d = 0$. All underlying scenarios are shown graphically in Supplementary Information section 1.3 and numerically in Supplementary Information section 1.4, abatement and interest costs are illustrated in Extended Data Fig. 6 for all scenarios.

A note on technological learning

Technological learning in most IAMs is either exogenous—that is, purely time dependent—or induced by learning-by-doing, which is strongly backed by empirical evidence. However, learning is best perceived as a complex interplay between research and development, learning-by-doing and different types of spillovers⁶², which only few models attempt to fully address. The MACCs derived here from SSP scenario results reflect learning rates in the IAMs that are used to generate these scenarios, resulting in typically decreasing marginal costs over time for similar abatement rates. Therefore, learning in our model is exogenous (purely time dependent), which is one of the main caveats of this model, because fixed learning rates over time imply an incentive to wait until abatement becomes cheaper. More-ambitious near-term mitigation under a CRO-ETS, however, would probably lead to earlier cost reductions than reflected in the model. Owing to the complexity of learning and the simplicity of our model, we disregard DACS-related technological change.

Software and solver

The model is solved using the CONOPT solver in GAMS v.26.1. CONOPT is based on the generalized reduced gradient algorithm, one of the most robust and commonly

applied methods for solving models with highly nonlinear objective functions or constraints⁶³.

Data availability

All data generated or analysed during this study are included in this published Article and its [Supplementary Information](#).

Code availability

The source code of the numerical model used for generating the data used in this study is available at <https://github.com/jobednar/CROmodel>. The numerical model was calibrated using scenarios from the SSP scenario database hosted by IIASA (<https://tntcat.iiasa.ac.at/SspDb/>).

References

1. 1.

Masson-Delmotte, V. et al. *Global warming of 1.5 °C. An IPCC Special Report* (IPCC, 2018).

2. 2.

Gasser, T. et al. Path-dependent reductions in CO₂ emission budgets caused by permafrost carbon release. *Nat. Geosci.* **11**, 830–835 (2018).

[ADS](#) [CAS](#) [Google Scholar](#)

3. 3.

Geden, O. The Paris Agreement and the inherent inconsistency of climate policymaking. *Wiley Interdiscip. Rev. Clim. Change* **7**, 790–797 (2016).

[Google Scholar](#)

4. 4.

Peters, G. P. & Geden, O. Catalysing a political shift from low to negative carbon. *Nat. Clim. Change* **7**, 619–621 (2017).

[ADS](#) [Google Scholar](#)

5. 5.

Bednar, J., Obersteiner, M. & Wagner, F. On the financial viability of negative emissions. *Nat. Commun.* **10**, 1783 (2019).

[ADS](#) [PubMed](#) [PubMed Central](#) [Google Scholar](#)

6. 6.

Black, R. et al. *Taking Stock: A Global Assessment of Net Zero Targets* [https://eciu.net/analysis/reports/2021/taking-stock-assessment-netzero-targets](https://eciu.net/analysis/reports/2021/taking-stock-assessment-net-zero-targets) (ECIU, 2021).

7. 7.

Rogelj, J., Geden, O., Cowie, A. & Reisinger, A. Three ways to improve net-zero emissions targets. *Nature* **591**, 365–368 (2021).

[ADS](#) [CAS](#) [PubMed](#) [PubMed Central](#) [Google Scholar](#)

8. 8.

McLaren, D. P., Tyfield, D. P., Willis, R., Szerszynski, B. & Markusson, N. O. Beyond “net-zero”: a case for separate targets for emissions reduction and negative emissions. *Front. Clim.* **1**, 4 (2019).

[Google Scholar](#)

9. 9.

Clarke, L. et al. *Climate Change 2014: Mitigation of Climate Change. Contribution of Working Group III to the Fifth Assessment Report of the Intergovernmental Panel on Climate Change* (eds Edenhofer, O. et al.) Ch. 6, 413–510 (Cambridge Univ. Press, 2014).

10. 10.

Rogelj, J., Forster, P. M., Kriegler, E., Smith, C. J. & Séférian, R. Estimating and tracking the remaining carbon budget for stringent climate targets. *Nature* **571**, 335–342 (2019).

[ADS](#) [CAS](#) [PubMed](#) [PubMed Central](#) [Google Scholar](#)

11. 11.

Rogelj, J. et al. Differences between carbon budget estimates unravelled. *Nat. Clim. Change* **6**, 245–252 (2016).

[ADS](#) [Google Scholar](#)

12. 12.

van Vuuren, D. P., Hof, A. F., van Sluisveld, M. A. E. & Riahi, K. Open discussion of negative emissions is urgently needed. *Nat. Energy* **2**, 902–904 (2017).

[ADS](#) [Google Scholar](#)

13. 13.

Honegger, M. & Reiner, D. The political economy of negative emissions technologies: consequences for international policy design. *Clim. Policy* **18**, 306–321 (2018).

[Google Scholar](#)

14. 14.

Anderson, K. & Peters, G. The trouble with negative emissions. *Science* **354**, 182–183 (2016).

[ADS](#) [CAS](#) [PubMed](#) [PubMed Central](#) [Google Scholar](#)

15. 15.

Fuss, S. et al. Betting on negative emissions. *Nat. Clim. Change* **4**, 850–853 (2014).

[ADS](#) [CAS](#) [Google Scholar](#)

16. 16.

Lawrence, M. G. et al. Evaluating climate geoengineering proposals in the context of the Paris Agreement temperature goals. *Nat. Commun.* **9**, 3734 (2018).

[ADS](#) [PubMed](#) [PubMed Central](#) [Google Scholar](#)

17. 17.

Lenzi, D., Lamb, W. F., Hilaire, J., Kowarsch, M. & Minx, J. C. Don't deploy negative emissions technologies without ethical analysis. *Nature* **561**, 303–305 (2018).

[ADS](#) [CAS](#) [PubMed](#) [PubMed Central](#) [Google Scholar](#)

18. 18.

Fuss, S. et al. Negative emissions—part 2: costs, potentials and side effects. *Environ. Res. Lett.* **13**, 063002 (2018).

[ADS](#) [Google Scholar](#)

19. 19.

Obersteiner, M. et al. How to spend a dwindling greenhouse gas budget. *Nat. Clim. Change* **8**, 7–10 (2018).

[ADS](#) [Google Scholar](#)

20. 20.

Rogelj, J. et al. A new scenario logic for the Paris Agreement long-term temperature goal. *Nature* **573**, 357–363 (2019).

[ADS](#) [CAS](#) [PubMed](#) [PubMed Central](#) [Google Scholar](#)

21. 21.

United Nations Environment Programme. *The Emissions Gap Report 2019, Annex B* (UN, 2019).

22. 22.

Hotelling, H. The economics of exhaustible resources. *J. Polit. Econ.* **39**, 137–175 (1931).

[MATH](#) [Google Scholar](#)

23. 23.

Mattauch, L. et al. *Steering The Climate System: An Extended Comment* Centre for Climate Change Economics and Policy Working Paper 347/Grantham

Research Institute on Climate Change and the Environment Working Paper 315 (London School of Economics and Political Science, 2018).

24. 24.

Rogelj, J. et al. Scenarios towards limiting global mean temperature increase below 1.5 °C. *Nat. Clim. Change* **8**, 325–332 (2018).

[ADS](#) [CAS](#) [Google Scholar](#)

25. 25.

Norges Bank Investment Management. *Investing with a Mandate*. https://www.nbim.no/contentassets/cd563b586fe34ce2bfea30df4c0a75db/investing-with-a-mandate_government-pension-fund-global_web.pdf (2020).

26. 26.

OECD. *OECD Sovereign Borrowing Outlook 2020* (2020).

27. 27.

Steitz, C. & Lewis, B. EU short of 118 billion euros in nuclear decommissioning funds - draft. *Reuters* (16 February 2016).

28. 28.

Fankhauser, S. & Hepburn, C. Designing carbon markets. Part I: carbon markets in time. *Energy Policy* **38**, 4363–4370 (2010).

[Google Scholar](#)

29. 29.

Murray, B., Newell, R. & Pizer, W. *Balancing Cost and Emissions Certainty: An Allowance Reserve for Cap-and-Trade*. NBER Working Paper 14258 <http://www.nber.org/papers/w14258.pdf> (National Bureau Of Economic Research, 2008).

30. 30.

Goulder, L. & Schein, A. *Carbon Taxes vs. Cap and Trade: A Critical Review*. NBER Working Paper 19338 <http://www.nber.org/papers/w19338.pdf> (National Bureau Of Economic Research, 2013).

31. 31.

Coffman, D. & Lockley, A. Carbon dioxide removal and the futures market. *Environ. Res. Lett.* **12**, 015003 (2017).

[ADS](#) [Google Scholar](#)

32. 32.

Emmerling, J. et al. The role of the discount rate for emission pathways and negative emissions. *Environ. Res. Lett.* **14**, 104008 (2019).

[ADS](#) [CAS](#) [Google Scholar](#)

33. 33.

Hilaire, J. et al. Negative emissions and international climate goals—learning from and about mitigation scenarios. *Clim. Change* **157**, 189–219 (2019).

[ADS](#) [Google Scholar](#)

34. 34.

Parson, E. A. & Buck, H. J. Large-scale carbon dioxide removal: the problem of phasedown. *Glob. Environ. Polit.* **20**, 70–92 (2020).

[Google Scholar](#)

35. 35.

Meinshausen, M. et al. The shared socio-economic pathway (SSP) greenhouse gas concentrations and their extensions to 2500. *Geosci. Model Dev.* **13**, 3571–3605 (2020).

[ADS](#) [CAS](#) [Google Scholar](#)

36. 36.

Workman, M., Dooley, K., Lomax, G., Maltby, J. & Darch, G. Decision making in contexts of deep uncertainty - an alternative approach for long-term climate policy. *Environ. Sci. Policy* **103**, 77–84 (2020).

[Google Scholar](#)

37. 37.

Butnar, I. et al. A deep dive into the modelling assumptions for biomass with carbon capture and storage (BECCS): a transparency exercise. *Environ. Res. Lett.* **15**, 084008 (2020).

[ADS](#) [CAS](#) [Google Scholar](#)

38. 38.

Gough, C. et al. Challenges to the use of BECCS as a keystone technology in pursuit of 1.5 °C. *Glob. Sustain.* **1**, e5 (2018).

[Google Scholar](#)

39. 39.

Friedlingstein, P. et al. Global carbon budget 2019. *Earth Syst. Sci. Data* **11**, 1783–1838 (2019).

[ADS](#) [Google Scholar](#)

40. 40.

Capros, P. et al. Energy-system modelling of the EU strategy towards climate-neutrality. *Energy Policy* **134**, 110960 (2019).

[Google Scholar](#)

41. 41.

European Commission. *A Clean Planet for All. A European Strategic Long-term Vision for a Prosperous, Modern, Competitive and Climate-neutral Economy* (EC, 2018).

42. 42.

European Environment Agency. *EEA Greenhouse Gas - Data Viewer*.
<https://www.eea.europa.eu/data-and-maps/data/data-viewers/greenhouse-gases-viewer> (EEA, 2021).

43. 43.

Geden, O. & Schenuit, F. *Unconventional Mitigation: Carbon Dioxide Removal as a New Approach in EU Climate Policy*. SWP Research Paper 2020/RP08
<https://www.swp-berlin.org/10.18449/2020RP08/> (SWP, 2020).

44. 44.

Rickels, W., Proelß, A., Geden, O., Burhenne, J. & Fridahl, M. Integrating carbon dioxide removal into European emissions trading. *Front. Clim.* **3**, 62 (2021).

[Google Scholar](#)

45. 45.

Davis, S. J. et al. Net-zero emissions energy systems. *Science* **360**, eaas9793 (2018).

[PubMed](#) [PubMed Central](#) [Google Scholar](#)

46. 46.

Luderer, G. et al. Residual fossil CO₂ emissions in 1.5–2 °C pathways. *Nat. Clim. Change* **8**, 626–633 (2018).

[ADS](#) [CAS](#) [Google Scholar](#)

47. 47.

Allen, M. R., Frame, D. J. & Mason, C. F. The case for mandatory sequestration. *Nat. Geosci.* **2**, 813–814 (2009).

[ADS](#) [CAS](#) [Google Scholar](#)

48. 48.

Friedmann, S. J. Engineered CO₂ removal, climate restoration, and humility. *Front. Clim.* **1**, 3 (2019).

[Google Scholar](#)

49. 49.

Beuttler, C., Charles, L. & Wurzbacher, J. The role of direct air capture in mitigation of anthropogenic greenhouse gas emissions. *Front. Clim.* **1**, 10 (2019).

[Google Scholar](#)

50. 50.

Levihn, F., Linde, L., Gustafsson, K. & Dahlen, E. Introducing BECCS through HPC to the research agenda: the case of combined heat and power in Stockholm. *Energy Rep.* **5**, 1381–1389 (2019).

[Google Scholar](#)

51. 51.

The World Bank. *Carbon Pricing Dashboard*.
<https://carbonpricingdashboard.worldbank.org/> (accessed 11 March 2020).

52. 52.

Newman, A. L. & Posner, E. Putting the EU in its place: policy strategies and the global regulatory context. *J. Eur. Public Policy* **22**, 1316–1335 (2015).

[Google Scholar](#)

53. 53.

Santikarn, M., Li, L., Theuer, S. L. H. & Haug, C. *A Guide to Linking Emissions Trading Systems* (ICAP, 2018).

54. 54.

Riahi, K. et al. The Shared Socioeconomic Pathways and their energy, land use, and greenhouse gas emissions implications: an overview. *Glob. Environ. Change* **42**, 153–168 (2017).

[Google Scholar](#)

55. 55.

Richards, F. J. A flexible growth function for empirical use. *J. Exp. Bot.* **10**, 290–301 (1959).

[Google Scholar](#)

56. 56.

Fujimori, S. et al. SSP3: AIM implementation of Shared Socioeconomic Pathways. *Glob. Environ. Change* **42**, 268–283 (2017).

[Google Scholar](#)

57. 57.

Calvin, K. et al. The SSP4: a world of deepening inequality. *Glob. Environ. Change* **42**, 284–296 (2017).

[Google Scholar](#)

58. 58.

Strefler, J. et al. Between Scylla and Charybdis: delayed mitigation narrows the passage between large-scale CDR and high costs. *Environ. Res. Lett.* **13**, 044015 (2018).

[ADS](#) [Google Scholar](#)

59. 59.

Marcucci, A., Kypreos, S. & Panos, E. The road to achieving the long-term Paris targets: energy transition and the role of direct air capture. *Clim. Change* **144**, 181–193 (2017).

[ADS](#) [Google Scholar](#)

60. 60.

Sanz-Pérez, E. S., Murdock, C. R., Didas, S. A. & Jones, C. W. Direct capture of CO₂ from ambient air. *Chem. Rev.* **116**, 11840–11876 (2016).

[PubMed](#) [PubMed Central](#) [Google Scholar](#)

61. 61.

Smith, P. et al. Biophysical and economic limits to negative CO₂ emissions. *Nat. Clim. Change* **6**, 42–50 (2016).

[ADS](#) [CAS](#) [Google Scholar](#)

62. 62.

Clarke, L., Weyant, J. & Birky, A. On the sources of technological change: assessing the evidence. *Energy Econ.* **28**, 579–595 (2006).

[Google Scholar](#)

63. 63.

Drud, A. S. CONOPT—a large-scale GRG code. *ORSA J. Comput.* **6**, 207–216 (1994).

[MATH](#) [Google Scholar](#)

[Download references](#)

Acknowledgements

We acknowledge financial support from the European Research Council Synergy grant ERC-SyG-2013-610028 IMBALANCE-P as well as from the FWF grant P-31796 Medium Complexity Earth System Risk Management (ERM) and support from the HSE University Basic Research Program for A.B.

Author information

Affiliations

1. International Institute for Applied Systems Analysis (IIASA), Laxenburg, Austria

Johannes Bednar, Michael Obersteiner, Artem Baklanov, Fabian Wagner & Oliver Geden

2. School of Geography and the Environment, University of Oxford, Oxford, UK

Johannes Bednar, Michael Obersteiner, Myles Allen & Jim W. Hall

3. HSE University, St Petersburg, Russian Federation

Artem Baklanov

4. National Center for Ecological Analysis and Synthesis (NCEAS), University of California, Santa Barbara, CA, USA

Marcus Thomson

5. German Institute for International and Security Affairs, Berlin, Germany

Oliver Geden

Authors

1. Johannes Bednar

[View author publications](#)

You can also search for this author in [PubMed](#) [Google Scholar](#)

2. Michael Obersteiner

[View author publications](#)

You can also search for this author in [PubMed](#) [Google Scholar](#)

3. Artem Baklanov

[View author publications](#)

You can also search for this author in [PubMed](#) [Google Scholar](#)

4. Marcus Thomson

[View author publications](#)

You can also search for this author in [PubMed](#) [Google Scholar](#)

5. Fabian Wagner

[View author publications](#)

You can also search for this author in [PubMed](#) [Google Scholar](#)

6. Oliver Geden

[View author publications](#)

You can also search for this author in [PubMed](#) [Google Scholar](#)

7. Myles Allen

[View author publications](#)

You can also search for this author in [PubMed](#) [Google Scholar](#)

8. Jim W. Hall

[View author publications](#)

You can also search for this author in [PubMed](#) [Google Scholar](#)

Contributions

M.O., F.W., M.T. and J.B. have contributed equally to identifying the knowledge gaps and main ideas of this Article, as well as sharpening the field of interest. J.B. acted as

lead author and was primarily involved in formalizing and quantifying the ideas of the Article, as well as in drafting the main paper and developing the analytical and numerical methods. J.W.H. and M.O. supervised the development of the paper from the first draft throughout the review process. J.W.H., O.G., M.A., F.W. and M.T. contributed to the framing, conception and design of the work, as well as to the interpretation of the results. A.B. provided quality control of methods and the presentation of the results and contributed the mathematical proof of the equations derived in the Methods. O.G. contributed by markedly improving the policy relevance of the Article (for instance, by developing the EU implementation scenario). All authors were equally involved in the revision process and have approved the submitted version of the Article.

Corresponding author

Correspondence to [Johannes Bednar](#).

Ethics declarations

Competing interests

The authors declare no competing interests.

Additional information

Peer review information *Nature* thanks David Stainforth and the other, anonymous, reviewer(s) for their contribution to the peer review of this work.

Publisher's note Springer Nature remains neutral with regard to jurisdictional claims in published maps and institutional affiliations.

Extended data figures and tables

[Extended Data Fig. 1 Schematic supply of emission allowances and CROs at a fixed point in time.](#)

The supply of allowances is completely inelastic (emission cap), whereas the supply elasticity of CROs is determined by discounted future abatement costs, which increase as the demand for CROs increases, as well as interest costs, which can be controlled by managing authorities and financial institutions (dashed blue CRO supply curves). If CROs are traded on a market, they clear at the same price as allowances and thereby reduce the price of allowances. The larger the elasticity of the CRO supply curve, the lower the potential for price volatility (red arrows), as—for example—induced by a demand shock (dashed orange line). The sum of allowances and CROs issued equals net emissions. Abated emissions equal the

difference between baseline emissions (green) and net emissions and consist of emission reductions and/or carbon removal.

Extended Data Fig. 2 Abatement costs and carbon debt of 1.5 °C (RCP 1.9) scenarios for six different MACCs of DACS and interest rates on carbon debt $r_d = 0$ and $r_d = 0.08$.

A definition of D is provided in the Methods. Abatement costs are discounted and expressed as a percentage of the GDP. Abatement costs are exclusive of interest costs. For each rate r_d , 78 scenarios (13 scenarios as for the RCP 2.6 analysis times 6 DACS parameters) are grouped by DACS costs (low to high, that is, ‘LoCost’, ‘MedCost’ and ‘HiCost’) and DACS capacity limits (10% and 30% of baseline emissions, that is, ‘LoCap’ and ‘HiCap’). **a, b**, Median abatement costs as a function of median carbon debt D for $r_d = 0$ (**a**) and $r_d = 0.08$ (**b**). For $r_d = 0$, we observe an inverse relation between the level of carbon debt and abatement costs; and the capacity limit is a stronger determinant of abatement costs than DACS deployment costs. This ‘discounting effect’ is reversed when $r_d = 0.08$ and high levels of $\backslash(D\backslash)$ are penalized. In this case, lower abatement costs are realized by lower carbon debt (and vice versa). For both rates r_d ‘LoCost_HiCap’ DACS scenarios are characterized by the lowest abatement costs, however, at very different levels of D . When interest is invoked, DACS deployments costs become an increasingly important determinant of total abatement costs. **c, d**, Distribution of total carbon debt D (**c**) and abatement costs (**d**) for the median values shown in **a, b**. Boxes indicate the 25–75% interquartile ranges around medians (bold solid line), whiskers indicate minimum to maximum ranges, black dots mark outliers.

Extended Data Fig. 3 The 1.5 °C (RCP 1.9) pathways under a conventional ETS or a CRO-ETS.

a, b, A conventional ETS is used. **c, d**, A CRO-ETS is used. The underlying set of scenarios was filtered for those scenarios that achieved at least a 5% reduction in total carbon debt compared with their baselines (see [Methods](#)). **a, c**, Geometric median net emissions (solid line) and gross emissions from

FFI, BECCS, LUC and DACS. Net emissions from **a** are also displayed in **c** (dashed line) and vice versa. The total carbon debt D is shown as a box-and-whiskers plot. Boxes indicate the 25–75% interquartile range around the median values (bold line), whiskers indicate minimum to maximum ranges, points mark the outliers. **b, d**, Annual mitigation costs as a percentage of GDP, including the share of average abatement costs attributed to emission reductions (ABM), to the compensation of residual emissions by CDR (RES) and to net-negative emissions (NNE) as well as expenditures for allowances (ETS) and interest costs (INT). Total mitigation costs (that is, ABM + RES + NNE + ETS + INT) from **d** are also displayed in **b** (dashed line) and vice versa. Box-and-whiskers plots show the total discounted abatement costs (that is, ABM + RES + NNE) as a percentage of GDP, the number above the chart indicates out-of-range outliers. Pie charts in **d** summarize the properties of the underlying set of scenarios (see [Methods](#)). The distribution of r_d in CRO-ETS scenarios is depicted in **c**.

Extended Data Fig. 4 The 1.5 °C (RCP 1.9) pathways under a conventional ETS or a CRO-ETS.

a, b, A conventional ETS is used. **c, d**, A CRO-ETS is used. The underlying set of scenarios was filtered for those scenarios that achieve at least a 15% reduction in total carbon debt compared with their baselines (see [Methods](#)). **a, c**, Geometric median net emissions (solid line) and gross emissions from FFI, BECCS, LUC and DACS. Net emissions from **a** are also displayed in **c** (dashed line) and vice versa. The total carbon debt D is shown as a box-and-whiskers plot. Boxes indicate the 25–75% interquartile range around the median values (bold line), whiskers indicate minimum to maximum ranges, points mark the outliers. **b, d**, Annual mitigation costs as a percentage of GDP, including the share of average abatement costs attributed to emission reductions (ABM), to the compensation of residual emissions by CDR (RES) and to net-negative emissions (NNE) as well as expenditures for allowances (ETS) and interest costs (INT). Total mitigation costs (that is, ABM + RES + NNE + ETS + INT) from **d** are also displayed in **b** (dashed line) and vice versa. Box-and-whiskers plots show the total discounted abatement costs (that is, ABM + RES + NNE) as a percentage of GDP, the number above the chart indicates out-of-range outliers. Pie charts

in **d** summarize the properties of the underlying set of scenarios (see [Methods](#)). The distribution of r_d in CRO-ETS scenarios is depicted in **c**.

[Extended Data Fig. 5 The 1.5 °C \(RCP1.9\) pathways under a conventional ETS or a CRO-ETS.](#)

a, b, A conventional ETS is used. **c, d**, A CRO-ETS is used. The underlying set of scenarios was filtered for those scenarios that achieve at least a 45% reduction in total carbon debt compared with their baselines (see [Methods](#)). **a, c**, Geometric median net emissions (solid line) and gross emissions from FFI, BECCS, LUC and DACS. Net emissions from **a** are also displayed in **c** (dashed line) and vice versa. The total carbon debt D is shown as a box-and-whiskers plot. Boxes indicate the 25–75% interquartile range around the median values (bold line), whiskers indicate minimum to maximum ranges, points mark the outliers. **b, d**, Annual mitigation costs as a percentage of GDP, including the share of average abatement costs attributed to emission reductions (ABM), to the compensation of residual emissions by CDR (RES) and to net-negative emissions (NNE) as well as expenditures for allowances (ETS) and interest costs (INT). Total mitigation costs (that is, ABM + RES + NNE + ETS + INT) from **d** are also displayed in **b** (dashed line) and vice versa. Box-and-whiskers plots show the total discounted abatement costs (that is, ABM + RES + NNE) as a percentage of GDP, the number above the chart indicates out-of-range outliers. Pie charts in **d** summarize the properties of the underlying set of scenarios (see [Methods](#)). The distribution of r_d in CRO-ETS scenarios is depicted in **c**.

[Extended Data Fig. 6 The abatement costs and interest costs of the 1.5 °C \(RCP 1.9\) scenarios as function of the percentage of carbon debt reduction compared with the baseline scenario.](#)

a, b, The abatement costs (**a**) and interest costs (**b**) of the 1.5 °C (RCP 1.9) scenarios is compared with the baseline scenario (in which $r_d = 0$) for all 468 RCP 1.9 scenarios, grouped by the carbon debt interest rate (r_d) and the cost and capacity parameters of DACS. DACS cost parameters range from

low to high (that is, LoCost, MedCost and HiCost); capacity limits include 10% and 30% of baseline emissions (that is, LoCap and HiCap). **a**, Total discounted abatement costs excluding interest costs (that is, ABM + RES + NNE as in Fig. 4 and Extended Data Figs. 3–5). **b**, Total discounted interest costs (that is, INT as in Fig. 4 and Extended Data Figs. 3–5).

Extended Data Fig. 7 Schematic overview and illustrative repayment terms of RCP 1.9 scenarios.

a, Schematic overview of the CRO-ETS. The physical overshoot of a cumulative emission target, potentially amplified by outgassing of CO₂ from the Earth’s stocks, subsequently necessitates carbon sequestration for returning to the target. For accrued carbon debt, CROs are issued, obliging emitters to compensate for a tonne of CO₂ before a specified maturity—for example, by physically removing atmospheric CO₂ or by acquiring an adequate quantity of allowances in the future. Similar to financial debt, CROs require debtors to pay interest to hedge physical and financial risks associated with carbon debt. Three earmarked financial resources are created under a CRO-ETS. (1) Revenues from auctioning allowances are recycled into the economy to the benefit of society. (2) Revenues from interest on carbon debt are targeted at managing risks—that is, by enabling additional carbon sequestration when Earth system risks (for example, permafrost thaw) and financial risks (for example, default risk of debtors) materialize. (3) Funds for repayment of the carbon debt are individually managed by debtors. **b–e**, The repayment term function $T_R(t)$ for the scenarios illustrated in Extended Data Fig. 3 (b), Extended Data Fig. 4 (c), Fig. 4 (d) and Extended Data Fig. 5 (e). Interest on carbon debt r_d reflects the mean values of the distributions shown in Fig. 4c and Extended Data Figs. 3c, 4c, 5c. Bold lines indicate geometric median repayment terms derived from the scenarios presented in Fig. 4 and Extended Data Figs. 3–5. $T_R(t)$ maps the timing of carbon debt accrual to the time of its compensation (see [Methods](#)). For instance, in c, the carbon debt accrued in 2020 is compensated approximately 40 years later in scenarios with interest ($r_d = 0.058$, yellow lines) and roughly 50 years later in scenarios for which

$r_d = 0$ (turquoise lines). As r_d is increased, the net-zero year moves closer, indicating that carbon debt in 2020 is compensated earlier, whereas, in general, T_R extends over longer periods. The increasingly flat net-negative emissions profile (when r_d is increased) suggests that T_R increases more rapidly in the beginning than when $r_d = 0$ because the cumulative carbon debt at t grows faster than the cumulative net-negative emissions at $t + T_R(t)$. The point of inflection indicates where cumulative carbon debt begins to grow more slowly than cumulative net-negative emissions that compensate for that carbon debt. For instance, in \mathbf{d} (yellow line), the cumulative carbon debt from 2030 onwards grows at a slower pace than the cumulative net-negative emissions approximately 63 years later.

Extended Data Fig. 8 MACCs.

a, The functional form of MACs, $\text{MAC}(a) = b[\frac{1}{\nu}((\frac{L-A}{A-\nu})^{\frac{1}{\nu}} - 1)]^c$, is derived from the inverse generalized logistic function. It is relatively flexible with respect to replicating a wide range of MACCs derived from the SSP database. Here $A = 1$ and $L = 0$ are upper and lower asymptotes along the y axis. Notably, $\text{MAC}(a = A) = \infty$; therefore, A is a maximum abatement rate built into the MAC curve. b defines the y position of the pivot point. The x position of the pivot point is determined by ν and for $\nu = 1$ it is exactly the middle of the interval (L, A) , $(L + A)/2$. c defines the level of rotation with respect to the pivot point. **b**, Six stylized MACCs for DACS covering the literature range for costs from US\$20 to US\$1,000 per t CO₂ (orange area). Low-cost MACCs (dotted lines) start at approximately US\$50 per t CO₂ and reach US\$1,000 per t CO₂ at abatement rates $a_{\text{DACS}} = 0.07$ (low capacity, blue line) and $a_{\text{DACS}} = 0.27$ (high capacity, red line) equivalent to approximately 3 and 12 Gt CO₂ yr⁻¹ at current emission levels, respectively. Medium-cost MACCs (dashed lines) start at US\$250 per t CO₂ and reach US\$1,000 t CO₂ at $a_{\text{DACS}} = 0.05$ (low capacity, blue line) and $a_{\text{DACS}} = 0.22$ (high capacity, red line), that is, roughly 2 and 10 Gt CO₂ yr⁻¹ at current emission levels, respectively. High-cost MACCs (solid lines) start at approximately US\$500 per t CO₂ and reach US\$1,000 per t CO₂ at $a_{\text{DACS}} = 0.03$ (low

capacity, blue line) and $a_{\text{DACS}} = 0.12$ (high capacity, red line), amounting to roughly 1 and 5 Gt CO₂ yr⁻¹ at current emission levels, respectively.

Extended Data Table 1 Net and gross emission removal in illustrative pathways from the IPCC's Special Report on global warming of 1.5 °C

[Full size table](#)

Extended Data Table 2 Combinations of models and SSPs used to calibrate the model in this study

[Full size table](#)

Supplementary information

[Supplementary Information](#)

This file contains a graphical representation of all 2 °C (RCP2.6) emission pathways discussed in the Results (specifically in Figure 3).

[Supplementary Data](#)

This file contains the data of all 2 °C (RCP2.6) pathways discussed in the Results as an Excel sheet.

[Supplementary Information](#)

SI1.3 contains a graphical representation of all 1.5 °C (RCP1.9) emission pathways discussed in the Results (specifically in Figure 4 and Extended Data Figures 7–9).

[Supplementary Data](#)

This file contains the data of all 1.5 °C (RCP1.9) pathways discussed in the Results as an Excel sheet.

[Supplementary Information](#)

This file contains a graphical representation of the marginal abatement cost (MAC) curves used in the numerical model of this study. The parameters of the MAC curves can be retrieved with the R package provided for using the numerical model.

Supplementary Information

This file illustrates carbon prices from the SSP scenarios compared to carbon prices and MAC from the numerical model of this study.

Supplementary Information

This file illustrates consumption loss and GDP loss from the SSP scenarios compared to abatement costs from the numerical model of this study.

Supplementary Information

This file illustrates net emissions from the SSP scenarios compared to net emissions from the numerical model of this study.

Supplementary Information

This file contains the analytical methods necessary to derive equation [16] in the Methods section.

Rights and permissions

Reprints and Permissions

About this article



Check for
updates

Cite this article

Bednar, J., Obersteiner, M., Baklanov, A. *et al.* Operationalizing the net-negative carbon economy. *Nature* **596**, 377–383 (2021).
<https://doi.org/10.1038/s41586-021-03723-9>

[Download citation](#)

- Received: 12 December 2019
- Accepted: 09 June 2021
- Published: 08 July 2021
- Issue Date: 19 August 2021
- DOI: <https://doi.org/10.1038/s41586-021-03723-9>

Comments

By submitting a comment you agree to abide by our [Terms](#) and [Community Guidelines](#). If you find something abusive or that does not comply with our terms or guidelines please flag it as inappropriate.

[Download PDF](#)

Associated Content

[‘Polluter pays’ policy could speed up emission reductions and removal of atmospheric CO₂](#)

- David A. Stainforth

News & Views 16 Aug 2021

Advertisement

This article was downloaded by **calibre** from <https://www.nature.com/articles/s41586-021-03723-9>

| [Section menu](#) | [Main menu](#) |

- Article
- [Published: 18 August 2021](#)

The Montreal Protocol protects the terrestrial carbon sink

- [Paul J. Young](#) [ORCID: orcid.org/0000-0002-5608-8887^{1,2,3}](#),
- [Anna B. Harper](#) [ORCID: orcid.org/0000-0001-7294-6039^{4,5}](#),
- [Chris Huntingford](#) [ORCID: orcid.org/0000-0002-5941-7770⁶](#),
- [Nigel D. Paul](#) [ORCID: orcid.org/0000-0001-6959-4239^{1,7}](#),
- [Olaf Morgenstern](#) [ORCID: orcid.org/0000-0002-9967-9740⁸](#),
- [Paul A. Newman](#) [ORCID: orcid.org/0000-0003-1139-2508⁹](#),
- [Luke D. Oman](#) [ORCID: orcid.org/0000-0002-5487-2598⁹](#),
- [Sasha Madronich](#) [ORCID: orcid.org/0000-0003-0983-1313¹⁰](#) &
- [Rolando R. Garcia](#) [ORCID: orcid.org/0000-0002-6963-4592¹⁰](#)

[Nature](#) volume **596**, pages 384–388 (2021) [Cite this article](#)

- 1639 Accesses
- 1435 Altmetric
- [Metrics details](#)

Subjects

- [Atmospheric chemistry](#)
- [Carbon cycle](#)
- [Climate and Earth system modelling](#)
- [Light responses](#)
- [Projection and prediction](#)

Abstract

The control of the production of ozone-depleting substances through the Montreal Protocol means that the stratospheric ozone layer is recovering¹ and that consequent increases in harmful surface ultraviolet radiation are being avoided^{2,3}. The Montreal Protocol has co-benefits for climate change mitigation, because ozone-depleting substances are potent greenhouse gases^{4,5,6,7}. The avoided ultraviolet radiation and climate change also have co-benefits for plants and their capacity to store carbon through photosynthesis⁸, but this has not previously been investigated. Here, using a modelling framework that couples ozone depletion, climate change, damage to plants by ultraviolet radiation and the carbon cycle, we explore the benefits of avoided increases in ultraviolet radiation and changes in climate on the terrestrial biosphere and its capacity as a carbon sink. Considering a range of strengths for the effect of ultraviolet radiation on plant growth^{8,9,10,11,12}, we estimate that there could have been 325–690 billion tonnes less carbon held in plants and soils by the end of this century (2080–2099) without the Montreal Protocol (as compared to climate projections with controls on ozone-depleting substances). This change could have resulted in an additional 115–235 parts per million of atmospheric carbon dioxide, which might have led to additional warming of global-mean surface temperature by 0.50–1.0 degrees. Our findings suggest that the Montreal Protocol may also be helping to mitigate climate change through avoided decreases in the land carbon sink.

Access options

Subscribe to Journal

Get full journal access for 1 year

\$199.00

only \$3.90 per issue

[Subscribe](#)

All prices are NET prices.
VAT will be added later in the checkout.
Tax calculation will be finalised during checkout.

Rent or Buy article

Get time limited or full article access on ReadCube.

from \$8.99

[Rent or Buy](#)

All prices are NET prices.

Additional access options:

- [Log in](#)
- [Access through your institution](#)
- [Learn about institutional subscriptions](#)

Fig. 1: The ozone, climate and biologically active UV levels of different futures.



Fig. 2: Effects on the productivity and stores of the terrestrial carbon cycle.

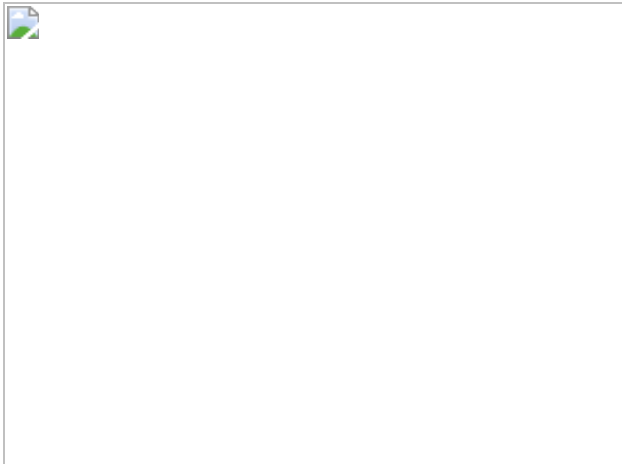
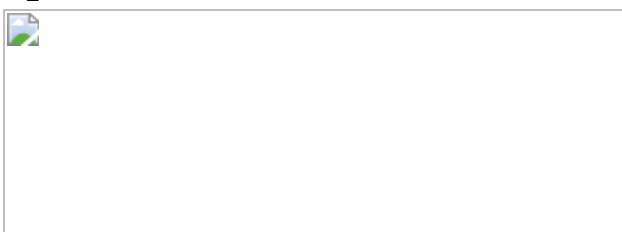


Fig. 3: The effect of UV-driven changes in vegetation on atmospheric CO₂ and surface temperature.



Data availability

All relevant JULES and NIWA–UKCA model output and input data have been archived (<https://doi.org/10.5281/zenodo.4733883>).

Code availability

The JULES code for these simulations is available on the Met Office Science Repository System (MOSRS; <https://code.metoffice.gov.uk/trac/jules>; registration required) in revision 15798. Simulations were run using the Rose suite u-bb620, also available through MOSRS. The NIWA–UKCA CCM is based on the HadGEM3 climate model, which is available under licence. Please contact O.M. (olaf.morgenstern@niwa.co.nz) for details.

References

1. 1.

World Meteorological Organization. *Scientific Assessment of Ozone Depletion: 2018*. Report No. 58 (Global Ozone and Research Monitoring Project, 2018).

2. 2.

van Dijk, A. et al. Skin cancer risks avoided by the Montreal Protocol—worldwide modeling integrating coupled climate-chemistry models with a risk model for UV. *Photochem. Photobiol.* **89**, 234–246 (2013).

[PubMed](#) [PubMed Central](#) [Google Scholar](#)

3. 3.

McKenzie, R. et al. Success of Montreal Protocol demonstrated by comparing high-quality UV measurements with ‘World Avoided’ calculations from two chemistry-climate models. *Sci. Rep.* **9**, 12332 (2019).

[ADS](#) [PubMed](#) [PubMed Central](#) [Google Scholar](#)

4. 4.

Ramanathan, V. Greenhouse effect due to chlorofluorocarbons: climatic implications. *Science* **190**, 50–52 (1975).

[ADS](#) [CAS](#) [Google Scholar](#)

5. 5.

Morgenstern, O. et al. The world avoided by the Montreal Protocol. *Geophys. Res. Lett.* **35**, L16811 (2008).

[ADS](#) [Google Scholar](#)

6. 6.

Newman, P. A. et al. What would have happened to the ozone layer if chlorofluorocarbons (CFCs) had not been regulated? *Atmos. Chem. Phys.* **9**, 2113–2128 (2009).

[ADS](#) [CAS](#) [Google Scholar](#)

7. 7.

Garcia, R. R., Kinnison, D. E. & Marsh, D. R. ‘World avoided’ simulations with the Whole Atmosphere Community Climate Model. *J. Geophys. Res.* **117**, D23303 (2012).

[ADS](#) [Google Scholar](#)

8. 8.

Ballaré, C. L., Caldwell, M. M., Flint, S. D., Robinson, S. A. & Bornman, J. F. Effects of solar ultraviolet radiation on terrestrial ecosystems. Patterns, mechanisms, and interactions with climate change. *Photochem. Photobiol. Sci.* **10**, 226–241 (2011).

[Google Scholar](#)

9. 9.

Newsham, K. K. & Robinson, S. A. Responses of plants in polar regions to UVB exposure: a meta-analysis. *Glob. Change Biol.* **15**, 2574–2589 (2009).

[ADS](#) [Google Scholar](#)

10. 10.

Li, F.-R., Peng, S.-L., Chen, B.-M. & Hou, Y.-P. A meta-analysis of the responses of woody and herbaceous plants to elevated ultraviolet-B radiation. *Acta Oecol.* **36**, 1–9 (2010).

[ADS](#) [Google Scholar](#)

11. 11.

Searles, P. S., Flint, S. D. & Caldwell, M. M. A meta-analysis of plant field studies simulating stratospheric ozone depletion. *Oecologia* **127**, 1–10 (2001).

[ADS](#) [PubMed](#) [PubMed Central](#) [Google Scholar](#)

12. 12.

Fu, G. & Shen, Z.-X. Effects of enhanced UV-B radiation on plant physiology and growth on the Tibetan Plateau: a meta-analysis. *Acta Physiol. Plant.* **39**, 85 (2017).

[Google Scholar](#)

13. 13.

Lucas, R. M. et al. Human health in relation to exposure to solar ultraviolet radiation under changing stratospheric ozone and climate. *Photochem. Photobiol. Sci.* **18**, 641–680 (2019).

[CAS](#) [PubMed](#) [PubMed Central](#) [Google Scholar](#)

14. 14.

Bornman, J. F. et al. Linkages between stratospheric ozone, UV radiation and climate change and their implications for terrestrial ecosystems. *Photochem. Photobiol. Sci.* **18**, 681–716 (2019).

[CAS](#) [PubMed](#) [PubMed Central](#) [Google Scholar](#)

15. 15.

Williamson, C. E. et al. The interactive effects of stratospheric ozone depletion, UV radiation, and climate change on aquatic ecosystems. *Photochem. Photobiol. Sci.* **18**, 717–746 (2019).

[CAS](#) [PubMed](#) [PubMed Central](#) [Google Scholar](#)

16. 16.

Molina, M. J. & Rowland, F. S. Stratospheric sink for chlorofluoromethanes: chlorine atom-catalysed destruction of ozone. *Nature* **249**, 810–812 (1974).

[ADS](#) [CAS](#) [Google Scholar](#)

17. 17.

Solomon, S., Garcia, R. R., Rowland, F. S. & Wuebbles, D. J. On the depletion of Antarctic ozone. *Nature* **321**, 755–758 (1986).

[ADS](#) [CAS](#) [Google Scholar](#)

18. 18.

Solomon, S. Stratospheric ozone depletion: a review of concepts and history. *Rev. Geophys.* **37**, 275–316 (1999).

[ADS](#) [CAS](#) [Google Scholar](#)

19. 19.

Velders, G. J. M., Andersen, S. O., Daniel, J. S., Fahey, D. W. & McFarland, M. The importance of the Montreal Protocol in protecting climate. *Proc. Natl Acad. Sci. USA* **104**, 4814–4819 (2007).

[ADS](#) [CAS](#) [PubMed](#) [PubMed Central](#) [Google Scholar](#)

20. 20.

Prather, M., Midgley, P., Rowland, F. S. & Stolarski, R. The ozone layer: the road not taken. *Nature* **381**, 551–554 (1996).

[ADS](#) [CAS](#) [Google Scholar](#)

21. 21.

Wu, Y., Polvani, L. M. & Seager, R. The importance of the Montreal Protocol in protecting Earth's hydroclimate. *J. Clim.* **26**, 4049–4068 (2013).

[ADS](#) [Google Scholar](#)

22. 22.

Polvani, L. M., Camargo, S. J. & Garcia, R. R. The importance of the Montreal Protocol in mitigating the potential intensity of tropical cyclones. *J. Clim.* **29**, 2275–2289 (2016).

[ADS](#) [Google Scholar](#)

23. 23.

Previdi, M. & Polvani, L. M. Impact of the Montreal Protocol on Antarctic surface mass balance and implications for global sea level rise. *J. Clim.* **30**, 7247–7253 (2017).

[ADS](#) [Google Scholar](#)

24. 24.

Chipperfield, M. P. et al. Quantifying the ozone and ultraviolet benefits already achieved by the Montreal Protocol. *Nat. Commun.* **6**, 7233 (2015).

[ADS](#) [CAS](#) [Google Scholar](#)

25. 25.

Newman, P. A. & McKenzie, R. UV impacts avoided by the Montreal Protocol. *Photochem. Photobiol. Sci.* **10**, 1152–1160 (2011).

[CAS](#) [PubMed](#) [PubMed Central](#) [Google Scholar](#)

26. 26.

Neugart, S. & Schreiner, M. UVB and UVA as eustressors in horticultural and agricultural crops. *Sci. Hortic.* **234**, 370–381 (2018).

[CAS](#) [Google Scholar](#)

27. 27.

Fiscus, E. L. & Booker, F. L. Is increased UV-B a threat to crop photosynthesis and productivity? *Photosynth. Res.* **43**, 81–92 (1995).

[CAS](#) [PubMed](#) [PubMed Central](#) [Google Scholar](#)

28. 28.

Morgenstern, O. et al. Review of the global models used within phase 1 of the Chemistry–Climate Model Initiative (CCMI). *Geosci. Model Dev.* **10**, 639–671 (2017).

[ADS](#) [Google Scholar](#)

29. 29.

Best, M. J. et al. The Joint UK Land Environment Simulator (JULES), model description—part 1: energy and water fluxes. *Geosci. Model Dev.* **4**, 677–699 (2011).

[ADS](#) [Google Scholar](#)

30. 30.

Clark, D. B. et al. The Joint UK Land Environment Simulator (JULES), model description—part 2: carbon fluxes and vegetation dynamics. *Geosci. Model Dev.* **4**, 701–722 (2011).

[ADS](#) [Google Scholar](#)

31. 31.

van Vuuren, D. P. et al. The representative concentration pathways: an overview. *Clim. Change* **109**, 5–31 (2011).

[ADS](#) [Google Scholar](#)

32. 32.

Barlow, J. et al. The future of hyperdiverse tropical ecosystems. *Nature* **559**, 517–526 (2018).

[ADS](#) [CAS](#) [PubMed](#) [PubMed Central](#) [Google Scholar](#)

33. 33.

Collins, M. et al. in *Climate Change 2013-The Physical Science Basis: Contribution of Working Group I to the Fifth Assessment Report of the Intergovernmental Panel on Climate Change* (eds Stocker, T. F. et al.) 1029–1136 (Cambridge Univ. Press, 2013).

34. 34.

Cox, P. M., Betts, R. A., Jones, C. D., Spall, S. A. & Totterdell, I. J. Acceleration of global warming due to carbon-cycle feedbacks in a coupled climate model. *Nature* **408**, 184–187 (2000); erratum **408**, 750 (2000).

[ADS](#) [CAS](#) [PubMed](#) [PubMed Central](#) [Google Scholar](#)

35. 35.

Heimann, M. & Reichstein, M. Terrestrial ecosystem carbon dynamics and climate feedbacks. *Nature* **451**, 289–292 (2008).

[ADS](#) [CAS](#) [PubMed](#) [PubMed Central](#) [Google Scholar](#)

36. 36.

Caldwell, M. M. in *Photophysiology, Current Topics in Photobiology and Photochemistry* Vol. VI (ed. Giese, A. C.) 131–177 (Academic

Press, 1971).

37. 37.

Caldwell, M. M., Camp, L. B., Warner, C. W. & Flint, S. D. in *Stratospheric Ozone Reduction, Solar Ultraviolet Radiation and Plant Life* Vol. 8 (eds Worrest, R. C. & Caldwell, M. M.) 87–111 (Springer, 1986).

38. 38.

Calbó, J., Pagès, D. & González, J. Empirical studies of cloud effects on UV radiation: a review. *Rev. Geophys.* **43**, RG2002 (2005).

[ADS](#) [Google Scholar](#)

39. 39.

Arora, V. K. et al. Carbon–concentration and carbon–climate feedbacks in CMIP5 Earth system models. *J. Clim.* **26**, 5289–5314 (2013).

[ADS](#) [Google Scholar](#)

40. 40.

Williamson, C. E. et al. Solar ultraviolet radiation in a changing climate. *Nat. Clim. Chang.* **4**, 434–441 (2014).

[ADS](#) [Google Scholar](#)

41. 41.

Rigby, M. et al. Increase in CFC-11 emissions from eastern China based on atmospheric observations. *Nature* **569**, 546–550 (2019).

[ADS](#) [CAS](#) [PubMed](#) [PubMed Central](#) [Google Scholar](#)

42. 42.

Tilmes, S., Garcia, R. R., Kinnison, D. E., Gettelman, A. & Rasch, P. J. Impact of geoengineered aerosols on the troposphere and stratosphere. *J. Geophys. Res.* **114**, D12305 (2009).

[ADS](#) [Google Scholar](#)

43. 43.

NASA. *Ozone Watch*
https://ozonewatch.gsfc.nasa.gov/meteorology/annual_data.html
(2019).

44. 44.

Morgenstern, O. et al. Evaluation of the new UKCA climate-composition model – part 1: the stratosphere. *Geosci. Model Dev.* **2**, 43–57 (2009).

[ADS](#) [Google Scholar](#)

45. 45.

Hewitt, H. T. et al. Design and implementation of the infrastructure of HadGEM3: the next-generation Met Office climate modelling system. *Geosci. Model Dev.* **4**, 223–253 (2011).

[ADS](#) [Google Scholar](#)

46. 46.

World Meteorological Organization. *Scientific Assessment of Ozone Depletion: 2010*. Report No. 52 (Global Ozone Research and Monitoring Project, 2011).

47. 47.

Morgenstern, O. et al. Ozone sensitivity to varying greenhouse gases and ozone-depleting substances in CCM1-1 simulations. *Atmos. Chem. Phys.* **18**, 1091–1114 (2018).

[ADS](#) [CAS](#) [Google Scholar](#)

48. 48.

Edwards, J. M. & Slingo, A. Studies with a flexible new radiation code. I: choosing a configuration for a large-scale model. *Q. J. R. Meteorol. Soc.* **122**, 689–719 (1996).

[ADS](#) [Google Scholar](#)

49. 49.

Forster, P. M. et al. Evaluation of radiation scheme performance within chemistry climate models. *J. Geophys. Res.* **116**, D10302 (2011).

[ADS](#) [Google Scholar](#)

50. 50.

Lauer, A. & Hamilton, K. Simulating clouds with global climate models: a comparison of CMIP5 results with CMIP3 and satellite data. *J. Clim.* **26**, 3823–3845 (2013).

[ADS](#) [Google Scholar](#)

51. 51.

Dee, D. P. et al. The ERA-Interim reanalysis: configuration and performance of the data assimilation system. *Q. J. R. Meteorol. Soc.* **137**, 553–597 (2011).

[ADS](#) [Google Scholar](#)

52. 52.

Flint, S. D. & Caldwell, M. M. A biological spectral weighting function for ozone depletion research with higher plants. *Physiol. Plant.* **117**, 137–144 (2003).

[CAS](#) [Google Scholar](#)

53. 53.

Kotilainen, T., Lindfors, A., Tegelberg, R. & Aphalo, P. J. How realistically does outdoor UV-B supplementation with lamps reflect ozone depletion: an assessment of enhancement errors. *Photochem. Photobiol.* **87**, 174–183 (2011).

[CAS](#) [PubMed](#) [PubMed Central](#) [Google Scholar](#)

54. 54.

Flint, S. D., Ryel, R. J. & Caldwell, M. M. Ecosystem UV-B experiments in terrestrial communities: a review of recent findings and methodologies. *Agric. For. Meteorol.* **120**, 177–189 (2003).

[ADS](#) [Google Scholar](#)

55. 55.

Poulter, B. et al. Plant functional type classification for earth system models: results from the European Space Agency's Land Cover Climate Change Initiative. *Geosci. Model Dev.* **8**, 2315–2328 (2015).

[ADS](#) [Google Scholar](#)

56. 56.

Harper, A. B. et al. Improved representation of plant functional types and physiology in the Joint UK Land Environment Simulator (JULES v4.2) using plant trait information. *Geosci. Model Dev.* **9**, 2415–2440 (2016).

[ADS](#) [Google Scholar](#)

57. 57.

Harper, A. B. et al. Vegetation distribution and terrestrial carbon cycle in a carbon cycle configuration of JULES4.6 with new plant functional types. *Geosci. Model Dev.* **11**, 2857–2873 (2018).

[ADS](#) [Google Scholar](#)

58. 58.

Huntingford, C. & Cox, P. M. An analogue model to derive additional climate change scenarios from existing GCM simulations. *Clim. Dyn.* **16**, 575–586 (2000).

[Google Scholar](#)

59. 59.

Meinshausen, M. et al. The RCP greenhouse gas concentrations and their extensions from 1765 to 2300. *Clim. Change* **109**, 213–241 (2011).

[ADS](#) [CAS](#) [Google Scholar](#)

60. 60.

Huntingford, C. et al. Using a GCM analogue model to investigate the potential for Amazonian forest dieback. *Theor. Appl. Climatol.* **78**, 177–185 (2004).

[ADS](#) [Google Scholar](#)

61. 61.

Friedlingstein, P. et al. Climate–carbon cycle feedback analysis: results from the C4MIP model intercomparison. *J. Clim.* **19**, 3337–3353 (2006).

[ADS](#) [Google Scholar](#)

[Download references](#)

Acknowledgements

P.J.Y. was supported by the UK Engineering and Physical Science Research Council (grant EP/R01860X/1), the Natural Environment Research Council (grant NE/R004927/1) and the Faculty of Science and Technology at Lancaster University. A.B.H. acknowledges funding from the UK Engineering and Physical Science Research Council (Fellowship EP/N030141/1) and the Natural Environment Research Council (grant NE/P019951/1). C.H. acknowledges a UK National Capability grant given to the UK Centre for Ecology and Hydrology. O.M. was supported by the NZ Government's Strategic Science Investment Fund (SSIF) through the NIWA programme CACV. L.D.O. is supported by the NASA Modeling, Analysis, and Prediction programme. S.M. and R.R.G. are supported by the National Center for Atmospheric Research, which is a major facility sponsored by the US National Science Foundation under cooperative agreement number 1852977. We acknowledge the contribution of New Zealand's national high-performance computing facilities to the results of this research, provided by the NZ eScience Infrastructure (NeSI) and funded jointly by NeSI's collaborator institutions and through the NZ Ministry for Business, Innovation and Employment's Research Infrastructure Programme.

Author information

Affiliations

1. Lancaster Environment Centre, Lancaster University, Lancaster, UK

Paul J. Young & Nigel D. Paul

2. Institute for Social Futures, Lancaster University, Lancaster, UK

Paul J. Young

3. Centre of Excellence for Environmental Data Science, Lancaster University and the UK Centre of Ecology and Hydrology, Lancaster,

UK

Paul J. Young

4. College of Engineering, Mathematics, and Physical Sciences,
University of Exeter, Exeter, UK

Anna B. Harper

5. Global Systems Institute, University of Exeter, Exeter, UK

Anna B. Harper

6. UK Centre for Ecology and Hydrology, Wallingford, UK

Chris Huntingford

7. Centre for Global Eco-Innovation, Lancaster University, Lancaster, UK

Nigel D. Paul

8. National Institute of Water and Atmospheric Research, Wellington, Aotearoa New Zealand

Olaf Morgenstern

9. NASA Goddard Space Flight Center, Greenbelt, MD, USA

Paul A. Newman & Luke D. Oman

10. National Center for Atmospheric Research, Boulder, CO, USA

Sasha Madronich & Rolando R. Garcia

Authors

1. Paul J. Young

[View author publications](#)

You can also search for this author in [PubMed](#) [Google Scholar](#)

2. Anna B. Harper

[View author publications](#)

You can also search for this author in [PubMed](#) [Google Scholar](#)

3. Chris Huntingford

[View author publications](#)

You can also search for this author in [PubMed](#) [Google Scholar](#)

4. Nigel D. Paul

[View author publications](#)

You can also search for this author in [PubMed](#) [Google Scholar](#)

5. Olaf Morgenstern

[View author publications](#)

You can also search for this author in [PubMed](#) [Google Scholar](#)

6. Paul A. Newman

[View author publications](#)

You can also search for this author in [PubMed](#) [Google Scholar](#)

7. Luke D. Oman

[View author publications](#)

You can also search for this author in [PubMed](#) [Google Scholar](#)

8. Sasha Madronich

[View author publications](#)

You can also search for this author in [PubMed](#) [Google Scholar](#)

9. Rolando R. Garcia

[View author publications](#)

You can also search for this author in [PubMed](#) [Google Scholar](#)

Contributions

P.J.Y. conceived the initial study on the basis of conversations with N.D.P. P.J.Y., A.B.H. and C.H. designed and constructed the modelling framework and the simulations, performed the analysis and, with N.D.P., wrote the manuscript. O.M., P.A.N., L.D.O., S.M. and R.R.G. provided model simulation data to run the framework and input to the parameterizations used, and contributed to writing the manuscript.

Corresponding author

Correspondence to [Paul J. Young](#).

Ethics declarations

Competing interests

The authors declare no competing interests.

Additional information

Peer review information *Nature* thanks Pedro J. Aphalo, Benjamin Felzer, Veerabhadran Ramanathan and the other, anonymous, reviewer(s) for their contribution to the peer review of this work. Peer reviewer reports are available.

Publisher's note Springer Nature remains neutral with regard to jurisdictional claims in published maps and institutional affiliations.

Extended data figures and tables

[Extended Data Fig. 1 Effects on NPP for different latitude bands.](#)

a–c, NPP time series data from JULES, as per Fig. [2a](#), but for 30°–60° N (**a**), 30° S–30° N (**b**) and 55°–30° S (**c**).

Extended Data Table 1 Effect of UV on CO₂ and global-mean air temperature for different scenarios

[Full size table](#)

Extended Data Table 2 The UV_{plant} meta-analyses that informed our simulations

[Full size table](#)

Supplementary information

[Peer Review File](#)

Rights and permissions

[Reprints and Permissions](#)

About this article



Check for
updates

Cite this article

Young, P.J., Harper, A.B., Huntingford, C. *et al.* The Montreal Protocol protects the terrestrial carbon sink. *Nature* **596**, 384–388 (2021).
<https://doi.org/10.1038/s41586-021-03737-3>

[Download citation](#)

- Received: 31 July 2020
- Accepted: 18 June 2021

- Published: 18 August 2021
- Issue Date: 19 August 2021
- DOI: <https://doi.org/10.1038/s41586-021-03737-3>

Comments

By submitting a comment you agree to abide by our [Terms](#) and [Community Guidelines](#). If you find something abusive or that does not comply with our terms or guidelines please flag it as inappropriate.

[Access through your institution](#)

[Change institution](#)

[Buy or subscribe](#)

Advertisement

This article was downloaded by **calibre** from <https://www.nature.com/articles/s41586-021-03737-3>

| [Section menu](#) | [Main menu](#) |

- Article
- [Published: 04 August 2021](#)

Agrochemicals interact synergistically to increase bee mortality

- [Harry Siviter](#) [ORCID: orcid.org/0000-0003-1088-7701^{1,2 na1}](#),
- [Emily J. Bailes^{1,3,4 na1}](#),
- [Callum D. Martin¹](#),
- [Thomas R. Oliver](#) [ORCID: orcid.org/0000-0002-3525-2692^{1,4,5}](#),
- [Julia Koricheva](#) [ORCID: orcid.org/0000-0002-9033-0171¹](#),
- [Ellouise Leadbeater](#) [ORCID: orcid.org/0000-0002-4029-7254¹](#) &
- [Mark J. F. Brown](#) [ORCID: orcid.org/0000-0002-8887-3628¹](#)

[Nature](#) volume 596, pages 389–392 (2021) [Cite this article](#)

- 3664 Accesses
- 711 Altmetric
- [Metrics details](#)

Subjects

- [Agroecology](#)
- [Conservation biology](#)
- [Ecosystem services](#)

Abstract

Global concern over widely documented declines in pollinators^{1,2,3} has led to the identification of anthropogenic stressors that, individually, are detrimental to bee populations^{4,5,6,7}. Synergistic interactions between these stressors could substantially amplify the environmental effect of these stressors and could therefore have important implications for policy decisions that aim to improve the health of pollinators^{3,8,9}. Here, to quantitatively assess the scale of this threat, we conducted a meta-analysis of 356 interaction effect sizes from 90 studies in which bees were exposed to combinations of agrochemicals, nutritional stressors and/or parasites. We found an overall synergistic effect between multiple stressors on bee mortality. Subgroup analysis of bee mortality revealed strong evidence for synergy when bees were exposed to multiple agrochemicals at field-realistic levels, but interactions were not greater than additive expectations when bees were exposed to parasites and/or nutritional stressors. All interactive effects on proxies of fitness, behaviour, parasite load and immune responses were either additive or antagonistic; therefore, the potential mechanisms that drive the observed synergistic interactions for bee mortality remain unclear. Environmental risk assessment schemes that assume additive effects of the risk of agrochemical exposure may underestimate the interactive effect of anthropogenic stressors on bee mortality and will fail to protect the pollinators that provide a key ecosystem service that underpins sustainable agriculture.

Access options

Subscribe to Journal

Get full journal access for 1 year

\$199.00

only \$3.90 per issue

[Subscribe](#)

All prices are NET prices.

VAT will be added later in the checkout.

Tax calculation will be finalised during checkout.

Rent or Buy article

Get time limited or full article access on ReadCube.

from \$8.99

[Rent or Buy](#)

All prices are NET prices.

Additional access options:

- [Log in](#)
- [Access through your institution](#)
- [Learn about institutional subscriptions](#)

Fig. 1: The interaction effects of parasites, agrochemicals and nutritional stressors on bee mortality.

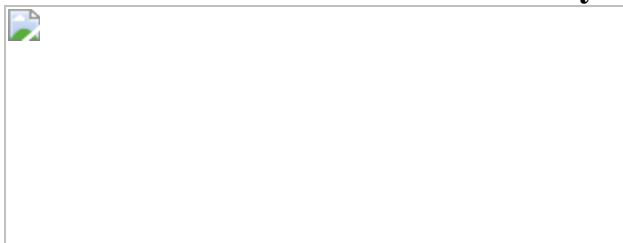


Fig. 2: The interaction effects of parasites, agrochemicals and nutritional stressors on non-mortality response measures.

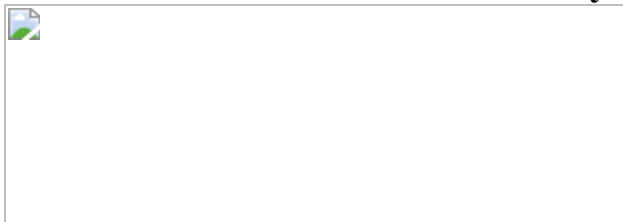
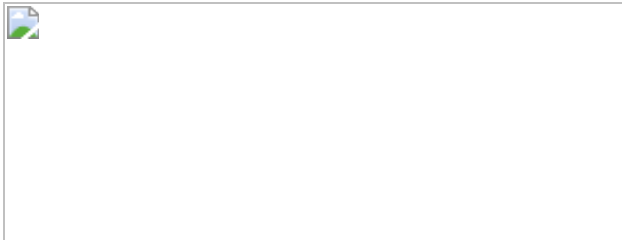


Fig. 3: Reversal interactions.



Data availability

All data used in this analysis are available at OSF (<https://osf.io/8xnua/>).

Code availability

All code used in this analysis is available at OSF (<https://osf.io/8xnua/>).

References

1. 1.

Holden, C. Report warns of looming pollination crisis in North America. *Science* **314**, 397 (2006).

[CAS](#) [PubMed](#) [PubMed Central](#) [Google Scholar](#)

2. 2.

Aizen, M. A. & Harder, L. D. The global stock of domesticated honey bees is growing slower than agricultural demand for pollination. *Curr. Biol.* **19**, 915–918 (2009).

[CAS](#) [PubMed](#) [PubMed Central](#) [Google Scholar](#)

3. 3.

Goulson, D., Nicholls, E., Botías, C. & Rotheray, E. L. Bee declines driven by combined stress from parasites, pesticides, and lack of flowers. *Science* **347**, 1255957 (2015).

[PubMed](#) [PubMed Central](#) [Google Scholar](#)

4. 4.

Woodcock, B. A. et al. Impacts of neonicotinoid use on long-term population changes in wild bees in England. *Nat. Commun.* **7**, 12459 (2016).

[ADS](#) [CAS](#) [PubMed](#) [PubMed Central](#) [Google Scholar](#)

5. 5.

Siviter, H., Brown, M. J. F. & Leadbeater, E. Sulfoxaflor exposure reduces bumblebee reproductive success. *Nature* **561**, 109–112 (2018).

[ADS](#) [CAS](#) [PubMed](#) [PubMed Central](#) [Google Scholar](#)

6. 6.

Cameron, S. A. et al. Patterns of widespread decline in North American bumble bees. *Proc. Natl Acad. Sci. USA* **108**, 662–667 (2011).

[ADS](#) [CAS](#) [PubMed](#) [PubMed Central](#) [Google Scholar](#)

7. 7.

Powney, G. D. et al. Widespread losses of pollinating insects in Britain. *Nat. Commun.* **10**, 1018 (2019).

[ADS](#) [PubMed](#) [PubMed Central](#) [Google Scholar](#)

8. 8.

Vanbergen, A. J. & The Insect Pollinators Initiative. Threats to an ecosystem service: pressures on pollinators. *Front. Ecol. Environ.* **11**, 251–259 (2013).

[Google Scholar](#)

9. 9.

EFSA. Bee health. <https://www.efsa.europa.eu/en/topics/topic/bee-health> (2019).

10. 10.

Foley, J. A. et al. Global consequences of land use. *Science* **309**, 570–574 (2005).

[ADS](#) [CAS](#) [PubMed](#) [Google Scholar](#)

11. 11.

Tilman, D., Cassman, K. G., Matson, P. A., Naylor, R. & Polasky, S. Agricultural sustainability and intensive production practices. *Nature* **418**, 671–677 (2002).

[ADS](#) [CAS](#) [PubMed](#) [PubMed Central](#) [Google Scholar](#)

12. 12.

Potts, S. G. et al. Safeguarding pollinators and their values to human well-being. *Nature* **540**, 220–229 (2016).

[ADS](#) [CAS](#) [PubMed](#) [PubMed Central](#) [Google Scholar](#)

13. 13.

Pettis, J. S. et al. Crop pollination exposes honey bees to pesticides which alters their susceptibility to the gut pathogen *Nosema ceranae*. *PLoS ONE* **8**, e70182 (2013).

[ADS](#) [CAS](#) [PubMed](#) [PubMed Central](#) [Google Scholar](#)

14. 14.

Siviter, H., Folly, A. J., Brown, M. J. F. & Leadbeater, E. Individual and combined impacts of sulfoxaflor and *Nosema bombi* on bumblebee

(*Bombus terrestris*) larval growth. *Proc. R. Soc. B* **287**, 20200935 (2020).

[CAS](#) [PubMed](#) [PubMed Central](#) [Google Scholar](#)

15. 15.

Retschnig, G. et al. Effects, but no interactions, of ubiquitous pesticide and parasite stressors on honey bee (*Apis mellifera*) lifespan and behaviour in a colony environment. *Environ. Microbiol.* **17**, 4322–4331 (2015).

[CAS](#) [PubMed](#) [PubMed Central](#) [Google Scholar](#)

16. 16.

Doublet, V., Labarussias, M., de Miranda, J. R., Moritz, R. F. A. & Paxton, R. J. Bees under stress: sublethal doses of a neonicotinoid pesticide and pathogens interact to elevate honey bee mortality across the life cycle. *Environ. Microbiol.* **17**, 969–983 (2015).

[CAS](#) [PubMed](#) [PubMed Central](#) [Google Scholar](#)

17. 17.

Folt, C. L., Chen, C. Y., Moore, M. V. & Burnaford, J. Synergism and antagonism among multiple stressors. *Limnol. Oceanogr.* **44**, 864–877 (1999).

[ADS](#) [Google Scholar](#)

18. 18.

Di Prisco, G. et al. Neonicotinoid clothianidin adversely affects insect immunity and promotes replication of a viral pathogen in honey bees. *Proc. Natl Acad. Sci. USA* **110**, 18466–18471 (2013).

[ADS](#) [PubMed](#) [PubMed Central](#) [Google Scholar](#)

19. 19.

Collison, E., Hird, H., Cresswell, J. & Tyler, C. Interactive effects of pesticide exposure and pathogen infection on bee health – a critical analysis. *Biol. Rev. Camb. Philos. Soc.* **91**, 1006–1019 (2016).

[PubMed](#) [PubMed Central](#) [Google Scholar](#)

20. 20.

Tsvetkov, N. et al. Chronic exposure to neonicotinoids reduces honey bee health near corn crops. *Science* **356**, 1395–1397 (2017).

[ADS](#) [CAS](#) [PubMed](#) [PubMed Central](#) [Google Scholar](#)

21. 21.

Carnesecchi, E. et al. Investigating combined toxicity of binary mixtures in bees: meta-analysis of laboratory tests, modelling, mechanistic basis and implications for risk assessment. *Environ. Int.* **133** (Pt B), 105256 (2019).

[CAS](#) [PubMed](#) [PubMed Central](#) [Google Scholar](#)

22. 22.

Jackson, M. C., Loewen, C. J. G., Vinebrooke, R. D. & Chimimba, C. T. Net effects of multiple stressors in freshwater ecosystems: a meta-analysis. *Glob. Change Biol.* **22**, 180–189 (2016).

[ADS](#) [Google Scholar](#)

23. 23.

Piggott, J. J., Townsend, C. R. & Matthaei, C. D. Reconceptualizing synergism and antagonism among multiple stressors. *Ecol. Evol.* **5**, 1538–1547 (2015).

[PubMed](#) [PubMed Central](#) [Google Scholar](#)

24. 24.

Ascher, J. S. & Pickering, J. Discover life: bee species guide and world checklist (Hymenoptera: Apoidea: Anthophila).
[https://www.discoverlife.org/mp/20q?
guide=Apoidea_species&flags=HAS](https://www.discoverlife.org/mp/20q?guide=Apoidea_species&flags=HAS) (2012).

25. 25.

Gill, R. J., Ramos-Rodriguez, O. & Raine, N. E. Combined pesticide exposure severely affects individual- and colony-level traits in bees. *Nature* **491**, 105–108 (2012).

[ADS](#) [CAS](#) [PubMed](#) [PubMed Central](#) [Google Scholar](#)

26. 26.

Schmid-Hempel, P. *Evolutionary Parasitology* (Oxford Univ. Press, 2011).

27. 27.

Sánchez-Bayo, F. et al. Are bee diseases linked to pesticides? — A brief review. *Environ. Int.* **89–90**, 7–11 (2016).

[PubMed](#) [PubMed Central](#) [Google Scholar](#)

28. 28.

Brandt, A., Gorenflo, A., Siede, R., Meixner, M. & Büchler, R. The neonicotinoids thiacloprid, imidacloprid, and clothianidin affect the immunocompetence of honey bees (*Apis mellifera L.*). *J. Insect Physiol.* **86**, 40–47 (2016).

[CAS](#) [PubMed](#) [PubMed Central](#) [Google Scholar](#)

29. 29.

Vaudo, A. D., Patch, H. M., Mortensen, D. A., Tooker, J. F. & Grozinger, C. M. Macronutrient ratios in pollen shape bumble bee (*Bombus impatiens*) foraging strategies and floral preferences. *Proc. Natl Acad. Sci. USA* **113**, E4035–E4042 (2016).

[CAS](#) [PubMed](#) [PubMed Central](#) [Google Scholar](#)

30. 30.

Fürst, M. A., McMahon, D. P., Osborne, J. L., Paxton, R. J. & Brown, M. J. F. Disease associations between honeybees and bumblebees as a threat to wild pollinators. *Nature* **506**, 364–366 (2014).

[ADS](#) [PubMed](#) [PubMed Central](#) [Google Scholar](#)

31. 31.

Cedergreen, N. Quantifying synergy: a systematic review of mixture toxicity studies within environmental toxicology. *PLoS ONE* **9**, e96580 (2014).

[ADS](#) [PubMed](#) [PubMed Central](#) [Google Scholar](#)

32. 32.

Carvell, C. et al. Declines in forage availability for bumblebees at a national scale. *Biol. Conserv.* **132**, 481–489 (2006).

[Google Scholar](#)

33. 33.

Baude, M. et al. Historical nectar assessment reveals the fall and rise of floral resources in Britain. *Nature* **530**, 85–88 (2016).

[ADS](#) [CAS](#) [PubMed](#) [PubMed Central](#) [Google Scholar](#)

34. 34.

Ovaskainen, O. et al. Community-level phenological response to climate change. *Proc. Natl Acad. Sci. USA* **110**, 13434–13439 (2013).

[ADS](#) [CAS](#) [PubMed](#) [PubMed Central](#) [Google Scholar](#)

35. 35.

Carvell, C. et al. Bumblebee family lineage survival is enhanced in high-quality landscapes. *Nature* **543**, 547–549 (2017).

[ADS](#) [CAS](#) [PubMed](#) [PubMed Central](#) [Google Scholar](#)

36. 36.

Siviter, H. & Muth, F. Do novel insecticides pose a threat to beneficial insects? *Proc. R. Soc. B* **287**, 20201265 (2020).

[PubMed](#) [PubMed Central](#) [Google Scholar](#)

37. 37.

Topping, C. J., Aldrich, A. & Berny, P. Overhaul environmental risk assessment for pesticides. *Science* **367**, 360–363 (2020).

[ADS](#) [CAS](#) [PubMed](#) [PubMed Central](#) [Google Scholar](#)

38. 38.

Sgolastra, F. et al. Bees and pesticide regulation: lessons from the neonicotinoid experience. *Biol. Conserv.* **241**, 108356 (2020).

[Google Scholar](#)

39. 39.

Mullin, C. A. Effects of ‘inactive’ ingredients on bees. *Curr. Opin. Insect Sci.* **10**, 194–200 (2015).

[PubMed](#) [PubMed Central](#) [Google Scholar](#)

40. 40.

Colin, T., Monchanin, C., Lihoreau, M. & Barron, A. B. Pesticide dosing must be guided by ecological principles. *Nat. Ecol. Evol.* **4**, 1575–1577 (2020).

[PubMed](#) [PubMed Central](#) [Google Scholar](#)

41. 41.

Milner, A. M. & Boyd, I. L. Toward pesticidovigilance. *Science* **357**, 1232–1234 (2017).

[ADS](#) [CAS](#) [PubMed](#) [PubMed Central](#) [Google Scholar](#)

42. 42.

Franklin, E. L. & Raine, N. E. Moving beyond honeybee-centric pesticide risk assessments to protect all pollinators. *Nat. Ecol. Evol.* **3**, 1373–1375 (2019)

[PubMed](#) [PubMed Central](#) [Google Scholar](#)

43. 43.

Brühl, C. A. & Zaller, J. G. Biodiversity decline as a consequence of an inappropriate environmental risk assessment of pesticides. *Front. Environ. Sci.* **7**, 177 (2019).

[Google Scholar](#)

44. 44.

OECD. *Test No. 245: Honey Bee (Apis Mellifera L.), Chronic Oral Toxicity Test (10-Day Feeding)* (OECD, 2017).

45. 45.

Viechtbauer, W. Conducting meta-analyses in R with the metafor package. *J. Stat. Softw.* **36**, 1–48 (2010).

[Google Scholar](#)

46. 46.

Duval, S. & Tweedie, R. Trim and fill: a simple funnel-plot-based method of testing and adjusting for publication bias in meta-analysis. *Biometrics* **56**, 455–463 (2000).

[CAS](#) [PubMed](#) [PubMed Central](#) [MATH](#) [Google Scholar](#)

47. 47.

Woodcock, B. A. et al. Meta-analysis reveals that pollinator functional diversity and abundance enhance crop pollination and yield. *Nat. Commun.* **10**, 1481 (2019).

[ADS](#) [CAS](#) [PubMed](#) [PubMed Central](#) [Google Scholar](#)

48. 48.

Siviter, H., Koricheva, J., Brown, M. J. F. & Leadbeater, E. Quantifying the impact of pesticides on learning and memory in bees. *J. Appl. Ecol.* **55**, 2812–2821 (2018).

[PubMed](#) [PubMed Central](#) [Google Scholar](#)

[Download references](#)

Acknowledgements

We thank all authors who made data available to us upon request (C. Alaux, K. Antunez, B. Baer, B. Blochtein, C. Botias, B. Dainat, M. Diogon, A. G. Dolezal, V. Doublet, K. Fent, D. C. de Graaf, G. de Grandi-Hoffman, P. Graystock, E. Guzman-Novoa, R. M. Johnson, E. G. Klinger, I. M. de Mattos, N. A. Moran, M. Natsopoulou, F. Nazzi, P. Neumann, R. Odemer,

R. Raimets, G. Retschnig, R. M. Roe, E. Ryabov, B. M. Sadd, C. Sandrock, F. Sgolastra, R. Siede, H. V. V. Tome, I. Toplak, S. Tosi, M. Tritschler, V. Zanni and Y. C. Zhu); and J. Bagi and A. J. Folly for helping with the initial screening of titles and abstracts. H.S. was supported by a Royal Holloway University of London Reid PhD Scholarship and by contributions from the High Wycombe Beekeeper's Association. This project has received funding from the European Horizon 2020 research and innovation programme under grant agreement no. 773921 and ERC Starting Grant BeeDanceGap 638873, and from the Biotechnology and Biological Sciences Research Council, grant/award number BB/N000668/1.

Author information

Author notes

1. These authors contributed equally: Harry Siviter, Emily J. Bailes

Affiliations

1. Department of Biological Sciences, Royal Holloway University of London, Egham, UK

Harry Siviter, Emily J. Bailes, Callum D. Martin, Thomas R. Oliver, Julia Koricheva, Ellouise Leadbeater & Mark J. F. Brown

2. Department of Integrative Biology, University of Texas at Austin, Austin, TX, USA

Harry Siviter

3. Department of Molecular Biology and Biotechnology, University of Sheffield, Sheffield, UK

Emily J. Bailes

4. School of Natural Sciences, Bangor University, Bangor, UK

Emily J. Bailes & Thomas R. Oliver

5. Rothamsted Research, Harpenden, UK

Thomas R. Oliver

Authors

1. Harry Siviter

[View author publications](#)

You can also search for this author in [PubMed](#) [Google Scholar](#)

2. Emily J. Bailes

[View author publications](#)

You can also search for this author in [PubMed](#) [Google Scholar](#)

3. Callum D. Martin

[View author publications](#)

You can also search for this author in [PubMed](#) [Google Scholar](#)

4. Thomas R. Oliver

[View author publications](#)

You can also search for this author in [PubMed](#) [Google Scholar](#)

5. Julia Koricheva

[View author publications](#)

You can also search for this author in [PubMed](#) [Google Scholar](#)

6. Ellouise Leadbeater

[View author publications](#)

You can also search for this author in [PubMed](#) [Google Scholar](#)

7. Mark J. F. Brown

[View author publications](#)

You can also search for this author in [PubMed](#) [Google Scholar](#)

Contributions

H.S., E.J.B., C.D.M., T.R.O. and M.J.F.B. conceived the idea for the study in a discussion group. H.S. and E.B. oversaw and managed the data collection. H.S., E.B., C.D.M. and T.R.O. carried out the literature search and collected the data. H.S. and E.L. conducted the statistical analysis and H.S. wrote the first version of the manuscript. H.S., E.J.B., J.K., E.L. and M.J.F.B. contributed to the writing of subsequent drafts.

Corresponding author

Correspondence to [Harry Siviter](#).

Ethics declarations

Competing interests

The authors declare no competing interests.

Additional information

Peer review information *Nature* thanks Antica Culina, Adam Vanbergen and the other, anonymous, reviewer(s) for their contribution to the peer review of this work. Peer reviewer reports are available.

Publisher's note Springer Nature remains neutral with regard to jurisdictional claims in published maps and institutional affiliations.

Extended data figures and tables

Extended Data Fig. 1 Distribution of Hedges' *d* values for the individual effect sizes included for the interaction effects of parasites, agrochemicals and nutritional stressors for bee response variables.

a–e, Distributions are shown for mortality (**a**), behaviour (**b**), fitness (**c**), parasite load (**d**) and immune responses (**e**). Data are shown as Hedges' *d* values \pm 95% CI. Effect sizes are sorted for each response variable from most negative to most positive. Each mean \pm 95% CI represents a different data point, hence there are more effect sizes than number of studies. Interactions are synergistic when the effect size is positive and the 95% CI does not include zero, antagonistic when the effect size is negative and the 95% CI does not include zero and additive when the 95% CI includes zero. Note that each panel is presented on a different scale.

Extended Data Fig. 2 Hedges' *d* values for interactions between specific stressors on bee mortality.

a, Interactions between combinations of parasite stressors. **b**, Interactions between combinations of parasite and nutritional stressors. Data are shown as Hedges' *d* values \pm 95% CI. The interactions are synergistic when the effect size is positive and the 95% CI does not include zero, antagonistic when the effect size is negative and the 95% CI does not include zero and additive when the 95% CI includes zero. Numbers next to the 95% CIs indicate the number of effect sizes in each category. Asterisks indicate that the 95% CI does not include zero.

Extended Data Fig. 3 Hedges' *d* values for different bee genera.

a–e, Data are shown as Hedges' *d* values \pm 95% CI for mortality (**a**), behaviour (**b**), fitness proxies (**c**), parasite load (**d**) and immune responses (**e**). The genus is indicated by the colour and shape of the symbol. Interactions are synergistic when the effect size is positive and the 95% CI does not include zero, antagonistic when the effect size is negative and the 95% CI does not include zero, and additive when the 95% CI includes zero. Numbers next to the 95% CIs indicate the number of effect sizes in each

category. Asterisks indicate that the 95% CI does not include zero. Note that each panel is presented on a different scale.

Extended Data Fig. 4 The interaction effects of different agrochemical classes on bee mortality response measures.

Hedges' d values \pm 95% CI are shown. Asterisks indicate that the 95% CI does not include zero. Numbers next to the 95% CIs indicate the number of effect sizes in each category. Note that effect sizes for azole fungicide \times pyrethroid are included in both groups.

Extended Data Fig. 5 Modified PRISMA flowchart.

A flowchart depicting the number of studies included or excluded at each stage of the literature search.

Extended Data Fig. 6 Funnel plots of the full models of the interactions between specific stressors.

a–e, Plots represent the models for mortality (**a**), behaviour (**b**), fitness proxies (**c**), parasite load (**d**) and immune responses (**e**).

Supplementary information

Supplementary Information

This file contains Supplementary Text, Supplementary Tables 1-6 and Supplementary References.

Reporting Summary

Peer Review File

Rights and permissions

[Reprints and Permissions](#)

About this article



Check for
updates

Cite this article

Siviter, H., Bailes, E.J., Martin, C.D. *et al.* Agrochemicals interact synergistically to increase bee mortality. *Nature* **596**, 389–392 (2021).
<https://doi.org/10.1038/s41586-021-03787-7>

[Download citation](#)

- Received: 06 October 2020
- Accepted: 30 June 2021
- Published: 04 August 2021
- Issue Date: 19 August 2021
- DOI: <https://doi.org/10.1038/s41586-021-03787-7>

Comments

By submitting a comment you agree to abide by our [Terms](#) and [Community Guidelines](#). If you find something abusive or that does not comply with our terms or guidelines please flag it as inappropriate.

[Access through your institution](#)

[Change institution](#)

[Buy or subscribe](#)

Associated Content

A cocktail of pesticides, parasites and hunger leaves bees down and out

- Adam J. Vanbergen

News & Views 04 Aug 2021

Advertisement

This article was downloaded by **calibre** from <https://www.nature.com/articles/s41586-021-03787-7>

| [Section menu](#) | [Main menu](#) |

- Article
- [Published: 04 August 2021](#)

Genetic insights into biological mechanisms governing human ovarian ageing

- [Katherine S. Ruth](#)^{1 na3},
- [Felix R. Day](#)^{2 na3},
- [Jazib Hussain](#)^{3 na3},
- [Ana Martínez-Marchal](#)^{4,5 na3},
- [Catherine E. Aiken](#)^{6,7},
- [Ajuna Azad](#)³,
- [Deborah J. Thompson](#)⁸,
- [Lucie Knoblochova](#)^{9,10},
- [Hironori Abe](#)¹¹,
- [Jane L. Tarry-Adkins](#)^{6,7},
- [Javier Martin Gonzalez](#)¹²,
- [Pierre Fontanillas](#)¹³,
- [Annique Claringbould](#)¹⁴,
- [Olivier B. Bakker](#)¹⁵,
- [Patrick Sulem](#)¹⁶,
- [Robin G. Walters](#)^{17,18},
- [Chikashi Terao](#)^{19,20,21},
- [Sandra Turon](#)²²,
- [Momoko Horikoshi](#)²³,
- [Kuang Lin](#)¹⁷,
- [N. Charlotte Onland-Moret](#)²⁴,
- [Aditya Sankar](#)³,
- [Emil Peter Thrane Hertz](#)^{3,25},

- Pascal N. Timsel²⁶,
- Vallari Shukla³,
- Rehannah Borup³,
- Kristina W. Olsen^{3,27},
- Paula Aguilera^{3,28},
- Mònica Ferrer-Roda^{4,5},
- Yan Huang^{4,5},
- Stasa Stankovic²,
- Paul R. H. J. Timmers^{29,30},
- Thomas U. Ahearn³¹,
- Behrooz Z. Alizadeh³²,
- Elnaz Naderi³²,
- Irene L. Andrulis^{33,34},
- Alice M. Arnold³⁵,
- Kristan J. Aronson^{36,37},
- Annelie Augustinsson³⁸,
- Stefania Bandinelli³⁹,
- Caterina M. Barbieri⁴⁰,
- Robin N. Beaumont¹,
- Heiko Becher⁴¹,
- Matthias W. Beckmann⁴²,
- Stefania Benonisdottir¹⁶,
- Sven Bergmann^{43,44},
- Murielle Bochud⁴⁵,
- Eric Boerwinkle⁴⁶,
- Stig E. Bojesen^{47,48,49},
- Manjeet K. Bolla⁸,
- Dorret I. Boomsma^{50,51,52},
- Nicholas Bowker²,
- Jennifer A. Brody⁵³,
- Linda Broer⁵⁴,
- Julie E. Buring^{55,56},
- Archie Campbell⁵⁷,
- Harry Campbell²⁹,

- Jose E. Castelao⁵⁸,
- Eulalia Catamo⁵⁹,
- Stephen J. Chanock³¹,
- Georgia Chenevix-Trench⁶⁰,
- Marina Ciullo^{61,62},
- Tanguy Corre^{43,44,45},
- Fergus J. Couch⁶³,
- Angela Cox⁶⁴,
- Laura Crisponi⁶⁵,
- Simon S. Cross⁶⁶,
- Francesco Cucca^{65,67},
- Kamila Czene⁶⁸,
- George Davey Smith^{69,70},
- Eco J. C. N. de Geus^{50,51,52},
- Renée de Mutsert⁷¹,
- Immaculata De Vivo^{72,73},
- Ellen W. Demerath⁷⁴,
- Joe Dennis⁸,
- Alison M. Dunning⁷⁵,
- Miriam Dwek⁷⁶,
- Mikael Eriksson⁷⁷,
- Tõnu Esko^{78,79},
- Peter A. Fasching^{42,80},
- Jessica D. Faul⁸¹,
- Luigi Ferrucci⁸²,
- Nora Franceschini⁸³,
- Timothy M. Frayling¹,
- Manuela Gago-Dominguez^{84,85},
- Massimo Mezzavilla⁸⁶,
- Montserrat García-Closas³¹,
- Christian Gieger^{87,88,89},
- Graham G. Giles^{90,91,92},
- Harald Grallert^{87,88,89},
- Daniel F. Gudbjartsson¹⁶,

- Vilmundur Gudnason^{93,94},
- Pascal Guénel⁹⁵,
- Christopher A. Haiman⁹⁶,
- Niclas Håkansson⁹⁷,
- Per Hall⁶⁸,
- Caroline Hayward³⁰,
- Chunyan He^{98,99},
- Wei He⁷⁷,
- Gerardo Heiss⁸³,
- Miya K. Høffding³,
- John L. Hopper⁹¹,
- Jouke J. Hottenga^{50,51,52},
- Frank Hu^{72,73,100},
- David Hunter^{17,73,100,101,102},
- Mohammad A. Ikram¹⁰³,
- Rebecca D. Jackson¹⁰⁴,
- Micaella D. R. Joaquim¹,
- Esther M. John^{105,106},
- Peter K. Joshi²⁹,
- David Karasik^{56,107},
- Sharon L. R. Kardia¹⁰⁸,
- Christiana Kartsonaki^{17,18},
- Robert Karlsson¹⁰⁹,
- Cari M. Kitahara¹¹⁰,
- Ivana Kolcic¹¹¹,
- Charles Kooperberg¹¹²,
- Peter Kraft^{72,113},
- Allison W. Kurian^{105,106},
- Zoltan Kutalik^{44,45},
- Martina La Bianca⁵⁹,
- Genevieve LaChance¹¹⁴,
- Claudia Langenberg²,
- Lenore J. Launer¹¹⁵,
- Joop S. E. Laven¹¹⁶,

- Deborah A. Lawlor^{69,70},
- Loic Le Marchand¹¹⁷,
- Jingmei Li⁶⁸,
- Annika Lindblom^{118,119},
- Sara Lindstrom¹²⁰,
- Tricia Lindstrom¹²¹,
- Martha Linet¹¹⁰,
- YongMei Liu¹²²,
- Simin Liu^{123,124},
- Jian'an Luan²,
- Reedik Mägi⁷⁹,
- Patrik K. E. Magnusson¹⁰⁹,
- Massimo Mangino^{114,125},
- Arto Mannermaa^{126,127,128},
- Brumat Marco⁸⁶,
- Jonathan Marten³⁰,
- Nicholas G. Martin¹²⁹,
- Hamdi Mbarek^{50,51,52},
- Barbara McKnight³⁵,
- Sarah E. Medland¹²⁹,
- Christa Meisinger^{88,130},
- Thomas Meitinger¹³¹,
- Cristina Menni¹¹⁴,
- Andres Metspalu⁷⁹,
- Lili Milani⁷⁹,
- Roger L. Milne^{90,91,92},
- Grant W. Montgomery¹³²,
- Dennis O. Mook-Kanamori^{71,133},
- Antonella Mulas⁶⁵,
- Anna M. Mulligan^{134,135},
- Alison Murray¹³⁶,
- Mike A. Nalls¹³⁷,
- Anne Newman^{138,139},
- Raymond Noordam¹⁴⁰,

- Teresa Nutile⁶¹,
- Dale R. Nyholt¹⁴¹,
- Andrew F. Olshan¹⁴²,
- Håkan Olsson³⁸,
- Jodie N. Painter¹²⁹,
- Alpa V. Patel¹⁴³,
- Nancy L. Pedersen¹⁰⁹,
- Natalia Perjakova⁷⁹,
- Annette Peters^{88,89},
- Ulrike Peters¹¹²,
- Paul D. P. Pharoah^{8,75},
- Ozren Polasek^{144,145},
- Eleonora Porcu⁶⁵,
- Bruce M. Psaty⁵³,
- Iffat Rahman¹⁴⁶,
- Gad Rennert¹⁴⁷,
- Hedy S. Rennert¹⁴⁷,
- Paul M. Ridker^{55,56},
- Susan M. Ring^{69,70},
- Antonietta Robino⁵⁹,
- Lynda M. Rose⁵⁵,
- Frits R. Rosendaal⁷¹,
- Jacques Rossouw¹⁴⁸,
- Igor Rudan²⁹,
- Rico Rueedi^{43,44},
- Daniela Ruggiero^{61,62},
- Cinzia F. Sala⁴⁰,
- Emmanouil Saloustros¹⁴⁹,
- Dale P. Sandler¹⁵⁰,
- Serena Sanna⁶⁵,
- Elinor J. Sawyer¹⁵¹,
- Chloé Sarnowski¹⁵²,
- David Schlessinger¹⁵³,
- Marjanka K. Schmidt^{154,155},

- Minouk J. Schoemaker¹⁵⁶,
- Katharina E. Schraut^{29,157},
- Christopher Scott¹²¹,
- Saleh Shekari¹,
- Amruta Shrikhande³,
- Albert V. Smith^{93,94},
- Blair H. Smith¹⁵⁸,
- Jennifer A. Smith¹⁰⁸,
- Rossella Sorice⁶¹,
- Melissa C. Southey^{90,92,159},
- Tim D. Spector¹¹⁴,
- John J. Spinelli^{160,161},
- Meir Stampfer^{72,73,100},
- Doris Stöckl^{88,162},
- Joyce B. J. van Meurs⁵⁴,
- Konstantin Strauch^{163,164,165},
- Unnur Styrkarsdottir¹⁶,
- Anthony J. Swerdlow^{156,166},
- Toshiko Tanaka⁸²,
- Lauren R. Teras¹⁴³,
- Alexander Teumer¹⁶⁷,
- Unnur Þorsteinsdottir^{16,168},
- Nicholas J. Timpson^{69,70},
- Daniela Toniolo⁴⁰,
- Michela Traglia⁴⁰,
- Melissa A. Troester¹⁴²,
- Thérèse Truong⁹⁵,
- Jessica Tyrrell¹,
- André G. Uitterlinden^{54,103},
- Sheila Ulivi⁵⁹,
- Celine M. Vachon¹⁶⁹,
- Veronique Vitart³⁰,
- Uwe Völker¹⁷⁰,
- Peter Vollenweider¹⁷¹,

- [Henry Völzke](#)¹⁶⁷,
- [Qin Wang](#)⁸,
- [Nicholas J. Wareham](#)²,
- [Clarice R. Weinberg](#)¹⁷²,
- [David R. Weir](#)⁸¹,
- [Amber N. Wilcox](#)³¹,
- [Ko Willems van Dijk](#)^{173,174,175},
- [Gonneke Willemsen](#)^{50,51,52},
- [James F. Wilson](#)^{29,30},
- [Bruce H. R. Wolffenbuttel](#)¹⁷⁶,
- [Alicja Wolk](#)^{97,177},
- [Andrew R. Wood](#)¹,
- [Wei Zhao](#)¹⁰⁸,
- [Marek Zygmunt](#)¹⁷⁸,
- [Biobank-based Integrative Omics Study \(BIOS\) Consortium](#),
- [eQTLGen Consortium](#),
- [The Biobank Japan Project](#),
- [China Kadoorie Biobank Collaborative Group](#),
- [kConFab Investigators](#),
- [The LifeLines Cohort Study](#),
- [The InterAct consortium](#),
- [23andMe Research Team](#),
- [Zhengming Chen](#)^{17,18},
- [Liming Li](#)^{179,180},
- [Lude Franke](#)^{15,181},
- [Stephen Burgess](#)^{182,183},
- [Patrick Deelen](#)^{15,184},
- [Tune H. Pers](#)²⁶,
- [Marie Louise Grøndahl](#)²⁷,
- [Claus Yding Andersen](#)¹⁸⁵,
- [Anna Pujol](#)²²,
- [Andres J. Lopez-Contreras](#)^{3,28},
- [Jeremy A. Daniel](#)²⁵,
- [Kari Stefansson](#)^{16,168},
- [Jenny Chang-Claude](#)^{186,187},

- [Yvonne T. van der Schouw²⁴](#),
- [Kathryn L. Lunetta^{152,188}](#),
- [Daniel I. Chasman^{55,56}](#),
- [Douglas F. Easton^{8,75}](#),
- [Jenny A. Visser⁵⁴](#),
- [Susan E. Ozanne⁶](#),
- [Satoshi H. Namekawa¹¹](#),
- [Petr Solc^{9 na2}](#),
- [Joanne M. Murabito^{188,189}](#),
- [Ken K. Ong^{2,190}](#),
- [Eva R. Hoffmann ORCID: orcid.org/0000-0002-2588-0652^{3 na1}](#),
- [Anna Murray ORCID: orcid.org/0000-0002-2351-2522^{1 na1}](#),
- [Ignasi Roig ORCID: orcid.org/0000-0003-0313-3581^{4,5 na1}](#) &
- [John R. B. Perry ORCID: orcid.org/0000-0001-6483-3771^{2,54 na1}](#)

[Nature](#) volume **596**, pages 393–397 (2021) [Cite this article](#)

- 12k Accesses
- 1206 Altmetric
- [Metrics details](#)

Subjects

- [Ageing](#)
- [Endocrine reproductive disorders](#)
- [Genome-wide association studies](#)
- [Reproductive biology](#)

Abstract

Reproductive longevity is essential for fertility and influences healthy ageing in women^{1,2}, but insights into its underlying biological mechanisms and treatments to preserve it are limited. Here we identify 290 genetic determinants of ovarian ageing, assessed using normal variation in age at

natural menopause (ANM) in about 200,000 women of European ancestry. These common alleles were associated with clinical extremes of ANM; women in the top 1% of genetic susceptibility have an equivalent risk of premature ovarian insufficiency to those carrying monogenic *FMR1* permutations³. The identified loci implicate a broad range of DNA damage response (DDR) processes and include loss-of-function variants in key DDR-associated genes. Integration with experimental models demonstrates that these DDR processes act across the life-course to shape the ovarian reserve and its rate of depletion. Furthermore, we demonstrate that experimental manipulation of DDR pathways highlighted by human genetics increases fertility and extends reproductive life in mice. Causal inference analyses using the identified genetic variants indicate that extending reproductive life in women improves bone health and reduces risk of type 2 diabetes, but increases the risk of hormone-sensitive cancers. These findings provide insight into the mechanisms that govern ovarian ageing, when they act, and how they might be targeted by therapeutic approaches to extend fertility and prevent disease.

Access options

Subscribe to Journal

Get full journal access for 1 year

\$199.00

only \$3.90 per issue

[Subscribe](#)

All prices are NET prices.

VAT will be added later in the checkout.

Tax calculation will be finalised during checkout.

Rent or Buy article

Get time limited or full article access on ReadCube.

from \$8.99

[Rent or Buy](#)

All prices are NET prices.

Additional access options:

- [Log in](#)
- [Access through your institution](#)
- [Learn about institutional subscriptions](#)

Fig. 1: Manhattan plot representing GWAS discovery analysis.

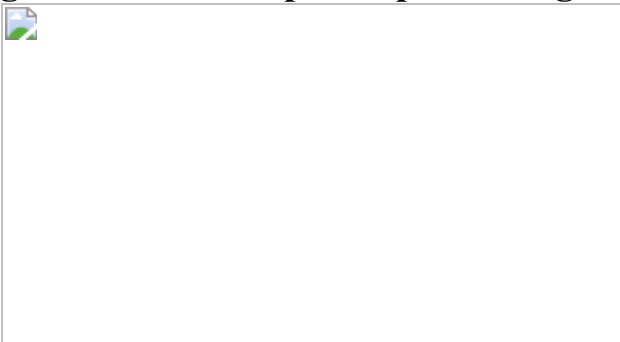


Fig. 2: Polygenic prediction of age at menopause.

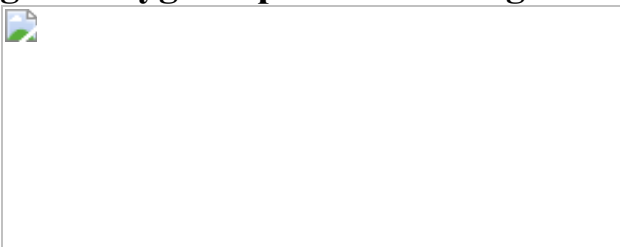


Fig. 3: Genetic manipulation of *Chek1* or *Chek2* extends reproductive lifespan in mice.



Data availability

Full genome-wide association summary statistics for the discovery meta-analysis are available from the ReproGen website (www.reprogen.org). The MII oocyte dataset is available from the European Genome-Phenome Archive under accession EGAS00001004947 (<https://ega-archive.org/studies/EGAS00001004947>). Access to these data is granted in accordance with the ethics permissions under which the data were collected from participants and under appropriate GDPR compliant data processing agreements. Data from the following sites were used: SMR (<https://cnsgenomics.com/software/smr/#eQTLsummarydata>); Tabula Muris (<https://tabula-muris.ds.czbiohub.org/>); LDSC-SEG (<https://github.com/bulik/ldsc/wiki/Cell-type-specific-analyses>); RNA-seq samples (<https://www.ebi.ac.uk/ena>); human oocyte expression analyses: Gene Expression Omnibus GSE86146, GSE107746. Source data are provided with this paper.

References

1. 1.

Lambalk, C. B., van Disseldorp, J., de Koning, C. H. & Broekmans, F. J. Testing ovarian reserve to predict age at menopause. *Maturitas* **63**, 280–291 (2009).

[CAS](#) [PubMed](#) [PubMed Central](#) [Google Scholar](#)

2. 2.

Collaborative Group on Hormonal Factors in Breast Cancer. Type and timing of menopausal hormone therapy and breast cancer risk: individual participant meta-analysis of the worldwide epidemiological evidence. *Lancet* **394**, 1159–1168 (2019).

[Google Scholar](#)

3. 3.

Murray, A. et al. Population-based estimates of the prevalence of FMR1 expansion mutations in women with early menopause and primary ovarian insufficiency. *Genet. Med.* **16**, 19–24 (2014).

[CAS](#) [PubMed](#) [PubMed Central](#) [Google Scholar](#)

4. 4.

Christensen, K., Doblhammer, G., Rau, R. & Vaupel, J. W. Ageing populations: the challenges ahead. *Lancet* **374**, 1196–1208 (2009).

[PubMed](#) [PubMed Central](#) [Google Scholar](#)

5. 5.

InterLACE Study Team. Variations in reproductive events across life: a pooled analysis of data from 505 147 women across 10 countries. *Hum. Reprod.* **34**, 881–893 (2019).

[Google Scholar](#)

6. 6.

Gruhn, J. R. et al. Chromosome errors in human eggs shape natural fertility over reproductive life span. *Science* **365**, 1466–1469 (2019).

[ADS](#) [CAS](#) [PubMed](#) [PubMed Central](#) [Google Scholar](#)

7. 7.

Donnez, J. & Dolmans, M.-M. Fertility preservation in women. *N. Engl. J. Med.* **377**, 1657–1665 (2017).

[PubMed](#) [PubMed Central](#) [Google Scholar](#)

8. 8.

Yding Andersen, C., Mamsen, L. S. & Kristensen, S. G. Fertility preservation: freezing of ovarian tissue and clinical opportunities. *Reproduction* **158**, F27–F34 (2019).

[CAS](#) [PubMed](#) [PubMed Central](#) [Google Scholar](#)

9. 9.

Argyle, C. E., Harper, J. C. & Davies, M. C. Oocyte cryopreservation: where are we now? *Hum. Reprod. Update* **22**, 440–449 (2016).

[CAS](#) [PubMed](#) [PubMed Central](#) [Google Scholar](#)

10. 10.

Stolk, L. et al. Meta-analyses identify 13 loci associated with age at menopause and highlight DNA repair and immune pathways. *Nat.*

Genet. **44**, 260–268 (2012).

[CAS](#) [PubMed](#) [PubMed Central](#) [Google Scholar](#)

11. 11.

Venturella, R. et al. The genetics of non-syndromic primary ovarian insufficiency: a systematic review. *Int. J. Fertil. Steril.* **13**, 161–168 (2019).

[CAS](#) [PubMed](#) [PubMed Central](#) [Google Scholar](#)

12. 12.

Titus, S. et al. Impairment of BRCA1-related DNA double-strand break repair leads to ovarian aging in mice and humans. *Sci. Transl. Med.* **5**, 172ra21 (2013).

[PubMed](#) [PubMed Central](#) [Google Scholar](#)

13. 13.

Day, F. R. et al. Large-scale genomic analyses link reproductive aging to hypothalamic signaling, breast cancer susceptibility and BRCA1-mediated DNA repair. *Nat. Genet.* **47**, 1294–1303 (2015).

[CAS](#) [PubMed](#) [PubMed Central](#) [Google Scholar](#)

14. 14.

Horikoshi, M. et al. Elucidating the genetic architecture of reproductive ageing in the Japanese population. *Nat. Commun.* **9**, 1977 (2018).

[ADS](#) [PubMed](#) [PubMed Central](#) [Google Scholar](#)

15. 15.

Caburet, S. et al. Homozygous hypomorphic *BRCA2* variant in primary ovarian insufficiency without cancer or Fanconi anaemia trait. *J. Med. Genet.* **58**, 125–134 (2020).

[Google Scholar](#)

16. 16.

Thompson, D. J. et al. Genetic predisposition to mosaic Y chromosome loss in blood. *Nature* **575**, 652–657 (2019).

[CAS](#) [PubMed](#) [PubMed Central](#) [Google Scholar](#)

17. 17.

Day, F. R. et al. Genomic analyses identify hundreds of variants associated with age at menarche and support a role for puberty timing in cancer risk. *Nat. Genet.* **49**, 834–841 (2017).

[CAS](#) [PubMed](#) [PubMed Central](#) [Google Scholar](#)

18. 18.

Boyle, E. A., Li, Y. I. & Pritchard, J. K. An expanded view of complex traits: from polygenic to omnigenic. *Cell* **169**, 1177–1186 (2017).

[CAS](#) [PubMed](#) [PubMed Central](#) [Google Scholar](#)

19. 19.

Reddy, P. et al. Oocyte-specific deletion of *Pten* causes premature activation of the primordial follicle pool. *Science* **319**, 611–613 (2008).

[CAS](#) [Google Scholar](#)

20. 20.

Suh, E.-K. et al. p63 protects the female germ line during meiotic arrest. *Nature* **444**, 624–628 (2006).

[ADS](#) [CAS](#) [PubMed](#) [PubMed Central](#) [Google Scholar](#)

21. 21.

Deutsch, G. B. et al. DNA damage in oocytes induces a switch of the quality control factor TAp63 α from dimer to tetramer. *Cell* **144**, 566–576 (2011).

[CAS](#) [PubMed](#) [PubMed Central](#) [Google Scholar](#)

22. 22.

Tuppi, M. et al. Oocyte DNA damage quality control requires consecutive interplay of CHK2 and CK1 to activate p63. *Nat. Struct. Mol. Biol.* **25**, 261–269 (2018).

[CAS](#) [Google Scholar](#)

23. 23.

Rinaldi, V. D., Bloom, J. C. & Schimenti, J. C. Oocyte elimination through DNA damage signaling from CHK1/CHK2 to p53 and p63. *Genetics* **215**, 373–378 (2020).

[CAS](#) [PubMed](#) [PubMed Central](#) [Google Scholar](#)

24. 24.

Aiken, C. E., Tarry-Adkins, J. L., Penfold, N. C., Dearden, L. & Ozanne, S. E. Decreased ovarian reserve, dysregulation of mitochondrial biogenesis, and increased lipid peroxidation in female mouse offspring exposed to an obesogenic maternal diet. *FASEB J.* **30**, 1548–1556 (2016).

[CAS](#) [PubMed](#) [PubMed Central](#) [Google Scholar](#)

25. 25.

Pittman, D. L. et al. Meiotic prophase arrest with failure of chromosome synapsis in mice deficient for Dmc1, a germline-specific RecA homolog. *Mol. Cell* **1**, 697–705 (1998).

[CAS](#) [PubMed](#) [PubMed Central](#) [Google Scholar](#)

26. 26.

Nakajo, N. et al. Absence of Wee1 ensures the meiotic cell cycle in *Xenopus* oocytes. *Genes Dev.* **14**, 328–338 (2000).

[CAS](#) [PubMed](#) [PubMed Central](#) [Google Scholar](#)

27. 27.

Ruth, K. S. et al. Events in early life are associated with female reproductive ageing: a UK Biobank study. *Sci. Rep.* **6**, 24710 (2016).

[ADS](#) [CAS](#) [PubMed](#) [PubMed Central](#) [Google Scholar](#)

28. 28.

Pan, Y. et al. A heterozygous hypomorphic mutation of Fanca causes impaired follicle development and subfertility in female mice. *Mol. Genet. Genomics* **296**, 103–112 (2021).

[CAS](#) [PubMed](#) [PubMed Central](#) [Google Scholar](#)

29. 29.

Bakker, S. T. et al. Fancm-deficient mice reveal unique features of Fanconi anemia complementation group M. *Hum. Mol. Genet.* **18**, 3484–3495 (2009).

[CAS](#) [PubMed](#) [PubMed Central](#) [Google Scholar](#)

30. 30.

Caburet, S. et al. Mutant cohesin in premature ovarian failure. *N. Engl. J. Med.* **370**, 943–949 (2014).

[CAS](#) [PubMed](#) [PubMed Central](#) [Google Scholar](#)

31. 31.

Bolcun-Filas, E., Rinaldi, V. D., White, M. E. & Schimenti, J. C. Reversal of female infertility by *Chk2* ablation reveals the oocyte DNA damage checkpoint pathway. *Science* **343**, 533–536 (2014).

[ADS](#) [CAS](#) [PubMed](#) [PubMed Central](#) [Google Scholar](#)

32. 32.

Adhikari, D. et al. Inhibitory phosphorylation of Cdk1 mediates prolonged prophase I arrest in female germ cells and is essential for female reproductive lifespan. *Cell Res.* **26**, 1212–1225 (2016).

[CAS](#) [PubMed](#) [PubMed Central](#) [Google Scholar](#)

33. 33.

Rinaldi, V. D., Bolcun-Filas, E., Kogo, H., Kurahashi, H. & Schimenti, J. C. The DNA damage checkpoint eliminates mouse oocytes with chromosome synapsis failure. *Mol. Cell* **67**, 1026–1036.e2 (2017).

[CAS](#) [PubMed](#) [PubMed Central](#) [Google Scholar](#)

34. 34.

Tharp, M. E., Malki, S. & Bortvin, A. Maximizing the ovarian reserve in mice by evading LINE-1 genotoxicity. *Nat. Commun.* **11**, 330 (2020).

[ADS](#) [CAS](#) [PubMed](#) [PubMed Central](#) [Google Scholar](#)

35. 35.

Liu, Q. et al. Chk1 is an essential kinase that is regulated by Atr and required for the G₂/M DNA damage checkpoint. *Genes Dev.* **14**, 1448–1459 (2000).

[CAS](#) [PubMed](#) [PubMed Central](#) [Google Scholar](#)

36. 36.

Abe, H. et al. CHEK1 coordinates DNA damage signaling and meiotic progression in the male germline of mice. *Hum. Mol. Genet.* **27**, 1136–1149 (2018).

[CAS](#) [PubMed](#) [PubMed Central](#) [Google Scholar](#)

37. 37.

Chen, L. et al. Checkpoint kinase 1 is essential for meiotic cell cycle regulation in mouse oocytes. *Cell Cycle* **11**, 1948–1955 (2012).

[CAS](#) [PubMed](#) [PubMed Central](#) [Google Scholar](#)

38. 38.

Pacheco, S. et al. ATR is required to complete meiotic recombination in mice. *Nat. Commun.* **9**, 2622 (2018).

[ADS](#) [PubMed](#) [PubMed Central](#) [Google Scholar](#)

39. 39.

Pacheco, S., Maldonado-Linares, A., Garcia-Caldés, M. & Roig, I. ATR function is indispensable to allow proper mammalian follicle development. *Chromosoma* **128**, 489–500 (2019).

[CAS](#) [PubMed](#) [PubMed Central](#) [Google Scholar](#)

40. 40.

López-Contreras, A. J., Gutierrez-Martinez, P., Specks, J., Rodrigo-Perez, S. & Fernandez-Capetillo, O. An extra allele of *Chk1* limits oncogene-induced replicative stress and promotes transformation. *J. Exp. Med.* **209**, 455–461 (2012).

[PubMed](#) [PubMed Central](#) [Google Scholar](#)

41. 41.

Salpeter, S. R. et al. Meta-analysis: effect of hormone-replacement therapy on components of the metabolic syndrome in postmenopausal women. *Diabetes Obes. Metab.* **8**, 538–554 (2006).

[CAS](#) [PubMed](#) [PubMed Central](#) [Google Scholar](#)

42. 42.

Manson, J. E. et al. Menopausal hormone therapy and health outcomes during the intervention and extended poststopping phases of the Women's Health Initiative randomized trials. *J. Am. Med. Assoc.* **310**, 1353–1368 (2013).

[ADS](#) [CAS](#) [Google Scholar](#)

43. 43.

Ruth, K. S. et al. Using human genetics to understand the disease impacts of testosterone in men and women. *Nat. Med.* **26**, 252–258 (2020).

[CAS](#) [PubMed](#) [PubMed Central](#) [Google Scholar](#)

44. 44.

Dam, V. et al. Association of menopausal characteristics and risk of coronary heart disease: a pan-European case-cohort analysis. *Int. J. Epidemiol.* **48**, 1275–1285 (2019).

[PubMed](#) [PubMed Central](#) [Google Scholar](#)

45. 45.

de Kat, A. C. et al. Unraveling the associations of age and menopause with cardiovascular risk factors in a large population-based study. *BMC Med.* **15**, 2 (2017).

[PubMed](#) [PubMed Central](#) [Google Scholar](#)

46. 46.

Atsma, F., Bartelink, M.-L. E. L., Grobbee, D. E. & van der Schouw, Y. T. Postmenopausal status and early menopause as independent risk factors for cardiovascular disease: a meta-analysis. *Menopause* **13**, 265–279 (2006).

[Google Scholar](#)

47. 47.

Ambikairajah, A., Walsh, E. & Cherbuin, N. Lipid profile differences during menopause: a review with meta-analysis. *Menopause* **26**, 1327–1333 (2019).

[PubMed](#) [PubMed Central](#) [Google Scholar](#)

48. 48.

Pike, C. J. Sex and the development of Alzheimer's disease. *J. Neurosci. Res.* **95**, 671–680 (2017).

[CAS](#) [PubMed](#) [PubMed Central](#) [Google Scholar](#)

49. 49.

Zhu, D. et al. Body mass index and age at natural menopause: an international pooled analysis of 11 prospective studies. *Eur. J. Epidemiol.* **33**, 699–710 (2018).

[PubMed](#) [PubMed Central](#) [Google Scholar](#)

50. 50.

Shadyab, A. H. et al. Ages at menarche and menopause and reproductive lifespan as predictors of exceptional longevity in women: the Women's Health Initiative. *Menopause* **24**, 35–44 (2017).

[PubMed](#) [PubMed Central](#) [Google Scholar](#)

51. 51.

Bycroft, C. et al. The UK Biobank resource with deep phenotyping and genomic data. *Nature* **562**, 203–209 (2018).

[ADS](#) [CAS](#) [PubMed](#) [PubMed Central](#) [Google Scholar](#)

52. 52.

Tyrrell, J. et al. Using genetics to understand the causal influence of higher BMI on depression. *Int. J. Epidemiol.* **48**, 834–848 (2019).

[PubMed](#) [PubMed Central](#) [Google Scholar](#)

53. 53.

Loh, P.-R. et al. Efficient Bayesian mixed-model analysis increases association power in large cohorts. *Nat. Genet.* **47**, 284–290 (2015).

[CAS](#) [PubMed](#) [PubMed Central](#) [Google Scholar](#)

54. 54.

Yang, J., Lee, S. H., Goddard, M. E. & Visscher, P. M. GCTA: a tool for genome-wide complex trait analysis. *Am. J. Hum. Genet.* **88**, 76–82 (2011).

[CAS](#) [PubMed](#) [PubMed Central](#) [Google Scholar](#)

55. 55.

Terao, C. et al. Chromosomal alterations among age-related haematopoietic clones in Japan. *Nature* **584**, 130–135 (2020).

[ADS](#) [CAS](#) [PubMed](#) [PubMed Central](#) [Google Scholar](#)

56. 56.

Wood, A. R. et al. Variants in the FTO and CDKAL1 loci have recessive effects on risk of obesity and type 2 diabetes, respectively. *Diabetologia* **59**, 1214–1221 (2016).

[CAS](#) [PubMed](#) [PubMed Central](#) [Google Scholar](#)

57. 57.

Szustakowski, J. D. et al. Advancing human genetics research and drug discovery through exome sequencing of the UK Biobank. *Nat. Genet.* <https://doi.org/10.1038/s41588-021-00885-0> (2021).

58. 58.

McLaren, W. et al. The Ensembl variant effect predictor. *Genome Biol.* **17**, 122 (2016).

[PubMed](#) [PubMed Central](#) [Google Scholar](#)

59. 59.

Zhou, W. et al. Scalable generalized linear mixed model for region-based association tests in large biobanks and cohorts. *Nat. Genet.* **52**, 634–639 (2020).

[CAS](#) [PubMed](#) [PubMed Central](#) [Google Scholar](#)

60. 60.

Zhu, Z. et al. Integration of summary data from GWAS and eQTL studies predicts complex trait gene targets. *Nat. Genet.* **48**, 481–487 (2016).

[CAS](#) [PubMed](#) [PubMed Central](#) [Google Scholar](#)

61. 61.

Võsa, U. et al. Unraveling the polygenic architecture of complex traits using blood eQTL metaanalysis. Preprint at <https://doi.org/10.1101/447367> (2018).

62. 62.

Pers, T. H. et al. Biological interpretation of genome-wide association studies using predicted gene functions. *Nat. Commun.* **6**, 5890 (2015).

[CAS](#) [PubMed](#) [PubMed Central](#) [Google Scholar](#)

63. 63.

Tabula Muris Consortium. Single-cell transcriptomics of 20 mouse organs creates a Tabula Muris. *Nature* **562**, 367–372 (2018).

[ADS](#) [Google Scholar](#)

64. 64.

Nestorowa, S. et al. A single-cell resolution map of mouse hematopoietic stem and progenitor cell differentiation. *Blood* **128**, e20–e31 (2016).

[CAS](#) [PubMed](#) [PubMed Central](#) [Google Scholar](#)

65. 65.

Finucane, H. K. et al. Heritability enrichment of specifically expressed genes identifies disease-relevant tissues and cell types. *Nat. Genet.* **50**, 621–629 (2018).

[CAS](#) [PubMed](#) [PubMed Central](#) [Google Scholar](#)

66. 66.

GTEx Consortium. The Genotype-Tissue Expression (GTEx) pilot analysis: multitissue gene regulation in humans. *Science* **348**, 648–660 (2015).

[PubMed](#) [PubMed Central](#) [Google Scholar](#)

67. 67.

Roadmap Epigenomics Consortium et al. Integrative analysis of 111 reference human epigenomes. *Nature* **518**, 317–330 (2015).

[Google Scholar](#)

68. 68.

Fehrman, R. S. N. et al. Gene expression analysis identifies global gene dosage sensitivity in cancer. *Nat. Genet.* **47**, 115–125 (2015).

[CAS](#) [PubMed](#) [PubMed Central](#) [Google Scholar](#)

69. 69.

Segrè, A. V., Groop, L., Mootha, V. K., Daly, M. J. & Altshuler, D. Common inherited variation in mitochondrial genes is not enriched for associations with type 2 diabetes or related glycemic traits. *PLoS Genet.* **6**, e1001058 (2010).

[PubMed](#) [PubMed Central](#) [Google Scholar](#)

70. 70.

de Leeuw, C. A., Mooij, J. M., Heskes, T. & Posthuma, D. MAGMA: generalized gene-set analysis of GWAS data. *PLOS Comput. Biol.* **11**, e1004219 (2015).

[PubMed](#) [PubMed Central](#) [Google Scholar](#)

71. 71.

Lamparter, D., Marbach, D., Rueedi, R., Kutalik, Z. & Bergmann, S. Fast and rigorous computation of gene and pathway scores from SNP-based summary statistics. *PLOS Comput. Biol.* **12**, e1004714 (2016).

[ADS](#) [PubMed](#) [PubMed Central](#) [Google Scholar](#)

72. 72.

Deelen, P. et al. Improving the diagnostic yield of exome- sequencing by predicting gene-phenotype associations using large-scale gene expression analysis. *Nat. Commun.* **10**, 2837 (2019).

[ADS](#) [PubMed](#) [PubMed Central](#) [Google Scholar](#)

73. 73.

Knijnenburg, T. A. et al. Genomic and molecular landscape of DNA damage repair deficiency across The Cancer Genome Atlas. *Cell Rep.* **23**, 239–254.e6 (2018).

[CAS](#) [PubMed](#) [PubMed Central](#) [Google Scholar](#)

74. 74.

Pearl, L. H., Schierz, A. C., Ward, S. E., Al-Lazikani, B. & Pearl, F. M. G. Therapeutic opportunities within the DNA damage response. *Nat. Rev. Cancer* **15**, 166–180 (2015).

[CAS](#) [PubMed](#) [PubMed Central](#) [Google Scholar](#)

75. 75.

Álvarez-Quilón, A. et al. Endogenous DNA 3' blocks are vulnerabilities for BRCA1 and BRCA2 deficiency and are reversed by the APE2 nuclease. *Mol. Cell* **78**, 1152–1165.e8 (2020).

[PubMed](#) [PubMed Central](#) [Google Scholar](#)

76. 76.

Vilhjálmsson, B. J. et al. Modeling linkage disequilibrium increases accuracy of polygenic risk scores. *Am. J. Hum. Genet.* **97**, 576–592 (2015).

[PubMed](#) [PubMed Central](#) [Google Scholar](#)

77. 77.

Purcell, S. et al. PLINK: a tool set for whole-genome association and population-based linkage analyses. *Am. J. Hum. Genet.* **81**, 559–575 (2007).

[CAS](#) [PubMed](#) [PubMed Central](#) [Google Scholar](#)

78. 78.

Burgess, S., Butterworth, A. & Thompson, S. G. Mendelian randomization analysis with multiple genetic variants using summarized data. *Genet. Epidemiol.* **37**, 658–665 (2013).

[PubMed](#) [PubMed Central](#) [Google Scholar](#)

79. 79.

Burgess, S. & Thompson, S. G. Interpreting findings from Mendelian randomization using the MR-Egger method. *Eur. J. Epidemiol.* **32**, 377–389 (2017).

[PubMed](#) [PubMed Central](#) [Google Scholar](#)

80. 80.

Bowden, J., Davey Smith, G., Haycock, P. C. & Burgess, S. Consistent estimation in Mendelian randomization with some invalid instruments using a weighted median estimator. *Genet. Epidemiol.* **40**, 304–314 (2016).

[PubMed](#) [PubMed Central](#) [Google Scholar](#)

81. 81.

Bowden, J. et al. Improving the visualization, interpretation and analysis of two-sample summary data Mendelian randomization via the radial plot and radial regression. *Int. J. Epidemiol.* **47**, 2100 (2018).

[PubMed](#) [PubMed Central](#) [Google Scholar](#)

82. 82.

Samuelsson, A.-M. et al. Diet-induced obesity in female mice leads to offspring hyperphagia, adiposity, hypertension, and insulin resistance: a novel murine model of developmental programming. *Hypertension* **51**, 383–392 (2008).

[CAS](#) [PubMed](#) [PubMed Central](#) [Google Scholar](#)

83. 83.

Sankar, A. et al. KDM4A regulates the maternal-to-zygotic transition by protecting broad H3K4me3 domains from H3K9me3 invasion in oocytes. *Nat. Cell Biol.* **22**, 380–388 (2020).

[MathSciNet](#) [CAS](#) [PubMed](#) [PubMed Central](#) [Google Scholar](#)

84. 84.

Li, L. et al. Single-cell RNA-seq analysis maps development of human germline cells and gonadal niche interactions. *Cell Stem Cell* **20**, 858–873.e4 (2017).

[CAS](#) [PubMed](#) [PubMed Central](#) [Google Scholar](#)

85. 85.

Zhang, Y. et al. Transcriptome landscape of human folliculogenesis reveals oocyte and granulosa cell interactions. *Mol. Cell* **72**, 1021–1034.e4 (2018).

[CAS](#) [PubMed](#) [PubMed Central](#) [Google Scholar](#)

86. 86.

Bolger, A. M., Lohse, M. & Usadel, B. Trimmomatic: a flexible trimmer for Illumina sequence data. *Bioinformatics* **30**, 2114–2120 (2014).

[CAS](#) [PubMed](#) [PubMed Central](#) [Google Scholar](#)

87. 87.

Chen, S. et al. AfterQC: automatic filtering, trimming, error removing and quality control for fastq data. *BMC Bioinformatics* **18**, 80 (2017).

[PubMed](#) [PubMed Central](#) [Google Scholar](#)

88. 88.

Pertea, M., Kim, D., Pertea, G. M., Leek, J. T. & Salzberg, S. L. Transcript-level expression analysis of RNA-seq experiments with HISAT, StringTie and Ballgown. *Nat. Protocols* **11**, 1650–1667 (2016).

[CAS](#) [PubMed](#) [PubMed Central](#) [Google Scholar](#)

89. 89.

Li, H. et al. The Sequence Alignment/Map format and SAMtools. *Bioinformatics* **25**, 2078–2079 (2009).

[PubMed](#) [PubMed Central](#) [Google Scholar](#)

90. 90.

Takai, H. et al. Chk2-deficient mice exhibit radioresistance and defective p53-mediated transcription. *EMBO J.* **21**, 5195–5205 (2002).

[CAS](#) [PubMed](#) [PubMed Central](#) [Google Scholar](#)

91. 91.

Lewandoski, M., Wassarman, K. M. & Martin, G. R. Zp3-cre, a transgenic mouse line for the activation or inactivation of loxP-flanked target genes specifically in the female germ line. *Curr. Biol.* **7**, 148–151 (1997).

[CAS](#) [PubMed](#) [PubMed Central](#) [Google Scholar](#)

92. 92.

Lam, M. H., Liu, Q., Elledge, S. J. & Rosen, J. M. Chk1 is haploinsufficient for multiple functions critical to tumor suppression. *Cancer Cell* **6**, 45–59 (2004).

[CAS](#) [PubMed](#) [PubMed Central](#) [Google Scholar](#)

93. 93.

Takeo, T. & Nakagata, N. Superovulation using the combined administration of inhibin antiserum and equine chorionic gonadotropin increases the number of ovulated oocytes in C57BL/6 female mice. *PLoS One* **10**, e0128330 (2015).

[PubMed](#) [PubMed Central](#) [Google Scholar](#)

94. 94.

Schindelin, J. et al. Fiji: an open-source platform for biological-image analysis. *Nat. Methods* **9**, 676–682 (2012).

[CAS](#) [PubMed](#) [PubMed Central](#) [Google Scholar](#)

[Download references](#)

Acknowledgements

This research was conducted using the UK Biobank resource under application numbers 871 (Exeter) and 9797 (Cambridge). Full individual study acknowledgements can be found in the Supplementary Information. The authors wish to dedicate this work to the memory of Professor P. Solc.

Author information

Author notes

1. These authors jointly supervised this work: Eva R. Hoffmann, Anna Murray, Ignasi Roig, John R. B. Perry
2. Deceased
3. These authors contributed equally: Katherine S. Ruth, Felix R. Day, Jazib Hussain, Ana Martínez-Marchal

Affiliations

1. Genetics of Human Complex Traits, University of Exeter Medical School, University of Exeter, Exeter, UK

Katherine S. Ruth, Robin N. Beaumont, Timothy M. Frayling, Micaella D. R. Joaquim, Saleh Shekari, Jessica Tyrrell, Andrew R. Wood & Anna Murray

2. MRC Epidemiology Unit, University of Cambridge School of Clinical Medicine, Institute of Metabolic Science, Cambridge Biomedical Campus, Cambridge, UK

Felix R. Day, Stasa Stankovic, Nicholas Bowker, Claudia Langenberg, Jian'an Luan, Nicholas J. Wareham, Ken K. Ong & John R. B. Perry

3. DNRF Center for Chromosome Stability, Department of Cellular and Molecular Medicine, Faculty of Health and Medical Sciences, University of Copenhagen, Copenhagen, Denmark

Jazib Hussain, Ajuna Azad, Aditya Sankar, Emil Peter Thrane Hertz, Vallari Shukla, Rehannah Borup, Kristina W. Olsen, Paula Aguilera, Miya K. Høffding, Amruta Shrikhande, Andres J. Lopez-Contreras & Eva R. Hoffmann

4. Genome Integrity and Instability Group, Institut de Biotecnologia i Biomedicina, Universitat Autònoma de Barcelona, Cerdanyola del Vallès, Spain

Ana Martínez-Marchal, Mònica Ferrer-Roda, Yan Huang & Ignasi Roig

5. Department of Cell Biology, Physiology and Immunology, Universitat Autònoma de Barcelona, Cerdanyola del Vallès, Spain

Ana Martínez-Marchal, Mònica Ferrer-Roda, Yan Huang & Ignasi Roig

6. University of Cambridge Metabolic Research Laboratories and MRC Metabolic Diseases Unit, Wellcome–MRC Institute of Metabolic Science, Addenbrooke's Hospital, Cambridge, UK

Catherine E. Aiken, Jane L. Tarry-Adkins & Susan E. Ozanne

7. Department of Obstetrics and Gynaecology, University of Cambridge, The Rosie Hospital and NIHR Cambridge Biomedical Research Centre, Cambridge, UK

Catherine E. Aiken & Jane L. Tarry-Adkins

8. Centre for Cancer Genetic Epidemiology, Department of Public Health and Primary Care, University of Cambridge, Cambridge, UK

Deborah J. Thompson, Manjeet K. Bolla, Joe Dennis, Paul D. P. Pharoah, Qin Wang & Douglas F. Easton

9. Institute of Animal Physiology and Genetics of the Czech Academy of Sciences, Libechov, Czech Republic

Lucie Knoblochova & Petr Solc

10. Faculty of Science, Charles University, Prague, Czech Republic

Lucie Knoblochova

11. Division of Reproductive Sciences, Cincinnati Children's Hospital Medical Center, Cincinnati, OH, USA

Hironori Abe & Satoshi H. Namekawa

12. Transgenic Core Facility, Department of Experimental Medicine, Faculty of Health and Medical Sciences, University of Copenhagen, Copenhagen, Denmark

Javier Martin Gonzalez

13. 23andMe Inc., Sunnyvale, CA, USA

Pierre Fontanillas

14. Structural and Computational Biology Unit, EMBL, Heidelberg, Germany

Annique Claringbould

15. University of Groningen, University Medical Center Groningen, Department of Genetics, Groningen, The Netherlands

Olivier B. Bakker, Lude Franke & Patrick Deelen

16. deCODE genetics/Amgen, Reykjavik, Iceland

Patrick Sulem, Stefania Benonisdottir, Daniel F. Gudbjartsson, Unnur Styrkarsdottir, Unnur Þorsteinsdottir & Kari Stefansson

17. Nuffield Department of Population Health, University of Oxford, Oxford, UK

Robin G. Walters, Kuang Lin, David Hunter, Christiana Kartsonaki & Zhengming Chen

18. MRC Population Health Research Unit, University of Oxford, Oxford, UK

Robin G. Walters, Christiana Kartsonaki & Zhengming Chen

19. Laboratory for Statistical and Translational Genetics, RIKEN Center for Integrative Medical Sciences, Yokohama, Japan

Chikashi Terao

20. Clinical Research Center, Shizuoka General Hospital, Shizuoka, Japan

Chikashi Terao

21. Department of Applied Genetics, School of Pharmaceutical Sciences, University of Shizuoka, Shizuoka, Japan

Chikashi Terao

22. Transgenic Animal Unit, Center of Animal Biotechnology and Gene Therapy, Universitat Autònoma de Barcelona, Cerdanyola del Vallès, Spain

Sandra Turon & Anna Pujol

23. Laboratory for Genomics of Diabetes and Metabolism, RIKEN Center for Integrative Medical Sciences, Yokohama, Japan

Momoko Horikoshi

24. Julius Center for Health Sciences and Primary Care, University Medical Center Utrecht, Utrecht University, Utrecht, the Netherlands

N. Charlotte Onland-Moret & Yvonne T. van der Schouw

25. The Novo Nordisk Foundation Center for Protein Research, Faculty of Health and Medical Sciences, University of Copenhagen, Copenhagen, Denmark

Emil Peter Thrane Hertz & Jeremy A. Daniel

26. The Novo Nordisk Foundation Center for Basic Metabolic Research, Faculty of Health and Medical Sciences, University of Copenhagen, Copenhagen, Denmark

Pascal N. Timshel & Tune H. Pers

27. Reproductive Medicine, Department of Obstetrics and Gynaecology, Herlev and Gentofte Hospital, Copenhagen University Hospital, Herlev, Denmark

Kristina W. Olsen & Marie Louise Grøndahl

28. Centro Andaluz de Biología Molecular y Medicina Regenerativa (CABIMER), Consejo Superior de Investigaciones Científicas (CSIC) – Universidad de Sevilla –Universidad Pablo de Olavide, Seville, Spain

Paula Aguilera & Andres J. Lopez-Contreras

29. Centre for Global Health Research, Usher Institute, University of Edinburgh, Edinburgh, UK

Paul R. H. J. Timmers, Harry Campbell, Peter K. Joshi, Igor Rudan, Katharina E. Schraut & James F. Wilson

30. MRC Human Genetics Unit, Institute of Genetics and Molecular Medicine, University of Edinburgh, Western General Hospital, Edinburgh, UK

Paul R. H. J. Timmers, Caroline Hayward, Jonathan Marten, Veronique Vitart & James F. Wilson

31. Division of Cancer Epidemiology and Genetics, National Cancer Institute, National Institutes of Health, Department of Health and Human Services, Bethesda, MD, USA

Thomas U. Ahearn, Stephen J. Chanock, Montserrat García-Closas & Amber N. Wilcox

32. Department of Epidemiology, University Medical Center Groningen, University of Groningen, Groningen, The Netherlands

Behrooz Z. Alizadeh & Elnaz Naderi

33. Fred A. Litwin Center for Cancer Genetics, Lunenfeld-Tanenbaum Research Institute of Mount Sinai Hospital, Toronto, Ontario, Canada

Irene L. Andrulis

34. Department of Molecular Genetics, University of Toronto, Toronto, Ontario, Canada

Irene L. Andrulis

35. Department of Biostatistics, University of Washington, Seattle, WA, USA

Alice M. Arnold & Barbara McKnight

36. Department of Public Health Sciences, Queen's University, Kingston, Ontario, Canada

Kristan J. Aronson

37. Cancer Research Institute, Queen's University, Kingston, Ontario, Canada

Kristan J. Aronson

38. Department of Cancer Epidemiology, Clinical Sciences, Lund University, Lund, Sweden

Annelie Augustinsson & Håkan Olsson

39. Geriatric Unit, Azienda Sanitaria Firenze (ASF), Florence, Italy

Stefania Bandinelli

40. Genetics of Common Disorders Unit, IRCCS San Raffaele Scientific Institute, Milan, Italy

Caterina M. Barbieri, Cinzia F. Sala, Daniela Toniolo & Michela Traglia

41. Institute of Medical Biometry and Epidemiology, University Medical Center Hamburg-Eppendorf, Hamburg, Germany

Heiko Becher

42. Department of Gynecology and Obstetrics, Comprehensive Cancer Center ER-EMN, University Hospital Erlangen, Friedrich-Alexander-University Erlangen-Nuremberg, Erlangen, Germany

Matthias W. Beckmann & Peter A. Fasching

43. Department of Computational Biology, University of Lausanne, Lausanne, Switzerland

Sven Bergmann, Tanguy Corre & Rico Rueedi

44. Swiss Institute of Bioinformatics, Lausanne, Switzerland

Sven Bergmann, Tanguy Corre, Zoltan Katalik & Rico Rueedi

45. University Center for Primary Care and Public Health, University of Lausanne, Lausanne, Switzerland

Murielle Bochud, Tanguy Corre & Zoltan Katalik

46. Human Genetics Center, School of Public Health, The University of Texas Health Science Center at Houston, Houston, TX, USA

Eric Boerwinkle

47. Copenhagen General Population Study, Herlev and Gentofte Hospital, Copenhagen University Hospital, Herlev, Denmark

Stig E. Bojesen

48. Department of Clinical Biochemistry, Herlev and Gentofte Hospital, Copenhagen University Hospital, Herlev, Denmark

Stig E. Bojesen

49. Faculty of Health and Medical Sciences, University of Copenhagen, Copenhagen, Denmark

Stig E. Bojesen

50. Department of Biological Psychology, Vrije Universiteit Amsterdam, Amsterdam, The Netherlands

Dorret I. Boomsma, Eco J. C. N. de Geus, Jouke J. Hottenga, Hamdi Mbarek & Gonneke Willemsen

51. Amsterdam Public Health (APH) Research Institute, Amsterdam, The Netherlands

Dorret I. Boomsma, Eco J. C. N. de Geus, Jouke J. Hottenga, Hamdi Mbarek & Gonneke Willemsen

52. Amsterdam Reproduction and Development (AR&D) Research Institute, Amsterdam, The Netherlands

Dorret I. Boomsma, Eco J. C. N. de Geus, Jouke J. Hottenga, Hamdi Mbarek & Gonneke Willemsen

53. Cardiovascular Health Research Unit, Departments of Medicine, Epidemiology, and Health Services, University of Washington, Seattle, WA, USA

Jennifer A. Brody & Bruce M. Psaty

54. Department of Internal Medicine, Erasmus MC, Rotterdam, The Netherlands

Linda Broer, Joyce B. J. van Meurs, André G. Uitterlinden, Jenny A. Visser & John R. B. Perry

55. Brigham and Women's Hospital, Boston, MA, USA

Julie E. Buring, Paul M. Ridker, Lynda M. Rose & Daniel I. Chasman

56. Harvard Medical School, Boston, MA, USA

Julie E. Buring, David Karasik, Paul M. Ridker & Daniel I. Chasman

57. Medical Genetics Section, Centre for Genomic and Experimental Medicine, Institute of Genetics and Molecular Medicine, University of Edinburgh, Edinburgh, UK

Archie Campbell

58. Oncology and Genetics Unit, Instituto de Investigacion Sanitaria Galicia Sur (IISGS), Xerencia de Xestion Integrada de Vigo-SERGAS, Vigo, Spain

Jose E. Castelao

59. Institute for Maternal and Child Health – IRCCS ‘Burlo Garofolo’, Trieste, Italy

Eulalia Catamo, Martina La Bianca, Antonietta Robino & Sheila Ulivi

60. Department of Genetics and Computational Biology, QIMR Berghofer Medical Research Institute, Brisbane, Queensland, Australia

Georgia Chenevix-Trench

61. Institute of Genetics and Biophysics – CNR, Naples, Italy

Marina Ciullo, Teresa Natile, Daniela Ruggiero & Rossella Sorice

62. IRCCS Neuromed, Pozzilli, Isernia, Italy

Marina Ciullo & Daniela Ruggiero

63. Department of Laboratory Medicine and Pathology, Mayo Clinic, Rochester, MN, USA

Fergus J. Couch

64. Sheffield Institute for Nucleic Acids (SInFoNiA), Department of Oncology and Metabolism, University of Sheffield, Sheffield, UK

Angela Cox

65. Institute of Genetics and Biomedical Research, National Research Council, Cagliari, Italy

Laura Crisponi, Francesco Cucca, Antonella Mulas, Eleonora Porcu & Serena Sanna

66. Academic Unit of Pathology, Department of Neuroscience, University of Sheffield, Sheffield, UK

Simon S. Cross

67. University of Sassari, Department of Biomedical Sciences, Sassari, Italy

Francesco Cucca

68. Karolinska Institutet, Department of Medical Epidemiology and Biostatistics, Stockholm, Sweden

Kamila Czene, Per Hall & Jingmei Li

69. MRC Integrative Epidemiology Unit, University of Bristol, Bristol, UK

George Davey Smith, Deborah A. Lawlor, Susan M. Ring & Nicholas J. Timpson

70. Population Health Science, Bristol Medical School, University of Bristol, Bristol, UK

George Davey Smith, Deborah A. Lawlor, Susan M. Ring & Nicholas J. Timpson

71. Department of Clinical Epidemiology, Leiden University Medical Center, Leiden, the Netherlands

Renée de Mutsert, Dennis O. Mook-Kanamori & Frits R. Rosendaal

72. Department of Epidemiology, Harvard T. H. Chan School of Public Health, Boston, MA, USA

Immaculata De Vivo, Frank Hu, Peter Kraft & Meir Stampfer

73. Channing Division of Network Medicine, Department of Medicine, Brigham and Women's Hospital and Harvard Medical School, Boston, MA, USA

Immaculata De Vivo, Frank Hu, David Hunter & Meir Stampfer

74. Division of Epidemiology & Community Health, University of Minnesota, Minneapolis, MN, USA

Ellen W. Demerath

75. Centre for Cancer Genetic Epidemiology, Department of Oncology, University of Cambridge, Cambridge, UK

Alison M. Dunning, Paul D. P. Pharoah & Douglas F. Easton

76. School of Life Sciences, University of Westminster, London, UK

Miriam Dwek

77. Department of Medical Epidemiology and Biostatistics, Karolinska Institutet, Stockholm, Sweden

Mikael Eriksson & Wei He

78. Population and Medical Genetics, Broad Institute, Cambridge, MA, USA

Tõnu Esko

79. Estonian Genome Center, Institute of Genomics, University of Tartu, Tartu, Estonia

Tõnu Esko, Reedik Mägi, Andres Metspalu, Lili Milani & Natalia Perjakova

80. David Geffen School of Medicine, Department of Medicine, Division of Hematology and Oncology, University of California at Los Angeles, Los Angeles, CA, USA

Peter A. Fasching

81. Survey Research Center, Institute for Social Research, Ann Arbor, MI, USA

Jessica D. Faul & David R. Weir

82. Translational Gerontology Branch, National Institute on Aging, Baltimore, MD, USA

Luigi Ferrucci & Toshiko Tanaka

83. Department of Epidemiology, Gillings School of Global Public Health, University of North Carolina, Chapel Hill, NC, USA

Nora Franceschini & Gerardo Heiss

84. Fundación Pública Galega de Medicina Xenómica, Instituto de Investigación Sanitaria de Santiago de Compostela (IDIS), Complejo Hospitalario Universitario de Santiago, SERGAS, Santiago de Compostela, Spain

Manuela Gago-Dominguez

85. Moores Cancer Center, University of California San Diego, La Jolla, CA, USA

Manuela Gago-Dominguez

86. Department of Medical Sciences, University of Trieste, Trieste, Italy

Massimo Mezzavilla & Brumat Marco

87. Research Unit of Molecular Epidemiology, Helmholtz Zentrum München–German Research Center for Environmental Health, Neuherberg, Germany
- Christian Gieger & Harald Grallert
88. Institute of Epidemiology II, Helmholtz Zentrum München–German Research Center for Environmental Health, Neuherberg, Germany
- Christian Gieger, Harald Grallert, Christa Meisinger, Annette Peters & Doris Stöckl
89. German Center for Diabetes Research (DZD), Neuherberg, Germany
- Christian Gieger, Harald Grallert & Annette Peters
90. Cancer Epidemiology Division, Cancer Council Victoria, Melbourne, Victoria, Australia
- Graham G. Giles, Roger L. Milne & Melissa C. Southey
91. Centre for Epidemiology and Biostatistics, Melbourne School of Population and Global Health, The University of Melbourne, Melbourne, Victoria, Australia
- Graham G. Giles, John L. Hopper & Roger L. Milne
92. Precision Medicine, School of Clinical Sciences at Monash Health, Monash University, Clayton, Victoria, Australia
- Graham G. Giles, Roger L. Milne & Melissa C. Southey
93. Icelandic Heart Association, Kopavogur, Iceland
- Vilmundur Gudnason & Albert V. Smith
94. Faculty of Medicine, University of Iceland, Reykjavik, Iceland
- Vilmundur Gudnason & Albert V. Smith

95. Cancer & Environment Group, Center for Research in Epidemiology and Population Health (CESP), INSERM, University Paris-Sud, University Paris-Saclay, Villejuif, France

Pascal Guénel & Thérèse Truong

96. Department of Preventive Medicine, Keck School of Medicine, University of Southern California, Los Angeles, CA, USA

Christopher A. Haiman

97. Institute of Environmental Medicine, Karolinska Institutet, Stockholm, Sweden

Niclas Håkansson & Alicja Wolk

98. Division of Medical Oncology, Department of Internal Medicine, University of Kentucky College of Medicine, Lexington, KY, USA

Chunyan He

99. The Cancer Prevention and Control Research Program, University of Kentucky Markey Cancer Center, Lexington, KY, USA

Chunyan He

100. Department of Nutrition, Harvard T. H. Chan School of Public Health, Boston, MA, USA

Frank Hu, David Hunter & Meir Stampfer

101. Department of Epidemiology, Harvard T. H. Chan School of Public Health, Boston, MA, USA

David Hunter

102. Broad Institute of Harvard and MIT, Cambridge, MA, USA

David Hunter

103. Department of Epidemiology, Erasmus MC, Rotterdam, The Netherlands

Mohammad A. Ikram & André G. Uitterlinden

104. Department of Internal Medicine, The Ohio State University, Columbus, OH, USA

Rebecca D. Jackson

105. Department of Epidemiology & Population Health, Stanford University School of Medicine, Stanford, CA, USA

Esther M. John & Allison W. Kurian

106. Department of Medicine, Division of Oncology, Stanford Cancer Institute, Stanford University School of Medicine, Stanford, CA, USA

Esther M. John & Allison W. Kurian

107. Hebrew SeniorLife Institute for Aging Research, Boston, MA, USA

David Karasik

108. Department of Epidemiology, School of Public Health, University of Michigan, Ann Arbor, MI, USA

Sharon L. R. Kardia, Jennifer A. Smith & Wei Zhao

109. Department of Medical Epidemiology and Biostatistics, Karolinska Institutet, Stockholm, Sweden

Robert Karlsson, Patrik K. E. Magnusson & Nancy L. Pedersen

110. Radiation Epidemiology Branch, Division of Cancer Epidemiology and Genetics, National Cancer Institute, Bethesda, MD, USA

Cari M. Kitahara & Martha Linet

111. Faculty of Medicine, University of Split, Split, Croatia

Ivana Kolcic

112. Division of Public Health Sciences, Fred Hutchinson Cancer Research Center, Seattle, WA, USA

Charles Kooperberg & Ulrike Peters

113. Department of Biostatistics, Harvard T. H. Chan School of Public Health, Boston, MA, USA

Peter Kraft

114. Department of Twin Research and Genetic Epidemiology, King's College London, London, UK

Genevieve LaChance, Massimo Mangino, Cristina Menni & Tim D. Spector

115. Laboratory of Epidemiology and Population Sciences, National Institute on Aging, Intramural Research Program, National Institutes of Health, Bethesda, MD, USA

Lenore J. Launer

116. Division of Reproductive Endocrinology and Infertility, Department of Obstetrics and Gynecology, Erasmus University Medical Center, Rotterdam, The Netherlands

Joop S. E. Laven

117. Epidemiology Program, University of Hawaii Cancer Center, Honolulu, HI, USA

Loic Le Marchand

118. Department of Molecular Medicine and Surgery, Karolinska Institutet, Stockholm, Sweden

Annika Lindblom

119. Department of Clinical Genetics, Karolinska University Hospital,
Stockholm, Sweden

Annika Lindblom

120. Department of Epidemiology, University of Washington, Seattle, WA,
USA

Sara Lindstrom

121. Department of Health Sciences Research, Mayo Clinic, Rochester,
MN, USA

Tricia Lindstrom & Christopher Scott

122. Center for Human Genetics, Division of Public Health Sciences, Wake
Forest School of Medicine, Wake Forest, NC, USA

YongMei Liu

123. Department of Epidemiology, Brown University, Providence, RI, USA

Simin Liu

124. Department of Medicine, Brown University, Providence, RI, USA

Simin Liu

125. NIHR Biomedical Research Centre at Guy's and St. Thomas'
Foundation Trust, London, UK

Massimo Mangino

126. Translational Cancer Research Area, University of Eastern Finland,
Kuopio, Finland

Arto Mannermaa

127. Institute of Clinical Medicine, Pathology and Forensic Medicine,
University of Eastern Finland, Kuopio, Finland

Arto Mannermaa

128. Biobank of Eastern Finland, Kuopio University Hospital, Kuopio,
Finland

Arto Mannermaa

129. QIMR Berghofer Medical Research Institute, Brisbane, Queensland,
Australia

Nicholas G. Martin, Sarah E. Medland & Jodie N. Painter

130. Central Hospital of Augsburg, MONICA/KORA Myocardial
Infarction Registry, Augsburg, Germany

Christa Meisinger

131. Institute of Human Genetics, Helmholtz Zentrum München, German
Research Center for Environmental Health, Neuherberg, Germany

Thomas Meitinger

132. Institute for Molecular Bioscience, The University of Queensland,
Brisbane, Queensland, Australia

Grant W. Montgomery

133. Department of Public Health and Primary Care, Leiden University
Medical Center, Leiden, the Netherlands

Dennis O. Mook-Kanamori

134. Department of Laboratory Medicine and Pathobiology, University of
Toronto, Toronto, Ontario, Canada

Anna M. Mulligan

135. Laboratory Medicine Program, University Health Network, Toronto, Ontario, Canada

Anna M. Mulligan

136. The Institute of Medical Sciences, Aberdeen Biomedical Imaging Centre, University of Aberdeen, Aberdeen, UK

Alison Murray

137. Laboratory of Neurogenetics, National Institute on Aging, National Institutes of Health, Bethesda, MD, USA

Mike A. Nalls

138. Department of Epidemiology, University of Pittsburgh, Pittsburgh, PA, USA

Anne Newman

139. Department of Medicine, University of Pittsburgh, Pittsburgh, PA, USA

Anne Newman

140. Department of Internal Medicine, Section of Gerontology and Geriatrics, Leiden University Medical Center, Leiden, the Netherlands

Raymond Noordam

141. Centre for Genomics and Personalised Health, School of Biomedical Sciences, Faculty of Health, Queensland University of Technology, Brisbane, Queensland, Australia

Dale R. Nyholt

142. Department of Epidemiology, Gillings School of Global Public Health and UNC Lineberger Comprehensive Cancer Center, University of North Carolina at Chapel Hill, Chapel Hill, NC, USA

Andrew F. Olshan & Melissa A. Troester

143. Department of Population Science, American Cancer Society, Atlanta, GA, USA

Alpa V. Patel & Lauren R. Teras

144. Faculty of Medicine, University of Split, Split, Croatia

Ozren Polasek

145. Gen-Info Ltd, Zagreb, Croatia

Ozren Polasek

146. Quantify Research, Stockholm, Sweden

Iffat Rahman

147. Clalit National Cancer Control Center, Carmel Medical Center and Technion Faculty of Medicine, Haifa, Israel

Gad Rennert & Hedy S. Rennert

148. Women's Health Initiative Branch, National Heart, Lung, and Blood Institute, Bethesda, MD, USA

Jacques Rossouw

149. Department of Oncology, University Hospital of Larissa, Larissa, Greece

Emmanouil Saloustros

150. Epidemiology Branch, National Institute of Environmental Health Sciences, NIH, Research Triangle Park, NC, USA

Dale P. Sandler

151. School of Cancer & Pharmaceutical Sciences, Comprehensive Cancer Centre, Guy's Campus, King's College London, London, UK

Elinor J. Sawyer

152. Department of Biostatistics, Boston University School of Public Health, Boston, MA, USA

Chloé Sarnowski & Kathryn L. Lunetta

153. National Institute on Aging, Intramural Research Program, Baltimore, MD, USA

David Schlessinger

154. Division of Molecular Pathology, The Netherlands Cancer Institute – Antoni van Leeuwenhoek Hospital, Amsterdam, The Netherlands

Marjanka K. Schmidt

155. Division of Psychosocial Research and Epidemiology, The Netherlands Cancer Institute – Antoni van Leeuwenhoek Hospital, Amsterdam, The Netherlands

Marjanka K. Schmidt

156. Division of Genetics and Epidemiology, The Institute of Cancer Research, London, UK

Minouk J. Schoemaker & Anthony J. Swerdlow

157. Centre for Cardiovascular Sciences, Queen's Medical Research Institute, University of Edinburgh, Royal Infirmary of Edinburgh, Edinburgh, UK

Katharina E. Schraut

158. Division of Population and Health Genomics, University of Dundee, Dundee, UK

Blair H. Smith

159. Department of Clinical Pathology, The University of Melbourne,
Melbourne, Victoria, Australia

Melissa C. Southey

160. Population Oncology, BC Cancer, Vancouver, British Columbia,
Canada

John J. Spinelli

161. School of Population and Public Health, University of British
Columbia, Vancouver, BC, Canada

John J. Spinelli

162. Department of Obstetrics and Gynaecology, Campus Grosshadern,
Ludwig-Maximilians-Universität, Munich, Germany

Doris Stöckl

1. Institute of Genetic Epidemiology, Helmholtz Zentrum München – German Research Center for Environmental Health, Neuherberg, Germany

Konstantin Strauch

2. Chair of Genetic Epidemiology, IBE, Faculty of Medicine, LMU Munich, Munich, Germany

Konstantin Strauch

3. Institute of Medical Biostatistics, Epidemiology and Informatics (IMBEI), University Medical Center, Johannes Gutenberg University, Mainz, Germany

Konstantin Strauch

4. Division of Breast Cancer Research, The Institute of Cancer Research, London, UK

Anthony J. Swerdlow

5. Institute for Community Medicine, University Medicine Greifswald, Greifswald, Germany

Alexander Teumer & Henry Völzke

6. Faculty of Medicine, School of Health Sciences, University of Iceland, Reykjavik, Iceland

Unnur Þorsteinsdóttir & Kari Stefansson

7. Department of Health Science Research, Division of Epidemiology, Mayo Clinic, Rochester, MN, USA

Celine M. Vachon

8. Interfaculty Institute for Genetics and Functional Genomics,
University Medicine Greifswald, Greifswald, Germany

Uwe Völker

9. Department of Medicine, Internal Medicine, Lausanne University Hospital and University of Lausanne, Lausanne, Switzerland

Peter Vollenweider

10. Biostatistics and Computational Biology Branch, National Institute of Environmental Health Sciences, NIH, Research Triangle Park, NC, USA

Clarice R. Weinberg

11. Department of Internal Medicine, Division of Endocrinology, Leiden University Medical Center, Leiden, the Netherlands

Ko Willems van Dijk

12. Einthoven Laboratory for Experimental Vascular Medicine, Leiden University Medical Center, Leiden, the Netherlands

Ko Willems van Dijk

13. Department of Human Genetics, Leiden University Medical Center, Leiden, the Netherlands

Ko Willems van Dijk

14. Department of Endocrinology, University Medical Center Groningen, University of Groningen, Groningen, The Netherlands

Bruce H. R. Wolffenduttle

15. Department of Surgical Sciences, Uppsala University, Uppsala, Sweden

Alicja Wolk

16. Department of Obstetrics and Gynecology, University Medicine
Greifswald, Greifswald, Germany

Marek Zygmunt

17. School of Public Health, Peking University Health Science Center,
Beijing, P.R. China

Liming Li

18. Peking University Center for Public Health and Epidemic
Preparedness & Response, Beijing, P.R. China

Liming Li

19. Oncode Institute, Utrecht, The Netherlands

Lude Franke

20. Department of Public Health and Primary Care, University of
Cambridge, Cambridge, UK

Stephen Burgess

21. MRC Biostatistics Unit, University of Cambridge, Cambridge, UK

Stephen Burgess

22. Department of Genetics, University Medical Centre Utrecht, Utrecht,
The Netherlands

Patrick Deelen

23. Laboratory of Reproductive Biology, The Juliane Marie Centre for
Women, Children and Reproduction, Copenhagen University Hospital
and Faculty of Health and Medical Sciences, University of
Copenhagen, Copenhagen, Denmark

Claus Yding Andersen

24. Division of Cancer Epidemiology, German Cancer Research Center (DKFZ), Heidelberg, Germany

Jenny Chang-Claude

25. Cancer Epidemiology Group, University Cancer Center Hamburg (UCCH), University Medical Center Hamburg-Eppendorf, Hamburg, Germany

Jenny Chang-Claude

26. NHLBI's and Boston University's Framingham Heart Study, Framingham, MA, USA

Kathryn L. Lunetta & Joanne M. Murabito

27. Boston University School of Medicine, Department of Medicine, Section of General Internal Medicine, Boston, MA, USA

Joanne M. Murabito

28. Department of Paediatrics, University of Cambridge, Cambridge, UK

Ken K. Ong

Authors

1. Katherine S. Ruth

[View author publications](#)

You can also search for this author in [PubMed](#) [Google Scholar](#)

2. Felix R. Day

[View author publications](#)

You can also search for this author in [PubMed](#) [Google Scholar](#)

3. Jazib Hussain

[View author publications](#)

You can also search for this author in [PubMed](#) [Google Scholar](#)

4. Ana Martínez-Marchal

[View author publications](#)

You can also search for this author in [PubMed](#) [Google Scholar](#)

5. Catherine E. Aiken

[View author publications](#)

You can also search for this author in [PubMed](#) [Google Scholar](#)

6. Ajuna Azad

[View author publications](#)

You can also search for this author in [PubMed](#) [Google Scholar](#)

7. Deborah J. Thompson

[View author publications](#)

You can also search for this author in [PubMed](#) [Google Scholar](#)

8. Lucie Knoblochova

[View author publications](#)

You can also search for this author in [PubMed](#) [Google Scholar](#)

9. Hironori Abe

[View author publications](#)

You can also search for this author in [PubMed](#) [Google Scholar](#)

10. Jane L. Tarry-Adkins

[View author publications](#)

You can also search for this author in [PubMed](#) [Google Scholar](#)

11. Javier Martin Gonzalez
[View author publications](#)

You can also search for this author in [PubMed](#) [Google Scholar](#)

12. Pierre Fontanillas
[View author publications](#)

You can also search for this author in [PubMed](#) [Google Scholar](#)

13. Annique Claringbould
[View author publications](#)

You can also search for this author in [PubMed](#) [Google Scholar](#)

14. Olivier B. Bakker
[View author publications](#)

You can also search for this author in [PubMed](#) [Google Scholar](#)

15. Patrick Sulem
[View author publications](#)

You can also search for this author in [PubMed](#) [Google Scholar](#)

16. Robin G. Walters
[View author publications](#)

You can also search for this author in [PubMed](#) [Google Scholar](#)

17. Chikashi Terao
[View author publications](#)

You can also search for this author in [PubMed](#) [Google Scholar](#)

18. Sandra Turon
[View author publications](#)

You can also search for this author in [PubMed](#) [Google Scholar](#)

19. Momoko Horikoshi

[View author publications](#)

You can also search for this author in [PubMed](#) [Google Scholar](#)

20. Kuang Lin

[View author publications](#)

You can also search for this author in [PubMed](#) [Google Scholar](#)

21. N. Charlotte Onland-Moret

[View author publications](#)

You can also search for this author in [PubMed](#) [Google Scholar](#)

22. Aditya Sankar

[View author publications](#)

You can also search for this author in [PubMed](#) [Google Scholar](#)

23. Emil Peter Thrane Hertz

[View author publications](#)

You can also search for this author in [PubMed](#) [Google Scholar](#)

24. Pascal N. Timshel

[View author publications](#)

You can also search for this author in [PubMed](#) [Google Scholar](#)

25. Vallari Shukla

[View author publications](#)

You can also search for this author in [PubMed](#) [Google Scholar](#)

26. Rehannah Borup

[View author publications](#)

You can also search for this author in [PubMed](#) [Google Scholar](#)

27. Kristina W. Olsen

[View author publications](#)

You can also search for this author in [PubMed](#) [Google Scholar](#)

28. Paula Aguilera

[View author publications](#)

You can also search for this author in [PubMed](#) [Google Scholar](#)

29. Mònica Ferrer-Roda

[View author publications](#)

You can also search for this author in [PubMed](#) [Google Scholar](#)

30. Yan Huang

[View author publications](#)

You can also search for this author in [PubMed](#) [Google Scholar](#)

31. Stasa Stankovic

[View author publications](#)

You can also search for this author in [PubMed](#) [Google Scholar](#)

32. Paul R. H. J. Timmers

[View author publications](#)

You can also search for this author in [PubMed](#) [Google Scholar](#)

33. Thomas U. Ahearn

[View author publications](#)

You can also search for this author in [PubMed](#) [Google Scholar](#)

34. Behrooz Z. Alizadeh

[View author publications](#)

You can also search for this author in [PubMed](#) [Google Scholar](#)

35. Elnaz Naderi

[View author publications](#)

You can also search for this author in [PubMed](#) [Google Scholar](#)

36. Irene L. Andrulis

[View author publications](#)

You can also search for this author in [PubMed](#) [Google Scholar](#)

37. Alice M. Arnold

[View author publications](#)

You can also search for this author in [PubMed](#) [Google Scholar](#)

38. Kristan J. Aronson

[View author publications](#)

You can also search for this author in [PubMed](#) [Google Scholar](#)

39. Annelie Augustinsson

[View author publications](#)

You can also search for this author in [PubMed](#) [Google Scholar](#)

40. Stefania Bandinelli

[View author publications](#)

You can also search for this author in [PubMed](#) [Google Scholar](#)

41. Caterina M. Barbieri

[View author publications](#)

You can also search for this author in [PubMed](#) [Google Scholar](#)

42. Robin N. Beaumont

[View author publications](#)

You can also search for this author in [PubMed](#) [Google Scholar](#)

43. Heiko Becher

[View author publications](#)

You can also search for this author in [PubMed](#) [Google Scholar](#)

44. Matthias W. Beckmann

[View author publications](#)

You can also search for this author in [PubMed](#) [Google Scholar](#)

45. Stefania Benonisdottir

[View author publications](#)

You can also search for this author in [PubMed](#) [Google Scholar](#)

46. Sven Bergmann

[View author publications](#)

You can also search for this author in [PubMed](#) [Google Scholar](#)

47. Murielle Bochud

[View author publications](#)

You can also search for this author in [PubMed](#) [Google Scholar](#)

48. Eric Boerwinkle

[View author publications](#)

You can also search for this author in [PubMed](#) [Google Scholar](#)

49. Stig E. Bojesen

[View author publications](#)

You can also search for this author in [PubMed](#) [Google Scholar](#)

50. Manjeet K. Bolla

[View author publications](#)

You can also search for this author in [PubMed](#) [Google Scholar](#)

51. Dorret I. Boomsma

[View author publications](#)

You can also search for this author in [PubMed](#) [Google Scholar](#)

52. Nicholas Bowker

[View author publications](#)

You can also search for this author in [PubMed](#) [Google Scholar](#)

53. Jennifer A. Brody

[View author publications](#)

You can also search for this author in [PubMed](#) [Google Scholar](#)

54. Linda Broer

[View author publications](#)

You can also search for this author in [PubMed](#) [Google Scholar](#)

55. Julie E. Buring

[View author publications](#)

You can also search for this author in [PubMed](#) [Google Scholar](#)

56. Archie Campbell

[View author publications](#)

You can also search for this author in [PubMed](#) [Google Scholar](#)

57. Harry Campbell

[View author publications](#)

You can also search for this author in [PubMed](#) [Google Scholar](#)

58. Jose E. Castelao

[View author publications](#)

You can also search for this author in [PubMed](#) [Google Scholar](#)

59. Eulalia Catamo

[View author publications](#)

You can also search for this author in [PubMed](#) [Google Scholar](#)

60. Stephen J. Chanock

[View author publications](#)

You can also search for this author in [PubMed](#) [Google Scholar](#)

61. Georgia Chenevix-Trench

[View author publications](#)

You can also search for this author in [PubMed](#) [Google Scholar](#)

62. Marina Ciullo

[View author publications](#)

You can also search for this author in [PubMed](#) [Google Scholar](#)

63. Tanguy Corre

[View author publications](#)

You can also search for this author in [PubMed](#) [Google Scholar](#)

64. Fergus J. Couch

[View author publications](#)

You can also search for this author in [PubMed](#) [Google Scholar](#)

65. Angela Cox

[View author publications](#)

You can also search for this author in [PubMed](#) [Google Scholar](#)

66. Laura Crisponi

[View author publications](#)

You can also search for this author in [PubMed](#) [Google Scholar](#)

67. Simon S. Cross

[View author publications](#)

You can also search for this author in [PubMed](#) [Google Scholar](#)

68. Francesco Cucca

[View author publications](#)

You can also search for this author in [PubMed](#) [Google Scholar](#)

69. Kamila Czene

[View author publications](#)

You can also search for this author in [PubMed](#) [Google Scholar](#)

70. George Davey Smith

[View author publications](#)

You can also search for this author in [PubMed](#) [Google Scholar](#)

71. Eco J. C. N. de Geus

[View author publications](#)

You can also search for this author in [PubMed](#) [Google Scholar](#)

72. Renée de Mutsert

[View author publications](#)

You can also search for this author in [PubMed](#) [Google Scholar](#)

73. Immaculata De Vivo

[View author publications](#)

You can also search for this author in [PubMed](#) [Google Scholar](#)

74. Ellen W. Demerath

[View author publications](#)

You can also search for this author in [PubMed](#) [Google Scholar](#)

75. Joe Dennis

[View author publications](#)

You can also search for this author in [PubMed](#) [Google Scholar](#)

76. Alison M. Dunning

[View author publications](#)

You can also search for this author in [PubMed](#) [Google Scholar](#)

77. Miriam Dwek

[View author publications](#)

You can also search for this author in [PubMed](#) [Google Scholar](#)

78. Mikael Eriksson

[View author publications](#)

You can also search for this author in [PubMed](#) [Google Scholar](#)

79. Tõnu Esko

[View author publications](#)

You can also search for this author in [PubMed](#) [Google Scholar](#)

80. Peter A. Fasching

[View author publications](#)

You can also search for this author in [PubMed](#) [Google Scholar](#)

81. Jessica D. Faul

[View author publications](#)

You can also search for this author in [PubMed](#) [Google Scholar](#)

82. Luigi Ferrucci

[View author publications](#)

You can also search for this author in [PubMed](#) [Google Scholar](#)

83. Nora Franceschini

[View author publications](#)

You can also search for this author in [PubMed](#) [Google Scholar](#)

84. Timothy M. Frayling

[View author publications](#)

You can also search for this author in [PubMed](#) [Google Scholar](#)

85. Manuela Gago-Dominguez

[View author publications](#)

You can also search for this author in [PubMed](#) [Google Scholar](#)

86. Massimo Mezzavilla

[View author publications](#)

You can also search for this author in [PubMed](#) [Google Scholar](#)

87. Montserrat García-Closas

[View author publications](#)

You can also search for this author in [PubMed](#) [Google Scholar](#)

88. Christian Gieger

[View author publications](#)

You can also search for this author in [PubMed](#) [Google Scholar](#)

89. Graham G. Giles

[View author publications](#)

You can also search for this author in [PubMed](#) [Google Scholar](#)

90. Harald Grallert

[View author publications](#)

You can also search for this author in [PubMed](#) [Google Scholar](#)

91. Daniel F. Gudbjartsson
[View author publications](#)

You can also search for this author in [PubMed](#) [Google Scholar](#)

92. Vilmundur Gudnason
[View author publications](#)

You can also search for this author in [PubMed](#) [Google Scholar](#)

93. Pascal Guénel
[View author publications](#)

You can also search for this author in [PubMed](#) [Google Scholar](#)

94. Christopher A. Haiman
[View author publications](#)

You can also search for this author in [PubMed](#) [Google Scholar](#)

95. Niclas Håkansson
[View author publications](#)

You can also search for this author in [PubMed](#) [Google Scholar](#)

96. Per Hall
[View author publications](#)

You can also search for this author in [PubMed](#) [Google Scholar](#)

97. Caroline Hayward
[View author publications](#)

You can also search for this author in [PubMed](#) [Google Scholar](#)

98. Chunyan He
[View author publications](#)

You can also search for this author in [PubMed](#) [Google Scholar](#)

99. Wei He

[View author publications](#)

You can also search for this author in [PubMed](#) [Google Scholar](#)

100. Gerardo Heiss

[View author publications](#)

You can also search for this author in [PubMed](#) [Google Scholar](#)

101. Miya K. Høffding

[View author publications](#)

You can also search for this author in [PubMed](#) [Google Scholar](#)

102. John L. Hopper

[View author publications](#)

You can also search for this author in [PubMed](#) [Google Scholar](#)

103. Jouke J. Hottenga

[View author publications](#)

You can also search for this author in [PubMed](#) [Google Scholar](#)

104. Frank Hu

[View author publications](#)

You can also search for this author in [PubMed](#) [Google Scholar](#)

105. David Hunter

[View author publications](#)

You can also search for this author in [PubMed](#) [Google Scholar](#)

106. Mohammad A. Ikram

[View author publications](#)

You can also search for this author in [PubMed](#) [Google Scholar](#)

107. Rebecca D. Jackson

[View author publications](#)

1. You can also search for this author in [PubMed](#) [Google Scholar](#)

2. Micaella D. R. Joaquim
[View author publications](#)

You can also search for this author in [PubMed](#) [Google Scholar](#)

3. Esther M. John
[View author publications](#)

You can also search for this author in [PubMed](#) [Google Scholar](#)

4. Peter K. Joshi
[View author publications](#)

You can also search for this author in [PubMed](#) [Google Scholar](#)

5. David Karasik
[View author publications](#)

You can also search for this author in [PubMed](#) [Google Scholar](#)

6. Sharon L. R. Kardia
[View author publications](#)

You can also search for this author in [PubMed](#) [Google Scholar](#)

7. Christiana Kartsonaki
[View author publications](#)

You can also search for this author in [PubMed](#) [Google Scholar](#)

8. Robert Karlsson
[View author publications](#)

You can also search for this author in [PubMed](#) [Google Scholar](#)

9. Cari M. Kitahara

[View author publications](#)

You can also search for this author in [PubMed](#) [Google Scholar](#)

10. Ivana Kolcic

[View author publications](#)

You can also search for this author in [PubMed](#) [Google Scholar](#)

11. Charles Kooperberg

[View author publications](#)

You can also search for this author in [PubMed](#) [Google Scholar](#)

12. Peter Kraft

[View author publications](#)

You can also search for this author in [PubMed](#) [Google Scholar](#)

13. Allison W. Kurian

[View author publications](#)

You can also search for this author in [PubMed](#) [Google Scholar](#)

14. Zoltan Katalik

[View author publications](#)

You can also search for this author in [PubMed](#) [Google Scholar](#)

15. Martina La Bianca

[View author publications](#)

You can also search for this author in [PubMed](#) [Google Scholar](#)

16. Genevieve LaChance

[View author publications](#)

You can also search for this author in [PubMed](#) [Google Scholar](#)

17. Claudia Langenberg

[View author publications](#)

You can also search for this author in [PubMed](#) [Google Scholar](#)

18. Lenore J. Launer

[View author publications](#)

You can also search for this author in [PubMed](#) [Google Scholar](#)

19. Joop S. E. Laven

[View author publications](#)

You can also search for this author in [PubMed](#) [Google Scholar](#)

20. Deborah A. Lawlor

[View author publications](#)

You can also search for this author in [PubMed](#) [Google Scholar](#)

21. Loic Le Marchand

[View author publications](#)

You can also search for this author in [PubMed](#) [Google Scholar](#)

22. Jingmei Li

[View author publications](#)

You can also search for this author in [PubMed](#) [Google Scholar](#)

23. Annika Lindblom

[View author publications](#)

You can also search for this author in [PubMed](#) [Google Scholar](#)

24. Sara Lindstrom

[View author publications](#)

You can also search for this author in [PubMed](#) [Google Scholar](#)

25. Tricia Lindstrom

[View author publications](#)

You can also search for this author in [PubMed](#) [Google Scholar](#)

26. Martha Linet

[View author publications](#)

You can also search for this author in [PubMed](#) [Google Scholar](#)

27. YongMei Liu

[View author publications](#)

You can also search for this author in [PubMed](#) [Google Scholar](#)

28. Simin Liu

[View author publications](#)

You can also search for this author in [PubMed](#) [Google Scholar](#)

29. Jian'an Luan

[View author publications](#)

You can also search for this author in [PubMed](#) [Google Scholar](#)

30. Reedik Mägi

[View author publications](#)

You can also search for this author in [PubMed](#) [Google Scholar](#)

31. Patrik K. E. Magnusson

[View author publications](#)

You can also search for this author in [PubMed](#) [Google Scholar](#)

32. Massimo Mangino

[View author publications](#)

You can also search for this author in [PubMed](#) [Google Scholar](#)

33. Arto Mannermaa

[View author publications](#)

You can also search for this author in [PubMed](#) [Google Scholar](#)

34. Brumat Marco

[View author publications](#)

You can also search for this author in [PubMed](#) [Google Scholar](#)

35. Jonathan Marten

[View author publications](#)

You can also search for this author in [PubMed](#) [Google Scholar](#)

36. Nicholas G. Martin

[View author publications](#)

You can also search for this author in [PubMed](#) [Google Scholar](#)

37. Hamdi Mbarek

[View author publications](#)

You can also search for this author in [PubMed](#) [Google Scholar](#)

38. Barbara McKnight

[View author publications](#)

You can also search for this author in [PubMed](#) [Google Scholar](#)

39. Sarah E. Medland

[View author publications](#)

You can also search for this author in [PubMed](#) [Google Scholar](#)

40. Christa Meisinger

[View author publications](#)

You can also search for this author in [PubMed](#) [Google Scholar](#)

41. Thomas Meitinger

[View author publications](#)

You can also search for this author in [PubMed](#) [Google Scholar](#)

42. Cristina Menni

[View author publications](#)

You can also search for this author in [PubMed](#) [Google Scholar](#)

43. Andres Metspalu

[View author publications](#)

You can also search for this author in [PubMed](#) [Google Scholar](#)

44. Lili Milani

[View author publications](#)

You can also search for this author in [PubMed](#) [Google Scholar](#)

45. Roger L. Milne

[View author publications](#)

You can also search for this author in [PubMed](#) [Google Scholar](#)

46. Grant W. Montgomery

[View author publications](#)

You can also search for this author in [PubMed](#) [Google Scholar](#)

47. Dennis O. Mook-Kanamori

[View author publications](#)

You can also search for this author in [PubMed](#) [Google Scholar](#)

48. Antonella Mulas

[View author publications](#)

You can also search for this author in [PubMed](#) [Google Scholar](#)

49. Anna M. Mulligan

[View author publications](#)

You can also search for this author in [PubMed](#) [Google Scholar](#)

50. Alison Murray

[View author publications](#)

You can also search for this author in [PubMed](#) [Google Scholar](#)

51. Mike A. Nalls

[View author publications](#)

You can also search for this author in [PubMed](#) [Google Scholar](#)

52. Anne Newman

[View author publications](#)

You can also search for this author in [PubMed](#) [Google Scholar](#)

53. Raymond Noordam

[View author publications](#)

You can also search for this author in [PubMed](#) [Google Scholar](#)

54. Teresa Nutile

[View author publications](#)

You can also search for this author in [PubMed](#) [Google Scholar](#)

55. Dale R. Nyholt

[View author publications](#)

You can also search for this author in [PubMed](#) [Google Scholar](#)

56. Andrew F. Olshan

[View author publications](#)

You can also search for this author in [PubMed](#) [Google Scholar](#)

57. Håkan Olsson

[View author publications](#)

You can also search for this author in [PubMed](#) [Google Scholar](#)

58. Jodie N. Painter

[View author publications](#)

You can also search for this author in [PubMed](#) [Google Scholar](#)

59. Alpa V. Patel

[View author publications](#)

You can also search for this author in [PubMed](#) [Google Scholar](#)

60. Nancy L. Pedersen

[View author publications](#)

You can also search for this author in [PubMed](#) [Google Scholar](#)

61. Natalia Perjakova

[View author publications](#)

You can also search for this author in [PubMed](#) [Google Scholar](#)

62. Annette Peters

[View author publications](#)

You can also search for this author in [PubMed](#) [Google Scholar](#)

63. Ulrike Peters

[View author publications](#)

You can also search for this author in [PubMed](#) [Google Scholar](#)

64. Paul D. P. Pharoah

[View author publications](#)

You can also search for this author in [PubMed](#) [Google Scholar](#)

65. Ozren Polasek

[View author publications](#)

You can also search for this author in [PubMed](#) [Google Scholar](#)

66. Eleonora Porcu

[View author publications](#)

You can also search for this author in [PubMed](#) [Google Scholar](#)

67. Bruce M. Psaty

[View author publications](#)

You can also search for this author in [PubMed](#) [Google Scholar](#)

68. Iffat Rahman

[View author publications](#)

You can also search for this author in [PubMed](#) [Google Scholar](#)

69. Gad Rennert

[View author publications](#)

You can also search for this author in [PubMed](#) [Google Scholar](#)

70. Hedy S. Rennert

[View author publications](#)

You can also search for this author in [PubMed](#) [Google Scholar](#)

71. Paul M. Ridker

[View author publications](#)

You can also search for this author in [PubMed](#) [Google Scholar](#)

72. Susan M. Ring

[View author publications](#)

You can also search for this author in [PubMed](#) [Google Scholar](#)

73. Antonietta Robino

[View author publications](#)

You can also search for this author in [PubMed](#) [Google Scholar](#)

74. Lynda M. Rose

[View author publications](#)

You can also search for this author in [PubMed](#) [Google Scholar](#)

75. Frits R. Rosendaal

[View author publications](#)

You can also search for this author in [PubMed](#) [Google Scholar](#)

76. Jacques Rossouw

[View author publications](#)

You can also search for this author in [PubMed](#) [Google Scholar](#)

77. Igor Rudan

[View author publications](#)

You can also search for this author in [PubMed](#) [Google Scholar](#)

78. Rico Rueedi

[View author publications](#)

You can also search for this author in [PubMed](#) [Google Scholar](#)

79. Daniela Ruggiero

[View author publications](#)

You can also search for this author in [PubMed](#) [Google Scholar](#)

80. Cinzia F. Sala

[View author publications](#)

You can also search for this author in [PubMed](#) [Google Scholar](#)

81. Emmanouil Saloustros

[View author publications](#)

You can also search for this author in [PubMed](#) [Google Scholar](#)

82. Dale P. Sandler

[View author publications](#)

1. You can also search for this author in [PubMed](#) [Google Scholar](#)

2. Serena Sanna

[View author publications](#)

You can also search for this author in [PubMed](#) [Google Scholar](#)

3. Elinor J. Sawyer

[View author publications](#)

You can also search for this author in [PubMed](#) [Google Scholar](#)

4. Chloé Sarnowski

[View author publications](#)

You can also search for this author in [PubMed](#) [Google Scholar](#)

5. David Schlessinger

[View author publications](#)

You can also search for this author in [PubMed](#) [Google Scholar](#)

6. Marjanka K. Schmidt

[View author publications](#)

You can also search for this author in [PubMed](#) [Google Scholar](#)

7. Minouk J. Schoemaker

[View author publications](#)

You can also search for this author in [PubMed](#) [Google Scholar](#)

8. Katharina E. Schraut

[View author publications](#)

You can also search for this author in [PubMed](#) [Google Scholar](#)

9. Christopher Scott

[View author publications](#)

You can also search for this author in [PubMed](#) [Google Scholar](#)

10. Saleh Shekari

[View author publications](#)

You can also search for this author in [PubMed](#) [Google Scholar](#)

11. Amruta Shrikhande

[View author publications](#)

You can also search for this author in [PubMed](#) [Google Scholar](#)

12. Albert V. Smith

[View author publications](#)

You can also search for this author in [PubMed](#) [Google Scholar](#)

13. Blair H. Smith

[View author publications](#)

You can also search for this author in [PubMed](#) [Google Scholar](#)

14. Jennifer A. Smith

[View author publications](#)

You can also search for this author in [PubMed](#) [Google Scholar](#)

15. Rossella Sorice

[View author publications](#)

You can also search for this author in [PubMed](#) [Google Scholar](#)

16. Melissa C. Southey

[View author publications](#)

You can also search for this author in [PubMed](#) [Google Scholar](#)

17. Tim D. Spector

[View author publications](#)

You can also search for this author in [PubMed](#) [Google Scholar](#)

18. John J. Spinelli

[View author publications](#)

You can also search for this author in [PubMed](#) [Google Scholar](#)

19. Meir Stampfer

[View author publications](#)

You can also search for this author in [PubMed](#) [Google Scholar](#)

20. Doris Stöckl

[View author publications](#)

You can also search for this author in [PubMed](#) [Google Scholar](#)

21. Joyce B. J. van Meurs

[View author publications](#)

You can also search for this author in [PubMed](#) [Google Scholar](#)

22. Konstantin Strauch

[View author publications](#)

You can also search for this author in [PubMed](#) [Google Scholar](#)

23. Unnur Styrkarsdottir

[View author publications](#)

You can also search for this author in [PubMed](#) [Google Scholar](#)

24. Anthony J. Swerdlow

[View author publications](#)

You can also search for this author in [PubMed](#) [Google Scholar](#)

25. Toshiko Tanaka

[View author publications](#)

You can also search for this author in [PubMed](#) [Google Scholar](#)

26. Lauren R. Teras

[View author publications](#)

You can also search for this author in [PubMed](#) [Google Scholar](#)

27. Alexander Teumer

[View author publications](#)

You can also search for this author in [PubMed](#) [Google Scholar](#)

28. Unnur Þorsteinsdóttir

[View author publications](#)

You can also search for this author in [PubMed](#) [Google Scholar](#)

29. Nicholas J. Timpson

[View author publications](#)

You can also search for this author in [PubMed](#) [Google Scholar](#)

30. Daniela Toniolo

[View author publications](#)

You can also search for this author in [PubMed](#) [Google Scholar](#)

31. Michela Traglia

[View author publications](#)

You can also search for this author in [PubMed](#) [Google Scholar](#)

32. Melissa A. Troester

[View author publications](#)

You can also search for this author in [PubMed](#) [Google Scholar](#)

33. Thérèse Truong

[View author publications](#)

You can also search for this author in [PubMed](#) [Google Scholar](#)

34. Jessica Tyrrell

[View author publications](#)

You can also search for this author in [PubMed](#) [Google Scholar](#)

35. André G. Uitterlinden

[View author publications](#)

You can also search for this author in [PubMed](#) [Google Scholar](#)

36. Sheila Ulivi

[View author publications](#)

You can also search for this author in [PubMed](#) [Google Scholar](#)

37. Celine M. Vachon

[View author publications](#)

You can also search for this author in [PubMed](#) [Google Scholar](#)

38. Veronique Vitart

[View author publications](#)

You can also search for this author in [PubMed](#) [Google Scholar](#)

39. Uwe Völker

[View author publications](#)

You can also search for this author in [PubMed](#) [Google Scholar](#)

40. Peter Vollenweider

[View author publications](#)

You can also search for this author in [PubMed](#) [Google Scholar](#)

41. Henry Völzke

[View author publications](#)

You can also search for this author in [PubMed](#) [Google Scholar](#)

42. Qin Wang

[View author publications](#)

You can also search for this author in [PubMed](#) [Google Scholar](#)

43. Nicholas J. Wareham

[View author publications](#)

You can also search for this author in [PubMed](#) [Google Scholar](#)

44. Clarice R. Weinberg

[View author publications](#)

You can also search for this author in [PubMed](#) [Google Scholar](#)

45. David R. Weir

[View author publications](#)

You can also search for this author in [PubMed](#) [Google Scholar](#)

46. Amber N. Wilcox

[View author publications](#)

You can also search for this author in [PubMed](#) [Google Scholar](#)

47. Ko Willems van Dijk

[View author publications](#)

You can also search for this author in [PubMed](#) [Google Scholar](#)

48. Gonneke Willemsen

[View author publications](#)

You can also search for this author in [PubMed](#) [Google Scholar](#)

49. James F. Wilson

[View author publications](#)

You can also search for this author in [PubMed](#) [Google Scholar](#)

50. Bruce H. R. Wolffentuttel

[View author publications](#)

You can also search for this author in [PubMed](#) [Google Scholar](#)

51. Alicja Wolk

[View author publications](#)

You can also search for this author in [PubMed](#) [Google Scholar](#)

52. Andrew R. Wood

[View author publications](#)

You can also search for this author in [PubMed](#) [Google Scholar](#)

53. Wei Zhao

[View author publications](#)

You can also search for this author in [PubMed](#) [Google Scholar](#)

54. Marek Zygmunt

[View author publications](#)

You can also search for this author in [PubMed](#) [Google Scholar](#)

55. Zhengming Chen

[View author publications](#)

You can also search for this author in [PubMed](#) [Google Scholar](#)

56. Liming Li

[View author publications](#)

You can also search for this author in [PubMed](#) [Google Scholar](#)

57. Lude Franke

[View author publications](#)

You can also search for this author in [PubMed](#) [Google Scholar](#)

58. Stephen Burgess

[View author publications](#)

You can also search for this author in [PubMed](#) [Google Scholar](#)

59. Patrick Deelen

[View author publications](#)

You can also search for this author in [PubMed](#) [Google Scholar](#)

60. Tune H. Pers

[View author publications](#)

You can also search for this author in [PubMed](#) [Google Scholar](#)

61. Marie Louise Grøndahl

[View author publications](#)

You can also search for this author in [PubMed](#) [Google Scholar](#)

62. Claus Yding Andersen

[View author publications](#)

You can also search for this author in [PubMed](#) [Google Scholar](#)

63. Anna Pujol

[View author publications](#)

You can also search for this author in [PubMed](#) [Google Scholar](#)

64. Andres J. Lopez-Contreras

[View author publications](#)

You can also search for this author in [PubMed](#) [Google Scholar](#)

65. Jeremy A. Daniel

[View author publications](#)

You can also search for this author in [PubMed](#) [Google Scholar](#)

66. Kari Stefansson

[View author publications](#)

You can also search for this author in [PubMed](#) [Google Scholar](#)

67. Jenny Chang-Claude

[View author publications](#)

You can also search for this author in [PubMed](#) [Google Scholar](#)

68. Yvonne T. van der Schouw

[View author publications](#)

You can also search for this author in [PubMed](#) [Google Scholar](#)

69. Kathryn L. Lunetta

[View author publications](#)

You can also search for this author in [PubMed](#) [Google Scholar](#)

70. Daniel I. Chasman

[View author publications](#)

You can also search for this author in [PubMed](#) [Google Scholar](#)

71. Douglas F. Easton

[View author publications](#)

You can also search for this author in [PubMed](#) [Google Scholar](#)

72. Jenny A. Visser

[View author publications](#)

You can also search for this author in [PubMed](#) [Google Scholar](#)

73. Susan E. Ozanne

[View author publications](#)

You can also search for this author in [PubMed](#) [Google Scholar](#)

74. Satoshi H. Namekawa

[View author publications](#)

You can also search for this author in [PubMed](#) [Google Scholar](#)

75. Petr Solc

[View author publications](#)

You can also search for this author in [PubMed](#) [Google Scholar](#)

76. Joanne M. Murabito

[View author publications](#)

You can also search for this author in [PubMed](#) [Google Scholar](#)

77. Ken K. Ong

[View author publications](#)

You can also search for this author in [PubMed](#) [Google Scholar](#)

78. Eva R. Hoffmann

[View author publications](#)

You can also search for this author in [PubMed](#) [Google Scholar](#)

79. Anna Murray

[View author publications](#)

You can also search for this author in [PubMed](#) [Google Scholar](#)

80. Ignasi Roig

[View author publications](#)

You can also search for this author in [PubMed](#) [Google Scholar](#)

81. John R. B. Perry

[View author publications](#)

You can also search for this author in [PubMed](#) [Google Scholar](#)

Consortia

Biobank-based Integrative Omics Study (BIOS) Consortium

eQTLGen Consortium

The Biobank Japan Project

China Kadoorie Biobank Collaborative Group

kConFab Investigators

The LifeLines Cohort Study

The InterAct consortium

23andMe Research Team

Contributions

All authors reviewed the original and revised manuscripts. Leads on manuscript writing: K.S.R., F.R.D., E.R.H., Anna Murray, I. Roig, J.R.B.P. Central statistical genetics analysis team: K.S.R., F.R.D., Anna Murray, J.R.B.P. Animal model working group: J.H., A.M.-M., C.E.A., L.K., H.A., J.L.T., J.M.G., S.T., E.P.T.H., M.F., Y.H., A.S., A. Pujol, A.J.L., J.A.D., S.E.O., S.H.N., P. Solc, E.R.H., I. Roig. Human oocyte expression working group: A. Azad, V.S., R.B., K.W.O., M.K.H., M.L.G., C.Y., E.R.H. Sample collection, genotyping, phenotyping and individual study analysis: K.S.R., F.R.D., D.J.T., P.F., A. Claringbould, O.B.B., P. Sulem, R.G.W., C.T., M.H., K.L., N.O., P.N.T., P.A., S. Stankovic, P.R.H.J.T., T.U.A., B.Z.A., E.N., I.L.A., A.M.A., K.J.A., A. Augustinsson, S. Bandinelli, C.M.B., R.N.B., H.B., M.W.B., S. Benonisdottir, S. Bergmann, M.B., E.B., S.E.B., M.K.B., D.I.B., N.B., J.A.B., L.B., J.E.B., A. Campbell, H.C., J.E.C., E.C., S.J.C., G.C., M.C., T.C., F.J.C., A. Cox, L.C., S.S.C., F.C., K.C., G.D., E.J.C.N.D., R.D., I.D., E.W.D., J.D., A.M.D., M.D., M.E., T.E., P.A.F., J.D.F., L. Ferrucci, N.F., T.M.F., M.G.-D., M. Mezzavilla, M.G.-C., C.G., G.G.G., H.G., D.F.G., V.G., P.G., C.A.H., N.H., P.H., C. Hayward, C. He, W.H., G.H., J.L.H., J.J.H., F.H., D.H., M.A.I., R.D.J., M.D.R.J., E.M.J., P.K.J., D.K., S.L.R.K., C. Kartsonaki, R.K., C.M.K., I.K., C. Kooperberg, P.K., A.W.K., Z.K., M. La Bianca, G.L., C.L., L.J.L., J.S.E.L., D.A.L., L.L.M., J. Li, A.L., S. Lindstrom, T.L., M. Linet, Y.L., S. Liu, J. Luan, R.M.,

P.K.E.M., M. Mangino, A. Mannermaa, B. Marco, J. Marten, N.G.M., H.M., B.McK., S.E.M., C. Meisinger, T.M., C. Menni, A. Metspalu, L.M., R.L.M., G.W.M., D.O.M., A. Mulas, A.M.M., Alison Murray, M.A.N., A.N., R.N., T.N., D.R.N., A.F.O., H.O., J.N.P., A.V.P., N.L.P., N.P., A. Peters, U.P., P.D.P.P., O.P., E. Porcu, B.M.P., I. Rahman, G.R., H.S.R., P.M.R., S.M.R., A.R., L.M.R., F.R.R., J.R., I. Rudan, R.R., D.R., C.F.S., E.S., D.P.S., S. Sanna, E.J.S., C. Sarnowski, D. Schlessinger, M.K.S., M.J.S., K.E.S., C. Scott, S. Shekari, A.V.S., B.H.S., J.A.S., R.S., M.C.S., T.D.S., J.J.S., M.S., D. Stöckl, J.B.J.v.M., K. Strauch, U.S., A.J.S., T. Tanaka, L.R.T., A.T., U.P., N.J.T., D.T., M.T., M.A.T., T. Truong, J.T., A.G.U., S.U., C.M.V., V.V., U.V., P.V., H.V., Q.W., N.J.W., C.R.W., D.R.W., A.N.W., K.W., G.W., J.F.W., B.H.R.W., A.W., A.R.W., W.Z., M.Z., Z.C., L. Li, L. Franke, S. Burgess, P.D., T.H.P., K. Stefansson, J.C., Y.T.v.d.S., K.L.L., D.I.C., D.F.E., J.A.V., J.M.M., K.K.O., Anna Murray, J.R.B.P.

Corresponding authors

Correspondence to [Eva R. Hoffmann](#) or [Anna Murray](#) or [Ignasi Roig](#) or [John R. B. Perry](#).

Ethics declarations

Competing interests

Full individual study and author disclosures can be found in the Supplementary Information.

Additional information

Peer review information *Nature* thanks Heng-Yu Fan and the other, anonymous, reviewer(s) for their contribution to the peer review of this work.

Publisher's note Springer Nature remains neutral with regard to jurisdictional claims in published maps and institutional affiliations.

Extended data figures and tables

Extended Data Fig. 1 Overview of ovarian reserve and follicular activity across reproductive life.

a, Key processes involved in follicular activity from fetal development to menopause showing the numbers of oocytes at each stage. **b**, Summary of key biological pathways involved in follicular activity and their relationship to stage of reproductive life. Follicles, consisting of oocytes and surrounding granulosa cells, are formed in utero and maintained as resting primordial follicles in the cortex, constituting the ovarian reserve. Follicles are sequentially recruited from the ovarian reserve at a rate of several hundred per month in childhood, peaking at around 900 per month at approximately 15 years of age. Following recruitment, follicles grow by mitotic division of granulosa cells and expansion of oocyte volume for almost six months until meiosis is reinitiated at ovulation and the mature oocyte is released into the oviduct. Waves of atresia (follicle death) accompany developmental transitions and growing follicles are continuously induced to undergo cell death such that, typically, only a single follicle matures to ovulate each month. As ovarian reserve declines, the rate of follicle recruitment decreases, but the preovulatory follicles continue to produce substantial amounts of oestrogen, while other important hormones such as anti-Müllerian hormone and inhibin-B decline, leading to upregulation of the hypothalamus–pituitary gonadal axis.

Extended Data Fig. 2 Overview of performed analyses.

Analyses are separated into those intended to lead to understanding of biological mechanisms, and those that lead to insights into population genetics or epidemiology.

Extended Data Fig. 3 Consistency of effect estimates across analysis methods and strata.

a–c, Comparison of effect estimates from: **a**, Cox proportional hazards regression in UK Biobank with linear regression effect estimates from the overall meta-analysis ('Effect full meta-analysis'); **b**, Cox proportional hazards regression in UK Biobank with linear regression effect estimates from the meta-analysis excluding UK Biobank ('Effect 1KG+BCAC'); **c**, linear regression in UK Biobank with linear regression effect estimates from the meta-analysis excluding UK Biobank ('Effect 1KG+BCAC'). **d–g**, Comparison of linear regression effect estimates from: **d**, UK Biobank GWAS versus the meta-analysis of 1000 Genomes imputed studies; **e**, UK Biobank GWAS versus meta-analysis of samples from the Breast Cancer Association Consortium (BCAC); **f**, meta-analysis of BCAC samples versus the meta-analysis of 1000 Genomes imputed studies; **g**, 23andMe replication analysis (rescaled) versus overall meta-analysis. HR, hazard ratio from Cox proportional hazards model; *r*, Pearson correlation coefficient; blue line is $y = x$ for reference. Note: *P* values $<1 \times 10^{-300}$ are shown as 1×10^{-300} .

Extended Data Fig. 4 Deviation from additive effects and distribution of estimated heritability across chromosomes.

a–d, Genome-wide significant signals showing departure from an additive model. We tested the identified signals for departure from an additive allelic model. **a**, rs11668344 shows no deviation from an additive allelic model, **b**, **c**, rs11670032 (**b**) and rs28416520 (**c**) show deviation from the additive allelic model and a recessive effect. **d**, rs75770066 shows a heterozygote effect. The mean and 95% confidence interval around the mean estimate are shown for each genotype. The expected mean ANM for the heterozygotes is the average of the mean ANM in the homozygote groups. The dashed orange line shows the effect estimate by genotype from linear regression based on an additive allelic model. Estimated ANM for each genotype was calculated as constant from regression model + number alleles × effect estimate from regression model. The dashed grey line indicates the additive

effect estimate by genotype from a model adjusting for the dominance deviation effect of the heterozygote group (solid grey line). All regression models were adjusted for centre, genotyping chip and genetic principal components. dom dev, dominance deviation. e, The percentage of the total heritability explained that was attributable to each chromosome (observed heritability) is compared with the expected proportion calculated on the basis of chromosome size. The heritability of ANM was not uniformly distributed across chromosomes in proportion to their size. The X chromosome did not explain more heritability than expected given its size, but chromosome 19 explained 2.36% (1.98–2.75) of the trait variance—greater than the individual contributions of nearly all larger chromosomes (weighted average for chromosomes 1–18: 1.7%, s.e 0.2%) and about 2.5 times more than expected given its size. This was partially attributable to a single locus at 19q13 which explained about 0.75% of trait variance and where we mapped six independent signals (Supplementary Table 2). The dashed line shows the mean ratio of expected to observed heritability across all chromosomes. Chromosome size was estimated based on the number of genetic variants.

[Source data](#)

[**Extended Data Fig. 5 Gene co-regulation networks for age at menopause genes with MCM8 highlighted.**](#)

a, Gene co-regulation network for genes relating to age at menopause. Nodes indicate genes that are either in a *cis* region from the GWAS or have been prioritized by Downstreamer; edges indicate a co-regulation relationship with a *z*-score > 4. Co-regulation is defined as the Pearson correlation between genes in a scaled eigenvector matrix derived from a multi-tissue gene network⁷². *cis* genes are defined as genes that are within 300 kb of a GWAS top hit for age at menopause. *trans* genes are defined as having been prioritized by Downstreamer's co-regulation analysis and not being within 300 kb of a GWAS top hit. Downstreamer prioritizes genes by associating the gene *P* value profile of the GWAS (calculated using PASCAL⁷¹) to the co-regulation profile of each protein-coding gene. Only genes for which this association passes Bonferroni significance are shown as *trans* genes. Teal, *cis* genes; dark teal, *trans* genes; yellow, genes with a

first-degree relation to *MCM8*. **b**, Gene co-regulation network showing the genes that have a first-degree relationship with *MCM8* with a *z*-score > 4. Edge width indicates the *z*-score of the co-regulation relationship. Colours as in **a**, with the exception of yellow, as all genes have a first-degree relation to *MCM8*.

Extended Data Fig. 6 DNA damage response and repair pathways implicated in reproductive ageing in humans.

a, Consequences of replication stress annotated with genes involved that were within 300 kb of the ANM signals. **b**, Genes involved in downstream DNA damage response and repair pathways with those within 300 kb of an ANM signal shown in blue. A full list of genes involved in DNA damage response and apoptosis annotated with genome-wide signals for ANM is provided in Supplementary Table 19. MRN, *MRN–MRE11–RAD50–NBS1* complex; RPA, replication protein A including a subunit encoded by *RPA1*; RFC, replication factor C including a subunit encoded by *RFC1*; 9-1-1, *RAD9–HUS1–RAD1* complex.

Extended Data Fig. 7 Cluster plot of expression of consensus genes identified from the genome-wide analyses in germ cells across different developmental stages.

Genes were selected from the GWAS signals, based on in silico prioritization (Supplementary Table 5). Of the 283 consensus genes highlighted by the GWAS, 258 passed QC and were available in the expression dataset. Gene expression was measured in human fetal primordial germ cells^{84,85} and in oocytes and granulosa cells in adult follicles (dataset generated in this study). Plot shows *z*-scores, calculated by subtracting the mean TPM in all samples for a gene and dividing by the s.d. GC, granulosa cell; MII, meiosis II; PGC, primordial germ cell; Wks, weeks.

Extended Data Fig. 8 Relationship between decreased ovarian reserve and gene expression.

Open bar/dot groups: control maternal diet, normal ovarian reserve. Grey bar/dot groups: obesogenic maternal diet, reduced ovarian reserve. Dots, individual observations. Bar heights and error bars: mean \pm s.e.m. **a**, Ovarian follicular reserve in young adulthood in wild-type mice. Total follicles per mm³ ovarian tissue at 12 weeks. $n = 8$ biologically independent animals from different litters in each group. $P = 0.0091$. **b**, *Brskl* expression in the same mice, measured using qRT–PCR and expressed as average copy number. $P = 0.0001$. **c**, *Weel* expression in the same mice, measured using qRT–PCR and expressed as average copy number. $P = 0.0256$. **d**, *Dmc1* expression in the same mice, measured using qRT–PCR and expressed as average copy number. $P = 0.00001$. **e**, *Mapt* expression in the same mice, measured using qRT-PCR and expressed as average copy number. $P = 0.0378$. All panels, two-way ANOVA after correction for multiple hypothesis testing. * $P < 0.05$, ** $P < 0.01$, *** $P < 0.001$.

Extended Data Fig. 9 *Chek2* deletion increases reproductive lifespan in mouse.

a, Representative images of ovarian sections of 1.5- and 13.5-month-old wild-type (WT) and *Chek2*^{-/-} mice stained with PAS-haematoxylin. Primordial follicles (inset (i)), primary follicles (inset (ii)), secondary follicle (white arrow) and antral follicle (black arrow) are shown. Scale bars, 200 μ m. **b–e**, Number of follicles (by class and total) present in WT and *Chek2*^{-/-} mouse ovaries. **b**, **c**, 1.5 months old; **d**, **e**, 13.5 months old. Numbers in parentheses show the total number of ovaries analysed. **f**, Serum AMH (ng ml⁻¹) in 16–17-month-old *Chek2*^{-/-} mice. Numbers in parentheses show the number of mice assessed. **g–i**, Gonadotrophin stimulation of 13.5-month-old females. Numbers in parentheses show: **g**, the number of MII oocytes retrieved per female; **h**, the number of MII oocytes fertilized; and **i**, the number of fertilized oocytes assessed for blastocyst formation. **j**, Litter size of WT and *Chek2*^{-/-} females throughout the reproductive lifespan. Litter sizes from nine WT and five *Chek2*^{-/-} females are shown. Breeding cages contained one male and one female. Generalized linear model analysis showed maternal age effect, but no effect of genotype on litter sizes. **k**, Image of healthy pups born to 13 month-old

Chek2^{-/-} females. **b–i**, Two-sample *t*-test and Fisher's exact test were used to compare WT and *Chek2*^{-/-} for statistical significance: **P* < 0.05, ***P* < 0.025, ****P* < 0.001. All *P* values are two-sided. Error bars indicate s.e.m. For boxplots: centre line, median; box limits, IQR; whiskers, 1.5 × IQR (**b–g**). an, antral follicle; pri, primary follicle; P0, primordial follicle; sec, secondary follicle. Mouse strain: maintained on a mixed background, C57BL/6 129Sv, accession number BRC03481 at the RIKEN Bioresource Centre.

[Source data](#)

[Extended Data Fig. 10 Conditional knockout *Chek1* females are infertile due to requirement for *Chek1* during preimplantation embryo development.](#)

a, Schematic of generation of conditional knockout mouse model of *Chek1* (*Chek1* cKO) in the female germline using *Ddx4-Cre*. A similar approach was used for *Zp3-Cre*. **b**, In ovarian sections stained with H&E, we found follicles, corpora lutea (CL) and oocytes which contain nuclear structures (arrowheads, magnified right panels). These findings suggest that oestrus cycles and ovulation followed by corpus luteum formation are independent of *Chek1* disruption in oocytes in vivo. **c**, Litter size of *Chek1* cKO females. Three females older than 5 weeks of age were mated with C57BL/6J males. Five independent littermate females (F/+; Tg-/Tg-; F/F; Tg-/Tg-; or F/+, Tg+/Tg-) were used as *Chek1* controls (ctrl). While *Chek1* control females delivered normally, *Chek1* cKO females delivered no litters (Mann–Whitney test, ***P* = 0.0179). Thus, these results indicate that *CHEK1* is essential in the female germline. **d**, Litter size of *Chek1*-cKO and control females using the *Zp3-Cre* during follicular growth. Three-month-old control (*Chek1* F/F; *Chek1* ctrl, *n* = 4) and conditional knockout (*Chek1* F/F; *Chek1* cKO with *Zp3-Cre*, *n* = 4) were consecutively mated three times with wild-type (*Chek1*^{+/+}) males, and the number of live (left) and dead (right) pups was monitored. While *Chek1* ctrl females delivered a normal number of live pups, *Chek1* cKO females had only a reduced number of perinatally dead pups (Mann–Whitney *U*-test: ****P* < 0.001, ***P* < 0.01). Numbers in parentheses show the number of litters. **e**, The mean number of

all ovulated eggs (sum of MII oocytes and fertilized MII oocytes) per mouse with s.e.m. (Mann–Whitney *U*-test, $P = 0.126$). Each data point represents the number of eggs per mouse. Three- to five-month-old *Chek1* ctrl ($n = 3$) and *Chek1* cKO ($n = 5$) females were mated with wild-type (*Chek1*^{+/+}) males after pMSG + hCG stimulation. The number of ovulated eggs isolated 18 h after hCG stimulation and additional 10 h cultured in vitro was scored. The number of mice is shown in parentheses. **f**, The proportion of fertilized MII oocytes to all ovulated eggs with a binomial confidence interval (Fisher’s exact test, $*P = 0.012$; 95% CI 1.9–6.0; OR, 2.62). Numbers in parentheses show the total number of analysed eggs. **g**, The proportion of embryos that developed to blastocysts with binomial confidence interval (Fisher’s exact test, $***P < 0.0001$). Fertilized MII oocytes (zygotes) were isolated from females stimulated with pMSG + hCG 18 h after hCG administration and cultured in vitro for 96 h (approximately embryonic day (E)3.5) when development to blastocyst was scored. Data are pooled from four independent experiments. The number of embryos is shown in parentheses. **h**, Fertilized eggs from *Chek1* ctrl ($n = 18$) and *Chek1* cKO ($n = 13$) females were fixed and stained for DNA (DAPI). All fertilized eggs from both genotypes showed normal pronucleus formation. The data were pooled from two independent experiments. Asterisks, polar bodies. **i**, The majority of *Chek1* ctrl embryos formed blastocysts (**g**), but *Chek1* cKO embryos were arrested mainly at the 3–8-cell stages. Representative bright-field images are shown. **j**, Proportion of developmental stages 2 cell, 3–4 cell and 5–8 cell (Cochran–Armitage trend test, $**P = 0.0073$). *Chek1* ctrl and *Chek1* cKO zygotes were isolated from 13 *Chek1* ctrl and 6 *Chek1* cKO females stimulated with pMSG + hCG 18 h after hCG administration and cultured in vitro for 49 h. Embryos were fixed and stained for γ H2AX by immunofluorescence. DNA was visualized by DAPI (**l**). **k**, Proportion of embryos with genome fragmentation with binomial confidence interval (Fisher’s exact test, $***P < 0.0001$). Data are pooled from two independent experiments. The number of embryos is shown in parentheses. **l**, *Chek1* ctrl and *Chek1* cKO zygotes (**j**, **k**) were fixed and stained for γ H2AX (magenta) by immunofluorescence. DNA (grey) was visualized by DAPI. Arrows, genome fragments; asterisks, polar bodies. These findings suggest that maternally expressed *Chek1* is critical for genome integrity protection during first divisions of preimplantation embryos in mice. All P values are two sided. For boxplots: centre line,

median; box limits, IQR; whiskers, $1.5 \times$ IQR. Strains: C57BL/6-FVB mixed background for **a–c** (*Chek1* cKO, *Ddx4-Cre*); C57BL6-CD1 mixed background (*Chek1* cKO, *Zp3-Cre*) for **d–l**.

[Source data](#)

Extended Data Fig. 11 Extended reproductive lifespan in females carrying an extra copy of *Chek1* (*sChek1*).

a, mRNA expression levels of *Chek1* in oocytes; numbers in parentheses show the number of mice stimulated for retrieval of oocytes. **b**, Representative images of ovarian sections from 1.5- and 13.5-month-old wild-type (WT) and *sChek1* mice stained with PAS-haematoxylin. Primordial follicles (inset (i)), primary follicles (inset (ii)), secondary follicle (white arrow) and antral follicle (black arrow) are shown. Scale bars, 200 μ m. **c–f**, Numbers of follicles (by class and total) in WT and *sChek1* littermates: **c**, **d**, 1.5 months old; **e**, **f**, 13.5 months old. Numbers in parentheses show the total number of ovaries analysed. **g–j**, MII oocytes retrieved in response to pMSG and hCG (**g**), proportion of euploid oocytes (**h**), proportion fertilized (**i**) and proportion developed to blastocysts (**j**) at different ages of WT and *sChek1* mice. Numbers in parentheses show: **g**, the number of female mice stimulated for retrieval of oocytes; **h**, the number of oocytes assessed for aneuploidy; **i**, the number of MII oocytes fertilized; and **j**, the number of fertilized oocytes assessed for blastocyst development. **k**, Proportion of live births relative to transferred embryos from in vitro fertilized oocytes from aged mice (16 months); numbers in parentheses show the number of embryos transferred. **l**, Healthy pups born to 16-month-old *sChek1* females after IVF. **m**, Litter sizes from F2 females or males from aged *sChek1* females after IVF treatment in **k**, compared to females of equivalent ages that were naturally breeding. Note that for natural breeding there were two females and one male per breeding cage, whereas F2 cages contained a single male and one female. Therefore, litter sizes are an underestimate for the IVF-conceived pups. **n**, Litter sizes of WT and *sChek1* females throughout their reproductive lifespan. Data are from six breeding cages, three for each genotype. Each breeding cage contained one WT male and two females that were either WT or *sChek1*. Generalized linear model analysis showed maternal age effect, but no effect

of genotype on litter sizes. **a–k**, Two-sample *t*-test and Fisher's exact test were used to compare WT and *sChek1* for statistical significance: * $P < 0.05$, ** $P < 0.025$, *** $P < 0.001$. All *P*-values are two sided. Error bars indicate s.e.m. For boxplots: centre line, median; box limits, IQR; whiskers, $1.5 \times$ IQR (**c–g, m**). NB, natural breeding; F2-f, F2 female; F2-m, F2 male. Mouse strain: inbred from mixed background C57BL/6 129Sv.

[Source data](#)

Supplementary information

[Supplementary Information](#)

This file contains Supplementary Results, Supplementary References and Supplementary Notes (acknowledgments, sources of funding, disclosures and consortium membership).

[Reporting Summary](#)

[Supplementary Tables](#)

This file contains Supplementary Tables 1-26 and a contents page.

Source data

[Source Data Fig. 2](#)

[Source Data Fig. 3](#)

[Source Data Extended Data Fig. 4](#)

[Source Data Extended Data Fig. 9](#)

[Source Data Extended Data Fig. 10](#)

[Source Data Extended Data Fig. 11](#)

Rights and permissions

[Reprints and Permissions](#)

About this article



Check for
updates

Cite this article

Ruth, K.S., Day, F.R., Hussain, J. *et al.* Genetic insights into biological mechanisms governing human ovarian ageing. *Nature* **596**, 393–397 (2021). <https://doi.org/10.1038/s41586-021-03779-7>

[Download citation](#)

- Received: 24 August 2020
- Accepted: 29 June 2021
- Published: 04 August 2021
- Issue Date: 19 August 2021
- DOI: <https://doi.org/10.1038/s41586-021-03779-7>

Comments

By submitting a comment you agree to abide by our [Terms](#) and [Community Guidelines](#). If you find something abusive or that does not comply with our terms or guidelines please flag it as inappropriate.

[Access through your institution](#)
[Change institution](#)
[Buy or subscribe](#)

Associated Content

[Genomic analysis identifies variants that can predict the timing of menopause](#)

- Krina T. Zondervan

News & Views 04 Aug 2021

[Genetics of female reproductive longevity](#)

- Anna Kriebs

Research Highlight 18 Aug 2021

Advertisement

This article was downloaded by **calibre** from <https://www.nature.com/articles/s41586-021-03779-7>

- Article
- [Published: 04 August 2021](#)

Deficient H2A.Z deposition is associated with genesis of uterine leiomyoma

- [Davide G. Berta](#) ORCID: [orcid.org/0000-0002-0847-998X^{1,2 na1}](https://orcid.org/0000-0002-0847-998X),
- [Heli Kuisma](#) ORCID: [orcid.org/0000-0002-9816-3777^{1,2 na1}](https://orcid.org/0000-0002-9816-3777),
- [Niko Välimäki](#) ORCID: [orcid.org/0000-0001-9200-9560^{1,2}](https://orcid.org/0000-0001-9200-9560),
- [Maritta Räisänen](#) ORCID: [orcid.org/0000-0002-2764-0433^{1,2}](https://orcid.org/0000-0002-2764-0433),
- [Maija Jäntti](#) ORCID: [orcid.org/0000-0001-7983-1998^{1,2}](https://orcid.org/0000-0001-7983-1998),
- [Annukka Pasanen](#)³,
- [Auli Karhu](#) ORCID: [orcid.org/0000-0002-7927-0796^{1,2}](https://orcid.org/0000-0002-7927-0796),
- [Jaana Kaukomaa](#) ORCID: [orcid.org/0000-0003-1183-4943^{1,2}](https://orcid.org/0000-0003-1183-4943),
- [Aurora Taira](#) ORCID: [orcid.org/0000-0002-1179-8500^{1,2}](https://orcid.org/0000-0002-1179-8500),
- [Tatiana Cajuso](#) ORCID: [orcid.org/0000-0002-6354-5572^{1,2}](https://orcid.org/0000-0002-6354-5572),
- [Sanna Nieminen](#) ORCID: [orcid.org/0000-0001-7341-8692^{1,2}](https://orcid.org/0000-0001-7341-8692),
- [Rosa-Maria Penttinen](#)^{1,2},
- [Saija Ahonen](#)^{1,2},
- [Rainer Lehtonen](#) ORCID: [orcid.org/0000-0002-8343-0318^{1,2}](https://orcid.org/0000-0002-8343-0318),
- [Miika Mehine](#) ORCID: [orcid.org/0000-0003-0443-0625^{1,2}](https://orcid.org/0000-0003-0443-0625),
- [Pia Vahteristo](#) ORCID: [orcid.org/0000-0002-4615-3825^{1,2}](https://orcid.org/0000-0002-4615-3825),
- [Jyrki Jalkanen](#) ORCID: [orcid.org/0000-0001-7452-442X⁴](https://orcid.org/0000-0001-7452-442X),
- [Biswajyoti Sahu](#) ORCID: [orcid.org/0000-0001-6576-5440²](https://orcid.org/0000-0001-6576-5440),
- [Janne Ravantti](#)^{1,2},
- [Netta Mäkinen](#) ORCID: [orcid.org/0000-0003-0104-7794^{1,2}](https://orcid.org/0000-0003-0104-7794),
- [Kristiina Rajamäki](#) ORCID: [orcid.org/0000-0001-5151-1220^{1,2}](https://orcid.org/0000-0001-5151-1220),
- [Kimmo Palin](#) ORCID: [orcid.org/0000-0002-4621-6128^{1,2,5}](https://orcid.org/0000-0002-4621-6128),
- [Jussi Taipale](#) ORCID: [orcid.org/0000-0003-4204-0951²](https://orcid.org/0000-0003-4204-0951),

- [Oskari Heikinheimo](#) ORCID: [orcid.org/0000-0002-8671-130X⁶](https://orcid.org/0000-0002-8671-130X),
- [Ralf Bützow](#) ORCID: [orcid.org/0000-0003-4366-5099^{2,3}](https://orcid.org/0000-0003-4366-5099),
- [Eevi Kaasinen](#) ORCID: [orcid.org/0000-0002-1333-8049^{1,2}](https://orcid.org/0000-0002-1333-8049) &
- [Lauri A. Aaltonen](#) ORCID: [orcid.org/0000-0001-6839-4286^{1,2,5}](https://orcid.org/0000-0001-6839-4286)

[Nature](#) volume **596**, pages 398–403 (2021) [Cite this article](#)

- 2981 Accesses
- 63 Altmetric
- [Metrics details](#)

Subjects

- [Cancer epigenetics](#)
- [Cancer genomics](#)
- [Disease genetics](#)
- [Infertility](#)

Abstract

One in four women suffers from uterine leiomyomas (ULs)—benign tumours of the uterine wall, also known as uterine fibroids—at some point in premenopausal life. ULs can cause excessive bleeding, pain and infertility¹, and are a common cause of hysterectomy². They emerge through at least three distinct genetic drivers: mutations in *MED12* or *FH*, or genomic rearrangement of *HMG A2*³. Here we created genome-wide datasets, using DNA, RNA, assay for transposase-accessible chromatin (ATAC), chromatin immunoprecipitation (ChIP) and HiC chromatin immunoprecipitation (HiChIP) sequencing of primary tissues to profoundly understand the genesis of UL. We identified somatic mutations in genes encoding six members of the SRCAP histone-loading complex⁴, and found that germline mutations in the SRCAP members *YEATS4* and *ZNHIT1* predispose women to UL. Tumours bearing these mutations showed defective deposition of the histone variant H2A.Z. In ULs, H2A.Z

occupancy correlated positively with chromatin accessibility and gene expression, and negatively with DNA methylation, but these correlations were weak in tumours bearing SRCAP complex mutations. In these tumours, open chromatin emerged at transcription start sites where H2A.Z was lost, which was associated with upregulation of genes. Furthermore, *YEATS4* defects were associated with abnormal upregulation of bivalent embryonic stem cell genes, as previously shown in mice⁵. Our work describes a potential mechanism of tumorigenesis—epigenetic instability caused by deficient H2A.Z deposition—and suggests that ULs arise through an aberrant differentiation program driven by deranged chromatin, emanating from a small number of mutually exclusive driver mutations.

Access options

Subscribe to Journal

Get full journal access for 1 year

\$199.00

only \$3.90 per issue

[Subscribe](#)

All prices are NET prices.

VAT will be added later in the checkout.

Tax calculation will be finalised during checkout.

Rent or Buy article

Get time limited or full article access on ReadCube.

from \$8.99

[Rent or Buy](#)

All prices are NET prices.

Additional access options:

- [Log in](#)
- [Access through your institution](#)
- [Learn about institutional subscriptions](#)

Fig. 1: Mutations in SRCAP complex genes identified as a driver of UL.

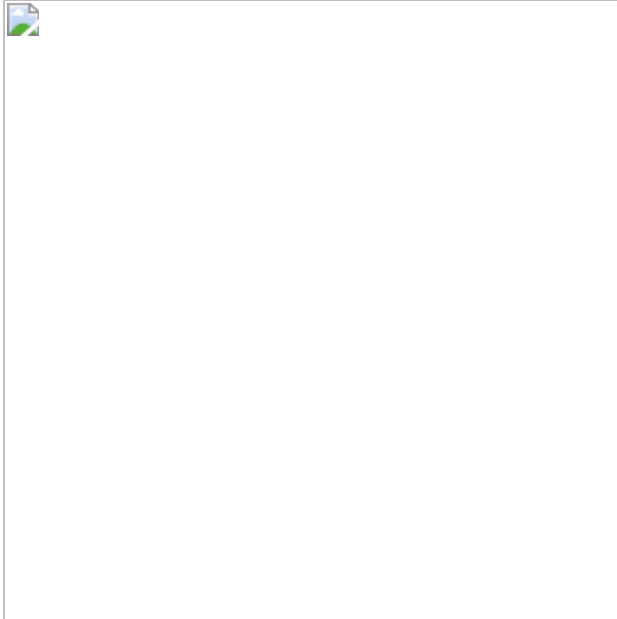


Fig. 2: H2A.Z binding on chromatin is changed in UL.

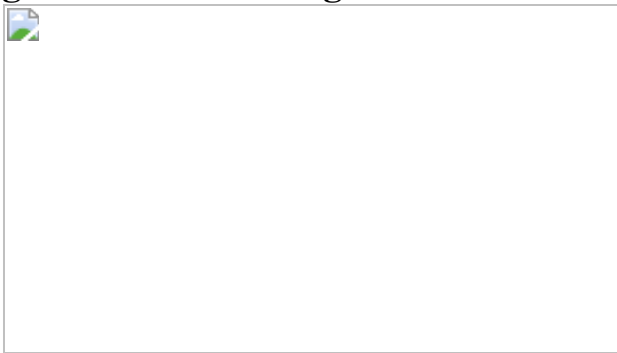


Fig. 3: Clues to the pathogenesis of UL derived from expression data.

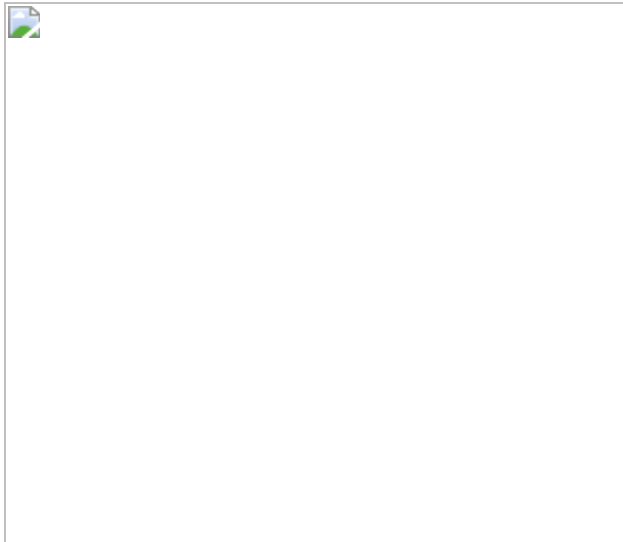
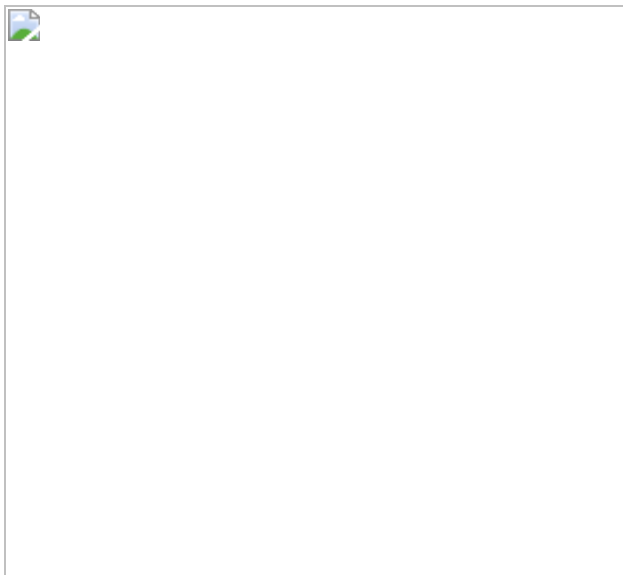


Fig. 4: Chromatin changes emerge at the locus containing *CBX2*, *CBX4* and *CBX8* in ULs.



Data availability

The peak level data used in the study are available for research use through Zenodo (<https://doi.org/10.5281/zenodo.4745433>). Genetic data presented in this manuscript have been deposited at the European Genome–phenome Archive (EGA; <https://www.ebi.ac.uk/ega/>) under accession number EGAS00001004499. A data access committee (DAC) has been established from two University of Helsinki representatives that are independent of the authors of the current study. See Supplementary Table [26](#) for EGA dataset

accession numbers. Requests for the data should be sent to the DAC via email (dac-finlandmyomastudy@helsinki.fi). The DAC ensures that the intended use of data as detailed in the request is compatible with the requirements of the European General Data Protection Regulation (GDPR), consistent with the consents given and otherwise ensures the protection of data subjects' rights as required by the GDPR. The DAC will always grant access to the data if the University is legally allowed to do so without infringing the rights and freedoms of data subjects. Subject to the requirements of the GDPR, the DAC grants access to the genetic data to non-commercial academic research on neoplasia and chromatin. Roadmap Epigenomics ChIP-seq and DNase-seq data

(<https://egg2.wustl.edu/roadmap/data/byFileType/peaks/consolidated/narrowPeak/>) provided in the LOLA extended and core databases were downloaded from <http://cloud.databio.org/regiondb/>. Chromatin states provided in mnemonics bed files by the Roadmap Epigenomics project were downloaded from

<https://egg2.wustl.edu/roadmap/data/byFileType/chromhmmSegmentations/ChmmModels/coreMarks/jointModel/final/>. GWAS cohort material was downloaded from <http://jenger.riken.jp/en/> (accessed on 2 September 2020) and <https://finngen.gitbook.io/documentation/v/r3/> (accessed on 2 September 2020). UK Biobank material access can be applied for at <https://www.ukbiobank.ac.uk/>. For RNA-seq, the reference annotation for GRCh37 was downloaded from Ensembl (ftp://ftp.ensembl.org/pub/release-75/gtf/homo_sapiens/) and for GRCh38 from GenBank (accession: GCA_000001405.15). For RNA-seq variant calling, the SNP and indel resources were downloaded from Broad institute (<https://console.cloud.google.com/storage/browser/gcp-public-data-broad-references/hg19/v0>). DAR annotation data are available from <http://homer.ucsd.edu/homer/data/genomes/hg19.v6.4.zip>. [Source data](#) are provided with this paper.

Code availability

Code for performing the analyses are available from Zenodo (<https://doi.org/10.5281/zenodo.4745433>).

References

1. 1.

Wallach, E. E., Buttram, V. C. Jr & Reiter, R. C. Uterine leiomyomata: etiology, symptomatology, and management. *Fertil. Steril.* **36**, 433–445 (1981).

[Google Scholar](#)

2. 2.

Gurusamy, K. S., Vaughan, J., Fraser, I. S., Best, L. M. J. & Richards, T. Medical therapies for uterine fibroids — a systematic review and network meta-analysis of randomised controlled trials. *PLoS ONE* **11**, e0149631 (2016).

[PubMed](#) [PubMed Central](#) [Google Scholar](#)

3. 3.

Mehine, M., Mäkinen, N., Heinonen, H.-R., Aaltonen, L. A. & Vahteristo, P. Genomics of uterine leiomyomas: insights from high-throughput sequencing. *Fertil. Steril.* **102**, 621–629 (2014).

[CAS](#) [PubMed](#) [PubMed Central](#) [Google Scholar](#)

4. 4.

Giaimo, B. D., Ferrante, F., Herchenröther, A., Hake, S. B. & Borggrefe, T. The histone variant H2A.Z in gene regulation. *Epigenetics Chromatin* **12**, 37 (2019).

[PubMed](#) [PubMed Central](#) [Google Scholar](#)

5. 5.

Hsu, C.-C. et al. Gas41 links histone acetylation to H2A.Z deposition and maintenance of embryonic stem cell identity. *Cell Discov.* **4**, 28 (2018).

[PubMed](#) [PubMed Central](#) [Google Scholar](#)

6. 6.

Baird, D. D., Dunson, D. B., Hill, M. C., Cousins, D. & Schectman, J. M. High cumulative incidence of uterine leiomyoma in black and white women: ultrasound evidence. *Am. J. Obstet. Gynecol.* **188**, 100–107 (2003).

[PubMed](#) [PubMed Central](#) [Google Scholar](#)

7. 7.

Okolo, S. Incidence, aetiology and epidemiology of uterine fibroids. *Best Pract. Res. Clin. Obstet. Gynaecol.* **22**, 571–588 (2008).

[PubMed](#) [PubMed Central](#) [Google Scholar](#)

8. 8.

Bertsch, E. et al. *MEDI2* and *HMGA2* mutations: two independent genetic events in uterine leiomyoma and leiomyosarcoma. *Mod. Pathol.* **27**, 1144–1153 (2014).

[CAS](#) [PubMed](#) [PubMed Central](#) [Google Scholar](#)

9. 9.

Lehtonen, R. et al. Biallelic inactivation of fumarate hydratase (FH) occurs in nonsyndromic uterine leiomyomas but is rare in other tumors. *Am. J. Pathol.* **164**, 17–22 (2004).

[CAS](#) [PubMed](#) [PubMed Central](#) [Google Scholar](#)

10. 10.

Hua, S. et al. Genomic analysis of estrogen cascade reveals histone variant H2A.Z associated with breast cancer progression. *Mol. Syst. Biol.* **4**, 188 (2008).

[PubMed](#) [PubMed Central](#) [Google Scholar](#)

11. 11.

Duncan, D. S., McWilliam, P., Tighe, O., Parle-McDermott, A. & Croke, D. T. Gene expression differences between the microsatellite instability (MIN) and chromosomal instability (CIN) phenotypes in colorectal cancer revealed by high-density cDNA array hybridization. *Oncogene* **21**, 3253–3257 (2002).

[CAS](#) [PubMed](#) [PubMed Central](#) [Google Scholar](#)

12. 12.

Yang, B. et al. H2A.Z regulates tumorigenesis, metastasis and sensitivity to cisplatin in intrahepatic cholangiocarcinoma. *Int. J. Oncol.* **52**, 1235–1245 (2018).

[CAS](#) [PubMed](#) [PubMed Central](#) [Google Scholar](#)

13. 13.

Vardabasso, C. et al. Histone variant H2A.Z.2 mediates proliferation and drug sensitivity of malignant melanoma. *Mol. Cell* **59**, 75–88 (2015).

[CAS](#) [PubMed](#) [PubMed Central](#) [Google Scholar](#)

14. 14.

Hsu, C.-C. et al. Recognition of histone acetylation by the GAS41 YEATS domain promotes H2A.Z deposition in non-small cell lung cancer. *Genes Dev.* **32**, 58–69 (2018).

[CAS](#) [PubMed](#) [PubMed Central](#) [Google Scholar](#)

15. 15.

Bellucci, L., Dalvai, M., Kocanova, S., Moutahir, F. & Bystricky, K. Activation of p21 by HDAC inhibitors requires acetylation of H2A.Z. *PLoS ONE* **8**, e54102 (2013).

[ADS](#) [CAS](#) [PubMed](#) [PubMed Central](#) [Google Scholar](#)

16. 16.

Ku, M. et al. H2A.Z landscapes and dual modifications in pluripotent and multipotent stem cells underlie complex genome regulatory functions. *Genome Biol.* **13**, R85 (2012).

[CAS](#) [PubMed](#) [PubMed Central](#) [Google Scholar](#)

17. 17.

Tomlinson, I. P. M. et al. Germline mutations in *FH* predispose to dominantly inherited uterine fibroids, skin leiomyomata and papillary renal cell cancer. *Nat. Genet.* **30**, 406–410 (2002).

[CAS](#) [PubMed](#) [PubMed Central](#) [Google Scholar](#)

18. 18.

Takahashi, D. et al. Quantitative regulation of histone variant H2A.Z during cell cycle by ubiquitin proteasome system and SUMO-targeted ubiquitin ligases. *Biosci. Biotechnol. Biochem.* **81**, 1557–1560 (2017).

[CAS](#) [PubMed](#) [PubMed Central](#) [Google Scholar](#)

19. 19.

Roadmap Epigenomics Consortium et al. Integrative analysis of 111 reference human epigenomes. *Nature* **518**, 317–330 (2015).

[Google Scholar](#)

20. 20.

Ye, B. et al. Suppression of SRCAP chromatin remodelling complex and restriction of lymphoid lineage commitment by Pcid2. *Nat. Commun.* **8**, 1518 (2017).

[ADS](#) [PubMed](#) [PubMed Central](#) [Google Scholar](#)

21. 21.

Bowman, T. A., Wong, M. M., Cox, L. K., Baldassare, J. J. & Chrivia, J. C. Loss of H2A.Z is not sufficient to determine transcriptional activity of Snf2-related CBP activator protein or p400 complexes. *Int. J. Cell Biol.* **2011**, 715642 (2011).

[PubMed](#) [PubMed Central](#) [Google Scholar](#)

22. 22.

Slupianek, A., Yerrum, S., Safadi, F. F. & Monroy, M. A. The chromatin remodeling factor SRCAP modulates expression of prostate specific antigen and cellular proliferation in prostate cancer cells. *J. Cell. Physiol.* **224**, 369–375 (2010).

[CAS](#) [PubMed](#) [PubMed Central](#) [Google Scholar](#)

23. 23.

Murphy, K. E., Meng, F. W., Makowski, C. E. & Murphy, P. J. Genome-wide chromatin accessibility is restricted by ANP32E. *Nat. Commun.* **11**, 5063 (2020).

[ADS](#) [CAS](#) [PubMed](#) [PubMed Central](#) [Google Scholar](#)

24. 24.

Brunelle, M. et al. The histone variant H2A.Z is an important regulator of enhancer activity. *Nucleic Acids Res.* **43**, 9742–9756 (2015).

[CAS](#) [PubMed](#) [PubMed Central](#) [Google Scholar](#)

25. 25.

Andersson, S., Berman, D. M., Jenkins, E. P. & Russell, D. W. Deletion of steroid 5 α -reductase 2 gene in male pseudohermaphroditism. *Nature* **354**, 159–161 (1991).

[ADS](#) [CAS](#) [PubMed](#) [PubMed Central](#) [Google Scholar](#)

26. 26.

Bauman, D. R., Steckelbroeck, S., Williams, M. V., Peehl, D. M. & Penning, T. M. Identification of the major oxidative 3 α -hydroxysteroid dehydrogenase in human prostate that converts 5 α -androstane-3 α ,17 β -diol to 5 α -dihydrotestosterone: a potential therapeutic target for androgen-dependent disease. *Mol. Endocrinol.* **20**, 444–458 (2006).

[CAS](#) [PubMed](#) [PubMed Central](#) [Google Scholar](#)

27. 27.

Weihua, Z., Lathe, R., Warner, M. & Gustafsson, J.-A. An endocrine pathway in the prostate, ER β , AR, 5 α -androstane-3 β ,17 β -diol, and CYP7B1, regulates prostate growth. *Proc. Natl Acad. Sci. USA* **99**, 13589–13594 (2002).

[ADS](#) [PubMed](#) [PubMed Central](#) [Google Scholar](#)

28. 28.

Solomon, M. J., Strauss, F. & Varshavsky, A. A mammalian high mobility group protein recognizes any stretch of six A.T base pairs in duplex DNA. *Proc. Natl Acad. Sci. USA* **83**, 1276–1280 (1986).

[ADS](#) [CAS](#) [PubMed](#) [PubMed Central](#) [Google Scholar](#)

29. 29.

Fowler, C. B., Evers, D. L., O’Leary, T. J. & Mason, J. T. Antigen retrieval causes protein unfolding: evidence for a linear epitope model of recovered immunoreactivity. *J. Histochem. Cytochem.* **59**, 366–381 (2011).

[CAS](#) [PubMed](#) [PubMed Central](#) [Google Scholar](#)

30. 30.

Kidder, B. L., Hu, G. & Zhao, K. ChIP-seq: technical considerations for obtaining high-quality data. *Nat. Immunol.* **12**, 918–922 (2011).

[CAS](#) [PubMed](#) [PubMed Central](#) [Google Scholar](#)

31. 31.

Kim, J. & Kingston, R. E. The CBX family of proteins in transcriptional repression and memory. *J. Biosci.* **45**, 16 (2020).

[CAS](#) [PubMed](#) [PubMed Central](#) [Google Scholar](#)

32. 32.

Klauke, K. et al. Polycomb Cbx family members mediate the balance between haematopoietic stem cell self-renewal and differentiation. *Nat. Cell Biol.* **15**, 353–362 (2013).

[CAS](#) [PubMed](#) [PubMed Central](#) [Google Scholar](#)

33. 33.

George, J. W. et al. Integrated epigenome, exome, and transcriptome analyses reveal molecular subtypes and homeotic transformation in uterine fibroids. *Cell Rep.* **29**, 4069–4085.e6 (2019).

[CAS](#) [PubMed](#) [PubMed Central](#) [Google Scholar](#)

34. 34.

Sato, S. et al. SATB2 and NGR1: potential upstream regulatory factors in uterine leiomyomas. *J. Assist. Reprod. Genet.* **36**, 2385–2397 (2019).

[PubMed](#) [PubMed Central](#) [Google Scholar](#)

35. 35.

Papadopoulou, T., Kaymak, A., Sayols, S. & Richly, H. Dual role of Med12 in PRC1-dependent gene repression and ncRNA-mediated transcriptional activation. *Cell Cycle* **15**, 1479–1493 (2016).

[CAS](#) [PubMed](#) [PubMed Central](#) [Google Scholar](#)

36. 36.

Tyagi, M., Cheema, M. S., Dryhurst, D., Eskiw, C. H. & Ausió, J. Metformin alters H2A.Z dynamics and regulates androgen dependent prostate cancer progression. *Oncotarget* **9**, 37054–37068 (2018).

[PubMed](#) [PubMed Central](#) [Google Scholar](#)

37. 37.

Tseng, C.-H. Metformin use is associated with a lower risk of uterine leiomyoma in female type 2 diabetes patients. *Ther. Adv. Endocrinol. Metab.* <https://doi.org/10.1177/2042018819895159> (2019).

38. 38.

Gormley, G. J. et al. The effect of finasteride in men with benign prostatic hyperplasia. *N. Engl. J. Med.* **327**, 1185–1191 (1992).

[CAS](#) [PubMed](#) [PubMed Central](#) [Google Scholar](#)

39. 39.

Tate, J. G. et al. COSMIC: the catalogue of somatic mutations in cancer. *Nucleic Acids Res.* **47**, D941–D947 (2019).

[CAS](#) [PubMed](#) [Google Scholar](#)

40. 40.

Ikeda, H., Sone, M., Yamanaka, S. & Yamamoto, T. Structural and spatial chromatin features at developmental gene loci in human pluripotent stem cells. *Nat. Commun.* **8**, 1616 (2017).

[ADS](#) [PubMed](#) [PubMed Central](#) [Google Scholar](#)

41. 41.

Ku, M. et al. Genomewide analysis of PRC1 and PRC2 occupancy identifies two classes of bivalent domains. *PLoS Genet.* **4**, e1000242 (2008).

[PubMed](#) [PubMed Central](#) [Google Scholar](#)

42. 42.

Surface, L. E. et al. H2A.Z.1 monoubiquitylation antagonizes BRD2 to maintain poised chromatin in ESCs. *Cell Rep.* **14**, 1142–1155 (2016).

[CAS](#) [PubMed](#) [PubMed Central](#) [Google Scholar](#)

43. 43.

Wang, K. et al. PennCNV: an integrated hidden Markov model designed for high-resolution copy number variation detection in whole-genome SNP genotyping data. *Genome Res.* **17**, 1665–1674 (2007).

[CAS](#) [PubMed](#) [PubMed Central](#) [Google Scholar](#)

44. 44.

Mäkinen, N. et al. *MED12*, the mediator complex subunit 12 gene, is mutated at high frequency in uterine leiomyomas. *Science* **334**, 252–255 (2011).

[ADS](#) [PubMed](#) [PubMed Central](#) [Google Scholar](#)

45. 45.

McGuire, M. M. et al. Whole exome sequencing in a random sample of North American women with leiomyomas identifies *MED12* mutations in majority of uterine leiomyomas. *PLoS ONE* **7**, e33251 (2012).

[ADS](#) [CAS](#) [PubMed](#) [PubMed Central](#) [Google Scholar](#)

46. 46.

Mehine, M. et al. Integrated data analysis reveals uterine leiomyoma subtypes with distinct driver pathways and biomarkers. *Proc. Natl Acad. Sci. USA* **113**, 1315–1320 (2016).

[ADS](#) [CAS](#) [PubMed](#) [PubMed Central](#) [Google Scholar](#)

47. 47.

Mäkinen, N., Kämpjärvi, K., Frizzell, N., Bützow, R. & Vahteristo, P. Characterization of *MED12*, *HMGA2*, and *FH* alterations reveals molecular variability in uterine smooth muscle tumors. *Mol. Cancer* **16**, 101 (2017).

[PubMed](#) [PubMed Central](#) [Google Scholar](#)

48. 48.

Kim, D., Langmead, B. & Salzberg, S. L. HISAT: a fast spliced aligner with low memory requirements. *Nat. Methods* **12**, 357–360 (2015).

[CAS](#) [PubMed](#) [PubMed Central](#) [Google Scholar](#)

49. 49.

Pertea, M. et al. StringTie enables improved reconstruction of a transcriptome from RNA-seq reads. *Nat. Biotechnol.* **33**, 290–295

(2015).

[CAS](#) [PubMed](#) [PubMed Central](#) [Google Scholar](#)

50. 50.

Van der Auwera, G. A. et al. From FastQ data to high confidence variant calls: the Genome Analysis Toolkit best practices pipeline. *Curr. Protoc. Bioinformatics* **43**, 11.10.1–11.10.33 (2013).

[Google Scholar](#)

51. 51.

Love, M. I., Huber, W. & Anders, S. Moderated estimation of fold change and dispersion for RNA-seq data with DESeq2. *Genome Biol.* **15**, 550 (2014).

[PubMed](#) [PubMed Central](#) [Google Scholar](#)

52. 52.

Ritchie, M. E. et al. limma powers differential expression analyses for RNA-sequencing and microarray studies. *Nucleic Acids Res.* **43**, e47 (2015).

[PubMed](#) [PubMed Central](#) [Google Scholar](#)

53. 53.

Witten, D. M. & Tibshirani, R. Penalized classification using Fisher's linear discriminant. *J. R. Stat. Soc. Series B Stat. Methodol.* **73**, 753–772 (2011).

[MathSciNet](#) [PubMed](#) [PubMed Central](#) [MATH](#) [Google Scholar](#)

54. 54.

Wilkerson, M. D. & Hayes, D. N. ConsensusClusterPlus: a class discovery tool with confidence assessments and item tracking. *Bioinformatics* **26**, 1572–1573 (2010).

[CAS](#) [PubMed](#) [PubMed Central](#) [Google Scholar](#)

55. 55.

Monti, S., Tamayo, P., Mesirov, J. & Golub, T. Consensus clustering: a resampling-based method for class discovery and visualization of gene expression microarray data. *Mach. Learn.* **52**, 91–118 (2003).

[MATH](#) [Google Scholar](#)

56. 56.

Van Hout, C. V. et al. Whole exome sequencing and characterization of coding variation in 49,960 individuals in the UK Biobank. Preprint at <https://doi.org/10.1101/572347> (2019).

57. 57.

Zhou, W. et al. Scalable generalized linear mixed model for region-based association tests in large biobanks and cohorts. *Nat. Genet.* **52**, 634–639 (2020).

[CAS](#) [PubMed](#) [PubMed Central](#) [Google Scholar](#)

58. 58.

Castel, S. E., Mohammadi, P., Chung, W. K., Shen, Y. & Lappalainen, T. Rare variant phasing and haplotypic expression from RNA sequencing with phASER. *Nat. Commun.* **7**, 12817 (2016).

[ADS](#) [PubMed](#) [PubMed Central](#) [Google Scholar](#)

59. 59.

Krämer, A., Green, J., Pollard, J., Jr & Tugendreich, S. Causal analysis approaches in Ingenuity Pathway Analysis. *Bioinformatics* **30**, 523–530 (2014).

[PubMed](#) [PubMed Central](#) [Google Scholar](#)

60. 60.

Mehine, M. et al. Characterization of uterine leiomyomas by whole-genome sequencing. *N. Engl. J. Med.* **369**, 43–53 (2013).

[CAS](#) [PubMed](#) [PubMed Central](#) [Google Scholar](#)

61. 61.

Drmanac, R. et al. Human genome sequencing using unchained base reads on self-assembling DNA nanoarrays. *Science* **327**, 78–81 (2010).

[ADS](#) [CAS](#) [PubMed](#) [PubMed Central](#) [Google Scholar](#)

62. 62.

Amemiya, H. M., Kundaje, A. & Boyle, A. P. The ENCODE Blacklist: identification of problematic regions of the genome. *Sci. Rep.* **9**, 9354 (2019).

[ADS](#) [PubMed](#) [PubMed Central](#) [Google Scholar](#)

63. 63.

Sheffield, N. C. & Bock, C. LOLA: enrichment analysis for genomic region sets and regulatory elements in R and Bioconductor. *Bioinformatics* **32**, 587–589 (2016).

[CAS](#) [PubMed](#) [PubMed Central](#) [Google Scholar](#)

64. 64.

Ernst, J. & Kellis, M. ChromHMM: automating chromatin-state discovery and characterization. *Nat. Methods* **9**, 215–216 (2012).

[CAS](#) [PubMed](#) [PubMed Central](#) [Google Scholar](#)

65. 65.

Ross-Innes, C. S. et al. Differential oestrogen receptor binding is associated with clinical outcome in breast cancer. *Nature* **481**, 389–393 (2012).

[ADS](#) [CAS](#) [PubMed](#) [PubMed Central](#) [Google Scholar](#)

66. 66.

Corces, M. R. et al. An improved ATAC-seq protocol reduces background and enables interrogation of frozen tissues. *Nat. Methods* **14**, 959–962 (2017).

[CAS](#) [PubMed](#) [PubMed Central](#) [Google Scholar](#)

67. 67.

Orchard, P., Kyono, Y., Hensley, J., Kitzman, J. O. & Parker, S. C. J. Quantification, dynamic visualization, and validation of bias in ATAC-seq data with ataqv. *Cell Syst.* **10**, 298–306.e4 (2020).

[CAS](#) [PubMed](#) [PubMed Central](#) [Google Scholar](#)

68. 68.

Corces, M. R. et al. The chromatin accessibility landscape of primary human cancers. *Science* **362**, eaav1898 (2018).

[ADS](#) [PubMed](#) [PubMed Central](#) [Google Scholar](#)

69. 69.

Buenrostro, J. D., Giresi, P. G., Zaba, L. C., Chang, H. Y. & Greenleaf, W. J. Transposition of native chromatin for fast and sensitive epigenomic profiling of open chromatin, DNA-binding proteins and nucleosome position. *Nat. Methods* **10**, 1213–1218 (2013).

[CAS](#) [PubMed](#) [PubMed Central](#) [Google Scholar](#)

70. 70.

Mumbach, M. R. et al. HiChIP: efficient and sensitive analysis of protein-directed genome architecture. *Nat. Methods* **13**, 919–922 (2016).

[CAS](#) [PubMed](#) [PubMed Central](#) [Google Scholar](#)

71. 71.

Servant, N. et al. HiC-Pro: an optimized and flexible pipeline for Hi-C data processing. *Genome Biol.* **16**, 259 (2015).

[PubMed](#) [PubMed Central](#) [Google Scholar](#)

72. 72.

Bhattacharyya, S., Chandra, V., Vijayanand, P. & Ay, F. Identification of significant chromatin contacts from HiChIP data by FitHiChIP. *Nat. Commun.* **10**, 4221 (2019).

[ADS](#) [PubMed](#) [PubMed Central](#) [Google Scholar](#)

73. 73.

Akdemir, K. C. & Chin, L. HiCPlotter integrates genomic data with interaction matrices. *Genome Biol.* **16**, 198 (2015).

[PubMed](#) [PubMed Central](#) [Google Scholar](#)

74. 74.

Li, H. Minimap2: pairwise alignment for nucleotide sequences. *Bioinformatics* **34**, 3094–3100 (2018).

[CAS](#) [PubMed](#) [PubMed Central](#) [Google Scholar](#)

75. 75.

De Coster, W., D’Hert, S., Schultz, D. T., Cruts, M. & Van Broeckhoven, C. NanoPack: visualizing and processing long-read sequencing data. *Bioinformatics* **34**, 2666–2669 (2018).

[PubMed](#) [PubMed Central](#) [Google Scholar](#)

76. 76.

Martin, M. et al. WhatsHap: fast and accurate read-based phasing. Preprint at <https://doi.org/10.1101/085050> (2016).

77. 77.

Simpson, J. T. et al. Detecting DNA cytosine methylation using nanopore sequencing. *Nat. Methods* **14**, 407–410 (2017).

[CAS](#) [PubMed](#) [PubMed Central](#) [Google Scholar](#)

78. 78.

Haeussler, M. et al. The UCSC Genome Browser database: 2019 update. *Nucleic Acids Res.* **47**, D853–D858 (2019).

[CAS](#) [PubMed](#) [PubMed Central](#) [Google Scholar](#)

79. 79.

Karolchik, D. et al. The UCSC Table Browser data retrieval tool. *Nucleic Acids Res.* **32**, D493–D496 (2004).

[CAS](#) [PubMed](#) [PubMed Central](#) [Google Scholar](#)

80. 80.

Park, Y. & Wu, H. Differential methylation analysis for BS-seq data under general experimental design. *Bioinformatics* **32**, 1446–1453 (2016).

[CAS](#) [PubMed](#) [PubMed Central](#) [Google Scholar](#)

81. 81.

Shabalin, A. A. Matrix eQTL: ultra fast eQTL analysis via large matrix operations. *Bioinformatics* **28**, 1353–1358 (2012).

[CAS](#) [PubMed](#) [PubMed Central](#) [Google Scholar](#)

82. 82.

Ishigaki, K. et al. Large-scale genome-wide association study in a Japanese population identifies novel susceptibility loci across different diseases. *Nat. Genet.* **52**, 669–679 (2020).

[CAS](#) [PubMed](#) [PubMed Central](#) [Google Scholar](#)

83. 83.

Välimäki, N. et al. Genetic predisposition to uterine leiomyoma is determined by loci for genitourinary development and genome stability. *eLife* **7**, e37110 (2018).

[PubMed](#) [PubMed Central](#) [Google Scholar](#)

[Download references](#)

Acknowledgements

The Finland Myoma Study has been made possible by professionals from operating theatre nurses to data scientists, and in particular the study participants, and we are deeply grateful for their vital support during the

years. We thank S. Marttinen, S. Soisalo, M. Rajalaakso, I.-L. Åberg, I. Vuoristo, A. London, J. Kolakowska, H. Metsola and K. Pylvänäinen for technical support; and P. Ikonen and the rest of the staff of the Kätilöopisto Maternity Hospital, and the staff of the Department of Pathology, University of Helsinki for technical assistance. Capillary sequencing was performed by the sequencing unit of FIMM Technology Centre, University of Helsinki supported by Biocenter Finland. This research was conducted using the UK Biobank Resource under Application Number 32506. We acknowledge the participants and investigators of the FinnGen study; the Biobank Japan Project for the ‘uterine fibroids’ GWAS summary statistics; and the computational resources provided by the ELIXIR node, hosted at the CSC–IT Center for Science, Finland. The study was supported by grants from Academy of Finland (Finnish Center of Excellence Program 2012–2017, 2018–2025, No. 250345 and 312041, Academy Professor grants No. 319083 and 320149), European Research Council (ERC, 695727), iCAN Digital Precision Cancer Medicine Flagship (320185), Cancer Society of Finland, Sigrid Juselius Foundation and Jane and Aatos Erkko Foundation.

Author information

Author notes

1. These authors contributed equally: Davide G. Berta, Heli Kuisma

Affiliations

1. Department of Medical and Clinical Genetics, University of Helsinki, Helsinki, Finland

Davide G. Berta, Heli Kuisma, Niko Välimäki, Maritta Räisänen, Maija Jäntti, Auli Karhu, Jaana Kaukomaa, Aurora Taira, Tatiana Cajuso, Sanna Nieminen, Rosa-Maria Penttinen, Saija Ahonen, Rainer Lehtonen, Miika Mehine, Pia Vahteristo, Janne Ravantti, Netta Mäkinen, Kristiina Rajamäki, Kimmo Palin, Eevi Kaasinen & Lauri A. Aaltonen

2. Applied Tumor Genomics Research Program, Research Programs Unit, University of Helsinki, Helsinki, Finland

Davide G. Berta, Heli Kuisma, Niko Välimäki, Maritta Räisänen, Maija Jäntti, Auli Karhu, Jaana Kaukomaa, Aurora Taira, Tatiana Cajuso, Sanna Nieminen, Rosa-Maria Penttinen, Saja Ahonen, Rainer Lehtonen, Miika Mehine, Pia Vahteristo, Biswajyoti Sahu, Janne Ravantti, Netta Mäkinen, Kristiina Rajamäki, Kimmo Palin, Jussi Taipale, Ralf Bützow, Eevi Kaasinen & Lauri A. Aaltonen

3. Department of Pathology, University of Helsinki and Helsinki University Hospital, Helsinki, Finland

Annukka Pasanen & Ralf Bützow

4. Department of Obstetrics and Gynecology, Central Finland Central Hospital, Jyväskylä, Finland

Jyrki Jalkanen

5. iCAN Digital Precision Cancer Medicine Flagship, University of Helsinki, Helsinki, Finland

Kimmo Palin & Lauri A. Aaltonen

6. Department of Obstetrics and Gynecology, University of Helsinki and Helsinki University Hospital, Helsinki, Finland

Oskari Heikinheimo

Authors

1. Davide G. Berta

[View author publications](#)

You can also search for this author in [PubMed](#) [Google Scholar](#)

2. Heli Kuisma

[View author publications](#)

You can also search for this author in [PubMed](#) [Google Scholar](#)

3. Niko Välimäki

[View author publications](#)

You can also search for this author in [PubMed](#) [Google Scholar](#)

4. Maritta Räisänen

[View author publications](#)

You can also search for this author in [PubMed](#) [Google Scholar](#)

5. Maija Jäntti

[View author publications](#)

You can also search for this author in [PubMed](#) [Google Scholar](#)

6. Annukka Pasanen

[View author publications](#)

You can also search for this author in [PubMed](#) [Google Scholar](#)

7. Auli Karhu

[View author publications](#)

You can also search for this author in [PubMed](#) [Google Scholar](#)

8. Jaana Kaukomaa

[View author publications](#)

You can also search for this author in [PubMed](#) [Google Scholar](#)

9. Aurora Taira

[View author publications](#)

You can also search for this author in [PubMed](#) [Google Scholar](#)

10. Tatiana Cajuso

[View author publications](#)

You can also search for this author in [PubMed](#) [Google Scholar](#)

11. Sanna Nieminen

[View author publications](#)

You can also search for this author in [PubMed](#) [Google Scholar](#)

12. Rosa-Maria Penttinen

[View author publications](#)

You can also search for this author in [PubMed](#) [Google Scholar](#)

13. Saija Ahonen

[View author publications](#)

You can also search for this author in [PubMed](#) [Google Scholar](#)

14. Rainer Lehtonen

[View author publications](#)

You can also search for this author in [PubMed](#) [Google Scholar](#)

15. Miika Mehine

[View author publications](#)

You can also search for this author in [PubMed](#) [Google Scholar](#)

16. Pia Vahteristo

[View author publications](#)

You can also search for this author in [PubMed](#) [Google Scholar](#)

17. Jyrki Jalkanen

[View author publications](#)

You can also search for this author in [PubMed](#) [Google Scholar](#)

18. Biswajyoti Sahu

[View author publications](#)

You can also search for this author in [PubMed](#) [Google Scholar](#)

19. Janne Ravantti

[View author publications](#)

You can also search for this author in [PubMed](#) [Google Scholar](#)

20. Netta Mäkinen

[View author publications](#)

You can also search for this author in [PubMed](#) [Google Scholar](#)

21. Kristiina Rajamäki

[View author publications](#)

You can also search for this author in [PubMed](#) [Google Scholar](#)

22. Kimmo Palin

[View author publications](#)

You can also search for this author in [PubMed](#) [Google Scholar](#)

23. Jussi Taipale

[View author publications](#)

You can also search for this author in [PubMed](#) [Google Scholar](#)

24. Oskari Heikinheimo

[View author publications](#)

You can also search for this author in [PubMed](#) [Google Scholar](#)

25. Ralf Bützow

[View author publications](#)

You can also search for this author in [PubMed](#) [Google Scholar](#)

26. Eevi Kaasinen

[View author publications](#)

You can also search for this author in [PubMed](#) [Google Scholar](#)

27. Lauri A. Aaltonen

[View author publications](#)

You can also search for this author in [PubMed](#) [Google Scholar](#)

Contributions

D.G.B., H.K., N.V., A.K., K.P., E.K. and L.A.A. conceived the ideas, planned the experiments and wrote the manuscript. D.G.B., M.R. and M.J. performed the ATAC and ChIP-seq experiments. D.G.B. performed HiChIP and western blot experiments. M.R., E.K., K.P and H.K. analysed ATAC, ChIP and HiChIP data. H.K., N.V. and T.C. performed the mutation analysis. H.K. and N.V. performed the gene expression analysis. R.-M.P. and N.V. performed the allele-specific expression analysis. A.T., K.P. and E.K. performed the methylation analysis. A.K., S.N. and T.C. performed the IHC experiments. R.B., A.K. and H.K. analysed the IHC data. N.V. analysed the germline predisposition data. J.K., S.A., P.V., M.M. and N.M. performed the mutation screening and managed clinical data. A.P., J.J., O.H. and R.B. collected the tissue samples. J.R. and R.L. provided support with analysis and management of data. J.T., K.R. and B.S. provided support with the experimental design and interpretation.

Corresponding authors

Correspondence to [Eevi Kaasinen](#) or [Lauri A. Aaltonen](#).

Ethics declarations

Competing interests

The authors declare no competing interests.

Additional information

Peer review information *Nature* thanks Zehra Ordulu and the other, anonymous, reviewer(s) for their contribution to the peer review of this work.

Publisher's note Springer Nature remains neutral with regard to jurisdictional claims in published maps and institutional affiliations.

Extended data figures and tables

[Extended Data Fig. 1 Overview of study material and somatic allelic imbalance.](#)

a, The sequential stages of UL subclass detection. Denominators are numbers of tumours screened at each stage; see [Methods](#) for a detailed description of data used at each stage. Percentages refer to proportions among all 2,263 tumours. HMGA1 subclass comprised 67 tumours without any other known driver change. Three tumours with an SRCAP complex gene mutation are shown here as one MED12 and two HMGA2 tumours as they also showed these driver changes. **b**, Germline LoF variants (blue; UK Biobank WES) compiled with somatic LoF (red) and missense (black) variants. Green boxes represent protein domains from Pfam. **c–e**, Overview of genome-wide somatic allelic imbalance in 2,186 SNP-arrayed ULs. **c**, y-axis gives the total length of the genome affected by somatic loss and gain aberrations per tumour, stratified by subclass (logarithmic and truncated to 10^5 bp). Dashed lines show the overall and subclass-specific mean values. Percentage units refer to the proportion of chromosomally stable tumours within each subclass. **d**, Estimated numbers of somatic DSBs. **e**, Subclass-specific enrichment of allelic loss: x-axis gives log-transformed, one-sided tests of loss-event enrichment in each subclass compared to the rest of the tumours (truncated to 1.0×10^{-20}). y-axis indicates the genomic position (autosomes and X). See Supplementary Table [6](#) for detailed statistics.

[Source data](#)

[Extended Data Fig. 2 H2AZ staining in myometrium, MED12, HMGA, FH, OM and YEATS4 tumours.](#)

a, Representative immunostaining of non-acetylated H2A.Z in normal myometrium and MED12, HMGA2, HMGA1, FH and YEATS4 ULs. The intensity of immunoreaction is given in parentheses: 0 = negative or weak, 1 = moderate, 2 = strong. YEATS4 mutated myoma displays negative or weak H2A.Z staining in neoplastic cells, but preserved staining in endothelial, perivascular and scattered inflammatory cells. 40× magnification. The scores for all the stained samples are given in **b** (left). MED12 ($n = 95$), HMGA2 ($n = 68$), HMGA1 ($n = 58$), FH ($n = 10$), OM ($n = 14$), YEATS4 ($n = 19$). **b**, Distribution of staining scores on non-acetylated H2A.Z antibody (left) and acetylated H2A.Z (H2A.Zac) antibody (right). **c**, H2A.Z (top) and H2A.Zac (bottom) staining intensity in HMGA2, HMGA1, HMGA2 and HMGA1 combined (HMGA2&1), YEATS4 and OM tumours compared to MED12 tumours (GEE-model). Nominal two-sided P values are shown. **d**, Western blot analysis of H2A.Z (left), H2A.Zac (right) and TBP (for both, as loading control) in chromatin fraction from MED12 and YEATS4 tumours and related normal myometrium, all from the same individual. Molecular weights of the protein ladder are indicated. Owing to the limited amount of the respective myometrium tissue as control, it was possible to perform the western blots only once. Uncropped blot available in Supplementary Fig. [30](#).

[Source data](#)

[Extended Data Fig. 3 Reduction in acetylated H2A.Z in MED12, HMGA, FH and YEATS4 tumours.](#)

Representative immunostaining of H2A.Zac in normal myometrium and MED12, HMGA, FH and YEATS4 ULs. The intensity of immunoreaction is shown in parentheses: 0 = negative or weak, 1 = moderate, 2 = strong. 40× magnification. The scores for all the stained samples are presented in Extended Data Fig. [2b](#) (right). MED12 ($n = 96$), HMGA2 ($n = 68$), HMGA1 ($n = 58$), FH ($n = 9$), OM ($n = 14$), YEATS4 ($n = 19$).

[Extended Data Fig. 4 Differences in H2A.Z binding between UL subclasses and normal samples.](#)

\log_2 FC and average binding strength (normalized read concentration) were calculated on each H2A.Z peak region and are represented by a dot. **a–d**, MED12 ($n = 3$) (**a**), HMGA2 ($n = 4$) (**b**), FH ($n = 4$) (**c**) and OM ($n = 3$) (**d**) tumours were separately compared to all normal samples ($n = 11$).

H2A.Z peak regions were stratified by five-state genome annotations from myometrium. States were annotated as bivalent TSS regions (TssBiv marked by both H3K4me3 and H3K27me3), active TSS regions (TssA marked by both H3K4me3 and H3K27ac), active chromatin outside TSS regions (OtherA marked by H3K27ac), repressed chromatin (Repr marked by H3K27me3) and other chromatin (Other).

Extended Data Fig. 5 Differential H2A.Z binding between tumours and myometria.

Volcano plots displaying differences in H2A.Z binding for MED12 ($n = 2$), YEATS4 ($n = 2$), HMGA2 ($n = 2$), HMGA1 ($n = 4$), OM ($n = 2$) and FH ($n = 2$) tumours against normal samples ($n = 4$) from the spike-in ChIP-seq experiments. FDR (y-axis) and \log_2 FC (x-axis) from DESeq2 analysis as implemented in the DiffBind R package. Violet dots represent differential H2A.Z binding sites ($FDR < 0.05, |\log_2\text{FC}| > 1$). The highlighted peaks (pink dots) are located close to *CBX8* and named as *S* with distance in kilobases from the *CBX8* TSS.

Extended Data Fig. 6 H2A.Z occupancy associates with chromatin opening and DNA methylation.

a, Chromatin accessibility as a function of H2A.Z occupancy. Chromatin accessibility $\log_2\text{FC}$ (y-axis) was measured by DESeq2-normalized ATAC-seq Tn5 insertion counts in MED12 ($n = 4$), HMGA2 ($n = 4$), FH ($n = 4$) and YEATS4 ($n = 4$) tumours compared with normal samples ($n = 15$) at H2A.Z peaks stratified into increased, no change and decreased binding. **b**, **c**, Pileup of H2A.Z ChIP fragments from pooled myometrium data at DARs shown by composite plots and heatmaps. DARs in each UL subclass (**b**) or in YEATS4 tumours stratified by overlap with other UL subclasses (**c**) are represented by heatmap rows over which mean H2A.Z fragment coverage is calculated. **d**, Differences in H2A.Z binding at DARs in UL subclasses as

compared to normal samples. Violet dots represent differential H2A.Z binding sites ($\text{FDR} < 0.05$, $|\log_2\text{FC}| > 1$). The highlighted peaks (pink dots) are located close to *CBX8* and named as *S* with distance in kilobases from the *CBX8* TSS. **e**, Mean sample-wise DNA methylation differences in MED12 ($n = 11$), HMGA2 ($n = 26$), FH ($n = 6$), YEATS4 ($n = 14$) and OM ($n = 8$) tumours compared with respective normal samples at H2A.Z peaks stratified into increased, no change and decreased binding. H2A.Z binding differences in **a**, **d**, **e** are from the spike-in ChIP-seq experiments comparing two tumours from each subclass to four normal samples. Increased, no change and decreased binding were defined using $\text{FDR} < 0.05$ and $|\log_2\text{FC}| > 1$ cutoffs. Boxplots show the median and the first and third quartiles. Error bars extend up to 1.5 IQR beyond the quartiles.

Extended Data Fig. 7 DNA methylation displays distinct patterns in UL subclasses.

a, Overall genome-wide DNA methylation in ULs and normal myometrium. Each dot represents a sample. **b**, Enrichment of hyper- and hypomethylated loci in different tumour subclasses on five chromatin states from normal myometrium. ORs and P values ($\log_{10}(\text{pvalue})$ stands for $-\log_{10}(P \text{ value})$) from one-sided Fisher's exact test implemented in the LOLA R package. **c–g**, Overall DNA methylation on active (**c**) and bivalent (**d**) TSSs, other active chromatin (**e**), repressed/poised chromatin (**f**) and other, quiescent, chromatin regions (**g**). Significance of methylation difference against normals evaluated by ordinary least squares regression: *** $P < 0.0001$, ** $P < 0.001$, * $P < 0.01$. Test controlled by global methylation levels. Sample sizes: normal 96, MED12 13, HMGA1 21, HMGA2 28, YEATS4 11, OM 9, FH 6, Unknown 14. Box covers the central two quartiles of the distribution. Median is highlighted. Whiskers extend to the minimum and maximum of the distribution or at most $1.5 \times \text{IQR}$ from the edge of the box, whichever is closer. Multiple testing correction was not performed. **h**, Mean sample-wise DNA methylation in ULs and normal myometrium at H2A.Z binding sites derived from pooled normal myometrium tissue samples. Asterisks, box-and-whiskers plots and sample sizes are as in **c–g**.

Extended Data Fig. 8 Clustering of RNA-seq samples.

a, $\log_2 FC$ of genes for which decreased ($FDR < 0.05$, $FC < -1$), increased ($FDR < 0.05$, $FC > 1$) or no-change H2A.Z peaks are located at the TSS. $\log_2 FC$ measured by differential expression analysis of tumours (MED12 ($n = 38$), HMGA2 ($n = 44$), HMGA1 ($n = 62$), FH ($n = 15$), OM ($n = 15$) and YEATS4 ($n = 16$)) against normal myometrium ($n = 162$). H2AZ binding differences are from the spike-in ChIP experiments comparing MED12 ($n = 2$), YEATS4 ($n = 2$), HMGA2 ($n = 2$), HMGA1 ($n = 4$), OM ($n = 2$) and FH ($n = 2$) tumours against normal samples ($n = 4$). Boxplots show the median and the first and third quartiles. Error bars extend up to $1.5 \times IQR$ beyond the quartiles. **b**, Heatmap presentation of 426 genes that separate myoma subclasses, selected on the basis of linear discriminant analysis. The ordering of samples and genes is based on an unsupervised hierarchical clustering of the 5% ($n = 1,355$) most variable genes. Two genes per gene cluster are highlighted on the basis of the highest absolute value in discriminant vectors. Patients from whom more than one tumour entered the analysis are highlighted in separate colours. All 426 genes are presented in Supplementary Table 20. **c**, Consensus clustering of RNA-seq samples. x -axis is sorted by subclass (from left to right: FH, HMGA1, HMGA2, MED12, normal myometrium, OM, YEATS4, and unknown; subclass labels are shown for reference). Item consensus is the mean consensus of an item with all the other items in the same cluster. For each sample, the item consensus value corresponding to each cluster ($k = 26$) is represented by a colour. For example, all FH samples have the largest item consensus on cluster 2, represented by dark green. Both YEATS4 and OM samples cluster predominantly to cluster 12, represented by blue. Unknown samples form several small clusters. The item consensus value (e_i) of each cluster (k) is presented on the y -axis. It is defined as: $\frac{1}{N_k} \sum_{j \in C_k} e_j$, where M is distance matrix and N_k is the number of items in the cluster. See Monti et al. 55 for further details.

[Source data](#)

Extended Data Fig. 9 Canonical IPA pathway comparison analyses.

Pathways are relevant to multiple UL subclasses. Pathways with the highest total score (P values; right-tailed Fisher's exact test) across the set of subclasses are sorted to the top. Heat map cells with insignificant P values ($-\log_{10} 1.3$) are marked with a dot.

Extended Data Fig. 10 H2A.Z ChIP-seq fragment pileup for individual samples at the locus harbouring *CBX2*, *CBX4* and *CBX8*.

Pink squares depict differential H2A.Z binding sites close to *CBX8* and the name of each of these sites refers to distance from the *CBX8* TSS in kilobases. UL subclasses are colour-coded as in the main Figures. Coordinates in GRCh38.

Supplementary information

Supplementary Information

This file contains a Supplementary Discussion, Supplementary Figures 1-30, Supplementary Tables (with descriptions) 3-7, 9-12, 15-18, 23 and Supplementary References.

Reporting Summary

Supplementary Table 1

Anonymized patient identifiers and background information. First eight columns give the patient identifier, sample series and denote (YES/NO) which of the myometrium tissue data types were generated per patient. Next two columns give patients' ancestry based on SNP chip genotypes (YES/NO; outliers identified in a principal components analysis, PLINK v1.90) and self-reported ancestry. The rest of the columns denote age at hysterectomy (years), height (cm), weight (kg), BMI (kg/m²), menopause status (pre/post/current hormone replacement therapy), parity, family history of ULs (YES/NO) and previous use of oral contraceptives (YES/NO). Note that all values were not available for all patients (empty fields denote missing data).

Supplementary Table 2

Tumour specimens utilized in the study. First three columns give the tumour identifier and subclass and denote which of the tumours were selected (YES/NO) for statistical analyses that rely on independent observations (one tumour per subclass per patient; see details in Methods). Next fourteen columns denote (YES/NO) which of the data types were generated per tumour and per paired-normal myometrium tissue. Patient identifiers (column J) refer to Supplementary Table 1. Next seven columns give the mutation statuses, and the following thirteen columns specify the mutation statuses used in the mutual exclusivity analysis. Next two columns specify, if available, tumour size (mm) and type (submucous/intramural/subserous). The rest of the columns summarize the WGS material (batch, sequencing

platform, library size, sequencing coverage at SRCAP complex genes, software versions).

Supplementary Table 8

Summary statistics of the gene-based UL association results. The columns give the p-values (SKAT-O test; combined burden and SKAT test, sidedness is not applicable), MAC distribution, and a list of LoF variants (at $\text{MAF} \leq 1\%$) identified in each gene. The results are based on the discovery set (50k UKBiobank). All genes with $\text{sum}(\text{MAC}) \geq 3$ among discovery set females of European ancestry were included. No adjustment for multiple comparisons.

Supplementary Table 13

Promoter-proximal open chromatin regions in YEATS4 tumours.
Differentially more accessible regions annotated to genes (RefSeq TSS + 1kb flank). Coordinates are in GRCh37.

Supplementary Table 14

Differentially expressed genes ($\text{FDR} < 0.05$) where significantly decreased ($\text{FDR} < 0.05$, $\text{Fold} < -1$) H2A.Z binding peak is located at TSS in YEATS4 tumours.

Supplementary Table 19

Per subclass differential expression of genes with differential HiCHIP links bridging (see Supplementary Figure 22b) a H2A.z peak and a TSS of the gene. Links (DiffLink) were derived from FitHiChIP differential analysis using $\text{FDR} < 0.05$ and fold change ($\text{FC} \geq \log_2(2)$) thresholds for EdgeR v3.26.5 statistics. The differential expression (DE) values were calculated with DESeq2 v1.22.2 utilizing Wald statistics.

Supplementary Table 20

The 426 genes that separate myoma subclasses (MED12, HMGA1, HMGA2, FH, YEATS4 + OM, and unknown) from each other based on linear discriminant analysis.

Supplementary Table 21

List of the differentially expressed (DE) genes in MED12, HMGA1, HMGA2, YEATS4, OM and FH UL subclasses as well as in all UL subclasses combined against myometrium. The values were calculated with DESeq2 v.1.22.2 utilizing Wald statistics.

Supplementary Table 22

Supplementary Tables 22.1 – 22.6 list the enriched pathways in MED12, HMGA1, HMGA2, YEATS4, OM and FH uterine leiomyoma subclasses. P-values were calculated with right-tailed Fisher's exact test and presented for each pathway on logarithmic scale.

Supplementary Table 24

Summary of allele-specific gene expression, including subclass-specific numbers. Table is sorted by genes with enrichment of ASE among tumours (log₂ fold-change with a pseudocount 1). The RNA-seq observations of tumours and normals were divided into five categories: i) allele-specific gene expression (ASE), ii) balanced gene expression (balancedE), iii) low gene expression (<16 coverage, lowE), iv) somatic allelic imbalance (AI), and v) no heterozygous markers to measure (homozygous), where the category iv) is applicable only among the tumour samples. Additionally, the number of tumors with ASE in each subclass and their proportions (prop; proportion of ASE per subclass after excluding chromosomal instability, low expression and homozygous samples) were listed. Genes with ASE in at least ten tumours were included in the table.

Supplementary Table 25

Meta-analysis results ($P < 1e-6$) from three independent cohorts: FINNNGEN (R3), UK Biobank and Biobank Japan. Each SNP was annotated for the

nearest DAR (among the common 156 DARs) and nearest entry in the GWAS catalog (v1.0 “uterine fibroid”; accessed on October 1, 2020) if any were found within a 3Mbp distance. Allele frequency (AF) and regression coefficient (BETA) base on the alternative allele. Coordinates are in GRCh37.

Supplementary Table 26

Summary of EGA study and dataset accession numbers. First spreadsheet gives the total numbers of samples. For the rest of the spreadsheets, rows follow the patient and tumour listing in Supplementary Table 1 and 2, respectively, and columns match the data type columns in Supplementary Table 1 and 2.

Source Data

This file contains Source Data for Supplementary Fig. 1.

Source data

Source Data Fig. 1

Source Data Fig. 3

Source Data Extended Data Fig. 1

Source Data Extended Data Fig. 2

Source Data Extended Data Fig. 8

Rights and permissions

Reprints and Permissions

About this article



Cite this article

Berta, D.G., Kuisma, H., Välimäki, N. *et al.* Deficient H2A.Z deposition is associated with genesis of uterine leiomyoma. *Nature* **596**, 398–403 (2021). <https://doi.org/10.1038/s41586-021-03747-1>

[Download citation](#)

- Received: 26 June 2020
- Accepted: 18 June 2021
- Published: 04 August 2021
- Issue Date: 19 August 2021
- DOI: <https://doi.org/10.1038/s41586-021-03747-1>

Comments

By submitting a comment you agree to abide by our [Terms](#) and [Community Guidelines](#). If you find something abusive or that does not comply with our terms or guidelines please flag it as inappropriate.

[Access through your institution](#)

[Change institution](#)

[Buy or subscribe](#)

Associated Content

Collection

Cancer at Nature Portfolio

Deranged chromatin drives uterine fibroid tumours

- Zehra Ordulu

News & Views 04 Aug 2021

Advertisement

This article was downloaded by **calibre** from <https://www.nature.com/articles/s41586-021-03747-1>

| [Section menu](#) | [Main menu](#) |

- Article
- [Published: 11 August 2021](#)

Locally ordered representation of 3D space in the entorhinal cortex

- [Gily Ginosar](#)¹,
- [Johnatan Aljadeff](#)^{1,2},
- [Yoram Burak](#)^{3,4},
- [Haim Sompolinsky](#)^{3,4,5},
- [Liora Las](#)¹ &
- [Nachum Ulanovsky](#) ORCID: orcid.org/0000-0001-8598-4667¹

[Nature](#) volume 596, pages 404–409 (2021) [Cite this article](#)

- 3058 Accesses
- 186 Altmetric
- [Metrics details](#)

Subjects

- [Computational neuroscience](#)
- [Cortex](#)
- [Hippocampus](#)
- [Neural circuits](#)
- [Spatial memory](#)

Abstract

As animals navigate on a two-dimensional surface, neurons in the medial entorhinal cortex (MEC) known as grid cells are activated when the animal passes through multiple locations (firing fields) arranged in a hexagonal lattice that tiles the locomotion surface¹. However, although our world is three-dimensional, it is unclear how the MEC represents 3D space². Here we recorded from MEC cells in freely flying bats and identified several classes of spatial neurons, including 3D border cells, 3D head-direction cells, and neurons with multiple 3D firing fields. Many of these multifield neurons were 3D grid cells, whose neighbouring fields were separated by a characteristic distance—forming a local order—but lacked any global lattice arrangement of the fields. Thus, whereas 2D grid cells form a global lattice—characterized by both local and global order—3D grid cells exhibited only local order, creating a locally ordered metric for space. We modelled grid cells as emerging from pairwise interactions between fields, which yielded a hexagonal lattice in 2D and local order in 3D, thereby describing both 2D and 3D grid cells using one unifying model. Together, these data and model illuminate the fundamental differences and similarities between neural codes for 3D and 2D space in the mammalian brain.

Access options

Subscribe to Journal

Get full journal access for 1 year

\$199.00

only \$3.90 per issue

[Subscribe](#)

All prices are NET prices.

VAT will be added later in the checkout.

Tax calculation will be finalised during checkout.

Rent or Buy article

Get time limited or full article access on ReadCube.

from \$8.99

[Rent or Buy](#)

All prices are NET prices.

Additional access options:

- [Log in](#)
- [Access through your institution](#)
- [Learn about institutional subscriptions](#)

Fig. 1: Experimental setup and behaviour.

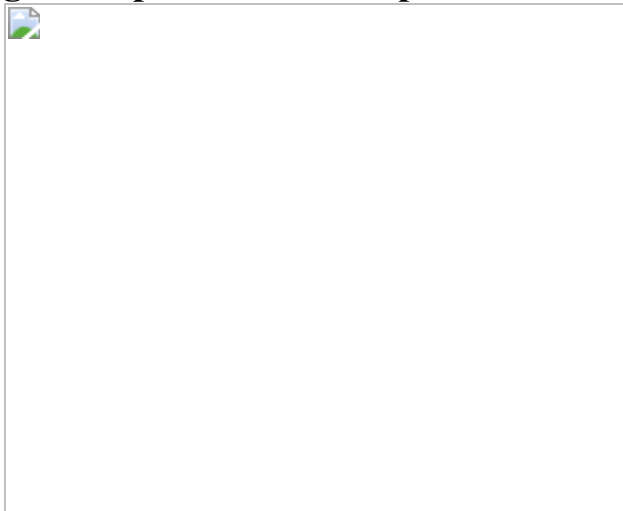


Fig. 2: 3D grid cells in flying bats exhibit fixed local distances but no global lattice.

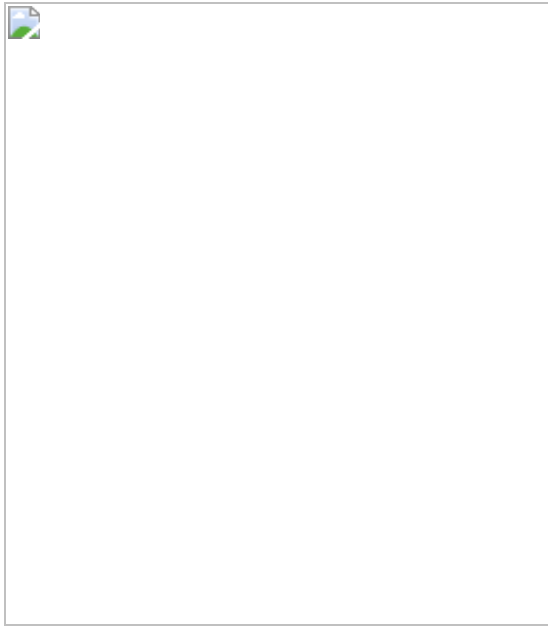


Fig. 3: Properties of 3D grid cells and non-grid multifield cells.



Fig. 4: 3D head-direction cells and 3D border cells in bat MEC.

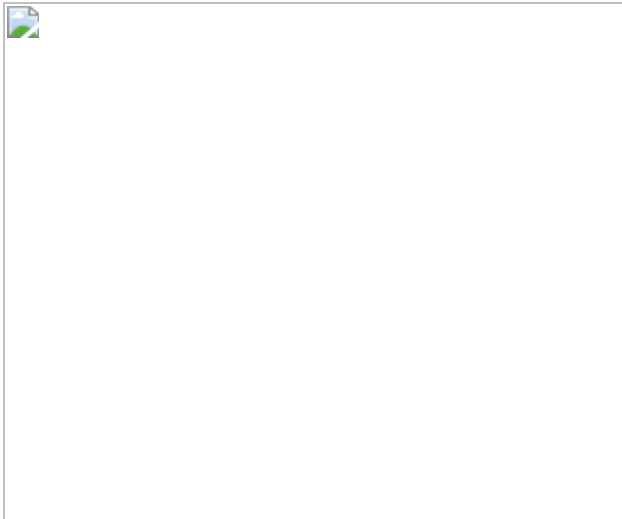
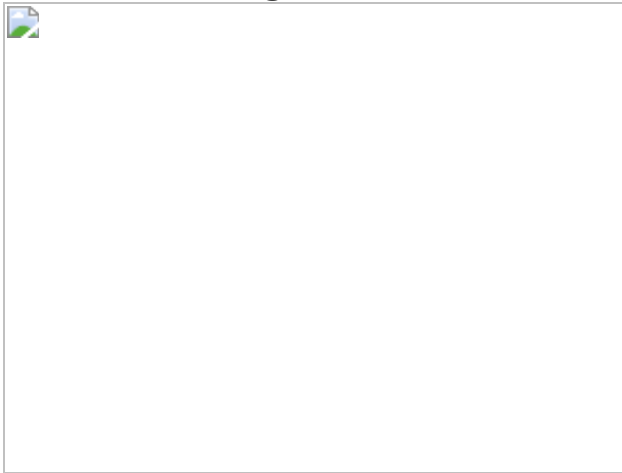


Fig. 5: A single model describes both grid-cell hexagonality in 2D and the local-but-not-global order in 3D.



Data availability

The data generated and analysed in the current study are available from the corresponding author on reasonable request. [Source data](#) are provided with this paper.

Code availability

The code generated for the current study is available from the corresponding author on reasonable request.

References

1. 1.

Hafting, T., Fyhn, M., Molden, S., Moser, M.-B. & Moser, E. I. Microstructure of a spatial map in the entorhinal cortex. *Nature* **436**, 801–806 (2005).

[ADS](#) [CAS](#) [PubMed](#) [Article](#) [PubMed Central](#) [Google Scholar](#)

2. 2.

Finkelstein, A., Las, L. & Ulanovsky, N. 3-D maps and compasses in the brain. *Annu. Rev. Neurosci.* **39**, 171–196 (2016).

[CAS](#) [PubMed](#) [Article](#) [PubMed Central](#) [Google Scholar](#)

3. 3.

Krupic, J., Burgess, N. & O’Keefe, J. Neural representations of location composed of spatially periodic bands. *Science* **337**, 853–857 (2012).

[ADS](#) [CAS](#) [PubMed](#) [PubMed Central](#) [Article](#) [Google Scholar](#)

4. 4.

Stensola, T., Stensola, H., Moser, M.-B. & Moser, E. I. Shearing-induced asymmetry in entorhinal grid cells. *Nature* **518**, 207–212 (2015).

[ADS](#) [CAS](#) [PubMed](#) [Article](#) [PubMed Central](#) [Google Scholar](#)

5. 5.

Hayman, R., Verriotis, M. A., Jovalekic, A., Fenton, A. A. & Jeffery, K. J. Anisotropic encoding of three-dimensional space by place cells and grid cells. *Nat. Neurosci.* **14**, 1182–1188 (2011).

[CAS](#) [PubMed](#) [PubMed Central](#) [Article](#) [Google Scholar](#)

6. 6.

Hayman, R. M., Casali, G., Wilson, J. J. & Jeffery, K. J. Grid cells on steeply sloping terrain: evidence for planar rather than volumetric encoding. *Front. Psychol.* **6**, 925 (2015).

[PubMed](#) [PubMed Central](#) [Article](#) [Google Scholar](#)

7. 7.

Casali, G., Bush, D. & Jeffery, K. Altered neural odometry in the vertical dimension. *Proc. Natl Acad. Sci. USA* **116**, 4631–4636 (2019).

[PubMed](#) [PubMed Central](#) [Article](#) [CAS](#) [Google Scholar](#)

8. 8.

Yartsev, M. M., Witter, M. P. & Ulanovsky, N. Grid cells without theta oscillations in the entorhinal cortex of bats. *Nature* **479**, 103–107 (2011).

[ADS](#) [CAS](#) [PubMed](#) [Article](#) [PubMed Central](#) [Google Scholar](#)

9. 9.

Taube, J. S., Muller, R. U. & Ranck, J. B. Jr Head-direction cells recorded from the postsubiculum in freely moving rats. I. Description and quantitative analysis. *J. Neurosci.* **10**, 420–435 (1990).

[CAS](#) [PubMed](#) [PubMed Central](#) [Article](#) [Google Scholar](#)

10. 10.

Sargolini, F. et al. Conjunctive representation of position, direction, and velocity in entorhinal cortex. *Science* **312**, 758–762 (2006).

[ADS](#) [CAS](#) [PubMed](#) [Article](#) [PubMed Central](#) [Google Scholar](#)

11. 11.

Finkelstein, A. et al. Three-dimensional head-direction coding in the bat brain. *Nature* **517**, 159–164 (2015).

[ADS](#) [CAS](#) [PubMed](#) [Article](#) [PubMed Central](#) [Google Scholar](#)

12. 12.

Solstad, T., Boccara, C. N., Kropff, E., Moser, M.-B. & Moser, E. I. Representation of geometric borders in the entorhinal cortex. *Science* **322**, 1865–1868 (2008).

[ADS](#) [CAS](#) [PubMed](#) [Article](#) [PubMed Central](#) [Google Scholar](#)

13. 13.

Savelli, F., Yoganarasimha, D. & Knierim, J. J. Influence of boundary removal on the spatial representations of the medial entorhinal cortex. *Hippocampus* **18**, 1270–1282 (2008).

[PubMed](#) [PubMed Central](#) [Article](#) [Google Scholar](#)

14. 14.

Yartsev, M. M. & Ulanovsky, N. Representation of three-dimensional space in the hippocampus of flying bats. *Science* **340**, 367–372 (2013).

[ADS](#) [CAS](#) [PubMed](#) [Article](#) [PubMed Central](#) [Google Scholar](#)

15. 15.

Hales, T. C. A proof of the Kepler conjecture. *Ann. Math.* **162**, 1065–1185 (2005).

[MathSciNet](#) [MATH](#) [Article](#) [Google Scholar](#)

16. 16.

Stella, F. & Treves, A. The self-organization of grid cells in 3D. *eLife* **4**, e05913 (2015).

[PubMed Central](#) [Article](#) [Google Scholar](#)

17. 17.

Mathis, A., Stemmler, M. B. & Herz, A. V. M. Probable nature of higher-dimensional symmetries underlying mammalian grid-cell activity patterns. *eLife* **4**, e05979 (2015).

[PubMed Central](#) [Article](#) [Google Scholar](#)

18. 18.

Horiuchi, T. K. & Moss, C. F. Grid cells in 3-D: reconciling data and models. *Hippocampus* **25**, 1489–1500 (2015).

[PubMed](#) [Article](#) [PubMed Central](#) [Google Scholar](#)

19. 19.

Boccara, C. N. et al. Grid cells in pre- and parasubiculum. *Nat. Neurosci.* **13**, 987–994 (2010).

[CAS](#) [PubMed](#) [Article](#) [PubMed Central](#) [Google Scholar](#)

20. 20.

Krupic, J., Bauza, M., Burton, S. & O’Keefe, J. Local transformations of the hippocampal cognitive map. *Science* **359**, 1143–1146 (2018).

[ADS](#) [CAS](#) [PubMed](#) [PubMed Central](#) [Article](#) [Google Scholar](#)

21. 21.

Boccara, C. N., Nardin, M., Stella, F., O’Neill, J. & Csicsvari, J. The entorhinal cognitive map is attracted to goals. *Science* **363**, 1443–1447 (2019).

[ADS](#) [CAS](#) [PubMed](#) [Article](#) [PubMed Central](#) [Google Scholar](#)

22. 22.

Sanguinetti-Scheck, J. I. & Brecht, M. Home, head direction stability, and grid cell distortion. *J. Neurophysiol.* **123**, 1392–1406 (2020).

[PubMed](#) [PubMed Central](#) [Article](#) [Google Scholar](#)

23. 23.

Krupic, J., Bauza, M., Burton, S., Lever, C. & O’Keefe, J. How environment geometry affects grid cell symmetry and what we can learn from it. *Phil. Trans. R. Soc. Lond. B* **369**, 20130188 (2013).

[Article](#) [Google Scholar](#)

24. 24.

Stensola, H. et al. The entorhinal grid map is discretized. *Nature* **492**, 72–78 (2012).

[ADS](#) [CAS](#) [PubMed](#) [Article](#) [PubMed Central](#) [Google Scholar](#)

25. 25.

Kropff, E. & Treves, A. The emergence of grid cells: intelligent design or just adaptation? *Hippocampus* **18**, 1256–1269 (2008).

[PubMed](#) [Article](#) [PubMed Central](#) [Google Scholar](#)

26. 26.

Burak, Y. & Fiete, I. R. Accurate path integration in continuous attractor network models of grid cells. *PLoS Comput. Biol.* **5**, e1000291 (2009).

[ADS](#) [MathSciNet](#) [PubMed](#) [PubMed Central](#) [Article](#) [CAS](#) [Google Scholar](#)

27. 27.

McNaughton, B. L., Battaglia, F. P., Jensen, O., Moser, E. I. & Moser, M.-B. Path integration and the neural basis of the ‘cognitive map’. *Nat. Rev. Neurosci.* **7**, 663–678 (2006).

[CAS](#) [PubMed](#) [Article](#) [PubMed Central](#) [Google Scholar](#)

28. 28.

Fiete, I. R., Burak, Y. & Brookings, T. What grid cells convey about rat location. *J. Neurosci.* **28**, 6858–6871 (2008).

[CAS](#) [PubMed](#) [PubMed Central](#) [Article](#) [Google Scholar](#)

29. 29.

Mathis, A., Herz, A. V. M. & Stemmler, M. B. Resolution of nested neuronal representations can be exponential in the number of neurons. *Phys. Rev. Lett.* **109**, 018103 (2012).

[ADS](#) [PubMed](#) [Article](#) [CAS](#) [PubMed Central](#) [Google Scholar](#)

30. 30.

Stemmler, M., Mathis, A. & Herz, A. V. M. Connecting multiple spatial scales to decode the population activity of grid cells. *Sci. Adv.* **1**, e1500816 (2015).

[ADS](#) [PubMed](#) [PubMed Central](#) [Article](#) [Google Scholar](#)

31. 31.

Sarel, A., Finkelstein, A., Las, L. & Ulanovsky, N. Vectorial representation of spatial goals in the hippocampus of bats. *Science* **355**, 176–180 (2017).

[ADS](#) [CAS](#) [PubMed](#) [Article](#) [PubMed Central](#) [Google Scholar](#)

32. 32.

Omer, D. B., Maimon, S. R., Las, L. & Ulanovsky, N. Social place-cells in the bat hippocampus. *Science* **359**, 218–224 (2018).

[ADS](#) [CAS](#) [PubMed](#) [Article](#) [PubMed Central](#) [Google Scholar](#)

33. 33.

Ulanovsky, N. & Moss, C. F. Hippocampal cellular and network activity in freely moving echolocating bats. *Nat. Neurosci.* **10**, 224–233 (2007).

[CAS](#) [PubMed](#) [Article](#) [PubMed Central](#) [Google Scholar](#)

34. 34.

Yovel, Y., Falk, B., Moss, C. F. & Ulanovsky, N. Optimal localization by pointing off axis. *Science* **327**, 701–704 (2010).

[ADS](#) [CAS](#) [PubMed](#) [Article](#) [PubMed Central](#) [Google Scholar](#)

35. 35.

Skaggs, W. E., McNaughton, B. L., Wilson, M. A. & Barnes, C. A. Theta phase precession in hippocampal neuronal populations and the compression of temporal sequences. *Hippocampus* **6**, 149–172 (1996).

[CAS](#) [PubMed](#) [Article](#) [PubMed Central](#) [Google Scholar](#)

36. 36.

Henriksen, E. J. et al. Spatial representation along the proximodistal axis of CA1. *Neuron* **68**, 127–137 (2010).

[CAS](#) [PubMed](#) [PubMed Central](#) [Article](#) [Google Scholar](#)

37. 37.

Stukowski, A. Visualization and analysis of atomistic simulation data with OVITO—the Open Visualization Tool. *Model. Simul. Mater. Sci. Eng.* **18**, 015012 (2010).

[ADS](#) [Article](#) [Google Scholar](#)

38. 38.

Larsen, P. M., Schmidt, S. & Schiøtz, J. Robust structural identification via polyhedral template matching. *Model. Simul. Mater. Sci. Eng.* **24**, 055007 (2016).

[ADS](#) [Article](#) [CAS](#) [Google Scholar](#)

39. 39.

Brandon, M. P. et al. Reduction of theta rhythm dissociates grid cell spatial periodicity from directional tuning. *Science* **332**, 595–599 (2011).

[ADS](#) [CAS](#) [PubMed](#) [PubMed Central](#) [Article](#) [Google Scholar](#)

40. 40.

Koenig, J., Linder, A. N., Leutgeb, J. K. & Leutgeb, S. The spatial periodicity of grid cells is not sustained during reduced theta oscillations. *Science* **332**, 592–595 (2011).

[ADS](#) [CAS](#) [PubMed](#) [Article](#) [PubMed Central](#) [Google Scholar](#)

41. 41.

Hansen, J.-P. & Verlet, L. Phase transitions of the Lennard-Jones system. *Phys. Rev.* **184**, 151–161 (1969).

[ADS](#) [CAS](#) [Article](#) [Google Scholar](#)

42. 42.

Langston, R. F. et al. Development of the spatial representation system in the rat. *Science* **328**, 1576–1580 (2010).

[ADS](#) [CAS](#) [PubMed](#) [Article](#) [PubMed Central](#) [Google Scholar](#)

43. 43.

Wills, T. J., Cacucci, F., Burgess, N. & O'Keefe, J. Development of the hippocampal cognitive map in preweanling rats. *Science* **328**, 1573–1576 (2010).

[ADS](#) [CAS](#) [PubMed](#) [PubMed Central](#) [Article](#) [Google Scholar](#)

44. 44.

Eliav, T. et al. Nonoscillatory phase coding and synchronization in the bat hippocampal formation. *Cell* **175**, 1119–1130 (2018).

[CAS](#) [PubMed](#) [Article](#) [PubMed Central](#) [Google Scholar](#)

45. 45.

Derdikman, D. et al. Fragmentation of grid cell maps in a multicompartment environment. *Nat. Neurosci.* **12**, 1325–1332 (2009).

[CAS](#) [PubMed](#) [Article](#) [PubMed Central](#) [Google Scholar](#)

46. 46.

Torquato, S. & Stillinger, F. H. Jammed hard-particle packings: from Kepler to Bernal and beyond. *Rev. Mod. Phys.* **82**, 2633 (2010).

[ADS](#) [Article](#) [Google Scholar](#)

47. 47.

D'Albis, T. & Kempter, R. A single-cell spiking model for the origin of grid-cell patterns. *PLoS Comput. Biol.* **13**, e1005782 (2017).

[ADS](#) [PubMed](#) [PubMed Central](#) [Article](#) [CAS](#) [Google Scholar](#)

48. 48.

Monsalve-Mercado, M. M. & Leibold, C. Hippocampal spike-timing correlations lead to hexagonal grid fields. *Phys. Rev. Lett.* **119**, 038101 (2017).

[ADS](#) [MathSciNet](#) [PubMed](#) [Article](#) [PubMed Central](#) [Google Scholar](#)

49. 49.

Weber, S. N. & Sprekeler, H. Learning place cells, grid cells and invariances with excitatory and inhibitory plasticity. *eLife* **7**, e34560 (2018).

[PubMed](#) [PubMed Central](#) [Article](#) [Google Scholar](#)

50. 50.

Yoon, K. et al. Specific evidence of low-dimensional continuous attractor dynamics in grid cells. *Nat. Neurosci.* **16**, 1077–1084 (2013).

[CAS](#) [PubMed](#) [PubMed Central](#) [Article](#) [Google Scholar](#)

51. 51.

Guanella, A., Kiper, D. & Verschure, P. A model of grid cells based on a twisted torus topology. *Int. J. Neural Syst.* **17**, 231–240 (2007).

[PubMed](#) [Article](#) [PubMed Central](#) [Google Scholar](#)

52. 52.

Fuhs, M. C. & Touretzky, D. S. A spin glass model of path integration in rat medial entorhinal cortex. *J. Neurosci.* **26**, 4266–4276 (2006).

[CAS](#) [PubMed](#) [PubMed Central](#) [Article](#) [Google Scholar](#)

53. 53.

Klukas, M., Lewis, M. & Fiete, I. Efficient and flexible representation of higher-dimensional cognitive variables with grid cells. *PLoS Comput. Biol.* **16**, e1007796 (2020).

[ADS](#) [PubMed](#) [PubMed Central](#) [Article](#) [CAS](#) [Google Scholar](#)

54. 54.

Burak, Y. & Fiete, I. Do we understand the emergent dynamics of grid cell activity? *J. Neurosci.* **26**, 9352–9354 (2006).

[CAS](#) [PubMed](#) [PubMed Central](#) [Article](#) [Google Scholar](#)

55. 55.

Rowland, D. C., Roudi, Y., Moser, M.-B. & Moser, E. I. Ten years of grid cells. *Annu. Rev. Neurosci.* **39**, 19–40 (2016).

[CAS](#) [PubMed](#) [Article](#) [PubMed Central](#) [Google Scholar](#)

[Download references](#)

Acknowledgements

We thank A. Treves for extensive discussions, A. V. M. Herz and E. Katzav for helpful suggestions; F. Stella, E. D. Karpas, T. Tamir, A. Rubin, A. Finkelstein, S. R. Maimon, S. Ray, D. Omer, S. Palgi and A. Sarel for comments on the manuscript; J.-M. Fellous for contributing to the initial stages of this project; S. Kaufman, O. Gobi and I. Shulman for bat training; A. Tuval for veterinary support; C. Ra’anan and R. Eilam for histology; M. P. Witter for advice on histological delineation of MEC borders; B. Pasmanirer and G. Ankaoua for mechanical designs; and G. Brodsky and N. David for graphics. We thank the Methods in Computational Neuroscience course at MBL, Woods Hole, where the modelling work was initiated. N.U. is the incumbent of the Barbara and Morris Levinson Professorial Chair in Brain Research. Y.B. is the incumbent of the William

N. Skirball Chair in Neurophysics. This study was supported by research grants to N.U. from the European Research Council (ERC-CoG – NATURAL_BAT_NAV), Israel Science Foundation (ISF 1319/13), and Minerva Foundation, and by the André Deloro Prize for Scientific Research and the Kimmel Award for Innovative Investigation to N.U. Y.B. acknowledges support from the Israel Science Foundation (ISF 1745/18), the European Research Council (ERC-SyG – KiloNeurons), and the Gatsby Charitable Foundation. H.S. acknowledges support from the Gatsby Charitable Foundation.

Author information

Affiliations

1. Department of Neurobiology, Weizmann Institute of Science, Rehovot, Israel

Gily Ginosar, Johnatan Aljadeff, Liora Las & Nachum Ulanovsky

2. Department of Bioengineering, Imperial College London, London, UK

Johnatan Aljadeff

3. The Edmond and Lily Safra Center for Brain Sciences, The Hebrew University of Jerusalem, Jerusalem, Israel

Yoram Burak & Haim Sompolinsky

4. Racah Institute of Physics, The Hebrew University of Jerusalem, Jerusalem, Israel

Yoram Burak & Haim Sompolinsky

5. Center for Brain Science, Harvard University, Cambridge, MA, USA

Haim Sompolinsky

Authors

1. Gily Ginosar

[View author publications](#)

You can also search for this author in [PubMed](#) [Google Scholar](#)

2. Johnatan Aljadeff

[View author publications](#)

You can also search for this author in [PubMed](#) [Google Scholar](#)

3. Yoram Burak

[View author publications](#)

You can also search for this author in [PubMed](#) [Google Scholar](#)

4. Haim Sompolinsky

[View author publications](#)

You can also search for this author in [PubMed](#) [Google Scholar](#)

5. Liora Las

[View author publications](#)

You can also search for this author in [PubMed](#) [Google Scholar](#)

6. Nachum Ulanovsky

[View author publications](#)

You can also search for this author in [PubMed](#) [Google Scholar](#)

Contributions

G.G, L.L. and N.U. conceived and designed the experiments. G.G. conducted the experiments, with contributions from L.L. G.G. analysed the experimental data. L.L. and N.U. guided the data analysis. J.A., Y.B. and H.S. conducted the theoretical modelling, and J.A. analysed the model results. G.G. and N.U. wrote the first draft of the manuscript, with major

input from L.L. All authors participated in writing and editing of the manuscript. N.U. supervised the project.

Corresponding author

Correspondence to [Nachum Ulanovsky](#).

Ethics declarations

Competing interests

The authors declare no competing interests.

Additional information

Peer review information *Nature* thanks Mark Brandon, Torkel Hafting and the other, anonymous, reviewer(s) for their contribution to the peer review of this work.

Publisher's note Springer Nature remains neutral with regard to jurisdictional claims in published maps and institutional affiliations.

Extended data figures and tables

[Extended Data Fig. 1 Expected properties of 3D grid cells, and coverage of 3D space by the bats' behaviour.](#)

a, Five basic properties of 2D grid cells. **b**, Expected properties of 3D grids under five hypothetical possibilities, ranging from highly ordered to random arrangement of fields. **c**, **d**, Bat behaviour covers 3D space. **c**, Examples of bat trajectories in the flight room. Rows: one example session from each of the four bats included in this study. Columns show different viewing perspectives: 3D view; top view of the room (xy); and side views of the room (xz and yz). Note that for bat 4 only, part of the room (grey area) was blocked off by a see-through nylon mesh (see [Methods](#)). **d**, Histograms of

distance flown per session, plotted separately for each of the four bats; we included here only sessions in which we recorded at least one of the 125 well-isolated neurons that passed the inclusion criteria for analysis.

Extended Data Fig. 2 A series of histological sections from one bat, showing two tetrode tracks in MEC layer 5.

Two tetrode tracks that enter from postrhinal cortex (POR) and progress along layer 5 of MEC in bat 2. Four sagittal Nissl-stained sections are arranged from medial (top) to lateral (bottom). Left, wide view (scale bar, 1,000 µm); right, zoom-in onto the region of the tetrode tracks (scale bar, 500 µm). The postrhinal (dorsal) border of MEC is marked by a black line. The combination of the angled tetrode penetration (see [Methods](#)) and the sagittal slicing of the brain resulted in tetrode tracks that are recognizable as a small hole (sometimes surrounded by glial scar) that proceeds over many consecutive sections. The distance of the hole (track) from the postrhinal border of MEC is indicated on the right. Coloured circles mark the tracks of the two tetrodes (purple, tetrode 1 (TT1); green, tetrode 4 (TT4)). The lesion at the end of the track of tetrode 1 (purple) is visible in section 31c (section numbers are indicated). The lesion at the end of the track of tetrode 4 (green) is visible in section 29b.

Extended Data Fig. 3 Firing fields, and additional examples of cells.

a, Peak detection: firing-rate map of an example cell, with overlaid black dots marking the positions of the detected field peaks (see [Methods](#)). Note that only the peaks of the visible fields are displayed here (not plotting the peaks for fields ‘buried’ deep inside the 3D volume of the map). **b**, Threshold for peak detection shuffle (one of three criteria for a field to be valid; these three criteria narrowed the $n = 125$ cells to $n = 78$ cells): an identified peak was included in the analysis if the firing rate in its peak voxel was higher than the firing rate in the same voxel in 75% of the spike shuffles (see [Methods](#)). Shown are the shuffle percentiles for all fields (both above and below this threshold); the 75% threshold was set at a natural kink in the distribution. **c**, Number of fields per neuron: a histogram for all the

neurons with valid fields ($n = 78$ cells), showing the number of fields per cell. A threshold of 10 fields was set for a neuron to be considered as ‘multifield’ ($n = 66$ cells, black bars; grey bars show cells below the threshold); see [Methods](#) for the rationale of setting this 10-field threshold. Example cells with varying numbers of fields are shown in **d**. **d**, Examples of cells with varying numbers of fields, including <10 fields (two left cells, not considered as multifield cells), and both grid and non-grid multifield cells with ≥ 10 fields. Plotted as in Fig. [2a, b](#). Top: 3D firing-rate maps. Bottom: box plots showing the median field sizes in the x , y and z directions. Horizontal line, median; box limits, 25th to 75th percentiles; whiskers, 10th to 90th percentiles. Shown are the results of Wilcoxon rank-sum tests comparing field dimensions in x vs. y , y vs. z and x vs. z , Bonferroni-corrected for three pairwise comparisons; n.s., non-significant; the number of fields for each cell (that is, the n for each test) is written above each firing-rate map. **e**, Two example neurons with significant field elongations; plotted as in **d** (overall, 9 out of 66 neurons showed significant field elongations). Note that these two neurons differed in their elongation direction. Wilcoxon rank-sum test comparing field dimensions in x vs. y , y vs. z and x vs. z , Bonferroni-corrected for three pairwise comparisons: left cell: $P_{yz} = 0.03$, $P_{xz} = 0.003$; right cell: $P_{xy} = 0.006$ (Bonferroni-corrected for three comparisons); the number of fields for each cell (that is, the n for each test) is written above each firing-rate map. In the 9 cells with significant field elongation, fields did not resemble columns and elongation was weak and not systematic, that is, the elongation direction was heterogeneous and differed across these 9 elongated neurons.

[Extended Data Fig. 4 Non-stereotypy of flights, and diversity of passes through fields: part I.](#)

a, Passes per field: histograms showing the number of flight passes creating each firing field (passes per field and passes with spikes per field serve as two of three criteria for a detected field to be considered valid). The four histograms correspond to all passes within the fields (top) and all passes with spikes within the field (bottom), computed for two different values of the radius from the field’s peak: 30 cm (left) and 50 cm (right). **b**, Flight non-stereotypy: a histogram showing the percentage of flights of each cell that passed through the same sequence of fields, within two different values

of the distance (radius) from the field's peak: 30 cm (left) and 50 cm (right). Flights that pass through the same sequence of fields correspond to a stereotypic trajectory of the bat: for example, if the same flight sequence repeats four times, it would appear here in the fourth bin, that is, with a value of 4 for 'No. of flights with same sequence'. The results here show that most flights are in fact unique and do not repeat more than once for the same cell (see large bin with value 1 for 'No. of flights with same sequence'), which suggests that the bats' flights were non-stereotypic. **c**, The *xy* projections of the trajectories that passed through 20 example fields. Shown are trajectories within a 0.5-m radius around the field's peak (this is the typical radius of grid fields in our data). We extracted the trajectories for all the 1,113 fields of the 66 multifield neurons, as follows: for each field we took a 3D sphere with 0.5-m radius around the field's peak, then extracted the 3D trajectories through this field, and then projected these 3D trajectories onto *xy* (2D projections). The Rayleigh vector length (RV) of the *xy*-projected trajectories was then computed for each field. Here we plotted one example field from approximately every fifth percentile of the RV distribution—a total of 20 example fields, ordered from low to high RV. The RV value and percentile (in parentheses) are indicated: top left example is from the first percentile of the RV = lowest RV (most isotropic trajectories); bottom right example is from the 99th percentile of the RV = highest RV (most uni-directional trajectories). Scale bar, 0.5 m. **d**, The RV distribution across all the fields ($n = 1,113$), calculated on the trajectories forming each field (see examples in **c**). Median RV of this distribution = 0.25: this is a relatively low value, indicating rather isotropic flights through most fields.

Extended Data Fig. 5 Non-stereotypy of flights, and diversity of passes through fields: part II.

a, Two examples of individual cells (columns), depicting the firing rates in each of the fields based on the trajectories coming from specific take-off balls (top matrices) or specific landing balls (bottom matrices); colour-coded from 0 (blue) to maximum firing rate (red; value indicated). In each matrix, the variety of firing rates in each row of the matrix (corresponding to each field) shows that the firing of each field was created by trajectories originating from a variety of take-off balls and ending on a variety of

landing balls. **b**, Percentage of fields per cell that are created from diverse trajectories. Box plots show the percentages of fields per cell whose behavioural trajectories involved at least 50% of the take-off balls (left) or landing balls (right). This analysis was done for the three bats for which we used landing balls. Horizontal line, median; box limits, 25th to 75th percentiles; whiskers, 10th to 90th percentiles. The high percentage shown here means that across cells, the large majority of fields per neuron involved most of the take-off balls and landing balls—that is, the bats' flights were diverse and non-stereotypic. **c**, Histograms showing the number of fields that were formed by trajectories that originated from various numbers of different take-off balls (top) and ending at various numbers of different landing balls (bottom). This analysis was done for the three bats for which we used landing-balls. **d–f**, As in **a–c**, but here instead of take-off and landing balls we examined the firing-rate at different directions of the trajectories passing through the field. This analysis was done on all the four bats. **d**, Examples of two individual cells. **e**, Percentage of fields in which the trajectories with spikes that occurred close to the field-peak (within 50 cm of the field peak) came from $\geq 50\%$ of the direction bins. **f**, Distribution of the percentage of direction bins for trajectories with spikes that passed through each field. For example, 60% on the x -axis means that the spikes of that field came from 60% of all the possible direction bins; that is, the flight trajectories with spikes that passed through that field spanned 60% of all the possible direction bins (60% of 360° ; we used here 36° bins)—a high diversity of directions.

Extended Data Fig. 6 Searching for global and local order.

a, Two lattices were proposed as theoretically probable structures of 3D grids^{16,17}: these lattices exhibit a hexagonal arrangement of spheres, and were proved to be the optimal arrangement for densest sphere packing in infinite 3D space¹⁵. These lattice arrangements—face centred cubic (FCC) and hexagonal close pack (HCP)—are widely found in chemistry. Both of these lattices are comprised of layers of spheres arranged in a hexagonal pattern (denoted here as layers A, B and C); the two lattices differ in the phase of these layers. Each layer is placed in one of two optional sets of holes created by the lower layer: the HCP lattice has an A–B–A pattern of layers (left); the FCC lattice has an A–B–C pattern of layers (right). **b**,

Illustration of the procedure of fitting data to hexagonal lattices (see [Methods](#)). Cartoon in 2D depicts the fitting that we used in 3D to fit the recorded 3D field arrangements to perfect FCC and HCP lattices. To find the best-fitting lattice for each of our recorded cells, we compared each cell with 3 million variations of FCC and HCP perfect lattices; this was done separately for FCC and HCP lattices (1.5 million variations for FCC and 1.5 million for HCP). In each iteration, we found for each of the recorded fields (purple spheres) the closest field in the perfect lattice (the simulated perfect lattice fields are depicted by dotted blue circles; red lines depict the distances between a recorded field and its nearest simulated lattice field). We then computed the squared distance from each recorded field to its closest simulated synthetic field; we summed these squared distances and computed the root, to yield the root mean square (RMS) error of each cell for each of the 1.5 million FCCs or 1.5 million HCPs. The cell's lowest RMS error across all the 1.5 million FCC lattices was termed the 'FCC fit error', and was then compared to the FCC fit errors that were analogously computed for all the shuffles (that is, for each shuffle we found the minimal FCC fit error over the 1.5 million synthetic FCC's). The same was done for HCP. **c**, Distribution of local angles. There was no angle-bias of local 3D angles, suggesting no local orientational (angular) order in the field arrangements. Top, local angles were computed between triplets of nearest-neighbouring fields; to avoid edge effects, we computed the angles only for fields that were within the convex hull of field arrangement. Grey, all recorded multifield cells; black line, shuffled data (using spike shuffling). Middle and bottom, distributions of local angles plotted separately for 3D grid cells (middle: red) and non-grid multifield cells (bottom: blue), together with shuffle data (black lines). The distributions for recorded cells did not differ significantly from the spike-shuffled data (black; indicated are the P values of Kolmogorov–Smirnov tests between data and shuffles). **d**, **e**, The calculation of the CV of distances to nearest neighbouring fields. **d**, Cartoon illustrating the three distances between each field and its three nearest neighbouring fields. These distances were then pooled across all fields (while avoiding double-counts), and the CV over these distances was calculated to quantify how fixed is the distance scale of the neuron (see [Methods](#)). **e**, Rationale for why the CV was computed over three nearest neighbours, and not 1, 2 or >3 nearest neighbours. Right, a perfect 2D lattice arrangement will yield low CV values regardless of how

many nearest neighbours are considered: three (bottom) or two (top). Left, a periodic 1D structure ('fields along a string')—which is not a 2D lattice—may still yield a low CV when considering only two neighbours (top left), but a high CV when considering three or more nearest neighbours (bottom left). Thus, three is the minimal number of nearest neighbours that can differentiate these possibilities, and unequivocally characterize the 3D arrangement of fields. We did not use more than three neighbours, because using a large number of neighbours may accentuate possible edge effects. **f**, Comparison of the CV measure and gridness score for cells in 2D. Left, scatter plot of the CV of nearest-neighbour distances versus the classical 2D gridness score, for medial entorhinal cortex neurons recorded in rats running in 2D in the Moser laboratory (courtesy of M.-B. Moser and E. I. Moser, from <https://www.ntnu.edu/kavli/research/grid-cell-data>; $n = 259$ cells; we excluded from analysis putative interneurons (mean firing rate >5 Hz), non-spatial neurons (cells with spatial information <0.2 bits per spike) and border cells (manually excluded)). The Pearson correlation of this scatter and its P value are given in the top-right corner. Right, example firing-rate maps of two cells. Top, a spatial non-grid cell with low gridness score and high CV; bottom, a grid cell with high gridness score and low CV. The locations of these two cells on the scatter plot are indicated. Here the gridness score was computed as described in the Methods, and the CV was computed using the distances of the two nearest neighbours of each field, rather than three nearest neighbours as done for 3D cells, because in 2D many cells did not have enough fields. **g, h**, The lack of global order could not be explained by proximity to room borders. **g**, Local angles throughout the room: shown is a scatter plot of the local angles between triplets of neighbouring fields as a function of their distance from the nearest wall. Points were slightly jittered in the x -axis, for display purposes only. Pearson correlation and significance are shown. The non-significant correlation suggests that the walls did not affect the 3D arrangement of fields. **h**, CV of nearest-neighbour distances throughout the room: shown is a histogram of the differences between CVs of fields at the edges of the room and the CVs of fields in the centre of the room ($\text{CV}_{\text{edges}} - \text{CV}_{\text{centre}}$). The border between 'centre' and 'edges' of the room was defined as the median distance of all the fields from their closest wall. Grey bars, histogram for all multifield cells ($n = 66$ cells); black line, histogram for shuffles done per neuron, using spike shuffling. P value of Kolmogorov–Smirnov test of data versus

shuffles is indicated. The non-significant difference suggests that the walls did not affect the 3D arrangement of fields.

Extended Data Fig. 7 The firing of 3D grid cells and non-grid multifield cells cannot be explained via a global lattice that undergoes distortions (scaling, shearing, or barrelling).

a–c, Mean CVs of distances between neighbouring fields, calculated after un-distorting the field positions of multifield cells ($n = 66$); shown separately for each individual bat (columns 1–4), and for all the cells from all bats pooled together (column 5). We did three types of un-distortion: un-scaling, un-shearing, and un-barrelling (see [Methods](#)). **a**, Un-scaling: field positions were scaled by a factor α along the specified axis. $\alpha < 1$ corresponds to shrinking towards the middle of the room along the specified axis, $\alpha > 1$ means expansion, $\alpha = 1$ corresponds to no change. The three rows correspond to un-scaling along three pairs of axes: xy , yz , and xz . Each heat-map describes the mean CV for all possible combinations of un-scaling of two axes: α_1 describes the first axis (in xy (first row) it corresponds to x), and α_2 describes the second axis (in xy it corresponds to y). CV is colour-coded from minimal value (blue) to maximal value (red), and these values are written above each matrix. White squares indicate no scaling ($\alpha_1 = \alpha_2 = 1$, that is, original data). **b**, Un-shearing: the fields of each cell underwent shearing/un-shearing as described⁴ (see [Methods](#)), where shearing was done by two walls simultaneously (yielding 15 possible combinations of shearing, all shown here (rows)); we computed the two possible shearing directions (positive and negative γ -factor, which can also be thought of as shearing and un-shearing). The writing on the left indicates the two walls that create the shearing and the axes in which the shearing is occurring (for example, xz shear x means that the xz wall is creating a shearing along the x -axis). Factor γ_1 corresponds to the first line (for example, xz shear x in the top row), and γ_2 corresponds to the second line (for example, yz shear y in the top row). Heat-map shows mean values of CV, colour-coded from minimum (blue) to maximum (red; values indicated above the panel). White squares indicate no shearing ($\gamma_1 = \gamma_2 = 0$, that is, original data). **c**, Un-barrelling: a barrelling transformation (also known as

fisheye lens distortion) and un-barrelling transformation (also known as pin-cushion distortion) was performed on the field arrangement of each cell. Plots show mean CV values as a function of the barrel and un-barrel factor β , for the different 2D planes along which the barrelling/un-barrelling was done (xy , yz , xz (rows)). All the transformations in **a–c** (scaling, shearing, barrelling) showed that distorting or un-distorting away from the original field arrangement increases the CV—which argues against the notion that the original field arrangements constitute a global lattice that underwent distortions.

Extended Data Fig. 8 Both 3D grid cells and non-grid multifield cells exhibit an anatomical gradient along the dorsoventral axis of MEC, as seen in rodent 2D grid cells.

a, Examples of recording sites and firing-rate maps of cells along the inter-field distance gradient, here using the spike-shuffling method as in Fig. 3b. Central scatterplot: both 3D grid cells (red) and non-grid multifield cells (blue) exhibited an increase in inter-field distance as a function of the recording depth along the dorsoventral axis of MEC—akin to what is known from rodent 2D grid cells¹. 3D grid cells were identified using spike shuffling; data points were pooled here across tetrodes and bats, and include only cells with high-quality histology that allowed precise assessment of recording depth within MEC ($n = 8$ grid cells, $n = 28$ non-grid multifield cells). Side panels: two histology examples, and their associated 3D firing-rate maps. Left, 3D grid cell recorded in layer 3; right, non-grid multifield cell recorded in layer 5. **b**, The increase in inter-field distance along the dorsoventral axis of MEC is also evident in individual tetrode tracks (TT). Shown are examples of three tetrode tracks, which proceeded mostly along a single cortical layer (indicated). Pearson correlation coefficients and their P values are indicated. **c**, Dorsoventral gradient, plotted as in Fig. 3b, but here classifying grid cells based on the field-shuffling method (rather than the spike-shuffling method as in Fig. 3b). We identified 20 neurons as 3D grid cells using field shuffling; included in these scatter-plots were only cells with high-quality histology that allowed precise assessment of recording depth within MEC ($n = 11$ grid cells, $n = 25$ non-grid multifield cells). Left, gradient of inter-field distances between neighbouring fields as a function of recording depth in MEC (distance from the postrhinal border

of MEC); right, gradient of number of fields per cell as a function of recording depth. Note that the gradient is exhibited by both 3D grid cells (red) and non-grid multifield cells (blue), suggesting they are not two separate populations of neurons, but a continuum. Shown are Pearson correlation coefficients and their P values.

Extended Data Fig. 9 Border cells and firing characteristics of the various cell classes.

a–c, Border cells. **a**, Definition of border cells in 3D arenas. We considered only neurons for which a 2D firing field was detected in each of the cell's 2D planes (see [Methods](#)). 2D firing-rate maps were plotted in the three principal 2D views of the room geometry: the top view xy , and the two side views xz and yz (green, orange and blue, respectively). We defined an elongation index for each field in each 2D plane as the field size along the more elongated axis/field size along the less elongated axis; the elongation index was computed separately for all three 2D planes (xy , xz , yz). A border field was defined as a field that was significantly elongated in exactly two out of the three views (for determining the significance we used the elongation index for each field and compared it to the elongation indices of spike shuffles; 99% criterion). Significant 1D border cells (left) were defined as 'sausage-shaped' neurons in which: (i) two of the 2D planes (2D views) exhibited firing fields with an elongation index > 2 , which was also significantly higher than shuffled data ($>99\%$ of the shuffles); and (ii) the third plane (2D view) exhibited a firing field that was non-elongated, and was smaller than in the two elongated planes (left, blue square), thus defining a 1D 'sausage'. Significant 2D planar border cells (right) were defined as 'pancake-shaped' neurons in which: (i) two of the 2D planes (2D views) exhibited firing fields with elongation index > 2 , which was also significantly higher than shuffled data ($>99\%$ of the shuffles); and (ii) the third plane (2D view) exhibited a firing field that was non-elongated, and was larger than in the two elongated planes (right, green square), thus defining a 2D 'pancake'. **b, c**, A full depiction of the example border cells plotted in Fig. [4b](#), here shown also with trajectories and spikes, as well as an additional example. **b**, Example of a border cell that exhibited firing along a 1D border of space—in this case, along the wall edge. Left, a top view of the room (xy); middle, right, side views (xz and yz). Top, flight

trajectory (grey) with spikes superimposed (red dots); bottom, firing rate maps, colour-coded from zero (blue) to the maximal firing rate across the three views of each cell (red). White line, edges of the detected firing field (enlarged by one bin for display purposes); indicated are the peak firing-rate and elongation index (EI; see [Methods](#)). Grey rectangle, area of the room that was made inaccessible for one of the four bats (see [Methods](#)). **c**, Examples of border cells that exhibited firing along a 2D planar border of space—in this case, the floor. Plotted as in **b**. Top cell also shown in Fig. [4b](#). **d, e**, Characteristics of the various cell classes. **d**, Firing characteristics for the different functional cell classes in MEC during 3D flight (mean \pm s.d. across cells; the column of head-direction cells is based on significant azimuthal head-direction cells). Peak firing rate (FR): the highest firing rate in the 3D firing rate map. Mean firing rate: the mean of the 3D firing rate map (second row) and the ratio of total spikes in flight/total time in flight (third row); these values were very similar because the 3D behaviour was quite uniform. Fourth row: Theta index^{[8,19,39,40](#)} (TI) computed as in ref. [19](#), where a criterion of $TI > 5$ was used as threshold for defining theta-modulated cells. All the cells in our study, including all the grid cells, exhibited $TI < 5$, indicating a lack of theta rhythmicity in the MEC of flying bats, consistent with previous findings on bat MEC cells in 2D^{[8,44](#)}. **e**, Examples of spike-train autocorrelations (top) and their power spectra (bottom) for the various cell classes. The theta index is indicated above the power spectra. Note that for the four grid cells, the two leftmost examples have theta index below the population mean (see **d**), whereas the two rightmost examples have theta index above the population mean; none of these four examples exhibited clear oscillations.

[Extended Data Fig. 10 Distribution of best-fitting temperatures in the Lennard–Jones pairwise interactions model, and comparison to alternative pairwise-interactions models.](#)

a–c, Simulations of highly structured cells with low CV ($CV < 0.25$, $n = 29$ neurons). **a**, Distribution of the best-fitting temperatures (T) in the Lennard–Jones (LJ) pairwise interactions model (red, 3D grid cells identified by spike shuffling; blue, non-grid multifield cells). The best-fitting temperature for the model ($\log_{10}T = 0.5$; black dashed line) was computed as the

average logarithm of the temperatures across all these cells; this temperature was consistent with the individual temperatures for almost all of the cells. The small variation in the fitted temperatures allowed us to use a single temperature for all the cells ($\log_{10}T = 0.5$, dashed line). **b, c,** Comparison of multiple models of short-range repulsion and long-range attraction (Lennard–Jones, modified Lennard–Jones, and difference-of-Gaussians (DOG) potentials). **b**, Quantifying the match between model and data. Three rightmost bars: distances between the RDF of the data and the RDFs of the pairwise interactions models: Lennard–Jones, modified Lennard–Jones, and DOG ($\log_{10}T = 0.5$ for all models). Left bar, distance between the RDF of the data and the RDF of the random Poisson model (in which the fields were randomly distributed in the 3D region visited by the bat). $N = 1,000$ simulated RDFs for each model; shown mean \pm s.e.m. The distance between the RDFs of the model simulations and the RDF of the data was substantially smaller for the three pairwise interactions models than for the random Poisson model (t -test: $P < 10^{-300}$ for all three comparisons). **c**, Best-fitting temperatures (in log scale, mean \pm s.d.) for neurons with $CV < 0.25$, plotted for the three pairwise interactions models. All these potentials yielded similar best-fitting temperatures: the Lennard–Jones and modified Lennard–Jones potentials yielded very similar best-fitting temperatures, and the DOG potential yielded a slightly lower temperature. The vertical dashed line denotes the temperature that was used for the bulk of the simulations in this study with the Lennard–Jones potential ($\log_{10}T = 0.5$). We note that for the modified Lennard–Jones and DOG potentials, the match between the RDF of the data and the RDF of the model was also very good for $\log_{10}T = 0.5$ (see **b**, where for all three pairwise interactions models we used $\log_{10}T = 0.5$). **d, e**, Simulations for high-CV cells ($CV > 0.25$, neurons not exhibiting an ordered arrangement of fields; $n = 37$ neurons). **d**, Distribution of the best-fitting temperatures in the Lennard–Jones pairwise interactions model (red, 3D grid cells; blue, non-grid multifield cells). The average logarithm of the best-fitting temperatures across these neurons was $\sim \log_{10}T = 3.5$ (black dashed line). **e**, Quantifying the match between model and data; t -test, P values indicated. Three rightmost bars: distances between the RDF of the data and the RDFs of the three pairwise interactions models (temperatures used here: Lennard–Jones, $\log_{10}T = 3.5$; modified Lennard–Jones, $\log_{10}T = 1.5$; DOG,

$\log_{10}T = 1$; these were the best-fitting temperatures for each of the models; note that these temperatures correspond to a much higher noise level than in the pairwise interactions models in **a–c**, where we considered neurons with $CV < 0.25$ and fitted a temperature of $\log_{10}T = 0.5$). Left bar, distance between the RDF of the data and the RDF of the random Poisson model. $N = 1,000$ simulated RDFs for each model; shown mean \pm s.e.m.

Extended Data Fig. 11 Modelling: index definitions, 2D grids, and effective density.

a, Definition of the regularity index (RI), computed as the relative height of the maximum versus the minimum in the RDF (excluding its first peak); that is, the RI reflects the modulation depth of the second (or third) peak of the RDF (see [Methods](#)). **b**, Definition of effective density ρ_{eff} , which is defined as $r_0/\text{mean inter-field distance}$ (see [Methods](#)). Note that when the fields are at their equilibrium position, at distances equalling the minimal energy of the Lennard–Jones potential, the effective density is $\rho_{\text{eff}} = 0.9$; that is, $\rho_{\text{eff}} = 0.9$ is the ‘natural’ effective density. **c**, Two examples of 2D simulated cells, showing field positions (bottom) and autocorrelograms (top, zoomed in on the centre). Numbers above autocorrelograms indicate the classical 2D gridness score (g). The left example is also shown in Fig. [5d](#). **d**, Distribution of gridness scores in all the pairwise-interaction 2D simulations (room size: 2×2 m). Many of the 2D simulations resulted in a high gridness score, indicating a highly ordered hexagonal organization. **e**, Plot of the classical 2D gridness score^{[8,10,19](#)} versus 2D room size, for our 2D model simulations (simulations in a room of size $a \times a \times 10$ -cm height; the gridness score was computed as described above (see [Methods](#)) and is shown as mean \pm s.e.m.; minimum 500 simulations per room size a (the number of simulations varied because they were chosen post hoc to match the nominal ρ_{eff})). This plot is shown for fixed effective density $\rho_{\text{eff}} = 0.9$, which is the ‘natural’ value for ρ_{eff} , where the local distances equal the minimal energy distance r_{\min} of the Lennard–Jones potential (see **b**; note that ρ_{eff} is defined as: $\rho_{\text{eff}} = r_0/d_{\text{NN}}$, where d_{NN} is the mean nearest neighbour distance (see [Methods](#)); because $r_{\min} = r_0 \times 1.12$ in the Lennard–Jones function, this yields: $\rho_{\text{eff}} = (r_{\min}/1.12)/d_{\text{NN}} \approx 0.9 \times r_{\min}/d_{\text{NN}}$. That is,

when $d_{\text{NN}} = r_{\min}$, this yields $\rho_{\text{eff}} = 0.9$). In other words, $\rho_{\text{eff}} = 0.9$ is the effective density that yields inter-field distances that match the minimum of the Lennard–Jones potential. We note that this effective density is also well within the empirically measured range of effective densities for our experimental data (see **f**). **f**, Distribution of effective density of fields ρ_{eff} in our experimental data, computed using the best-fitted scale parameter r_0 for each neuron (shown here are the $n = 29$ multifield cells with $\text{CV} < 0.25$). **g**, Regularity index as a function of room height. Simulations were done in 10-cm increments of room height, going from effectively 2D arena (0.1 m ceiling) to a full 3D room (2.5 m ceiling), as in Fig. [5e](#). Each curve was computed for a fixed effective density ρ_{eff} (see **b**); different curve shading corresponds to different ρ_{eff} values, from light to dark grey ($\rho_{\text{eff}} = 0.75$ to $\rho_{\text{eff}} = 1$). Thick curve (shown in Fig. [5e](#)): $\rho_{\text{eff}} = 0.9$, a value within the range seen in our data (see **f**), and which is the ‘natural’ effective density corresponding to the equilibrium positions of the fields (see **b**). Left, computed for parameters corresponding to the 3D data, using $r_0 = 1$ m and a 5×5 m floor (with varying ceiling height). Right: computed for parameters corresponding to 2D data, using $r_0 = 0.5$ m and a 2×2 m floor (with varying ceiling height). Dashed line marks the value of r_0 used. Note the drop in regularity values when going from 2D to 3D; at this transition point the room height is slightly smaller than the distance parameter r_0 of the Lennard–Jones potential (and thus the room height allowed a second layer of fields).

[Extended Data Fig. 12 3D grid cells are better explained by the pairwise interactions model than by jittered FCC or jittered HCP models; and pairwise interactions lead to a local but not global order at low temperatures of the model.](#)

a, RDF plots for three models (top row, green: Lennard–Jones pairwise interactions model; middle and bottom rows, dark and light purple: jittered FCC and jittered HCP models, where the RDFs were computed for jittered FCC and jittered HCP models with the same nearest-neighbour mean distance (d_{NN}) and CV of distances (CV_{NN}) as used in the pairwise interactions model). Each model was simulated using three temperatures (T)

of the model (left, zero temperature $T = 0$, a non-biological scenario with no noise; middle, low temperature ($\log_{10}T = -1$) with little noise; right, the higher temperature that fitted well our experimental 3D data ($\log_{10}T = 0.5$)). For the temperature fitted to the data ($\log_{10}T = 0.5$), note the comparison of the RDF for the pairwise interactions model (top right, green) to the RDF for a random Poisson model (grey): the peak of the RDF is much sharper around $r = 1$ in the pairwise interactions model (green), indicating preserved local distances between nearby fields. Note that for very low temperatures with little or no jitter (left, middle), the jittered FCC and jittered HCP models showed very repetitive and distinct peaks in the RDF as a function of distance r , indicating a near-perfect lattice—as expected from FCC and HCP with no jitter ($T = 0$) or very small jitter (low temperature $\log_{10}T = -1$). By contrast, for the pairwise interactions model, at low temperatures (both at $\log_{10}T = -1$ and $T = 0$) the RDF was non-zero at all distances (see insets), which is not consistent with a perfect global lattice. At $T = 0$, the RDF seems more consistent with a distorted FCC lattice, but with preserved local distances. In other words, even at very low temperatures, the pairwise interactions model exhibited local distances without a global lattice. **b**, Distributions of local angles for the different models, following the same organization as **a**. Even at $T = 0$, the pairwise interactions model yielded field arrangements with a continuous angle distribution, with all possible angles (except very small angles that cannot occur for nearest-neighbour triangles)—in contrast to the jittered FCC and jittered HCP arrangements where angles concentrated solely in discrete values, which indicates again that even at $T = 0$, the pairwise interactions model does not exhibit a perfect global lattice. Here again, at the temperature fitted to the 3D data ($\log_{10}T = 0.5$), the pairwise interactions model yielded a more ordered arrangement than the random Poisson (top right, green curve for Lennard–Jones: see the mild peak at an angle of 60° , as compared to the grey curve for random Poisson: no peak). This means that the pairwise interactions model yielded stronger local orientational order than randomly arranged fields. **c, d**, Energy convergence of the Lennard–Jones pairwise interactions model at the temperature that best fitted the 3D data ($\log_{10}T = 0.5$, orange) and at $T = 0$ (light blue). **c**, Energy per pair of fields versus the step number of the simulation. **d**, Left, energy change versus the step number of the simulation, plotted in linear–log scale

for both temperatures. Right, energy change of the simulations for $T = 0$, plotted in log–log scale. Shading in **c**, **d** depicts s.e.m. Note that **c**, **d** show that for the temperature which was used to fit our model to the data ($\log_{10}T = 0.5$, orange), the system converged to an asymptote very rapidly, long before we finished running the simulations—that is, the system rapidly reached equilibrium; therefore, the simulations reported in this study correspond to a system in equilibrium.

Extended Data Fig. 13 Comparing the pairwise interactions model for 3D versus 2D, for six combinations of model parameters T and r_0 (varying the number of fields).

a–f, Regularity phase planes for 2D and 3D (see Extended Data Fig. [11a](#) for illustration of the regularity index)—plotted as a function of room size, a , and number of fields, N . Room dimensions: 2D, $a \times a \times 10\text{-cm}$ height; 3D, room-size $a \times a \times a/2$. The three rows (**a**, **b** and **c**, **d** and **e**, **f**) correspond to a changing temperature parameter T (**c**, **d** show the temperature that was best fitted to the experimental data: $\log_{10}T = 0.5$). The two columns (**a**, **c**, **e** and **b**, **d**, **f**) correspond to a changing distance parameter r_0 of the Lennard–Jones potential (values of T and r_0 are indicated). For each panel, we compared simulations in 2D (left) and in 3D (right). The top graphs in each panel show the regularity index (grey scale) for various combinations of a and N (we conducted simulations for $N \geq 10$, corresponding to multifield cells, which have ≥ 10 fields). Note that all these simulations exhibited much higher regularity of field arrangements in 2D than in 3D. Red hatched area denotes a non-plausible region, where the experimentally observed field diameters (~ 20 cm for published 2D rat grid cells²⁴ and ~ 1 m in our 3D bat grid cells) do not allow fitting N such fields into a room of size a (see [Methods](#)). The bottom graphs show the RDF as a function of r (normalized distance) for two specific values of a , N (marked by small squares in the top graphs). Left, 2D simulation for $a = 2$ m, $N = 30$ fields (the approximate arena size and number of fields for a typical rat 2D grid cell from dorsal MEC²⁴); right, 3D simulation for $a = 5$ m, $N = 20$ fields (corresponding to our typical 3D data from bats). RDFs plotted as in Fig. [5d](#). Note that for all six parameter combinations (T , r_0 ; **a–f**), the 2D

simulations showed a high regularity index (owing to a prominent second peak emerging in the RDF in 2D) for a large portion of the phase plane, and in particular in the a, N combination corresponding to a typical 2D grid cell from rat dorsal-MEC²⁴ (black pixel in the left panels)—whereas all 3D simulations showed a low regularity index for a, N corresponding to our data (white pixel in the right panels). A similar difference between 2D and 3D was also found when plotting phase planes of room size a versus the linear density of fields, ρ_0 (Extended Data Fig. 14).

Extended Data Fig. 14 Comparing the pairwise interactions model for 3D versus 2D, for six combinations of model parameters T and r_0 (varying the linear field density).

a–f, Similar phase plane plots as in Extended Data Fig. 13, comparing 2D and 3D, where now the regularity index was plotted as a function of room size a and linear field density ρ_0 (with ρ_0 defined as the square root of the field density in 2D and cubic root of the field density in 3D). We used $r_0 = 1$ m in the right column (**b, d, f**) and $r_0 = 0.5$ m in the left column (**a, c, e**), for three temperatures T (rows; **c, d** show the temperature that was best fitted to the experimental data: $\log_{10}T = 0.5$). Similarly to the plots of the regularity index as a function of room size a and particle number N (Extended Data Fig. 13), these plots show the following: (i) arrangements in 2D are more ordered than in 3D (for matched density); (ii) decreasing the temperature increases the amount of order (compare the three rows); and (iii) increasing the density increases the amount of order (see monotonic dependence of the regularity index on ρ_0 within each panel).

Supplementary information

Reporting Summary

Source data

Source Data Fig. 1

[**Source Data Fig. 2**](#)

[**Source Data Fig. 3**](#)

[**Source Data Fig. 4**](#)

[**Source Data Fig. 5**](#)

Rights and permissions

[Reprints and Permissions](#)

About this article



Check for
updates

Cite this article

Ginosar, G., Aljadeff, J., Burak, Y. *et al.* Locally ordered representation of 3D space in the entorhinal cortex. *Nature* **596**, 404–409 (2021).
<https://doi.org/10.1038/s41586-021-03783-x>

[Download citation](#)

- Received: 08 January 2020
- Accepted: 29 June 2021
- Published: 11 August 2021
- Issue Date: 19 August 2021
- DOI: <https://doi.org/10.1038/s41586-021-03783-x>

Comments

By submitting a comment you agree to abide by our [Terms](#) and [Community Guidelines](#). If you find something abusive or that does not comply with our terms or guidelines please flag it as inappropriate.

[Access through your institution](#)

[Change institution](#)

[Buy or subscribe](#)

Advertisement

This article was downloaded by **calibre** from <https://www.nature.com/articles/s41586-021-03783-x>

| [Section menu](#) | [Main menu](#) |

Systems vaccinology of the BNT162b2 mRNA vaccine in humans

[Download PDF](#)

- Article
- [Published: 12 July 2021](#)

Systems vaccinology of the BNT162b2 mRNA vaccine in humans

- [Prabhu S. Arunachalam](#) ORCID: [orcid.org/0000-0003-0090-5689](#)^{1 na1},
- [Madeleine K. D. Scott](#)^{1,2 na1},
- [Thomas Hagan](#) ORCID: [orcid.org/0000-0002-5254-5251](#)^{3,4 na1},
- [Chunfeng Li](#)¹,
- [Yupeng Feng](#) ORCID: [orcid.org/0000-0001-8550-2787](#)¹,
- [Florian Wimmers](#) ORCID: [orcid.org/0000-0002-6482-2228](#)¹,
- [Lilit Grigoryan](#)¹,
- [Meera Trisal](#)¹,
- [Venkata Viswanadh Edara](#) ORCID: [orcid.org/0000-0001-9321-7839](#)⁵,
- [Lilin Lai](#)⁵,
- [Sarah Esther Chang](#)^{1,6},
- [Allan Feng](#)^{1,6},
- [Shaurya Dhingra](#)^{1,6},
- [Mihir Shah](#)⁷,
- [Alexandra S. Lee](#) ORCID: [orcid.org/0000-0003-4526-3800](#)⁷,
- [Sharon Chinthrajah](#)⁷,
- [Sayantani B. Sindher](#)⁷,
- [Vamsee Mallajosyula](#) ORCID: [orcid.org/0000-0002-0658-3652](#)¹,
- [Fei Gao](#)¹,
- [Natalia Siga](#)¹,
- [Sangeeta Kowli](#)¹,
- [Sheena Gupta](#)¹,
- [Kathryn Pellegrini](#)⁵,
- [Gregory Tharp](#) ORCID: [orcid.org/0000-0003-3075-755X](#)⁵,
- [Sofia Maysel-Auslender](#)¹,
- [Sydney Hamilton](#)⁵,
- [Hadj Aoued](#)⁵,

- [Kevin Hrusovsky](#)⁸,
- [Mark Roskey](#)⁸,
- [Steven E. Bosinger](#) ORCID: orcid.org/0000-0002-2116-5061^{4,9},
- [Holden T. Maecker](#)¹,
- [Scott D. Boyd](#) ORCID: orcid.org/0000-0003-0963-044X^{7,10},
- [Mark M. Davis](#) ORCID: orcid.org/0000-0001-6868-657X^{1,10,11},
- [Paul J. Utz](#) ORCID: orcid.org/0000-0003-1181-1565^{1,6},
- [Mehul S. Suthar](#)⁵,
- [Purvesh Khatri](#) ORCID: orcid.org/0000-0002-4143-4708^{1,2},
- [Kari C. Nadeau](#) ORCID: orcid.org/0000-0002-2146-2955^{7,12,13} &
- [Bali Pulendran](#) ORCID: orcid.org/0000-0001-6517-4333^{1,10,11}

Nature volume **596**, pages 410–416 (2021) [Cite this article](#)

- 51k Accesses
- 1079 Altmetric
- [Metrics details](#)

Subjects

- [RNA vaccines](#)
- [SARS-CoV-2](#)
- [Vaccines](#)

Abstract

The emergency use authorization of two mRNA vaccines in less than a year from the emergence of SARS-CoV-2 represents a landmark in vaccinology^{1,2}. Yet, how mRNA vaccines stimulate the immune system to elicit protective immune responses is unknown. Here we used a systems vaccinology approach to comprehensively profile the innate and adaptive immune responses of 56 healthy volunteers who were vaccinated with the Pfizer–BioNTech mRNA vaccine (BNT162b2). Vaccination resulted in the robust production of neutralizing antibodies against the wild-type SARS-CoV-2 (derived from 2019-nCOV/USA_WA1/2020) and, to a lesser extent, the B.1.351 strain, as well as significant increases in antigen-specific polyfunctional CD4 and CD8 T cells after the second dose. Booster vaccination stimulated a notably enhanced innate immune response as compared to primary vaccination, evidenced by (1) a greater frequency of CD14⁺CD16⁺ inflammatory monocytes; (2) a higher concentration of plasma IFN γ ; and (3) a transcriptional signature of innate antiviral

immunity. Consistent with these observations, our single-cell transcriptomics analysis demonstrated an approximately 100-fold increase in the frequency of a myeloid cell cluster enriched in interferon-response transcription factors and reduced in AP-1 transcription factors, after secondary immunization. Finally, we identified distinct innate pathways associated with CD8 T cell and neutralizing antibody responses, and show that a monocyte-related signature correlates with the neutralizing antibody response against the B.1.351 variant. Collectively, these data provide insights into the immune responses induced by mRNA vaccination and demonstrate its capacity to prime the innate immune system to mount a more potent response after booster immunization.

[Download PDF](#)

Main

BNT162b2 has demonstrated 95% efficacy in preventing severe COVID-19¹. Although adaptive immunity to BNT162b2 has been characterized in humans^{2,3}, little is known about the innate immune response to this vaccine (or to any mRNA vaccine). Systems immunology enables the comprehensive characterization of the cellular and molecular networks that drive innate and adaptive immunity to vaccines and infections^{4,5,6,7,8}. Here we used systems tools to analyse immune responses in 56 volunteers (Extended Data Table 1) who received two doses of BNT162b2 (Extended Data Fig. 1a). More volunteers reported mild side effects after secondary than after primary vaccination (Extended Data Table 2).

Antibody and T cell responses

Primary vaccination induced binding antibody and neutralizing antibody responses in all but three individuals; these responses were boosted significantly after the secondary vaccination (Fig. 1a,b, Extended Data Fig. 1b–d). The neutralizing antibody response reduced about 2-fold by days 90–120, this being comparable to the response to the Moderna mRNA-1273 vaccine⁹ (Fig. 1b, Extended Data Fig. 1c). There was no gender-associated difference in antibody responses; however, the neutralizing antibody response inversely correlated with age (Extended Data Fig. 1e). Four participants with previous confirmed SARS-CoV-2 infection did not have high baseline titres, but after the first immunization three of these individuals had titres that were greater than 30-fold the geometric mean titres of uninfected individuals following the first dose, but did not increase further after the boost¹⁰ (filled black circles in Extended Data Fig. 1b,c). BNT162b2 vaccination also induced a neutralizing antibody response against the B.1.351 variant of concern, albeit at a tenfold-lower magnitude than against the wild-type WA1/2020 (WA1) strain (Fig. 1c,

Extended Data Fig. 1f), consistent with previous studies¹¹. The cross-neutralization potential, calculated as a ratio of neutralizing antibody responses between B.1.351 and WA1 strains, also showed a negative association with age (Extended Data Fig. 1g). Vaccination also stimulated spike-specific T cell responses, which were more readily detectable seven days after the secondary immunization (Fig. 1d,e, Extended Data Fig. 2a–e). Consistent with previous studies³, the CD4 T cell responses were primarily of the T-helper-1 type, although there was a low-level T-helper-2 (IL-4) response (Extended Data Fig. 2b). IFN γ and TNF were the dominant responses in CD8 T cells; three individuals with no known exposure to SARS-CoV-2 responded even at baseline, suggestive of CD8 T cells that are cross-reactive to related viruses, as has previously been shown¹² (Extended Data Fig. 2d). There was no significant correlation between T cell responses and age or neutralizing antibodies (Extended Data Fig. 2f–k).

Fig. 1: BNT162b2 vaccination induces robust antibody and T cell responses.



a, b, Serum anti-S IgG titres (a) (half-maximal effective concentration (EC_{50})) and live-virus neutralizing antibody titres (b) (half-maximal inhibitory concentration

(IC_{50})), measured by enzyme-linked immunosorbent assay and focus reduction neutralization titre assays, respectively. **c**, Live-virus neutralizing antibody response against the wild-type (WA1) or B.1.351 variant measured in day-42 sera. **d, e**, Spike-specific CD4 (**d**) and CD8 (**f**) T cell IFN γ response in blood. Each dot represents a participant ($n = 56$ (**a, b**), 30 (**c**) and 38 (**d, e**)). Statistical differences were calculated using two-sided Wilcoxon matched-pairs signed-rank test. * $P < 0.05$, ** $P < 0.01$, *** $P < 0.001$, **** $P < 0.0001$. Boxes show median and 25th–75th percentiles, and whiskers show the range.

[Source data](#)

[Full size image](#)

Lack of autoantibodies or anticytokine antibodies

Several studies have demonstrated the presence of serum autoantibodies^{13,14} and anticytokine antibodies¹⁵ in individuals infected with SARS-CoV-2, and the development of new-onset antibodies in a subset of patients who are hospitalized with COVID-19¹⁶. We screened sera of 31 vaccinated individuals for IgG autoantibodies and anticytokine antibodies on days 0, 21 and 42 using a 55-plex antigen and 58-plex cytokine arrays. We included sera of 17 patients with autoimmune and immunodeficiency disorders as positive controls. Five vaccinated individuals had pre-existing autoantibodies (suggestive of autoimmune thyroiditis, primary biliary cirrhosis or connective tissue disease) (Extended Data Fig. [3a](#)). Anticytokine antibodies were largely absent or were observed at a low mean fluorescence intensity with no significant changes (Extended Data Fig. [3b](#)). Two individuals had anti-IL-21 autoantibodies, and two additional individuals had anti-IL-1 antibodies (Extended Data Fig. [4](#)). Importantly, none of the individuals with pre-existing autoantibodies or anticytokine antibodies experienced adverse events, nor did levels of pre-existing autoantibodies or anticytokine antibodies change in response to vaccination.

Innate immune responses

We first assessed whole-blood samples of 27 individuals using cytometry by time of flight (CyTOF). Unsupervised clustering identified 14 major cell types (Fig. [2a](#), Extended Data Fig. [5a, b](#)), which we further subtyped manually (Extended Data Fig. [5c](#)). The frequency of intermediate monocytes ($CD14^+CD16^+$ monocytes) increased significantly two days after the primary vaccination, and was substantially higher two days after the secondary vaccination (Fig. [2b](#), Extended Data Figs. [5d, 6](#)). In addition, there were enhanced levels of phosphorylated (p)STAT3 and pSTAT1 in multiple cell types on day 1 after secondary vaccination, relative to day 1 after primary vaccination

(Fig. 2c, d). These data suggested that BNT162b2 vaccination induced a heightened innate immune response after secondary immunization relative to primary immunization.

Fig. 2: Innate immune responses induced by BNT162b2 vaccination.



a, CyTOF-identified cell clusters from whole blood visualized by uniform manifold approximation and projection (UMAP). HPCs, haematopoietic progenitor cells; NK, natural killer. **b**, Frequency of inflammatory monocytes ($CD14^+CD16^+$ monocytes) as a proportion of live $CD45^+$ cells. Boxes show median and 25th–75th percentiles, and whiskers show the range. **c**, Heat map of fold change of pSTAT3 and pSTAT1 levels in comparison to baseline in the cell types indicated on the y axis. Only statistically significant changes between the increase on day 1 after primary and day 1 after secondary immunizations, as measured using two-sided Mann–Whitney rank-sum test ($P < 0.05$), were plotted. mDC, myeloid dendritic cell; pDC, plasmacytoid dendritic cell; T_{reg} , regulatory T. **d**, Fold change in pSTAT3 levels on days 1 and 22, compared to primary and secondary baselines, respectively. **e**, Volcano plots showing plasma cytokines significantly increased after primary (left) and secondary (right) vaccinations versus day 0 and day 21, respectively. **f**, Plasma IFN γ levels measured by Olink. NPX, normalized protein expression. **g**, Heat map of two-sided Spearman’s correlation between increase in plasma IFN γ and pSTAT3 or pSTAT1 levels in different cell types, shown on the y axis, on day 1 after secondary vaccination. The P values were corrected for multiple testing. **h**, Spearman’s correlation between pSTAT3 levels in CD4 T cells and plasma IFN γ levels. The error bands represent 95% confidence limits. In **b**, **f**, statistical differences between the peak and baseline time points were measured using two-sided Wilcoxon matched-pairs signed-rank test. The differences between peak time points were measured using two-sided Mann–Whitney rank-sum test. * $P < 0.05$, ** $P < 0.01$, *** $P < 0.001$, **** $P < 0.0001$. Blue and red

dots indicate female and male participants, respectively. $n = 27$ and 31 participants for CyTOF and Olink.

[Source data](#)

[Full size image](#)

To further investigate this phenomenon, we measured plasma cytokines in 31 vaccinated individuals using Olink (<https://www.olink.com/products/target/inflammation/>). Of the 67 cytokines detected, the concentration of 2 cytokines (IFN γ and CXCL10) were increased significantly on days 1 and 2 after primary vaccination (Fig. 2e left). Similar to our observations on intermediate monocytes and pSTAT1 and pSTAT3, the concentrations of these cytokines were increased even further after the secondary immunization (Fig. 2e right). The concentration of plasma IFN γ was 11.3-fold higher at day 22 relative to day 1 (Fig. 2f). CXCL10 peaked on day 23 (Extended Data Fig. 7a). The anti-inflammatory cytokine IL-10 showed a similar trend with enhanced response following secondary immunization, although this did not reach statistical significance (Extended Data Fig. 7b). The concentration of IFN α 2 (type I interferon) was not significantly increased on days 1 and 2 after vaccination, and the responses were just over the assay limit of the highly sensitive single-molecule array (SIMOA) (16 fg ml $^{-1}$) (Extended Data Fig. 7c, d). Furthermore, there was a correlation between plasma IFN γ levels and pSTAT1 and pSTAT3 expression levels across several cell types (Fig. 2g, h, Extended Data Fig. 7e). Collectively, these data demonstrate that vaccination with BNT162b2 stimulates modest innate immune responses after primary immunization, which increase notably after the secondary immunization.

Transcriptional signatures of vaccination

Next, we performed bulk mRNA sequencing of whole blood from 31 participants. Six of 185 samples did not pass quality control and were removed from the analysis (Extended Data Fig. 8a, b). Secondary vaccination generated a greater transcriptional response (as has previously been seen in a recent study of adjuvanted hepatitis B vaccine¹⁷), with nearly a fourfold increase of differentially expressed genes at day 22 as compared to day 1 (Fig. 3a); this is consistent with the increased markers of innate immunity detected by both CyTOF and Olink (Fig. 2). Gene-set enrichment analysis (GSEA) revealed that both doses of BNT162b2 stimulated antiviral and interferon response modules¹⁸ (Fig. 3b). However, the booster immunization led to a broader innate response. In addition to the induction of antiviral pathways, secondary vaccination led to increases in signatures of dendritic cell activation and the upregulation of Toll-like receptor signalling, monocyte and neutrophil modules on days 22 and 23 (Fig. 3b, Extended Data Fig. 8c, d). The results were consistent

regardless of the baseline time point (that is, day 0 or 21) that we used (Extended Data Fig. 8e,f, Supplementary Table 1).

Fig. 3: Transcriptional signatures of BNT162b2 vaccination.

 [figure3](#)

a, Number of differentially expressed genes (DEGs) (absolute \log_2 -transformed fold change > 0.2 and Wald $P < 0.01$) at each time point after prime (left) and boost (right). d, day. **b**, Interferon and innate BTMs that were significantly enriched (false discovery rate (FDR) < 0.05 , absolute normalized enrichment score (NES) > 2) after prime (left) and boost (right) vaccination. Days 1, 2 and 7 were compared against day 0; days 22, 23 and 28 were compared against day 21 in **a**, **b**. **c**, BTMs on day 22 that were significantly associated with plasma IFN γ . GSEA was used to identify enrichment of BTMs within gene lists ranked by correlation with fold change in IFN γ between days 22 and 21.

[Source data](#)

[Full size image](#)

As mortality to COVID-19 is highest among individuals who are elderly and older populations are known to mount suboptimal responses to many vaccines¹⁹, we examined whether there were age-associated differences in response to mRNA vaccination. On day 22, younger participants tended to have greater changes in monocyte and inflammatory modules, whereas older individuals had increased expression of B and T cell modules (Extended Data Fig. 8g). Given that the plasma IFN γ concentration was significantly higher after secondary vaccination, we asked whether there was an association between IFN γ and the increased innate responses

after the boost. Both interferon and inflammatory modules were significantly enriched by GSEA when using genes ranked by correlation with IFN γ on day 22 (Fig. 3c). The average fold changes of these modules also correlated with IFN γ (Extended Data Fig. 8h,i), which suggests that IFN γ may have a role in driving enhanced innate and antiviral responses after the boost.

Single-cell transcriptional response

Bulk transcriptomics signatures could reflect changes in cell composition as well as alterations in transcriptional activity within cells. We performed cellular indexing of transcriptomes and epitopes by sequencing (CITE-seq) of 45 peripheral blood mononuclear cell (PBMC) samples from 6 individuals (Extended Data Fig. 1a) to disentangle these two effects and to examine transcriptional changes at the single-cell level. We enriched dendritic cells and mixed them with total PBMCs at a ratio of 1:2 to represent minor subsets of dendritic cells sufficiently⁴. After quality control, we obtained 242,479 high-quality transcriptomes that segregated into 18 cell clusters (Fig. 4a, Extended Data Fig. 9a–c). Notably, cluster C8 (which expressed *CD14*, *VCAN*, *CD1C*, *FCGR1A* and *CD274* mRNA or protein) emerged on day 22, one day after secondary vaccination (Fig. 4b). These cells uniquely expressed interferon-stimulated genes, including *WARS* (also known as *WARS1*), *GBPI*, *IFI30* and *IFITM3* (Extended Data Fig. 9d), and constituted about 0.01% of the Lin $^-$ HLA-DR $^+$ population on day 1 after primary vaccination but increased almost 100-fold to about 1% one day after secondary vaccination (Fig. 4c). Iterative removal of each cluster from a pseudobulk score showed that C8 contributed to the increased interferon as well as monocyte blood transcriptional modules (BTMs) that we observed in the bulk transcriptomics data on day 22 (Extended Data Fig. 9e). To examine whether these cells uniquely emerge in response to mRNA vaccination or whether they are seen in natural SARS-CoV-2 infection (because they expressed *CD14*, *CD1C* and *CD274*, which are known to be expressed by myeloid-derived suppressor cells observed at elevated frequencies in the blood of patients infected with SARS-CoV-2^{4,20,21,22}), we combined and analysed innate immune cells (myeloid cells and plasmacytoid dendritic cells) from this study with data from two previous studies^{4,23} after batch correction using Harmony²⁴. Well-annotated cell types such as monocytes and dendritic cells overlapped between the datasets, but the C8 cluster did not overlap (Extended Data Fig. 10a,b). The cluster closest to C8 was IFN-experienced CD14 $^+$ monocytes, previously defined in patients with COVID-19⁴ (Extended Data Fig. 10b). Although the partial overlap was due to expression of interferon-stimulated genes in both clusters, C8 expressed higher levels of HLA-DR and other activation molecules and lower levels of S100 genes that are known to be expressed in myeloid-derived suppressor cells induced in patients with COVID-19 (Extended Data Fig. 10c). These

data suggest that cluster C8 is not present in COVID-19 infection, and does not represent myeloid-derived suppressor cells.

Fig. 4: Single-cell transcriptional response to BNT162b2 vaccination.

 figure4



a, UMAP representation of cell types identified by single-cell transcriptional profiling. **b**, Feature plots across time points, showing cluster C8 in red. **c**, Frequency of C8 as a proportion of Lin⁻HLA-DR⁺ cell clusters (C3, C4, C7, C8, C11 and C13). Each dot or line represents an individual. Blue and red indicate female and male participants, respectively. **d**, UMAP representation of subclusters within C8 resolved using Louvain clustering. **e**, Heat map showing Euclidean distance between C8 subclusters and the rest of the cell types identified by single-cell profiling. **f**, DEGs determined between C8_2 and C8_1, and their closest cell clusters ranked by fold change between C8 and their parental clusters, are plotted. Genes in red, green and blue represent genes

upregulated, unchanged and downregulated, respectively, in the C8 subcluster as compared to its closest parental cluster. **g**, Heat map showing scaled expression of key interferon-response and AP-1 transcription factors. **h**, Heat map showing an extended set of genes from ref. [25](#) that showed enhanced accessibility on day 42 after H5N1 + AS03 vaccination. **i**, Significantly enriched interferon BTMs (FDR < 0.05, absolute NES > 2) across clusters over time. Days 1 and 7 were compared against day 0; days 22 and 28 were compared against day 21.

[Source data](#)

[Full size image](#)

To further delineate the cellular composition of C8, we re-embedded C8 with uniform manifold approximation and projection using participant-corrected principal component analyses. Using Louvain community detection, we resolved seven distinct clusters within the original C8 cluster (Fig. [4d](#)). C8 was a heterogeneous mix of classical monocytes (C8_0, C8_1 and C8_3), a classical dendritic cell subtype (cDC2; C8_2) and intermediate monocytes (C8_4), as evidenced by proximity to the original clusters calculated by Euclidean distance (Fig. [4e](#), Extended Data Fig. [10d–f](#)). We analysed subclusters C8_1 and C8_2, which are closer to CD14⁺ monocytes and cDC2, respectively. In addition to expressing higher interferon-stimulated genes as compared to their parent clusters, they had a reduced expression of the AP-1 transcription factors *FOS* and *JUN* (Fig. [4f](#)). This C8 population is similar to an epigenetically remodelled monocyte population in the blood of humans, 21 days after vaccination with two doses of an AS03-adjuvanted H5N1 pandemic influenza vaccine (H5N1 + AS03)[25](#). These monocytes demonstrated an enhanced chromatin accessibility of interferon-stimulated genes and reduced accessibility of AP-1 transcription factors, and showed heightened resistance to infection with unrelated blood-borne viruses, such as dengue virus and Zika virus[25](#). We asked whether C8 represents an analogous cell type at the transcriptional level. C8 had a relatively higher expression of *IRF1*, *STAT1*, *STAT2*, *STAT3* and *IRF8* and reduced levels of *FOS*, *JUNB*, *JUND* and *ATF3*—the same transcription factors that defined the monocyte population in the previous study[25](#) (Fig. [4g](#)). We confirmed this using an extended set of genes for which the chromatin accessibility profile was higher 21 days after H5N1 + AS03 vaccination (Fig. [4h](#)). Notably, the emergence of C8 correlated with plasma IFNγ levels (Extended Data Fig. [10g, h](#)). In vitro stimulation of purified healthy monocytes with IFNγ or day-22 plasma also induced a C8 signature, which suggests that IFNγ has a key role in inducing cluster C8, in response to mRNA vaccination (Extended Data Fig. [10i, j](#)).

In addition to the emergence of C8, our CITE-seq analysis demonstrated that the interferon signature was broadly induced across cell types on day 1 and day 22, and

the higher magnitude of response on day 22 was more evident (Fig. 4*i*). Furthermore, there was activation of natural killer cells on day 22, as observed by downregulation of natural-killer-cell-associated gene modules, and upregulation of AP-1 transcription factors²⁶ on day 22 (Extended Data Fig. 10*k,l*).

Comparison with other vaccines

As mRNA vaccines have only recently received approval for use in humans, the degree to which these vaccines induce similar or distinct immune responses compared to other vaccine types (such as inactivated or live-attenuated vaccines) is unknown. To address this, we performed a comparative analysis of a set of published vaccine trials with BNT162b2 (Extended Data Table 3) by generating similarity matrices through pairwise correlations of mean gene fold changes between vaccines at days 1 and 7 after vaccination. Although the day-1 response to the first dose of BNT162b2 showed little overlap with that of other vaccines, the response at day 1 after the boost was broadly similar to the response induced by vaccination with adjuvanted vaccines (H5N1 + AS03), live viral vectors (Ebola and HIV vaccines), or inactivated influenza (which stimulates a recall response) (Extended Data Fig. 11*a*). At the BTM level, the shared signature consisted of innate immunity modules, including interferon signalling, dendritic cell activation and inflammatory responses (Fig. 5). Meanwhile, day-7 responses to both the prime and boost doses of BNT162b2 exhibited weak correlation both between themselves and with other vaccines (Extended Data Fig. 11*b*), with cell-cycle-related transcriptional modules after the prime dose being the signature shared with many vaccines (Extended Data Fig. 11*c*). With most vaccines, this cell cycle signature is also associated with upregulation of B and plasma cell modules, reflecting the expansion of antibody-secreting cells^{18,27}. However, this induction of B and plasma cell modules was absent in BNT162b2 (Extended Data Fig. 11*d,e*). Given that BNT162b2 successfully promoted a robust antibody response (Fig. 1), the lack of detectable plasma cell or B cell signature on day 7 (particularly after the boost) was surprising. Consistent with this, we observed less than a twofold increase in plasmablast responses by CyTOF (Extended Data Fig. 11*f*), in contrast to seasonal influenza or other vaccines that induce a higher frequency of plasmablasts²⁷.

Fig. 5: Comparison of transcriptional responses with other vaccines.

 [figure5](#)

Circos plot of the overlap across vaccines in BTMs enriched on day 1. GSEA was performed on genes ranked by day 1 versus baseline *t*-statistic in each vaccine. Each segment of the circle represents one vaccine, and each point in a segment represents a single BTM. Bars in outer circle represent the NES of significantly enriched BTMs (FDR < 0.05). Lines connect BTMs with a significant positive enrichment shared between vaccines. Inner circle boxes and line colours represent the functional groups of the BTMs. ECM, extracellular matrix.

[Source data](#)

[Full size image](#)

Transcriptional correlates of adaptive immunity

As cellular and humoral immunity are the chief functional components that mediate protection from infection, we used GSEA to identify early transcriptional responses correlated with day-42 neutralizing antibody or day-28 CD8⁺IFN γ ⁺ T cell responses. On day 22 (one day after the boost), monocyte-related modules correlated with neutralizing antibody responses, whereas interferon and antiviral signatures were associated with the CD8 T cell response (Extended Data Fig. [12a, b](#)). The emergence of SARS-CoV-2 variants poses a serious challenge for the success of ongoing vaccination efforts. We asked whether there are early transcriptional correlates of the cross-neutralization potential induced by BNT162b2. We defined a cross-neutralization index (a ratio of variant-to-WA1 neutralizing antibody titres) and, using GSEA, found that monocyte and inflammatory modules were highly associated with this index (Extended Data Fig. [12c](#)). In addition, the peak frequency of classical monocytes at two days after the boost correlated with cross-neutralization index (Extended Data Fig. [12d, e](#)). Consistent with this, a gene score that defines C3 (the classical monocyte cluster in the CITE-seq data) also correlated with cross-neutralization (Extended Data Fig. [12f](#)).

Discussion

Our study represents, to our knowledge, the first systems-level analysis of innate and adaptive immunity to an mRNA vaccine. In contrast to the dysregulated innate immune responses to SARS-CoV-2 infection^{[4,20,28,29](#)}, BNT162b2 vaccination stimulated antiviral immunity with little type I IFN response after the first dose, but a notably enhanced innate response after the secondary immunization. Cluster C8, defined by single-cell transcriptional profiling, is a heterogenous mixture of myeloid cells that are uniquely induced by mRNA vaccination and are distinct from the IFN-experienced HLA-DR^{low} myeloid cells observed in natural infection^{[4,20](#)}. A previous study has shown that vaccination with H5N1 + AS03 induces a similar transcriptional signature (enriched interferon-stimulated genes and diminished expression of AP-1 transcription factors) in monocytes and myeloid dendritic cells^{[25](#)}. In that study, vaccination induced epigenetic reprogramming of these myeloid cells, leading to enhanced resistance against heterologous viruses such as dengue virus and Zika virus, even several weeks later^{[25](#)}. In the case of BNT162b2, whether epigenetic reprogramming underlies the enhanced interferon-stimulated gene response in C8 after secondary immunization, and whether this confers enhanced resistance to viruses, remains an open question. Alternatively, it is conceivable that the enhanced myeloid cell response after secondary immunization reflects the response of these cells to a systemic cytokine response. Consistent with this, plasma IFN γ concentration was significantly higher one day after secondary immunization and associated with the

emergence of C8. Thus, these data provide a model in which ‘cytokine feedback’ regulates the enhanced innate immune responses to secondary vaccination (Extended Data Fig. 10h–j). Whether or not T cells provide this feedback warrants further investigation, but we did not detect IFN γ within PBMCs (data not shown). Natural killer cells, tissue-resident T cells or innate lymphoid cells at the site of vaccination or draining lymphoid tissues could be potential sources of the rapidly induced circulating IFN γ . This model does not preclude complementary mechanisms, such as persistent epigenetic changes^{25,30}. Finally, our analysis of transcriptional signatures of BNT162b2 vaccination relative to those induced by six other vaccines provides a useful benchmark to assess human immunity to mRNA vaccination in the broader context of immune responses to other vaccines.

Methods

No statistical methods were used to predetermine sample size. The experiments were not randomized, and investigators were not blinded to allocation during experiments and outcome assessment.

Human subjects and experimentation

Fifty-six healthy volunteers were recruited for the study under informed consent. The study was approved by Stanford University Institutional Review Board (IRB 8269) and was conducted within full compliance of Good Clinical Practice as per the Code of Federal Regulations. The demographics of all participants are provided in Extended Data Table 1.

Anti-spike binding enzyme-linked immunosorbent assay

SARS-CoV-2 spike protein was purchased from Sino Biologicals. Ninety-six-well high binding plates were coated with 100 ng of spike protein diluted at a concentration of 2 μ g ml⁻¹ in PBS. The next morning, the plates were washed once, blocked with 3% non-fat milk in PBS containing 0.1% Tween 20 (PBST) for 1 h at room temperature. Sera samples serially diluted in 1% non-fat milk containing PBST were added to the plates and incubated at 37 °C for 1 h. The plates were washed 3× with PBST, horseradish peroxidase conjugated goat anti-monkey IgG (γ -chain specific, Alpha Diagnostics, 1:4,000 dilution), in PBS-T containing 1% non-fat milk was added and incubated for 1 h at room temperature. Wells were washed 3× with PBST before addition of 3,3',5,5'-tetramethylbenzidine (TMB) substrate solution. The reaction was stopped after 12 min by addition of 0.16 M sulfuric acid or 1 M hydrochloric acid. The optical density at 450 nanometres was measured with a Biorad microplate reader.

Focus reduction neutralization titre assay

Neutralization assays with authentic SARS-CoV-2 virus (infectious clone SARS-CoV-2 derived from 2019-nCoV/USA_WA1/2020 strain) were performed as previously described³¹. Sera samples were serially diluted (threefold) in serum-free Dulbecco's modified Eagle's medium (DMEM) in duplicate wells and incubated with 100–200 focus-forming units infectious clone derived SARS-CoV-2-mNG virus³² at 37 °C for 1 h. The antibody–virus mixture was added to Vero E6 cell (C1008, ATCC, no. CRL-1586) monolayers seeded in 96-well blackout plates and incubated at 37 °C for 1 h. After incubation, the inoculum was removed and replaced with pre-warmed complete DMEM containing 0.85% methylcellulose. Plates were incubated at 37 °C for 24 h. After 24 h, methylcellulose overlay was removed, cells were washed twice with PBS and fixed with 2% paraformaldehyde in PBS for 30 min at room temperature. Following fixation, plates were washed twice with PBS and foci were visualized on a fluorescence ELISPOT reader (CTL ImmunoSpot S6 Universal Analyzer) and enumerated using Viridot³³. The neutralization titres were calculated as follows: 1 – (ratio of the mean number of foci in the presence of sera and foci at the highest dilution of respective sera sample). Each specimen was tested in two independent assays performed at different times. The focus reduction neutralization titre (FRNT)–mNeonGreen 50% (mNG₅₀) titres were interpolated using a four-parameter nonlinear regression in GraphPad Prism 8.4.3. Samples with an FRNT–mNG₅₀ value that was below the limit of detection were plotted at 10. For these samples, this value was used in fold reduction calculations.

FRNT assay against the variants of concern

The wild-type infectious clone SARS-CoV-2, derived from the 2019-nCoV/USA_WA1/2020 strain, was propagated in Vero E6 cells (ATCC) and sequenced³². The B.1.351 variant was isolated as previously described³⁴. Our laboratory plaque-isolated the virus on VeroE6 cells followed by a single round of propagation on Vero E6 cells (multiplicity of infection of 0.05), aliquoted to generate a working stock and sequenced. Viral titres were determined by focus-forming assay on Vero E6 cells. Viral stocks were stored at –80 °C until use.

FRNT assays were performed as described for the wild-type FRNT assay. The assay with each variant was performed simultaneously with wild-type controls. The samples were diluted at 3-fold in 8 serial dilutions using DMEM in duplicates with an initial dilution of 1:10 in a total volume of 60 µl. Serially diluted samples were incubated with an equal volume of SARS-CoV-2 (wild type or the variant) (100–200 foci per well) at 37 °C for 1 h in a round-bottomed 96-well culture plate. The antibody–virus mixture was then added to Vero cells and incubated at 37 °C for 1 h. After incubation,

the antibody–virus mixture was removed and 100 µl of prewarmed 0.85% overlay was added to each well. Plates were incubated at 37 °C for 24 h. After 24 h, methylcellulose overlay was removed, and cells were washed 3 times with PBS. Cells were then fixed with 2% paraformaldehyde in PBS (Electron Microscopy Sciences) for 30 min. Following fixation, plates were washed twice with PBS and 100 µl of permeabilization buffer (0.1% bovine serum albumin (BSA), saponin in PBS), was added to the fixed Vero cells for 20 min. Cells were incubated with an anti-SARS-CoV spike primary antibody directly conjugated to biotin (CR3022–biotin) for 1 h at room temperature. Next, the cells were washed 3 times in PBS and avidin–HRP was added for 1 h at room temperature followed by 3 washes in PBS. Foci were visualized using TrueBlue HRP substrate (KPL, no. 5510-0050) and imaged on an ELISPOT reader (CTL).

Intracellular cytokine staining assay

Antigen-specific T cell responses were measured using the intracellular cytokine staining assay as previously described³⁵. Live frozen PBMCs were revived, counted and resuspended at a density of 2 million live cells per ml in complete RPMI (RPMI supplemented with 10% FBS and antibiotics). The cells were rested overnight at 37 °C in a CO₂ incubator. The next morning, the cells were counted again, resuspended at a density of 15 million cells per ml in complete RPMI and 100 µl of cell suspension containing 1.5 million cells was added to each well of a 96-well round-bottomed tissue culture plate. Each sample was treated with two conditions, no stimulation and a peptide pool spanning the spike protein at a concentration of 1 µg ml⁻¹ of each peptide in the presence of 1 µg ml⁻¹ of anti-CD28 (clone CD28.2, BD Biosciences) and anti-CD49d (clone 9F10, BD Biosciences) as well as anti-CXCR3 and anti-CXCR5. The peptides were custom-synthesized to 90% purity using GenScript, a commercial vendor. All samples contained 0.5% v/v DMSO in total volume of 200 µl per well. The samples were incubated at 37 °C in CO₂ incubators for 2 h before addition of 10 µg ml⁻¹ brefeldin-A. The cells were incubated for an additional 4 h. The cells were washed with PBS and stained with Zombie UV fixable viability dye (Biolegend). The cells were washed with PBS containing 5% FCS, before the addition of surface antibody cocktail. The cells were stained for 20 min at 4 °C in 100-µl volume. Subsequently, the cells were washed, fixed and permeabilized with cytofix/cytoperm buffer (BD Biosciences) for 20 min. The permeabilized cells were stained with intracellular cytokine staining antibodies for 20 min at room temperature in 1× perm/wash buffer (BD Biosciences). Cells were then washed twice with perm/wash buffer and once with staining buffer before acquisition using the BD Symphony Flow Cytometer and the associated BD FACS Diva software. All flow cytometry data were analysed using Flowjo software v.10 (TreeStar).

Bead-based antigen arrays

We used an existing bead-based autoantigen array, and a cytokine array with expanded content that was based on recent COVID-19 studies¹⁶. A complete list of all antigens, vendors and catalogue numbers can be found in Supplementary Tables 2, 3. The ‘COVID-19 Autoantigen Array’ included 55 commercial protein antigens associated with connective tissue diseases (Supplementary Table 2). The ‘COVID-19 Cytokine Array’ comprised 58 proteins including cytokines, chemokines, growth factors, acute phase proteins and cell surface proteins (Supplementary Table 3). Antigens were coupled to carboxylated magnetic beads (MagPlex-C, Luminex) such that each antigen was linked to beads with unique barcodes, as previously described^{16,36,37}. Prototype human plasma samples derived from participants with autoimmune diseases with known reactivity patterns were purchased from ImmunoVision or were obtained from Stanford rheumatology clinics and had previously been characterized¹⁶. Serum samples from individuals with autoimmune polyendocrine syndrome type 1 (APS1), pulmonary alveolar proteinosis (PAP) or atypical mycobacterial infection (AMI) were used for validation of anticytokine antibodies¹⁶. Serum samples were tested at 1:100 dilution in 0.05% PBS-Tween supplemented with 1% (w/v) BSA. Bound antibody was detected using R-phycoerythrin (R-PE) conjugated Fcγ-specific goat anti-human IgG F(ab')2 fragment (Jackson ImmunoResearch) before analysis using a FlexMap3D instrument (Luminex). A minimum of 100 events per bead identifier were counted, and samples were studied in duplicate. Binding events were displayed as mean fluorescence intensity (MFI). All data analysis and statistics were performed using R and various R packages³⁸. For normalization, average MFI values for ‘bare bead’ identifier were subtracted from average MFI values for antigen-conjugated bead identifiers.

CyTOF analysis of whole-blood samples

Fresh whole-blood samples collected in sodium citrate cell preparation tubes (CPT) were fixed in proteomic stabilizer buffer. Two hundred and seventy µl of whole-blood samples were mixed with 420 µl of smart buffer, mixed and incubated at room temperature for 12 min and frozen at –80 °C until processing. Fixed frozen cells were thawed by gentle resuspension in CSM (PBS supplemented with 2% BSA, 2 mM EDTA and 0.1% sodium azide), washed twice with CSM and counted. Cells were permeabilized and barcoded using Cell-IDTM 20-Plex Pd Barcoding Kit (Fluidigm). The samples were washed with CSM, pooled and counted. One pooled sample containing a mix of all barcoded PBMC samples was stained for 30 min with surface antibody cocktail at room temperature. The sample was then fixed with 4% freshly prepared paraformaldehyde (Alfa Aesar) for 10 min at room temperature, washed with CSM, permeabilized with 100% methanol (Sigma) and kept at –80 °C overnight. The next day, the cells were washed with CSM, counted and stained with pre-titrated

intracellular antibody cocktail for 30 min at room temperature. Cells were then washed with CSM, stained with iridium-containing DNA intercalator (Fluidigm), washed with MilliQ water and acquired on Helios mass cytometer (Fluidigm) in MilliQ water supplemented with 1× EQ four element calibration beads (Fluidigm).

The FCS files were bead-normalized before data export. The data were processed for debarcoding in Flowjo software v.10 (TreeStar). In brief, the bead-normalized file was used to gate single cells on the basis of DNA content and event length using FlowJo. The single cells were reimported and debarcoded using Helios software version 7.0.5189. The debarcoded samples were analysed using FlowJo or R version 1.2.1335 for analysis and visualization.

CyTOF data analysis

High-dimensional analysis of phospho-CyTOF data was performed using a previously described R-based pipeline³⁹. In brief, the raw .fcs files were imported into R and the data were transformed to normalize marker intensities using arcsinh with a cofactor of 5. For visualization, another transformation was applied that scales the expression of all values between 0 and 1 using percentiles as the boundary. Cell clustering was performed with 4,000 cells randomly selected from each sample using FlowSom and ConsensusClusterPlus. The transformed matrix was used as an input for FlowSom and cells were separated into 20 clusters. To obtain reproducible results (avoid random start), a seed was set for each clustering. The 20 clusters were manually annotated on the basis of the lineage marker expression, and were merged to produce the final clusters. The clusters were visualized in two-dimensional space using UMAP. The abundance of cell populations was determined using Plotabundance function. In parallel, the data were manually gated to identify 25 immune cell subpopulations that were not well-distinguished in UMAP and used for all quantification purposes.

Plasma protein profiling using multiplex Olink panel

We measured cytokines in plasma using Olink multiplex proximity extension assay (PEA) inflammation panel (Olink proteomics: www.olink.com) according to the manufacturer's instructions. The PEA is a dual-recognition immunoassay, in which two matched antibodies labelled with unique DNA oligonucleotides simultaneously bind to a target protein in solution. This brings the two antibodies into proximity, allowing their DNA oligonucleotides to hybridize, serving as template for a DNA polymerase-dependent extension step. This creates a double-stranded DNA 'barcode' that is unique for the specific antigen and quantitatively proportional to the initial concentration of target protein. The hybridization and extension are immediately followed by PCR amplification and the amplicon is then finally quantified by microfluidic qPCR using Fluidigm BioMark HD system (Fluidigm).

Bulk transcriptomics

RNA was isolated from blood samples stored in Paxgene tubes at the Yerkes Genomics Core (http://www.yerkes.emory.edu/nhp_genomics_core/). RNA quality was assessed using an Agilent 4200 TapeStation and concentration via the RNA HS assay on the Qubit. Globin transcripts in blood RNA were blocked with the FastSelect Globin Reagent (Qiagen) before library preparation. Libraries were prepared using the Clontech SMART-Seq v.4 Ultra Low Input RNA kit (Takara Bio) in combination with the NexteraXT DNA Library Preparation kit to append dual-indexed adaptor sequences (Illumina). Libraries were validated by capillary electrophoresis on an Agilent 4200 TapeStation, pooled at equimolar concentrations, and sequenced on an Illumina NovaSeq6000 at 100SR, yielding 25–30 million reads per sample.

Bulk transcriptomics analysis

Gene-level counts were filtered to remove those with a median expression less than 32. Principal component analysis (PCA) was performed on baseline samples to identify outliers. Three samples were more than 1.5 s.d. away from the mean and were removed from the analysis. Relative log expression (RLE) plots were generated with EDASEq⁴⁰; samples with an RLE > 0.6 were removed from the analysis. Differential gene analysis was performed using DESeq2⁴¹ (v.1.26.0), incorporating participant identifier into the model to account for inter-participant bias. Genes were ranked by the Wald statistic as reported by DESeq2 for GSEA using the BTMs¹⁸. Per-participant fold changes were computed by dividing the DESeq2 normalized expression data for the day of interest by either day 0 (for day 1, day2 and day 7) or day 21 (for day 22, 28 and 42). To obtain BTM correlates with age, the age of each participant was compared against the per-participant fold changes for day 22. The resulting correlation values were ranked by *t*-statistic and analysed with GSEA. The same method was employed to obtain BTM correlates with IFN γ . IFN scores were computed by taking the per-participant mean fold change on day 22 of the unique set of genes present in the 5 interferon BTMs (M75, M111.1, M150, M127 and M68) that significantly correlated with day-22 IFN γ fold change. Similarly, the per-participant M16 gene score was computed using average fold change on day 22 of the genes present in M16.

Vaccine dataset meta-analysis

Datasets were obtained from Gene Expression Omnibus (GEO) via the accession identifiers in Supplementary Table 4. CEL files of all the samples belonging to the same trial were grouped and normalized in Bioconductor by RMA⁴², which includes global background adjustment and quantile normalization. Probes mapping to multiple genes were discarded, and the remaining probes were collapsed to gene level in each

dataset by selecting the probe for each gene with the highest mean expression across all subjects. The only non-microarray dataset was GSE97590, for which the normalized count matrix from GEO was used. Genes not present in all datasets were removed. Baseline normalized \log_2 -transformed fold changes were then computed per subject for all genes. GSEA was then performed to identify enriched BTMs using gene lists for each dataset ranked by *t*-statistic from two-sided Student's *t*-tests on the post-vaccination \log_2 -transformed fold changes.

CITE-seq

CITE-seq analysis of PBMCs were assayed exactly as previously described⁴. In brief, live frozen PBMCs were thawed and 2× washed with RPMI supplemented with 10% FBS and 20 $\mu\text{g ml}^{-1}$ DNase I (Sigma Aldrich). Dendritic cells were enriched using the Dynabeads DC Enrichment Kit (Invitrogen, 11308D) according to manufacturer's instructions with 3–4 million PBMCs as starting material. The enriched cells were mixed with total PBMCs at a ratio of 1:2 and mixed cells were stained with a cocktail of TotalSeq-A antibodies in PBS supplemented with 5% FBS, 2 mM EDTA and 5 mg ml^{-1} human IgG, washed twice with PBS supplemented with 5% FBS, and 2 mM EDTA, and resuspended in PBS supplemented with 1% BSA (Miltenyi), and 0.5 U μl^{-1} RNase Inhibitor (Sigma Aldrich). About 9,000 cells were targeted for each experiment.

Cells were mixed with the reverse transcription mix and subjected to partitioning along with the Chromium gel-beads using the 10X Chromium system to generate the gel-bead in emulsions (GEMs) using the 3' V3 chemistry (10X Genomics). The reverse transcription reaction was conducted in the C1000 touch PCR instrument (BioRad). Barcoded cDNA was extracted from the GEMs by post-GEM reverse transcription cleanup and amplified for 12 cycles. Before amplification, the cDNA amplification mix was spiked in with ADT additive primer (0.2 μM stock) to amplify the antibody barcodes. Amplified cDNA was subjected to 0.6× SPRI beads cleanup (Beckman, B23318). Amplified antibody barcodes were recovered from the supernatant and were processed to generate TotalSeq-A libraries as instructed by the manufacturer (BioLegend, TotalSeq-A antibodies with 10x Single Cell 3' Reagent Kit v.3 3.1 protocol). The rest of the amplified cDNA was subjected to enzymatic fragmentation, end repair, A tailing, adaptor ligation and 10X-specific sample indexing as per manufacturer's protocol. Libraries were quantified using Bioanalyzer (Agilent) analysis.

10x Genomics scRNA-seq and TotalSeq-A libraries were pooled and sequenced on an Illumina HiSeq 4000 using the recommended sequencing read lengths of 28 bp (read 1), 8 bp (i7IndexRead) and 91 bp (read 2). CellRanger v.3.1.0 (10xGenomics) was

used to demultiplex raw sequencing data and quantify transcript levels against the 10x Genomics GRCh38 reference v.3.0.0.

CITE-seq analysis

10x Genomics scRNA-seq and TotalSeq-A libraries were pooled and sequenced on a Novaseq S4. Cell Ranger v.3.1.0 (10x Genomics) was used to quantify transcript levels against the 10x Genomics GRCh38 reference (v.3.0.0.) Raw count data were filtered to remove cells with a mitochondrial RNA fraction greater than 20% of total RNA counts per cell, cells with fewer than 100 unique features and cells with fewer than 200 total reads. The filtered count matrix was used to create a Seurat⁴³ (v.3.1.4) object. Filtered read counts were scaled by a factor of 10,000 and log-transformed. The antibody-derived tag matrix was normalized per feature using centre log normalization. Doublets were identified with scds⁴⁴ (v.1.2.0); cells with a doublet score in the top decile were removed. The remaining 242,479 cells were processed with the default Seurat pipeline. Specifically, the most variable 2,000 RNA features were used to perform PCA on the log-transformed counts. The first 25 principal components were used further downstream analyses, including clustering and UMAP projections. Clusters were identified with Seurat SNN graph construction followed by Louvain community detection on the resultant graph with a resolution of 0.2, yielding 18 clusters. Differential expression across time points was calculated with MAST⁴⁵ (v.1.12.0) to account for inter-participant heterogeneity.

Pseudobulk profiles were constructed by taking the average expression across all cells in each participant, per day. When computing fold changes across time points, the pseudobulk profile of each participant was compared to their baseline profile to reduce participant-specific biases. To calculate the effect of removing a cluster, each cluster across all time points was iteratively removed and resulting fold changes were recomputed.

C8 was re-embedded and reclustered with UMAP and Louvain community detection, respectively. Distances from each subcluster to the other clusters was calculated as the Euclidean distance between the average expression of all genes of each cluster. The Euclidean distances were calculated in the original data space. Specifically, the Euclidean distance was calculated using all genes as input to the dist function in R. The dist function calculates Euclidean distance $d(x, y)$ as:

$$d(x,y)=\sqrt{\sum_{i=1}^n ((y_i-x_i))^2}$$

in which x is the value for gene i in cluster A and y is the value for gene i in cluster B.

Complexheatmap (v.2.2.0) was used for all heat maps. All analysis was performed in R (v.3.6.3).

Combined analysis of single-cell RNA sequencing

Data from ref. ²³ were downloaded from <https://covid19cellatlas.org/> as an .h5ad file and converted to a Seurat object in R. Both the resulting Seurat object and the vaccine data were subset to include only myeloid cells and combined using Harmony.

Similarly, the data from ref. ⁴ were integrated with the myeloid cells from the vaccine study using Harmony²⁴. Lymphoid cells from ref. ⁴ were removed after integration. For both integrations, UMAP was performed on the Harmony-corrected embeddings.

Monocyte purification and stimulation

Monocytes were negatively enriched from healthy PBMCs using Dynabeads Untouched Human Monocyte kit (Invitrogen, cat. no. 11350D) following manufacturer's instructions. In brief, 50 million live PBMCs were stained with the antibody cocktail for 20 min at 4 °C. The cells were washed and mixed with 0.5 ml of premixed Dynabeads. The samples were incubated in a hulamixer for 15 min at 4 °C. The tubes were placed on the magnet and the unbound fraction containing purified CD14⁺ monocytes was aspirated using a pipette. The purified monocytes were washed thoroughly and resuspended at a density of 5 million per ml for stimulation. The purity of monocytes was estimated by flow cytometry and was over 95% in all the samples.

Monocytes (0.5 million) were stimulated per condition in 96-well round-bottomed plate for 24 h in 100 µl complete RPMI. Different concentrations of IFNγ, as shown in Extended Data Fig. ^{7j}, were added in 100 µl complete RPMI. Day 0, 1 or 22 plasma samples were from the participant 2055 with <10 pg ml⁻¹, <10 pg ml⁻¹ and 300 pg ml⁻¹ IFNγ, respectively, as measured by enzyme-linked immunosorbent assay. Fifty µl of plasma samples was added to appropriate wells. Fifty µl of complete medium was added to make up the volume to 0.2 ml in total. The plates were incubated at 37 °C, 5% CO₂ cell culture incubators.

RNA isolation and qPCR

RNA was isolated using Aurum Total RNA minikit (Biorad, cat. no. 7326820) following the manufacturer's protocol. cDNA was synthesized using iScript Advanced cDNA synthesis kit (Biorad, cat. no. 1725038) using 150 ng total RNA in 20 µl volume. The cDNA samples were diluted 5-fold by adding 80 µl sterile nuclease-free water and 5 µl of cDNA was used for PCR reaction. The PCRs were carried out using Biorad Prime PCR reagents and SYBR green chemistry (SsoAdvanced Universal SYBR Green Supermix (cat. no. 1725272)) in Biorad CFX384 real-time PCR.

Reporting summary

Further information on research design is available in the [Nature Research Reporting Summary](#) linked to this paper.

Data availability

CITE-seq and bulk RNA data are publicly accessible in the GEO under accession numbers [GSE171964](#) and [GSE169159](#), respectively. Any other relevant data are available from the corresponding authors upon reasonable request. [Source data](#) are provided with this paper.

Code availability

The codes used in the study are available in GitHub (<https://github.com/scottmk777/PfizerCovid>). Some codes used for meta-analysis can be obtained from the corresponding authors upon reasonable request.

References

1. 1.

Polack, F. P. et al. Safety and efficacy of the BNT162b2 mRNA Covid-19 vaccine. *N. Engl. J. Med.* **383**, 2603–2615 (2020).

[CAS](#) [Article](#) [Google Scholar](#)

2. 2.

Mulligan, M. J. et al. Phase I/II study of COVID-19 RNA vaccine BNT162b1 in adults. *Nature* **586**, 589–593 (2020).

[CAS](#) [Article](#) [ADS](#) [Google Scholar](#)

3. 3.

Sahin, U. et al. COVID-19 vaccine BNT162b1 elicits human antibody and T_H1 T cell responses. *Nature* **586**, 594–599 (2020).

[CAS](#) [Article](#) [ADS](#) [Google Scholar](#)

4. 4.

Arunachalam, P. S. et al. Systems biological assessment of immunity to mild versus severe COVID-19 infection in humans. *Science* **369**, 1210–1220 (2020).

[CAS](#) [Article](#) [ADS](#) [Google Scholar](#)

5. 5.

Nakaya, H. I. et al. Systems biology of vaccination for seasonal influenza in humans. *Nat. Immunol.* **12**, 786–795 (2011).

[CAS](#) [Article](#) [Google Scholar](#)

6. 6.

Querec, T. D. et al. Systems biology approach predicts immunogenicity of the yellow fever vaccine in humans. *Nat. Immunol.* **10**, 116–125 (2009).

[CAS](#) [Article](#) [Google Scholar](#)

7. 7.

Gaucher, D. et al. Yellow fever vaccine induces integrated multilineage and polyfunctional immune responses. *J. Exp. Med.* **205**, 3119–3131 (2008).

[CAS](#) [Article](#) [Google Scholar](#)

8. 8.

Tsang, J. S. et al. Global analyses of human immune variation reveal baseline predictors of postvaccination responses. *Cell* **157**, 499–513 (2014).

[CAS](#) [Article](#) [Google Scholar](#)

9. 9.

Doria-Rose, N. et al. Antibody persistence through 6 months after the second dose of mRNA-1273 vaccine for Covid-19. *N. Engl. J. Med.* **384**, 2259–2261 (2021).

[Article](#) [Google Scholar](#)

10. 10.

Samanovic, M. I. et al. Poor antigen-specific responses to the second BNT162b2 mRNA vaccine dose in SARS-CoV-2-experienced individuals. Preprint at

<https://doi.org/10.1101/2021.02.07.21251311> (2021).

11. 11.

Liu, Y. et al. Neutralizing activity of BNT162b2-elicited serum. *N. Engl. J. Med.* **384**, 1466–1468 (2021).

[Article](#) [Google Scholar](#)

12. 12.

Sette, A. & Crotty, S. Pre-existing immunity to SARS-CoV-2: the knowns and unknowns. *Nat. Rev. Immunol.* **20**, 457–458 (2020).

[CAS](#) [Article](#) [Google Scholar](#)

13. 13.

Woodruff, M. C., Ramonell, R. P., Lee, F. E.-H. & Sanz, I. Clinically identifiable autoreactivity is common in severe SARS-CoV-2 infection. Preprint at <https://doi.org/10.1101/2020.10.21.20216192> (2020).

14. 14.

Zuo, Y. et al. Prothrombotic autoantibodies in serum from patients hospitalized with COVID-19. *Sci. Transl. Med.* **12**, eabd3876 (2020).

[CAS](#) [Article](#) [Google Scholar](#)

15. 15.

Wang, E. Y. et al. Diverse functional autoantibodies in patients with COVID-19. *Nature* **595**, 283–288 (2021).

16. 16.

Chang, S. E. et al. New-onset IgG autoantibodies in hospitalized patients with COVID-19. Preprint at <https://doi.org/10.1101/2021.01.27.21250559> (2021).

17. 17.

De Mot, L. et al. Transcriptional profiles of adjuvanted hepatitis B vaccines display variable interindividual homogeneity but a shared core signature. *Sci. Transl. Med.* **12**, eaay8618 (2020).

[Article](#) [Google Scholar](#)

18. 18.

Li, S. et al. Molecular signatures of antibody responses derived from a systems biology study of five human vaccines. *Nat. Immunol.* **15**, 195–204 (2014).

[Article](#) [Google Scholar](#)

19. 19.

Boraschi, D. & Italiani, P. Immunosenescence and vaccine failure in the elderly: strategies for improving response. *Immunol. Lett.* **162**, 346–353 (2014).

[CAS](#) [Article](#) [Google Scholar](#)

20. 20.

Schulte-Schrepping, J. et al. Severe COVID-19 is marked by a dysregulated myeloid cell compartment. *Cell* **182**, 1419–1440 (2020).

[CAS](#) [Article](#) [Google Scholar](#)

21. 21.

Wilk, A. J. et al. A single-cell atlas of the peripheral immune response in patients with severe COVID-19. *Nat. Med.* **26**, 1070–1076 (2020).

[CAS](#) [Article](#) [Google Scholar](#)

22. 22.

Bakdash, G. et al. Expansion of a BDCA1⁺CD14⁺ myeloid cell population in melanoma patients may attenuate the efficacy of dendritic cell vaccines. *Cancer Res.* **76**, 4332–4346 (2016).

[CAS](#) [Article](#) [Google Scholar](#)

23. 23.

Stephenson, E. et al. Single-cell multi-omics analysis of the immune response in COVID-19. *Nat. Med.* **27**, 904–916 (2021).

[CAS](#) [Article](#) [Google Scholar](#)

24. 24.

Korsunsky, I. et al. Fast, sensitive and accurate integration of single-cell data with Harmony. *Nat. Methods* **16**, 1289–1296 (2019).

[CAS Article](#) [Google Scholar](#)

25. 25.

Wimmers, F. et al. The single-cell epigenomic and transcriptional landscape of immunity to influenza vaccination. *Cell* **184**, 3915–3935 (2021).

26. 26.

Ponti, C. et al. Role of CREB transcription factor in c-fos activation in natural killer cells. *Eur. J. Immunol.* **32**, 3358–3365 (2002).

[CAS Article](#) [Google Scholar](#)

27. 27.

Nakaya, H. I. et al. Systems analysis of immunity to influenza vaccination across multiple years and in diverse populations reveals shared molecular signatures. *Immunity* **43**, 1186–1198 (2015).

[CAS Article](#) [Google Scholar](#)

28. 28.

Hadjadj, J. et al. Impaired type I interferon activity and inflammatory responses in severe COVID-19 patients. *Science* **369**, 718–724 (2020).

[CAS Article](#) [ADS](#) [Google Scholar](#)

29. 29.

Mathew, D. et al. Deep immune profiling of COVID-19 patients reveals distinct immunotypes with therapeutic implications. *Science* **369**, eabc8511 (2020).

[CAS Article](#) [Google Scholar](#)

30. 30.

Domínguez-Andrés, J. & Netea, M. G. The specifics of innate immune memory. *Science* **368**, 1052–1053 (2020).

[Article](#) [ADS](#) [Google Scholar](#)

31. 31.

Vanderheiden, A. et al. Development of a rapid focus reduction neutralization test assay for measuring SARS-CoV-2 neutralizing antibodies. *Curr. Protoc. Immunol.* **131**, e116 (2020).

[CAS](#) [Article](#) [Google Scholar](#)

32. 32.

Xie, X. et al. An infectious cDNA clone of SARS-CoV-2. *Cell Host Microbe* **27**, 841–848 (2020).

[CAS](#) [Article](#) [Google Scholar](#)

33. 33.

Katzelnick, L. C. et al. Viridot: an automated virus plaque (immunofocus) counter for the measurement of serological neutralizing responses with application to dengue virus. *PLoS Negl. Trop. Dis.* **12**, e0006862 (2018).

[Article](#) [Google Scholar](#)

34. 34.

Tegally, H. et al. Emergence and rapid spread of a new severe acute respiratory syndrome-related coronavirus 2 (SARS-CoV-2) lineage with multiple spike mutations in South Africa. Preprint at <https://doi.org/10.1101/2020.12.21.20248640> (2020).

35. 35.

Arunachalam, P. S. et al. Adjuvanting a subunit COVID-19 vaccine to induce protective immunity. *Nature* **594**, 253–258 (2021).

[CAS](#) [Article](#) [ADS](#) [Google Scholar](#)

36. 36.

Ayoglu, B. et al. Anoctamin 2 identified as an autoimmune target in multiple sclerosis. *Proc. Natl Acad. Sci. USA* **113**, 2188–2193 (2016).

[CAS](#) [Article](#) [ADS](#) [Google Scholar](#)

37. 37.

Degn, S. E. et al. Clonal evolution of autoreactive germinal centers. *Cell* **170**, 913–926 (2017).

[CAS](#) [Article](#) [Google Scholar](#)

38. 38.

R Core Team. R: A Language and Environment for Statistical Computing (R Foundation for Statistical Computing, 2013).

39. 39.

Nowicka, M. et al. CyTOF workflow: differential discovery in high-throughput high-dimensional cytometry datasets. *F1000Res.* **6**, 748 (2017).

[Article](#) [Google Scholar](#)

40. 40.

Risso, D., Schwartz, K., Sherlock, G. & Dudoit, S. GC-content normalization for RNA-seq data. *BMC Bioinformatics* **12**, 480 (2011).

[CAS](#) [Article](#) [Google Scholar](#)

41. 41.

Love, M. I., Huber, W. & Anders, S. Moderated estimation of fold change and dispersion for RNA-seq data with DESeq2. *Genome Biol.* **15**, 550 (2014).

[Article](#) [Google Scholar](#)

42. 42.

Irizarry, R. A. et al. Exploration, normalization, and summaries of high density oligonucleotide array probe level data. *Biostatistics* **4**, 249–264 (2003).

[Article](#) [Google Scholar](#)

43. 43.

Stuart, T. et al. Comprehensive integration of single-cell data. *Cell* **177**, 1888–1902 (2019).

[CAS](#) [Article](#) [Google Scholar](#)

44. 44.

Bais, A. S. & Kostka, D. scds: computational annotation of doublets in single-cell RNA sequencing data. *Bioinformatics* **36**, 1150–1158 (2020).

[CAS](#) [Article](#) [Google Scholar](#)

45. 45.

Finak, G. et al. MAST: a flexible statistical framework for assessing transcriptional changes and characterizing heterogeneity in single-cell RNA sequencing data. *Genome Biol.* **16**, 278 (2015).

[Article](#) [Google Scholar](#)

[Download references](#)

Acknowledgements

We thank all participants as well as the clinical staff who helped throughout the study; J. Francis, M. Mahoney, J. Liu, J. Gonzalez, A. Buccanzo, E. Tkachenko, I. Chang, D. Dunham, E. Smith, E. Do, S. Jane, M. Manohar, C. Joffe, C. Schumacher, W. Collins, W. Yu, K. Jia, R. Hoh, M. Shoura, F. Yang, O. Fabian Wirz, K. Mathi, C. Dault, T. Audrey Liu and all members of the groups of B.P., K.C.N., S.D.B. and M.M.D. for their contribution to coordination, blood collection and processing of samples; D. Wagh, M. Blanco and J. Collier for assistance with single-cell RNA sequencing; the Yerkes Nonhuman Primate (NHP) Genomics Core (supported in part by National Institutes of Health (NIH) grant P51 OD011132) for assistance with bulk transcriptomics; the HIMC and the Parker Institute for Cancer Immunotherapy (PICI) for maintenance and access to the flow cytometer; and the Stanford Biobank (principal investigator, R. O'Hara) for processing and storing of samples (funded through NIH CTSA). This work was supported by NIH grants HIPC U19AI090023 (to B.P.), U19AI057266 (to B.P. and principal investigator R. Ahmed (Emory University)), Open Philanthropy (to M.M.D. and B.P.) and U24AI120134 (to S.E.B.); the Sean Parker Cancer Institute; the Soffer endowment (to B.P.); and the Violetta Horton endowment (to B.P.). Next-generation sequencing services were provided by the Yerkes NHP Genomics Core, which is supported in part by NIH P51 OD 011132, and the data were acquired on a NovaSeq 6000 funded by NIH S10 OD 026799. A.F. was funded by Stanford University and the Vice Provost for Undergraduate Education's (VPUE) 2019-2020 Major Grant. P.J.U. was supported by the National Institute of Allergy and Infectious Diseases of the NIH, R01 AI125197-04, NIH U01 AI150741-01S1 and the Henry Gustav Floren Trust. This study was partially funded by the Parker Foundation (K.C.N. and B.P.), CCHI (principal investigator, M.M.D.) and the Crown Foundation (K.C.N.).

Author information

Author notes

1. These authors contributed equally: Prabhu S. Arunachalam, Madeleine K. D. Scott, Thomas Hagan

Affiliations

1. Institute for Immunity, Transplantation and Infection, Stanford University, Stanford, CA, USA

Prabhu S. Arunachalam, Madeleine K. D. Scott, Chunfeng Li, Yupeng Feng, Florian Wimmers, Lilit Grigoryan, Meera Trisal, Sarah Esther Chang, Allan Feng, Shaurya Dhingra, Vamsee Mallajosyula, Fei Gao, Natalia Sigal, Sangeeta Kowli, Sheena Gupta, Sofia Maysel-Auslender, Holden T. Maecker, Mark M. Davis, Paul J. Utz, Purvesh Khatri & Bali Pulendran

2. Center for Biomedical Informatics, Department of Medicine, Stanford University School of Medicine, Stanford University, Stanford, CA, USA

Madeleine K. D. Scott & Purvesh Khatri

3. Division of Infectious Diseases, Cincinnati Children's Hospital Medical Center, Cincinnati, OH, USA

Thomas Hagan

4. Department of Pediatrics, University of Cincinnati College of Medicine, Cincinnati, OH, USA

Thomas Hagan & Steven E. Bosinger

5. Yerkes National Primate Research Center, Atlanta, GA, USA

Venkata Viswanadh Edara, Lilin Lai, Kathryn Pellegrini, Gregory Tharp, Sydney Hamilton, Hadj Aoued & Mehul S. Suthar

6. Department of Medicine, Division of Immunology and Rheumatology, Stanford University School of Medicine, Stanford University,

Stanford, CA, USA

Sarah Esther Chang, Allan Feng, Shaurya Dhingra & Paul J. Utz

7. Sean N. Parker Center for Allergy and Asthma Research, Stanford University, Stanford, CA, USA

Mihir Shah, Alexandra S. Lee, Sharon Chinthurajah, Sayantani B. Sindher, Scott D. Boyd & Kari C. Nadeau

8. Quanterix, Billerica, MA, USA

Kevin Hrusovsky & Mark Roskey

9. Department of Pathology, Emory University School of Medicine, Atlanta, GA, USA

Steven E. Bosingier

10. Department of Pathology, Stanford University School of Medicine, Stanford University, Stanford, CA, USA

Scott D. Boyd, Mark M. Davis & Bali Pulendran

11. Department of Microbiology and Immunology, Stanford University School of Medicine, Stanford University, Stanford, CA, USA

Mark M. Davis & Bali Pulendran

12. Howard Hughes Medical Institute, Stanford University, Stanford, CA, USA

Kari C. Nadeau

13. Department of Medicine, Division of Pulmonary, Allergy and Critical Care Medicine, Stanford University School of Medicine, Stanford University, Stanford, CA, USA

Kari C. Nadeau

Authors

1. Prabhu S. Arunachalam

[View author publications](#)

You can also search for this author in [PubMed](#) [Google Scholar](#)

2. Madeleine K. D. Scott

[View author publications](#)

You can also search for this author in [PubMed](#) [Google Scholar](#)

3. Thomas Hagan

[View author publications](#)

You can also search for this author in [PubMed](#) [Google Scholar](#)

4. Chunfeng Li

[View author publications](#)

You can also search for this author in [PubMed](#) [Google Scholar](#)

5. Yupeng Feng

[View author publications](#)

You can also search for this author in [PubMed](#) [Google Scholar](#)

6. Florian Wimmers

[View author publications](#)

You can also search for this author in [PubMed](#) [Google Scholar](#)

7. Lilit Grigoryan

[View author publications](#)

You can also search for this author in [PubMed](#) [Google Scholar](#)

8. Meera Trisal

[View author publications](#)

You can also search for this author in [PubMed](#) [Google Scholar](#)

9. Venkata Viswanadh Edara
[View author publications](#)

You can also search for this author in [PubMed](#) [Google Scholar](#)

10. Lilin Lai
[View author publications](#)

You can also search for this author in [PubMed](#) [Google Scholar](#)

11. Sarah Esther Chang
[View author publications](#)

You can also search for this author in [PubMed](#) [Google Scholar](#)

12. Allan Feng
[View author publications](#)

You can also search for this author in [PubMed](#) [Google Scholar](#)

13. Shaurya Dhingra
[View author publications](#)

You can also search for this author in [PubMed](#) [Google Scholar](#)

14. Mihir Shah
[View author publications](#)

You can also search for this author in [PubMed](#) [Google Scholar](#)

15. Alexandra S. Lee
[View author publications](#)

You can also search for this author in [PubMed](#) [Google Scholar](#)

16. Sharon Chinthrajah
[View author publications](#)

You can also search for this author in [PubMed](#) [Google Scholar](#)

17. Sayantani B. Sindher

[View author publications](#)

You can also search for this author in [PubMed](#) [Google Scholar](#)

18. Vamsee Mallajosyula

[View author publications](#)

You can also search for this author in [PubMed](#) [Google Scholar](#)

19. Fei Gao

[View author publications](#)

You can also search for this author in [PubMed](#) [Google Scholar](#)

20. Natalia Sigal

[View author publications](#)

You can also search for this author in [PubMed](#) [Google Scholar](#)

21. Sangeeta Kowli

[View author publications](#)

You can also search for this author in [PubMed](#) [Google Scholar](#)

22. Sheena Gupta

[View author publications](#)

You can also search for this author in [PubMed](#) [Google Scholar](#)

23. Kathryn Pellegrini

[View author publications](#)

You can also search for this author in [PubMed](#) [Google Scholar](#)

24. Gregory Tharp

[View author publications](#)

You can also search for this author in [PubMed](#) [Google Scholar](#)

25. Sofia Maysel-Auslender
[View author publications](#)

You can also search for this author in [PubMed](#) [Google Scholar](#)

26. Sydney Hamilton
[View author publications](#)

You can also search for this author in [PubMed](#) [Google Scholar](#)

27. Hadj Aoued
[View author publications](#)

You can also search for this author in [PubMed](#) [Google Scholar](#)

28. Kevin Hrusovsky
[View author publications](#)

You can also search for this author in [PubMed](#) [Google Scholar](#)

29. Mark Roskey
[View author publications](#)

You can also search for this author in [PubMed](#) [Google Scholar](#)

30. Steven E. Bosingr
[View author publications](#)

You can also search for this author in [PubMed](#) [Google Scholar](#)

31. Holden T. Maecker
[View author publications](#)

You can also search for this author in [PubMed](#) [Google Scholar](#)

32. Scott D. Boyd
[View author publications](#)

You can also search for this author in [PubMed](#) [Google Scholar](#)

33. Mark M. Davis

[View author publications](#)

You can also search for this author in [PubMed](#) [Google Scholar](#)

34. Paul J. Utz

[View author publications](#)

You can also search for this author in [PubMed](#) [Google Scholar](#)

35. Mehul S. Suthar

[View author publications](#)

You can also search for this author in [PubMed](#) [Google Scholar](#)

36. Purvesh Khatri

[View author publications](#)

You can also search for this author in [PubMed](#) [Google Scholar](#)

37. Kari C. Nadeau

[View author publications](#)

You can also search for this author in [PubMed](#) [Google Scholar](#)

38. Bali Pulendran

[View author publications](#)

You can also search for this author in [PubMed](#) [Google Scholar](#)

Contributions

B.P., K.C.N., M.M.D., S.D.B. and P.S.A. conceptualized and designed the trial; P.S.A. and B.P. designed the study; P.S.A., M.S., A.S.L., S.C. and S.B.S. coordinated and performed blood collections under the supervision of K.C.N.; P.S.A., C.L., Y.F., F.W., L.G., V.M. and F.G. processed blood and prepared all samples; P.S.A., C.L., Y.F. and L.G. performed enzyme-linked

immunosorbent assays; V.V.E. and L.L. performed neutralization assays under the guidance of M.S.S.; P.S.A., C.L., M.T., S.G. and S.M.-A. performed T cell assays; P.S.A., N.S. and S.K. performed CyTOF under the guidance of H.T.M.; K.H. and M.R. performed SIMOA; S.E.C., A.F. and S.D. performed autoantibody assays under the guidance of P.J.U.; K.P., G.T., H.A. and S.H. performed bulk transcriptomics under the guidance of S.E.B.; P.S.A., F.W., C.L. and Y.F. performed CITE-seq; P.S.A. performed monocyte stimulation experiments; P.S.A. analysed antibody responses, T cell responses, CyTOF and Olink; M.K.D.S. and T.H. analysed bulk transcriptomics; M.K.D.S. and P.S.A. analysed CITE-seq; T.H. performed vaccine response meta-analysis; P.S.A., M.S. and T.H. performed data visualization. B.P., K.C.N., P.K., M.S.S., P.J.U., M.M.D., S.D.B., H.T.M. and S.E.B. supervised the project. P.S.A., M.S., T.H. and B.P wrote the paper. B.P., K.C.N. and P.K. acquired funding. All the authors read and accepted the manuscript.

Corresponding authors

Correspondence to [Purvesh Khatri](#) or [Kari C. Nadeau](#) or [Bali Pulendran](#).

Ethics declarations

Competing interests

B.P. serves on the External Immunology Board of GlaxoSmithKline, and on the Scientific Advisory Board of Medicago.

Additional information

Peer review information *Nature* thanks Petter Brodin, Rik Lindeboom, Waradon Sungnak, Sarah Teichmann and the other, anonymous, reviewer(s) for their contribution to the peer review of this work. Peer reviewer reports are available.

Publisher's note Springer Nature remains neutral with regard to jurisdictional claims in published maps and institutional affiliations.

Extended data figures and tables

Extended Data Fig. 1 Antibody responses to BNT162b2 vaccination.

a, Schematic of the study design and the number of participants used in various assays. **b, c**, Binding (**b**) and neutralizing (**c**) antibody responses to BNT162b2 vaccination in female and male participants ($n = 56$). **d, e**, Correlation between binding antibody and neutralizing antibody titres (**d**) and neutralizing antibody responses and age (**e**). **f**, Neutralizing antibody response to B.1.351 variant of concern in female and male participants ($n = 30$). **g**, Correlation between age and cross-neutralization index, defined as the ratio of neutralizing antibody response to B.1.351 versus WA1 strains. Each dot represents an individual in all plots. Blue and red colour denote female and male participants, respectively. Boxes show median and 25th–75th percentiles, and whiskers show the range in all box plots. All correlations are two-sided Spearman’s correlations. The error bands represent 95% confidence limits. The statistical difference between time points is calculated using two-sided Wilcoxon matched-pairs signed-rank test and the statistical differences between groups were calculated using two-sided Mann–Whitney rank-sum test. *** $P < 0.001$, **** $P < 0.0001$.

Extended Data Fig. 2 T cell responses to BNT162b2 vaccination.

a, Frequency of spike-specific CD4 T cell responses measured in blood at time points indicated on the x axis. **b**, Polyfunctional profiles of CD4 T cells. **c**, Frequency of spike-specific CD8 T cell responses measured in blood at time points indicated on the x axis. **d**, Polyfunctional profiles of CD8 T cells. **e**, Frequency of spike-specific CD4 T cells secreting IL-21 and CD154 at time points indicated on x -axis. **f**, Correlation between spike-specific CD4 (left) and CD8 (right) T cell frequencies and neutralizing antibody responses. **g**, Correlation between cross-neutralization index, ratio between neutralizing antibody responses against B.1.351 to WA1 strains, and spike-specific CD4 T cell frequencies, IFN γ^+ (left) or polyfunctional CD4 T cells expressing IL-2, IFN γ and TNF (right). **h**, Correlation of spike-

specific CD4 (left) and CD8 (right) T cell responses with age. **i**, Correlation of spike-specific IL-21⁺CD154⁺ T follicular helper-like cells on day 28 and neutralizing antibody response on day 42. **j**, Frequency of CXCR5⁺ CD4 T cells in PBMCs in DMSO-stimulation condition. **k**, Correlation of peak (day 7) CXCR5⁺ CD4 T cells and neutralizing antibody response on day 42. Each dot represents an individual in all plots. Blue and red colour denote female and male participants, respectively. Boxes show median and 25th–75th percentiles, and whiskers show the range in all box plots. The IFN γ response plots in CD4 (**a**) and CD8 (**c**) T cells are from Fig. [1d, e](#) repeated here for completeness. The pie charts in **b**, **d** represent the proportion of T cells expressing one, two or three cytokines as shown in the legend. All correlations are two-sided Spearman’s correlations. The error bands represent 95% confidence limits. The statistical difference between time points is calculated using two-sided Wilcoxon matched-pairs signed-rank test. * $P < 0.05$, ** $P < 0.01$, *** $P < 0.001$, **** $P < 0.0001$. $n = 38$. Number of samples differ between time points as shown in Extended Data Fig. [1a](#).

Extended Data Fig. 3 Autoantibodies and anticytokine antibodies in vaccinated individuals.

a, Heat map depicting serum IgG antibodies discovered using a 55-plex bead-based protein array containing the indicated autoantigens (y axis). Autoantigens are grouped on the basis of disease (for example, scleroderma, myositis and overlap syndromes such as mixed connective tissue disease, systemic lupus erythematosus (SLE) and Sjögren’s, and gastrointestinal and endocrine disorders), DNA-associated antigens and antigens associated with tissue inflammation or stress responses. Vaccinated individuals are shown on the left ($n = 30$ individuals, on day 0, day 21, and day 42 and $n = 1$ on day 0 and day 21), and eight prototype autoimmune disorders are shown on the right. Colours correspond to the MFI values shown at far right. **b**, Heat map using a 58-plex array of cytokines, chemokines, growth factors and receptors. Cytokines are grouped on the y axis by category (interferons, interleukins and other cytokines, growth factors and receptors), and serum samples are shown on the x axis. Vaccinated individuals are shown on the left ($n = 30$ individuals, on day 0, day 21 and day 42 and $n = 1$ on day 0 and day 21). Data are displayed as

fold change over baseline. Prototype samples from patients with immunodeficiency disorders are shown on the right, and include three patients with AMI, three patients with PAP and three patients with APS1. Colours for the prototype samples correspond to the MFI values shown at far right.

Extended Data Fig. 4 Pre-existing autoantibodies and autocytokine antibodies do not change in vaccinated individuals.

a–f, Bar plots (mean of two technical replicates) of representative patients with high baseline MFI autoantibodies for select antigens. **a**, Anti-RPP25 (Th/To). **b**, Anti-PM/Scl-75. **c**, Anti-SSB/La. **d**, Anti-PDC-E2. **e**, Anti-thyroperoxidase, TPO. **f**, Anti-thyroglobulin, TG. **g–j**, Bar plots (mean of two technical replicates) of representative patients with high baseline MFI autocytokine antibodies. Group bars represent antigens for baseline (black), day 21 (grey), and day 42 (white) time points. **g**, Individual 2012, anticytokine antibody measurements. **h**, Individual 2043, anticytokine antibody measurements. **i**, Individual 2052, anticytokine antibody measurements; **j**, Individual 2053, anticytokine antibody measurements.

Extended Data Fig. 5 Innate immune responses to BNT162b2 vaccination.

a, Representation of CyTOF-identified cell clusters in Lin[−] (CD3[−]CD20[−]CD66b[−]) HLA-DR⁺ cells visualized by UMAP in two-dimensional space. **b**, Heat map showing expression of markers in the different cell clusters identified in the CyTOF dataset. **c**, Gating strategy identifying immune cell populations by the CyTOF panel. **d**, Mass cytometry plots showing CD14 and CD16 expression of Lin[−] HLA-DR⁺ population. $n = 27$.

Extended Data Fig. 6 Frequency of all cell types identified by CyTOF.

Frequency of all major cell types measured in whole blood by CyTOF. Each dot represents an individual in all plots. Blue and red colour denote female and male participants, respectively. Boxes show median and 25th–75th percentiles, and whiskers show the range in all box plots. $n = 27$; some time points have a smaller n value (as shown in Extended Data Fig. 1a).

Extended Data Fig. 7 Plasma cytokine analysis.

a–c, Plasma levels of CXCL10 (**a**) and IL-10 (**b**) determined by Olink, and IFN α 2 measured by SIMOA (**c**). **d**, Kinetic plots of IFN α 2 in plasma of female or male participants measured by SIMOA. **e**, Scatter plots showing two-sided Spearman's correlation between pSTAT3 level in intermediate monocytes and plasma IFN γ levels. The error bands represent 95% confidence limits. Each dot represents an individual in all plots. Blue and red colour denote female and male participants, respectively. Boxes show median and 25th–75th percentiles, and whiskers show the range in all box plots. The statistically significant differences between the peak and baseline time points were measured using two-sided Wilcoxon matched-pairs signed-rank test. The differences between peak time points were measured using two-sided Mann–Whitney rank-sum test. * $P < 0.05$, ** $P < 0.01$, *** $P < 0.001$ and **** $P < 0.0001$. $n = 31$.

Extended Data Fig. 8 Transcriptional signatures induced by BNT162b2 vaccination.

a, PCA analysis of bulk RNA-sequencing samples. **b**, RLE analysis of bulk RNA-sequencing data. **c**, **d**, Temporal expression patterns of genes within modules M111.0 (**c**) or M16 (**d**). Black lines represent the median fold change of all genes. **e**, Number of genes differentially expressed (absolute log₂-transformed fold change > 0.2 and Wald $P < 0.01$) at each time point. All time points were compared to universal baseline, day 0. Number of upregulated and downregulated genes are shown in orange and green, respectively. **f**, BTMs that were significantly enriched (FDR < 0.05 , absolute NES > 2) after vaccination. GSEA was used to identify increased (red) or decreased (blue) enrichment of BTMs within gene lists ranked by Wald statistic between before and after vaccination at each time point. **g**,

BTMs on day 22 relative to day 21 that were significantly associated with age. **h, i**, Scatter plots showing two-sided Pearson correlation of the mean fold change between day 22 and day 21 of genes in interferon modules M127, M75, M150, M111.1 and M68 (**h**) or module M16 (**i**) with IFN γ . Each dot represents an individual in all plots. Blue and red colour denote female and male participants, respectively.

Extended Data Fig. 9 CITE-seq analysis of PBMCS.

a, b, Fraction of cells in each cluster of CITE-seq data classified by subject (**a**) or time point (**b**), determined from all single cells that passed quality control. **c**, Proportion of cells in each cluster at different time points indicated on x axis. **d**, Heat map showing top 10 cluster-defining genes in each cluster. **e**, Pseudobulk gene expression score showing the contribution from each cluster after iterative removal of each cluster.

Extended Data Fig. 10 Analysis of gene expression within cluster C8.

a, b, UMAP representation of 71,276 innate immune cells (myeloid cells + pDCs) from this study combined with innate cells from ref. ²³ (**a**, 154,108 cells) or ref. ⁴ (**b**, 18,926 cells). Red and blue fonts on the legends denote cell clusters defined in the current study versus previously published studies. **c**, Rank plot showing genes overexpressed in cluster C8 from this study in comparison to IFN-experienced monocyte cluster ('C11_C Mono_IFN'). Genes expressed more in C8 are in red font; genes in blue font are expressed at a higher level in C11_C Mono_IFN. **d**, Heat map showing genes in C3 CD14 $^{+}$ monocytes, C4 CD16 $^{+}$ monocytes, C7 cDC2 and C13 cDC1 that are shared with C8 subclusters and are closest with the parental clusters on the basis of Euclidean distance. **e**, Feature plots showing expression of CD14, CD1c or CD16 within C8 subclusters. **f**, Fraction of cells in each subcluster of C8 classified by subject. **g**, Frequency of C8 as a proportion of Lin $^{-}$ HLA-DR $^{+}$ population (bottom) or plasma IFN γ levels (top) as measured in Olink. **h**, Correlation between C8 frequency and plasma IFN γ levels measured by enzyme-linked immunosorbent assay. **i**, Schematic of the experimental set up for in vitro

stimulation of purified healthy monocytes with IFN γ and day-22 plasma from vaccinated participants. **j**, Heat maps showing expression of genes measured by quantitative real-time PCR (qRT–PCR) relative to the ‘no stimulation’ condition. Each column shows the condition as shown on the top. Each row represents a gene quantified by qRT–PCR. Five hundred thousand PBMCs from four donors were treated with different concentration of IFN γ , 1:4 diluted plasma sample from day 0, 1 or 22. **k**, Significantly enriched natural killer cell modules (FDR < 0.05, absolute NES >2) within the natural killer cell cluster. Days 1 and 7 were compared against day 0; days 22 and 28 were compared against day 21. GSEA was used to identify increased (red) or decreased (blue) enrichment of interferon BTMs. **l**, log₂-transformed fold change of top 50 DEGs between natural killer cells from day 22 samples versus day 1 samples.

Extended Data Fig. 11 Comparison of transcriptional responses with other vaccines.

a, Correlation matrix of vaccines on day 1. Spearman’s correlation was computed using mean fold changes over all genes between each pair of vaccines. Circle size and colour represents the correlation coefficient. **b**, Correlation matrix of vaccines on day 7. **c**, Circos plot of the overlap across vaccines in enriched BTMs on day 7. GSEA was performed on genes ranked by day 7 versus baseline *t*-statistic in each vaccine. Each segment of the circle represents one vaccine, and each point in a segment represents a single BTM. Bars in outer circle represent the NES of significantly enriched BTMs (FDR < 0.05). Lines connect BTMs with a significant positive enrichment shared between vaccines. Inner circle boxes and line colours represent the functional groups of the BTMs. **d**, Heat map of cell cycle, B cell and plasma cell BTMs on day 7. Cell cycle, B cell and plasma cell BTMs that were significantly enriched (FDR < 0.05) on day 7 after either dose of BNT162b2 are shown. Colour represents significant NES. **e**, Expression of genes in the plasma cell module M156 across different vaccines on day 7 after vaccination. The asterisks denote statistical significance measured by two-sided Wilcoxon test between baseline and day-7 samples within each vaccine group. **f**, Plasmablast frequencies measured by CyTOF in whole-blood samples. The numbers within plots indicate geometric mean ± s.e.m. at the time points as indicated. Each dot

represents an individual in all plots. Blue and red colour denote female and male participants, respectively. Boxes show median and 25th–75th percentiles, and whiskers show the range in all box plots. The statistically significant differences between the peak and baseline time points were measured using two-sided Wilcoxon matched-pairs signed-rank test.

Extended Data Fig. 12 Transcriptional correlates of neutralizing antibody and T cell responses.

a, BTMs (day 22 relative to day 21) associated with the neutralizing antibody or CD8 IFN γ T cell response to BNT162b2. GSEA was run using BTMs on gene lists ranked by correlation with either day-42 neutralizing antibody titres or day-28 antigen-specific CD8 $^+$ IFN γ $^+$ T cell frequencies. Modules shown are those with NES > 2 and FDR < 0.05. **b**, Correlation of genes in M75, an antiviral BTM, on day 22 with the day-42 neutralizing antibody response (top) or day-28 antigen-specific CD8 $^+$ IFN γ $^+$ T cell frequencies (bottom). Colour represents two-sided Pearson correlation coefficient. Each edge (grey line) represents a co-expression relationship, as previously described¹⁸. **c**, BTMs correlated with cross-neutralization index, ratio of B.1.351:WA1 neutralizing antibody titres, analysed as in **a**. Modules shown are those with NES > 2 and FDR < 0.05. **d**, Frequency of classical monocytes (Lin $^-$ HLA-DR $^+$ CD14 $^+$ CD16 $^-$ cells) in whole-blood samples analysed by CyTOF. **e**, **f**, Scatter plots of two-sided Spearman's correlation between cross-neutralization index and peak (day 23) classical monocyte frequency (**e**) or a gene score created in the bulk RNA-sequencing data using the cluster-defining genes of the classical monocyte cluster, C3, in CITE-seq (**f**). The error bands represent 95% confidence limits. Each dot represents an individual in all plots. Blue and red colour denote female and male participants, respectively in **d–f**. Boxes show median and 25th–75th percentiles, and whiskers show the range in **d**.

Extended Data Table 1 Participant demographics

[Full size table](#)

Extended Data Table 2 Vaccine side effects and symptoms

[Full size table](#)

Extended Data Table 3 Vaccine meta-analysis datasets

[Full size table](#)

Supplementary information

[Reporting Summary](#)

[Supplementary Table 1](#)

List of all differentially expressed blood-transcriptional modules identified by bulk transcriptomics analysis.

[Peer Review File](#)

Source data

[Source Data Fig. 1](#)

[Source Data Fig. 2](#)

[Source Data Fig. 3](#)

[Source Data Fig. 4](#)

[Source Data Fig. 5](#)

Rights and permissions

[Reprints and Permissions](#)

About this article



Check for
updates

Cite this article

Arunachalam, P.S., Scott, M.K.D., Hagan, T. *et al.* Systems vaccinology of the BNT162b2 mRNA vaccine in humans. *Nature* **596**, 410–416 (2021). <https://doi.org/10.1038/s41586-021-03791-x>

[Download citation](#)

- Received: 19 April 2021
- Accepted: 01 July 2021
- Published: 12 July 2021
- Issue Date: 19 August 2021
- DOI: <https://doi.org/10.1038/s41586-021-03791-x>

Comments

By submitting a comment you agree to abide by our [Terms](#) and [Community Guidelines](#). If you find something abusive or that does not comply with our terms or guidelines please flag it as inappropriate.

[Download PDF](#)

Advertisement

This article was downloaded by **calibre** from <https://www.nature.com/articles/s41586-021-03791-x>

Age-related immune response heterogeneity to SARS-CoV-2 vaccine BNT162b2

[Download PDF](#)

- Article
- Open Access
- [Published: 30 June 2021](#)

Age-related immune response heterogeneity to SARS-CoV-2 vaccine BNT162b2

- [Dami A. Collier](#) [ORCID: orcid.org/0000-0001-5446-4423](#)^{1,2,3 na1},
- [Isabella A. T. M. Ferreira](#)^{1,2 na1},
- [Prasanti Kotagiri](#)^{1,2 na1},
- [Rawlings P. Dahir](#) [ORCID: orcid.org/0000-0003-0521-2144](#)^{1,2,3 na1},
- [Eleanor Y. Lim](#)^{2 na1},
- [Emma Touizer](#)³,
- [Bo Meng](#)^{1,2},
- [Adam Abdullahi](#)¹,
- [The CITIID-NIHR BioResource COVID-19 Collaboration](#),
- [Anne Elmer](#)^{4,5},
- [Nathalie Kingston](#)^{4,5},
- [Barbara Graves](#)⁴,
- [Emma Le Gresley](#)^{4,5},
- [Daniela Caputo](#)^{4,5},
- [Laura Bergamaschi](#)¹,
- [Kenneth G. C. Smith](#) [ORCID: orcid.org/0000-0003-3829-4326](#)^{1,2},
- [John R. Bradley](#)^{2,4},
- [Lourdes Ceron-Gutierrez](#)⁶,
- [Paulina Cortes-Acevedo](#)⁷,
- [Gabriela Barcenas-Morales](#)⁷,
- [Michelle A. Linterman](#) [ORCID: orcid.org/0000-0001-6047-1996](#)⁸,
- [Laura E. McCoy](#) [ORCID: orcid.org/0000-0001-9503-7946](#)³,
- [Chris Davis](#)⁹,
- [Emma Thomson](#) [ORCID: orcid.org/0000-0003-1482-0889](#)⁹,

- [Paul A. Lyons](#) ORCID: orcid.org/0000-0001-7035-8997^{1,2},
- [Eoin McKinney](#) ^{1,2},
- [Rainer Doffinger](#) ⁵,
- [Mark Wills](#) ^{1,2} &
- [Ravindra K. Gupta](#) ORCID: orcid.org/0000-0001-9751-1808^{1,2}

Nature volume **596**, pages 417–422 (2021) [Cite this article](#)

- 53k Accesses
- 1168 Altmetric
- [Metrics details](#)

Subjects

- [Antibodies](#)
- [SARS-CoV-2](#)

Abstract

Although two-dose mRNA vaccination provides excellent protection against SARS-CoV-2, there is little information about vaccine efficacy against variants of concern (VOC) in individuals above eighty years of age¹. Here we analysed immune responses following vaccination with the BNT162b2 mRNA vaccine² in elderly participants and younger healthcare workers. Serum neutralization and levels of binding IgG or IgA after the first vaccine dose were lower in older individuals, with a marked drop in participants over eighty years old. Sera from participants above eighty showed lower neutralization potency against the B.1.1.7 (Alpha), B.1.351 (Beta) and P.1. (Gamma) VOC than against the wild-type virus and were more likely to lack any neutralization against VOC following the first dose. However, following the second dose, neutralization against VOC was detectable regardless of age. The frequency of SARS-CoV-2 spike-specific memory B cells was higher in elderly responders (whose serum showed neutralization activity) than in non-responders after the first dose. Elderly participants showed a clear reduction in somatic hypermutation of class-switched cells. The production of interferon- γ and interleukin-2 by SARS-CoV-2 spike-specific T cells was lower in older participants, and both cytokines were secreted primarily by CD4 T cells. We conclude that the elderly are a high-risk population and that specific measures to boost vaccine responses in this population are warranted, particularly where variants of concern are circulating.

[Download PDF](#)

Main

Vaccines designed to elicit protective immune responses remain the key hope for containing the COVID-19 pandemic caused by SARS-CoV-2. In particular, mRNA vaccines have shown excellent efficacy when administered as two doses separated by a three- or four-week gap^{2,3}. There is increasing evidence that neutralizing responses are a correlate of protection^{4,5,6}. Few trial data on neutralizing responses or vaccine efficacy in individuals above the age of 80 are available¹. This is even more pertinent for settings in which a dosing interval of 12–16 weeks or more has been implemented to maximize the administration of first doses⁷. In addition, the emergence of new variants with increased transmissibility⁸ and reduced sensitivity to vaccine-elicited antibodies⁹, and for which vaccines are less able to prevent infection¹⁰, has raised fears for vulnerable groups in whom the magnitude and quality of immune responses may be suboptimal.

Neutralization following immunization

We studied 140 participants who had received at least one vaccination (median age 72 years (interquartile range (IQR) 44–83), 51% female; Extended Data Fig. 1). We first validated the use of a pseudotyped virus (PV) system to investigate neutralization, by comparing geometric mean titres (GMTs) between PVs expressing the Wuhan-1 D614G spike (referred to here as wild-type) and a B.1 lineage live virus isolate, using sera isolated from thirteen individuals after two vaccine doses (Extended Data Fig. 2). We observed a high correlation between the two approaches, consistent with other findings¹¹, and proceeded with the PV system.

We explored the association between age and ability to neutralize virus by plotting the proportion of individuals whose sera produced detectable virus neutralization after the first dose at a given age. This analysis showed a nonlinear relationship with a marked drop around the age of 80 years (Fig. 1a). Given this nonlinear change in a correlate of protection, we performed selected subsequent analyses with age both as a continuous variable and as a categorical variable. When individuals aged 80 years or more were tested between 3 and 12 weeks after their first dose, around half showed no evidence of neutralization (Extended Data Fig. 2). Geometric mean neutralization titre (GMT) was lower in participants aged 80 years or more than in younger individuals (48.2 (95% confidence interval (CI) 34.6–67.1) versus 104.1 (95% CI 69.7–155.2), $P = 0.004$; Extended Data Table 1, Fig. 1b). GMT showed evidence of an inverse association with age (Extended Data Fig. 2). The GMT following the second dose was significantly higher in individuals for whom there had been a 12-week interval between doses compared with a 3-week interval between doses (Extended Data Fig. 2). A clinically accredited assay for N antibodies⁹ showed evidence that five

individuals in each group had previously been infected with SARS-CoV-2 (Extended Data Table 1), and we adjusted for this in multivariable analyses (Extended Data Tables 2, 3). Neutralizing titres for sera from vaccinated individuals were higher after the second dose than after the first dose, regardless of age (Fig. 1b). In participants who had suboptimal or no neutralization after dose 1, and who subsequently received the second dose within the study period (Fig. 1c), all but two elderly participants responded with an increase in neutralization activity (Extended Data Table 1, Fig. 1b).

Fig. 1: SARS-CoV-2 neutralization by sera from BNT162b2 vaccinated individuals.

 figure1

a. Proportion of individuals with detectable serum neutralization of PV after the first dose of Pfizer BNT162b2 vaccine by age. Cut-off for serum neutralization is an

inhibitory dilution at which 50% inhibition of infection is achieved (ID50) of 20. Shading, 95% CI. **b**, Serum neutralization of PV after dose 1 (blue) and dose 2 (red) by age group (<80 years ($n = 79$), ≥ 80 years ($n = 59$)). **c**, Neutralization curves for serum from two individuals (ID 4 and ID 8) with lower responses after the first dose (blue) and increased neutralization activity after the second dose (red) of BNT162b2 against pseudovirus expressing wild-type spike protein (D614G). Data shown as mean \pm s.e.m. of technical replicates. **d**, **f**, Neutralization of SARS-CoV-2 VOCs by sera after dose 1 (**d**) and dose 2 (**f**) of BNT162b2. **d**, WT, $n = 138$; B.1.1.7, $n = 135$; B.1.351, $n = 82$; P.1, $n = 82$. **f**, WT, $n = 64$; B.1.1.7, $n = 53$; B.1.351, $n = 32$; P.1, $n = 32$. Data shown as GMT \pm s.d. **e**, **g**, The proportion of participant vaccine sera with neutralization activity against wild-type and mutant spike proteins after dose 1 (**e**) and dose 2 (**g**) (ID50 > 1 in 20 dilution of sera). GMT \pm s.d. are representative of two independent experiments each with two technical repeats. Mann–Whitney test was used for unpaired comparisons and Wilcoxon matched-pairs signed rank test for paired comparisons. * $P < 0.05$, ** $P < 0.01$, *** $P < 0.0001$; NS, not significant. HS, human AB serum control.

[Full size image](#)

Given our observation that participants aged 80 years or more had lower neutralization responses following the first dose than younger individuals, we hypothesized that this could lead to sub-protective neutralizing responses against the B.1.1.7, B.1.351 and P.1 VOCs, which were first identified in the UK, South Africa and Brazil, respectively (Extended Data Fig. 2). We therefore examined serum neutralization by age group against PVs bearing the wild-type spike protein or spike proteins from the three VOCs (Fig. 1d, e). There was a clear reduction in neutralizing titres against VOCs (Fig. 1d), and titres were lower for individuals over 80 years old than for younger individuals. The proportions of individuals with detectable neutralization showed a similar pattern (Fig. 1e, Extended Data Tables 2, 3). Following the second dose, although there were differences in GMT for the VOCs between the age groups (Fig. 1f), nearly all participants across age groups had detectable neutralization responses across the VOCs tested (Fig. 1g).

B cell responses to mRNA vaccination

We measured binding antibody responses to the full-length wild-type (Wuhan-1) spike protein⁹. Levels of IgG and all IgG subclasses against spike protein increased between vaccine doses (Fig. 2a), and were similar after the second dose to those observed following natural infection. Like the neutralization titres, levels of IgG against spike declined with age (Fig. 2b, Extended Data Fig. 3). IgG and its subclasses correlated with serum neutralization (Fig. 2c, Extended Data Fig. 3). The concentrations of total and subclass anti-spike IgGs were significantly lower in participants aged 80 or older

than in the younger group (Fig. 2d). IgA responses also increased between the two doses and correlated with neutralization after dose 1 (Extended Data Fig. 3). In addition, phenotyping of peripheral blood mononuclear cells (PBMCs) by flow cytometry showed that neutralization in the over-80 age group was associated with a higher proportion of spike-specific IgG⁺IgM⁻CD19⁺ memory B cells (Fig. 3e). Notably, the proportion of these cells did not differentiate neutralizers from non-neutralizers in the under-80 group (Fig. 3e, Extended Data Fig. 4).

Fig. 2: SARS-CoV-2 spike-binding antibody responses and SARS-CoV-2 spike-specific memory B cells in blood following vaccination with BNT162b2.

 figure2

a, Total anti-spike IgG and subclasses after first and second doses of vaccine and in individuals with prior COVID-19. MFI, mean fluorescence intensity. **b**, Pearson's correlation (r) between anti-spike IgG binding antibody responses after first dose and age ($n = 134$). **c**, Pearson's correlation between anti-spike IgG ($n = 134$) binding antibody responses and neutralization by sera against SARS-CoV-2 in a spike lentiviral pseudotyping assay expressing wild-type spike (D614G). **d**, Anti-spike IgG subclass responses to first dose vaccine stratified by age (<80 and ≥ 80 years). **e**, CD19⁺ memory B cells (left, as percentage of PBMCs) and SARS-CoV-2 spike-specific CD19⁺IgG⁺IgM⁻ memory B cells (right, as percentage of all memory B cells) from FACS-sorted PBMCs. $n = 16$ for ≥ 80 years, $n = 16$ for <80 years; stratified by neutralizing response after first dose, $n = 8$ in each category. MFI – mean fluorescence intensity. Mann–Whitney test was used for unpaired comparisons. * $P < 0.05$, ** $P < 0.01$, *** $P < 0.001$, **** $P < 0.0001$; NS, not significant. Scatter plots show linear correlation line bounded by 95% CI; β , slope/regression coefficient. Error bars, s.d.

[Full size image](#)

Fig. 3: B cell repertoire following vaccination with first dose of BNT162b2.

 figure3

a, Isotype usage according to unique VDJ sequence in participants <80 ($n = 22$) or ≥ 80 years old ($n = 28$) and association with neutralization of spike pseudotyped virus. Neutralization cut-off for 50% neutralization was set at 20. Mann–Whitney U -test. **b**, Heat map showing differences in V gene usage between the <80 and ≥ 80 groups. Mann–Whitney U -test with Benjamini–Hochberg false discovery rate (FDR) correction; * $P < 0.1$. **c**, Mean somatic hypermutation for participants <80 or ≥ 80 years old, grouped according to isotype class. Mann–Whitney U -test. **d**, Diversity indices for neutralizing and non-neutralizing groups. The inverse is depicted for Simpson’s index. t -test. **e**, BCR comparison of patients in the two age groups for the first 50 days after vaccination (<80, $n = 27$; ≥ 80 , $n = 5$) with public clones known to be associated

with SARS-CoV-2 using the CoV-AbDab database¹². Clones from participants and the database were co-clustered based on matching IGHV andIGHJ segments, matching CDR-H3 region length and 85% CDR-H3 sequence amino acid homology. One-sided *t*-test. For boxplots: centre line, median; box, 25th–75th percentile; whiskers, 1.5× IQR.

[Full size image](#)

We performed B cell repertoire sequencing on bulk PBMCs to assess isotype and variable gene usage, somatic hypermutation and diversity of the repertoire between the two age groups and in relation to neutralization. There were no differences in isotype proportions between the two age groups (Extended Data Fig. 5), or by neutralization (Fig. 3a). We found an increase in usage of the immunoglobulin heavy variable 4 (IGHV4) family in the older age group, with an increased proportion of IGHV4.34, IGHV4.39, IGHV4.59 and IGHV4.61, whereas in the younger age group there was an increase in usage of the IGHV1 family, with increases in IGHV1.18 and IGHV1.69D (Fig. 3b). We did not find any significant differences in V gene usage associated with neutralization (Extended Data Fig. 5).

Differences in somatic hypermutation could affect neutralization through antibody affinity maturation. We found that participants aged 80 years or more had a lower level of somatic hypermutation in class-switched B cell receptors (BCRs) than the younger group, and that the difference was driven by the IgA1/2 isotype (Fig. 3c). We also did not find any relationship between measures of diversity and neutralization potency or age group (Fig. 3d, Extended Data Fig. 5). We next examined the B cell repertoire for public clones known to be associated with SARS-CoV-2 neutralization. We explored the convergence between BCR clones in our study and the CoV-AbDab database¹² and found that participants under 80 years of age had a higher frequency of convergent clones, in keeping with increased neutralization, when compared with the older group (Fig. 3e).

T cell responses to mRNA vaccination

Although it is increasingly recognized that neutralizing antibodies dominate protection against initial infection^{4,13}, T cells might limit disease progression⁵ when neutralizing antibody titres are low¹⁴. We therefore determined the T cell response to SARS-CoV-2 spike protein in vaccinated individuals by stimulating PBMCs with overlapping peptide pools to the wild-type SARS-CoV-2 spike, using an interferon- γ (IFN γ) and interleukin-2 (IL-2) FluoroSpot assay to count spike-specific T cells. When we plotted IFN γ -spike specific T cell responses against age as a continuous variable, there was a negative correlation with a drop-off at around 80 years (Fig. 4a). A similar effect, albeit less pronounced, was seen for IL-2 (Fig. 4b). However, there did not appear to

be a relationship between cytokine production by PBMCs and neutralization titre after the first dose (Extended Data Fig. 6).

Fig. 4: T cell responses to BNT162b2 vaccine after the first and second doses.

 figure4

a, b, FluoroSpot analysis by age for IFN γ (**a**) and IL-2 (**b**) T cell responses specific to SARS-CoV-2 spike protein peptide pool following PBMC stimulation. SFU, spot-forming units. Scatter plots show linear correlation line bounded by 95% CI; β , slope/regression coefficient. **c, d**, FluoroSpot analysis for IFN γ (**c**) and IL-2 (**d**) T cell responses specific to SARS-CoV-2 spike protein peptide pool following stimulation of unexposed PBMCs (stored PBMCs from 2014–2016, $n = 20$) and PBMCs from vaccinated individuals (<80 IFN γ , $n = 46$; <80 IL-2, $n = 44$; ≥ 80 IFN γ , $n = 35$; ≥ 80 IL-2, $n = 27$) three weeks or more after the first dose of BNT162b2. **e, f**, FluoroSpot analysis for IFN γ (**e**) and IL-2 (**f**) T cell responses specific to SARS-CoV-2 spike protein peptide pool following stimulation of unexposed PBMCs ($n = 20$) and PBMCs from vaccinated individuals three weeks after the first or second dose (first dose: <80 IFN γ , $n = 46$; <80 IL-2, $n = 45$; ≥ 80 IFN γ , $n = 31$; ≥ 80 IL-2, $n = 19$; second dose: <80 IFN γ , $n = 15$; <80 IL-2, $n = 15$; ≥ 80 IFN γ , $n = 24$; ≥ 80 IL-2, $n = 24$). **g, h**, FluoroSpot analysis for IL-2 (**g**) and IFN γ (**h**) CD4 and CD8 T cell responses specific to SARS-CoV-2 spike protein peptide pool following stimulation after column-based PBMC separation. Mann–Whitney test was used for unpaired comparisons and Wilcoxon matched-pairs signed rank test for paired comparisons. * $P < 0.05$, ** $P < 0.001$, *** $P < 0.0001$; NS, not significant. Error bars, s.d.

[Full size image](#)

Following the first dose of vaccine, the frequency of IFN γ -secreting T cells against a CEF+ peptide pool that included cytomegalovirus (CMV)-, Epstein-Barr virus (EBV)- and influenza-specific peptides did not differ by age category and was similar to healthy SARS-CoV-2 unexposed controls (Extended Data Fig. 6). This indicates that differences in observed responses were likely to be vaccine-specific rather than

resulting from generalized suboptimal T cell responses or immune paresis. However, IFN γ spike-specific T cell responses were significantly larger in immunized individuals below 80 years of age than in an unexposed population of the same age (Fig. 4c). However, in participants aged 80 years or more, the IFN γ spike-specific T cell response following the first dose did not differ from that of unexposed controls (Fig. 4c). By contrast, spike-specific IL-2 T cell frequencies were significantly higher in both vaccinated groups than in unexposed controls (Fig. 4d). Notably, although spike-specific IFN γ and IL-2 responses in PBMCs after the first dose of vaccine were similar to those found after natural infection (Extended Data Fig. 6), the second dose did not appear to increase these responses, either overall (Extended Data Fig. 6) or within age categories (Fig. 4e,f). Following depletion of CD4 or CD8 T cells, the majority of IFN γ and IL-2 production was from CD4 $^{+}$ T cells in vaccinated individuals (Fig. 4g,h). Those aged 80 or more had markedly lower spike-specific IL-2 CD4 $^{+}$ T cell responses than their younger counterparts (Fig. 4g).

CMV serostatus has been associated with poorer responses to vaccination and infections^{15,16}. The rate of CMV IgG positivity was higher in the older age group (Extended Data Fig. 6); unexpectedly, though, CMV-positive individuals in this group had significantly higher IFN γ , but not IL-2, responses to SARS-CoV-2 spike peptides than CMV-negative individuals in the same age group (Extended Data Fig. 6).

Autoantibodies and inflammatory molecules

Finally, we investigated the possibility of interactions between senescence and mRNA vaccine responses. Autoantibodies and inflammatory cytokines or chemokines are associated with immune senescence¹⁷. We first measured a panel of autoantibodies in the sera of 101 participants following the first dose of the BNT162b2 vaccine. Eight participants had autoantibodies against myeloperoxidase (anti-MPO), two against fibrillarin and one against cardiolipin (Extended Data Fig. 7). As expected, all but one of the participants with anti-MPO autoantibodies were over the age of 80 years (Extended Data Fig. 7). There was a trend towards reduced anti-spike IgG levels and serum neutralization against the wild-type and B.1.17 spike proteins in participants with autoantibodies, although this did not reach statistical significance (probably owing to the small sample size; Extended Data Fig. 7). Next, we explored the association between serum cytokines or chemokines and neutralization of SARS-CoV-2 PV, as well as their association with age. PIDF, a known senescence-associated secretory phenotype (SASP) molecule, was the only molecule that was enriched in sera from participants aged over 80 years, and there was no association between any of these molecules and the ability of sera to neutralize SARS-CoV-2 PVs (Extended Data Fig. 7).

Discussion

Neutralizing antibodies are a likely correlate of protection against SARS-CoV-2 infection, as suggested by vaccine efficacy studies, preclinical studies in mice and non-human primates, and data from the early use of convalescent plasma in elderly patients^{4,5,10,13,14,18,23}. There is a lack of data on neutralizing antibody immune responses following mRNA vaccination in the elderly, and no data, to our knowledge, on variants of concern in this group. In a clinical study that specifically looked at older adults vaccinated with BNT162b2, the GMT after the first dose was 12 in a set of 12 subjects between ages of 65 and 85 years, rising to 149 seven days after the second dose¹. Furthermore, in a study of the Moderna 1273 mRNA vaccine in individuals above 55 years of age, neutralization was detectable only after the second dose, whereas binding antibodies were detectable after both doses¹⁹. In a randomized phase I study on BNT162b1 in younger (18–55 years) and older adults (65–85 years), virus neutralization was lower in the older age group 22 days after the first dose²⁰. These data reflect the finding that responses to the ChAdOx1 nCov-19 (AZD-1222) vaccine were lower in older than in younger mice, and the difference was overcome by booster dosing²¹.

Here, in a cohort of 140 individuals, we have shown not only an inverse relationship between age and neutralizing responses following the first dose of BNT162b2, but also a more precipitous decline around the age of 80 years. Individuals aged 80 or more were prioritized for vaccination in the UK and elsewhere, as they represented the group at greatest risk of severe COVID-19²². We found that around half of those above the age of 80 have a suboptimal neutralizing antibody response after the first dose of BNT162b2, accompanied by lower T cell responses compared to younger individuals. Individuals over 80 years of age differed from the younger group in four main respects that could explain poorer neutralization of SARS-CoV-2. First, serum IgG levels were lower, accompanied by a lower proportion of peripheral spike-specific IgG⁺IgM⁻CD19⁺ memory B cells. Second, the elderly displayed lower somatic hypermutation in the *BCR* gene. Third, the elderly had lower enrichment for public BCR clonotypes that are associated with neutralization. And fourth, the older group displayed a marked reduction in IL-2-producing spike-reactive CD4⁺ T cells. Therefore, possible explanations for their poorer neutralizing responses include lower concentrations of antibodies (quantity) and/or lower-affinity antibodies (quality) resulting from B cell selection, reduced CD4⁺ T cell help, or a combination of both. These data parallel those in aged mice, where ChAdOx1 nCov-19 (AZD-1222) vaccine responses were reported to be lower than in younger mice, and this was overcome by booster dosing²¹.

Critically, we show that elderly individuals are likely to be at greater risk from VOCs, as a greater proportion of individuals in the over-80 age group showed no neutralizing activity to P.1 and B.1.1.7 after the first dose. Reassuringly, we observed neutralizing responses across all age groups after the second dose, although further work is needed to understand the effect of age on the durability of immune responses following vaccination.

Methods

Study design

Community participants or healthcare workers who received their first dose of the BNT162b2 vaccine between 14 December 2020 and 10 February 2021 were consecutively recruited at Addenbrooke's Hospital into the COVID-19 cohort of the NIHR Bioresource. Participants were followed up for up to 3 weeks after receiving their second dose of the BNT162b2 vaccine. They provided blood samples 3 to 12 weeks after their first dose and again 3 weeks after the second dose of the vaccine. Consecutive participants were eligible without exclusion. The exposure of interest was age, categorized into two exposure levels (<80 and \geq 80 years). The outcome of interest was inadequate vaccine-elicited serum antibody neutralization activity at least 3 weeks after the first dose. This was measured as the dilution of serum required to inhibit infection by 50% (ID50) in an in vitro neutralization assay. An ID50 of 20 or below was deemed inadequate neutralization. Binding antibody responses to the spike, receptor-binding domain (RBD) and nucleocapsid were measured by multiplex particle-based flow cytometry and spike-specific T cell responses were measured by IFN γ and IL-2 FluoroSpot assays. Measurement of serum autoantibodies and characterization of the B cell receptor (BCR) repertoire following the first vaccine dose were exploratory outcomes.

We assumed a risk ratio of non-neutralization in the \geq 80 years group compared with the <80 years group of 5. Using an alpha of 0.05 and power of 90% required a sample size of 50 with a 1:1 ratio in each group.

Ethical approval

The study was approved by the East of England – Cambridge Central Research Ethics Committee (17/EE/0025). PBMCs from unexposed volunteers previously recruited by the NIHR BioResource Centre Cambridge through the ARIA study (2014–2016) were used with ethical approval from the Cambridge Human Biology Research Ethics Committee (HBREC.2014.07) and currently North of Scotland Research Ethics Committee 1 (NS/17/0110).

Statistical analyses

Descriptive analyses of demographic and clinical data are presented as median and IQR when continuous and as frequency and proportion (%) when categorical. Differences between continuous and categorical data were tested using Wilcoxon rank sum and Chi-square tests, respectively. Logistic regression was used to model the association between age group and neutralization by vaccine-elicited antibodies after the first dose of the BNT162b2 vaccine. The effects of sex and time interval from vaccination to sampling as confounders were adjusted for. Linear regression was also used to explore the association between age as a continuous variable and log-transformed ID50, binding antibody levels, antibody subclass levels and T cell response after dose 1 and dose 2 of the BNT162b2 vaccine. Bonferroni adjustment was made for multiple comparisons in the linear correlation analyses between binding antibody levels, ID50, age and T cell responses. The Pearson's normally distributed correlation coefficient for linear data and Spearman's non-normally distributed correlation for nonlinear data were reported. Statistical analyses were done using Stata v13, Prism v9 and R (version 3.5.1).

Generation of mutants and pseudotyped viruses

Wild-type pseudotyped virus (bearing mutation D614G), B.1.1.7 pseudotyped viruses (bearing mutations Δ69/70, Δ144, N501Y, A570D, D614G, P681H, T716I and S982A and D1118H), B.1.351 pseudotyped virus (bearing mutations L18F, D80A, D215G, Δ242-4, R246I, K417N, E484K, N501Y, D614G, A701V) and P.1 pseudotyped virus (bearing mutations L18F, T20N, P26S, D138Y, R190S, K417T, E484K, N501Y, D614G, H655Y, T1027I and V1176F) were generated. In brief, amino acid substitutions were introduced into the D614G pCDNA_SARS-CoV-2_S plasmid as previously described²³ using the QuikChange Lightening Site-Directed Mutagenesis kit, according to the manufacturer's instructions (Agilent Technologies). Sequences were verified by Sanger sequencing. The pseudoviruses were generated in a triple plasmid transfection system whereby the spike-expressing plasmid along with a lentviral packaging vector (p8.9) and luciferase expression vector (psCSFLW) were transfected into 293T cells (a gift from Greg Towers; tested for mycoplasma) with Fugene HD transfection reagent (Promega). The viruses were harvested after 48 h and stored at -80 °C. TCID50 was determined by titration of the viruses on 293T cells expressing ACE-2 and TMPRSS2²⁴.

Pseudotyped virus neutralization assays

Spike pseudotype assays have been shown to have similar characteristics as neutralization testing using fully infectious wild-type SARS-CoV-2¹¹. Virus neutralization assays were performed on 293T cells transiently transfected with ACE2

and TMPRSS2 using SARS-CoV-2 spike pseudotyped virus expressing luciferase²⁴. Pseudotyped virus was incubated with serial dilutions of heat-inactivated human serum samples or sera from vaccinated individuals in duplicate for 1 h at 37 °C. Virus and cell-only controls were also included. Then, freshly trypsinized 293T ACE2/TMPRSS2-expressing cells were added to each well. Following 48 h incubation with 5% CO₂ at 37 °C, luminescence was measured using the Steady-Glo Luciferase assay system (Promega). Neutralization was calculated relative to virus-only controls. Dilution curves were presented as a mean neutralization with s.e.m. ID50 values were calculated in GraphPad Prism. The limit of detection for 50% neutralization was set at an ID50 of 20. The ID50 within groups were summarized as a geometric mean titre (GMT) and statistical comparison between groups were made with Mann–Whitney or Wilcoxon ranked sign tests.

Live virus serum neutralization assays

A549-ACE2-TMPRSS2 cells were seeded at a cell density of 2.4×10^4 per well in a 96-well plate 24 h before inoculation. Serum was titrated starting at a final dilution of 1:50 with live B.1 virus PHE2 (EPI_ISL_407073) isolate being added at a multiplicity of infection (MOI) of 0.01. The mixture was then incubated for 1 h before being added to the cells. Seventy-two hours after infection, the plates were fixed with 8% formaldehyde and then stained with Coomassie blue for 30 min. The plates were washed and dried overnight before using a Celigo Imaging Cytometer (Nexcelom) to measure the staining intensity. Percentage cell survival was determined by comparing the intensity of the staining to an uninfected well. A nonlinear sigmoidal 4PL model (Graphpad Prism 9) was used to determine the IC₅₀ for each serum. The correlation between log-transformed ID50 obtained from the pseudotyped virus and live virus systems were explored using linear regression. Pearson's correlation coefficient was determined.

SARS-CoV-2 serology by multiplex particle-based flow cytometry (Luminex)

Recombinant SARS-CoV-2 nucleocapsid, spike and RBD were covalently coupled to distinct carboxylated bead sets (Luminex) to form a 3-plex and analysed as previously described²⁵. Specific binding was reported as mean fluorescence intensities (MFI).

CMV serology

HCMV IgG levels were determined using an IgG enzyme-linked immunosorbent assay (ELISA), HCMV Captia (Trinity Biotech) according to the manufacturer's instructions, on plasma derived from clotted blood samples.

Serum autoantibodies

Serum was screened for the presence of autoantibodies using the ProtoPlex autoimmune panel (Life Technologies) according to the manufacturer's instructions. In brief, 2.5 µl serum was incubated with Luminex MagPlex magnetic microspheres in a multiplex format conjugated to 19 full-length human autoantigens (cardiolipin, CENP B, H2a(F2A2) and H4 (F2A1), Jo-1, La/SS-B, Mi-2b, myeloperoxidase, proteinase-3, pyruvate dehydrogenase, RNP complex, Ro52/SS-A, Scl-34, Scl-70, Smith antigen, thyroglobulin, thyroid peroxidase, transglutaminase, U1-snRNP 68, and whole histone) along with bovine serum albumin (BSA). Detection was undertaken using goat-anti-human IgG-RPE in a 96-well flat-bottomed plate and the plate was read in a Luminex xMAP 200 system. Raw fluorescence intensities (FI) were further processed in R (version 3.5.1) Non-specific BSA-bound FI was subtracted from background-corrected total FI for each antigen before log₂ transformation and thresholding. Outlier values (Q3 + 1.5 × IQR) in each distribution were defined as positive.

Serum chemokine and cytokine analysis

Serum proteins were quantified using a validated electrochemiluminescent sandwich assay quantification kit (Mesoscale Discovery VPlex) according to the manufacturer's instructions. In brief, both sera and standard calibration controls were incubated with SULFO-tagged antibodies targeting IFN γ , IL-10, IL-12p70, IL-13, IL-1 β , IL-2, IL-4, IL-6, IL-8, TNF α , GC-CSF, IL-1 α , IL-12, IL-15, IL-16, IL-17A, IL-5, IL-7, TNF β , VEGF, MCP1, MCP4, eotaxin, eotaxin3, IP10, MDC, MIP1 α , MIP1 β , TARC, IL-17B, IL-17C, IL-17D, IL-1RA, IL-3, IL-9, TSLP, VEGFA, VEGFC, VEGFD, VEGFR1/FLT1, PIGF, TIE2, FGF, ICAM1, VCAM1, SAA and CRP and read using an MSD MESO S600 instrument. Concentrations were calculated by comparison with an internal standard calibration curve fitted to a four-parameter logistic model. Values below (19%) or above (0%) the reference range were imputed at the lower/upper limit of detection, respectively. Association of each cytokine level with SARS-CoV-2 neutralizing antibody titre, neutralization status (1/0) and age was undertaken using Kendall's tau and Wilcoxon tests with FDR <5% considered significant.

B cell receptor repertoire library preparation

PBMCs were lysed and RNA extracted using Qiagen AllPrep DNA/RNA mini kits and Allprep DNA/RNA Micro kits according to the manufacturer's protocol. The RNA was quantified using a Qubit. B cell receptor repertoire libraries were generated for 52 COVID-19 vaccinated individuals (58 samples) as follows: 200 ng total RNA from PAXgenes (14 µl volume) was combined with 1 µl 10 mM dNTP and 10 µM reverse primer mix (2 µl) and incubated for 5 min at 70 °C. The mixture was immediately placed on ice for 1 min and then subsequently combined with 1 µl DTT

(0.1 M), 1 µl SuperScriptIV (Thermo Fisher Scientific), 4 µl SSIV Buffer (Thermo Fisher Scientific) and 1 µl RNase inhibitor. The solution was incubated at 50 °C for 60 min followed by 15 min inactivation at 70 °C. cDNA was cleaned with AMPure XP beads and PCR-amplified with a 5' V-gene multiplex primer mix and 3' universal reverse primer using the KAPA protocol and the following thermal cycling conditions: 1 cycle (95 °C, 5 min); 5 cycles (98 °C, 20 s; 72 °C, 30 s); 5 cycles (98 °C, 15 s; 65 °C, 30 s; 72 °C, 30 s); 19 cycles (98 °C, 15 s; 60 °C, 30 s; 72 °C, 30 s); 1 step (72 °C, 5 min). Sequencing libraries were prepared using Illumina protocols and sequenced using 300-bp paired-end sequencing on a MiSeq machine.

Sequence analysis

Raw reads were filtered for base quality using a median Phred score of ≥ 32 (<http://sourceforge.net/projects/quasr/>). Forward and reverse reads were merged where a minimum 20-bp identical overlapping region was present. Sequences were retained where more than 80% base sequence similarity was present between all sequences with the same barcode. The constant-region allele with highest sequence similarity was identified by 10-mer matching to the reference constant-region genes from the IMGT database. Sequences without complete reading frames and non-immunoglobulin sequences were removed and only reads with significant similarity to reference IGHV and J genes from the IMGT database using BLAST were retained. Immunoglobulin gene use and sequence annotation were performed in IMGT V-QUEST, and repertoire differences were analysed by custom scripts in Python.

Public BCR analysis

Convergent clones were annotated with the same IGHV andIGHJ segments, had the same CDR-H3 region length and were clustered based on 85% CDR-H3 sequence amino acid homology. A cluster was considered convergent with the CoV-AbDab database if it contained sequences from post-vaccinated individuals and from the database.

Flow cytometry

The following antibodies or staining reagents were purchased from BioLegend: CD19 (SJ25C, 363028), CD3 (OKT3, 317328), CD11C (3.9, 301608), CD25 (M-A251, 356126), CD14 (M5E2,301836), and IgM (IgG1-k, 314524). CCR7 (150503, 561143) and IgG (G18-145, 561297) were obtained from BD Bioscience, CD45RA (T6D11, 130-113-359) from Miltenyi Biotech, and CD8A (SK1, 48-0087-42) from eBiosciences. The LIVE/DEAD Fixable Aqua Dead Cell Stain Kit was obtained from Invitrogen. Biotinylated spike protein expressed and purified as previously described²⁶ was conjugated to streptavidin R-phycoerythrin (PJRS25-1) or streptavidin APC

obtained from Agilent Technologies. PBMCs were isolated from study participants and stored in liquid nitrogen. Aliquots containing 10^7 cells were thawed and stained in PBS containing 2 mM EDTA at 4 °C with the above antibody panel and then transferred to 0.04% BSA in PBS. Events were acquired on a FACSaria Fusion (BD Biosciences). Analyses were carried out in FlowJo version 10.7.1.

IFN γ and IL-2 FluoroSpot T cell assays

PBMCs were isolated from the heparinized blood samples using Histopaque-1077 (Sigma-Aldrich) and SepMate-50 tubes (StemCell Technologies). Frozen PBMCs were rapidly thawed and diluted into 10 ml TexMACS medium (Miltenyi Biotech), centrifuged and resuspended in 10 ml fresh medium with 10 U/ml DNase (Benzonase, Merck-Millipore via Sigma-Aldrich). PBMCs were then incubated at 37 °C for 1 h, followed by centrifugation and resuspension in fresh medium supplemented with 5% human AB serum (Sigma Aldrich) before being counted. PBMCs were stained with 2 μ l LIVE/DEAD Fixable Far Red Dead Cell Stain Kit (Thermo Fisher Scientific) and live PBMCs were enumerated on the BD Accuri C6 flow cytometer.

Overlapping spike SARS-CoV-2 peptide stimulation

A peptide pool was generated using the following: 1. PepTivator SARS-CoV-2 Prot_S containing the sequence domains (amino acids) 304–338, 421–475, 492–519, 683–707, 741–770, 785–802, and 885–1,273 and the N-terminal S1 domain of the surface glycoprotein (S) of SARS-CoV-2 (GenBank MN908947.3, Protein QHD43416.1). 2. The PepTivator SARS-CoV-2 Prot_S1 containing amino acids 1–692. The peptides used are 15 amino acids with 11-amino acid overlaps.

We incubated 1.0 to 2.5×10^5 PBMCs from vaccinated individuals in pre-coated FluoroSpot^{FLEX} plates (anti-IFN γ and anti-IL-2 capture antibodies, Mabtech) in duplicate with the spike peptide pool mix as described above (specific for Wuhan-1, QHD43416.1 spike SARS-CoV-2 protein; Miltenyi Biotech) or a mixture of peptides specific for cytomegalovirus, Epstein–Barr virus and influenza virus (CEF+, Miltenyi Biotech) (final peptide concentration as recommended by the manufacturer: 1 μ g/ml peptide) in addition to an unstimulated (medium only) and positive control mix (containing anti-CD3 (Mabtech AB) and *Staphylococcus* Enterotoxin B (SEB, Sigma Aldrich)) at 37 °C in a humidified CO₂ atmosphere for 42 h. The cells and medium were then decanted from the plate and the assay developed according to the manufacturer's instructions. Developed plates were read using an AID iSpot reader (Oxford Biosystems) and counted using AID EliSpot v7 software (Autoimmun Diagnostika). Peptide-specific frequencies were calculated by subtracting for background cytokine-specific spots (unstimulated control) and expressed as SFU per 10^6 PBMCs. With the same peptide pool, we also stimulated PBMC that had been

collected and biobanked between 2014 and 2016, representing a healthy population that had not been exposed to SARS-CoV-2, and PBMCs from donors who had been infected with SARS-CoV-2 (confirmed by RT-PCR) for comparison of T cell responses following natural infection.

CD4 and CD8 depletion from PBMCs for subsequent FluoroSpot analysis

Peripheral blood mononuclear cells were depleted of either CD4⁺ or CD8⁺ T cells by magnetic-activated cell sorting (MACS) using anti-CD4 or anti-CD8 direct beads (Miltenyi Biotec), according to the manufacturer's instructions, and separated using an AutoMACS Pro (Miltenyi Biotec). The efficiency of depletion was determined by staining cells with a mix of CD3-FITC, CD4-PE, and CD8-PerCP Cy5.5 antibodies (all BioLegend) and analysing by flow cytometry.

Reporting summary

Further information on research design is available in the [Nature Research Reporting Summary](#) linked to this paper.

Data availability

Sequence data have been deposited at the European Genome-Phenome Archive (<https://ega-archive.org/>) which is hosted by the EBI and the CRG under accession number EGAS00001005380. Data are available without restriction.

References

1. 1.

Walsh, E. E. et al. Safety and immunogenicity of two RNA-based Covid-19 vaccine candidates. *N. Engl. J. Med.* **383**, 2439–2450 (2020).

[CAS Article](#) [Google Scholar](#)

2. 2.

Polack, F. P. et al. Safety and efficacy of the BNT162b2 mRNA Covid-19 vaccine. *N. Engl. J. Med.* **383**, 2603–2615 (2020).

[CAS Article](#) [Google Scholar](#)

3. 3.

Baden, L. R. et al. Efficacy and safety of the mRNA-1273 SARS-CoV-2 vaccine. *N. Engl. J. Med.* **384**, 403–416 (2021).

[CAS](#) [Article](#) [Google Scholar](#)

4. 4.

Khoury, D. S. et al. Neutralizing antibody levels are highly predictive of immune protection from symptomatic SARS-CoV-2 infection. *Nat. Med.* <https://doi.org/10.1038/s41591-021-01377-8> (2021).

[Article](#) [PubMed](#) [Google Scholar](#)

5. 5.

Israelow, B. et al. Adaptive immune determinants of viral clearance and protection in mouse models of SARS-CoV-2. Preprint at <https://doi.org/10.1101/2021.05.19.444825> (2021).

6. 6.

Feng, S. et al. Correlates of protection against symptomatic and asymptomatic SARS-CoV-2 infection. Preprint at <https://doi.org/10.1101/2021.06.21.21258528> (2021).

7. 7.

Department of Health. *Briefing on Rescheduling of Second Doses of the Pfizer/BioNTech Covid-19 Vaccine* <https://www.health-ni.gov.uk/news/briefing-rescheduling-second-doses-pfizerbiotech-covid-19-vaccine> (2021).

8. 8.

Volz, E. et al. Assessing transmissibility of SARS-CoV-2 lineage B.1.1.7 in England. *Nature* **593**, 266–269 (2021).

[CAS](#) [Article](#) [ADS](#) [Google Scholar](#)

9. 9.

Collier, D. A. et al. Sensitivity of SARS-CoV-2 B.1.1.7 to mRNA vaccine-elicited antibodies. *Nature* **593**, 136–141 (2021).

[CAS](#) [Article](#) [ADS](#) [Google Scholar](#)

10. 10.

Madhi, S. A. et al. Efficacy of the ChAdOx1 nCoV-19 Covid-19 vaccine against the B.1.351 variant. *N. Engl. J. Med.* **384**, 1885–1898 (2021).

[CAS](#) [Article](#) [Google Scholar](#)

11. 11.

Schmidt, F. et al. Measuring SARS-CoV-2 neutralizing antibody activity using pseudotyped and chimeric viruses. *J. Exp. Med.* **217**, e20201181 (2020).

[Article](#) [Google Scholar](#)

12. 12.

Raybould, M. I. J., Kovaltsuk, A., Marks, C. & Deane, C. M. CoV-AbDab: the coronavirus antibody database. *Bioinformatics* **37**, 734–735 (2021).

[Article](#) [Google Scholar](#)

13. 13.

Mercado, N. B. et al. Single-shot Ad26 vaccine protects against SARS-CoV-2 in rhesus macaques. *Nature* **586**, 583–588 (2020).

[CAS](#) [Article](#) [ADS](#) [Google Scholar](#)

14. 14.

McMahan, K. et al. Correlates of protection against SARS-CoV-2 in rhesus macaques. *Nature* **590**, 630–634 (2021).

[CAS](#) [Article](#) [ADS](#) [Google Scholar](#)

15. 15.

Merani, S., Pawelec, G., Kuchel, G. A. & McElhaney, J. E. Impact of aging and cytomegalovirus on immunological response to influenza vaccination and infection. *Front. Immunol.* **8**, 784 (2017).

[Article](#) [Google Scholar](#)

16. 16.

Kadambari, S., Klennerman, P. & Pollard, A. J. Why the elderly appear to be more severely affected by COVID-19: the potential role of immunosenescence and CMV. *Rev. Med. Virol.* **30**, e2144 (2020).

[CAS Article](#) [Google Scholar](#)

17. 17.

Ray, D. & Yung, R. Immune senescence, epigenetics and autoimmunity. *Clin. Immunol.* **196**, 59–63 (2018).

[CAS Article](#) [Google Scholar](#)

18. 18.

Libster, R. et al. Early high-titer plasma therapy to prevent severe Covid-19 in older adults. *N. Engl. J. Med.* **384**, 610–618 (2021).

[CAS Article](#) [Google Scholar](#)

19. 19.

Anderson, E. J. et al. Safety and immunogenicity of SARS-CoV-2 mRNA-1273 vaccine in older adults. *N. Engl. J. Med.* **383**, 2427–2438 (2020).

[CAS Article](#) [Google Scholar](#)

20. 20.

Li, J. et al. Safety and immunogenicity of the SARS-CoV-2 BNT162b1 mRNA vaccine in younger and older Chinese adults: a randomized, placebo-controlled, double-blind phase 1 study. *Nat. Med.* **27**, 1062–1070 (2021).

[CAS Article](#) [Google Scholar](#)

21. 21.

Silva-Cayetano, A. et al. A booster dose enhances immunogenicity of the COVID-19 vaccine candidate ChAdOx1 nCoV-19 in aged mice. *Med* **2**, 243–262 (2020).

[Article](#) [Google Scholar](#)

22. 22.

Docherty, A. B. et al. Features of 20 133 UK patients in hospital with COVID-19 using the ISARIC WHO Clinical Characterisation Protocol: prospective observational cohort study. *Br. Med. J.* **369**, m1985 (2020)

[Article](#) [Google Scholar](#)

23. 23.

Kemp, S. A. et al. SARS-CoV-2 evolution during treatment of chronic infection. *Nature* **592**, 277–282 (2021).

[CAS](#) [Article](#) [Google Scholar](#)

24. 24.

Mlcochova, P. et al. Combined point of care nucleic acid and antibody testing for SARS-CoV-2 following emergence of D614G spike variant. *Cell Rep Med* **1**, 100099 (2020).

[Article](#) [Google Scholar](#)

25. 25.

Xiong, X. et al. A thermostable, closed SARS-CoV-2 spike protein trimer. *Nat. Struct. Mol. Biol.* **27**, 934–941 (2020).

[CAS](#) [Article](#) [Google Scholar](#)

26. 26.

Graham, C. et al. Neutralization potency of monoclonal antibodies recognizing dominant and subdominant epitopes on SARS-CoV-2 Spike is impacted by the B.1.1.7 variant. *Immunity* **54**, 1276–1289.e6 (2021).

[CAS](#) [Article](#) [Google Scholar](#)

[Download references](#)

Acknowledgements

We thank the Cambridge University Hospitals NHS Trust Occupational Health Department; the NIHR Cambridge Clinical Research Facility and staff at CUH; the

Cambridge NIHR BRC Stratified Medicine Core Laboratory NGS Hub; the NIHR Cambridge BRC Phenotyping Hub; P. Mlcochova, S. A. Kemp, M. Potts, B. Krishna, M. Perera and G. Okecha; and J. Nathan, L. James and J. Briggs. R.K.G. is supported by a Wellcome Trust Senior Fellowship in Clinical Science (WT108082AIA). D.A.C. is supported by a Wellcome Trust Clinical PhD Research Fellowship. K.G.C.S. is the recipient of a Wellcome Investigator Award (200871/Z/16/Z). M.A.L. is supported by the Biotechnology and Biological Sciences Research Council (BBS/E/B/000C0427, BBS/E/B/000C0428). This research was supported by the National Institute for Health Research (NIHR) Cambridge Biomedical Research Centre, the Cambridge Clinical Trials Unit (CCTU), the NIHR BioResource and Addenbrooke's Charitable Trust, the Evelyn Trust (20/75), and the UKRI COVID Immunology Consortium. G.B.-M. and P.C.-A. were supported by UNAM-FESC-PIAPI Program Code PIAPI2009 and by a CONACyT 829997 Fellowship. The views expressed are those of the authors and not necessarily those of the NIHR or the Department of Health and Social Care. I.A.T.M.F. is funded by a Sub-Saharan African Network for TB/HIV Research Excellence (SANTHE, a DELTAS Africa Initiative (grant DEL-15-006)) Fellowship. We thank D. Corti for the VOC plasmids. P.K. is the recipient of a Jacquot Research Entry Scholarship from the Royal Australasian College of Physicians Foundation.

Author information

Author notes

1. These authors contributed equally: Dami A. Collier, Isabella A. T. M. Ferreira, Prasanti Kotagiri, Rawlings Datir, Eleanor Lim

Affiliations

1. Cambridge Institute of Therapeutic Immunology and Infectious Disease (CITIID), Cambridge, UK

Dami A. Collier, Isabella A. T. M. Ferreira, Prasanti Kotagiri, Rawlings P. Datir, Bo Meng, Adam Abdullahi, Laura Bergamaschi, Kenneth G. C. Smith, Paul A. Lyons, Eoin McKinney, Mark Wills & Ravindra K. Gupta

2. Department of Medicine, University of Cambridge, Cambridge, UK

Dami A. Collier, Isabella A. T. M. Ferreira, Prasanti Kotagiri, Rawlings P. Datir, Eleanor Y. Lim, Bo Meng, Stephen Baker, Gordon Dougan, Christoph Hess, Paul J. Lehner, Paul A. Lyons, Nicholas J. Matheson, James E. D. Thaventhiran, Michael P. Weekes, Ben Bullman, Kelvin Hunter, Federica Mescia, Nicole Pond, Laura Bergamaschi, Ariana Betancourt, Georgie

Bower, Chiara Cossetti, Madeline Epping, Andrew Hinch, Veronika Romashova, Lori Turner, Kenneth G. C. Smith, John R. Bradley, Paul A. Lyons, Eoin McKinney, Mark Wills & Ravindra K. Gupta

3. Division of Infection and Immunity, University College London, London, UK

Dami A. Collier, Rawlings P. Datir, Emma Touizer, Stephen Baker, Gordon Dougan, Christoph Hess, Paul J. Lehner, Paul A. Lyons, Nicholas J. Matheson, Charlotte Summers, James E. D. Thaventhiran, Mark Toshner, Benjamin J. Dunmore, Stefan Gräf, Josh Hodgson, Christopher Huang, Kelvin Hunter, Ekaterina Legchenko, Cecilia Matara, Jennifer Martin, Federica Mescia, Ciara O'Donnell, Linda Pointon, Nicole Pond, Joy Shih, Rachel Sutcliffe, Tobias Tilly, Carmen Treacy, Zhen Tong, Jennifer Wood, Laura Bergamaschi, Ariana Betancourt, Georgie Bower, Chiara Cossetti, Aloka De Sa, Madeline Epping, Andrew Hinch, Sarah Jackson, Isobel Jarvis, Ben Krishna, Daniel Lewis, Joe Marsden, Francesca Nice, Georgina Okecha, Ommar Omarjee, Marianne Perera, Martin Potts, Nathan Richoz, Veronika Romashova, Natalia Savinykh Yarkoni, Rahul Sharma, Lori Turner, Eckart M. D. D. De Bie, Katherine Bunclark, Masa Josipovic, Michael Mackay, Mayurun Selvan & Laura E. McCoy

4. NIHR Bioresource, Cambridge, UK

John Allison, Helen Butcher, Kathleen E. Stirrups, Paul Townsend, Neil Walker, Anne Elmer, Nathalie Kingston, Barbara Graves, Emma Le Gresley, Daniela Caputo & John R. Bradley

5. Department of Public Health and Primary Care, School of Clinical Medicine, University of Cambridge, Cambridge Biomedical Campus, Cambridge, UK

Daniela Caputo, Debbie Clapham-Riley, Eleanor Dewhurst, Anita Furlong, Barbara Graves, Jennifer Gray, Tasmin Ivers, Mary Kasanicki, Emma Le Gresley, Rachel Linger, Sarah Meloy, Francesca Muldoon, Nigel Ovington, Sofia Papadia, Isabel Phelan, Hannah Stark, Jennifer Webster, Anne Elmer, Nathalie Kingston, Emma Le Gresley, Daniela Caputo & Rainer Doffinger

6. Department of Clinical Biochemistry and Immunology, Addenbrookes Hospital, Cambridge, UK

Lourdes Ceron-Gutierrez

7. Laboratorio de Inmunología, FES-Cuautitlán, UNAM, Mexico City, Mexico

Paulina Cortes-Acevedo & Gabriela Barcenas-Morales

8. Immunology Programme, Babraham Institute, Cambridge, UK

Michelle A. Linterman

9. MRC Centre for Virus Research, University of Glasgow, Glasgow, UK

Chris Davis & Emma Thomson

10. Cambridge Clinical Research Centre, NIHR Clinical Research Facility,
Cambridge University Hospitals NHS Foundation Trust, Addenbrooke's Hospital,
Cambridge, UK

Caroline Saunders, Ashlea Bucke, Jo Calder, Laura Canna, Jason Domingo, Anne Elmer, Stewart Fuller, Sarah Hewitt, Jane Kennet, Sherly Jose, Jenny Kourampa, Anne Meadows, Criona O'Brien, Jane Price, Cherry Publico, Rebecca Rastall, Carla Ribeiro, Jane Rowlands, Valentina Ruffolo & Hugo Tordesillas

11. University of Cambridge, Cambridge Biomedical Campus, Cambridge, UK

Nathalie Kingston, Willem H. Owehand, Patrick Maxwell, Stefan Gräf, Stuart Fawke, Nick Gleadall, Luca Stefanucci, Jonathan Stephens, John Allison, Helen Butcher, Daniela Caputo, Debbie Clapham-Riley, Eleanor Dewhurst, Anita Furlong, Barbara Graves, Jennifer Gray, Tasmin Ivers, Emma Le Gresley, Rachel Linger, Sarah Meloy, Francesca Muldoon, Nigel Ovington, Sofia Papadia, Isabel Phelan, Hannah Stark & Jennifer Webster

12. Australian National Phenome Centre, Murdoch University, Murdoch, Western Australia, Australia

Sze-How Bong

13. MRC Toxicology Unit, School of Biological Sciences, University of Cambridge, Cambridge, UK

James E. D. Thaventhiran

14. R&D Department, Hycult Biotech, Uden, The Netherlands

Sarah Spencer

15. Heart and Lung Research Institute, Cambridge Biomedical Campus, Cambridge, UK

Charlotte Summers & Mark Toshner

16. Royal Papworth Hospital NHS Foundation Trust, Cambridge Biomedical Campus, Cambridge, UK

Charlotte Summers, Mark Toshner, Alice Michael, Ali Ansaripour, Alice Michael, Lucy Mwaura, Caroline Patterson & Gary Polwarth

17. Department of Biomedicine, University and University Hospital Basel, Basel, Switzerland

Christoph Hess

18. Botnar Research Centre for Child Health (BRCCH), University Basel & ETH Zurich, Basel, Switzerland

Christoph Hess

19. Addenbrooke's Hospital, Cambridge, UK

Charlotte Summers, Patrick Maxwell, Ashley Shaw, Petra Polgarova & Giovanni di Stefano

20. Department of Veterinary Medicine, Cambridge, UK

Emma Jones

21. Cambridge Institute for Medical Research, Cambridge Biomedical Campus, Cambridge, UK

Stuart Fawke

22. Cancer Research UK, Cambridge Institute, University of Cambridge, Cambridge, UK

Julie Harris, Richard Grenfell & Mateusz Strezlecki

23. Department of Obstetrics & Gynaecology, The Rosie Maternity Hospital, Cambridge, UK

Oisin Huhn

24. Centre for Molecular Medicine and Innovative Therapeutics, Health Futures Institute, Murdoch University, Perth, Western Australia, Australia

Jerome D. Coudert

25. Cambridge and Peterborough Foundation Trust, Fulbourn Hospital, Cambridge, UK

Codie Fahey & Rachel Michel

26. Department of Surgery, Addenbrooke's Hospital, Cambridge, UK

Sabrina Rossi & Cissy Yong

27. Department of Biochemistry, University of Cambridge, Cambridge, UK

Marta Wylot

28. Centre of Computational and Systems Medicine, Health Futures Institute, Murdoch University, Perth, Western Australia, Australia

Elaine Holmes

Authors

1. Dami A. Collier

[View author publications](#)

You can also search for this author in [PubMed](#) [Google Scholar](#)

2. Isabella A. T. M. Ferreira

[View author publications](#)

You can also search for this author in [PubMed](#) [Google Scholar](#)

3. Prasanti Kotagiri

[View author publications](#)

You can also search for this author in [PubMed](#) [Google Scholar](#)

4. Rawlings P. Datin

[View author publications](#)

You can also search for this author in [PubMed](#) [Google Scholar](#)

5. Eleanor Y. Lim

[View author publications](#)

You can also search for this author in [PubMed](#) [Google Scholar](#)

6. Emma Touizer

[View author publications](#)

You can also search for this author in [PubMed](#) [Google Scholar](#)

7. Bo Meng

[View author publications](#)

You can also search for this author in [PubMed](#) [Google Scholar](#)

8. Adam Abdullahi

[View author publications](#)

You can also search for this author in [PubMed](#) [Google Scholar](#)

9. Anne Elmer

[View author publications](#)

You can also search for this author in [PubMed](#) [Google Scholar](#)

10. Nathalie Kingston

[View author publications](#)

You can also search for this author in [PubMed](#) [Google Scholar](#)

11. Barbara Graves

[View author publications](#)

You can also search for this author in [PubMed](#) [Google Scholar](#)

12. Emma Le Gresley

[View author publications](#)

You can also search for this author in [PubMed](#) [Google Scholar](#)

13. Daniela Caputo

[View author publications](#)

You can also search for this author in [PubMed](#) [Google Scholar](#)

14. Laura Bergamaschi

[View author publications](#)

You can also search for this author in [PubMed](#) [Google Scholar](#)

15. Kenneth G. C. Smith

[View author publications](#)

You can also search for this author in [PubMed](#) [Google Scholar](#)

16. John R. Bradley

[View author publications](#)

You can also search for this author in [PubMed](#) [Google Scholar](#)

17. Lourdes Ceron-Gutierrez

[View author publications](#)

You can also search for this author in [PubMed](#) [Google Scholar](#)

18. Paulina Cortes-Acevedo

[View author publications](#)

You can also search for this author in [PubMed](#) [Google Scholar](#)

19. Gabriela Barcenas-Morales

[View author publications](#)

You can also search for this author in [PubMed](#) [Google Scholar](#)

20. Michelle A. Linterman

[View author publications](#)

You can also search for this author in [PubMed](#) [Google Scholar](#)

21. Laura E. McCoy

[View author publications](#)

You can also search for this author in [PubMed](#) [Google Scholar](#)

22. Chris Davis

[View author publications](#)

You can also search for this author in [PubMed](#) [Google Scholar](#)

23. Emma Thomson

[View author publications](#)

You can also search for this author in [PubMed](#) [Google Scholar](#)

24. Paul A. Lyons

[View author publications](#)

You can also search for this author in [PubMed](#) [Google Scholar](#)

25. Eoin McKinney

[View author publications](#)

You can also search for this author in [PubMed](#) [Google Scholar](#)

26. Rainer Doffinger

[View author publications](#)

You can also search for this author in [PubMed](#) [Google Scholar](#)

27. Mark Wills

[View author publications](#)

You can also search for this author in [PubMed](#) [Google Scholar](#)

28. Ravindra K. Gupta

[View author publications](#)

You can also search for this author in [PubMed](#) [Google Scholar](#)

Consortia

The Citiid-Nihr BioResource COVID-19 Collaboration

- Principal Investigators

- Stephen Baker
- , Gordon Dougan
- , Christoph Hess
- , Nathalie Kingston
- , Paul J. Lehner
- , Paul A. Lyons
- , Nicholas J. Matheson
- , Willem H. Owehand
- , Caroline Saunders
- , Charlotte Summers
- , James E. D. Thaventhiran
- , Mark Toshner

- , Michael P. Weekes
- , Patrick Maxwell
- & Ashley Shaw

- **CRF and Volunteer Research Nurses**

- Ashlea Bucke
- , Jo Calder
- , Laura Canna
- , Jason Domingo
- , Anne Elmer
- , Stewart Fuller
- , Julie Harris
- , Sarah Hewitt
- , Jane Kennet
- , Sherly Jose
- , Jenny Kourampa
- , Anne Meadows
- , Criona O'Brien
- , Jane Price
- , Cherry Publico
- , Rebecca Rastall
- , Carla Ribeiro
- , Jane Rowlands
- , Valentina Ruffolo
- & Hugo Tordesillas

- **Sample Logistics**

- Ben Bullman
- , Benjamin J. Dunmore
- , Stuart Fawke
- , Stefan Gräf
- , Josh Hodgson
- , Christopher Huang
- , Kelvin Hunter
- , Emma Jones
- , Ekaterina Legchenko
- , Cecilia Matara
- , Jennifer Martin
- , Federica Mescia
- , Ciara O'Donnell

- , Linda Pointon
- , Nicole Pond
- , Joy Shih
- , Rachel Sutcliffe
- , Tobias Tilly
- , Carmen Treacy
- , Zhen Tong
- , Jennifer Wood
- & Marta Wylot

- **Sample Processing and Data Acquisition**

- Laura Bergamaschi
- , Ariana Betancourt
- , Georgie Bower
- , Chiara Cossetti
- , Aloka De Sa
- , Madeline Epping
- , Stuart Fawke
- , Nick Gleadall
- , Richard Grenfell
- , Andrew Hinch
- , Oisin Huhn
- , Sarah Jackson
- , Isobel Jarvis
- , Ben Krishna
- , Daniel Lewis
- , Joe Marsden
- , Francesca Nice
- , Georgina Okecha
- , Ommar Omarjee
- , Marianne Perera
- , Martin Potts
- , Nathan Richoz
- , Veronika Romashova
- , Natalia Savinykh Yarkoni
- , Rahul Sharma
- , Luca Stefanucci
- , Jonathan Stephens
- , Mateusz Strezlecki
- & Lori Turner

- **Clinical Data Collection**
 - Eckart M. D. D. De Bie
 - , Katherine Bunclark
 - , Masa Josipovic
 - , Michael Mackay
 - , Federica Mescia
 - , Alice Michael
 - , Sabrina Rossi
 - , Mayurun Selvan
 - , Sarah Spencer
 - & Cissy Yong
- **Royal Papworth Hospital ICU**
 - Ali Ansaripour
 - , Alice Michael
 - , Lucy Mwaura
 - , Caroline Patterson
 - & Gary Polwarth
- **Addenbrooke's Hospital ICU**
 - Petra Polgarova
 - & Giovanni di Stefano
- **Cambridge and Peterborough Foundation Trust**
 - Codie Fahey
 - & Rachel Michel
- **ANPC and Centre for Molecular Medicine and Innovative Therapeutics**
 - Sze-How Bong
 - , Jerome D. Coudert
 - & Elaine Holmes
- **NIHR BioResource4**
 - John Allison
 - , Helen Butcher

- , Daniela Caputo
- , Debbie Clapham-Riley
- , Eleanor Dewhurst
- , Anita Furlong
- , Barbara Graves
- , Jennifer Gray
- , Tasmin Ivers
- , Mary Kasanicki
- , Emma Le Gresley
- , Rachel Linger
- , Sarah Meloy
- , Francesca Muldoon
- , Nigel Ovington
- , Sofia Papadia
- , Isabel Phelan
- , Hannah Stark
- , Kathleen E. Stirrups
- , Paul Townsend
- , Neil Walker
- & Jennifer Webster

Contributions

Conceived study: R.K.G., D.A.C., I.A.T.M.F., E.M., R.D., M.W. Designed study and experiments: R.K.G., I.A.T.M.F., P.K., D.A.C., L.E.M., J.R.B., E. Thomson, M.W., D.C., E.L.G., M.A.L., L.C.-G., G.B.-M., R.P.D., A.E. Performed experiments: B.M., E.Y.L., L.B., A.A., P.C.-A., G.B.-M., P.A.L., C.D., D.A.C., E. Touizer, R.P.D., P.K., I.A.T.M.F., N.K., B.G., L.C.-G.. Interpreted data: R.K.G., D.A.C., B.M., R.P.D., E.M., R.D., I.A.T.M.F., M.W., E.Y.L., L.E.M., J.R.B., K.G.C.S.

Corresponding authors

Correspondence to [Eoin McKinney](#) or [Rainer Doffinger](#) or [Mark Wills](#) or [Ravindra K. Gupta](#).

Ethics declarations

Competing interests

The authors declare no competing interests.

Additional information

Peer review information *Nature* thanks Thushan de Silva, Julie Ledgerwood and the other, anonymous, reviewer(s) for their contribution to the peer review of this work. Peer reviewer reports are available.

Publisher's note Springer Nature remains neutral with regard to jurisdictional claims in published maps and institutional affiliations.

Extended data figures and tables

[Extended Data Fig. 1 Study flow diagram for samples and analyses.](#)

n values are shown for each analysis.

[Extended Data Fig. 2 SARS-CoV-2 neutralization by serum from individuals vaccinated with Pfizer BNT162b2 vaccine.](#)

a, Linear correlation of live virus neutralization with SARS-CoV-2 spike PV neutralization for 13 sera from individuals vaccinated with BNT162b2. Linear regression line plotted bounded by 95% CI. **b**, SARS-CoV-2 PV neutralization by sera from individuals vaccinated with first dose of BNT162b2 (*n* = 140) plotted against time since first dose. **c**, Correlation of SARS-CoV-2 neutralization by sera from individuals vaccinated with BNT162b2 with age. Serum neutralization of spike (D614G) pseudotyped lentiviral particles (ID50) after dose 1 (top, *n* = 138) or dose 2 (bottom, *n* = 64) by age. Linear regression line plotted bounded by 95% CI. Bonferroni adjustment was made for multiple comparisons in linear regression. **d**, ID50 against wild-type (D614G) PV following the second dose of vaccine stratified by age and interval between vaccine doses (3 weeks (*n* = 21) and 12 weeks (*n* = 43)). GMT ± s.d., Mann–Whitney test. **e**, Spike mutations in VOCs, along with number of sequences in GISAID database.

[Extended Data Fig. 3 Binding IgG and IgA spike antibody responses following BNT162b2 vaccination.](#)

a, Correlations between serum binding IgG subclass 1–4 antibody responses following vaccination with first dose of BNT162b2 and age in years (*n* = 133). **b**, Correlations between serum binding IgG subclass 1–4 antibody responses following vaccination with first dose of BNT162b2 and serum neutralization using a PV system (*n* = 133). **c**, IgA responses to spike, nucleocapsid and RBD after first dose (light green, *n* = 133) and second dose (dark green, *n* = 21) compared to individuals with prior infection (red,

$n = 18$) and negative controls (grey, $n = 18$) at serum dilution of 1 in 100. **d**, Correlations between serum binding IgA spike antibody responses following vaccination with first dose of BNT162b2 and serum neutralization using a PV system ($n = 133$). Bonferroni adjustment was made for multiple comparisons. Spike proteins tested are Wuhan-1 with D614G (WT). Linear regression lines plotted bounded by 95% CI.

[Extended Data Fig. 4 Peripheral blood lymphocyte subsets following first dose of BNT162b2.](#)

PBMCs were sorted by FACS ($n = 16$ above 80 years of age, $n = 16$ below 80 years of age). **a**, Gating strategy for flow cytometry analysis of human immune cells after vaccination. **b**, Data for indicated sorted cell subsets stratified by neutralizing response after first dose ($n = 8$ in each category). NK cells, natural killer cells; Treg cells, regulatory T cells. Error bars, s.d.

[Extended Data Fig. 5 B cell repertoire following vaccination with first dose of BNT162b2.](#)

a, Isotype usage according to unique VDJ sequence in <80-year-old ($n = 22$) and ≥ 80 -year-old groups ($n = 28$). Differences between groups were calculated using Mann–Whitney *U*-test. **b**, V gene usage as a proportion, by neutralization of spike PV. Neutralization cut-off for 50% neutralization was set at 20. Differences between groups were calculated using Mann–Whitney *U*-test. **c**, Diversity indices comparing the two age groups. The inverse is depicted for Simpson’s index and the Shannon–Weiner index is normalized. Differences between groups were calculated using a *t*-test. For boxplots: centre line, median; box, 25th–75th percentile; whiskers, $1.5 \times$ IQR.

[Extended Data Fig. 6 T cell responses following vaccination with BNT162b2.](#)

Correlation between T cell responses against SARS-CoV-2 spike peptide pool and serum neutralization of spike (D614G) pseudotyped lentiviral particles (ID50). **a, b**, Correlation of IFN γ (**a**, $n = 79$) and IL-2 (**b**, $n = 69$) FluoroSpot and ID50 after first dose. Linear regression lines with 95% CI are plotted. Bonferroni adjustment was made for multiple comparisons. **c**, FluoroSpot IFN γ PBMC responses to peptide pool of CEF peptide pool. Responses from unexposed PBMCs (stored from 2014–2016, $n = 20$), <80 years group ($n = 46$) and ≥ 80 years group ($n = 35$) three weeks after the first dose of vaccine. **d, e**, FluoroSpot analysis for IFN γ (**d**) and IL-2 T cell responses (**e**) specific to SARS-CoV-2 spike protein peptide pool following stimulation of PBMCs from infected donors ($n = 46$), unexposed donors ($n = 20$) and vaccinated

individuals three weeks or more after the first dose (IFN γ , $n = 77$; IL-2, $n = 64$) and three weeks after the second dose (IFN γ and IL-2, $n = 39$). **f–i**, Human cytomegalovirus serostatus, T cell responses and serum neutralization of spike (D614G) pseudotyped lentiviral particles (ID50) after the first dose of vaccine. **f**, HCMV serostatus for <80- and \geq 80-year age groups ($n = 72$). **g, h**, IFN γ (**g**, $n = 72$) and IL-2 (**h**, $n = 64$) FluoroSpot responses after the first dose. **i**, ID50 after the first dose by CMV serostatus. Error bars, s.d.

Extended Data Fig. 7 Autoantibodies and inflammatory markers in participants who received at least one dose of the BNT162b2 vaccine and relationship to SARS-CoV-2 spike-specific IgG and SARS-CoV-2 PV neutralization.

$n = 101$. **a**, Heatmap of log₂-transformed fluorescence intensity of 19 autoantibodies; red, positive; blue, negative. **b**, Age (mean \pm s.d.) in years by anti-MPO antibody-positive (red) or -negative (blue) status. **c**, IgG subclass responses to spike after first dose of BNT162b2 vaccine in individuals with or without anti-MPO antibodies ($n = 100$). **d**, GMT \pm s.d of sera from individuals after their first dose of vaccine against wild-type and B.1.1.7 spike mutant SARS-CoV-2 PVs by anti-MPO antibody status. **e**, Nonparametric rank correlation (Kendall's tau- b) of wild-type (WT) PV neutralization, variant (B.1.17) PV neutralization and age (<80 or \geq 80 years) against each of 53 cytokines or chemokines. Heatmaps illustrate Tau- b statistic (left) and significance (right, $-\log_{10}$ FDR).

Extended Data Table 1 Characteristics of study participants and neutralization data for wild-type SARS-CoV-2

[Full size table](#)

Extended Data Table 2 Neutralization after the first dose of BNT162b2 vaccine against wild-type and B1.1.7 PVs

[Full size table](#)

Extended Data Table 3 Neutralization in participants after the first dose of BNT162b2 vaccine against wild-type and B.1.1.7, B.1.351 and P.1 spike mutant PVs

[Full size table](#)

Supplementary information

Reporting Summary

Peer Review File

Rights and permissions

Open Access This article is licensed under a Creative Commons Attribution 4.0 International License, which permits use, sharing, adaptation, distribution and reproduction in any medium or format, as long as you give appropriate credit to the original author(s) and the source, provide a link to the Creative Commons license, and indicate if changes were made. The images or other third party material in this article are included in the article's Creative Commons license, unless indicated otherwise in a credit line to the material. If material is not included in the article's Creative Commons license and your intended use is not permitted by statutory regulation or exceeds the permitted use, you will need to obtain permission directly from the copyright holder. To view a copy of this license, visit <http://creativecommons.org/licenses/by/4.0/>.

Reprints and Permissions

About this article



Check for
updates

Cite this article

Collier, D.A., Ferreira, I.A.T.M., Kotagiri, P. *et al.* Age-related immune response heterogeneity to SARS-CoV-2 vaccine BNT162b2. *Nature* **596**, 417–422 (2021).
<https://doi.org/10.1038/s41586-021-03739-1>

Download citation

- Received: 16 April 2021
- Accepted: 18 June 2021
- Published: 30 June 2021
- Issue Date: 19 August 2021
- DOI: <https://doi.org/10.1038/s41586-021-03739-1>

Comments

By submitting a comment you agree to abide by our [Terms](#) and [Community Guidelines](#). If you find something abusive or that does not comply with our terms or guidelines please flag it as inappropriate.

[Download PDF](#)

Advertisement

This article was downloaded by **calibre** from <https://www.nature.com/articles/s41586-021-03739-1>

| [Section menu](#) | [Main menu](#) |

Protective efficacy of Ad26.COV2.S against SARS-CoV-2 B.1.351 in macaques
[Download PDF](#)

- Article
- Open Access
- [Published: 23 June 2021](#)

Protective efficacy of Ad26.COV2.S against SARS-CoV-2 B.1.351 in macaques

- [Jingyou Yu¹](#),
- [Lisa H. Tostanoski](#) ORCID: [orcid.org/0000-0001-9255-5684](#)¹,
- [Noe B. Mercado](#) ORCID: [orcid.org/0000-0001-7769-7326](#)¹,
- [Katherine McMahan](#)¹,
- [Jinyan Liu](#)¹,
- [Catherine Jacob-Dolan](#) ORCID: [orcid.org/0000-0001-6641-0342](#)^{1,2},
- [Abishek Chandrashekar](#) ORCID: [orcid.org/0000-0001-7821-5552](#)¹,
- [Caroline Atyeo](#)^{2,3},
- [David R. Martinez](#)⁴,
- [Tochi Anioke](#)¹,
- [Esther A. Bondzie](#)¹,
- [Aiquan Chang](#)^{1,2},
- [Sarah Gardner](#)¹,
- [Victoria M. Giffin](#) ORCID: [orcid.org/0000-0002-9783-302X](#)¹,
- [David L. Hope](#) ORCID: [orcid.org/0000-0001-5654-1744](#)¹,
- [Felix Nampanya](#)¹,
- [Joseph Nkolola](#)¹,
- [Shivani Patel](#) ORCID: [orcid.org/0000-0003-3475-1016](#)¹,
- [Owen Sanborn](#)¹,
- [Daniel Sellers](#)¹,
- [Huahua Wan](#) ORCID: [orcid.org/0000-0001-6958-9464](#)¹,
- [Tammy Hayes](#) ORCID: [orcid.org/0000-0002-8397-696X](#)⁵,
- [Katherine Bauer](#)⁵,
- [Laurent Pessaint](#)⁶,

- [Daniel Valentin⁶](#),
- [Zack Flinchbaugh⁶](#),
- [Renita Brown⁶](#),
- [Anthony Cook⁶](#),
- [Deandre Bueno-Wilkerson⁶](#),
- [Elyse Teow⁶](#),
- [Hanne Andersen](#) [ORCID: orcid.org/0000-0003-1103-9608⁶](#),
- [Mark G. Lewis](#) [ORCID: orcid.org/0000-0001-7852-0135⁶](#),
- [Amanda J. Martinot](#) [ORCID: orcid.org/0000-0001-6237-6191⁵](#),
- [Ralph S. Baric](#) [ORCID: orcid.org/0000-0001-6827-8701⁴](#),
- [Galit Alter](#) [ORCID: orcid.org/0000-0002-7680-9215³](#),
- [Frank Wegmann](#) [ORCID: orcid.org/0000-0002-9821-1492⁷](#),
- [Roland Zahn](#) [ORCID: orcid.org/0000-0003-2822-6231⁷](#),
- [Hanneke Schuitemaker](#) [ORCID: orcid.org/0000-0001-8563-2266⁷](#) &
- [Dan H. Barouch](#) [ORCID: orcid.org/0000-0001-5127-4659^{1,2,3}](#)

Nature volume **596**, pages 423–427 (2021) [Cite this article](#)

- 11k Accesses
- 125 Altmetric
- [Metrics details](#)

Subjects

- [SARS-CoV-2](#)
- [Vaccines](#)

Abstract

The emergence of SARS-CoV-2 variants that partially evade neutralizing antibodies poses a threat to the efficacy of current COVID-19 vaccines^{1,2}. The Ad26.COV2.S vaccine expresses a stabilized spike protein from the WA1/2020 strain of SARS-CoV-2, and has recently demonstrated protective efficacy against symptomatic COVID-19 in humans in several geographical regions—including in South Africa, where 95% of sequenced viruses in cases of COVID-19 were the B.1.351 variant³. Here we show that Ad26.COV2.S elicits humoral and cellular immune responses that cross-react with the B.1.351 variant and protects against B.1.351 challenge in rhesus macaques. Ad26.COV2.S induced lower binding and neutralizing antibodies against B.1.351 as compared to WA1/2020, but elicited comparable CD8 and CD4 T cell responses

against the WA1/2020, B.1.351, B.1.1.7, P.1 and CAL.20C variants. B.1.351 infection of control rhesus macaques resulted in higher levels of virus replication in bronchoalveolar lavage and nasal swabs than did WA1/2020 infection. Ad26.COV2.S provided robust protection against both WA1/2020 and B.1.351, although we observed higher levels of virus in vaccinated macaques after B.1.351 challenge. These data demonstrate that Ad26.COV2.S provided robust protection against B.1.351 challenge in rhesus macaques. Our findings have important implications for vaccine control of SARS-CoV-2 variants of concern.

[Download PDF](#)

Main

SARS-CoV-2 variants of concern have shown increased transmissibility and pathogenicity in humans^{4,5}, and some variants have also demonstrated partial evasion of natural and vaccine-elicited neutralizing antibodies^{1,2,6,7}. Ad26.COV2.S is a replication-incompetent human adenovirus type 26 vector⁸ that expresses a prefusion stabilized SARS-CoV-2 spike protein (S)^{9,10} from the Wuhan 2019 strain of SARS-CoV-2. It was previously reported that Ad26.COV2.S demonstrated protective efficacy against SARS-CoV-2 WA1/2020 challenges in hamsters and nonhuman primates^{11,12,13}, and also showed safety and immunogenicity in humans^{14,15}. A recent phase III efficacy trial has shown that Ad26.COV2.S provided 86%, 88% and 82% protection against severe COVID-19 disease by day 28 after vaccination in the USA, Brazil and South Africa, respectively³.

We developed a B.1.351 challenge stock by expansion of a seed stock (BEI Resources, NR-54974) in Calu-3 cells (ATCC HTB-55). We immunized 24 rhesus macaques in 4 experimental groups ($n = 6$ macaques per group) as follows: groups 1 and 3 received a sham vaccine (sham control macaques), and groups 2 and 4 received a single immunization with 5×10^{10} viral particles of Ad26.COV2.S; after vaccination, groups 1 and 2 were challenged with the original SARS-CoV 2 strain WA1/2020, and groups 3 and 4 were challenged with the SARS-CoV-2 variant B.1.351.

Ad26.COV2.S immunogenicity and cross-reactivity

We assessed vaccine-induced antibody responses against the SARS-CoV-2 WA1/2020 strain as well as against B.1.351. Using a luciferase-based pseudovirus neutralizing antibody assay^{12,16,17,18}, we found that the median neutralizing antibody titres in macaques that received Ad26.COV2.S vaccine were less than 20 at week 0, and were 693, 561, and 155 against the WA1/2020, D614G and B.1.351 strains, respectively, in Ad26.COV2.S-vaccinated macaques at week 6 (Fig. 1a). These data show a median

4.5-fold reduction of neutralizing antibody titres against B.1.351 as compared to WA1/2020 ($P = 0.0002$, Wilcoxon rank-sum test). Live-virus neutralizing antibody assays¹⁹ showed a greater reduction of neutralizing antibody titres against B.1.351 (Extended Data Fig. 1).

Fig. 1: Antibody responses in vaccinated rhesus macaques.

 **figure1**

a, Pseudovirus neutralizing antibody (nAb) assays against the SARS-CoV-2 WA1/2020, D614G and B.1.351 variants were assessed at week 0 (top panels) and week 6 (bottom panels) in macaques that received a single immunization of sham vaccine (left panels) or 5×10^{10} viral particles of Ad26.COV2.S (right panels). **b**,

RBD-specific binding antibody responses of sham control (left panels) or Ad26.COV2.S-vaccinated (right panels) macaques against WA1/2020, B.1.1.7, and B.1.351 were assessed by ELISA at week 0 (top panels) and week 6 (bottom panels). **c**, Antibody-dependent cellular phagocytosis (ADCP) (phagocytic score) and antibody-dependent complement deposition (ADCD) (mean fluorescence intensity) were evaluated against WA1/2020 and B.1.351 at week 6. Macaques that eventually were challenged with WA1/2020 (triangles) or B.1.351 (squares) are depicted. Horizontal red bars reflect median responses. *P* values reflect two-sided Wilcoxon rank-sum tests. Dotted lines reflect the limits of quantification of the assay. *n* = 24 independent samples (12 sham and 12 Ad26.COV2.S).

[Source data](#)

[Full size image](#)

Median receptor-binding domain (RBD)-specific enzyme-linked immunosorbent assay (ELISA) titres in macaques that received Ad26.COV2.S vaccine were less than 25 at week 0, and were 4,050, 3,186 and 805 against the WA1/2020, B.1.1.7 and B.1.351 strains, respectively, in Ad26.COV2.S-vaccinated macaques at week 6 (Fig. 1b). These data show a median 5.0-fold reduction of RBD-specific ELISA titres against B.1.351 as compared to WA1/2020 ($P < 0.0001$, Wilcoxon rank-sum test). We also used an electrochemiluminescence assay (ECLA)²⁰ to evaluate S- and RBD-specific binding antibody responses to WA1/2020, B.1.1.7, P.1. and B.1.351 (Extended Data Fig. 2). Similar to the ELISA titres, median RBD-specific ECLA responses were reduced against P.1 and B.1.351 as compared to WA1/2020 at week 6, whereas we observed a smaller effect with S-specific ECLA responses. Antibody-dependent cellular phagocytosis and antibody-dependent complement deposition responses²¹ were more comparable against WA1/2020 and B.1.351 than were ELISA titres or ECLA responses (Fig. 1c).

We assessed S-specific cellular immune responses using pooled peptide IFN γ enzyme-linked immunospot (ELISPOT) assays in peripheral blood mononuclear cells at week 4. ELISPOT responses were comparable among the WA1/2020, B.1.351, B.1.1.7, P.1 and CAL.20C strains, with no evidence of decreased responses against the variants (Fig. 2a). We also evaluated S-specific CD8 $^{+}$ and CD4 $^{+}$ T cell responses using multi-parameter intracellular cytokine staining assays at week 6 (Supplementary Fig. 1). IFN γ CD8 $^{+}$ and CD4 $^{+}$ T cell responses were comparable among the WA1/2020, B.1.351, B.1.1.7, P.1 and CAL.20C strains (Fig. 2b). Similarly, IFN γ central memory CD28 $^{+}$ CD95 $^{+}$ CD4 $^{+}$ and CD28 $^{+}$ CD95 $^{+}$ CD8 $^{+}$ T cell responses were comparable across these variants (Fig. 2c). These data show that S-specific cellular immune responses were comparable for these SARS-CoV-2 variants.

Fig. 2: T cell responses in vaccinated rhesus macaques.

 figure2

a–c, Cellular immune responses to pooled S peptides of sham control (left) or Ad26.COV2.S-vaccinated (right) macaques were assessed by IFN γ ELISPOT assays at week 4 (**a**) and IFN γ intracellular cytokine staining assays at week 6 (**b, c**) to

WA1/2020, B.1.351, B.1.1.7, P.1, and CAL.20C variants. Intracellular cytokine staining assays show IFN γ responses in CD4 $^{+}$ (left) and CD8 $^{+}$ (right) T cells (**b**) and CD28 $^{+}$ CD95 $^{+}$ CD4 $^{+}$ (left) or CD28 $^{+}$ CD95 $^{+}$ CD8 $^{+}$ (right) central memory (CM) T cells (**c**). Macaques that eventually were challenged with WA1/2020 (triangles) or B.1.351 (squares) are depicted. Horizontal red bars reflect median responses. Dotted lines reflect assay limits of quantification. $n = 24$ independent samples (12 sham and 12 Ad26.COV2.S). SPCs, spot-forming cells; PBMCs, peripheral blood mononuclear cells.

[Source data](#)

[Full size image](#)

Homologous and heterologous SARS-CoV-2 challenges

We challenged all macaques at week 6 with a 5×10^5 50% tissue culture infectious dose (TCID₅₀) of SARS-CoV-2 WA1/2020^{12,16,17,22} or B.1.351 by the intranasal and intratracheal routes. We assessed viral loads in bronchoalveolar lavage (BAL) and nasal swabs by reverse-transcription PCR (RT-PCR) specific for subgenomic mRNA (sgRNA), which is believed to measure replicating virus^{16,23,24}. All sham control macaques were infected and showed higher median peak sgRNA of 6.16 (range of 4.93–6.80) log₁₀(sgRNA copies per ml) in BAL for B.1.351, as compared to 4.80 (range of 4.70–5.52) log₁₀(sgRNA copies per ml) for WA1/2020 (Fig. 3a). By contrast, vaccinated macaques demonstrated a median peak of 3.62 (range of 3.37–4.43) log₁₀(sgRNA copies per ml) in BAL for B.1.351, as compared with less than 1.69 (range of <1.69 to 3.23) log₁₀(sgRNA copies per ml) in BAL for WA1/2020 (Fig. 3a). Sham control macaques also showed a trend towards a higher median peak sgRNA of 5.90 (range of 4.73–6.47) log₁₀(sgRNA copies per swab) in nasal swabs for B.1.351, as compared with 5.48 (range of 4.44–6.00) log₁₀(sgRNA copies per swab) for WA1.2020 (Fig. 3b). Vaccinated macaques demonstrated a median peak of 3.57 (range of 2.41–4.21) log₁₀(sgRNA copies per swab) in nasal swabs for B.1.351, as compared with 2.64 (range of <1.69 to 3.89) log₁₀(sgRNA copies per swab) in nasal swabs for WA1/2020 (Fig. 3b).

Fig. 3: Protective efficacy after SARS-CoV-2 challenge.

 **figure3**

Rhesus macaques were challenged by the intranasal and intratracheal routes with 5×10^5 TCID₅₀ SARS-CoV-2 WA1/2020 or B.1.351. **a**, log₁₀(sgRNA copies per ml) (limit of quantification of 50 copies per ml) are shown in BAL of sham control (left) or Ad26.COV2.S-vaccinated (right) macaques after challenge with WA1/2020 (top) or

B.1.351 (bottom). **b**, \log_{10} (sgRNA copies per swab) (limit of quantification 50 copies per swab) are shown in nasal swabs of sham control (left) or Ad26.COV2.S-vaccinated (right) macaques after challenge with WA1/2020 (top) or B.1.351 (bottom). Red lines reflect median values. $n = 24$ independent samples (12 sham and 12 Ad26.COV2.S).

[Source data](#)

[Full size image](#)

B.1.351 led to higher peak viral loads, faster kinetics of viral replication and a longer duration of viral replication as compared with WA1/2020 in sham control macaques, which suggests that B.1.351 is a more stringent challenge in the macaque model. Ad26.COV2.S provided robust protection against peak viral replication for both strains, including a 3.13 and 2.54 log reduction of peak sgRNA copies per ml in BAL for WA1/2020 and B.1.351, respectively, and a 2.84 and 2.33 log reduction of peak sgRNA copies per swab in nasal swabs for WA1/2020 and B.1.351, respectively ($P = 0.0022$ for both BAL and nasal swabs for both WA1/2020 and B.1.351, Wilcoxon rank-sum tests) (Fig. 4a). By day 4 after challenge, viral loads were undetectable in Ad26.COV2.S-vaccinated macaques after both WA1/2020 and B.1.351 challenge, whereas viral loads were positive in most sham control macaques for WA1/2020 and in all sham control macaques for B.1.351 (Fig. 4b). Ad26.COV2.S also provided similar robust protection against day 2 infectious virus titres, as assessed by TCID₅₀ assays (Extended Data Fig. 3).

Fig. 4: Summary of protective efficacy after SARS-CoV-2 challenge.

 **figure4**

a, b, Peak (**a**) and day 4 (**b**) viral loads in BAL (left) and nasal swabs (right) of sham control (sham) and Ad26.COV2.S-vaccinated (Ad26) macaques after challenge with WA1/2020 or B.1.351. Horizontal red bars reflect median values. *P* values reflect two-sided Wilcoxon rank-sum tests. Dotted lines reflect the limits of quantification of the assay. *n* = 24 independent samples (12 sham and 12 Ad26.COV2.S).

[Source data](#)

[Full size image](#)

Correlates of protection

On day 10 after challenge (study week 8), sham control macaques developed both humoral and cellular immune responses, as expected (Extended Data Figs. 4–6). In sham control macaques, WA1/2020 challenge led to higher neutralizing antibody titres to WA1/2020 than to B.1.351, whereas B.1.351 challenge led to higher neutralizing antibody titres to B.1.351 than to WA1/2020 (Extended Data Fig. 4a), and cellular responses were comparable across all strains regardless of the challenge virus (Extended Data Fig. 6), consistent with the vaccine immunogenicity data.

Ad26.COV2.S-vaccinated macaques developed increased humoral and cellular immune responses after challenge. The low ELISA titres in sham control macaques probably reflect the early (day 10) time point after challenge (Extended Data Fig. 4b).

Peak \log_{10} (sgRNA) in BAL (Extended Data Fig. 7) and in nasal swabs (Extended Data Fig. 8) after challenge inversely correlated with \log_{10} ELISA, neutralizing antibody and ELISPOT responses at week 6, which suggests that both antibody and T cell responses correlate with protection. Correlations were slightly stronger for immune responses against the homologous challenge virus as compared with the heterologous challenge virus.

Histopathology

Ad26.COV2.S-vaccinated macaques demonstrated reduced lung histopathology compared with sham control macaques at necropsy on day 10 after WA1/2020 or B.1.351 challenge (Fig. 5a,b), although viral replication had largely resolved by day 10. Sham control macaques infected with WA1/2020 and B.1.351 had histopathological lesions that were consistent with previous reports¹⁶, including focal to locally extensive interstitial pneumonia with neutrophilic and mononuclear interstitial infiltrates, alveolar syncytia, and increased numbers of alveolar macrophages. Perivascular inflammation and type II pneumocyte hyperplasia were prominent features in both groups of sham control macaques, as were multifocal regions of fibrosis (Fig. 5c,d, Extended Data Fig. 9). Ad26.COV2.S-vaccinated macaques had only rare lesions, predominantly small and focal regions of interstitial inflammation, and rare syncytia in isolated lung lobes (Fig. 5e,f, Extended Data Fig. 10). No evidence of eosinophilic infiltrates or enhanced respiratory disease was observed in Ad26.COV2.S-vaccinated macaques.

Fig. 5: Histopathology after SARS-CoV-2 challenge.

 figure5

a, Cumulative histopathologic scoring of lung lesions from eight representative lung lobes from Ad26.COV2.S-vaccinated (Ad26) and sham control (sham) macaques on day 10 after challenge with WA1/2020 or B.1.351 SARS CoV-2 variants. **b**, Eight representative samples from cranial, middle and caudal lung lobes from the left and

right lungs were evaluated from each macaque, and were scored independently for each of the following lesions: interstitial inflammation and septal thickening, interstitial infiltrate (eosinophils), interstitial infiltrate (neutrophils), hyaline membranes, interstitial fibrosis, alveolar infiltrate (macrophages), bronchoalveolar infiltrate (neutrophils), epithelial syncytia, type II pneumocyte hyperplasia, bronchi infiltrate (macrophages), bronchi infiltrate (neutrophils), bronchi (hyperplasia of bronchus-associated lymphoid tissue), bronchiolar or peribronchiolar infiltrate (mononuclear cells), perivascular infiltrate (mononuclear cells) and endothelialitis. Each feature assessed was assigned a score of: 0, no substantial findings; 1, minimal; 2, mild; 3, moderate; 4, moderate to severe; 5, marked or severe. Scores were added for all lesions across all lung lobes for each macaque, for a maximum possible score of 600 for each macaque. Horizontal red lines reflect median values. *P* values reflect two-sided Wilcoxon rank-sum tests. **c–f**, Representative lung histopathology from at least eight evaluated tissues from sham control (**c, d**) and Ad26.COV2.S-vaccinated (**e, f**) macaques challenged with WA1/2020 (**c, e**) or B.1.351 (**d, f**) (on day 10 after the challenge), showing increased alveolar macrophages and thickened alveolar septa with inflammatory infiltrates and fibrosis (**c**), increased alveolar macrophages and epithelial syncytia within alveolar spaces, thickened and fibrotic alveolar septa with inflammatory infiltrates, focal alveolar and perivascular inflammatory infiltrates (**d**), focal perivascular inflammation (**e**) and focal expansion of alveolar septa with inflammatory infiltrates (**f**). Lungs evaluated were inflated or suffused with 10% formalin. In **c–f**, tissues were stained with haematoxylin and eosin. Scale bars, 20 µm. *n* = 24 independent samples (12 sham and 12 Ad26.COV2.S) (**a, b**); *n* = 4 representative samples (2 sham and 2 Ad26.COV2.S) (**c–f**).

[Source data](#)

[Full size image](#)

Discussion

It has previously been reported that Ad26.COV2.S provided robust protection against challenge with SARS-CoV-2 WA1/2020 in both rhesus macaques and hamsters^{11,12,13}. In this study, we show that Ad26.COV2.S induced cross-reactive antibody and T cell responses against SARS-CoV-2 variants of concern—including the B.1.351 variant, which has several mutations (including E484K) that lead to partial evasion of natural and vaccine-elicited neutralizing antibodies^{1,2,6,7}. Binding and neutralizing antibody titres were suppressed 4–5-fold against B.1.351 as compared to WA1/2020, but Fc functional antibody responses were affected less, and T cell responses were not affected at all by the SARS-CoV-2 variants. Ad26.COV2.S provided robust protection against both high-dose WA1/2020 and B.1.351 challenges. These data have important

implications for the potential utility of current vaccines and inform boosting strategies against SARS-CoV-2 variants of concern.

Our data are consistent with findings in humans in a recent phase III clinical trial of Ad26.COV2.S that was conducted in the USA, Latin America (Argentina, Brazil, Chile, Colombia, Mexico and Peru) and South Africa³. Robust protection was observed in all geographical regions, with similar levels of protection against severe COVID-19 disease regardless of variant, including in the USA, in Brazil (where 69% of cases with sequence data were the P.2 variant) and in South Africa (where 95% of cases with sequence data were the B.1.351 variant). In the current study in macaques, B.1.351 infection led to a higher magnitude of and more prolonged viral replication in the upper and lower respiratory tracts than did WA1/2020. Nevertheless, Ad26.COV2.S provided robust protection against both viruses, although levels of virus in BAL and nasal swabs were higher after B.1.351 challenge than after WA1/2020 challenge.

To the best of our knowledge, this is the first report of a SARS-CoV-2 vaccine evaluated for efficacy against a SARS-CoV-2 variant of concern in macaques. Several SARS-CoV-2 vaccines have previously been reported to protect against homologous WA1/2020 challenges, but have not yet been reported against B.1.351 challenges. Our study does not define mechanistic correlates of protection against SARS-CoV-2 variants, but it has previously been reported that IgG was sufficient for protection against homologous SARS-CoV-2 challenge in macaques and that CD8 T cell responses also contributed to protection if antibody titres were subprotective²².

In conclusion, Ad26.COV2.S induced cross-reactive humoral and cellular immune responses and provided robust protection against the heterologous SARS-CoV-2 variant B.1.351 in rhesus macaques. Future studies will determine whether Ad26.COV2.S, as well as other vaccines, protect against other SARS-CoV-2 variants of concern.

Methods

No statistical methods were used to predetermine sample size. Macaques were randomized into groups. All immunological, virological and histopathological studies were performed blinded.

Macaques and study design

Twenty-four outbred Indian-origin adult male and female rhesus macaques (*Macaca mulatta*) (3–11 years old) were randomly allocated to groups. All macaques were housed at Bioqual. Macaques received a single immunization of 5×10^{10} viral

particles of Ad26.COV2.S ($n = 12$) or sham ($n = 12$) by the intramuscular route without adjuvant at week 0. At week 6, all macaques were challenged with 5×10^5 TCID₅₀ SARS-CoV-2 from strains USA-WA1/2020 (BEI Resources; NR-5228) (which was grown in VeroE6 cells and deep sequenced as previously described¹⁶) or B.1.351 (BEI Resources; NR-54974). The B.1.351 stock was grown in Calu-3 cells and was deep-sequenced, which confirmed the expected sequence identity with no mutations in the S greater than 2.5% frequency and no mutations elsewhere in the virus at greater than 13% frequency. Virus was administered as 1 ml by the intranasal route (0.5 ml in each nare) and 1 ml by the intratracheal route. All immunological, virological and histopathological studies were performed blinded. Animal studies were conducted in compliance with all relevant local, state and federal regulations and were approved by the Bioqual Institutional Animal Care and Use Committee.

Pseudovirus-based virus neutralization assay

The SARS-CoV-2 pseudoviruses expressing a luciferase reporter gene were generated essentially as previously described^{12,16,17,18}. In brief, the packaging plasmid psPAX2 (AIDS Resource and Reagent Program), luciferase reporter plasmid pLenti-CMV Puro-Luc (Addgene) and S expressing pcDNA3.1-SARS CoV-2 SΔCT of variants were co-transfected into HEK293T cells by lipofectamine 2000 (ThermoFisher). Pseudoviruses of SARS-CoV-2 variants were generated by using WA1/2020 strain (Wuhan/WIV04/2019, GISAID accession identifier EPI_ISL_402124), D614G mutation, B.1.1.7 variant (GISAID accession identifier EPI_ISL_601443) or B.1.351 variant (GISAID accession identifier EPI_ISL_712096). The supernatants containing the pseudotype viruses were collected 48 h after transfection, and were purified by centrifugation and filtration with a 0.45-μm filter. To determine the neutralization activity of the plasma or serum samples from participants, HEK293T cells expressing human ACE2 (HEK293-hACE2 cells) were seeded in 96-well tissue culture plates at a density of 1.75×10^4 cells per well overnight. Threefold serial dilutions of heat-inactivated serum or plasma samples were prepared and mixed with 50 μl of pseudovirus. The mixture was incubated at 37 °C for 1 h before adding to HEK293T-hACE2 cells. Forty-eight hours after infection, cells were lysed in Steady-Glo Luciferase Assay (Promega) according to the manufacturer's instructions. SARS-CoV-2 neutralization titres were defined as the sample dilution at which a 50% reduction in relative light units (RLU) was observed relative to the average of the virus control wells.

Live virus neutralization assay

Full-length SARS-CoV-2 WA1/2020, B.1.351 and B.1.1.7, viruses were designed to express nanoluciferase (nLuc) and were recovered via reverse genetics¹⁹. One day

before the assay, Vero E6 USAMRID cells were plated at 20,000 cells per well in clear-bottom black-walled plates. Cells were inspected to ensure confluence on the day of assay. Serum samples were tested at a starting dilution of 1:20 and were serially diluted threefold up to nine dilution spots. Serially diluted serum samples were mixed in equal volume with diluted virus. Antibody–virus and virus-only mixtures were then incubated at 37 °C with 5% CO₂ for 1 h. After incubation, serially diluted sera and virus-only controls were added in duplicate to the cells at 75 plaque-forming units at 37 °C with 5% CO₂. Twenty-four hours later, the cells were lysed, and luciferase activity was measured via Nano-Glo Luciferase Assay System (Promega) according to the manufacturer specifications. Luminescence was measured by a Spectramax M3 plate reader (Molecular Devices). Virus neutralization titres were defined as the sample dilution at which a 50% reduction in RLU was observed relative to the average of the virus control wells.

ELISA

WA1/2020, B.1.1.7 and B.1.351 RBD-specific binding antibodies were assessed by ELISA essentially as previously described^{12,16,17}. In brief, 96-well plates were coated with 0.5 µg ml⁻¹ RBD protein in 1× DPBS and incubated at 4 °C overnight. After incubation, plates were washed once with wash buffer (0.05% Tween-20 in 1× DPBS) and blocked with 350 µl casein block per well for 2–3 h at room temperature. After incubation, block solution was discarded and plates were blotted dry. Serial dilutions of heat-inactivated serum diluted in casein block were added to wells and plates were incubated for 1 h at room temperature, before three further washes and a 1-h incubation with a 1 µg ml⁻¹ dilution of anti-macaque IgG HRP (Nonhuman Primate Reagent Resource) at room temperature in the dark. Plates were then washed three times, and 100 µl of SeraCare KPL TMB SureBlue Start solution was added to each well; plate development was halted by the addition of 100 µl SeraCare KPL TMB Stop solution per well. The absorbance at 450 nm was recorded using a VersaMax microplate reader. For each sample, ELISA endpoint titre was calculated in GraphPad Prism software, using a four-parameter logistic curve fit to calculate the reciprocal serum dilution that yields an absorbance value of 0.2 at 450 nm. log₁₀-transformed endpoint titres are reported.

ECLA

ECLA plates (MesoScale Discovery SARS-CoV-2 IgG Cat No: N05CA-1; panel 7) were designed and produced with up to nine antigen spots in each well, and assays were performed essentially as previously described²⁰. The antigens included were WA1/2020, B.1.1.7, P.1, and B.1.351 S and RBD. The plates were blocked with 50 µl of blocker A (1% BSA in MilliQ water) solution for at least 30 m at room temperature

shaking at 700 rpm with a digital microplate shaker. During blocking, the serum was diluted 1:5,000 in diluent 100. The plates were then washed 3 times with 150 µl of the MSD kit wash buffer, blotted dry, and 50 µl of the diluted samples were added in duplicate to the plates and set to shake at 700 rpm at room temperature for at least 2 h. The plates were again washed 3 times and 50 µl of SULFO-tagged anti-human IgG detection antibody (MesoScale Discovery) diluted to 1× in diluent 100 was added to each well and incubated shaking at 700 rpm at room temperature for at least 1 h. Plates were then washed 3 times and 150 µl of MSD GOLD read buffer B was added to each well and the plates were read immediately after on a MESO QuickPlex SQ 120 machine. MSD titres for each sample are reported as RLU_s, which were calculated as sample RLU minus blank RLU for each spot for each sample. The limit of detection was defined as 1,000 RLU for each assay.

Fc functional antibody assays

Fc functional profiling included the assessment of antibody-dependent monocyte phagocytosis and antibody-dependent complement deposition²¹. In brief, fluorescent beads (LifeTechnologies) were coupled via carboxy-coupling, and plasma were added, allowing immune complex formation, excess antibodies were washed away, followed by the addition of THP1 monocytes, primary neutrophils or guinea pig complement, individually, respectively. The level of phagocytosis and complement deposition was assessed by flow cytometry.

IFN γ ELISPOT assay

Pooled peptide ELISPOT assays were performed essentially as previously described^{12,16,17}. Peptide pools consisted of 15 amino acid peptides overlapping by 11 amino acids spanning the SARS-CoV-2 S from the WA1/2020 strain or variant strains. ELISPOT plates were coated with mouse anti-human IFN γ monoclonal antibody from BD Pharmigen at 5 µg per well and incubated overnight at 4 °C. Plates were washed with DPBS wash buffer (DPBS with 0.25% Tween-20), and blocked with R10 medium (RPMI with 10% heat-inactivated FBS with 1% of 100× penicillin–streptomycin) for 1–4 h at 37 °C. SARS-CoV-2 peptides (21st Century Biochemicals) were prepared and plated at a concentration of 1 µg per well, and 200,000 cells per well were added to the plate. The peptides and cells were incubated for 18–24 h at 37 °C. All steps after this incubation were performed at room temperature. The plates were washed with ELISPOT wash buffer (11% 10× DPBS and 0.3% Tween-20 in 1 l MilliQ water) and incubated for 2 h with rabbit polyclonal anti-human IFN γ biotin from U-Cytech (1 µg ml⁻¹). The plates were washed a second time and incubated for 2 h with streptavidin–alkaline phosphatase from Southern Biotech (2 µg ml⁻¹). The final wash was followed by the addition of nitor-blue tetrazolium chloride or 5-bromo-4-chloro 3' indolylphosphate *p*-toluidine salt (NBT/BCIP chromagen) substrate solution

for 7 min. The chromagen was discarded and the plates were washed with water and dried in a dim place for 24 h. Plates were scanned and counted on a Cellular Technologies Limited Immunospot Analyzer.

Intracellular cytokine staining assay

Multi-parameter pooled-peptide intracellular cytokine staining assays were performed essentially as previously described^{12,16,17}. Peptide pools consisted of 15 amino acid peptides overlapping by 11 amino acids spanning the SARS-CoV-2 S from the WA1/2020 strain or variant strains. Then, 10^6 PBMCs per well were resuspended in 100 μ l of R10 medium supplemented with CD49d monoclonal antibody (1 μ g ml⁻¹). Each sample was assessed with mock (100 μ l of R10 plus 0.5% DMSO; background control), peptide pools (2 μ g ml⁻¹), or 10 pg ml⁻¹ phorbol myristate acetate and 1 μ g ml⁻¹ ionomycin (Sigma-Aldrich) (100 μ l; positive control) and incubated at 37 °C for 1 h. After incubation, 0.25 μ l of GolgiStop and 0.25 μ l of GolgiPlug in 50 μ l of R10 was added to each well and incubated at 37 °C for 8 h and then held at 4 °C overnight. The next day, the cells were washed twice with DPBS, stained with near-IR live/dead dye for 10 min and then stained with predetermined titres of monoclonal antibodies against CD279 (clone EH12.1, BB700), CD38 (clone OKT10, PE), CD28 (clone 28.2, PE CY5), CD4 (clone L200, BV510), CD95 (clone DX2, BUV737) and CD8 (clone SK1, BUV805), for 30 min. Cells were then washed twice with 2% FBS in DPBS buffer and incubated for 15 min with 200 μ l of BD CytoFix/CytoPerm Fixation/Permeabilization solution. Cells were washed twice with 1× Perm Wash buffer (BD Perm/Wash Buffer 10× in the CytoFix/CytoPerm Fixation/Permeabilization kit diluted with MilliQ water and passed through a 0.22- μ m filter) and stained with intracellularly with monoclonal antibodies against Ki67 (clone B56, FITC), CD69 (clone TP1.55.3, ECD), IL-10 (clone JES3-9D7, PE CY7), IL-13 (clone JES10-5A2, BV421), TNF (clone Mab11, BV650), IL-4 (clone MP4-25D2, BV711), IFN γ (clone B27; BUV395), CD45 (clone D058-1283, BUV615), IL-2 (clone MQ1-17H12, APC) and CD3 (clone SP34.2, Alexa 700), for 30 min. Cells were washed twice with 1× Perm Wash buffer and fixed with 250 μ l of freshly prepared 1.5% formaldehyde. Fixed cells were transferred to a 96-well round-bottom plate and analysed by BD FACSymphony system. Central memory T cells were defined as CD28⁺CD95⁺ T cells. Data were analysed with FlowJo v.9.9.

sgRNA assay

SARS-CoV-2 *E* gene sgRNA was assessed by RT-PCR using primers and probes as previously described^{23,24}. A standard was generated by first synthesizing a gene fragment of the subgenomic *E* gene²³. The gene fragment was subsequently cloned into a pcDNA3.1+ expression plasmid using restriction site cloning (Integrated DNA

Techonologies). The insert was in vitro-transcribed to RNA using the AmpliCap-Max T7 High Yield Message Maker Kit (CellScript). log dilutions of the standard were prepared for RT-PCR assays ranging from 1×10^{10} copies to 1×10^{-1} copies. Viral loads were quantified from BAL fluid and nasal swabs. RNA extraction was performed on a QIAcube HT using the IndiSpin QIAcube HT Pathogen Kit according to manufacturer's specifications (Qiagen). The standard dilutions and extracted RNA samples were reverse-transcribed using SuperScript VILO Master Mix (Invitrogen) following the cycling conditions described by the manufacturer, 25 °C for 10 min, 42 °C for 1 h, then 85 °C for 5 min. A Taqman custom gene expression assay (Thermo Fisher Scientific) was designed using the sequences targeting the *E* gene sgRNA²³. The sequences for the custom assay were as follows, forward primer, sgLeadCoV2.Fwd: CGATCTCTGTAGATCTGTTCTC, E_Sarboco_R: ATATTGCAGCAGTACGCACACA, E_Sarboco_P1 (probe): VIC-ACACTAGCCATCCTTACTGCGCTTCG-MGB. These primers and probes were equally reactive for both variants. Reactions were carried out in duplicate for samples and standards on the QuantStudio 6 and 7 Flex Real-Time PCR Systems (Applied Biosystems) with the thermal cycling conditions, initial denaturation at 95 °C for 20 s, then 45 cycles of 95 °C for 1 s and 60 °C for 20 s. Standard curves were used to calculate sgRNA copies per ml or per swab; the quantitative assay sensitivity was 50 copies per ml or per swab.

TCID₅₀ assay

Vero TMPRSS2 cells (obtained from A. Creanga) were plated at 25,000 cells per well in DMEM with 10% FBS and gentamicin, and the cultures were incubated at 37 °C, 5.0% CO₂. Medium was aspirated and replaced with 180 µl of DMEM with 2% FBS and gentamicin. Serial dilution of samples as well as positive (virus stock of known infectious titre) and negative (medium only) controls were included in each assay. The plates are incubated at 37 °C, 5.0% CO₂ for 4 days. Cell monolayers were visually inspected for cytopathic effect. The TCID₅₀ was calculated using the Read–Muench formula.

Histopathology

Lungs on day 10 after SARS-CoV-2 challenge were evaluated by histopathology. At the time of fixation, lungs were suffused with 10% formalin to expand the alveoli. All tissues were fixed in 10% formalin and blocks sectioned at 5 µm. Slides were incubated for 30–60 min at 65 °C then deparaffinized in xylene and rehydrated through a series of graded ethanol to distilled water. Sections were stained with haematoxylin and eosin. Blinded evaluation and scoring was performed by a board-certified veterinary pathologist (A.J.M.).

Statistical analyses

Comparisons of virological, immunological and histopathological data were performed using GraphPad Prism 8.4.2 (GraphPad Software). Comparison of data between groups was performed using two-sided Wilcoxon rank-sum tests. Correlation analyses were performed using two-sided Spearman rank-correlation tests. *P* values of less than 0.05 were considered significant.

Reporting summary

Further information on research design is available in the [Nature Research Reporting Summary](#) linked to this paper.

Data availability

All relevant data are available in the Article and its [Supplementary Information](#). Any additional data are available from the corresponding author upon reasonable request. [Source data](#) are provided with this paper.

References

1. 1.

Wang, P. et al. Antibody resistance of SARS-CoV-2 variants B.1.351 and B.1.1.7. *Nature* **593**, 130–135 (2021).

[CAS](#) [Article](#) [ADS](#) [Google Scholar](#)

2. 2.

Wibmer, C. K. et al. SARS-CoV-2 501Y.V2 escapes neutralization by South African COVID-19 donor plasma. *Nat. Med.* **27**, 622–625 (2021).

[CAS](#) [Article](#) [Google Scholar](#)

3. 3.

Sadoff, J. et al. Safety and efficacy of single-dose Ad26.COV2.S vaccine against Covid-19. *N. Engl. J. Med.* **384**, 2187–2201 (2021).

[CAS](#) [Article](#) [Google Scholar](#)

4. 4.

Korber, B. et al. Tracking changes in SARS-CoV-2 spike: evidence that D614G increases infectivity of the COVID-19 virus. *Cell* **182**, 812–827.e19 (2020).

[CAS](#) [Article](#) [Google Scholar](#)

5. 5.

Davies, N. G. et al. Estimated transmissibility and impact of SARS-CoV-2 lineage B.1.1.7 in England. *Science* **372**, eabg3055 (2021).

[CAS](#) [Article](#) [Google Scholar](#)

6. 6.

Wu, K. et al. Serum neutralizing activity elicited by mRNA-1273 vaccine. *N. Engl. J. Med.* **384**, 1468–1470 (2021).

[Article](#) [Google Scholar](#)

7. 7.

Liu, Y. et al. Neutralizing activity of BNT162b2-elicited serum. *N. Engl. J. Med.* **384**, 1466–1468 (2021).

[Article](#) [Google Scholar](#)

8. 8.

Abbink, P. et al. Comparative seroprevalence and immunogenicity of six rare serotype recombinant adenovirus vaccine vectors from subgroups B and D. *J. Virol.* **81**, 4654–4663 (2007).

[CAS](#) [Article](#) [Google Scholar](#)

9. 9.

Bos, R. et al. Ad26 vector-based COVID-19 vaccine encoding a prefusion-stabilized SARS-CoV-2 spike immunogen induces potent humoral and cellular immune responses. *NPJ Vaccines* **5**, 91 (2020).

[CAS](#) [Article](#) [Google Scholar](#)

10. 10.

Wrapp, D. et al. Cryo-EM structure of the 2019-nCoV spike in the prefusion conformation. *Science* **367**, 1260–1263 (2020).

[CAS](#) [Article](#) [ADS](#) [Google Scholar](#)

11. 11.

Tostanoski, L. H. et al. Ad26 vaccine protects against SARS-CoV-2 severe clinical disease in hamsters. *Nat. Med.* **26**, 1694–1700 (2020).

[CAS](#) [Article](#) [Google Scholar](#)

12. 12.

Mercado, N. B. et al. Single-shot Ad26 vaccine protects against SARS-CoV-2 in rhesus macaques. *Nature* **586**, 583–588 (2020).

[CAS](#) [Article](#) [ADS](#) [Google Scholar](#)

13. 13.

van der Lubbe, J. E. M. et al. Ad26.COV2.S protects Syrian hamsters against G614 spike variant SARS-CoV-2 and does not enhance respiratory disease. *NPJ Vaccines* **6**, 39 (2021).

[Article](#) [Google Scholar](#)

14. 14.

Sadoff, J. et al. Interim results of a phase 1-2a trial of Ad26.COV2.S Covid-19 vaccine. *N. Engl. J. Med.* **384**, 1824–1835 (2021).

[CAS](#) [Article](#) [Google Scholar](#)

15. 15.

Stephenson, K. E. et al. Immunogenicity of the Ad26.COV2.S vaccine for COVID-19. *J. Am. Med. Assoc.* **325**, 1535–1544 (2021).

[CAS](#) [Article](#) [Google Scholar](#)

16. 16.

Chandrashekhar, A. et al. SARS-CoV-2 infection protects against rechallenge in rhesus macaques. *Science* **369**, 812–817 (2020).

[CAS](#) [Article](#) [ADS](#) [Google Scholar](#)

17. 17.

Yu, J. et al. DNA vaccine protection against SARS-CoV-2 in rhesus macaques. *Science* **369**, 806–811 (2020).

[CAS](#) [Article](#) [ADS](#) [Google Scholar](#)

18. 18.

Yu, J. et al. Deletion of the SARS-CoV-2 spike cytoplasmic tail increases infectivity in pseudovirus neutralization assays. *J. Virol.* **95**, JVI.00044-21 (2021).

[Article](#) [Google Scholar](#)

19. 19.

Martinez, D. R. et al. Chimeric spike mRNA vaccines protect against sarbecovirus challenge in mice. Preprint at <https://doi.org/10.1101/2021.03.11.434872> (2021).

20. 20.

Jacob-Dolan, C. et al. Coronavirus-specific antibody cross reactivity in Rhesus macaques following SARS-CoV-2 vaccination and infection. *J. Virol.* JVI.00117-21 (2021).

21. 21.

Chung, A. W. et al. Dissecting polyclonal vaccine-induced humoral immunity against HIV using systems serology. *Cell* **163**, 988–998 (2015).

[CAS](#) [Article](#) [Google Scholar](#)

22. 22.

McMahan, K. et al. Correlates of protection against SARS-CoV-2 in rhesus macaques. *Nature* **590**, 630–634 (2021).

[CAS](#) [Article](#) [ADS](#) [Google Scholar](#)

23. 23.

Wölfel, R. et al. Virological assessment of hospitalized patients with COVID-2019. *Nature* **581**, 465–469 (2020).

[Article](#) [ADS](#) [Google Scholar](#)

24. 24.

Dagotto, G. et al. Comparison of subgenomic and total RNA in SARS-CoV-2 challenged rhesus macaques. *J. Virol.* **95**, JVI.02370-20 (2021).

[Article](#) [Google Scholar](#)

[Download references](#)

Acknowledgements

We thank J. Muench, F. Paz, J. Valley-Ogunro, S. O'Connor, A. Sigal, T. de Oliveira, J. Barrett, M. Gebre and M. Lifton for advice, assistance, and reagents; and Mesoscale Discovery for the ECLA kits. This project was funded in part by the Department of Health and Human Services Biomedical Advanced Research and Development Authority (BARDA) under contract HHS0100201700018C. We also acknowledge support from Janssen Vaccines & Prevention BV, Ragon Institute of MGH, MIT and Harvard, Musk Foundation, Massachusetts Consortium on Pathogen Readiness (MassCPR) and the National Institutes of Health (CA260476).

Author information

Author notes

1. These authors contributed equally: Jingyou Yu, Lisa H. Tostanoski, Noe B. Mercado, Katherine McMahan, Jinyan Liu, Catherine Jacob-Dolan, Abishek Chandrashekar

Affiliations

1. Center for Virology and Vaccine Research, Beth Israel Deaconess Medical Center, Harvard Medical School, Boston, MA, USA

Jingyou Yu, Lisa H. Tostanoski, Noe B. Mercado, Katherine McMahan, Jinyan Liu, Catherine Jacob-Dolan, Abishek Chandrashekar, Tochi Anioke, Esther A. Bondzie, Aiquan Chang, Sarah Gardner, Victoria M. Giffin, David L. Hope, Felix

Nampanya, Joseph Nkolola, Shivani Patel, Owen Sanborn, Daniel Sellers, Huahua Wan & Dan H. Barouch

2. Harvard Medical School, Boston, MA, USA

Catherine Jacob-Dolan, Caroline Atyeo, Aiquan Chang & Dan H. Barouch

3. Ragon Institute of MGH, MIT and Harvard, Cambridge, MA, USA

Caroline Atyeo, Galit Alter & Dan H. Barouch

4. University of North Carolina at Chapel Hill, Chapel Hill, NC, USA

David R. Martinez & Ralph S. Baric

5. Tufts University Cummings School of Veterinary Medicine, North Grafton, MA, USA

Tammy Hayes, Katherine Bauer & Amanda J. Martinot

6. Bioqual, Rockville, MD, USA

Laurent Pessant, Daniel Valentin, Zack Flinchbaugh, Renita Brown, Anthony Cook, Deandre Bueno-Wilkerson, Elyse Teow, Hanne Andersen & Mark G. Lewis

7. Janssen Vaccines & Prevention, Leiden, The Netherlands

Frank Wegmann, Roland Zahn & Hanneke Schuitemaker

Authors

1. Jingyou Yu

[View author publications](#)

You can also search for this author in [PubMed](#) [Google Scholar](#)

2. Lisa H. Tostanoski

[View author publications](#)

You can also search for this author in [PubMed](#) [Google Scholar](#)

3. Noe B. Mercado

[View author publications](#)

You can also search for this author in [PubMed](#) [Google Scholar](#)

4. Katherine McMahan

[View author publications](#)

You can also search for this author in [PubMed](#) [Google Scholar](#)

5. Jinyan Liu

[View author publications](#)

You can also search for this author in [PubMed](#) [Google Scholar](#)

6. Catherine Jacob-Dolan

[View author publications](#)

You can also search for this author in [PubMed](#) [Google Scholar](#)

7. Abishek Chandrashekhar

[View author publications](#)

You can also search for this author in [PubMed](#) [Google Scholar](#)

8. Caroline Atyeo

[View author publications](#)

You can also search for this author in [PubMed](#) [Google Scholar](#)

9. David R. Martinez

[View author publications](#)

You can also search for this author in [PubMed](#) [Google Scholar](#)

10. Tochi Anioke

[View author publications](#)

You can also search for this author in [PubMed](#) [Google Scholar](#)

11. Esther A. Bondzie

[View author publications](#)

You can also search for this author in [PubMed](#) [Google Scholar](#)

12. Aiquan Chang

[View author publications](#)

You can also search for this author in [PubMed](#) [Google Scholar](#)

13. Sarah Gardner

[View author publications](#)

You can also search for this author in [PubMed](#) [Google Scholar](#)

14. Victoria M. Giffin

[View author publications](#)

You can also search for this author in [PubMed](#) [Google Scholar](#)

15. David L. Hope

[View author publications](#)

You can also search for this author in [PubMed](#) [Google Scholar](#)

16. Felix Nampanya

[View author publications](#)

You can also search for this author in [PubMed](#) [Google Scholar](#)

17. Joseph Nkolola

[View author publications](#)

You can also search for this author in [PubMed](#) [Google Scholar](#)

18. Shivani Patel

[View author publications](#)

You can also search for this author in [PubMed](#) [Google Scholar](#)

19. Owen Sanborn

[View author publications](#)

You can also search for this author in [PubMed](#) [Google Scholar](#)

20. Daniel Sellers

[View author publications](#)

You can also search for this author in [PubMed](#) [Google Scholar](#)

21. Huahua Wan

[View author publications](#)

You can also search for this author in [PubMed](#) [Google Scholar](#)

22. Tammy Hayes

[View author publications](#)

You can also search for this author in [PubMed](#) [Google Scholar](#)

23. Katherine Bauer

[View author publications](#)

You can also search for this author in [PubMed](#) [Google Scholar](#)

24. Laurent Pessant

[View author publications](#)

You can also search for this author in [PubMed](#) [Google Scholar](#)

25. Daniel Valentin

[View author publications](#)

You can also search for this author in [PubMed](#) [Google Scholar](#)

26. Zack Flinchbaugh

[View author publications](#)

You can also search for this author in [PubMed](#) [Google Scholar](#)

27. Renita Brown

[View author publications](#)

You can also search for this author in [PubMed](#) [Google Scholar](#)

28. Anthony Cook

[View author publications](#)

You can also search for this author in [PubMed](#) [Google Scholar](#)

29. Deandre Bueno-Wilkerson

[View author publications](#)

You can also search for this author in [PubMed](#) [Google Scholar](#)

30. Elyse Teow

[View author publications](#)

You can also search for this author in [PubMed](#) [Google Scholar](#)

31. Hanne Andersen

[View author publications](#)

You can also search for this author in [PubMed](#) [Google Scholar](#)

32. Mark G. Lewis

[View author publications](#)

You can also search for this author in [PubMed](#) [Google Scholar](#)

33. Amanda J. Martinot

[View author publications](#)

You can also search for this author in [PubMed](#) [Google Scholar](#)

34. Ralph S. Baric

[View author publications](#)

You can also search for this author in [PubMed](#) [Google Scholar](#)

35. Galit Alter

[View author publications](#)

You can also search for this author in [PubMed](#) [Google Scholar](#)

36. Frank Wegmann

[View author publications](#)

You can also search for this author in [PubMed](#) [Google Scholar](#)

37. Roland Zahn

[View author publications](#)

You can also search for this author in [PubMed](#) [Google Scholar](#)

38. Hanneke Schuitemaker

[View author publications](#)

You can also search for this author in [PubMed](#) [Google Scholar](#)

39. Dan H. Barouch

[View author publications](#)

You can also search for this author in [PubMed](#) [Google Scholar](#)

Contributions

D.H.B., F.W. and R.Z. designed the study. J.Y., L.H.T., N.B.M., K.M., J.L., C.J.-D., A. Chandrashekhar, T.A., E.A.B., A. Chang, S.G., V.M.G., D.L.H., F.N., J.N., S.P., O.S., D.S. and H.W. performed the immunological and virological assays. D.R.M. and R.S.B. performed the live virus neutralization assays. C.A. and G.A. performed the Fc functional antibody assays. L.P., D.V., Z.F., R.B., A. Cook, D.B.-W., E.T., H.A. and M.G.L. led the clinical care of the macaques. F.W., R.Z. and H.S. provided the vaccine. T.H., K.B. and A.J.M. led the histopathology. D.H.B. wrote the paper with all co-authors.

Corresponding author

Correspondence to [Dan H. Barouch](#).

Ethics declarations

Competing interests

D.H.B., R.Z., F.W. and H.S. are co-inventors on provisional vaccine patents (63/121,482; 63/133,969; 63/135,182). R.Z., F.W. and H.S. are employees of Janssen Vaccines & Prevention BV and may hold stock in Johnson & Johnson.

Additional information

Peer review information *Nature* thanks Wolfgang Baumgärtner, Andrianus Boon and the other, anonymous, reviewer(s) for their contribution to the peer review of this work.

Publisher's note Springer Nature remains neutral with regard to jurisdictional claims in published maps and institutional affiliations.

Extended data figures and tables

[Extended Data Fig. 1 Live virus neutralizing antibody responses in vaccinated rhesus macaques.](#)

Live virus neutralizing antibody responses against the SARS-CoV-2 WA1/2020, B.1.1.7 and B.1.351 variants were assessed at week 6 in macaques that received a single immunization of sham vaccine or 5×10^{10} viral particles of Ad26.COV2.S. Macaques that eventually were challenged with WA1/2020 (triangles) or B.1.351 (squares) are depicted. Horizontal red bars reflect median responses. Dotted lines reflect assay limits of quantification. $n = 24$ independent samples (12 sham, 12 Ad26.COV2.S).

Extended Data Fig. 2 Binding antibody responses in vaccinated rhesus macaques by ECLA.

a, b, S- and RBD-specific binding antibody responses against the SARS-CoV-2 WA1/2020, B.1.1.7, B.1.351 and P.1 variants were assessed by ECLA at week 0 (**a**) and week 6 (**b**) in macaques that received a single immunization of sham-negative control or 5×10^{10} viral particles of Ad26.COV2.S. Macaques that eventually were challenged with WA1/2020 (triangles) or B.1.351 (squares) are depicted. Horizontal red bars reflect median responses. Dotted lines reflect assay limits of quantification.

Extended Data Fig. 3 Infectious virus titres after SARS-CoV-2 challenge.

Day 2 infectious virus titres by TCID₅₀ assays in BAL and nasal swabs after challenge. Horizontal red bars reflect median values. *P* values reflect two-sided Wilcoxon rank-sum tests. Dotted lines reflect assay limits of quantification. $n = 24$ independent samples (12 sham, 12 Ad26.COV2.S).

Extended Data Fig. 4 Binding and neutralizing antibody responses in challenged rhesus macaques.

a, b, Pseudovirus neutralizing antibody assays against the SARS-CoV-2 WA1/2020, D614G, and B.1.351 variants were assessed (**a**) and RBD-specific binding antibody responses against the SARS-CoV-2 WA1/2020, B.1.1.7, and B.1.351 variants were assessed by ELISA (**b**) on day 10 after challenge in macaques that received a single immunization of sham vaccine or 5×10^{10} viral particles of Ad26.COV2.S. Macaques that were challenged with WA1/2020 or B.1.351 are shown in separate graphs. Horizontal red bars reflect median responses. Dotted lines reflect assay limits of quantification. $n = 24$ independent samples (12 sham, 12 Ad26.COV2.S).

Extended Data Fig. 5 Binding antibody responses in challenged rhesus macaques by ECLA.

S- and RBD-specific binding antibody responses against the SARS-CoV-2 WA1/2020, B.1.1.7, B.1.351 and P.1 variants were assessed by ECLA on day 10 after challenge in macaques that received a single immunization of sham vaccine or 5×10^{10} viral particles of Ad26.COV2.S. Macaques that were challenged with WA1/2020 or B.1.351 are shown in separate graphs. Horizontal red bars reflect median responses. Dotted lines reflect assay limit of quantification. $n = 24$ independent samples (12 sham, 12 Ad26.COV2.S).

Extended Data Fig. 6 T cell responses in vaccinated rhesus macaques by ELISPOT assays.

a, Cellular immune responses to pooled S peptides were assessed by IFN γ ELISPOT assays on day 10 after challenge to WA1/2020, B.1.351, B.1.1.7, P.1 and CAL.20C variants. **b**, CD4 $^+$ and CD8 $^+$ T cell responses to pooled S peptides were assessed by IFN γ intracellular cytokine staining assays on day 10 after challenge to WA1/2020, B.1.351, B.1.1.7, P.1 and CAL.20C variants. Horizontal red bars reflect median responses. $n = 24$ independent samples (12 sham, 12 Ad26.COV2.S).

Extended Data Fig. 7 Correlates of protection in BAL.

a, b, Correlations of log(peak sgRNA copies per ml) in BAL after challenge versus log-transformed ELISA titres, neutralizing antibody titres or ELISPOT responses to the homologous (**a**) or heterologous (**b**) challenge virus (WA1/2020, B.1.351) at week 6 after vaccination. Red lines reflect the best linear fit relationship between these variables. P and R values reflect two-sided Spearman rank-correlation tests.

Extended Data Fig. 8 Correlates of protection in nasal swabs.

a, b, Correlations of log(peak sgRNA copies per ml) in nasal swabs after challenge versus log-transformed ELISA titres, neutralizing antibody titres or ELISPOT responses to the homologous (**a**) or heterologous (**b**) challenge virus (WA1/2020, B.1.351) at week 6 after vaccination. Red lines reflect the best linear fit relationship between these variables. P and R values reflect two-sided Spearman rank-correlation tests.

Extended Data Fig. 9 Representative histopathology in sham control macaques after SARS-CoV-2 challenge.

a–f, Locally extensive moderate-to-severe lesions were observed in sham control macaques challenged with WA1/2020 (**a–c**) or B.1.351 (**d–f**), on day 10 after challenge. **a**, Syncytia, lymphoid proliferation and locally extensive interstitial

inflammation. **b**, Type II pneumocyte hyperplasia and lymphoid proliferation. **c**, Perivascular alveolar infiltrates and interstitial inflammation. **d**, Alveolar macrophage infiltrates. **e**, Severe mononuclear alveolar infiltrates and pneumocyte hyperplasia. **f**, Perivascular infiltrates and interstitial inflammation. At least eight tissues were assessed per macaques. Haematoxylin and eosin staining. Scale bars, 20 µm.

[Extended Data Fig. 10 Representative histopathology in Ad26.COV2.S-vaccinated macaques after SARS-CoV-2 challenge.](#)

a–f, Focal minimal-to-mild lesions were observed in Ad26.COV2.S-vaccinated macaques challenged with WA1/2020 (**a–c**) or B.1.351 (**d–f**), on day 10 after challenge. **a**, Interstitial inflammation. **b**, Syncytia. **c**, Perivascular neutrophilic infiltrates. **d**, Perivascular mononuclear inflammation. **e**, Type II pneumocyte hyperplasia. **f**, Alveolar macrophage infiltrates. At least eight tissues were assessed per macaque. Haematoxylin and eosin staining. Scale bar, 20 µm.

Supplementary information

[Supplementary Figure 1](#)

Sample Raw Flow Cytometry Data.

[Reporting Summary](#)

Source data

[Source Data Fig. 1](#)

[Source Data Fig. 2](#)

[Source Data Fig. 3](#)

[Source Data Fig. 4](#)

[Source Data Fig. 5](#)

Rights and permissions

Open Access This article is licensed under a Creative Commons Attribution 4.0 International License, which permits use, sharing, adaptation, distribution and reproduction in any medium or format, as long as you give appropriate credit to the original author(s) and the source, provide a link to the Creative Commons license, and indicate if changes were made. The images or other third party material in this article are included in the article's Creative Commons license, unless indicated otherwise in a credit line to the material. If material is not included in the article's Creative Commons license and your intended use is not permitted by statutory regulation or exceeds the permitted use, you will need to obtain permission directly from the copyright holder. To view a copy of this license, visit <http://creativecommons.org/licenses/by/4.0/>.

Reprints and Permissions

About this article



Check for
updates

Cite this article

Yu, J., Tostanoski, L.H., Mercado, N.B. *et al.* Protective efficacy of Ad26.COV2.S against SARS-CoV-2 B.1.351 in macaques. *Nature* **596**, 423–427 (2021).
<https://doi.org/10.1038/s41586-021-03732-8>

Download citation

- Received: 15 April 2021
- Accepted: 16 June 2021
- Published: 23 June 2021
- Issue Date: 19 August 2021
- DOI: <https://doi.org/10.1038/s41586-021-03732-8>

Comments

By submitting a comment you agree to abide by our [Terms](#) and [Community Guidelines](#). If you find something abusive or that does not comply with our terms or guidelines please flag it as inappropriate.

[Download PDF](#)

Advertisement

This article was downloaded by **calibre** from <https://www.nature.com/articles/s41586-021-03732-8>

| [Section menu](#) | [Main menu](#) |

- Article
- [Published: 28 July 2021](#)

In silico saturation mutagenesis of cancer genes

- [Ferran Muiños](#) [ORCID: orcid.org/0000-0002-4651-4168](#)^{1, na1},
- [Francisco Martínez-Jiménez](#)^{1, na1},
- [Oriol Pich](#) [ORCID: orcid.org/0000-0002-1956-1882](#)¹,
- [Abel Gonzalez-Perez](#) [ORCID: orcid.org/0000-0002-8582-4660](#)^{1,2} &
- [Nuria Lopez-Bigas](#) ^{1,2,3}

[Nature](#) volume **596**, pages 428–432 (2021) [Cite this article](#)

- 8328 Accesses
- 300 Altmetric
- [Metrics details](#)

Subjects

- [Cancer genomics](#)

Abstract

Despite the existence of good catalogues of cancer genes^{1,2}, identifying the specific mutations of those genes that drive tumorigenesis across tumour types is still a largely unsolved problem. As a result, most mutations identified in cancer genes across tumours are of unknown significance to tumorigenesis³. We propose that the mutations observed in thousands of tumours—natural experiments testing their oncogenic potential replicated

across individuals and tissues—can be exploited to solve this problem. From these mutations, features that describe the mechanism of tumorigenesis of each cancer gene and tissue may be computed and used to build machine learning models that encapsulate these mechanisms. Here we demonstrate the feasibility of this solution by building and validating 185 gene–tissue-specific machine learning models that outperform experimental saturation mutagenesis in the identification of driver and passenger mutations. The models and their assessment of each mutation are designed to be interpretable, thus avoiding a black-box prediction device. Using these models, we outline the blueprints of potential driver mutations in cancer genes, and demonstrate the role of mutation probability in shaping the landscape of observed driver mutations. These blueprints will support the interpretation of newly sequenced tumours in patients and the study of the mechanisms of tumorigenesis of cancer genes across tissues.

Access options

Subscribe to Journal

Get full journal access for 1 year

\$199.00

only \$3.90 per issue

[Subscribe](#)

All prices are NET prices.

VAT will be added later in the checkout.

Tax calculation will be finalised during checkout.

Rent or Buy article

Get time limited or full article access on ReadCube.

from \$8.99

[Rent or Buy](#)

All prices are NET prices.

Additional access options:

- [Log in](#)
- [Access through your institution](#)
- [Learn about institutional subscriptions](#)

Fig. 1: Building and evaluating boostDM models.



Fig. 2: The features of driver mutations.

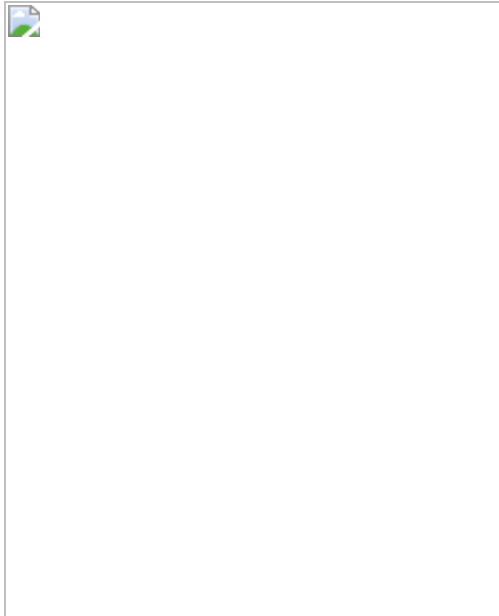


Fig. 3: Blueprints of driver mutations of cancer genes.

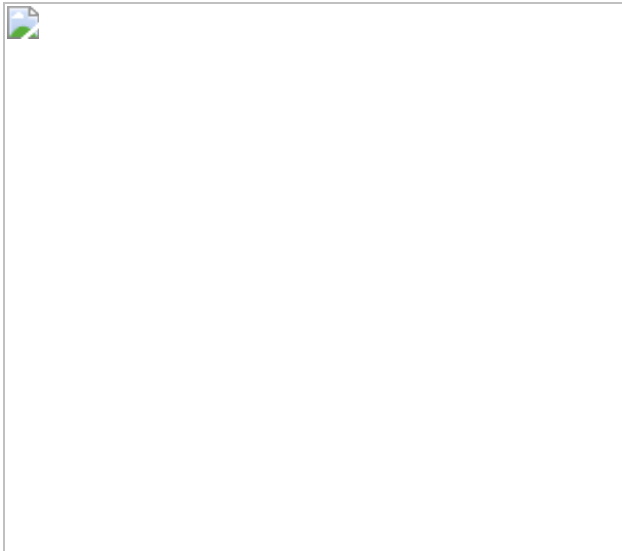
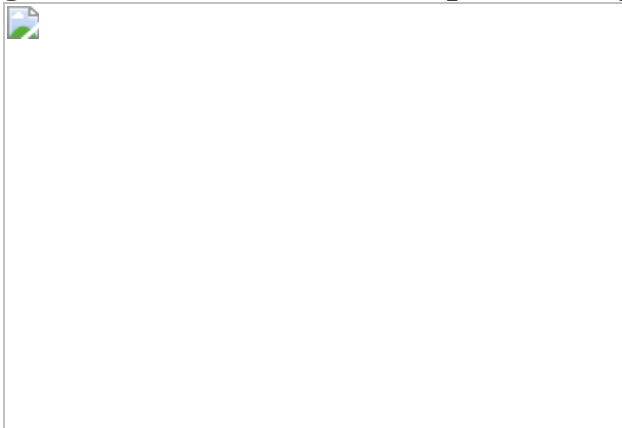


Fig. 4: The role of mutation probability in observed driver mutations.



Data availability

Cancer genes and their observed mutations across ~28,000 tumours of 66 cancer types (the starting point to train boostDM models) are available through IntOGen (<https://intogen.org/>). Mutational features computed across cancer genes, and positive and negative sets needed to train boostDM models, are available in a Zenodo repository (<https://doi.org/10.5281/zenodo.4813082>). Data source files point towards this repository. Blueprints may be browsed and downloaded at <https://www.intogen.org/boostdm/> ([including all protein sequence affecting mutations](#)), and newly sequenced tumours may be analysed using boostDM models via the Cancer Genome Interpreter

(<https://www.cancergenomeinterpreter.org/>). [Source data](#) are provided with this paper.

Code availability

All code needed to train and test boostDM models, as well as python scripts and jupyter notebooks necessary to reproduce all figures of the paper in conjunction with the data, are available in the aforementioned Zenodo repository (<https://doi.org/10.5281/zenodo.4813082>).

References

1. 1.

Sondka, Z. et al. The COSMIC Cancer Gene Census: describing genetic dysfunction across all human cancers. *Nat. Rev. Cancer* **18**, 696–705 (2018).

[CAS Article](#) [Google Scholar](#)

2. 2.

Martínez-Jiménez, F. et al. A compendium of mutational cancer driver genes. *Nat. Rev. Cancer* **20**, 555–572 (2020).

[Article](#) [Google Scholar](#)

3. 3.

Tamborero, D. et al. Cancer Genome Interpreter annotates the biological and clinical relevance of tumor alterations. *Genome Med.* **10**, 25 (2018).

[Article](#) [Google Scholar](#)

4. 4.

Alexandrov, L. B. et al. The repertoire of mutational signatures in human cancer. *Nature* **578**, 94–101 (2020).

[CAS](#) [Article](#) [ADS](#) [Google Scholar](#)

5. 5.

Gonzalez-Perez, A., Sabarinathan, R. & Lopez-Bigas, N. Local determinants of the mutational landscape of the human genome. *Cell* **177**, 101–114 (2019).

[CAS](#) [Article](#) [Google Scholar](#)

6. 6.

Lawrence, M. S. et al. Mutational heterogeneity in cancer and the search for new cancer-associated genes. *Nature* **499**, 214–218 (2013).

[CAS](#) [Article](#) [ADS](#) [Google Scholar](#)

7. 7.

Polak, P. et al. Cell-of-origin chromatin organization shapes the mutational landscape of cancer. *Nature* **518**, 360–364 (2015).

[CAS](#) [Article](#) [ADS](#) [Google Scholar](#)

8. 8.

Supek, F. & Lehner, B. Scales and mechanisms of somatic mutation rate variation across the human genome. *DNA Repair* **81**, 102647 (2019).

[CAS](#) [Article](#) [Google Scholar](#)

9. 9.

Martincorena, I. et al. Universal patterns of selection in cancer and somatic tissues. *Cell* **171**, 1029–1041.e21 (2017).

[CAS](#) [Article](#) [Google Scholar](#)

10. 10.

Sabarinathan, R. et al. The whole-genome panorama of cancer drivers. Preprint at <https://doi.org/10.1101/190330> (2017).

11. 11.

Kato, S. et al. Understanding the function-structure and function-mutation relationships of p53 tumor suppressor protein by high-resolution missense mutation analysis. *Proc. Natl Acad. Sci. USA* **100**, 8424–8429 (2003).

[CAS](#) [Article](#) [ADS](#) [Google Scholar](#)

12. 12.

Giacomelli, A. O. et al. Mutational processes shape the landscape of TP53 mutations in human cancer. *Nat. Genet.* **50**, 1381–1387 (2018).

[CAS](#) [Article](#) [Google Scholar](#)

13. 13.

Berger, A. H. et al. High-throughput phenotyping of lung cancer somatic mutations. *Cancer Cell* **30**, 214–228 (2016).

[CAS](#) [Article](#) [Google Scholar](#)

14. 14.

Kim, E. et al. Systematic functional interrogation of rare cancer variants identifies oncogenic alleles. *Cancer Discov.* **6**, 714–726 (2016).

[CAS](#) [Article](#) [Google Scholar](#)

15. 15.

Mighell, T. L., Evans-Dutson, S. & O'Roak, B. J. A saturation mutagenesis approach to understanding PTEN lipid phosphatase activity and genotype-phenotype relationships. *Am. J. Hum. Genet.* **102**, 943–955 (2018).

[CAS](#) [Article](#) [Google Scholar](#)

16. 16.

Boettcher, S. et al. A dominant-negative effect drives selection of *TP53* missense mutations in myeloid malignancies. *Science* **365**, 599–604 (2019).

[CAS](#) [Article](#) [ADS](#) [Google Scholar](#)

17. 17.

Chen, H. et al. Comprehensive assessment of computational algorithms in predicting cancer driver mutations. *Genome Biol.* **21**, 43 (2020).

[Article](#) [Google Scholar](#)

18. 18.

Tokheim, C. & Karchin, R. CHASMplus reveals the scope of somatic missense mutations driving human cancers. *Cell Syst.* **9**, 9–23.e8 (2019).

[CAS](#) [Article](#) [Google Scholar](#)

19. 19.

Vaser, R., Adusumalli, S., Leng, S. N., Sikic, M. & Ng, P. C. SIFT missense predictions for genomes. *Nat. Protocols* **11**, 1–9 (2016).

[CAS](#) [Article](#) [Google Scholar](#)

20. 20.

Adzhubei, I., Jordan, D. M. & Sunyaev, S. R. Predicting functional effect of human missense mutations using PolyPhen-2. *Curr. Protoc. Hum. Genet.* **76**, 7.20.1–7.20.41 (2013).

[Google Scholar](#)

21. 21.

Rentzsch, P., Witten, D., Cooper, G. M., Shendure, J. & Kircher, M. CADD: predicting the deleteriousness of variants throughout the human genome. *Nucleic Acids Res.* **47**, D886–D894 (2019).

[CAS Article](#) [Google Scholar](#)

22. 22.

Bandaru, P. et al. Deconstruction of the Ras switching cycle through saturation mutagenesis. *eLife* **6**, e27810 (2017).

[Article](#) [Google Scholar](#)

23. 23.

Shihab, H. A. et al. Predicting the functional, molecular, and phenotypic consequences of amino acid substitutions using hidden Markov models. *Hum. Mutat.* **34**, 57–65 (2013).

[CAS Article](#) [Google Scholar](#)

24. 24.

Carter, H., Douville, C., Stenson, P. D., Cooper, D. N. & Karchin, R. Identifying Mendelian disease genes with the variant effect scoring tool. *BMC Genomics* **14** (Suppl. 3), S3 (2013).

[Article](#) [Google Scholar](#)

25. 25.

Reva, B., Antipin, Y. & Sander, C. Predicting the functional impact of protein mutations: application to cancer genomics. *Nucleic Acids Res.* **39**, e118 (2011).

[CAS](#) [Article](#) [Google Scholar](#)

26. 26.

Landrum, M. J. et al. ClinVar: improving access to variant interpretations and supporting evidence. *Nucleic Acids Res.* **46**, D1062–D1067 (2018).

[CAS](#) [Article](#) [Google Scholar](#)

27. 27.

Chakravarty, D. et al. OncoKB: a precision oncology knowledge base. *JCO Precis. Oncol.* <https://doi.org/10.1200/PO.17.00011> (2017).

28. 28.

Pollard, K. S., Hubisz, M. J., Rosenbloom, K. R. & Siepel, A. Detection of nonneutral substitution rates on mammalian phylogenies. *Genome Res.* **20**, 110–121 (2010).

[CAS](#) [Article](#) [Google Scholar](#)

29. 29.

Hornbeck, P. V. et al. PhosphoSitePlus, 2014: mutations, PTMs and recalibrations. *Nucleic Acids Res.* **43**, D512–D520 (2015).

[CAS](#) [Article](#) [Google Scholar](#)

30. 30.

McLaren, W. et al. Deriving the consequences of genomic variants with the Ensembl API and SNP Effect Predictor. *Bioinformatics* **26**, 2069–2070 (2010).

[CAS](#) [Article](#) [Google Scholar](#)

31. 31.

Lundberg, S. M. & Lee, S.-I. A unified approach to interpreting model predictions. In *Advances in Neural Information Processing Systems 30* (eds. Guyon, I. et al.) 4765–4774 (Curran, 2017).

32. 32.

Ng, P. C. & Henikoff, S. SIFT: predicting amino acid changes that affect protein function. *Nucleic Acids Res.* **31**, 3812–3814 (2003).

[CAS](#) [Article](#) [Google Scholar](#)

33. 33.

Liu, X., Li, C., Mou, C., Dong, Y. & Tu, Y. dbNSFP v4: a comprehensive database of transcript-specific functional predictions and annotations for human nonsynonymous and splice-site SNVs. *Genome Med.* **12**, 103 (2020).

[CAS](#) [Article](#) [Google Scholar](#)

34. 34.

Chen, T. & Guestrin, C. XGBoost: a scalable tree boosting system. In *Proc. 22nd ACM SIGKDD Intl Conf. on Knowledge Discovery and Data Mining* 785–794 (Association for Computing Machinery, 2016).

35. 35.

Di Tommaso, P. et al. Nextflow enables reproducible computational workflows. *Nat. Biotechnol.* **35**, 316–319 (2017).

[Article](#) [Google Scholar](#)

36. 36.

Rosenthal, R., McGranahan, N., Herrero, J., Taylor, B. S. & Swanton, C. DeconstructSigs: delineating mutational processes in single tumors distinguishes DNA repair deficiencies and patterns of carcinoma evolution. *Genome Biol.* **17**, 31 (2016).

[Article](#) [Google Scholar](#)

37. 37.

Alexandrov, L. B. et al. Signatures of mutational processes in human cancer. *Nature* **500**, 415–421 (2013).

[CAS](#) [Article](#) [Google Scholar](#)

38. 38.

Tate, J. G. et al. COSMIC: the catalogue of somatic mutations in cancer. *Nucleic Acids Res.* **47**, D941–D947 (2019).

[CAS](#) [Article](#) [Google Scholar](#)

39. 39.

Pich, O. et al. Somatic and germline mutation periodicity follow the orientation of the DNA minor groove around nucleosomes. *Cell* **175**, 1074–1087.e18 (2018).

[CAS](#) [Article](#) [Google Scholar](#)

40. 40.

Hunter, J. D. Matplotlib: a 2D graphics environment. *Comput. Sci. Eng.* **9**, 90–95 (2007).

[Article](#) [Google Scholar](#)

41. 41.

Oliphant, T. E. *Guide to NumPy* (Open Source Book, 2006).

42. 42.

McKinney, W. *Python for Data Analysis: Data Wrangling with Pandas, NumPy, and IPython* (O'Reilly Media, 2017).

43. 43.

Virtanen, P. et al. SciPy 1.0: fundamental algorithms for scientific computing in Python. *Nat. Methods* **17**, 261–272 (2020).

[CAS](#) [Article](#) [Google Scholar](#)

44. 44.

Pedregosa, F. et al. Scikit-learn: machine learning in Python. *J. Mach. Learn. Res.* **12**, 2825–2830 (2011).

[MathSciNet](#) [MATH](#) [Google Scholar](#)

[Download references](#)

Acknowledgements

N.L.-B. acknowledges funding from the European Research Council (consolidator grant 682398) and ERDF/Spanish Ministry of Science, Innovation and Universities – Spanish State Research Agency/DamReMap Project (RTI2018-094095-B-I00) and Asociación Española Contra el Cáncer (AECC) (GC16173697BIGA). IRB Barcelona is a recipient of a Severo Ochoa Centre of Excellence Award from the Spanish Ministry of Economy and Competitiveness (MINECO; Government of Spain) and is supported by CERCA (Generalitat de Catalunya). O.P. is the recipient of a BIST PhD fellowship supported by the Secretariat for Universities and Research of the Ministry of Business and Knowledge of the Government of Catalonia, and the Barcelona Institute of Science and Technology (BIST). This publication and the underlying research were partly facilitated by the Cancer Genome Atlas project, the TARGET project and the Hartwig Medical Foundation and the Center for Personalized Cancer Treatment (CPCT), which have generated, analysed and made available data for this

purpose. The schematic DNA double helices in Extended Data Fig. 9a, e were created using Biorender (N.L.-B. premium membership).

Author information

Author notes

1. These authors contributed equally: Ferran Muiños, Francisco Martínez-Jiménez

Affiliations

1. Institute for Research in Biomedicine (IRB Barcelona), The Barcelona Institute of Science and Technology, Barcelona, Spain

Ferran Muiños, Francisco Martínez-Jiménez, Oriol Pich, Abel Gonzalez-Perez & Nuria Lopez-Bigas

2. Research Program on Biomedical Informatics, Universitat Pompeu Fabra, Barcelona, Spain

Abel Gonzalez-Perez & Nuria Lopez-Bigas

3. Institució Catalana de Recerca i Estudis Avançats (ICREA), Barcelona, Spain

Nuria Lopez-Bigas

Authors

1. Ferran Muiños

[View author publications](#)

You can also search for this author in [PubMed](#) [Google Scholar](#)

2. Francisco Martínez-Jiménez

[View author publications](#)

You can also search for this author in [PubMed](#) [Google Scholar](#)

3. Oriol Pich

[View author publications](#)

You can also search for this author in [PubMed](#) [Google Scholar](#)

4. Abel Gonzalez-Perez

[View author publications](#)

You can also search for this author in [PubMed](#) [Google Scholar](#)

5. Nuria Lopez-Bigas

[View author publications](#)

You can also search for this author in [PubMed](#) [Google Scholar](#)

Contributions

A.G.-P. and N.L.-B. conceptualized the project. F.M. conceived, implemented and tested boostDM. F.M.-J. participated in the implementation and testing of boostDM code. All authors participated in the conceptualization of boostDM. F.M. and O.P. benchmarked boostDM. F.M. computed the mutation probability bias. O.P. performed the analyses of mutational signatures. F.M.-J. performed the analysis of variants of unknown significance. F.M. and F.M.-J. designed the visualization of blueprints and radial plots to interpret the results of boostDM. F.M., F.M.-J. and O.P. prepared the figures. All authors participated in the design of the analyses and in the interpretation of the results. A.G.-P. and N.L.-B. drafted the manuscript. F.M., F.M.-J. and O.P. edited the manuscript. A.G.-P. and N.L.-B. supervised the project.

Corresponding authors

Correspondence to [Ferran Muiños](#) or [Abel Gonzalez-Perez](#) or [Nuria Lopez-Bigas](#).

Ethics declarations

Competing interests

The authors declare no competing interests.

Additional information

Peer review information *Nature* thanks Moritz Gerstung and the other, anonymous, reviewer(s) for their contribution to the peer review of this work. Peer reviewer reports are available.

Publisher's note Springer Nature remains neutral with regard to jurisdictional claims in published maps and institutional affiliations.

Extended data figures and tables

[Extended Data Fig. 1 Specific models encapsulate the features of driver mutations.](#)

a, Flow chart describing the construction of specific models from all possible cancer gene–tumour type combinations in the compendium of mutational cancer genes. **b**, Discovery index of ten cancer gene–tumour type combinations (trend of the number of unique mutations as a function of the size of bootstrapped subsets of samples). **c**, As in **b** for *TP53* across ten tumour types. **d**, Distribution of discovery index resulting from 100 iterations in each example (see [Methods](#)). **e**, As in **d** for *TP53* across 10 tumour types. **f**, Schematic depiction of the calculation of the F_{50} value used to measure the performance of the models. Fifty subsets of observed and synthetic mutations are randomly divided into training and test sets, and used in cross validations, from which a family of values of F_{50} are derived (Fig. [1c](#) and [e](#)). **g**, Fraction of mutations observed in 50 cancer gene–tissue combinations that are classified as drivers by the corresponding boostDM models. These include all mutations observed in the gene (including synonymous variants), not only those employed in the training. **h**,

Performance (median and IQR F_{50} of base classifiers) of 282 gene–tissue models as a function of the number of observed mutations. Boxplots: centre line, median; box limits, first and third quartiles; whiskers, lowest/highest data points at first quartile minus/plus $1.5 \times$ IQR.

Extended Data Fig. 2 The complexity of trained models.

a, Schematics depicting the calculation of the complexity index of models from the assessed compressibility of SHAP values for the 18 mutational features of a given model. Specifically, the smaller the number of principal components explaining a larger fraction of variance, the smaller the complexity index. **b**, Effect of reducing the size of observed mutations available for training on the performance and complexity index of three models. The circle and bars represent the median and IQR of F_{50} values computed from the cross-validation. As the size of the set of mutations available to train the models is reduced, the performance and complexity of built models decrease, demonstrating that as more cancer genomes are sequenced, more good-quality specific boostDM models will be within reach. **c**, Comparison of the performance of the cross-validation of *TP53* high-confidence models (median F_{50} and IQR of values obtained from the base classifiers) with models trained and tested on randomly drawn 90% of the samples of each tumour type, leaving the remaining 10% held out as external datasets for validation. **d**, Distribution of median F_{50} of cross-validation and re-trained models (as in **c**) for 155 cancer gene–tumour type combinations for which re-training with 90% of the original samples is possible, respecting the conditions set out in Extended Data Fig. [1a](#). Boxplots: centre line, median; box limits, first and third quartiles; whiskers, lowest/highest data points at first quartile minus/plus $1.5 \times$ IQR.

Extended Data Fig. 3 Performance of boostDM models on observed cancer mutations.

a, Comparison of performance of boostDM *TP53* models and saturation mutagenesis experiments (left) or computational tools (right) using PRCs. The PRCs represent median values of the base classifiers. **b**, Comparison of the performance of absolute classification (F_{50}) of *TP53* boostDM models

and two saturation mutagenesis experiments^{11,12} ([Supplementary Note](#)). F_{50} values represent the median of the base classifiers. The F_{50} values for all base classifiers of the colorectal model are compared to both experimental saturation mutagenesis assays (middle). BoostDM score and classification of six *TP53* driver mutations (experimentally validated in Boettcher et al.¹⁶) by 33 *TP53*-specific models. Points represent the scores from models and boxplots their distribution (bottom). **c**, PRCs (as in **a**) resulting from scoring *KRAS*, *HRAS* and *NRAS* mutations using boostDM models, a saturation mutagenesis experiment, and computational tools. **d**, Distribution of auPRC of *KRAS*, *HRAS* and *NRAS* boostDM models, a saturation mutagenesis experiment and bioinformatics tools across seven tumour types. **e**, As in **a**, **b** for *PTEN*. **f**, Comparison of performance (PRCs) of boostDM models and computational tools on mutations in several cancer genes. **g**, Comparison of the performance of absolute classification (F_{50} values) of boostDM models and the CHASMplus tool (using two different CHASMplus q values as threshold). **h**, Comparison of the performance of absolute classification (F_{50} values) of boostDM models and CHASMplus (q -value = 0). **i**, As in **h** for CADD score (CADD > 10). Boxplots: centre line, median; box limits, first and third quartiles; whiskers, lowest/highest data points at first quartile minus/plus 1.5× IQR.

[Extended Data Fig. 4 Performance of boostDM models on other sets of variants.](#)

a, Left, boostDM scores of rare experimentally validated oncogenic and benign variants^{13,14} and absolute performance of boostDM models (precision, recall and F_{50}). Right, performance of specific models. In parentheses, sizes of positive and negative sets of mutations. **b**, Performance of boostDM models (precision, recall and F_{50}) in the discrimination between pathogenic somatic and benign germline variants (ClinVar). **c**, Distribution of predicted drivers across polymorphisms with different allele frequencies across the population. The bars represent the effect size of a logistic regression of the categorical frequency of the polymorphisms on their boostDM classification. Bars with positive effect size represent genes (or pooled cancer genes, in red, with regression P value

indicated) across which very rare polymorphisms have an increased likelihood of being classified as drivers by boostDM models. The *P* value of the logistic regression corresponding to polymorphisms across all cancer genes is shown. Boxplots: centre line, median; box limits, first and third quartiles; whiskers, lowest/highest data points at first quartile minus/plus $1.5 \times \text{IQR}$.

Extended Data Fig. 5 Features of driver mutations.

a, Radial plots representing the contributions of different features (via SHAP values) to the classification of five selected driver mutations. **b**, Two-dimensional representation (via *t*-distributed stochastic neighbour embedding; *t*-SNE) of the combination of features relevant to the classification of all driver mutations across genes and tumour types. Mutations are coloured according to the mode of action (left) of the genes they affect, clusters (centre) resulting from the similarity of their SHAP values (Fig. 2d) and the complexity index (right) of the model used to classify them

[Source data.](#)

Extended Data Fig. 6 Blueprints of driver mutations of cancer genes.

a–d, Blueprints of potential driver mutations in *EGFR* across lung adenocarcinomas (**a**), in *KRAS* across pancreatic adenocarcinomas (**b**), in *RBI* across bladder tumours (**c**), and in *PIK3CA* across breast adenocarcinomas (**d**). Blueprints of all cancer genes with models are available at <https://intogen.org/boostdm>. **e**, Comparison of the fraction of potential driver mutations (from all possible) in tumour suppressors and oncogenes. The former exhibit significantly larger fractions of potential driver mutations than the latter. **f**, Distribution of potential driver mutations along the sequence of *TP53* across 33 tumour types. The dendrogram represents the similarity in distribution of potential driver mutations between malignancies. Boxplots: centre line, median; box limits, first and third quartiles; whiskers, lowest/highest data points at first quartile minus/plus $1.5 \times \text{IQR}$.

Extended Data Fig. 7 Mutational processes.

a, Left, distribution of mutation probability bias of observed versus unobserved mutations across all non-cancer genes. Middle, distribution of mutation probability bias of observed versus unobserved mutations (irrespective of their classification by boostDM models) across all cancer genes. Right, comparison of the distributions of mutation probability bias of all observed versus unobserved mutations in cancer genes (185) and non-cancer genes (3,035) and the distributions of mutation probability bias of potential driver observed versus unobserved mutations and all observed and unobserved mutations (irrespective of their classification by boostDM models) in cancer genes. Potential driver mutations show the lowest mutation probability bias of the three, which is evidence of the activity of selection. **b**, Selected driver mutations and the most likely mutational signature contributing them (colour) across tissues. The diameter of the circles is proportional to their frequency. **c**, Selected driver mutations across bladder adenocarcinomas are likely to be contributed by different mutational processes. The diameter of each circle represents the likelihood that the mutation is contributed by the corresponding (colour-coded) signature. **d**, Frequency (top) of different mutations affecting a section of the sequence of *PIK3CA* (bottom) in breast adenocarcinomas. Middle, the probability that each mutation is contributed by different signatures that are active in breast tumours. Boxplots: centre line, median; box limits, first and third quartiles; whiskers, lowest/highest data points at first quartile minus/plus $1.5 \times$ IQR.

Extended Data Fig. 8 General models.

a, Schematic representation of the process followed to build and select gene-specific models or gene–other tumour type models. If a high-confidence model is available for a cancer gene in a specific tumour type (that is, through completion of the process represented in Extended Data Fig. 1a), no general gene model is built to represent this gene–tumour type combination (*FBXW7* in uterine carcinosarcomas). We call these models gene–tumour type-specific. Conversely, if no specific model is available (*FBXW7* in oesophageal adenocarcinomas), a gene–general model is trained on mutations pooled from tumour types at the leaves of the oncotre

([Supplementary Note](#)). For example, a model of *FBXW7* across solid tumours may be trained on the features computed for the gene in oesophageal adenocarcinomas. If several gene-specific models can be built for the gene–tissue combination (for example, *FBXW7* across solid tumours and *FBXW7* across all cancer), the model built on a general tumour type that is closest to the tumour type in question and with F_{50} greater than 0.8 will be chosen. In total, 48 gene-specific models represent 72 gene–tumour type cases not covered by gene–tumour type-specific models. Finally, if neither a gene–tumour type-specific model nor a gene-specific model is available, a model trained on a different tumour type may be used (gene–other tumour type model). **b**, The types of model selected to classify the mutations observed in 20 cancer genes across 32 tumour types.

Extended Data Fig. 9 Interpretation of variants using boostDM models.

a, BoostDM models can be used to interpret the mutations observed in a newly sequenced tumour genome. Classifications and their explanation (represented via radial plots) may be useful for an expert with other ancillary information. **b**, Number of models of each type (gene–tumour type-specific, gene-specific or gene–other tumour type) selected across tumour types in a pan-cancer cohort of about 28,000 tumours to classify mutations observed in cancer genes (numbers below the plot). At least one model is available to classify mutations across 2,080 cancer gene–tissue combinations. **c**, Fraction of all mutations in cancer genes (variants of unknown significance, or VUS) that are covered by either type of model across tumour types. Fractions for the entire cohort appear in the right-hand barplot. Specifically, 14,757 (26%) are classified by specific boostDM models, while a further 2,588 (4%) may be classified by models trained by pooling mutations and features of several related tumour types; 20% more may be classified by a model trained on a different tumour type. In the entire cohort, 28,080 VUSs (about 50%) are covered for interpretation by at least one boostDM model. These are compared to the fraction of VUSs covered by interpretation using two curated datasets of known oncogenic mutations (ClinVar and OncoKB). **d**, Comparison of the number of driver mutations identified by boostDM per sample across the cohort with the number of excess mutations (over the expectation provided under the

hypothesis of neutrality) identified by a dNdS approach. The numbers identified are of the same order of magnitude as the numbers of driver mutations predicted by dNdScv. Points, median; bars, extending between 10th and 90th percentiles of the distribution. e, The interpretation of newly sequenced tumour genomes is implemented within the Cancer Genome Interpreter platform. VUSs not covered by boostDM models are interpreted following a simple rule-based approach (OncodriveMut).

Supplementary information

[Supplementary Information](#)

This file contains Supplementary Notes, Supplementary Figures 1-4 and Supplementary References – see Contents page for details.

[Reporting Summary](#)

[Supplementary Tables](#)

This file contains Supplementary Tables 1-2.

[Peer Review File](#)

Source data

[Source Data Extended Data Fig. 5](#)

Rights and permissions

[Reprints and Permissions](#)

About this article



Check for
updates

Cite this article

Muiños, F., Martínez-Jiménez, F., Pich, O. *et al.* In silico saturation mutagenesis of cancer genes. *Nature* **596**, 428–432 (2021).
<https://doi.org/10.1038/s41586-021-03771-1>

[Download citation](#)

- Received: 02 July 2020
- Accepted: 25 June 2021
- Published: 28 July 2021
- Issue Date: 19 August 2021
- DOI: <https://doi.org/10.1038/s41586-021-03771-1>

Comments

By submitting a comment you agree to abide by our [Terms](#) and [Community Guidelines](#). If you find something abusive or that does not comply with our terms or guidelines please flag it as inappropriate.

[Access through your institution](#)

[Change institution](#)

[Buy or subscribe](#)

Advertisement

| [Section menu](#) | [Main menu](#) |

- Article
- [Published: 28 July 2021](#)

BARD1 reads H2A lysine 15 ubiquitination to direct homologous recombination

- [Jordan R. Becker](#) [ORCID: orcid.org/0000-0002-6827-0002^{1,2}](#),
- [Gillian Clifford³](#),
- [Clara Bonnet](#) [ORCID: orcid.org/0000-0002-9197-485X^{1,2}](#),
- [Anja Groth](#) [ORCID: orcid.org/0000-0003-0577-1771^{4,5}](#),
- [Marcus D. Wilson³](#) &
- [J. Ross Chapman](#) [ORCID: orcid.org/0000-0002-6477-4254^{1,2,6}](#)

[Nature](#) volume **596**, pages 433–437 (2021) [Cite this article](#)

- 4658 Accesses
- 56 Altmetric
- [Metrics details](#)

Subjects

- [Double-strand DNA breaks](#)
- [Homologous recombination](#)
- [Non-homologous-end joining](#)

Abstract

Protein ubiquitination at sites of DNA double-strand breaks (DSBs) by RNF168 recruits BRCA1 and 53BP1^{1,2}, which are mediators of the homologous recombination and non-homologous end joining DSB repair pathways, respectively³. Non-homologous end joining relies on 53BP1 binding directly to ubiquitinated lysine 15 on H2A-type histones (H2AK15ub)^{4,5} (which is an RNF168-dependent modification⁶), but how RNF168 promotes BRCA1 recruitment and function remains unclear. Here we identify a tandem BRCT-domain-associated ubiquitin-dependent recruitment motif (BUDR) in BRCA1-associated RING domain protein 1 (BARD1) (the obligate partner protein of BRCA1) that, by engaging H2AK15ub, recruits BRCA1 to DSBs. Disruption of the BUDR of BARD1 compromises homologous recombination and renders cells hypersensitive to PARP inhibition and cisplatin. We further show that BARD1 binds nucleosomes through multivalent interactions: coordinated binding of H2AK15ub and unmethylated H4 lysine 20 by its adjacent BUDR and ankyrin repeat domains, respectively, provides high-affinity recognition of DNA lesions in replicated chromatin and promotes the homologous recombination activities of the BRCA1–BARD1 complex. Finally, our genetic epistasis experiments confirm that the need for BARD1 chromatin-binding activities can be entirely relieved upon deletion of RNF168 or 53BP1. Thus, our results demonstrate that by sensing DNA-damage-dependent and post-replication histone post-translation modification states, BRCA1–BARD1 complexes coordinate the antagonization of the 53BP1 pathway with promotion of homologous recombination, establishing a simple paradigm for the governance of the choice of DSB repair pathway.

Access options

Subscribe to Journal

Get full journal access for 1 year

\$199.00

only \$3.90 per issue

[Subscribe](#)

All prices are NET prices.
VAT will be added later in the checkout.
Tax calculation will be finalised during checkout.

Rent or Buy article

Get time limited or full article access on ReadCube.

from \$8.99

[Rent or Buy](#)

All prices are NET prices.

Additional access options:

- [Log in](#)
- [Access through your institution](#)
- [Learn about institutional subscriptions](#)

Fig. 1: Residues in the inter- $\beta 2'$ - $\beta 3'$ loop of the BRCT2 of BARD1 are essential for homologous recombination.

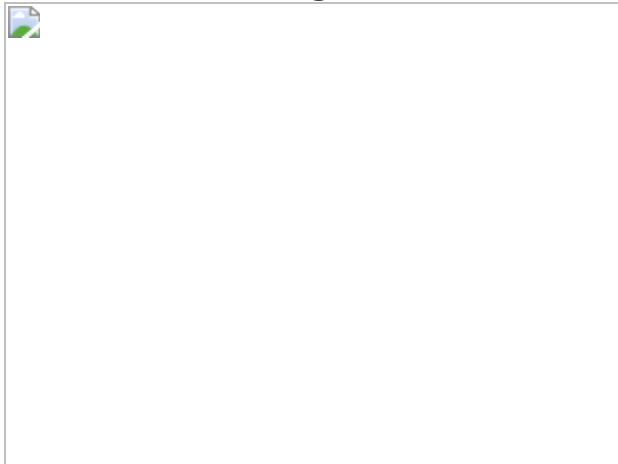


Fig. 2: ARD and BRCTs in BARD1 co-recruit BRCA1 during homologous recombination.

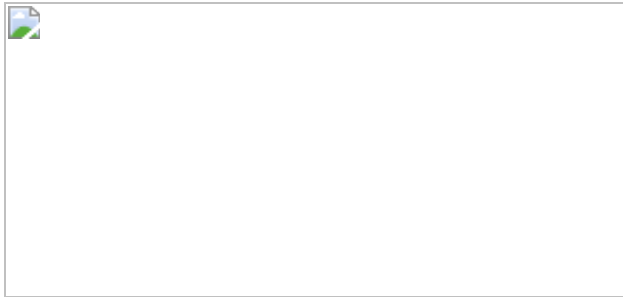


Fig. 3: Specific recognition of ubiquitinated lysine 15 on histone H2A by the BRCTs of BARD1.

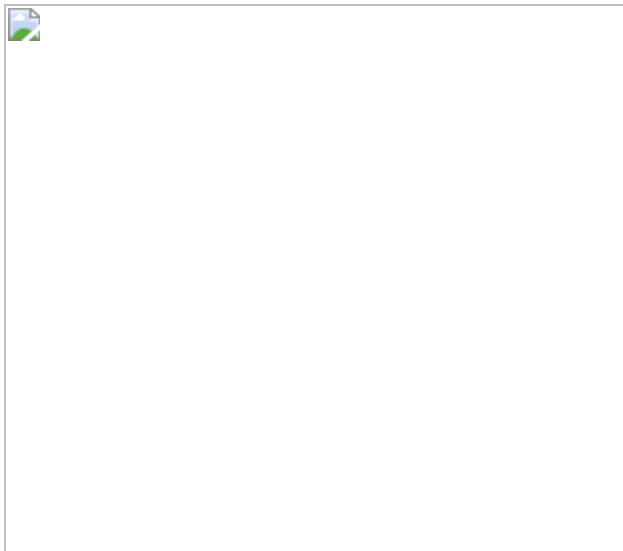
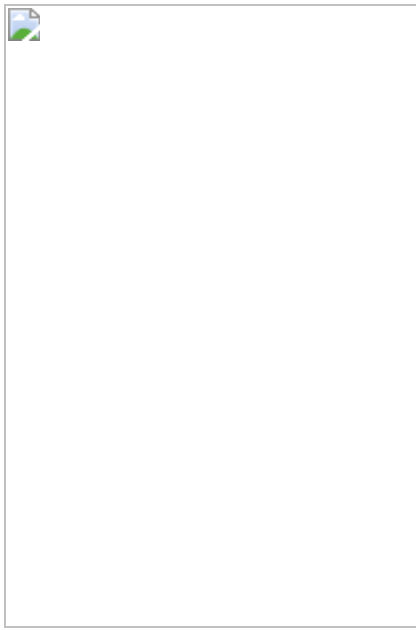


Fig. 4: Control of selection of DSB repair pathway by two histone-modification states and their readers.



Data availability

All data are available in the Article and its [Supplementary Information](#). [Source data](#) are provided with this paper.

References

1. 1.

Doil, C. et al. RNF168 binds and amplifies ubiquitin conjugates on damaged chromosomes to allow accumulation of repair proteins. *Cell* **136**, 435–446 (2009).

[CAS](#) [Article](#) [Google Scholar](#)

2. 2.

Stewart, G. S. et al. The RIDDLE syndrome protein mediates a ubiquitin-dependent signaling cascade at sites of DNA damage. *Cell* **136**, 420–434 (2009).

[CAS](#) [Article](#) [Google Scholar](#)

3. 3.

Hustedt, N. & Durocher, D. The control of DNA repair by the cell cycle. *Nat. Cell Biol.* **19**, 1–9 (2017).

[CAS](#) [Article](#) [Google Scholar](#)

4. 4.

Fradet-Turcotte, A. et al. 53BP1 is a reader of the DNA-damage-induced H2A Lys 15 ubiquitin mark. *Nature* **499**, 50–54 (2013).

[CAS](#) [Article](#) [ADS](#) [Google Scholar](#)

5. 5.

Wilson, M. D. et al. The structural basis of modified nucleosome recognition by 53BP1. *Nature* **536**, 100–103 (2016).

[CAS](#) [Article](#) [ADS](#) [Google Scholar](#)

6. 6.

Mattioli, F. et al. RNF168 ubiquitinates K13-15 on H2A/H2AX to drive DNA damage signaling. *Cell* **150**, 1182–1195 (2012).

[CAS](#) [Article](#) [Google Scholar](#)

7. 7.

Botuyan, M. V. et al. Structural basis for the methylation state-specific recognition of histone H4-K20 by 53BP1 and Crb2 in DNA repair. *Cell* **127**, 1361–1373 (2006).

[CAS](#) [Article](#) [Google Scholar](#)

8. 8.

Bothmer, A. et al. Regulation of DNA end joining, resection, and immunoglobulin class switch recombination by 53BP1. *Mol. Cell* **42**, 319–329 (2011).

[CAS](#) [Article](#) [Google Scholar](#)

9. 9.

Dimitrova, N., Chen, Y.-C. M., Spector, D. L. & de Lange, T. 53BP1 promotes non-homologous end joining of telomeres by increasing chromatin mobility. *Nature* **456**, 524–528 (2008).

[CAS](#) [Article](#) [ADS](#) [Google Scholar](#)

10. 10.

Nakamura, K. et al. H4K20me0 recognition by BRCA1–BARD1 directs homologous recombination to sister chromatids. *Nat. Cell Biol.* **21**, 311–318 (2019).

[CAS](#) [Article](#) [Google Scholar](#)

11. 11.

Manke, I. A., Lowery, D. M., Nguyen, A. & Yaffe, M. B. BRCT repeats as phosphopeptide-binding modules involved in protein targeting. *Science* **302**, 636–639 (2003).

[CAS](#) [Article](#) [ADS](#) [Google Scholar](#)

12. 12.

Yu, X., Chini, C. C. S., He, M., Mer, G. & Chen, J. The BRCT domain is a phospho-protein binding domain. *Science* **302**, 639–642 (2003).

[CAS](#) [Article](#) [ADS](#) [Google Scholar](#)

13. 13.

Glover, J. N. M., Williams, R. S. & Lee, M. S. Interactions between BRCT repeats and phosphoproteins: tangled up in two. *Trends Biochem. Sci.* **29**, 579–585 (2004).

[CAS](#) [Article](#) [Google Scholar](#)

14. 14.

Wu, Q., Jubb, H. & Blundell, T. L. Phosphopeptide interactions with BRCA1 BRCT domains: more than just a motif. *Prog. Biophys. Mol. Biol.* **117**, 143–148 (2015).

[Article](#) [Google Scholar](#)

15. 15.

Li, M. & Yu, X. Function of BRCA1 in the DNA damage response is mediated by ADP-ribosylation. *Cancer Cell* **23**, 693–704 (2013).

[CAS](#) [Article](#) [Google Scholar](#)

16. 16.

Billing, D. et al. The BRCT domains of the BRCA1 and BARD1 tumor suppressors differentially regulate homology-directed repair and stalled fork protection. *Mol. Cell* **72**, 127–139 (2018).

[CAS](#) [Article](#) [Google Scholar](#)

17. 17.

Natsume, T., Kiyomitsu, T., Saga, Y. & Kanemaki, M. T. Rapid protein depletion in human cells by auxin-inducible degron tagging with short homology donors. *Cell Rep.* **15**, 210–218 (2016).

[CAS](#) [Article](#) [Google Scholar](#)

18. 18.

Laufer, M. et al. Structural requirements for the BARD1 tumor suppressor in chromosomal stability and homology-directed DNA repair. *J. Biol. Chem.* **282**, 34325–34333 (2007).

[CAS](#) [Article](#) [Google Scholar](#)

19. 19.

Birrane, G., Varma, A. K., Soni, A. & Ladias, J. A. A. Crystal structure of the BARD1 BRCT domains. *Biochemistry* **46**, 7706–7712 (2007).

[CAS](#) [Article](#) [Google Scholar](#)

20. 20.

Sobhian, B. et al. RAP80 targets BRCA1 to specific ubiquitin structures at DNA damage sites. *Science* **316**, 1198–1202 (2007).

[CAS](#) [Article](#) [ADS](#) [Google Scholar](#)

21. 21.

Wang, B. et al. Abraxas and RAP80 form a BRCA1 protein complex required for the DNA damage response. *Science* **316**, 1194–1198 (2007).

[CAS](#) [Article](#) [ADS](#) [Google Scholar](#)

22. 22.

Kim, H., Chen, J. & Yu, X. Ubiquitin-binding protein RAP80 mediates BRCA1-dependent DNA damage response. *Science* **316**, 1202–1205 (2007).

[CAS](#) [Article](#) [ADS](#) [Google Scholar](#)

23. 23.

Sims, J. J. & Cohen, R. E. Linkage-specific avidity defines the lysine 63-linked polyubiquitin-binding preference of rap80. *Mol. Cell* **33**, 775–783 (2009).

[CAS](#) [Article](#) [Google Scholar](#)

24. 24.

Sato, Y. et al. Structural basis for specific recognition of Lys 63-linked polyubiquitin chains by tandem UIMs of RAP80. *EMBO J.* **28**, 2461–2468 (2009).

[CAS](#) [Article](#) [Google Scholar](#)

25. 25.

Hu, Y. et al. RAP80-directed tuning of BRCA1 homologous recombination function at ionizing radiation-induced nuclear foci. *Genes Dev.* **25**, 685–700 (2011).

[CAS](#) [Article](#) [Google Scholar](#)

26. 26.

Shao, G. et al. MERIT40 controls BRCA1-Rap80 complex integrity and recruitment to DNA double-strand breaks. *Genes Dev.* **23**, 740–754 (2009).

[CAS](#) [Article](#) [Google Scholar](#)

27. 27.

Zgheib, O., Pataky, K., Brugger, J. & Halazonetis, T. D. An oligomerized 53BP1 Tudor domain suffices for recognition of DNA double-strand breaks. *Mol. Cell. Biol.* **29**, 1050–1058 (2009).

[CAS](#) [Article](#) [Google Scholar](#)

28. 28.

Hu, Q., Botuyan, M. V., Cui, G., Zhao, D. & Mer, G. Mechanisms of ubiquitin-nucleosome recognition and regulation of 53BP1 chromatin recruitment by RNF168/169 and RAD18. *Mol. Cell* **66**, 473–487 (2017).

[CAS](#) [Article](#) [Google Scholar](#)

29. 29.

Cao, J. & Yan, Q. Histone ubiquitination and deubiquitination in transcription, DNA damage response, and cancer. *Front. Oncol.* **2**, 26 (2012).

[Article](#) [Google Scholar](#)

30. 30.

Densham, R. M. et al. Human BRCA1–BARD1 ubiquitin ligase activity counteracts chromatin barriers to DNA resection. *Nat. Struct. Mol. Biol.* **23**, 647–655 (2016).

[CAS](#) [Article](#) [Google Scholar](#)

31. 31.

Kalb, R., Mallory, D. L., Larkin, C., Huang, J. T. & Hiom, K. BRCA1 is a histone-H2A-specific ubiquitin ligase. *Cell Rep.* **8**, 999–1005 (2014).

[CAS](#) [Article](#) [Google Scholar](#)

32. 32.

Witus, S. R. et al. BRCA1/BARD1 site-specific ubiquitylation of nucleosomal H2A is directed by BARD1. *Nat. Struct. Mol. Biol.* **28**, 268–277 (2021).

[CAS](#) [Article](#) [Google Scholar](#)

33. 33.

Chapman, J. R., Sossick, A. J., Boulton, S. J. & Jackson, S. P. BRCA1-associated exclusion of 53BP1 from DNA damage sites underlies temporal control of DNA repair. *J. Cell Sci.* **125**, 3529–3534 (2012).

[CAS](#) [PubMed](#) [PubMed Central](#) [Google Scholar](#)

34. 34.

Pellegrino, S., Michelena, J., Teloni, F., Imhof, R. & Altmeyer, M. Replication-coupled dilution of H4K20me2 guides 53BP1 to pre-replicative chromatin. *Cell Rep.* **19**, 1819–1831 (2017).

[CAS](#) [Article](#) [Google Scholar](#)

35. 35.

Nacson, J. et al. BRCA1 mutation-specific responses to 53BP1 loss-induced homologous recombination and PARP inhibitor resistance. *Cell Rep.* **24**, 3513–3527 (2018).

[CAS](#) [Article](#) [Google Scholar](#)

36. 36.

Chen, J. et al. 53BP1 loss rescues embryonic lethality but not genomic instability of BRCA1 total knockout mice. *Cell Death Differ.* **27**, 2552–2567 (2020).

[CAS](#) [Article](#) [Google Scholar](#)

37. 37.

Dyer, P. N. et al. in *Methods in Enzymology* Vol. 375 (eds Allis, C. D. & Wu, C.) 23–44 (Academic, 2003).

38. 38.

Simon, M. D. et al. The site-specific installation of methyl-lysine analogs into recombinant histones. *Cell* **128**, 1003–1012 (2007).

[CAS](#) [Article](#) [Google Scholar](#)

39. 39.

Long, L., Furgason, M. & Yao, T. Generation of nonhydrolyzable ubiquitin-histone mimics. *Methods* **70**, 134–138 (2014).

[CAS](#) [Article](#) [Google Scholar](#)

40. 40.

Wilson, M. D. et al. Retroviral integration into nucleosomes through DNA looping and sliding along the histone octamer. *Nat. Commun.* **10**,

4189 (2019).

[Article](#) [ADS](#) [Google Scholar](#)

[Download references](#)

Acknowledgements

We thank all members of the laboratory of J.R.C. for discussions; D. Durocher for plasmid reagents; N. Johnson for discussions regarding unpublished data; and T. Humphrey for comments on the manuscript. This work was funded by a Cancer Research UK (CRUK) Career Development Fellowship (C52690/A19270 to J.R.C.), which previously provided salary support to J.R.B., and CRUK Oxford Centre funding (C5255/A18085 to J.R.B. and J.R.C.). J.R.B.’s salary is provided by a Ruth L. Kirschstein NRSA Individual Postdoctoral Fellowship (F32) (NIH/NCI - F32CA239339). The laboratory of J.R.C. is also supported by the Medical Research Council (MRC - MR/R017549/1), the MRC Molecular Haematology Unit (MRC MHU, UK) and the National Institute for Health Research (NIHR) Oxford Biomedical Research Centre (BRC). J.R.C. holds a Lister Institute Research Prize Fellowship. The Wellcome Centre for Human Genetics (WHG) is supported by Wellcome core award 090532/Z/09/Z. C.B. was sponsored by an ERASMUS+ internship. M.D.W.’s work is supported by the Wellcome Trust (210493), the MRC (T029471/1) and the University of Edinburgh. The Wellcome Centre for Cell Biology is supported by core funding from the Wellcome Trust (203149). A.G.’s research is supported by the Lundbeck Foundation (R198-2015-269 and R313-2019-448), the European Research Council (ERC CoG no. 724436) and Independent Research Fund Denmark (7016-00042B and 4092-00404B). Research at CPR is supported by the Novo Nordisk Foundation (NNF14CC0001). We also acknowledge the BHF Centre of Research Excellence, Oxford (RE/13/1/30181), and the WHG Cellular Imaging core for equipment access and support.

Author information

Affiliations

1. Medical Research Council (MRC) Molecular Haematology Unit, Weatherall Institute of Molecular Medicine, University of Oxford, Oxford, UK

Jordan R. Becker, Clara Bonnet & J. Ross Chapman

2. Wellcome Centre for Human Genetics, University of Oxford, Oxford, UK

Jordan R. Becker, Clara Bonnet & J. Ross Chapman

3. Wellcome Centre for Cell Biology, University of Edinburgh, Edinburgh, UK

Gillian Clifford & Marcus D. Wilson

4. The Novo Nordisk Center for Protein Research (CPR), Faculty of Health Sciences, University of Copenhagen, Copenhagen, Denmark

Anja Groth

5. Biotech Research and Innovation Centre (BRIC), Faculty of Health Sciences, University of Copenhagen, Copenhagen, Denmark

Anja Groth

6. NIHR Biomedical Research Centre, University of Oxford, Oxford, UK

J. Ross Chapman

Authors

1. Jordan R. Becker

[View author publications](#)

You can also search for this author in [PubMed](#) [Google Scholar](#)

2. Gillian Clifford

[View author publications](#)

You can also search for this author in [PubMed](#) [Google Scholar](#)

3. Clara Bonnet

[View author publications](#)

You can also search for this author in [PubMed](#) [Google Scholar](#)

4. Anja Groth

[View author publications](#)

You can also search for this author in [PubMed](#) [Google Scholar](#)

5. Marcus D. Wilson

[View author publications](#)

You can also search for this author in [PubMed](#) [Google Scholar](#)

6. J. Ross Chapman

[View author publications](#)

You can also search for this author in [PubMed](#) [Google Scholar](#)

Contributions

J.R.B. designed and analysed the majority of experiments, and supervised experiments performed by C.B. M.D.W. and G.C. undertook and analysed all *in vitro* nucleosome binding experiments. The project was initiated in collaboration with A.G. J.R.C. conceived and supervised the project, and designed and analysed experiments. J.R.B. and J.R.C. co-wrote the manuscript, with author input.

Corresponding author

Correspondence to [J. Ross Chapman](#).

Ethics declarations

Competing interests

A.G. is co-founder and CSO in Ankrin Therapeutics. No other authors have competing interests.

Additional information

Peer review information *Nature* thanks Daniel Durocher, Joanna Morris and the other, anonymous, reviewer(s) for their contribution to the peer review of this work.

Publisher's note Springer Nature remains neutral with regard to jurisdictional claims in published maps and institutional affiliations.

Extended data figures and tables

[Extended Data Fig. 1 BARD1 BRCT-mutated transgenes are stably expressed in *BARD1^{AID/AID}* HCT-116 cells.](#)

Related to Fig. 1. **a**, Immunoblots of whole-cell lysates collected at the indicated time points after IAA addition. Expression of the auxin-degron-targeting SCF-complex E3 ligase *Oryza sativa* TIR1 was induced using doxycycline ($2 \mu\text{g ml}^{-1}$), 24 h before the depletion of endogenous BARD1–AID protein with IAA (1 mM). Representative of two biological repeats. **b**, Immunoblot from whole-cell lysates of BARD1 BRCT mutants screened for olaparib sensitivity. **c**, Immunoblot of whole cell lysates from *BARD1^{AID/AID}* cells expressing the indicated transgenes. Cells were seeded in the presence of doxycycline ($2 \mu\text{g ml}^{-1}$) and IAA (1 mM) was added after 24 h. Lysates were collected at the indicated time points after IAA addition. Representative of two biological repeats.

Extended Data Fig. 2 ARD and BRCTs in BARD1 cooperate in recruiting BRCA1 to post-replicative chromatin during homologous recombination.

Related to Fig. 2. **a–c**, Survival of the indicated *BARD1*^{AID/AID} cell lines grown for 7 days without IAA in the presence of the indicated doses of olaparib or cisplatin. Cell lines were seeded in doxycycline (2 µg ml⁻¹) for 24 h before olaparib or cisplatin addition. Resazurin cell viability assay, *n* = 3 biological experiments, mean ± s.d. **d**, High-content immunofluorescent microscopy of BRCA1 IRIF in H4K20me0⁺ *BARD1*^{AID/AID} cells expressing the indicated transgenes. Cultures were grown in the presence of doxycycline (2 µg ml⁻¹) for 24 h before IAA (1 mM) addition, irradiated 2 h later, and fixed following irradiation. Scale bar, 5 µm. Representative of *n* = 2 biological experiments. **e**, Top, quantification of BRCA1 IRIF from **d**. Boxes indicate the 25th–75th percentiles with the median denoted, and whiskers indicate the 10th–90th percentiles. BRCA1 foci measurements are made for nuclei in the bottom quartile of H4K20me0 integrated staining intensity (≥ 172 nuclei per condition). Foci quantification and H4K20me0 integrated intensity measurements were performed with CellProfiler. Bottom, mean number of BRCA1 foci per cell from two independent experiments ± s.d. **f, g**, Same as in **d, e**, respectively, in *RAP80*^{-/-} cells. ≥ 179 nuclei per condition. **h, i**, Survival of the indicated *BARD1*^{AID/AID} cell lines grown for 7 days without IAA in the presence of olaparib. Cell lines were seeded in doxycycline (2 µg ml⁻¹) for 24 h before olaparib addition. Resazurin cell viability assay, *n* = 3 biological experiments, mean ± s.d.

[Source data](#).

Extended Data Fig. 3 Purification of BARD1 and 53BP1 fragments and assembly of modified nucleosomes.

Related to Fig. 3. **a**, Western blot of HA-tagged 53BP1–BARD1 fusion proteins used in **b** stably expressed in *BARD1*^{AID/AID} 53BP1^{-/-} cells. **b**, Top, model depicting the 53BP1–BARD1 fusion protein. The fusion is a chimera composed of the 53BP1 minimal focus-forming region (amino

acids 1220–1711) and BARD1 BRCTs (amino acids 555–777). Expressed form includes an N-terminal 2×HA–Flag epitope tag. Bottom, confocal immunofluorescent microscopy of 53BP1–BARD1 chimeric fusion proteins in irradiated *BARD1*^{AID/AID}*53BP1*^{−/−} cells. Cultures were grown in the presence of doxycycline (2 µg ml^{−1}) for 24 h before IAA (1 mM) addition and irradiated (5 Gy) 2 h later. Cells were fixed 2 h following irradiation. Scale bar, 10 µm. Representative of $n = 2$ biological experiments. **c**, SDS–PAGE gel, stained with InstantBlue protein stain of proteins used in Fig. [3a](#). **d**, SDS–PAGE gel, stained with InstantBlue protein stain of nucleosomes used in this study. **e**, Native gel electrophoresis of Widom 601 DNA in isolation and wrapped with nucleosomes used in this study. **f**, Representative gel images from EMSA experiments quantified in Fig. [3b](#). H2AKc15ub-modified, or H2AKc15ub- and H4Kc20me2-modified, nucleosomes (or control DNA) were incubated with increasing concentrations of 6×His–MBP–BARD1(ARD–BRCT) or GST–53BP1(TTD–UDR). Complexes were resolved by native PAGE and visualized using Diamond DNA stain. **g**, SDS–PAGE gel, stained with InstantBlue protein stain of BARD1 variants used in Fig. [3c](#). Neighbouring lanes were loaded with two different concentrations.

Extended Data Fig. 4 BRCA1 recruitment to IRIF is RNF168-dependent, but independent of PRC1 and BRCA1–BARD1 ubiquitin ligase activity.

Related to Fig. [4](#). **a**, Model indicating the three major known sites of ubiquitin attachment on histone H2A and the genetic manipulations used to block each individually in our experiments. *PRC1*^{−/−} indicates *RING1A*^{−/−}*RING1B*^{−/−} double knockout. **b**, Immunoblot of whole-cell lysates from *BARD1*^{AID/AID} parental cells and *RNF168*^{−/−} derivatives. Cells were seeded in the presence of doxycycline (2 µg ml^{−1}) and IAA (1 mM) was added after 24 h. Lysates were collected 8 h after IAA addition. Representative of two biological repeats. **c**, Immunofluorescent microscopy of *BARD1*^{AID/AID} parental cells and *RNF168*^{−/−} derivatives. Cultures were seeded 24 h before irradiation (5 Gy), and fixed 2 h later. Representative of $n = 3$ biological experiments. Scale bar, 10 µm. **d**, Quantification of BRCA1 and 53BP1 IRIF from **c**. Boxes indicate the 25th–75th percentiles with the median

denoted, and whiskers indicate the 10th–90th percentiles. BRCA1 foci measurements are made for EdU-positive nuclei. Foci quantification was performed using CellProfiler. Significance was determined by two-sided Kruskal–Wallis *H* test with Dunn’s correction for multiple comparisons. *** $P \leq 0.0001$. Representative of $n = 3$ biological replicates. **e**, Immunoblot of whole-cell lysates from *BARD1*^{AID/AID} parental cells and *RING1A*^{-/-}, *RING1B*^{-/-} and *RING1A*^{-/-}*RING1B*^{-/-} (denoted as *PRCI*^{-/-}) derivatives. Cultures were seeded 24 h before irradiation (10 Gy), and collected 2 h later. **f, g**, The indicated cell lines were treated as in **d**. Representative of $n = 3$ biological replicates

[Source data](#).

[Extended Data Fig. 5 The \$\beta\$ 2'- \$\beta\$ 3' loop and ARD counteract toxic 53BP1-dependent non-homologous end joining.](#)

Related to Fig. 4. **a**, Immunofluorescent microscopy of RAD51 IRIF in *BARD1*^{AID/AID} cells expressing the indicated transgenes. Cultures were grown in the presence of doxycycline (2 μ g ml⁻¹) for 24 h before IAA (1 mM) addition, irradiated 2 h later (5 Gy), and fixed with PFA 2 h following irradiation. Data were collected from the same experiment as Fig. 2*i, j*. Scale bar, 5 μ m. Representative of $n = 3$ biological experiments. **b**, Top, quantification of RAD51 foci per cell from **a**. Per condition, ≥ 255 nuclei. Boxes indicate the 25th–75th percentiles with the median denoted, and whiskers indicate the 10th–90th percentiles. Significance was determined by two-sided Kruskal–Wallis *H* test with Dunn’s correction for multiple comparisons. *** $P \leq 0.0001$, *** $P = 0.0003$. Data are from same experiment presented in Fig. 2*i, j*. *BARD1*^{AID/AID} cells expressing GST and *BARD1* are displayed in both for comparison. Representative of $n = 3$ biological experiments. Bottom, mean number of RAD51 IRIF from three independent biological experiments \pm s.d. **c, d**, Immunoblot of whole-cell lysates from *BARD1*^{AID/AID} (top) or *BARD1*^{AID/AID}*53BP1*^{-/-} (bottom) cells expressing the indicated transgenes. Cells were seeded in the presence of doxycycline (2 μ g ml⁻¹) and IAA (1 mM) was added after 24 h. Lysates were collected at the indicated time points after IAA addition. Representative of two biological repeats. **e–h**, Survival of the indicated

BARD1^{AID/AID} cell lines grown without IAA for 7 days in the presence of the indicated doses of olaparib or cisplatin. Cultures were seeded in doxycycline (2 µg ml⁻¹) and olaparib or cisplatin was added 24 h later. Survival was measured after 7 days by resazurin cell viability assay (*n* = 3 biological experiments) mean ± s.d

[Source data](#).

Supplementary information

[Supplementary Figure](#)

This file contains the uncropped blots shown in Fig. 3 and Extended Data Figs 1, 3, 4 and 5.

[Reporting Summary](#)

Source data

[Source Data Fig. 2](#)

[Source Data Fig. 4](#)

[Source Data Extended Data Fig. 2](#)

[Source Data Extended Data Fig. 4](#)

[Source Data Extended Data Fig. 5](#)

Rights and permissions

[Reprints and Permissions](#)

About this article



Check for
updates

Cite this article

Becker, J.R., Clifford, G., Bonnet, C. *et al.* BARD1 reads H2A lysine 15 ubiquitination to direct homologous recombination. *Nature* **596**, 433–437 (2021). <https://doi.org/10.1038/s41586-021-03776-w>

[Download citation](#)

- Received: 05 May 2020
- Accepted: 28 June 2021
- Published: 28 July 2021
- Issue Date: 19 August 2021
- DOI: <https://doi.org/10.1038/s41586-021-03776-w>

Comments

By submitting a comment you agree to abide by our [Terms](#) and [Community Guidelines](#). If you find something abusive or that does not comply with our terms or guidelines please flag it as inappropriate.

[Access through your institution](#)

[Change institution](#)

[Buy or subscribe](#)

Advertisement

| [Section menu](#) | [Main menu](#) |

- Article
- [Published: 28 July 2021](#)

Mechanisms of BRCA1–BARD1 nucleosome recognition and ubiquitylation

- [Qi Hu](#) [ORCID: orcid.org/0000-0003-3647-8471](#)¹ natl,
- [Maria Victoria Botuyan](#) [ORCID: orcid.org/0000-0002-6466-7432](#)¹ natl,
- [Debiao Zhao](#)¹ natl,
- [Gaofeng Cui](#)¹,
- [Elie Mer](#) [ORCID: orcid.org/0000-0003-2339-9547](#)¹ &
- [Georges Mer](#) [ORCID: orcid.org/0000-0002-1900-1578](#)^{1,2}

[Nature](#) volume **596**, pages 438–443 (2021) [Cite this article](#)

- 6505 Accesses
- 134 Altmetric
- [Metrics details](#)

Subjects

- [Cryoelectron microscopy](#)
- [Double-strand DNA breaks](#)
- [Nucleosomes](#)
- [Solution-state NMR](#)
- [Ubiquitylation](#)

An [Author Correction](#) to this article was published on 17 August 2021

This article has been [updated](#)

Abstract

The BRCA1–BARD1 tumour suppressor is an E3 ubiquitin ligase necessary for the repair of DNA double-strand breaks by homologous recombination^{1,2,3,4,5,6,7,8,9,10}. The BRCA1–BARD1 complex localizes to damaged chromatin after DNA replication and catalyses the ubiquitylation of histone H2A and other cellular targets^{11,12,13,14}. The molecular bases for the recruitment to double-strand breaks and target recognition of BRCA1–BARD1 remain unknown. Here we use cryo-electron microscopy to show that the ankyrin repeat and tandem BRCT domains in BARD1 adopt a compact fold and bind to nucleosomal histones, DNA and monoubiquitin attached to H2A amino-terminal K13 or K15, two signals known to be specific for double-strand breaks^{15,16}. We further show that RING domains¹⁷ in BRCA1–BARD1 orient an E2 ubiquitin-conjugating enzyme atop the nucleosome in a dynamic conformation, primed for ubiquitin transfer to the flexible carboxy-terminal tails of H2A and variant H2AX. Our work reveals a regulatory crosstalk in which recognition of monoubiquitin by BRCA1–BARD1 at the N terminus of H2A blocks the formation of polyubiquitin chains and cooperatively promotes ubiquitylation at the C terminus of H2A. These findings elucidate the mechanisms of BRCA1–BARD1 chromatin recruitment and ubiquitylation specificity, highlight key functions of BARD1 in both processes and explain how BRCA1–BARD1 promotes homologous recombination by opposing the DNA repair protein 53BP1 in post-replicative chromatin^{18,19,20,21,22}. These data provide a structural framework to evaluate BARD1 variants and help to identify mutations that drive the development of cancer.

Access options

Subscribe to Journal

Get full journal access for 1 year

\$199.00

only \$3.90 per issue

[Subscribe](#)

All prices are NET prices.

VAT will be added later in the checkout.

Tax calculation will be finalised during checkout.

Rent or Buy article

Get time limited or full article access on ReadCube.

from \$8.99

[Rent or Buy](#)

All prices are NET prices.

Additional access options:

- [Log in](#)
- [Access through your institution](#)
- [Learn about institutional subscriptions](#)

Fig. 1: Cryo-EM structure of the BRCA1^R–BARD1^R–UbcH5c–nucleosome complex.

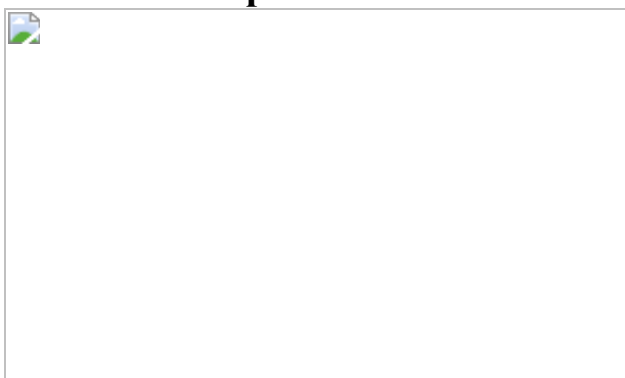


Fig. 2: Cryo-EM structure of BARD1 (ARD–BRCT) in complex with the nucleosome ubiquitylated at H2A K13 and K15.



Fig. 3: Intramolecular and intermolecular interfaces in the cryo-EM structure of BARD1 bound to the nucleosome ubiquitylated at H2A K13 and K15.

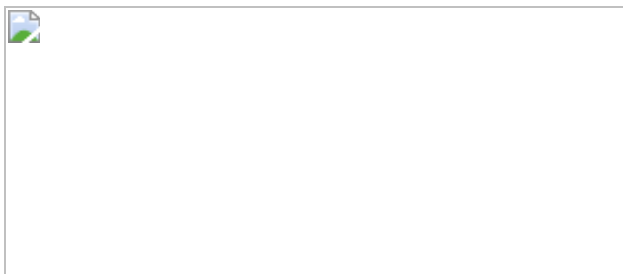
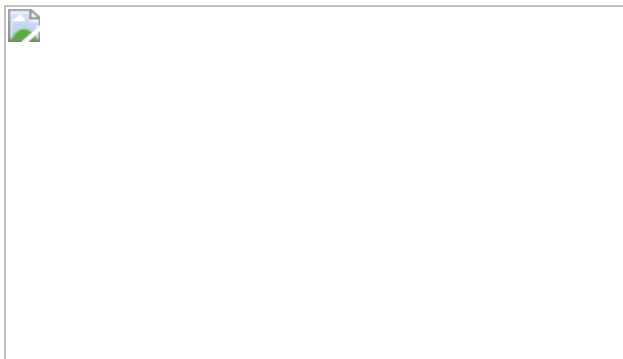


Fig. 4: BRCA1–BARD1 multivalent recognition of the NCP ubiquitylated at the H2A N terminus promotes NCP ubiquitylation at the H2A C terminus.



Data availability

The atomic coordinates and EM maps have been deposited in the Protein Data Bank under accession codes [7LYA](#) (NCP), [7LYB](#) (BRCA1^R–BARD1^R–UbcH5c–NCP) and [7LYC](#) (BARD1(ARD–BRCT)–NCP^{H2AK13ubK15ub}), and in the Electron Microscopy Data Bank under corresponding accession codes [EMD-23590](#), [EMD-23591](#) and [EMD-23592](#). Raw gels and blots are provided in Supplementary Figs. [1–6](#). Reagents from this study are available from the corresponding author on request.

Change history

- [**17 August 2021**](#)

[A Correction to this paper has been published:](#)
<https://doi.org/10.1038/s41586-021-03881-w>

References

1. 1.
Hall, J. M. et al. Linkage of early-onset familial breast cancer to chromosome 17q21. *Science* **250**, 1684–1689 (1990).
[ADS](#) [CAS](#) [PubMed](#) [Article](#) [Google Scholar](#)
2. 2.
Miki, Y. et al. A strong candidate for the breast and ovarian cancer susceptibility gene BRCA1. *Science* **266**, 66–71 (1994).
[ADS](#) [CAS](#) [PubMed](#) [Article](#) [Google Scholar](#)
3. 3.
Futreal, P. A. et al. BRCA1 mutations in primary breast and ovarian carcinomas. *Science* **266**, 120–122 (1994).
[ADS](#) [CAS](#) [PubMed](#) [Article](#) [Google Scholar](#)

4. 4.

Friedman, L. S. et al. Confirmation of BRCA1 by analysis of germline mutations linked to breast and ovarian cancer in ten families. *Nat. Genet.* **8**, 399–404 (1994).

[CAS](#) [PubMed](#) [Article](#) [Google Scholar](#)

5. 5.

Wu, L. C. et al. Identification of a RING protein that can interact in vivo with the BRCA1 gene product. *Nat. Genet.* **14**, 430–440 (1996).

[CAS](#) [PubMed](#) [Article](#) [Google Scholar](#)

6. 6.

Scully, R. et al. Association of BRCA1 with Rad51 in mitotic and meiotic cells. *Cell* **88**, 265–275 (1997).

[CAS](#) [PubMed](#) [Article](#) [Google Scholar](#)

7. 7.

Zhao, W. et al. BRCA1–BARD1 promotes RAD51-mediated homologous DNA pairing. *Nature* **550**, 360–365 (2017).

[ADS](#) [CAS](#) [PubMed](#) [PubMed Central](#) [Article](#) [Google Scholar](#)

8. 8.

Moynahan, M. E., Chiu, J. W., Koller, B. H. & Jasin, M. Brca1 controls homology-directed DNA repair. *Mol. Cell* **4**, 511–518 (1999).

[CAS](#) [PubMed](#) [Article](#) [Google Scholar](#)

9. 9.

Paull, T. T., Cortez, D., Bowers, B., Elledge, S. J. & Gellert, M. Direct DNA binding by Brca1. *Proc. Natl Acad. Sci. USA* **98**, 6086–6091 (2001).

[ADS](#) [CAS](#) [PubMed](#) [PubMed Central](#) [Article](#) [Google Scholar](#)

10. 10.

Tarsounas, M. & Sung, P. The antitumorigenic roles of BRCA1–BARD1 in DNA repair and replication. *Nat. Rev. Mol. Cell Biol.* **21**, 284–299 (2020).

[CAS](#) [PubMed](#) [PubMed Central](#) [Article](#) [Google Scholar](#)

11. 11.

Nakamura, K. et al. H4K20me0 recognition by BRCA1–BARD1 directs homologous recombination to sister chromatids. *Nat. Cell Biol.* **21**, 311–318 (2019).

[CAS](#) [PubMed](#) [PubMed Central](#) [Article](#) [Google Scholar](#)

12. 12.

Saredi, G. et al. H4K20me0 marks post-replicative chromatin and recruits the TONSL–MMS22L DNA repair complex. *Nature* **534**, 714–718 (2016).

[ADS](#) [CAS](#) [PubMed](#) [PubMed Central](#) [Article](#) [Google Scholar](#)

13. 13.

Kalb, R., Mallory, D. L., Larkin, C., Huang, J. T. & Hiom, K. BRCA1 is a histone-H2A-specific ubiquitin ligase. *Cell Rep.* **8**, 999–1005 (2014).

[CAS](#) [PubMed](#) [PubMed Central](#) [Article](#) [Google Scholar](#)

14. 14.

Densham, R. M. et al. Human BRCA1–BARD1 ubiquitin ligase activity counteracts chromatin barriers to DNA resection. *Nat. Struct. Mol. Biol.* **23**, 647–655 (2016).

[CAS](#) [PubMed](#) [PubMed Central](#) [Article](#) [Google Scholar](#)

15. 15.

Mattioli, F. et al. RNF168 ubiquitinates K13-15 on H2A/H2AX to drive DNA damage signaling. *Cell* **150**, 1182–1195 (2012).

[CAS](#) [PubMed](#) [Article](#) [PubMed Central](#) [Google Scholar](#)

16. 16.

Gatti, M. et al. A novel ubiquitin mark at the N-terminal tail of histone H2As targeted by RNF168 ubiquitin ligase. *Cell Cycle* **11**, 2538–2544 (2012).

[CAS](#) [PubMed](#) [PubMed Central](#) [Article](#) [Google Scholar](#)

17. 17.

Brzovic, P. S., Rajagopal, P., Hoyt, D. W., King, M. C. & Klevit, R. E. Structure of a BRCA1–BARD1 heterodimeric RING–RING complex. *Nat. Struct. Biol.* **8**, 833–837 (2001).

[CAS](#) [PubMed](#) [Article](#) [Google Scholar](#)

18. 18.

Bunting, S. F. et al. 53BP1 inhibits homologous recombination in *Brcal*-deficient cells by blocking resection of DNA breaks. *Cell* **141**, 243–254 (2010).

[CAS](#) [PubMed](#) [PubMed Central](#) [Article](#) [Google Scholar](#)

19. 19.

Bouwman, P. et al. 53BP1 loss rescues BRCA1 deficiency and is associated with triple-negative and BRCA-mutated breast cancers. *Nat. Struct. Mol. Biol.* **17**, 688–695 (2010).

[CAS](#) [PubMed](#) [PubMed Central](#) [Article](#) [Google Scholar](#)

20. 20.

Chapman, J. R., Sossick, A. J., Boulton, S. J. & Jackson, S. P. BRCA1-associated exclusion of 53BP1 from DNA damage sites underlies temporal control of DNA repair. *J. Cell Sci.* **125**, 3529–3534 (2012).

[CAS](#) [PubMed](#) [PubMed Central](#) [Article](#) [Google Scholar](#)

21. 21.

Pellegrino, S., Michelena, J., Teloni, F., Imhof, R. & Altmeyer, M. Replication-coupled dilution of H4K20me2 guides 53BP1 to pre-replicative chromatin. *Cell Rep.* **19**, 1819–1831 (2017).

[CAS](#) [PubMed](#) [PubMed Central](#) [Article](#) [Google Scholar](#)

22. 22.

Greenberg, R. A. Assembling a protective shield. *Nat. Cell Biol.* **20**, 862–863 (2018).

[CAS](#) [PubMed](#) [PubMed Central](#) [Article](#) [Google Scholar](#)

23. 23.

Liang, Y. et al. Structural analysis of BRCA1 reveals modification hotspot. *Sci. Adv.* **3**, e1701386 (2017).

[ADS](#) [PubMed](#) [PubMed Central](#) [Article](#) [CAS](#) [Google Scholar](#)

24. 24.

Hashizume, R. et al. The RING heterodimer BRCA1–BARD1 is a ubiquitin ligase inactivated by a breast cancer-derived mutation. *J. Biol. Chem.* **276**, 14537–14540 (2001).

[CAS](#) [PubMed](#) [Article](#) [PubMed Central](#) [Google Scholar](#)

25. 25.

Mallery, D. L., Vandenberg, C. J. & Hiom, K. Activation of the E3 ligase function of the BRCA1/BARD1 complex by polyubiquitin chains. *EMBO J.* **21**, 6755–6762 (2002).

[CAS](#) [PubMed](#) [PubMed Central](#) [Article](#) [Google Scholar](#)

26. 26.

Stewart, M. D. et al. BARD1 is necessary for ubiquitylation of nucleosomal histone H2A and for transcriptional regulation of estrogen metabolism genes. *Proc. Natl Acad. Sci. USA* **115**, 1316–1321 (2018).

[CAS](#) [PubMed](#) [PubMed Central](#) [Article](#) [Google Scholar](#)

27. 27.

Fradet-Turcotte, A. et al. 53BP1 is a reader of the DNA-damage-induced H2A Lys 15 ubiquitin mark. *Nature* **499**, 50–54 (2013).

[ADS](#) [CAS](#) [PubMed](#) [PubMed Central](#) [Article](#) [Google Scholar](#)

28. 28.

Wilson, M. D. et al. The structural basis of modified nucleosome recognition by 53BP1. *Nature* **536**, 100–103 (2016).

[ADS](#) [CAS](#) [PubMed](#) [Article](#) [Google Scholar](#)

29. 29.

Botuyan, M. V. et al. Structural basis for the methylation state-specific recognition of histone H4-K20 by 53BP1 and Crb2 in DNA repair. *Cell* **127**, 1361–1373 (2006).

[CAS](#) [PubMed](#) [PubMed Central](#) [Article](#) [Google Scholar](#)

30. 30.

Stewart, G. S. et al. The RIDDLE syndrome protein mediates a ubiquitin-dependent signaling cascade at sites of DNA damage. *Cell* **136**, 420–434 (2009).

[CAS](#) [PubMed](#) [Article](#) [Google Scholar](#)

31. 31.

Doil, C. et al. RNF168 binds and amplifies ubiquitin conjugates on damaged chromosomes to allow accumulation of repair proteins. *Cell* **136**, 435–446 (2009).

[CAS](#) [PubMed](#) [Article](#) [PubMed Central](#) [Google Scholar](#)

32. 32.

Becker, J. R. et al. BARD1 links histone H2A lysine-15 ubiquitination to initiation of BRCA1-dependent homologous recombination. Preprint at <https://doi.org/10.1101/2020.06.01.127951> (2020).

33. 33.

Luger, K., Mäder, A. W., Richmond, R. K., Sargent, D. F. & Richmond, T. J. Crystal structure of the nucleosome core particle at 2.8 Å resolution. *Nature* **389**, 251–260 (1997).

[ADS](#) [CAS](#) [PubMed](#) [Article](#) [PubMed Central](#) [Google Scholar](#)

34. 34.

McGinty, R. K., Henrici, R. C. & Tan, S. Crystal structure of the PRC1 ubiquitylation module bound to the nucleosome. *Nature* **514**, 591–596 (2014).

[ADS](#) [CAS](#) [PubMed](#) [PubMed Central](#) [Article](#) [Google Scholar](#)

35. 35.

Punjani, A. & Fleet, D. J. 3D variability analysis: resolving continuous flexibility and discrete heterogeneity from single particle cryo-EM. *J. Struct. Biol.* **213**, 107702 (2021).

[CAS](#) [PubMed](#) [Article](#) [PubMed Central](#) [Google Scholar](#)

36. 36.

Nakane, T., Kimanius, D., Lindahl, E. & Scheres, S. H. Characterisation of molecular motions in cryo-EM single-particle data by multi-body refinement in RELION. *eLife* **7**, e36861 (2018).

[PubMed](#) [PubMed Central](#) [Article](#) [Google Scholar](#)

37. 37.

Paull, T. T. et al. A critical role for histone H2AX in recruitment of repair factors to nuclear foci after DNA damage. *Curr. Biol.* **10**, 886–895 (2000).

[CAS](#) [PubMed](#) [Article](#) [PubMed Central](#) [Google Scholar](#)

38. 38.

Fox, D., III et al. Crystal structure of the BARD1 ankyrin repeat domain and its functional consequences. *J. Biol. Chem.* **283**, 21179–21186 (2008).

[CAS](#) [PubMed](#) [PubMed Central](#) [Article](#) [Google Scholar](#)

39. 39.

Li, M. & Yu, X. Function of BRCA1 in the DNA damage response is mediated by ADP-ribosylation. *Cancer Cell* **23**, 693–704 (2013).

[CAS](#) [PubMed](#) [PubMed Central](#) [Article](#) [Google Scholar](#)

40. 40.

Billing, D. et al. The BRCT domains of the BRCA1 and BARD1 tumor suppressors differentially regulate homology-directed repair and stalled fork protection. *Mol. Cell* **72**, 127–139.e8 (2018).

[CAS](#) [PubMed](#) [PubMed Central](#) [Article](#) [Google Scholar](#)

41. 41.

Eddins, M. J., Carlile, C. M., Gomez, K. M., Pickart, C. M. & Wolberger, C. Mms2–Ubc13 covalently bound to ubiquitin reveals the structural basis of linkage-specific polyubiquitin chain formation. *Nat. Struct. Mol. Biol.* **13**, 915–920 (2006).

[CAS](#) [PubMed](#) [Article](#) [Google Scholar](#)

42. 42.

Sobhian, B. et al. RAP80 targets BRCA1 to specific ubiquitin structures at DNA damage sites. *Science* **316**, 1198–1202 (2007).

[ADS](#) [CAS](#) [PubMed](#) [PubMed Central](#) [Article](#) [Google Scholar](#)

43. 43.

Wang, B. et al. Abraxas and RAP80 form a BRCA1 protein complex required for the DNA damage response. *Science* **316**, 1194–1198 (2007).

[ADS](#) [CAS](#) [PubMed](#) [PubMed Central](#) [Article](#) [Google Scholar](#)

44. 44.

Kim, H., Chen, J. & Yu, X. Ubiquitin-binding protein RAP80 mediates BRCA1-dependent DNA damage response. *Science* **316**, 1202–1205 (2007).

[ADS](#) [CAS](#) [PubMed](#) [Article](#) [Google Scholar](#)

45. 45.

Coleman, K. A. & Greenberg, R. A. The BRCA1–RAP80 complex regulates DNA repair mechanism utilization by restricting end resection. *J. Biol. Chem.* **286**, 13669–13680 (2011).

[CAS](#) [PubMed](#) [PubMed Central](#) [Article](#) [Google Scholar](#)

46. 46.

Hu, Y. et al. RAP80-directed tuning of BRCA1 homologous recombination function at ionizing radiation-induced nuclear foci. *Genes Dev.* **25**, 685–700 (2011).

[CAS](#) [PubMed](#) [PubMed Central](#) [Article](#) [Google Scholar](#)

47. 47.

Xu, M. et al. Partitioning of histone H3–H4 tetramers during DNA replication-dependent chromatin assembly. *Science* **328**, 94–98 (2010).

[ADS](#) [CAS](#) [PubMed](#) [Article](#) [Google Scholar](#)

48. 80.

Witus, S. R. et al. BRCA1/BARD1 site-specific ubiquitylation of nucleosomal H2A is directed by BARD1. *Nat. Struct. Mol. Biol.* **28**, 268–277 (2021).

[CAS](#) [PubMed](#) [PubMed Central](#) [Article](#) [Google Scholar](#)

49. 48.

Hu, Q., Botuyan, M. V., Cui, G., Zhao, D. & Mer, G. Mechanisms of ubiquitin -nucleosome recognition and regulation of 53BP1 chromatin recruitment by RNF168/169 and RAD18. *Mol. Cell* **66**, 473–487.e9 (2017).

[CAS](#) [PubMed](#) [PubMed Central](#) [Article](#) [Google Scholar](#)

50. 49.

Sundd, M., Iverson, N., Ibarra-Molero, B., Sanchez-Ruiz, J. M. & Robertson, A. D. Electrostatic interactions in ubiquitin: stabilization of carboxylates by lysine amino groups. *Biochemistry* **41**, 7586–7596 (2002).

[CAS](#) [PubMed](#) [Article](#) [Google Scholar](#)

51. 50.

Cui, G. et al. Structural basis of ubiquitin recognition by translesion synthesis DNA polymerase 1. *Biochemistry* **49**, 10198–10207 (2010).

[CAS](#) [PubMed](#) [Article](#) [PubMed Central](#) [Google Scholar](#)

52. 51.

Berndsen, C. E. & Wolberger, C. A spectrophotometric assay for conjugation of ubiquitin and ubiquitin-like proteins. *Anal. Biochem.* **418**, 102–110 (2011).

[CAS](#) [PubMed](#) [PubMed Central](#) [Article](#) [Google Scholar](#)

53. 52.

Bentley, M. L. et al. Recognition of UbcH5c and the nucleosome by the Bmi1/Ring1b ubiquitin ligase complex. *EMBO J.* **30**, 3285–3297 (2011).

[CAS](#) [PubMed](#) [PubMed Central](#) [Article](#) [Google Scholar](#)

54. 53.

Benirschke, R. C. et al. Molecular basis for the association of human E4B U box ubiquitin ligase with E2-conjugating enzymes UbcH5c and Ubc4. *Structure* **18**, 955–965 (2010).

[CAS](#) [PubMed](#) [PubMed Central](#) [Article](#) [Google Scholar](#)

55. 54.

Su, D. et al. Structure and histone binding properties of the Vps75–Rtt109 chaperone–lysine acetyltransferase complex. *J. Biol. Chem.* **286**, 15625–15629 (2011).

[CAS](#) [PubMed](#) [PubMed Central](#) [Article](#) [Google Scholar](#)

56. 55.

Su, D. et al. Structural basis for recognition of H3K56-acetylated histone H3–H4 by the chaperone Rtt106. *Nature* **483**, 104–107 (2012).

[ADS](#) [CAS](#) [PubMed](#) [PubMed Central](#) [Article](#) [Google Scholar](#)

57. 56.

Luger, K., Rechsteiner, T. J. & Richmond, T. J. Preparation of nucleosome core particle from recombinant histones. *Methods Enzymol.* **304**, 3–19 (1999).

[CAS](#) [PubMed](#) [Article](#) [PubMed Central](#) [Google Scholar](#)

58. 57.

Makde, R. D., England, J. R., Yennawar, H. P. & Tan, S. Structure of RCC1 chromatin factor bound to the nucleosome core particle. *Nature* **467**, 562–566 (2010).

[ADS](#) [CAS](#) [PubMed](#) [PubMed Central](#) [Article](#) [Google Scholar](#)

59. 58.

Matsumoto, S. et al. DNA damage detection in nucleosomes involves DNA register shifting. *Nature* **571**, 79–84 (2019).

[CAS](#) [PubMed](#) [PubMed Central](#) [Article](#) [Google Scholar](#)

60. 59.

Marks, B. D. et al. Multiparameter analysis of a screen for progesterone receptor ligands: comparing fluorescence lifetime and fluorescence polarization measurements. *Assay Drug Dev. Technol.* **3**, 613–622 (2005).

[CAS](#) [PubMed](#) [Article](#) [PubMed Central](#) [Google Scholar](#)

61. 60.

Shukla, A. K. et al. Visualization of arrestin recruitment by a G-protein-coupled receptor. *Nature* **512**, 218–222 (2014).

[ADS](#) [CAS](#) [PubMed](#) [PubMed Central](#) [Article](#) [Google Scholar](#)

62. 61.

Punjani, A., Rubinstein, J. L., Fleet, D. J. & Brubaker, M. A. cryoSPARC: algorithms for rapid unsupervised cryo-EM structure determination. *Nat. Methods* **14**, 290–296 (2017).

[CAS](#) [PubMed](#) [Article](#) [PubMed Central](#) [Google Scholar](#)

63. 62.

Scheres, S. H. RELION: implementation of a Bayesian approach to cryo-EM structure determination. *J. Struct. Biol.* **180**, 519–530 (2012).

[CAS](#) [PubMed](#) [PubMed Central](#) [Article](#) [Google Scholar](#)

64. 63.

Zivanov, J. et al. New tools for automated high-resolution cryo-EM structure determination in RELION-3. *eLife* **7**, e42166 (2018).

[PubMed](#) [PubMed Central](#) [Article](#) [Google Scholar](#)

65. 64.

Zheng, S. Q. et al. MotionCor2: anisotropic correction of beam-induced motion for improved cryo-electron microscopy. *Nat. Methods* **14**, 331–332 (2017).

[CAS](#) [PubMed](#) [PubMed Central](#) [Article](#) [Google Scholar](#)

66. 65.

Tan, Y. Z. et al. Addressing preferred specimen orientation in single-particle cryo-EM through tilting. *Nat. Methods* **14**, 793–796 (2017).

[CAS](#) [PubMed](#) [PubMed Central](#) [Article](#) [Google Scholar](#)

67. 66.

Liebschner, D. et al. Macromolecular structure determination using X-rays, neutrons and electrons: recent developments in Phenix. *Acta Crystallogr. D* **75**, 861–877 (2019).

[CAS](#) [Article](#) [Google Scholar](#)

68. 67.

Emsley, P. & Cowtan, K. Coot: model-building tools for molecular graphics. *Acta Crystallogr. D* **60**, 2126–2132 (2004).

[PubMed](#) [Article](#) [CAS](#) [PubMed Central](#) [Google Scholar](#)

69. 68.

Birrane, G., Varma, A. K., Soni, A. & Ladias, J. A. Crystal structure of the BARD1 BRCT domains. *Biochemistry* **46**, 7706–7712 (2007).

[CAS](#) [PubMed](#) [Article](#) [PubMed Central](#) [Google Scholar](#)

70. 69.

Edwards, R. A. et al. The BARD1 C-terminal domain structure and interactions with polyadenylation factor CstF-50. *Biochemistry* **47**, 11446–11456 (2008).

[CAS](#) [PubMed](#) [Article](#) [PubMed Central](#) [Google Scholar](#)

71. 70.

Vijay-Kumar, S., Bugg, C. E. & Cook, W. J. Structure of ubiquitin refined at 1.8 Å resolution. *J. Mol. Biol.* **194**, 531–544 (1987).

[CAS](#) [PubMed](#) [Article](#) [PubMed Central](#) [Google Scholar](#)

72. 71.

Chen, V. B. et al. MolProbity: all-atom structure validation for macromolecular crystallography. *Acta Crystallogr. D* **66**, 12–21 (2010).

[CAS](#) [PubMed](#) [Article](#) [Google Scholar](#)

73. 72.

Pettersen, E. F. et al. UCSF Chimera—a visualization system for exploratory research and analysis. *J. Comput. Chem.* **25**, 1605–1612 (2004).

[CAS](#) [Article](#) [Google Scholar](#)

74. 73.

Goddard, T. D. et al. UCSF ChimeraX: meeting modern challenges in visualization and analysis. *Protein Sci.* **27**, 14–25 (2018).

[CAS](#) [PubMed](#) [Article](#) [PubMed Central](#) [Google Scholar](#)

75. 74.

Delaglio, F. et al. NMRPipe: a multidimensional spectral processing system based on UNIX pipes. *J. Biomol. NMR* **6**, 277–293 (1995).

[CAS](#) [PubMed](#) [PubMed Central](#) [Article](#) [Google Scholar](#)

76. 75.

Lee, W., Tonelli, M. & Markley, J. L. NMRFAM-SPARKY: enhanced software for biomolecular NMR spectroscopy. *Bioinformatics* **31**, 1325–1327 (2015).

[PubMed](#) [PubMed Central](#) [Article](#) [Google Scholar](#)

77. 76.

Schanda, P., Kupce, E. & Brutscher, B. SOFAST-HMQC experiments for recording two-dimensional heteronuclear correlation spectra of proteins within a few seconds. *J. Biomol. NMR* **33**, 199–211 (2005).

[CAS](#) [PubMed](#) [Article](#) [Google Scholar](#)

78. 77.

Berendsen, H. J. C., van der Spoel, D. & van Drunen, R. GROMACS: a message-passing parallel molecular dynamics implementation. *Comput. Phys. Commun.* **91**, 43–56 (1995).

[ADS](#) [CAS](#) [Article](#) [Google Scholar](#)

79. 78.

Mukherjee, R. et al. Calmodulin regulates MGRN1–GP78 interaction mediated ubiquitin proteasomal degradation system. *FASEB J.* **33**, 1927–1945 (2019).

[CAS](#) [PubMed](#) [Article](#) [Google Scholar](#)

80. 79.

Landrum, M. J. et al. ClinVar: improving access to variant interpretations and supporting evidence. *Nucleic Acids Res.* **46**, D1062–D1067 (2018).

[CAS](#) [PubMed](#) [Article](#) [Google Scholar](#)

[Download references](#)

Acknowledgements

We are indebted to H. Scott, J. Myers and N. Meyer at the Pacific Northwest Cryo-EM Center (PNCC) for cryo-EM screenings and data collections, and to H. Scott for his invaluable advice throughout this project; we are grateful to A. Sundborger-Lunna, P.-L. Chiu and A. Alam for providing instrument access and for collaboration on other cryo-EM projects; and thank M. Schellenberg for generous instrument access and B. Bragantini for sharing unpublished findings. This research was supported by the US National Institutes of Health (NIH) grants R01 CA132878, R01 GM116829 and R35 GM136262 to G.M.; the Ovarian Cancer Research Alliance Liz Tilberis Award to M.V.B.; an Edward C. Kendall Fellowship in Biochemistry to Q.H.; and a Mayo Clinic Cancer Center and Center for Biomedical Discovery Eagles Fellowship to D.Z. Cryo-EM screenings and data collections were supported by the NIH grant U24GM129547 and performed at the PNCC at Oregon Health & Science University (OHSU) and accessed through the EMSL (grid.436923.9), a DOE Office of Science User Facility sponsored by the Office of Biological and Environmental Research.

Author information

Author notes

1. These authors contributed equally: Qi Hu, Maria Victoria Botuyan, Debiao Zhao

Affiliations

1. Department of Biochemistry and Molecular Biology, Mayo Clinic, Rochester, MN, USA

Qi Hu, Maria Victoria Botuyan, Debiao Zhao, Gaofeng Cui, Elie Mer & Georges Mer

2. Department of Cancer Biology, Mayo Clinic, Rochester, MN, USA

Georges Mer

Authors

1. Qi Hu

[View author publications](#)

You can also search for this author in [PubMed](#) [Google Scholar](#)

2. Maria Victoria Botuyan

[View author publications](#)

You can also search for this author in [PubMed](#) [Google Scholar](#)

3. Debiao Zhao

[View author publications](#)

You can also search for this author in [PubMed](#) [Google Scholar](#)

4. Gaofeng Cui

[View author publications](#)

You can also search for this author in [PubMed](#) [Google Scholar](#)

5. Elie Mer

[View author publications](#)

You can also search for this author in [PubMed](#) [Google Scholar](#)

6. Georges Mer

[View author publications](#)

You can also search for this author in [PubMed](#) [Google Scholar](#)

Contributions

G.M. conceived and supervised this work. G.M., Q.H., M.V.B. and D.Z. designed the experiments. Q.H. determined the cryo-EM structures. G.C. and Q.H. performed the NMR spectroscopy experiments. M.V.B. cloned the different constructs. M.V.B., D.Z., Q.H. and E.M. produced and purified all samples. M.V.B., Q.H., D.Z. and E.M. performed the functional assays. G.M. wrote the manuscript with major contributions from M.V.B. and Q.H., and input from all authors.

Corresponding author

Correspondence to [Georges Mer](#).

Ethics declarations

Competing interests

The authors declare no competing interests.

Additional information

Peer review information *Nature* thanks Daniel Durocher and the other, anonymous, reviewer(s) for their contribution to the peer review of this work. Peer reviewer reports are available.

Publisher's note Springer Nature remains neutral with regard to jurisdictional claims in published maps and institutional affiliations.

Extended data figures and tables

Extended Data Fig. 1 Site-specific ubiquitylation of nucleosomal histones H2A and H2AX by BRCA1^R-BARD1^R and UbcH5c.

a, Left: time-course ubiquitylation of nucleosomal H2A catalysed by BRCA1^R-BARD1^R-UbcH5c probed using NMR spectroscopy at 25 °C. Changes in signal intensities in the ¹H - ¹⁵N heteronuclear single quantum coherence (HSQC) spectra of the NCP harbouring ¹⁵N-labelled H2A-H2B were monitored. Right: overlay of the ¹H - ¹⁵N HSQC spectra before and 1,000 min after the start of the ubiquitylation reaction. Signals from remnant tag residues are labelled in black. **b**, Left: Coomassie-stained gels as readout of the ubiquitylation of wild-type (WT) NCP and NCPs harbouring double-point and triple-point mutations in H2A as indicated, using BRCA1^R-BARD1^R and UbcH5c. The lysine residues being monoubiquitylated are indicated in red. Right: quantification of the NCP ubiquitylation from $n = 3$ independent experiments. Bar graphs show the mean and s.d. for each data point. P values were calculated using a two-sample, two-tailed Student t -test; * $P < 0.05$, ** $P < 0.01$, *** $P < 0.001$, NS means not significant. Exact P values are provided in Supplementary Table 1. For gel source data, see Supplementary Fig. 3. **c**, Estimation by simulation of the conformational space sampled by fluctuating conformations of H2A, H2AX and UbcH5c in BRCA1^R-BARD1^R-UbcH5c-bound NCP (see [Methods](#)). The graph shows the ubiquitylation space accessible to the C-terminal tails of H2A (residues 118–129) and H2AX (residues 118–142). The red dashed line indicates a 3–5 Å distance between the thiol group of the active site cysteine C85 of UbcH5c and an acceptor lysine ε-amino group that allows ubiquitin transfer. The cyan shaded area below this line shows the histone residues accessible for ubiquitylation. A negative distance indicates that the distance between the sulfur atom of C85 and an α-carbon of H2A or H2AX can be short enough to permit ubiquitylation if the corresponding acceptor residue is a lysine. Only H2A and H2AX residues 123–129 and 123–142, respectively, satisfy this condition. Three of these residues are lysines in H2A (K125, K127 and K129) and H2AX (K127, K133 and K134). The conformational variability of UbcH5c was accounted for in these calculations. **d**, Left: amino acid sequence alignment of H2A and H2AX C-terminal tails and time-course

ubiquitylation of nucleosomal H2AX catalysed by BRCA1^R-BARD1^R-UbcH5c probed using NMR spectroscopy at 25 °C. Changes in signal intensities in the ¹H - ¹⁵N HSQC spectra of the NCP harbouring ¹⁵N-labelled H2AX-H2B were monitored. Right: overlay of the ¹H - ¹⁵N HSQC spectra before and 1,000 min after the start of the ubiquitylation reaction. Signals from remnant tag residues are labelled in black. e, Left: Coomassie-stained gels as readout of the ubiquitylation of the NCPs harbouring WT and double-point and triple-point mutations in H2AX as indicated, using BRCA1^R-BARD1^R and UbcH5c. The lysine residues being monoubiquitylated are indicated in red. Right: quantification of the NCP ubiquitylation from $n = 3$ independent experiments. Bar graphs show the mean and s.d. for each data point. P values were calculated using a two-sample, two-tailed Student *t*-test; * $P < 0.05$, ** $P < 0.01$, *** $P < 0.001$, NS means not significant. Exact P values are provided in Supplementary Table 1. For gel source data, see Supplementary Fig. 3.

Extended Data Fig. 2 Processing of cryo-EM data for the BRCA1^R-BARD1^R-UbcH5c-nucleosome complex.

a, Flow chart showing the stages of cryo-EM image processing. A total of 5,490 micrographs was collected on a Titan Krios 300 kV microscope and subjected to beam-induced motion correction. Data processing was done using cryoSPARC (v2.14) and RELION 3.0. The reconstruction of BRCA1^R-BARD1^R-UbcH5c-NCP with the highest resolution was selected for building an atomic model. Cryo-EM density reconstruction for the apo NCP (particles with no detectable density for BRCA1^R-BARD1^R-UbcH5c) was also carried out and is schematized by blue arrows. After 3D models were built, the r.m.s.d. over all NCP backbone atoms between the apo and complex states is 0.29 Å, not including the histone tails, which are not detected in the two densities. b, Multibody refinement and conformational dynamics analysis of BRCA1^R-BARD1^R-UbcH5c-NCP using RELION 3.1. Six principal components were used to describe motions among three rigid bodies corresponding to BRCA1^R-BARD1^R, UbcH5c and the NCP, with the two extreme conformations for each rigid body displayed in grey and blue. Rigid body movements of BRCA1^R-BARD1^R, UbcH5c and BRCA1^R-

BARD1^R-UbcH5c as a whole are indicated by orange, red and black curved arrows, respectively.

Extended Data Fig. 3 Validation of EM data and sample cryo-EM density for the BRCA1^R-BARD1^R-UbcH5c-nucleosome complex.

a, Local resolution distribution displayed on the reconstructed cryo-EM density map of the BRCA1^R-BARD1^R-UbcH5c-nucleosome complex. **b**, Top: Euler angle distribution generated using RELION 3.0 for the particles used in the final reconstruction. Each bar has a height and colour indicative of the number of particles (increasing from blue to red) in a defined orientation. Bottom: particle angular distribution heatmap generated using cryoSPARC (v2.14). **c**, Gold-standard Fourier shell correlation (GSFSC) curves for the final refinement in cryoSPARC (v2.14). Non-uniform refinement led to a 3.28 Å resolution map. **d**, Quantification of directional resolution anisotropy using a 3D Fourier shell correlation (3DFSC) algorithm in the 3DFSC server⁶⁵. **e**, Fourier shell correlation (FSC) curves between model-calculated density and the final cryo-EM density map generated using PHENIX. Resolution at FSC 0.5 is indicated. **f**, Representative regions of the cryo-EM density map for the nucleosome components (histones and DNA) of the complex. **g**, Representative regions of the cryo-EM density map for the BRCA1^R, BARD1^R and UbcH5c interfaces. The four-helix bundle of BRCA1^R-BARD1^R is highlighted on the left. **h**, Representative regions of the cryo-EM density map for the interfaces involving BRCA1^R and BARD1^R interactions with the nucleosome. The first and second representations from the left highlight BRCA1^R interaction with the nucleosome acidic patch and BARD1^R interaction with H2B, respectively.

Extended Data Fig. 4 Effects of structure-based mutations in BRCA1^R, BARD1^R and nucleosomal histone proteins H2A and H2B on ubiquitin conjugation to H2A.

a, Top: representative Coomassie-stained gel of time-course ubiquitylation assays of the NCP using UbcH5c and BRCA1^R-BARD1^R, wild type (WT) and with indicated mutations in BRCA1^R. Bottom: quantification of the NCP ubiquitylation from $n = 3$ independent experiments. Bar graphs show the mean and s.d. for each data point. P values were calculated using a two-sample, two-tailed Student t -test; * $P < 0.05$, ** $P < 0.01$, *** $P < 0.001$, NS means not significant. Exact P values are provided in Supplementary Table 1. For gel source data, see Supplementary Fig. 4. **b**, Left: representative Coomassie-stained gels of time-course ubiquitylation assays of WT and indicated H2A mutant NCPs by WT BRCA1^R-BARD1^R and UbcH5c. Right: quantification of the NCP ubiquitylation from $n = 3$ independent experiments. Bar graphs show the mean and s.d. for each data point. P values were calculated using a two-sample, two-tailed Student t -test; * $P < 0.05$, ** $P < 0.01$, *** $P < 0.001$, NS means not significant. Exact P values are provided in Supplementary Table 1. For gel source data, see Supplementary Fig. 4. **c**, Similar to b but using WT and indicated H2B mutations in the NCP. Exact P values are provided in Supplementary Table 1. For gel source data, see Supplementary Fig. 4. **d**, Top: representative Coomassie-stained gel of time-course ubiquitylation assays of the NCP using UbcH5c and BRCA1^R-BARD1^R, with the indicated mutations in BARD1^R. The ubiquitylation assay carried out with WT BRCA1^R-BARD1^R is shown in a. Bottom: quantification of the NCP ubiquitylation from $n = 3$ independent experiments. Bar graphs show the mean and s.d. for each data point. P values were calculated using a two-sample, two-tailed Student t -test; * $P < 0.05$, ** $P < 0.01$, *** $P < 0.001$, NS means not significant. Exact P values are provided in Supplementary Table 1. For gel source data, see Supplementary Fig. 4. **e**, Overlays of ^1H - ^{15}N HSQC NMR spectra of WT BRCA1^R-BARD1^R versus BRCA1^R-BARD1^R harbouring the BARD1^R P89A or W91A mutation. BRCA1^R and BARD1^R signals for which there was a change in chemical shift are labelled with BC and BD prefixes, respectively. The spectra demonstrate that the mutant proteins are well folded. The changes in chemical shifts for the W91A mutant map to residues close in space to the mutation site and can be attributed to altered ring current effect. These affected residues are coloured red and cyan on the NMR structure of BRCA1^R-BARD1^R. The multiple side-chain conformations of W91 in the NMR ensemble are displayed.

Extended Data Fig. 5 Structural and functional comparison of BRCA1^R-BARD1^R-UbcH5c and RING1B^R-BMI1^R-UbcH5c in association with the nucleosome and dynamics of the BRCA1^R-UbcH5c interaction.

a, Top: fluorescence polarization nucleosome-binding curves showing that BRCA1^R-BARD1^R and BRCA1^R-BARD1^R-UbcH5c bind to the NCP with similar affinities, lower than the affinity of RING1B^R-BMI1^R for the NCP. Data are mean and s.d. for each data point ($n = 3$ independent experiments). K_d values are indicated. Bottom: control binding curves for the RING1B^R-BMI1^R-NCP interaction at two salt concentrations. While our experiments were done with 50 mM NaCl, previously published experiments probing the RING1B^R-BMI1^R-NCP interaction were done with 100 mM NaCl. The higher RING1B^R-BMI1^R-NCP K_d that we obtained at 100 mM NaCl is similar to published data³⁴. **b**, Surface representations of the 3D structures of BRCA1^R-BARD1^R-UbcH5c-NCP and RING1B^R-BMI1^R-UbcH5c-NCP shown side-by-side with identical orientations of the NCP to highlight the radically different positioning of UbcH5c relative to the NCP in the two complexes. **c**, Left: representative Coomassie-stained gels of ubiquitylation assays of the NCP by UbcH5c and BRCA1^R-BARD1^R or RING1B^R-BMI1^R using wild-type (WT) proteins and the indicated UbcH5c and BRCA1^R mutants. Right: quantification of the NCP ubiquitylation from $n = 3$ independent experiments. Bar graphs show the mean and s.d. for each data point. P values were calculated using a two-sample, two-tailed Student t -test; * $P < 0.05$, ** $P < 0.01$, *** $P < 0.001$, NS means not significant. Exact P values are provided in Supplementary Table 1. For gel source data, see Supplementary Fig. 5. **d**, Top: overlay of the ^1H - ^{15}N NMR HSQC spectra of BRCA1^R-BARD1^R-UbcH5c (red), BRCA1^R-BARD1^R (cyan) and UbcH5c (gold) highlighting 12 residues (black labels) near the BRCA1^R-UbcH5c interface for which NMR signals disappear or become very weak due to exchange broadening upon formation of the BRCA1^R-BARD1^R-UbcH5c complex, consistent with motions on the microsecond-to-millisecond timescale. The signals of seven other UbcH5c residues (blue labels), distant from the interface with BRCA1^R, are also exchange

broadened because of allosteric effects as previously noted for other UbcH5c and related complexes^{53,78}. Bottom: surface representation of the BRCA1^R-BARD1^R-UbcH5c complex. The regions for which NMR signals disappear due to exchange broadening upon formation of the BRCA1^R-BARD1^R-UbcH5c complex are highlighted in yellow. The active site C85 of UbcH5c is shown in red.

Extended Data Fig. 6 Flow chart showing the stages of cryo-EM image processing for BARD1 (ARD-BRCT) in complex with the nucleosome ubiquitylated at H2A K13 and K15.

A total of 5,051 micrographs was collected on a Titan Krios 300 kV microscope and subjected to beam-induced motion correction. Data processing was done using cryoSPARC (v2.15). The reconstruction with the highest resolution was selected for building an atomic model.

Extended Data Fig. 7 Validation of EM data for BARD1 (ARD-BRCT) in complex with the nucleosome ubiquitylated at H2A K13 and K15.

a, Local resolution distribution displayed on the reconstructed cryo-EM density map of BARD1 (ARD-BRCT) bound to the H2AK13ubK15ub-containing NCP. **b**, Top: Euler angle distribution generated using RELION 3.0 for the particles used in the final reconstruction. Each bar has a height and colour indicative of the number of particles (increasing from blue to red) in a defined orientation. Bottom: particle angular distribution heatmap generated using cryoSPARC (v2.15). **c**, Gold-standard Fourier shell correlation (GSFSC) curves for the final refinement in cryoSPARC (v2.14). Non-uniform refinement led to a 2.94 Å resolution map. **d**, Quantification of directional resolution anisotropy using a 3D Fourier shell correlation (3DFSC) algorithm in the 3DFSC server⁶⁵. **e**, Fourier shell correlation (FSC) curves between model-calculated density and the final cryo-EM density map generated using PHENIX. Resolution at FSC 0.5 is indicated.

Extended Data Fig. 8 Sample cryo-EM density of the BARD1 (ARD-BRCT)-ubiquitylated nucleosome complex.

a, Representative regions of the cryo-EM density map for the different components (histones, DNA, BARD1-ARD, BARD1-BRCT and ubiquitin) of the complex. **b**, Representative regions of the cryo-EM density map highlighting global interfaces. **c**, Representative regions of the cryo-EM density map highlighting details of the various interfaces in the complex.

Extended Data Fig. 9 Ubiquitylated nucleosome-binding properties of BARD1 (ARD-BRCT) and associated inhibition of K63-mediated polyubiquitin chain formation.

a, Top: fluorescence polarization binding curves for BARD1 (ARD-BRCT), wild type (WT) and with the indicated mutations in the ARD domain, added to fluorescently labelled H2AK13ubK15ub-bearing NCP. GST was used as a control since BARD1 (ARD-BRCT) was GST-tagged. Data are mean and s.d. for each data point ($n = 3$ independent experiments). K_d values are indicated. ND, not determined. Bottom: similar to the top panel but with the indicated mutations in the tandem BRCT domain. **b**, Left: cryo-EM density near the ubiquitin isopeptide bond linkage in the structure of BARD1 (ARD-BRCT) in complex with H2AK13ubK15ub-bearing NCP. Only one ubiquitin molecule, interacting with BARD1 and NCP surfaces (that is, bound ubiquitin), is detected in the density. The weak and blurry density for the isopeptide bond region is compatible with the bound ubiquitin being linked to H2A K13 or H2A K15, suggesting binding exchange between H2AK13ub and H2AK15ub. Lack of density for a second ubiquitin molecule is probably due to flexibility in the unbound state. Right: ubiquitylation reaction of BARD1 (ARD-BRCT)-H2A-H2B fusion (labelled as Fusion) by RNF168, UbcH5c and UBA1 showing that there are two ubiquitin molecules attached to H2A (at K13 and K15) in the purified samples used for cryo-EM. Data shown are representative of $n = 5$ independent experiments. For gel source data, see Supplementary Fig. 6. **c**, Cryo-EM density at BARD1 BRCT-ubiquitin (left) and H2B-ubiquitin (right) interfaces in the structure of BARD1 (ARD-BRCT) bound to the NCP ubiquitylated at H2A K13 and K15. Ubiquitin K63 and E64 contact

BARD1 while ubiquitin I44, G47, H68 and V70 contact H2B. **d**, Location of the putative phosphate-binding site in the BARD1 tandem BRCT domain. The predicted phosphate-binding residues S575, G576, L618 and K619 are highlighted in red. **e**, Left: MMS2-Ubc13-catalysed polyubiquitin chain elongation at H2AK13ubK15ub in the NCP was inhibited by adding increasing amounts of GST-tagged BARD1 (ARD-BRCT), up to 16 times molar excess. Ubiquitylation efficiency was calculated as a ratio of the total intensities of the ubiquitylated products in that particular western blot (WB) lane against the lane with uninhibited MMS2-Ubc13 activity. Data are mean and s.d. for each data point from $n = 3$ independent experiments. P values were calculated using a two-sample, two-tailed Student t -test; $^*P < 0.05$, $^{**}P < 0.01$, $^{***}P < 0.001$, NS means not significant. Exact P values are provided in Supplementary Table 1. Right: representative WB images depicting inhibition of the MMS2-Ubc13-catalysed polyubiquitin chain elongation at H2AK13ubK15ub in the NCP by GST-tagged BARD1 (ARD-BRCT) but not by GST. The non-ubiquitylated NCP, used as a control substrate, shows chain elongation of free ubiquitin only by MMS2-Ubc13, uninhibited by BARD1 (ARD-BRCT). All lanes with ATP show formation of di-ubiquitin with additional chain extension by MMS2-Ubc13, demonstrating that BARD1 or GST do not inhibit MMS2-Ubc13. For gel source data, see Supplementary Fig. 6.

[Extended Data Fig. 10 BARD1 missense variants that map near the interdomain and intermolecular interfaces in the 3D structure of BARD1 \(ARD-BRCT\) in complex with the ubiquitylated nucleosome.](#)

The side chains of BARD1 (ARD-BRCT) residues for which missense variants were identified in patients with cancer are highlighted on the 3D structure of BARD1 (ARD-BRCT)-ubiquitylated NCP. Only variants that are located near the interdomain and intermolecular interfaces are shown with a different colour for each interface. The amino acids are labelled when they are directly involved in interdomain or intermolecular interactions in the BARD1 (ARD-BRCT)-ubiquitylated NCP structure. The variants were obtained from the ClinVar database maintained at the US National Institutes of Health⁷⁹.

Extended Data Table 1 Cryo-EM data collection, refinement and validation statistics

[Full size table](#)

Supplementary information

Supplementary Information

This file contains Supplementary Text, Supplementary Figures 1-7 and Supplementary Tables 1-2.

Reporting Summary

Peer Review File

Video 1

Three-dimensional variability analysis of the BRCA1-BARD1-UbcH5c-nucleosome complex.

Video 2

Multi-body analysis of the BRCA1-BARD1-UbcH5c-nucleosome complex.

Rights and permissions

Reprints and Permissions

About this article



Check for
updates

Cite this article

Hu, Q., Botuyan, M.V., Zhao, D. *et al.* Mechanisms of BRCA1–BARD1 nucleosome recognition and ubiquitylation. *Nature* **596**, 438–443 (2021). <https://doi.org/10.1038/s41586-021-03716-8>

[Download citation](#)

- Received: 17 September 2020
- Accepted: 10 June 2021
- Published: 28 July 2021
- Issue Date: 19 August 2021
- DOI: <https://doi.org/10.1038/s41586-021-03716-8>

Comments

By submitting a comment you agree to abide by our [Terms](#) and [Community Guidelines](#). If you find something abusive or that does not comply with our terms or guidelines please flag it as inappropriate.

[Access through your institution](#)

[Change institution](#)

[Buy or subscribe](#)

Advertisement

This article was downloaded by **calibre** from <https://www.nature.com/articles/s41586-021-03716-8>

- Article
- [Published: 04 August 2021](#)

Structure and mechanism of blood–brain-barrier lipid transporter MFSD2A

- [Chase A. P. Wood¹](#), ✉ [Email](#)
- [Jinru Zhang¹](#), ✉ [Email](#)
- [Deniz Aydin](#) [ORCID: orcid.org/0000-0002-2758-2480](#)^{1,2,3,4},
- [Yan Xu¹](#),
- [Benjamin J. Andreone⁵](#),
- [Urs H. Langen](#) [ORCID: orcid.org/0000-0002-7412-276X](#)⁵,
- [Ron O. Dror](#) [ORCID: orcid.org/0000-0002-6418-2793](#)^{1,2,3,4},
- [Chenghua Gu](#) [ORCID: orcid.org/0000-0002-4212-7232](#)⁵ &
- [Liang Feng](#) [ORCID: orcid.org/0000-0001-6171-2050](#)^{1,2}

[Nature](#) volume **596**, pages 444–448 (2021) [Cite this article](#)

- 4794 Accesses
- 18 Altmetric
- [Metrics details](#)

Subjects

- [Blood–brain barrier](#)
- [Cryoelectron microscopy](#)
- [Transporters](#)

Abstract

MFSD2A is a sodium-dependent lysophosphatidylcholine symporter that is responsible for the uptake of docosahexaenoic acid into the brain^{1,2}, which is crucial for the development and performance of the brain³. Mutations that affect MFSD2A cause microcephaly syndromes^{4,5}. The ability of MFSD2A to transport lipid is also a key mechanism that underlies its function as an inhibitor of transcytosis to regulate the blood–brain barrier^{6,7}. Thus, MFSD2A represents an attractive target for modulating the permeability of the blood–brain barrier for drug delivery. Here we report the cryo-electron microscopy structure of mouse MFSD2A. Our structure defines the architecture of this important transporter, reveals its unique extracellular domain and uncovers its substrate-binding cavity. The structure—together with our functional studies and molecular dynamics simulations—identifies a conserved sodium-binding site, reveals a potential lipid entry pathway and helps to rationalize *MFSD2A* mutations that underlie microcephaly syndromes. These results shed light on the critical lipid transport function of MFSD2A and provide a framework to aid in the design of specific modulators for therapeutic purposes.

Access options

Subscribe to Journal

Get full journal access for 1 year

\$199.00

only \$3.90 per issue

[Subscribe](#)

All prices are NET prices.

VAT will be added later in the checkout.

Tax calculation will be finalised during checkout.

Rent or Buy article

Get time limited or full article access on ReadCube.

from \$8.99

[Rent or Buy](#)

All prices are NET prices.

Additional access options:

- [Log in](#)
- [Access through your institution](#)
- [Learn about institutional subscriptions](#)

Fig. 1: Overall structure and substrate translocation pathway.

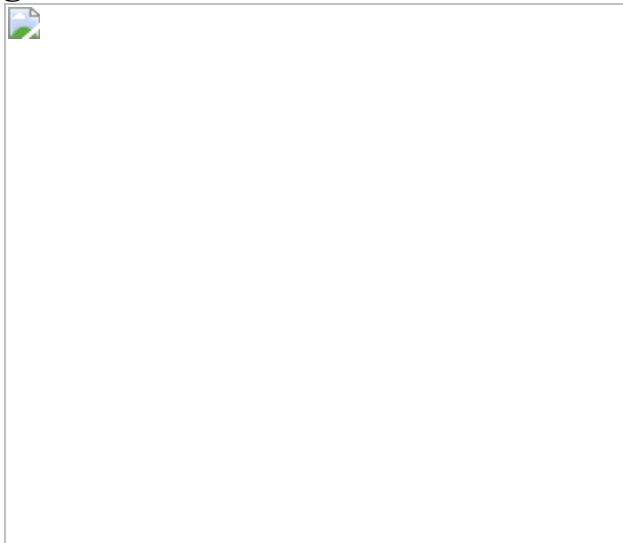


Fig. 2: Lateral side openings.

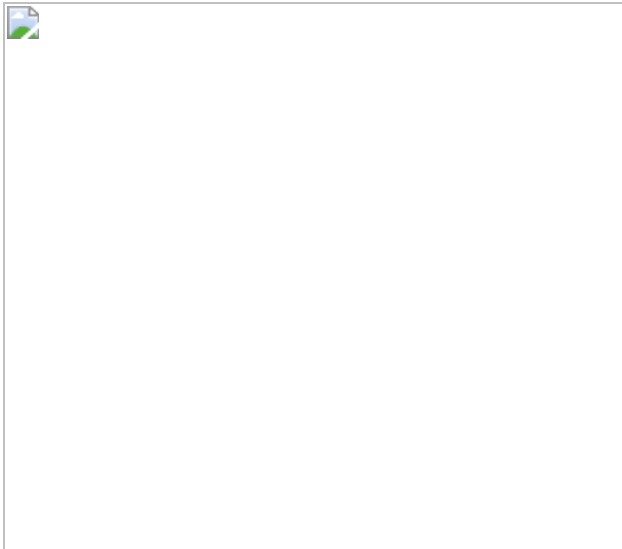
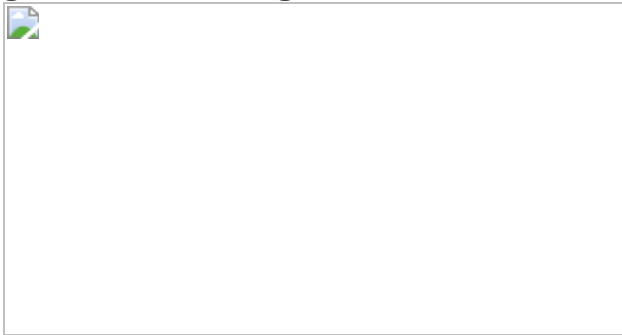


Fig. 3: Na^+ -binding site.



Data availability

The cryo-EM map has been deposited into the Electron Microscopy Data Bank (accession number [EMD-24252](#)). The coordinates have been deposited into the Protein Data Bank (accession number [7N98](#)). Any other relevant data are available from the corresponding author upon reasonable request.

References

1. 1.

Nguyen, L. N. et al. Mfsd2a is a transporter for the essential omega-3 fatty acid docosahexaenoic acid. *Nature* **509**, 503–506 (2014).

[CAS](#) [PubMed](#) [Article](#) [ADS](#) [PubMed Central](#) [Google Scholar](#)

2. 2.

Quek, D. Q., Nguyen, L. N., Fan, H. & Silver, D. L. Structural insights into the transport mechanism of the human sodium-dependent lysophosphatidylcholine transporter MFSD2A. *J. Biol. Chem.* **291**, 9383–9394 (2016).

[CAS](#) [PubMed](#) [PubMed Central](#) [Article](#) [Google Scholar](#)

3. 3.

Horrocks, L. A. & Yeo, Y. K. Health benefits of docosahexaenoic acid (DHA). *Pharmacol. Res.* **40**, 211–225 (1999).

[CAS](#) [PubMed](#) [Article](#) [PubMed Central](#) [Google Scholar](#)

4. 4.

Guemez-Gamboa, A. et al. Inactivating mutations in MFSD2A, required for omega-3 fatty acid transport in brain, cause a lethal microcephaly syndrome. *Nat. Genet.* **47**, 809–813 (2015).

[CAS](#) [PubMed](#) [PubMed Central](#) [Article](#) [Google Scholar](#)

5. 5.

Alakbarzade, V. et al. A partially inactivating mutation in the sodium-dependent lysophosphatidylcholine transporter MFSD2A causes a non-lethal microcephaly syndrome. *Nat. Genet.* **47**, 814–817 (2015).

[CAS](#) [PubMed](#) [Article](#) [PubMed Central](#) [Google Scholar](#)

6. 6.

Ben-Zvi, A. et al. Mfsd2a is critical for the formation and function of the blood-brain barrier. *Nature* **509**, 507–511 (2014).

[CAS](#) [PubMed](#) [PubMed Central](#) [Article](#) [ADS](#) [Google Scholar](#)

7. 7.

Andreone, B. J. et al. Blood-brain barrier permeability is regulated by lipid transport-dependent suppression of caveolae-mediated transcytosis. *Neuron* **94**, 581–594 (2017).

[CAS](#) [PubMed](#) [PubMed Central](#) [Article](#) [Google Scholar](#)

8. 8.

Andreone, B. J., Lacoste, B. & Gu, C. Neuronal and vascular interactions. *Annu. Rev. Neurosci.* **38**, 25–46 (2015).

[CAS](#) [PubMed](#) [PubMed Central](#) [Article](#) [Google Scholar](#)

9. 9.

Reese, T. S. & Karnovsky, M. J. Fine structural localization of a blood-brain barrier to exogenous peroxidase. *J. Cell Biol.* **34**, 207–217 (1967).

[CAS](#) [PubMed](#) [PubMed Central](#) [Article](#) [Google Scholar](#)

10. 10.

Brightman, M. W. & Reese, T. S. Junctions between intimately apposed cell membranes in the vertebrate brain. *J. Cell Biol.* **40**, 648–677 (1969).

[CAS](#) [PubMed](#) [PubMed Central](#) [Article](#) [Google Scholar](#)

11. 11.

Chow, B. W. & Gu, C. Gradual suppression of transcytosis governs functional blood-retinal barrier formation. *Neuron* **93**, 1325–1333 (2017).

[CAS](#) [PubMed](#) [PubMed Central](#) [Article](#) [Google Scholar](#)

12. 12.

Yang, Y. R. et al. Mfsd2a (major facilitator superfamily domain containing 2a) attenuates intracerebral hemorrhage-induced blood-brain barrier disruption by inhibiting vesicular transcytosis. *J. Am. Heart Assoc.* **6**, e005811 (2017).

[PubMed](#) [PubMed Central](#) [Google Scholar](#)

13. 13.

Yan, N. Structural biology of the major facilitator superfamily transporters. *Annu. Rev. Biophys.* **44**, 257–283 (2015).

[CAS](#) [PubMed](#) [Article](#) [PubMed Central](#) [Google Scholar](#)

14. 14.

Deng, D. et al. Crystal structure of the human glucose transporter GLUT1. *Nature* **510**, 121–125 (2014).

[CAS](#) [PubMed](#) [Article](#) [ADS](#) [PubMed Central](#) [Google Scholar](#)

15. 15.

Ethayathulla, A. S. et al. Structure-based mechanism for Na^+ /melibiose symport by MelB. *Nat. Commun.* **5**, 3009 (2014).

[PubMed](#) [Article](#) [ADS](#) [CAS](#) [PubMed Central](#) [Google Scholar](#)

16. 16.

Granell, M., León, X., Leblanc, G., Padrós, E. & Lórenz-Fonfría, V. A. Structural insights into the activation mechanism of melibiose permease by sodium binding. *Proc. Natl Acad. Sci. USA* **107**, 22078–22083 (2010).

[CAS](#) [PubMed](#) [PubMed Central](#) [Article](#) [ADS](#) [Google Scholar](#)

17. 17.

Harding, M. M. Metal-ligand geometry relevant to proteins and in proteins: sodium and potassium. *Acta Crystallogr. D* **58**, 872–874 (2002).

[PubMed](#) [Article](#) [CAS](#) [PubMed Central](#) [Google Scholar](#)

18. 18.

Vu, T. M. et al. Mfsd2b is essential for the sphingosine-1-phosphate export in erythrocytes and platelets. *Nature* **550**, 524–528 (2017).

[CAS](#) [PubMed](#) [Article](#) [ADS](#) [PubMed Central](#) [Google Scholar](#)

19. 19.

Kobayashi, N. et al. MFSD2B is a sphingosine 1-phosphate transporter in erythroid cells. *Sci. Rep.* **8**, 4969 (2018).

[PubMed](#) [PubMed Central](#) [Article](#) [ADS](#) [CAS](#) [Google Scholar](#)

20. 20.

Scala, M. et al. Biallelic *MFSD2A* variants associated with congenital microcephaly, developmental delay, and recognizable neuroimaging features. *Eur. J. Hum. Genet.* **28**, 1509–1519 (2020).

[CAS](#) [PubMed](#) [Article](#) [PubMed Central](#) [Google Scholar](#)

21. 21.

Riazuddin, S. et al. Exome sequencing of Pakistani consanguineous families identifies 30 novel candidate genes for recessive intellectual disability. *Mol. Psychiatry* **22**, 1604–1614 (2017).

[CAS](#) [PubMed](#) [Article](#) [PubMed Central](#) [Google Scholar](#)

22. 22.

Hu, H. et al. Genetics of intellectual disability in consanguineous families. *Mol. Psychiatry* **24**, 1027–1039 (2019).

[CAS](#) [PubMed](#) [Article](#) [PubMed Central](#) [Google Scholar](#)

23. 23.

Harel, T. et al. Homozygous mutation in *MFSD2A*, encoding a lysolipid transporter for docosahexanoic acid, is associated with microcephaly and hypomyelination. *Neurogenetics* **19**, 227–235 (2018).

[PubMed](#) [Article](#) [PubMed Central](#) [Google Scholar](#)

24. 24.

Drew, D. & Boudker, O. Shared molecular mechanisms of membrane transporters. *Annu. Rev. Biochem.* **85**, 543–572 (2016).

[CAS](#) [PubMed](#) [Article](#) [PubMed Central](#) [Google Scholar](#)

25. 25.

Deng, D. et al. Molecular basis of ligand recognition and transport by glucose transporters. *Nature* **526**, 391–396 (2015).

[CAS](#) [PubMed](#) [Article](#) [ADS](#) [PubMed Central](#) [Google Scholar](#)

26. 26.

Plummer, A. M., Culbertson, A. T. & Liao, M. The ABCs of sterol transport. *Annu. Rev. Physiol.* **83**, 153–181 (2021).

[CAS](#) [PubMed](#) [Article](#) [PubMed Central](#) [Google Scholar](#)

27. 27.

Andersen, J. P. et al. P4-ATPases as phospholipid flippases—structure, function, and enigmas. *Front. Physiol.* **7**, 275 (2016).

[PubMed](#) [PubMed Central](#) [Article](#) [Google Scholar](#)

28. 28.

Nikaido, H. Structure and mechanism of RND-type multidrug efflux pumps. *Adv. Enzymol.* **77**, 1–60 (2011).

[CAS](#) [PubMed](#) [PubMed Central](#) [Google Scholar](#)

29. 29.

Pardridge, W. M. The blood-brain barrier: bottleneck in brain drug development. *NeuroRx* **2**, 3–14 (2005).

[PubMed](#) [PubMed Central](#) [Article](#) [Google Scholar](#)

30. 30.

Banks, W. A. From blood-brain barrier to blood-brain interface: new opportunities for CNS drug delivery. *Nat. Rev. Drug Discov.* **15**, 275–292 (2016).

[CAS](#) [PubMed](#) [Article](#) [PubMed Central](#) [Google Scholar](#)

31. 31.

Goehring, A. et al. Screening and large-scale expression of membrane proteins in mammalian cells for structural studies. *Nat. Protocols* **9**, 2574–2585 (2014).

[CAS](#) [PubMed](#) [Article](#) [PubMed Central](#) [Google Scholar](#)

32. 32.

Tucker, D. F. et al. Isolation of state-dependent monoclonal antibodies against the 12-transmembrane domain glucose transporter 4 using

virus-like particles. *Proc. Natl Acad. Sci. USA* **115**, E4990–E4999 (2018).

[CAS](#) [PubMed](#) [PubMed Central](#) [Article](#) [Google Scholar](#)

33. 33.

Mastronarde, D. N. Automated electron microscope tomography using robust prediction of specimen movements. *J. Struct. Biol.* **152**, 36–51 (2005).

[PubMed](#) [PubMed Central](#) [Article](#) [Google Scholar](#)

34. 34.

Zheng, S. Q. et al. MotionCor2: anisotropic correction of beam-induced motion for improved cryo-electron microscopy. *Nat. Methods* **14**, 331–332 (2017).

[CAS](#) [PubMed](#) [PubMed Central](#) [Article](#) [ADS](#) [Google Scholar](#)

35. 35.

Zhang, K. Gctf: real-time CTF determination and correction. *J. Struct. Biol.* **193**, 1–12 (2016).

[CAS](#) [PubMed](#) [PubMed Central](#) [Article](#) [ADS](#) [Google Scholar](#)

36. 36.

Grant, T., Rohou, A. & Grigorieff, N. *cisTEM*, user-friendly software for single-particle image processing. *eLife* **7**, e35383 (2018).

[PubMed](#) [PubMed Central](#) [Article](#) [Google Scholar](#)

37. 37.

Scheres, S. H. A Bayesian view on cryo-EM structure determination. *J. Mol. Biol.* **415**, 406–418 (2012).

[CAS](#) [PubMed](#) [PubMed Central](#) [Article](#) [Google Scholar](#)

38. 38.

Punjani, A., Rubinstein, J. L., Fleet, D. J. & Brubaker, M. A. cryoSPARC: algorithms for rapid unsupervised cryo-EM structure determination. *Nat. Methods* **14**, 290–296 (2017).

[CAS](#) [PubMed](#) [PubMed Central](#) [Article](#) [Google Scholar](#)

39. 39.

Ru, H. et al. Molecular mechanism of V(D)J recombination from synaptic RAG1-RAG2 complex structures. *Cell* **163**, 1138–1152 (2015).

[CAS](#) [PubMed](#) [PubMed Central](#) [Article](#) [Google Scholar](#)

40. 40.

Emsley, P., Lohkamp, B., Scott, W. G. & Cowtan, K. Features and development of Coot. *Acta Crystallogr. D* **66**, 486–501 (2010).

[CAS](#) [PubMed](#) [PubMed Central](#) [Article](#) [Google Scholar](#)

41. 41.

Adams, P. D. et al. PHENIX: a comprehensive Python-based system for macromolecular structure solution. *Acta Crystallogr. D* **66**, 213–221 (2010).

[CAS](#) [PubMed](#) [PubMed Central](#) [Article](#) [Google Scholar](#)

42. 42.

Chen, V. B. et al. MolProbity: all-atom structure validation for macromolecular crystallography. *Acta Crystallogr. D* **66**, 12–21 (2010).

[CAS](#) [Article](#) [Google Scholar](#)

43. 43.

The PyMOL Molecular Graphics System v.2.0 (Schrödinger, 2017).

44. 44.

Pettersen, E. F. et al. UCSF Chimera—a visualization system for exploratory research and analysis. *J. Comput. Chem.* **25**, 1605–1612 (2004).

[CAS](#) [PubMed](#) [PubMed Central](#) [Article](#) [Google Scholar](#)

45. 45.

Minitab 17 Statistical Software (Minitab, 2010).

46. 46.

Ashkenazy, H. et al. ConSurf 2016: an improved methodology to estimate and visualize evolutionary conservation in macromolecules. *Nucleic Acids Res.* **44**, W344–W350 (2016).

[CAS](#) [PubMed](#) [PubMed Central](#) [Article](#) [Google Scholar](#)

47. 47.

Landau, M. et al. ConSurf 2005: the projection of evolutionary conservation scores of residues on protein structures. *Nucleic Acids Res.* **33**, W299–W302 (2005).

[CAS](#) [PubMed](#) [PubMed Central](#) [Article](#) [ADS](#) [Google Scholar](#)

48. 48.

Lomize, M. A., Lomize, A. L., Pogozheva, I. D. & Mosberg, H. I. OPM: orientations of proteins in membranes database. *Bioinformatics* **22**, 623–625 (2006).

[CAS](#) [Article](#) [Google Scholar](#)

49. 49.

Zhang, B. et al. Structure of a proton-dependent lipid transporter involved in lipoteichoic acids biosynthesis. *Nat. Struct. Mol. Biol.* **27**, 561–569 (2020).

[CAS](#) [PubMed](#) [PubMed Central](#) [Article](#) [Google Scholar](#)

50. 50.

Jacobson, M. P., Friesner, R. A., Xiang, Z. & Honig, B. On the role of the crystal environment in determining protein side-chain conformations. *J. Mol. Biol.* **320**, 597–608 (2002).

[CAS](#) [PubMed](#) [Article](#) [PubMed Central](#) [Google Scholar](#)

51. 51.

Zhang, L. & Hermans, J. Hydrophilicity of cavities in proteins. *Proteins* **24**, 433–438 (1996).

[CAS](#) [PubMed](#) [Article](#) [PubMed Central](#) [Google Scholar](#)

52. 52.

Betz, R. Dabble (v.2.6.3), <https://doi.org/10.5281/zenodo.836914> (2017).

53. 53.

Huang, J. et al. CHARMM36m: an improved force field for folded and intrinsically disordered proteins. *Nat. Methods* **14**, 71–73 (2017).

[CAS](#) [PubMed](#) [Article](#) [PubMed Central](#) [Google Scholar](#)

54. 54.

Klauda, J. B. et al. Update of the CHARMM all-atom additive force field for lipids: validation on six lipid types. *J. Phys. Chem. B* **114**, 7830–7843 (2010).

[CAS](#) [PubMed](#) [PubMed Central](#) [Article](#) [Google Scholar](#)

55. 55.

Guvenc, O., Hatcher, E. R., Venable, R. M., Pastor, R. W. & Mackerell, A. D. CHARMM additive all-atom force field for glycosidic linkages between hexopyranoses. *J. Chem. Theory Comput.* **5**, 2353–2370 (2009).

[CAS](#) [PubMed](#) [PubMed Central](#) [Article](#) [Google Scholar](#)

56. 56.

Case, D. A. et al. AMBER 2018 (University of California, 2018).

57. 57.

Hopkins, C. W., Le Grand, S., Walker, R. C. & Roitberg, A. E. Long-time-step molecular dynamics through hydrogen mass repartitioning. *J. Chem. Theory Comput.* **11**, 1864–1874 (2015).

[CAS](#) [PubMed](#) [Article](#) [PubMed Central](#) [Google Scholar](#)

58. 58.

Ryckaert, J., Ciccotti, G. & Berendsen, H. J. Numerical integration of the Cartesian equations of motion of a system with constraints: molecular dynamics of n-alkanes. *J. Comput. Phys.* **23**, 327–341 (1977).

[CAS](#) [Article](#) [ADS](#) [Google Scholar](#)

59. 59.

Roe, D. R. & Cheatham, T. E. III. PTraj and CPPtraj: software for processing and analysis of molecular dynamics trajectory data. *J. Chem. Theory Comput.* **9**, 3084–3095 (2013).

[CAS](#) [PubMed](#) [Article](#) [PubMed Central](#) [Google Scholar](#)

60. 60.

Humphrey, W., Dalke, A. & Schulten, K. VMD: visual molecular dynamics. *J. Mol. Graph.* **14**, 33–38, 27–28 (1996).

[CAS](#) [PubMed](#) [Article](#) [PubMed Central](#) [Google Scholar](#)

61. 61.

Vilas, J. L. et al. MonoRes: automatic and accurate estimation of local resolution for electron microscopy maps. *Structure* **26**, 337–344 (2018).

[CAS](#) [PubMed](#) [Article](#) [PubMed Central](#) [Google Scholar](#)

[Download references](#)

Acknowledgements

We thank L. Montabana and D.-H. Chen for help with EM data collection. This work was made possible by support from Stanford University, the Harold and Leila Y. Mathers Charitable Foundation and NIA DP2AG052940 to L.F., a Dean’s fellowship to J.Z., the EMBO Long-Term Fellowship ALTF 544-2019 to D.A., an EMBO long-term fellowship to U.H.L., the NIH DP1 NS092473 Pioneer Award, the NIH/NINDS R35NS116820 grant, the Blavatnik Biomedical Accelerator grant and the QFASTR grant from Harvard Medical School to C.G. The research of C.G. was also supported in part by a Faculty Scholar grant from the Howard Hughes Medical Institute.

Author information

Author notes

1. These authors contributed equally: Chase A. P. Wood, Jinru Zhang

Affiliations

1. Department of Molecular and Cellular Physiology, Stanford University School of Medicine, Stanford, CA, USA

Chase A. P. Wood, Jinru Zhang, Deniz Aydin, Yan Xu, Ron O. Dror & Liang Feng

2. Department of Structural Biology, Stanford University School of Medicine, Stanford, CA, USA

Deniz Aydin, Ron O. Dror & Liang Feng

3. Department of Computer Science, Stanford University, Stanford, CA, USA

Deniz Aydin & Ron O. Dror

4. Institute for Computational and Mathematical Engineering, Stanford University, Stanford, CA, USA

Deniz Aydin & Ron O. Dror

5. Department of Neurobiology, Harvard Medical School, Boston, MA, USA

Benjamin J. Andreone, Urs H. Langen & Chenghua Gu

Authors

1. Chase A. P. Wood

[View author publications](#)

You can also search for this author in [PubMed](#) [Google Scholar](#)

2. Jinru Zhang

[View author publications](#)

You can also search for this author in [PubMed](#) [Google Scholar](#)

3. Deniz Aydin

[View author publications](#)

You can also search for this author in [PubMed](#) [Google Scholar](#)

4. Yan Xu

[View author publications](#)

You can also search for this author in [PubMed](#) [Google Scholar](#)

5. Benjamin J. Andreone

[View author publications](#)

You can also search for this author in [PubMed](#) [Google Scholar](#)

6. Urs H. Langen

[View author publications](#)

You can also search for this author in [PubMed](#) [Google Scholar](#)

7. Ron O. Dror

[View author publications](#)

You can also search for this author in [PubMed](#) [Google Scholar](#)

8. Chenghua Gu

[View author publications](#)

You can also search for this author in [PubMed](#) [Google Scholar](#)

9. Liang Feng

[View author publications](#)

You can also search for this author in [PubMed](#) [Google Scholar](#)

Contributions

C.A.P.W. and J.Z. carried out biochemical, functional and cryo-EM studies. D.A. carried out and analysed molecular dynamics simulations under the guidance of R.O.D. Y.X. assisted with functional and biochemical studies. B.A. and U.H.L. characterized the scFv. C.G. supervised the generation and characterizations of scFv. L.F. directed biochemical, functional and structural studies. C.A.P.W., J.Z. and L.F. wrote the manuscript with input from all authors.

Corresponding author

Correspondence to [Liang Feng](#).

Ethics declarations

Competing interests

The authors declare no competing interests.

Additional information

Peer review information *Nature* thanks Diwakar Shukla and the other, anonymous, reviewer(s) for their contribution to the peer review of this work.

Publisher's note Springer Nature remains neutral with regard to jurisdictional claims in published maps and institutional affiliations.

Extended data figures and tables

[**Extended Data Fig. 1 Sequence alignment of MFSD2A and MFSD2B homologues.**](#)

Sequence alignments of MFSD2A and MFSD2B from *M. musculus* (Mm), *Homo sapiens* (Hs), *Danio rerio* (Dr), *Xenopus laevis* (Xl), *Bos taurus* (Bt) and *Gallus gallus* (Gg) are shown.

Extended Data Fig. 2 Biochemical and functional characterizations of MFSD2A.

a, Size-exclusion chromatography profile of MFSD2A. **b**, Size-exclusion chromatography profile of MFSD2A in complex with scFv. **c**, Representative SDS-PAGE gel of purified MFSD2A–scFv complex. This was carried out four times in independent experiments. **d**, Uptake activity of Q67H used for structural studies. Uptake activity was normalized to that of the wild type (mean \pm s.e.m., $n = 4$ biologically independent experiments). P values from one-way ANOVA followed by Tukey's post hoc multiple comparison test are indicated on bar chart.

Extended Data Fig. 3 Single-particle cryo-EM analysis of MFSD2A.

a, Representative cryo-EM image of MFSD2A. **b**, Two-dimensional class averages of MFSD2A in CryoSparc. **c**, The workflow of classification and refinement. **d**, Angle distributions of the particles for the final reconstruction. **e**, Local resolution of the MFSD2A map calculated by MonoRes⁶¹. **f**, FSC of the final reconstruction as a function of resolution. Orange, gold-standard FSC curve between two half-maps from masked MFSD2A, with indicated resolution at FSC = 0.143; blue, FSC curve between the final atomic model and the local map masked on MFSD2A only, with indicated resolution at FSC = 0.5. FSC calculation performed by SAMUEL (SAM script)³⁹.

Extended Data Fig. 4 Representative cryo-EM density maps of MFSD2A transmembrane helices.

Electron microscopy map density for 12 transmembrane helices of MFSD2A.

Extended Data Fig. 5 Conservation analysis of mouse MFSD2A structure.

Residues are coloured from variable to conserved according to the palette below the structure.

Extended Data Fig. 6 Intracellular elements of MFSD2A.

Ribbon representation (left) and cylindrical representation (right) of MFSD2A viewed from the intracellular side. N- and C-domains are coloured in cyan and green, respectively. IL, intracellular linker (orange). The helix after the last transmembrane helix is also coloured in orange.

Extended Data Fig. 7 Sodium-binding sites in molecular dynamics simulations.

a, Shaded regions (black, blue and green) indicate points in time during each simulation when a sodium ion was present at the Na1 site—in particular, points at which a sodium ion at a distance of 2–5 Å from the T95 side-chain oxygen formed a salt bridge with D92 and/or D96. **b**, Shaded regions indicate points in time during each simulation when a sodium ion was present at the Na2 site—in particular, points at which a sodium ion at a distance of 5–8 Å from the T95 side-chain oxygen formed a salt bridge with D92 and/or E159. Both **a** and **b** show data for simulations under three conditions. In the first two conditions (black and blue), a sodium ion is initially placed in the binding pocket at a position suggested by the potential coordination environment and the cryo-EM density, whereas in the third (black), no sodium ions are initially placed in the binding pocket. The first and third conditions (black and green) used a 9 Å nonbonded interaction cut-off, whereas the second (blue) used a 12 Å cut-off. Plots include equilibration as well as production phases of each simulation. **c**, Sodium positions from simulation no. 2 of the first condition (highlighted by red box), in which sodium ions bind simultaneously at the Na1 and Na2 sites. Positions of sodium bound at the Na1 site are shown as purple spheres, and positions of sodium bound at the Na2 site are shown as orange spheres (Methods). In this simulation, a Na^+ ion was initially placed at a position

proposed on the basis of the potential coordination environment and the cryo-EM density map, shown as a yellow circle. **d**, Sodium-binding sites in a representative frame from the same simulation. Sodium-coordinating residues are shown as sticks. Sodium bound at the Na1 site is shown as a purple sphere and sodium bound at the Na2 site is shown as an orange sphere. Oxygen atoms of water molecules are shown as red spheres.

[Extended Data Fig. 8 Structural mapping of disease-causing mutations.](#)

a, Close-up view of S170. S170 and R190 (sticks) are within hydrogen-bond distance. **b**, Zoomed-in view of S343, near the helical bend of TM8 that gives rise to lateral opening. **c**, Uptake activities of mouse MFSD2A variants with equivalent point mutations to human microcephaly-associated mutations. Uptake activities are normalized to that of the wild type (mean \pm s.e.m., $n = 6$ biologically independent experiments). P values from one-way ANOVA followed by Tukey's post hoc multiple comparison test are indicated on bar chart.

[Extended Data Fig. 9 Structure of MFSD2A in complex with scFv.](#)

a, The cryo-EM map of the MFSD2A–scFv complex. **b**, The ribbon representations of the MFSD2A–scFv complex. A model scFv was docked into the density.

Extended Data Table 1 Cryo-EM data collection, refinement and validation statistics

[Full size table](#)

Supplementary information

[Supplementary Figure 1](#)

This file contains an example of the gating strategy for flow cytometry in uptake assays.

Reporting Summary

Rights and permissions

Reprints and Permissions

About this article



Check for
updates

Cite this article

Wood, C.A.P., Zhang, J., Aydin, D. *et al.* Structure and mechanism of blood–brain-barrier lipid transporter MFSD2A. *Nature* **596**, 444–448 (2021). <https://doi.org/10.1038/s41586-021-03782-y>

Download citation

- Received: 18 December 2020
- Accepted: 29 June 2021
- Published: 04 August 2021
- Issue Date: 19 August 2021
- DOI: <https://doi.org/10.1038/s41586-021-03782-y>

Comments

By submitting a comment you agree to abide by our [Terms](#) and [Community Guidelines](#). If you find something abusive or that does not comply with our terms or guidelines please flag it as inappropriate.

[Access through your institution](#)

[Change institution](#)

[Buy or subscribe](#)

Advertisement

This article was downloaded by **calibre** from <https://www.nature.com/articles/s41586-021-03782-y>.

| [Section menu](#) | [Main menu](#) |

Amendments & Corrections

- [**Author Correction: Climate-driven flyway changes and memory-based long-distance migration**](#) [02 August 2021]
Author Correction •
- [**Author Correction: Blastocyst-like structures generated from human pluripotent stem cells**](#) [02 August 2021]
Author Correction •
- [**Author Correction: Quantum distance and anomalous Landau levels of flat bands**](#) [02 August 2021]
Author Correction •
- [**Author Correction: Summertime increases in upper-ocean stratification and mixed-layer depth**](#) [02 August 2021]
Author Correction •
- [**Publisher Correction: Global absence and targeting of protective immune states in severe COVID-19**](#) [02 August 2021]
Publisher Correction •

Author Correction: Climate-driven flyway changes and memory-based long-distance migration

[Download PDF](#)

- Author Correction
- [Published: 02 August 2021](#)

Author Correction: Climate-driven flyway changes and memory-based long-distance migration

- [Zhongru Gu](#)^{1,2,3 na1},
- [Shengkai Pan](#)^{1,2 na1},
- [Zhenzhen Lin](#)^{1,2 na1},
- [Li Hu](#)^{1,2,3},
- [Xiaoyang Dai](#)⁴,
- [Jiang Chang](#) ORCID: orcid.org/0000-0001-7064-9321⁵,
- [Yuanchao Xue](#) ORCID: orcid.org/0000-0002-8113-2333⁶,
- [Han Su](#)^{1,2,3},
- [Juan Long](#)^{1,2,3},
- [Mengru Sun](#)^{3,6},
- [Sergey Ganusevich](#)⁷,
- [Vasiliy Sokolov](#) ORCID: orcid.org/0000-0002-0115-3151⁸,
- [Aleksandr Sokolov](#)⁹,
- [Ivan Pokrovsky](#) ORCID: orcid.org/0000-0002-6533-674X^{9,10,11},
- [Fen Ji](#)¹²,
- [Michael W. Bruford](#)^{2,13},
- [Andrew Dixon](#)^{2,14,15,16} &
- [Xiangjiang Zhan](#) ORCID: orcid.org/0000-0002-4517-1626^{1,2,3,17}

- 379 Accesses
- 1 Altmetric
- [Metrics details](#)

Subjects

- [Animal migration](#)
- [Evolutionary genetics](#)

The [Original Article](#) was published on 03 March 2021

[Download PDF](#)

Correction to: *Nature* <https://doi.org/10.1038/s41586-021-03265-0>

Published online 3 March 2021

In this Article, there were several errors in Fig. 2. In Fig. 2d, the order of the middle and right panels was incorrect; these have been swapped. In Fig. 2f, the distribution map was incorrect, and has been replaced. In Fig. 2k, the order of Kola and Kolguev labels was incorrect; these labels have been swapped.

The legends of Figs. 1, 2 and 3 have also been amended. In the legend of Fig. 1e, ‘ $n = 12$ individual birds’ was updated to ‘ $n = 11$ individual birds’, and ‘ $n = 32$ individual birds’ was updated to ‘ $n = 33$ individual birds’. The text ‘The haplotypes were phased using BEAGLE.’ has been added to legend of Fig. 2k. In the legend of Fig. 2l, ‘Haplotype frequency in the identified segment’ has been changed to ‘**Haplotype (10x Genomics phased) frequency in the identified segment**’. In the legend of Fig. 3b, ‘long-distance peregrines’ has been replaced by ‘**the studied** peregrines’.

In the section titled ‘Migration patterns of Arctic peregrines’, the text ‘we identified 150 completed migration paths’ has been updated to ‘we identified **151** completed migration paths’. In the Methods section titled

‘Identification of selective sweeps and detection of selected SNPs between short-distance and long-distance peregrines’, the text ‘10x genomics’ has been updated to ‘10x **Genomics**’.

Reference 59 (‘Cao, X., Tian, F., Dallmeyer, A. & Herzschuh, U. Northern Hemisphere biome changes ($> 30^\circ$ N) since 40 cal ka bp and their driving factors inferred from model-data comparisons. *Quat. Sci. Rev.* **220**, 291–309 (2019)’) has been replaced with ‘Tarasov, P. E. et al. Last glacial maximum biomes reconstructed from pollen and plant macrofossil data from northern Eurasia. *J. Biogeogr.* **27**, 609–620 (2000)’.

Several amendments have been made to the [Supplementary Information](#) of this Article. In [Supplementary Fig. 6](#), owing to an error in the calculation of N_e and breeding area, the values have been recalculated and the plot has been replaced; ‘kya’ has also been replaced with ‘ka’. The original, incorrect, [Supplementary Information](#) is shown as [Supplementary Information](#) to this Amendment, for transparency. In [Supplementary Table 1](#), the migration status for transmitter 49116 has been changed from ‘Incomplete’ to ‘Autumn’. In [Supplementary Table 2](#), the ‘Autumn tracks’ and ‘Autumn arrival’ values for individual ‘49116_Plinka-Gaungdong’ have both been updated from 0 to 1. In the section titled ‘Satellite tracking’ in the Supplementary Information, the text ‘we identified 150 complete migration paths, comprising 87 autumn’ has been updated to ‘we identified **151** complete migration paths, comprising **88** autumn’. In the legend of Supplementary Fig. 17, ‘Isolation-By-State’ has been updated to ‘**Identity-By-State**’.

The original Article has been corrected online.

Supplementary information is available in the online version of this Amendment.

Author information

Author notes

1. These authors contributed equally: Zhongru Gu, Shengkai Pan, Zhenzhen Lin

Affiliations

1. Key Laboratory of Animal Ecology and Conservation Biology, Institute of Zoology, Chinese Academy of Sciences, Beijing, China

Zhongru Gu, Shengkai Pan, Zhenzhen Lin, Li Hu, Han Su, Juan Long & Xiangjiang Zhan

2. Cardiff University–Institute of Zoology Joint Laboratory for Biocomplexity Research, Chinese Academy of Sciences, Beijing, China

Zhongru Gu, Shengkai Pan, Zhenzhen Lin, Li Hu, Han Su, Juan Long, Michael W. Bruford, Andrew Dixon & Xiangjiang Zhan

3. University of the Chinese Academy of Sciences, Beijing, China

Zhongru Gu, Li Hu, Han Su, Juan Long, Mengru Sun & Xiangjiang Zhan

4. School of Biological Sciences, University of Bristol, Bristol, UK

Xiaoyang Dai

5. State Key Laboratory of Environmental Criteria and Risk Assessment, Chinese Research Academy of Environmental Sciences, Beijing, China

Jiang Chang

6. Key Laboratory of RNA Biology, CAS Center for Excellence in Biomacromolecules, Institute of Biophysics, Chinese Academy of Sciences, Beijing, China

Yuanchao Xue & Mengru Sun

7. Wild Animal Rescue Centre, Moscow, Russia

Sergey Ganusevich

8. Institute of Plant and Animal Ecology, Ural Division Russian Academy of Sciences, Ekaterinburg, Russia

Vasiliy Sokolov

9. Arctic Research Station of the Institute of Plant and Animal Ecology, Ural Division Russian Academy of Sciences, Labytnangi, Russia

Aleksandr Sokolov & Ivan Pokrovsky

10. Department of Migration, Max Planck Institute of Animal Behavior, Radolfzell, Germany

Ivan Pokrovsky

11. Laboratory of Ornithology, Institute of Biological Problems of the North FEB RAS, Magadan, Russia

Ivan Pokrovsky

12. State Key Laboratory of Stem Cell and Reproductive Biology, Institute of Zoology, Chinese Academy of Sciences, Beijing, China

Fen Ji

13. School of Biosciences and Sustainable Places Institute, Cardiff University, Cardiff, UK

Michael W. Bruford

14. Emirates Falconers' Club, Abu Dhabi, United Arab Emirates

Andrew Dixon

15. Reneco International Wildlife Consultants, Abu Dhabi, United Arab Emirates

Andrew Dixon

16. International Wildlife Consultants, Carmarthen, UK

Andrew Dixon

17. Center for Excellence in Animal Evolution and Genetics, Chinese Academy of Sciences, Kunming, China

Xiangjiang Zhan

Authors

1. Zhongru Gu

[View author publications](#)

You can also search for this author in [PubMed](#) [Google Scholar](#)

2. Shengkai Pan

[View author publications](#)

You can also search for this author in [PubMed](#) [Google Scholar](#)

3. Zhenzhen Lin

[View author publications](#)

You can also search for this author in [PubMed](#) [Google Scholar](#)

4. Li Hu

[View author publications](#)

You can also search for this author in [PubMed](#) [Google Scholar](#)

5. Xiaoyang Dai

[View author publications](#)

You can also search for this author in [PubMed](#) [Google Scholar](#)

6. Jiang Chang

[View author publications](#)

You can also search for this author in [PubMed](#) [Google Scholar](#)

7. Yuanchao Xue

[View author publications](#)

You can also search for this author in [PubMed](#) [Google Scholar](#)

8. Han Su

[View author publications](#)

You can also search for this author in [PubMed](#) [Google Scholar](#)

9. Juan Long

[View author publications](#)

You can also search for this author in [PubMed](#) [Google Scholar](#)

10. Mengru Sun

[View author publications](#)

You can also search for this author in [PubMed](#) [Google Scholar](#)

11. Sergey Ganusevich

[View author publications](#)

You can also search for this author in [PubMed](#) [Google Scholar](#)

12. Vasiliy Sokolov

[View author publications](#)

You can also search for this author in [PubMed](#) [Google Scholar](#)

13. Aleksandr Sokolov

[View author publications](#)

You can also search for this author in [PubMed](#) [Google Scholar](#)

14. Ivan Pokrovsky

[View author publications](#)

You can also search for this author in [PubMed](#) [Google Scholar](#)

15. Fen Ji

[View author publications](#)

You can also search for this author in [PubMed](#) [Google Scholar](#)

16. Michael W. Bruford

[View author publications](#)

You can also search for this author in [PubMed](#) [Google Scholar](#)

17. Andrew Dixon

[View author publications](#)

You can also search for this author in [PubMed](#) [Google Scholar](#)

18. Xiangjiang Zhan

[View author publications](#)

You can also search for this author in [PubMed](#) [Google Scholar](#)

Corresponding author

Correspondence to [Xiangjiang Zhan](#).

Supplementary information

[Supplementary Information](#)

This file contains the original, incorrect Supplementary Information.

Rights and permissions

[Reprints and Permissions](#)

About this article



Check for
updates

Cite this article

Gu, Z., Pan, S., Lin, Z. *et al.* Author Correction: Climate-driven flyway changes and memory-based long-distance migration. *Nature* **596**, E4 (2021). <https://doi.org/10.1038/s41586-021-03599-9>

[Download citation](#)

- Published: 02 August 2021
- Issue Date: 19 August 2021
- DOI: <https://doi.org/10.1038/s41586-021-03599-9>

Comments

By submitting a comment you agree to abide by our [Terms](#) and [Community Guidelines](#). If you find something abusive or that does not comply with our terms or guidelines please flag it as inappropriate.

[Download PDF](#)

Advertisement

| [Section menu](#) | [Main menu](#) |

Author Correction: Blastocyst-like structures generated from human pluripotent stem cells

[Download PDF](#)

- Author Correction
- [Published: 02 August 2021](#)

Author Correction: Blastocyst-like structures generated from human pluripotent stem cells

- [Leqian Yu^{1,2}](#) na1,
- [Yulei Wei^{1,3,4}](#) na1,
- [Jialei Duan](#) [ORCID: orcid.org/0000-0003-4086-7461](#) 5 na1,
- [Daniel A. Schmitz^{1,2}](#),
- [Masahiro Sakurai](#) [ORCID: orcid.org/0000-0002-6376-0299](#) ¹,
- [Lei Wang⁵](#),
- [Kunhua Wang⁶](#),
- [Shuhua Zhao⁷](#),
- [Gary C. Hon](#) 5,8,9 &
- [Jun Wu](#) [ORCID: orcid.org/0000-0001-9863-1668](#) ^{1,2}

[Nature](#) volume **596**, page E5 (2021) [Cite this article](#)

- 468 Accesses
- 1 Altmetric
- [Metrics details](#)

Subjects

- [Embryonic stem cells](#)
- [Pluripotent stem cells](#)
- [Stem cells](#)

The [Original Article](#) was published on 17 March 2021

[Download PDF](#)

Correction to: *Nature* <https://doi.org/10.1038/s41586-021-03356-y>
Published online 17 March 2021

In the Acknowledgements section of this Article, grant number ‘NIH (DP2GM128203)’ was erroneously cited and has been removed. The Article has been corrected online.

Author information

Author notes

1. These authors contributed equally: Leqian Yu, Yulei Wei, Jialei Duan

Affiliations

1. Department of Molecular Biology, University of Texas Southwestern Medical Center, Dallas, TX, USA

Leqian Yu, Yulei Wei, Daniel A. Schmitz, Masahiro Sakurai & Jun Wu

2. Hamon Center for Regenerative Science and Medicine, University of Texas Southwestern Medical Center, Dallas, TX, USA

Leqian Yu, Daniel A. Schmitz & Jun Wu

3. School of Biotechnology and Health Sciences, Wuyi University, Jiangmen, China

Yulei Wei

4. International Healthcare Innovation Institute, Jiangmen, China

Yulei Wei

5. Cecil H. and Ida Green Center for Reproductive Biology Sciences,
University of Texas Southwestern Medical Center, Dallas, TX, USA

Jialei Duan, Lei Wang & Gary C. Hon

6. NHC Key Laboratory of Drug Addiction Medicine, First Affiliated
Hospital of Kunming Medical University, Kunming Medical
University, Kunming, China

Kunhua Wang

7. Department of Reproduction and Genetics, First Affiliated Hospital of
Kunming Medical University, Kunming Medical University, Kunming,
China

Shuhua Zhao

8. Department of Obstetrics and Gynecology, University of Texas
Southwestern Medical Center, Dallas, TX, USA

Gary C. Hon

9. Department of Bioinformatics, University of Texas Southwestern
Medical Center, Dallas, TX, USA

Gary C. Hon

Authors

1. Leqian Yu

[View author publications](#)

You can also search for this author in [PubMed](#) [Google Scholar](#)

2. Yulei Wei

[View author publications](#)

You can also search for this author in [PubMed](#) [Google Scholar](#)

3. Jialei Duan

[View author publications](#)

You can also search for this author in [PubMed](#) [Google Scholar](#)

4. Daniel A. Schmitz

[View author publications](#)

You can also search for this author in [PubMed](#) [Google Scholar](#)

5. Masahiro Sakurai

[View author publications](#)

You can also search for this author in [PubMed](#) [Google Scholar](#)

6. Lei Wang

[View author publications](#)

You can also search for this author in [PubMed](#) [Google Scholar](#)

7. Kunhua Wang

[View author publications](#)

You can also search for this author in [PubMed](#) [Google Scholar](#)

8. Shuhua Zhao

[View author publications](#)

You can also search for this author in [PubMed](#) [Google Scholar](#)

9. Gary C. Hon

[View author publications](#)

You can also search for this author in [PubMed](#) [Google Scholar](#)

10. Jun Wu

[View author publications](#)

You can also search for this author in [PubMed](#) [Google Scholar](#)

Corresponding authors

Correspondence to [Gary C. Hon](#) or [Jun Wu](#).

Rights and permissions

[Reprints and Permissions](#)

About this article



Check for
updates

Cite this article

Yu, L., Wei, Y., Duan, J. *et al.* Author Correction: Blastocyst-like structures generated from human pluripotent stem cells. *Nature* **596**, E5 (2021).
<https://doi.org/10.1038/s41586-021-03635-8>

[Download citation](#)

- Published: 02 August 2021
- Issue Date: 19 August 2021
- DOI: <https://doi.org/10.1038/s41586-021-03635-8>

Comments

By submitting a comment you agree to abide by our [Terms](#) and [Community Guidelines](#). If you find something abusive or that does not comply with our terms or guidelines please flag it as inappropriate.

[Download PDF](#)

Advertisement

This article was downloaded by **calibre** from <https://www.nature.com/articles/s41586-021-03635-8>

| [Section menu](#) | [Main menu](#) |

Author Correction: Quantum distance and anomalous Landau levels of flat bands

[Download PDF](#)

- Author Correction
- [Published: 02 August 2021](#)

Author Correction: Quantum distance and anomalous Landau levels of flat bands

- [Jun-Won Rhim](#) ORCID: orcid.org/0000-0001-9094-0650^{1,2},
- [Kyoo Kim](#)³ &
- [Bohm-Jung Yang](#) ^{1,2,4}

[Nature](#) volume **596**, page E6 (2021)[Cite this article](#)

- 317 Accesses
- 5 Altmetric
- [Metrics details](#)

Subjects

- [Electronic properties and materials](#)
- [Metamaterials](#)
- [Quantum mechanics](#)
- [Topological matter](#)

The [Original Article](#) was published on 05 August 2020

[Download PDF](#)

Correction to: *Nature* <https://doi.org/10.1038/s41586-020-2540-1> Published online 5 August 2020

In the Acknowledgements section of this Article, the statement ‘B.-J.Y. was supported by the Institute for Basic Science (IBS-R009-D1), the Basic Science Research Program through the NRF (grant number 0426-20200003) and the US Army Research Office under grant number W911NF-18-1-0137.’ has been replaced by ‘B.-J.Y. was supported by the Institute for Basic Science (IBS-R009-D1), the **National Research Foundation of Korea (NRF) grant funded by the Korea government (MSIT) (grant number 2018R1C1B6005663)** and the US Army Research Office and Asian Office of Aerospace Research & Development (AOARD) under grant number W911NF-18-1-0137.’. The Article has been corrected online.

Author information

Affiliations

1. Center for Correlated Electron Systems, Institute for Basic Science (IBS), Seoul, Korea

Jun-Won Rhim & Bohm-Jung Yang

2. Department of Physics and Astronomy, Seoul National University, Seoul, Korea

Jun-Won Rhim & Bohm-Jung Yang

3. Korea Atomic Energy Research Institute, Daejeon, Korea

Kyoo Kim

4. Center for Theoretical Physics (CTP), Seoul National University, Seoul, Korea

Bohm-Jung Yang

Authors

1. Jun-Won Rhim

[View author publications](#)

You can also search for this author in [PubMed](#) [Google Scholar](#)

2. Kyoo Kim

[View author publications](#)

You can also search for this author in [PubMed](#) [Google Scholar](#)

3. Bohm-Jung Yang

[View author publications](#)

You can also search for this author in [PubMed](#) [Google Scholar](#)

Corresponding author

Correspondence to [Bohm-Jung Yang](#).

Rights and permissions

[Reprints and Permissions](#)

About this article



Check for
updates

Cite this article

Rhim, JW., Kim, K. & Yang, BJ. Author Correction: Quantum distance and anomalous Landau levels of flat bands. *Nature* **596**, E6 (2021).
<https://doi.org/10.1038/s41586-021-03690-1>

[Download citation](#)

- Published: 02 August 2021
- Issue Date: 19 August 2021
- DOI: <https://doi.org/10.1038/s41586-021-03690-1>

Comments

By submitting a comment you agree to abide by our [Terms](#) and [Community Guidelines](#). If you find something abusive or that does not comply with our terms or guidelines please flag it as inappropriate.

[Download PDF](#)

Advertisement

This article was downloaded by **calibre** from <https://www.nature.com/articles/s41586-021-03690-1>

Author Correction: Summertime increases in upper-ocean stratification and mixed-layer depth

[Download PDF](#)

- Author Correction
- [Published: 02 August 2021](#)

Author Correction: Summertime increases in upper-ocean stratification and mixed-layer depth

- [Jean-Baptiste Sallée](#) ORCID: [orcid.org/0000-0002-6109-5176¹](https://orcid.org/0000-0002-6109-5176),
- [Violaine Pelichero^{2,3}](#),
- [Camille Akhoudas¹](#),
- [Etienne Pauthenet](#) ORCID: [orcid.org/0000-0002-0531-3810¹](https://orcid.org/0000-0002-0531-3810),
- [Lucie Vignes¹](#),
- [Sunke Schmidtko](#) ORCID: [orcid.org/0000-0003-3272-7055⁴](https://orcid.org/0000-0003-3272-7055),
- [Alberto Naveira Garabato](#) ORCID: [orcid.org/0000-0001-6071-605X⁵](https://orcid.org/0000-0001-6071-605X),
- [Peter Sutherland⁶](#) &
- [Mikael Kuusela⁷](#)

[Nature](#) volume 596, page E7 (2021) [Cite this article](#)

- 296 Accesses
- 2 Altmetric
- [Metrics details](#)

Subjects

- [Physical oceanography](#)

The [Original Article](#) was published on 24 March 2021

[Download PDF](#)

Correction to: *Nature* <https://doi.org/10.1038/s41586-021-03303-x>

Published online 24 March 2021

In this Article, the code used to compute stratification values omitted the gravitational acceleration coefficient. All values for mean stratification or change in stratification should have been multiplied by the appropriate coefficient (9.81 m s^{-2}); the values on colour scale bars of Figs. 2a–d, 3a, b, Extended Data Figs. 4e–h, 5a, b, 9a, and on the x axes in Fig. 3a, b, have therefore been increased by an order of magnitude.

In the Abstract, the text ‘we find that the summertime density contrast increased by 8.9 ± 2.7 per cent per decade (10^{-6} – 10^{-5} per second squared per decade, depending on region)’ has been changed to ‘we find that the summertime density contrast increased by 8.9 ± 2.7 per cent per decade (10^{-5} – 10^{-4} per second squared per decade, depending on region)’. In the section titled ‘Seasonal pycnocline changes’, the text ‘Summertime pycnocline stratification has increased worldwide across all ocean basins since 1970, at a rate ranging from $10^{-6} \text{ s}^{-2} \text{ dec}^{-1}$ to $10^{-5} \text{ s}^{-2} \text{ dec}^{-1}$ (Fig. 3b). Trends display a marked regional pattern, with greater trends in the tropics (about 10^{-5} s^{-2}) than at high latitudes (about 10^{-6} s^{-2}). Consistent with pycnocline stratification, the 0–200 m stratification also shows a global increase, although at a lower rate, ranging from $10^{-7} \text{ s}^{-2} \text{ dec}^{-1}$ to $10^{-6} \text{ s}^{-2} \text{ dec}^{-1}$ (Fig. 3a).’ has been changed to ‘Summertime pycnocline stratification has increased worldwide across all ocean basins since 1970, at a rate ranging from $10^{-5} \text{ s}^{-2} \text{ dec}^{-1}$ to $10^{-4} \text{ s}^{-2} \text{ dec}^{-1}$ (Fig. 3b). Trends display a marked regional pattern, with greater trends in the tropics (about 10^{-4} s^{-2}) than at high latitudes (about 10^{-5} s^{-2}). Consistent with pycnocline stratification, the 0–200 m stratification also shows a global increase,

although at a lower rate, ranging from 10^{-6} s⁻² dec⁻¹ to 10^{-5} s⁻² dec⁻¹ (Fig. 3a)'.

We thank L. Cheng, K. E. Trenberth, M. E. Mann, J. Abraham, J. Zhu and G. Li for identifying these errors.

The original Article has been corrected online.

Author information

Affiliations

1. Sorbonne Université, CNRS/IRD/MNHN, LOCEAN, IPSL, Paris, France

Jean-Baptiste Sallée, Camille Akhoudas, Etienne Pauthenet & Lucie Vignes

2. Institute for Marine and Antarctic Studies, University of Tasmania, Hobart, Tasmania, Australia

Violaine Pellichero

3. CSIRO Oceans and Atmosphere, Hobart, Tasmania, Australia

Violaine Pellichero

4. GEOMAR Helmholtz Centre for Ocean Research Kiel, Kiel, Germany

Sunke Schmidtko

5. Ocean and Earth Science, National Oceanography Centre, University of Southampton, Southampton, UK

Alberto Naveira Garabato

6. Ifremer, Université Brest, CNRS, IRD, Laboratoire d'Océanographie Physique et Spatiale (LOPS), IUEM, Brest, France

Peter Sutherland

7. Department of Statistics and Data Science, Carnegie Mellon University, Pittsburgh, PA, USA

Mikael Kuusela

Authors

1. Jean-Baptiste Sallée

[View author publications](#)

You can also search for this author in [PubMed](#) [Google Scholar](#)

2. Violaine Pellichero

[View author publications](#)

You can also search for this author in [PubMed](#) [Google Scholar](#)

3. Camille Akhoudas

[View author publications](#)

You can also search for this author in [PubMed](#) [Google Scholar](#)

4. Etienne Pauthenet

[View author publications](#)

You can also search for this author in [PubMed](#) [Google Scholar](#)

5. Lucie Vignes

[View author publications](#)

You can also search for this author in [PubMed](#) [Google Scholar](#)

6. Sunke Schmidtko

[View author publications](#)

You can also search for this author in [PubMed](#) [Google Scholar](#)

7. Alberto Naveira Garabato

[View author publications](#)

You can also search for this author in [PubMed](#) [Google Scholar](#)

8. Peter Sutherland

[View author publications](#)

You can also search for this author in [PubMed](#) [Google Scholar](#)

9. Mikael Kuusela

[View author publications](#)

You can also search for this author in [PubMed](#) [Google Scholar](#)

Corresponding author

Correspondence to [Jean-Baptiste Sallée](#).

Rights and permissions

[Reprints and Permissions](#)

About this article



Check for
updates

Cite this article

Sallée, JB., Pelichero, V., Akhoudas, C. *et al.* Author Correction: Summertime increases in upper-ocean stratification and mixed-layer depth. *Nature* **596**, E7 (2021). <https://doi.org/10.1038/s41586-021-03745-3>

[Download citation](#)

- Published: 02 August 2021
- Issue Date: 19 August 2021
- DOI: <https://doi.org/10.1038/s41586-021-03745-3>

Comments

By submitting a comment you agree to abide by our [Terms](#) and [Community Guidelines](#). If you find something abusive or that does not comply with our terms or guidelines please flag it as inappropriate.

[Download PDF](#)

Advertisement

This article was downloaded by **calibre** from <https://www.nature.com/articles/s41586-021-03745-3>

| [Section menu](#) | [Main menu](#) |

Publisher Correction: Global absence and targeting of protective immune states in severe COVID-19

[Download PDF](#)

- Publisher Correction
- [Published: 02 August 2021](#)

Publisher Correction: Global absence and targeting of protective immune states in severe COVID-19

- [Alexis J. Combes](#) ORCID: orcid.org/0000-0002-9110-6542^{1,2,3 na1},
- [Tristan Courau](#) ORCID: orcid.org/0000-0003-1819-9516^{1,2,3 na1},
- [Nicholas F. Kuhn](#)^{1,2 na1},
- [Kenneth H. Hu](#) ORCID: orcid.org/0000-0002-0294-0202^{1,2 na1},
- [Arja Ray](#)^{1,2 na1},
- [William S. Chen](#)^{2,4},
- [Nayvin W. Chew](#)^{1,2,3},
- [Simon J. Cleary](#) ORCID: orcid.org/0000-0001-5573-6363^{2,5,6},
- [Divyashree Kushnoor](#)^{1,2,3},
- [Gabriella C. Reeder](#)^{1,2,3},
- [Alan Shen](#)^{1,2,3},
- [Jessica Tsui](#)^{1,2,3},
- [Kamir J. Hiam-Galvez](#) ORCID: orcid.org/0000-0002-1956-0257^{2,7,8},
- [Priscila Muñoz-Sandoval](#)^{2,8,9},
- [Wandi S. Zhu](#)^{2,8,9},
- [David S. Lee](#) ORCID: orcid.org/0000-0001-6539-4272^{2,10,11},
- [Yang Sun](#)^{2,10,11},
- [Ran You](#)^{1,2},
- [Mélia Magnen](#)^{2,5,6},
- [Lauren Rodriguez](#)^{2,7},

- [K. W. Im](#)^{1,2,3},
- [Nina K. Serwas](#) [ORCID: orcid.org/0000-0003-2243-5446](#)^{1,2},
- [Aleksandra Leligdowicz](#)^{5,6},
- [Colin R. Zamecnik](#) [ORCID: orcid.org/0000-0002-9477-1388](#)^{2,12},
- [Rita P. Loudermilk](#) [ORCID: orcid.org/0000-0001-9970-5112](#)^{2,12},
- [Michael R. Wilson](#) [ORCID: orcid.org/0000-0002-8705-5084](#)^{2,12},
- [Chun J. Ye](#) [ORCID: orcid.org/0000-0001-6560-3783](#)^{2,10,11},
- [Gabriela K. Fragiadakis](#)^{2,3,10,11},
- [Mark R. Looney](#) [ORCID: orcid.org/0000-0003-0241-9190](#)^{2,5,6},
- [Vincent Chan](#) [ORCID: orcid.org/0000-0002-0823-6726](#)^{1,2},
- [Alyssa Ward](#)^{10,11},
- [Sidney Carrillo](#)^{5,6},
- [The UCSF COMET Consortium](#),
- [Michael Matthay](#) [ORCID: orcid.org/0000-0003-3039-8155](#)^{5,6},
- [David J. Erle](#) [ORCID: orcid.org/0000-0002-2171-0648](#)^{2,3,5,6},
- [Prescott G. Woodruff](#)^{2,5,6},
- [Charles Langelier](#)¹³,
- [Kirsten Kangelaris](#)¹⁴,
- [Carolyn M. Hendrickson](#)^{5,6},
- [Carolyn Calfee](#)^{5,6},
- [Arjun Arkal Rao](#) [ORCID: orcid.org/0000-0003-4480-3190](#)^{1,2,3} &
- [Matthew F. Krummel](#) [ORCID: orcid.org/0000-0001-7915-3533](#)^{1,2}

[Nature volume 596](#), page E8 (2021) [Cite this article](#)

- 349 Accesses
- 3 Altmetric
- [Metrics details](#)

Subjects

- [Infection](#)
- [Infectious diseases](#)
- [SARS-CoV-2](#)

The [Original Article](#) was published on 25 January 2021

[Download PDF](#)

Correction to: *Nature* <https://doi.org/10.1038/s41586-021-03234-7>
Published online 25 January 2021

In this Article, in the Methods section ‘Patients, participants, severity score and clinical data collection’, the word ‘mild–moderate’ should be replaced by ‘severe’ in the sentence ‘Patients classified as … (typically five days or more).’. The corrected sentence should read: ‘Patients classified as having **severe** disease are patients who required intensive care and mechanical ventilation (typically five days or more).’. The Article has been corrected online.

Author information

Author notes

1. These authors contributed equally: Alexis J. Combes, Tristan Courau, Nicholas F. Kuhn, Kenneth H. Hu, Arja Ray

Affiliations

1. Department of Pathology, University of California San Francisco, San Francisco, CA, USA

Alexis J. Combes, Tristan Courau, Nicholas F. Kuhn, Kenneth H. Hu, Arja Ray, Nayvin W. Chew, Divyashree Kushnoor, Gabriella C. Reeder, Alan Shen, Jessica Tsui, Ran You, K. W. Im, Nina K. Serwas, Vincent Chan, Cai Cathy, Jenny Zhan, Bushra Samad, Tasha Lea, Arjun Arkal Rao & Matthew F. Krummel

2. ImmunoX Initiative, University of California San Francisco, San Francisco, CA, USA

Alexis J. Combes, Tristan Courau, Nicholas F. Kuhn, Kenneth H. Hu, Arja Ray, William S. Chen, Nayvin W. Chew, Simon J. Cleary, Divyashree Kushnoor, Gabriella C. Reeder, Alan Shen, Jessica Tsui, Kamir J. Hiam-Galvez, Priscila Muñoz-Sandoval, Wandi S. Zhu, David S. Lee, Yang Sun, Ran You, Mélia Magnen, Lauren Rodriguez, K. W. Im, Nina K. Serwas, Colin R. Zamecnik, Rita P. Loudermilk, Michael R. Wilson, Chun J. Ye, Gabriela K. Fragiadakis, Mark R. Looney, Vincent Chan, Cai Cathy, Jenny Zhan, Bushra Samad, David J. Erle, Prescott G. Woodruff, Arjun Arkal Rao & Matthew F. Krummel

3. UCSF CoLabs, University of California San Francisco, San Francisco, CA, USA

Alexis J. Combes, Tristan Courau, Nayvin W. Chew, Divyashree Kushnoor, Gabriella C. Reeder, Alan Shen, Jessica Tsui, K. W. Im, Gabriela K. Fragiadakis, Walter Eckalbar, David J. Erle & Arjun Arkal Rao

4. Department of Radiation Oncology, University of California San Francisco, San Francisco, CA, USA

William S. Chen

5. Division of Pulmonary and Critical Care Medicine, Department of Medicine, University of California San Francisco, San Francisco, CA, USA

Simon J. Cleary, Mélia Magnen, Aleksandra Lelidowicz, Mark R. Looney, Sidney Carrillo, Suzanna Chak, Rajani Ghale, Jeremy Giberson, Ana Gonzalez, Alejandra Jauregui, Deanna Lee, Viet Nguyen, Kimberly Yee, Pratik Sinha, Alexander Beagle, Austin Sigman, Chayse Jones, Walter Eckalbar, Michael Matthay, David J. Erle, Prescott G. Woodruff, Carolyn M. Hendrickson & Carolyn Calfee

6. Cardiovascular Research Institute, University of California San Francisco, San Francisco, CA, USA

Simon J. Cleary, Mélia Magnen, Aleksandra Lelidowicz, Mark R. Looney, Sidney Carrillo, Deanna Lee, Viet Nguyen, Kimberly Yee, Michael Matthay, David J. Erle, Prescott G. Woodruff, Carolyn M. Hendrickson & Carolyn Calfee

7. Department of Otolaryngology, University of California San Francisco, San Francisco, CA, USA

Kamir J. Hiam-Galvez & Lauren Rodriguez

8. Department of Microbiology and Immunology, University of California San Francisco, San Francisco, CA, USA

Kamir J. Hiam-Galvez, Priscila Muñoz-Sandoval & Wandi S. Zhu

9. Sandler Asthma Basic Research Center, University of California San Francisco, San Francisco, CA, USA

Priscila Muñoz-Sandoval & Wandi S. Zhu

10. Institute for Human Genetics, University of California San Francisco, San Francisco, CA, USA

David S. Lee, Yang Sun, Chun J. Ye, Gabriela K. Fragiadakis & Alyssa Ward

11. Division of Rheumatology, Department of Medicine, University of California San Francisco, San Francisco, CA, USA

David S. Lee, Yang Sun, Chun J. Ye, Gabriela K. Fragiadakis & Alyssa Ward

12. Department of Neurology, Weill Institute for Neurosciences, University of California San Francisco, San Francisco, CA, USA

Colin R. Zamecnik, Rita P. Loudermilk & Michael R. Wilson

13. Division of Infectious Disease, Department of Medicine, University of California San Francisco, San Francisco, CA, USA

Charles Langelier

14. Division of Hospital Medicine, Department of Medicine, University of California San Francisco, San Francisco, CA, USA

Yumiko Abe-Jones, Logan Pierce, Priya Prasad, Armond Esmalii, Kattie Raffel & Kirsten Kangelaris

15. Zuckerberg San Francisco General Hospital and Trauma Center, University of California San Francisco, San Francisco, California, USA

Jeremy Giberson, Ana Gonzalez, Deanna Lee, Viet Nguyen & Gabriel M. Ortiz

16. Division of Nephrology, Department of Medicine, University of California San Francisco, San Francisco, California, USA

Kathleen Liu

17. Division of Critical Care Medicine, Department of Anesthesia, University of California at San Francisco, San Francisco, CA, USA

Kathleen Liu

Authors

1. Alexis J. Combes

[View author publications](#)

You can also search for this author in [PubMed](#) [Google Scholar](#)

2. Tristan Courau

[View author publications](#)

You can also search for this author in [PubMed](#) [Google Scholar](#)

3. Nicholas F. Kuhn

[View author publications](#)

You can also search for this author in [PubMed](#) [Google Scholar](#)

4. Kenneth H. Hu

[View author publications](#)

You can also search for this author in [PubMed](#) [Google Scholar](#)

5. Arja Ray

[View author publications](#)

You can also search for this author in [PubMed](#) [Google Scholar](#)

6. William S. Chen

[View author publications](#)

You can also search for this author in [PubMed](#) [Google Scholar](#)

7. Nayvin W. Chew

[View author publications](#)

You can also search for this author in [PubMed](#) [Google Scholar](#)

8. Simon J. Cleary

[View author publications](#)

You can also search for this author in [PubMed](#) [Google Scholar](#)

9. Divyashree Kushnoor

[View author publications](#)

You can also search for this author in [PubMed](#) [Google Scholar](#)

10. Gabriella C. Reeder

[View author publications](#)

You can also search for this author in [PubMed](#) [Google Scholar](#)

11. Alan Shen

[View author publications](#)

You can also search for this author in [PubMed](#) [Google Scholar](#)

12. Jessica Tsui

[View author publications](#)

You can also search for this author in [PubMed](#) [Google Scholar](#)

13. Kamir J. Hiam-Galvez

[View author publications](#)

You can also search for this author in [PubMed](#) [Google Scholar](#)

14. Priscila Muñoz-Sandoval

[View author publications](#)

You can also search for this author in [PubMed](#) [Google Scholar](#)

15. Wandi S. Zhu

[View author publications](#)

You can also search for this author in [PubMed](#) [Google Scholar](#)

16. David S. Lee

[View author publications](#)

You can also search for this author in [PubMed](#) [Google Scholar](#)

17. Yang Sun

[View author publications](#)

You can also search for this author in [PubMed](#) [Google Scholar](#)

18. Ran You

[View author publications](#)

You can also search for this author in [PubMed](#) [Google Scholar](#)

19. Mélia Magnen

[View author publications](#)

You can also search for this author in [PubMed](#) [Google Scholar](#)

20. Lauren Rodriguez

[View author publications](#)

You can also search for this author in [PubMed](#) [Google Scholar](#)

21. K. W. Im

[View author publications](#)

You can also search for this author in [PubMed](#) [Google Scholar](#)

22. Nina K. Serwas

[View author publications](#)

You can also search for this author in [PubMed](#) [Google Scholar](#)

23. Aleksandra Leligdowicz

[View author publications](#)

You can also search for this author in [PubMed](#) [Google Scholar](#)

24. Colin R. Zamecnik

[View author publications](#)

You can also search for this author in [PubMed](#) [Google Scholar](#)

25. Rita P. Loudermilk

[View author publications](#)

You can also search for this author in [PubMed](#) [Google Scholar](#)

26. Michael R. Wilson

[View author publications](#)

You can also search for this author in [PubMed](#) [Google Scholar](#)

27. Chun J. Ye

[View author publications](#)

You can also search for this author in [PubMed](#) [Google Scholar](#)

28. Gabriela K. Fragiadakis
[View author publications](#)

You can also search for this author in [PubMed](#) [Google Scholar](#)

29. Mark R. Looney
[View author publications](#)

You can also search for this author in [PubMed](#) [Google Scholar](#)

30. Vincent Chan
[View author publications](#)

You can also search for this author in [PubMed](#) [Google Scholar](#)

31. Alyssa Ward
[View author publications](#)

You can also search for this author in [PubMed](#) [Google Scholar](#)

32. Sidney Carrillo
[View author publications](#)

You can also search for this author in [PubMed](#) [Google Scholar](#)

33. Michael Matthay
[View author publications](#)

You can also search for this author in [PubMed](#) [Google Scholar](#)

34. David J. Erle
[View author publications](#)

You can also search for this author in [PubMed](#) [Google Scholar](#)

35. Prescott G. Woodruff
[View author publications](#)

You can also search for this author in [PubMed](#) [Google Scholar](#)

36. Charles Langelier

[View author publications](#)

You can also search for this author in [PubMed](#) [Google Scholar](#)

37. Kirsten Kangelaris

[View author publications](#)

You can also search for this author in [PubMed](#) [Google Scholar](#)

38. Carolyn M. Hendrickson

[View author publications](#)

You can also search for this author in [PubMed](#) [Google Scholar](#)

39. Carolyn Calfee

[View author publications](#)

You can also search for this author in [PubMed](#) [Google Scholar](#)

40. Arjun Arkal Rao

[View author publications](#)

You can also search for this author in [PubMed](#) [Google Scholar](#)

41. Matthew F. Krummel

[View author publications](#)

You can also search for this author in [PubMed](#) [Google Scholar](#)

Consortia

The UCSF COMET Consortium

- Cai Cathy
- , Jenny Zhan

- , Bushra Samad
- , Suzanna Chak
- , Rajani Ghale
- , Jeremy Giberson
- , Ana Gonzalez
- , Alejandra Jauregui
- , Deanna Lee
- , Viet Nguyen
- , Kimberly Yee
- , Yumiko Abe-Jones
- , Logan Pierce
- , Priya Prasad
- , Pratik Sinha
- , Alexander Beagle
- , Tasha Lea
- , Armond Esmalii
- , Austin Sigman
- , Gabriel M. Ortiz
- , Kattie Raffel
- , Chayse Jones
- , Kathleen Liu
- & Walter Eckalbar

Corresponding authors

Correspondence to [Alexis J. Combes](#) or [Arjun Arkal Rao](#) or [Matthew F. Krummel](#).

Rights and permissions

[Reprints and Permissions](#)

About this article



Check for
updates

Cite this article

Combes, A.J., Courau, T., Kuhn, N.F. *et al.* Publisher Correction: Global absence and targeting of protective immune states in severe COVID-19. *Nature* **596**, E8 (2021). <https://doi.org/10.1038/s41586-021-03718-6>

[Download citation](#)

- Published: 02 August 2021
- Issue Date: 19 August 2021
- DOI: <https://doi.org/10.1038/s41586-021-03718-6>

Comments

By submitting a comment you agree to abide by our [Terms](#) and [Community Guidelines](#). If you find something abusive or that does not comply with our terms or guidelines please flag it as inappropriate.

[Download PDF](#)

Advertisement

This article was downloaded by **calibre** from <https://www.nature.com/articles/s41586-021-03718-6>